WAVE VELOCITIES IN HYDROCARBONS AND HYDROCARBON SATURATED ROCKS
– WITH APPLICATIONS TO EOR MONITORING

A DISSERTATION

SUBMITTED TO THE DEPARTMENT OF GEOPHYSICS

AND THE COMMITTEE ON GRADUATE STUDIES

OF STANFORD UNIVERSITY

IN PARTIAL FULFILLMENT OF THE REQUIREMENTS

FOR THE DEGREE OF

DOCTOR OF PHILOSOPHY

By

Zhijing Wang

April, 1988

TABLE OF CONTENTS

ABSTRACT

In order to effectively utilize many new seismic technologies and interpret the results, acoustic properties of both reservoir fluids and rocks must be well understood. It is the main purpose of this dissertation to investigate acoustic wave velocities in different hydrocarbons and hydrocarbon saturated rocks under various reservoir conditions.

The investigation consists of six laboratory experiments, followed by a series of theoretical and application analyses. All the experiments involve acoustic velocity measurements in hydrocarbons and rocks with different hydrocarbons, using the ultrasonic pulse-transmission methods, at elevated temperatures and pressures.

In the experiments, wave velocities are measured versus both temperature and pressure in 50 hydrocarbons. The relations among the acoustic velocity, temperature, pressure, API gravity, and the molecular weight of the hydrocarbons are studied, and empirical equations are established which allow one to calculate the acoustic velocities in hydrocarbons with known API gravities. Wave velocities in hydrocarbon mixtures are related to the composition and the velocities in the components. The experimental results are also analyzed in terms of various existing theories and models of the liquid state.

Wave velocities are also measured in various rocks saturated with different hydrocarbons. The compressional wave velocities in rocks saturated with pure hydrocarbons increase with increasing the carbon number of the hydrocarbons. They decrease markedly in all the heavy hydrocarbon saturated rocks as temperature increases. Such velocity decreases set the petrophysical basis for in-situ seismic monitoring thermal enhanced oil recovery processes.

The effects of carbon dioxide flooding and different pore fluids on wave velocities in rocks are also investigated. It is highly possible that there exist reflections of seismic waves at the light-heavy oil saturation interfaces in-situ. It is also possible to use seismic methods to monitor carbon dioxide flooding processes.

Velocity dispersions are analyzed theoretically in rocks saturated with different pore fluids. The results are discussed in terms of the Biot theory and the "local flow" mechanism. Applications of the results and the applicability of using seismic methods to monitor various enhanced oil recovery and production processes are also discussed.

CHAPTER 1

INTRODUCTION

During the past years, seismic methods have been playing a major role in the exploration for hydrocarbon reservoirs. However, little success would have been achieved without knowing and understanding seismic velocities and their behaviors with various parameters in various rocks. There is little doubt that seismic velocities and their variations with different parameters are the main cause of the success of seismic methods in explorations. Extended studies on velocities in various rocks have been done by numerous investigators. Some of the references of these studies are listed in the bibliography.

Furthermore, seismic methods have almost never been used in hydrocarbon recovery assessment, in spite of the growing need to better understand various recovery processes. A major problem in the area of reservoir evaluation and production is the realization of the complexity of most reservoirs, leading to large uncertainties in estimated total recovery, recovery rates, and recovery methods. There is little doubt that seismic methods will play, in the near future, a major role in helping to solve production and recovery problems. But we first need to understand what seismic waves can tell us about reservoir rocks, and how to extract the desired information.

With the rapid development in seismic and well logging technologies, detailed studies on hydrocarbon reservoirs are getting more and more attention. In recent years, seismic borehole to borehole tomography, 3-D seismic reservoir imaging, seismic delineation of reservoir fluid saturations, seismic evaluation and characterization of hydrocarbon reservoirs, seismically monitoring production and enhanced oil recovery (EOR)

processes in time, and detailed borehole sonic loggings have begun to emerge. There is little doubt that these technologies will become routine in the near future. However, acoustic properties of both reservoir fluids and rocks must be understood in order to utilize these new methods and interpret their results. Therefore, it is the main purpose of this thesis to investigate acoustic wave velocities in different hydrocarbons and reservoir fluids and in rocks saturated with hydrocarbons under various reservoir conditions.

The importance of the acoustic properties of reservoir liquids have not gotten enough attention thus far. There are very few experimental data of acoustic velocities in crude oils, and no systematic studies. The reason for this is that, as has been well known, the acoustic velocities in fluids are in fact pure thermodynamic quantities. From this point of view measurements of acoustic velocities in fluids can not give more information than that included in the data of the equation of state. However, the precision of the information on the fluids actually obtained by acoustic experiments is often one or two orders of magnitude higher than that of direct thermodynamic measurements. For this reason, even if complete pressure-volume-temperature (P-V-T) data are available, acoustic velocity experiments are useful as an independent check of these data. If no complete P-V-T data are available, the interest of acoustic velocity measurements is of course obvious. On the other side, if acoustic velocity data are available, one can use these data to derive more accurate P-V-T properties of the fluids.

There is at present no completely satisfactory theory or model of the liquid state which can give precise acoustic velocity data. Acoustic velocities calculated by the equation of state based on various liquid theories or models usually deviate from those actually measured substantially. Furthermore, such velocity calculations require measurements of other thermal properties of the liquid such as the specific heat ratio, thermal expansivity, and heat capacity. These measurements are often much more complicated than acoustic measurements. Therefore, from this point of view, the advantage of measuring acoustic velocities in crude oils is obvious.

Although many experiments and investigations have been done in the past years on acoustic velocities in rocks, most of such experiments and investigations were done for rocks saturated with water. That is, very few laboratory experiments have been carried out on velocities in rocks saturated with various hydrocarbons. The reasons for this situation may be because (1) the velocities in water and heavy oils are about the same at room condition, people generally make the assumption that velocities in rocks saturated with heavy oils should also be about the same as those in the same rocks with water, according to the Biot theory; (2) the measurement for velocities in hydrocarbon saturated rocks is more difficult and complicated, due to the high viscosities of the hydrocarbons; and (3) hydrocarbons are usually hazardous, especially at high temperatures. However, the major purpose of the seismic explorations is to find hydrocarbon reservoirs. Without knowing the acoustic properties of hydrocarbons and hydrocarbon saturated rocks, it is more difficult and impractical to apply the laboratory data to the field. Furthermore, even if the acoustic velocities in water and heavy oils are about the same at room condition, their temperature and pressure responses are different. Therefore, it is necessary and important to study the acoustic velocities in rocks saturated with various hydrocarbons in order to better apply the laboratory results to the field in seismic exploration, acoustic well logging, and production assessment.

In this thesis, acoustic velocities in 50 different hydrocarbons were measured versus temperature and pressure. The hydrocarbons include pure hydrocarbons, hydrocarbon mixtures, light and heavy crude oils, and solid paraffin wax. Furthermore, wave velocities were also measured in several rocks saturated with different hydrocarbons and water. The results, along with the interpretations, discussions, and applications of the results, are shown in chapters 2 through 10.

In chapter 2, wave velocities are measured in 26 pure hydrocarbons with different molecular weights. The relations among the velocity, temperature, and the molecular weight (or carbon number) of the hydrocarbons are studied and established. The

experimental results of the wave velocities in 9 pure hydrocarbon mixtures show that the velocity in a hydrocarbon mixture is related to the composition and the velocities in the components.

Chapter 3 studies the wave velocities in crude oils with API gravity ranging from 5 to 62°. The velocities in the crude oils are systematically related to the temperature, pressure, API gravity, and molecular weight. The experimental results are discussed and interpreted in terms of various existing theories of the liquid state. Empirical equations are established which can be used to calculate the acoustic velocities in oils with known API gravity (or density) as a function of temperature and pressure. Furthermore, using the acoustic velocity information, one can calculate the pressure-volume-temperature relations of the oils. Other applications of the results are also discussed.

The experimental results shown in chapter 4 reveal that the compressional wave velocities in rocks saturated with pure hydrocarbons increase with increasing the carbon number (or molecular weight) of the hydrocarbons. Even though the rocks are saturated with light hydrocarbons, the compressional wave velocities in the rocks still decrease substantially as temperature increases. The amount of such velocity decrease sets the lower bond of the temperature effect on the compressional wave velocities in rocks saturated with hydrocarbons.

In chapter 5, wave velocities in 4 heavy hydrocarbons and rocks saturated with these hydrocarbons are measured versus temperature at fixed pressures. The velocities in the solid hydrocarbons decrease sharply as the hydrocarbons are melted. And the same happens to the velocities in rocks saturated with the solid hydrocarbons. The compressional wave velocities in all the heavy hydrocarbon saturated rocks decrease markedly as temperature increases. Such velocity decreases set the petrophysical basis for in-situ seismic monitoring thermal enhanced oil recovery processes.

Chapter 6 investigates the effect of CO_2 flooding on wave velocities in rocks with hydrocarbons. The experimental results show that CO_2 flooding decreases the

compressional wave velocities in reservoir rocks markedly. Therefore, it is possible to use seismic methods to locate the CO_2 zones, to track the movement of the CO_2 bank, and to monitor the flooding processes in reservoirs subject to CO_2 floodings.

In chapter 7, the effect of different pore fluids on wave velocities in rocks is investigated. The experimental results reveal that the compressional wave velocities differ pronouncedly in rocks saturated with different pore fluids. It is highly possible that there exist reflections of seismic waves at the light-heavy oil saturation interfaces in-situ: Such reflections could be as strong as, or even stronger than, those at the air-water saturation interfaces. The results suggest that on seismograms, "bright spots" could not only appear at the gas-water (or oil), but also the light-heavy oil, saturation interfaces. It is also suggested that one should specify if it is light oil or heavy oil when referring to oil saturations of rocks.

Chapter 8 studies the velocity dispersions in rocks saturated with different fluids. In order to apply the laboratory results to the field in-situ, such study is very important since the wave characters measured in the field are in different frequency bands from those measured in the laboratory. The results show that the velocity dispersions in rocks are directly related to the viscosity of the pore fluids, the permeability and pore geometry of the rock, the thin crack appearance in the rock, and temperature and pressure. The results are discussed in terms of the Biot theory and the "local flow" mechanism. According to either the Biot theory or the "local flow" mechanism, laboratory results of velocities in heavy oil saturated rocks measured at 1 MHz can be directly applied to the field in-situ at seismic or sonic logging frequencies.

Chapter 9 summarizes and discusses the applicability of using seismic methods to monitor various enhanced oil recovery and production processes. It also discusses the factors affecting seismic wave velocities in hydrocarbon reservoirs.

In chapter 10, abstracts of other related publications and reports by me and my co-authors are presented. These publications and reports are related to the content of

this thesis and were written during the period of my stay at Stanford as a graduate student.

The richness of the seismic effects discussed in this thesis and the sensitivity of velocity to reservoir parameters clearly indicate the future direction of reservoir seismology: growing efforts to describe reservoirs in more detail, and monitoring their recovery processes, using high resolution seismic methods. However, much of the methodology required still remains to be developed. Although 3-D and vertical seismic profiling (VSP) surveys already contribute significantly to reservoir description, cross-hole tomography and inverted VSP, using downhole sources and a very large number of surface receivers, are just beginning to emerge. With data densities which are much greater than those needed for exploration through rock volumes (reservoirs, production zones, etc.) which are quite small, it should thus become very practical to use seismic probing routinely in development and production of hydrocarbon reservoirs. The velocities and amplitude data obtained can then be converted to desired reservoir parameters, using the effects described in this thesis and elsewhere.

REFERENCES

Nur, A., 1987. Seismic rock properties for reservoir descriptions and monitoring. In: Seismic Tomography, edited by G. Nolet, p203-238. D. Reidel Pub. Co., Dordrecht.

Nur, A. and Z. Wang, 1987. In-situ seismic monitoring EOR: The petrophysical basis. SPE Paper No. 16865. Proc. of the 62nd Annual Conf. and Exhib., Vol. Φ, p307-313.

CHAPTER 2

WAVE VELOCITIES IN PURE HYDROCARBONS AND MIXTURES

ABSTRACT

Wave velocities were measured in hydrocarbons of the Alkane, Alkene, and Naphthene (Cycloparaffin) families as a function of temperature, using the ultrasonic pulse transmission method. It was found that the wave velocities in all the hydrocarbons measured decreased with increasing temperature approximately linearly, though the slopes of the decreases were different.

By plotting the velocities as a function of both temperature and the carbon number (or the molecular weight), one could see that the velocities increased with increasing the carbon number of the hydrocarbons. This suggests that hydrocarbons of the same family with higher carbon content have higher elastic modulus (or lower compressibility).

Wave velocities in hydrocarbon mixtures were also measured. The measured velocities had very small deviation from the following empirical formula

$$V = \sum_{i=1}^{n} X_i V_i \ ,$$

where V is the velocity in the hydrocarbon mixture, X_i is the volume fraction and V_i is the velocity, respectively, of the ith component.

INTRODUCTION

The variation of ultrasonic wave velocities with temperature changes in liquids has long been a research subject for many scientists. In recent years, with the rapid development in petroleum technologies, seismic-acoustical methods are becoming more and more important in both exploration and experimental geophysics. Therefore, it is necessary to study the acoustical properties of both hydrocarbons and hydrocarbon-saturated rocks. In a series of such studies, we carried out some ultrasonic measurements on the velocities in petroleum-forming hydrocarbons as a function of temperature.

Wave velocities in thirteen n-alkane, ten 1-alkene, and three cycloparaffin hydrocarbon samples were measured in the temperature range of as low as -12 to up to 132° C. It was found that the velocities in all the hydrocarbons decreased approximately linearly as the temperature increased, with slopes ranging from -3.43 to -4.86 $[m/sec]/^{\circ} C$.

The velocities in the hydrocarbons increased with increasing the carbon numbers or the molecular weights, and a linear (or approximately linear) relationship between the velocities and the inverse of the carbon numbers or molecular weights was found. By combining the effects of temperature and carbon number or molecular weights on the velocities together, an empirical model for the velocities in pure hydrocarbons was proposed. This model allows one to calculate velocities in pure hydrocarbons of various molecular weights or carbon numbers at various temperatures, if the temperature coefficient, the molecular weight coefficient or carbon number coefficient, and a reference velocity are known.

Although both the densities of and the velocities in the hydrocarbons vary with the temperature changes approximately linearly, one may not expect the same relationship to exist between the bulk moduli (or compressibility) and temperature. The experimental results show that the bulk moduli of the hydrocarbons decrease non-linearly

with increasing temperature, and that they increase with increasing carbon numbers or molecular weights.

The wave velocities in nine mixtures of pure hydrocarbons were also measured, either as a function of the volume fraction of one of the components or as a function of temperature. The measured velocity data were fitted by a simple linear equation

$$V = \sum_{i=1}^{n} X_i V_i \ ,$$

where X_i and V_i are the volume fraction and velocity, respectively, of the ith hydrocarbon component in the mixture. It was found that the fit was surprisingly well, with the biggest deviation of only 0.52%.

Although several linear relationships have been found, all of them may be applicable only when the hydrocarbons are in the liquid state.

PHYSICAL PROPERTIES OF THE HYDROCARBONS

In the experiments, three types of hydrocarbons were selected, namely, n-alkanes, 1-alkenes, and cycloparaffins. Of them, cycloparaffins and alkanes are among the most common constituents of crude oils. All the hydrocarbon samples were bought from a major chemical company.

n-Alkanes

The alkanes are a homologous series* of saturated open-chain hydrocarbons of general formula $C_n H_{2n+2}$. They are also called paraffins which dominate the gasoline fraction of crude oils. Generally, they are the principal hydrocarbons in the oldest, most deeply buried reservoirs. On average, a crude oil contains somewhere between 15-20% (by weight) alkanes; however, this figure may rise to as high as 35% in very paraffinic crude oils, or drop to zero in the case of heavily biodegraded oils.

* - In organic chemistry, a homologous series is a series of compounds in which each member differs from the next member by a constant amount.

The alkanes which have straight-chain molecular structures are called normal alkanes (n-alkanes) or normal paraffins (n-paraffins). A typical crude oil contains normal alkanes with carbon numbers ranging from 1 to about 40 (a few beyond 40). At room temperature and pressure, normal alkanes of $C_1 - C_4$, $C_5 - C_{16}$, and C_{16} above are in the state of gas, liquid, and solid, respectively.

Table 1 lists the physical properties of the n-alkanes tested in our experiments. From this table, one can see that the boiling point, melting point, and density of the n-alkanes all increase with increasing carbon numbers (hence molecular weight), which is related to the van der Waals forces between the hydrocarbon molecules.

All the n-alkanes tested are basically non-soluble in water. The densities are all less than that of water (1 $grams/cm^3$), and decrease with increasing temperature (figure 1).

1-Alkenes

The alkenes are a homologous series of unsaturated open-chain hydrocarbons of general formula $C_n H_{2n}$. They are also called olefins. Alkenes have a double bond between two of the carbon atoms (i.e., $-C=C-$) in structure (this is what "unsaturated" actually means) and therefore are chemically reactive. They are rarely seen in crude oils due to their chemical reactivity; however, small quantities of hexene (C_6H_{12}), heptene (C_7H_{14}), and octene (C_8H_{16}) have been identified.

The 1-alkenes in the experiments are straight-chain hydrocarbons and have the double bond between their first and second carbon atoms (or the last and the second last ones) in the molecular structure. Their physical properties (table 2) are similar to those of n-alkanes. The melting point of a 1-alkene is much lower, the boiling point is slightly lower, and the density is higher, than those of the n-alkane with the same carbon number, which is caused by the double bond in the molecular structure of the 1-alkenes.

Figure 2 shows the density-temperature relation of the 1-alkenes. This relationship is approximately linear.

Cycloparaffins

The cycloparaffins are formed by joining the carbon atoms in a ring. They are also called naphthenes. They are saturated hydrocarbons with general formula $C_n H_{2n}$. Usually, crude oils can contain up to 50% (by weight) of naphthene compounds.

Three samples of cycloparaffins (cyclohexane, cycloheptane, and cyclooctane) were selected for the experiments. Their physical properties are listed in table 3. Note that their physical properties are quite different from those of n-alkanes and 1-alkenes with the same carbon numbers, due to the differences between their molecular structures.

EXPERIMENTS

The pulse transmission method was employed in the experiments. The apparatus consists of a pair of acoustic transducers, a pulse transmitter/receiver, a signal amplifier, and an oscilloscope. The transducers used are a pair of identical, wide band piezoelectric immersion transducers with a central frequency of 2.25 *MHz* and diameters of 19.05 *mm* (0.75 *in.*), and attached with two identical high-temperature buffers.

In the measurements, the two transducers, attached with the high-temperature buffers, were built in and locked on a heat-conductive cylindrical container, and the distance between them were precisely measured. The ultrasonic pulse of 1 *MHz* frequency was sent to one of the transducers to generate the ultrasonic waves traveling through the hydrocarbons under test. The waves were picked up by the other transducer and sent to the amplifier and then to the digital oscilloscope. The travel times of the waves therefore were measured on the oscilloscope, with precision of 0.05 $\mu sec.$.

At one temperature point, two travel times of the waves were measured; one was the two-way travel time Δt_R in one of the high-temperature buffers (the reflection time

at the interface of the high-temperature buffer and the hydrocarbon under test), and the other was the transmission time Δt_T in the hydrocarbon sample and the two buffers. The ultrasonic velocity was calculated by

$$V = \frac{l}{\Delta t_T - \Delta t_R}$$

where l is the distance through which the waves traveled in the hydrocarbon sample.

The hydrocarbons of low melting points were pre-cooled in a refrigerator and those of high melting points were pre-melted in a vacuum oven. Once the hydrocarbon sample was prepared, it was poured into the container in which the transducers were built. The temperature of the sample was gradually increased by a heating tape which surrounded the heat-conducting container homogeneously. The heating rate was about 0.5 - 0.8° C/minute. Once a temperature point was reached, we waited for about 10-15 minutes to measure the travel times to assure temperature equilibrium inside the sample. Owing to these procedures and since the volume of the hydrocarbon sample was small (about 110 ml), the temperature gradient in the sample at the measuring point was very small.

The travel times were also measured when the temperature decreased from the highest measuring point to room temperature (22° C). No velocity hysteresis was found in the experiments.

RESULTS AND DISCUSSIONS

Wave Velocities in Pure Hydrocarbons

The compressional wave velocities in 26 pure hydrocarbon samples (thirteen n-alkanes, ten 1-alkenes, and three cycloparaffins) were measured as a function of temperature, with accuracy of about 0.1%. The complete data were listed in tables 4 to 6.

Figure 3 shows the velocities in the thirteen n-alkanes as a function of temperature. The velocities in all the liquid n-alkanes decrease approximately linearly with increasing temperature, i.e., the data can be fitted by straight lines of expression

$$V_T = V_o - b\,\Delta T, \tag{1}$$

where V_T and V_o are the velocities at temperatures T and T_o (a reference temperature point), respectively, $\Delta T = T - T_o$, and b is called the temperature coefficient of the velocity.

Figures 4 and 5 plot the velocity data of 1-alkenes and cycloparaffins listed in tables 5 and 6, respectively as a function of temperature. Again, the velocities decrease with increasing temperature approximately linearly.

The linear relation between wave velocities in the hydrocarbons and temperature is restricted in the region of the hydrocarbons being in the state of liquid only. Therefore, one does not expect this linearity to span on the whole three-state region.

The linear (or approximately linear) variation of wave velocities with temperature has also been observed in many liquids. The ultrasonic velocities in nitrobenzene, methyl acetate, ethyl acetate, diethylene glycol monoethyl ether, etc., nine organic compounds, measured by Rao and Rao (1959), all showed a linear decrease with increasing temperature (ranging 25 - 110° C). Bradley (1963) showed that the sound velocities in a Dow Corning 200 fluid also decrease approximately linearly with increasing temperature. Although he fitted the data by high order polynomials, the constant and the first order terms were obviously dominant in his expressions. In our experiments, we did not feel it necessary to fit the data by polynomials since the data measured were not that highly accurate (the accuracy was about 0.1%). The sound velocities in liquid trichlorofluoromethane, measured by Chavez et al (1981), also showed a linear relationship with temperature in the range of -25 to 25° C (not in the whole temperature range). Even in mercury, the velocity also decreases linearly with

increasing temperature (Hunter et al, 1963).

One also notices that the wave velocities in all the measured 26 hydrocarbon samples decrease with increasing temperature very fast, generally by 35-45% in the temperature interval of 100° C. For different hydrocarbons, the degree of the velocity decrease is different. This degree of decrease is measured by a parameter called the temperature coefficient, b. Figure 6 plots the temperature coefficients of all the 26 hydrocarbon samples. It shows that the temperature coefficient decreases (while the velocity increases) with increasing carbon number (or molecular weight) of the hydrocarbons of the same series, which means that the heavier the hydrocarbon is, the less sensitive the velocity is to temperature changes.

Figure 6 shows that the temperature coefficients of the velocities in the n-alkanes and the 1-alkenes vary with the molecular weight changes in a similar nature. These coefficients are also plotted against the molecular weights of the hydrocarbons (figure 7). The continuous line in figure 7 represents the fitted data by an empirical equation

$$\frac{1}{b} = 0.306 - \frac{7.6}{M},$$

where b is the temperature coefficient and M the molecular weight. This equation allows one to calculate the temperature coefficient of the wave velocities in hydrocarbons of the n-alkane and 1-alkene series, with a reasonable accuracy.

The velocities in all the hydrocarbons measured increase with increasing the carbon number at all temperatures. In lighter hydrocarbons (with carbon numbers less than 16), the velocities increase very fast as the carbon number increases, and in the heavier ones, this increase becomes less sensitive to the carbon number changes.

Figures 8, 9, and 10 show that the velocities at different temperatures are linear function of the inverse of the carbon number ($\frac{1}{C}$) of the hydrocarbons. In figures 8 to 10, the velocity data are fitted by straight lines and the deviation of the data from these straight lines is small (the largest one is about 1.5%). Therefore, equation (1) is

modified as a 2-dimensional function of temperature and carbon number,

$$V_{T,C} = V_{T_o,C_o} - b\,(T - T_o) - a\,(\frac{1}{C} - \frac{1}{C_o}), \tag{2}$$

where a is called the carbon number coefficient of the velocity; C is the carbon number, and C_o is a reference carbon number. In equation (2), b is a function of carbon number, and a is a function of temperature.

Equation (2) can also be written as

$$V_{T,C} = V_{T_o,C_o} - b\,\Delta T + a\frac{\Delta C}{CC_o}, \tag{3}$$

where $\Delta T = T - T_o$ and $\Delta C = C - C_o$.

Equations (2) and (3) illustrate the variations of the wave velocities in hydrocarbons with both temperature and carbon numbers. Knowing the coefficients a and b and a reference velocity V_o, one can calculate the wave velocities in hydrocarbons of various carbon numbers at different temperatures. However, they can be used only when the hydrocarbons are in the state of liquid.

Figure 11 shows a 3-dimensional plot of the velocities in the n-alkanes as a function of both temperature and carbon number. Figures 12 and 13 are the 3-dimensional plots for the 1-alkenes and cycloparaffins, respectively.

Since the wave velocities are related to the carbon numbers of the hydrocarbons, they must have the similar relationship with the molecular weights of the hydrocarbons. Figures 14 and 15 illustrate the variations of the velocities in the n-alkanes and the 1-alkenes, respectively, with the the inverse of the molecular weight at different temperatures. The shapes of the velocity curves are very similar to those shown in figures 8 and 9.

Figures 14 and 15 show that the wave velocities are linear (or approximately linear) functions of the inverse of the molecular weights of the n-alkanes and 1-alkenes. Therefore, equations (2) and (3) can also be written as a 2-dimensional function of

temperature and molecular weight of the hydrocarbons,

$$V_{T,M} = V_{T_o,M_o} - b\,(T - T_o) - a_M\,(\frac{1}{M} - \frac{1}{M_o}), \tag{4}$$

or

$$V_{T,M} = V_{T_o,M_o} - b\,\Delta T - a_M\,\frac{\Delta M}{MM_o}, \tag{5}$$

where a_M is the molecular weight coefficient of the velocity and is different from a, the carbon number coefficient. a_M is also a function of temperature. M and M_o are the molecular weight and a reference molecular weight, respectively, and $\Delta M = M - M_o$. V_{T_o,M_o} is a reference velocity (velocity in hydrocarbon of molecular weight M_o at temperature T_o). All other notations in equation (4) and (5) mean the same as in (2) and (3).

Like equations (2) and (3), equations (4) and (5) also allow one to calculate the velocities in the hydrocarbons of various molecular weights at different temperatures if a reference velocity and the coefficients b and a_M are known.

Plotting the velocities in the n-alkanes and the 1-alkenes in a same figure as a function of molecular weight (figure 16), one can see that all the data points at a given temperature point lie on a fairly smooth line. This means that for the hydrocarbons which have the similar molecular structures, the velocities are mainly determined by their molecular weights, at a given temperature and pressure point. Comparing the physical properties of an n-alkane and a 1-alkene of the same carbon number, their melting points and densities are quite different, while the molecular weights differ only by 2 and the boiling points by a few degree C (tables 1 and 2). Therefore, one can conclude that, besides the ambient environments such as temperature and pressure, the velocities in hydrocarbons are determined by their molecular weights and molecular structures.

Bulk Moduli of the n-Alkanes and 1-Alkenes

Having both the density and velocity data, one can calculate the adiabatic bulk moduli of the hydrocarbons by using the equation

$$K = \rho V^2, \tag{6}$$

where ρ and V represent density and velocity, respectively.

The calculated bulk moduli of the n-alkanes with carbon numbers ranging 6 to 18 are plotted in figure 17. Although both the densities of and the velocities in the n-alkanes decrease with increasing temperature approximately linearly, the bulk moduli of the hydrocarbons decrease with increasing temperature non-linearly. However, similar to the densities and velocities, the bulk moduli of the n-alkanes decrease with increasing temperature also very fast, and increase with increasing carbon numbers (and hence molecular weights).

Figure 18 plots the bulk moduli of the 1-alkenes as a function of temperature. Again, systematic decrease of the bulk moduli with increasing temperature was found. The bulk moduli also increase with increasing carbon numbers (molecular weights) systematically, as found in the n-alkanes (figure 27).

Plotting the bulk moduli of both the n-alkanes and 1-alkenes in the same figure (figure 19), one can see that for the hydrocarbons which have the same molecular weights, the bulk moduli are very close to each other, and also vary in the same way with temperature changes. However, as one can see in figure 19, the bulk moduli of the n-alkanes are a little smaller than those of the 1-alkenes of the same molecular weights. This is obviously caused by the density effect: Since at a given molecular weight the density of the n-alkane is lower than, while the velocity is about the same as, that of the 1-alkene, the bulk moduli of the n-alkane should be a little smaller than that of the 1-alkene due to its lower density. Therefore, one can conclude that for the hydrocarbons which have the same molecular structures (e.g., open-chain, number of double or

triple bonds) and the same molecular weights, at the same temperature and pressure, their bulk moduli are affected by the densities.

The densities of the hydrocarbons are related to the molecular structures. For example, the double bond increases the densities of the 1-alkenes (also lowers the melting and boiling points). However, the density may not affect the velocities if the molecular structures are similar (e.g., open-chain, straight-chain), though it may have effects on the bulk moduli. The molecular structures of a 1-alkene and an n-alkane of the same carbon number differ each other only by a double bond. Our results show that this double bond does not affect the velocities (the slight differences in velocities are caused by the molecular weight difference) but does affect the bulk moduli.

Wave Velocities in Hydrocarbon Mixtures

The wave velocities in hydrocarbon mixtures were also measured in the experiments. The volumes of the pure hydrocarbon components were precisely measured and the mixtures were well-stirred. All other measuring procedures were the same as in the measurements on the pure hydrocarbons.

The velocities in the binary mixture of 1-decene ($C_{10}H_{20}$) and 1-octadecene ($C_{18}H_{36}$) are listed in table 7. The measured velocities are fitted by

$$V = X_1V_1 + X_2V_2, \tag{7}$$

where X_1 and V_1, X_2 and V_2 are the volume fractions and velocities of the first and second pure hydrocarbon components, respectively. The data (both measured and calculated) are also plotted in figure 20 which shows the velocities in the binary mixture behave as a linear function of the volume fraction of 1-decene ($C_{10}H_{20}$). The calculated velocities by equation (7) fit the measured very well, with the biggest deviation of 0.31%.

The velocities measured in 50% (by volume) 1-decene ($C_{10}H_{20}$) and 50% 1-hexadecene ($C_{16}H_{32}$), along with those calculated by equation (7), are plotted in figure

21 as a function of temperature (the data are listed in table 8). Again, the measured velocities are well-fitted by equation (7), with the biggest deviation of 0.38%.

To test the applicability of equation (7), the velocities in the binary mixture of 35% (by volume) 1-dodecene ($C_{12}H_{24}$) and 65% 1-tetradecene ($C_{14}H_{28}$) were also measured as a function of temperature (figure 22, table 8). The biggest deviation of the measured velocity data from the calculated by equation (7) is about 0.52%.

Equation (7) is applicable to the binary mixtures, both as a function of the volume fraction of one of the pure hydrocarbon components and as a function of temperature. The velocities in multi-component mixtures of pure hydrocarbons were also measured. Table 9 lists the velocities in six multi-component mixtures of the pure hydrocarbons, at temperature of 20° C, along with those calculated by

$$V = \sum_{i=1}^{n} X_i V_i , \tag{8}$$

where X_i and V_i are the volume fraction of and velocity in the ith hydrocarbon component, and n is the number of the components in the mixture. From table 9, one can see that the measured velocities are also well-fitted by equation (8), with the biggest deviation of 0.31%. Therefore, one may conclude that one can calculate the velocities in the hydrocarbon mixtures by equation (8) very precisely, if the composition of the mixtures is known.

SUMMARIES AND CONCLUSION

Linear (or approximately linear) decreases of the wave velocities in pure hydrocarbons with increasing temperature were found. This linearity allows one to extrapolate the velocity values in a hydrocarbon at various temperatures if a reference velocity (velocity value at a given temperature point) and the temperature coefficient are known. However, this extrapolation may be made only when the hydrocarbon is in the state of liquid.

The wave velocities in hydrocarbons of the same series increase non-linearly with increasing the carbon numbers or the molecular weights of the hydrocarbons. However. if the velocities are plotted as a function of the inverse of the carbon numbers or the molecular weights, again linear relationships are found. Combining the effects of temperature and the carbon numbers or molecular weights on the velocities, one can calculate the velocities in hydrocarbons of various carbon numbers or molecular weights at various temperatures if the temperature and carbon number (or molecular weight) coefficients and a reference velocity are known.

Although both the densities of and the velocities in the measured hydrocarbons decrease with increasing temperature linearly (or approximately linearly), the same relationship does not exist between the bulk moduli (or compressibilities) and temperature.

The velocities in the hydrocarbon mixtures have also linear (or approximately linear) relationships with temperature and the volume fraction of one of the components. The empirical equation established in this study allows one to calculate the velocities in hydrocarbon mixtures at given temperatures if the compositions of the mixtures are known.

REFERENCES

Bradley, D. L., 1963; Velocity of sound in a Dow Corning 200 fluid as a function of temperature and pressure, Journal Acoust. Soc. Am., vol. 35, no. 10, p1565-1567.

Hunt, J. M., 1979; Petroleum geochemistry and geology. W. H. Freeman and Co., San Francisco, Calif..

Hunter, J. L., T. J. Welch, and C. J. Montrose, 1963; Excess absorption in mercury, Journal Acoust. Soc. Am., vol. 35, no. 10, p1568-1570.

Kinghorn, R. R. F., 1983; An introduction to the physics and chemistry of petroleum,

John Wiley & Sons, New York.

Rao, K. S. and B. R. Rao, 1959; Study of temperature variation of ultrasonic velocities in some organic liquids by modified fixed-path interferometer method, Journal Acoust. Soc. Am., vol. 31, no. 4, p439-441.

Rossini, F. D., K. S. Pitzer, R. L. Arnett, R. M. Braun, and G. C. Pimentel. 1953: Selected values of physical and thermodynamic properties of hydrocarbons and related compounds, Carnegie Press, Pittsburgh, Pennsylvania.

Vargaftik, N. B., 1975; Tables on the thermophysical properties of liquids and gases. 2nd ed., John Wiley & Sons, New York.

TABLE AND FIGURE CAPTIONS

TABLES

Table 1. Physical properties of the n-Alkanes.

Table 2. Physical properties of the 1-Alkenes.

Table 3. Physical properties of the Cycloparaffins.

Table 4. Measured velocities as a function of temperature in the n-Alkanes.

Table 5. Measured velocities as a function of temperature in the 1-Alkenes.

Table 6. Measured velocities as a function of temperature in the Cycloparaffins.

Table 7. Measured and calculated velocities in the binary mixtures of $C_{10}H_{20}$ and $C_{18}H_{36}$.

Table 8. Measured and calculated velocities as a function of temperature in the binary mixtures of 50% $C_{10}H_{20}$ and 50% $C_{16}H_{32}$ and 35% $C_{12}H_{24}$ and 65% $C_{14}H_{28}$.

Table 9. Measured and calculated velocities in the multi-component mixtures of selected n-Alkanes, 1-Alkenes, and Cycloparaffins.

FIGURES

Figure 1. Density of the n-Alkanes *vs.* temperature. The numbers in the figure represent carbon numbers.

Figure 2. Density of the 1-Alkenes *vs.* temperature. The numbers in the figure represent carbon numbers.

Figure 3. Velocities in the n-Alkanes *vs.* temperature. The numbers in the figure represent carbon numbers.

Figure 4. Velocities in the 1-Alkenes *vs.* temperature. The numbers in the figure represent carbon numbers.

Figure 5. Velocities in the Cycloparaffins *vs.* temperature. The numbers in the figure represent carbon numbers.

Figure 6. Temperature coefficient b of the velocities in the measured hydrocarbons as a function of the carbon number.

Figure 7. Temperature coefficient b of the velocities in the measured hydrocarbons as a function of the molecular weight.

Figure 8. Velocities in the n-Alkanes plotted as a function of the inverse of the carbon numbers, at different temperatures.

Figure 9. Velocities in the 1-Alkenes plotted as a function of the inverse of the carbon numbers, at different temperatures.

Figure 10. Velocities in the Cycloparaffins plotted as a function of the inverse of the carbon numbers, at different temperatures.

Figure 11. Three-dimensional plot of the velocities in the n-Alkanes as a function of both temperature and the carbon number.

Figure 12. Three-dimensional plot of the velocities in the 1-Alkenes as functions of temperature and the carbon number.

Figure 13. Three-dimensional plot of the velocities in the cycloparaffins as a function of both temperature and the carbon number, in the temperature interval of 15 to 120° C.

Figure 14. Velocities in the n-Alkanes *vs.* the inverse of the molecular weight (multiplied by 10) at different temperatures.

Figure 15. Velocities in the 1-Alkenes *vs.* the inverse of the molecular weight (multiplied by 10) at different temperatures.

Figure 16. Comparison of the velocities in the 1-Alkenes with those in the n-Alkanes, as a function of molecular weight at different temperatures.

Figure 17. The calculated bulk moduli of the n-Alkanes *vs.* temperature. The numbers in the figure represent carbon numbers.

Figure 18. The calculated bulk moduli of the 1-Alkenes *vs.* temperature. The numbers in the figure represent carbon numbers.

Figure 19. Comparison of bulk moduli of the 1-Alkenes with those of the n-Alkanes, as a function of temperature.

Figure 20. The measured and calculated velocities in the binary mixture of $C_{10}H_{20}$ and $C_{18}H_{36}$.

Figure 21. The measured and calculated velocities as a function of temperature in the binary mixture of 50% $C_{10}H_{20}$ and 50% $C_{16}H_{32}$.

Figure 22. The measured and calculated velocities as a function of temperature in the binary mixture of 35% $C_{12}H_{24}$ and 65% $C_{14}H_{28}$.

Name	Formula	Purity (%)	Molecular Weight	Melting Point (° C)*	Boiling Point (° C)*	Density at 20° C**
n -Hexane	C_6H_{14}	99+	86.06	-95	69	0.659
n -Heptane	C_7H_{16}	99+	100.07	-91	98	0.684
n -Octane	C_8H_{18}	99+	114.08	-57	126	0.703
n -Decane	$C_{10}H_{22}$	99+	142.10	-30	174	0.730
n -Undecane	$C_{11}H_{24}$	99	156.11	-26	196	0.740
n -Dodecane	$C_{12}H_{26}$	99	170.12	-12	216	0.749
n -Tetradecane	$C_{14}H_{30}$	99	198.14	-6	253	0.763
n -Pentadecane	$C_{15}H_{32}$	99+	212.15	10	270	0.769
n -Hexadecane	$C_{16}H_{34}$	99	226.16	18	287	0.773
n -Octadecane	$C_{18}H_{38}$	97	254.18	30	317	0.782
n -Docosane	$C_{22}H_{46}$	99	310.22	44	369	0.794
n -Octacosane	$C_{28}H_{58}$	97	394.28	62	429	0.807
n -Hexatriacontane	$C_{36}H_{74}$	98	506.36	74	493	0.817

*: at 760 mmHg. **: at 760 mmHg, unit: $Grams/cm^3$.

Table 1

Name	Formula	Purity (%)	Molecular Weight	Melting Point (° C)*	Boiling Point (° C)*	Density at 20° C**
1-Hexene	C_6H_{12}	97	84.06	-140	64	0.673
1-Heptene	C_7H_{14}	97	98.07	-119	94	0.697
1-Octene	C_8H_{16}	97	112.08	-101	122	0.715
1-Decene	$C_{10}H_{20}$	96	140.10	-66	171	0.741
1-Undecene	$C_{11}H_{22}$	99	154.11	-49	192	0.750
1-Dodecene	$C_{12}H_{24}$	95	168.12	-35	213	0.758
1-Tetradecene	$C_{14}H_{28}$	95	196.14	-13	251	0.775
1-Hexadecene	$C_{16}H_{32}$	94	224.16	4	274	0.783
1-Octadecene	$C_{18}H_{36}$	90	252.18	16	314	0.789
1-Eicosene	$C_{20}H_{40}$	...	280.20	28	341	0.795

*: at 760 mmHg. **: at 760 mmHg, unit: *Grams* /cm^3.

Table 2

Name	Formula	Purity (%)	Molecular Weight	Melting Point ($^{\circ}C$)*	Boiling Point ($^{\circ}C$)*	Density at 20$^{\circ}C$**
Cyclohexane	C_6H_{12}	99.9	84.06	-18	81	0.779
Cycloheptane	C_7H_{14}	98	98.07	-12	118	0.811
Cyclooctane	C_8H_{16}	99	112.08	12	151***	0.834

*: at 760 mmHg. **: at 760 mmHg, unit: $Grams/cm^3$. ***: at 740 mmHg.

Table 3

C_6H_{14}		C_7H_{16}		C_8H_{18}		$C_{10}H_{22}$	
T	Vp	T	Vp	T	Vp	T	Vp
-10	1224	-8	1270	-8	1314	-5	1342
-5	1204	0	1235	-6	1305	10	1281
0	1184	7	1203	-2	1289	22	1241
3	1171	12	1178	5	1253	27	1224
6	1160	18	1157	12	1228	38	1178
12	1131	28	1109	18	1200	49	1137
19	1102	36	1078	24	1177	56	1108
26	1070	43	1047	31	1147	64	1076
34	1035	50	1019	41	1105	69	1059
40	1005	59	979	52	1059	78	1023
45	983	65	951	61	1020	89	976
50	960	73	917	74	965	95	951
55	937	85	863	86	916	106	908
61	910	92	833	102	846	118	859
64	894	95	820	113	797	...	...
68	882	...	...	119	776	...	...

Units: T - Degree C, V - Meters/second.

Table 4

$C_{11}H_{24}$		$C_{12}H_{26}$		$C_{14}H_{30}$		$C_{15}H_{32}$	
T	Vp	T	Vp	T	Vp	T	Vp
-2	1357	...	...	10	1370	...	...
0	1348	4	1359	22	1324	...	...
6	1323	13	1327	27	1304	...	...
14	1296	22	1288	30	1295	14	1364
18	1280	28	1261	36	1267	25	1323
31	1223	37	1220	42	1248	33	1290
44	1180	45	1194	49	1220	48	1236
55	1135	54	1157	59	1186	57	1205
68	1086	65	1118	71	1139	71	1152
76	1055	73	1086	83	1091	82	1111
87	1008	83	1051	90	1064	89	1085
93	989	92	1011	103	1016	91	1075
101	955	100	978	110	986	102	1038
112	910	110	940	120	951	112	1000
121	875	119	907	...	...	121	967

Units: T - Degree C, V - Meters/second.

Table 4

$C_{16}H_{34}$		$C_{18}H_{38}$		$C_{22}H_{46}$		$C_{28}H_{58}$		$C_{36}H_{74}$	
T	Vp	T	Vp	T	Vp	T	Vp	T	Vp
23	1343	...	...	...	...	...	...	...	...
27	1328	28	1340	...	...	...	...	...	...
33	1304	29	1338	...	...	...	...	...	...
36	1288	38	1302	44	1316	61	1301	74	1275
45	1258	48	1263	48	1301	67	1275	80	1249
52	1234	58	1228	55	1278	74	1244	85	1232
62	1192	68	1194	65	1242	83	1215	90	1211
73	1152	77	1161	72	1217	90	1188	95	1197
83	1118	90	1111	82	1182	96	1169	101	1172
93	1081	93	1104	93	1142	101	1148	110	1144
104	1041	104	1060	104	1105	108	1126	117	1121
110	1016	114	1027	111	1077	115	1102	124	1097
119	982	122	996	120	1047	120	1082	132	1076

Units: T - Degree C, V - Meters/second.

Table 4

C_6H_{12}		C_7H_{14}		C_8H_{16}		$C_{10}H_{20}$		$C_{11}H_{22}$	
T	Vp	T	Vp	T	Vp	T	Vp	T	Vp
-12	1241	...	...	-12	1323	...	...	...	...
-8	1222	...	...	-4	1291	...	...	0	1345
-4	1203	-8	1261	0	1275	-8	1355	8	1320
2	1175	0	1226	5	1249	0	1324	12	1293
8	1147	8	1191	12	1220	12	1277	16	1281
11	1133	11	1180	19	1188	22	1238	22	1257
18	1102	17	1155	31	1136	28	1213	34	1207
24	1074	25	1120	44	1084	36	1181	47	1153
30	1048	33	1085	53	1047	47	1137	57	1118
33	1031	42	1047	64	999	60	1087	62	1103
39	1004	53	1000	73	960	72	1039	75	1052
47	968	63	958	84	914	84	993	87	1007
50	954	74	910	92	878	96	943	100	956
56	927	84	870	108	814	108	896	114	896
63	896	92	833	115	784	120	849	121	868

Unit: T - Degree C. V - Meters/second

Table 5

$C_{12}H_{24}$		$C_{14}H_{28}$		$C_{16}H_{32}$		$C_{18}H_{36}$		$C_{20}H_{40}$	
T	Vp	T	Vp	T	Vp	T	Vp	T	Vp
-4	1380	0	1397	...	...	...	...	...	...
0	1365	13	1349	10	1385	...	...	...	...
8	1335	23	1312	22	1341	...	...	...	...
15	1309	29	1288	30	1309	...	...	...	...
22	1282	36	1261	38	1279	17	1381	...	...
28	1261	43	1236	46	1248	23	1361	32	1356
36	1229	49	1215	49	1240	30	1336	35	1343
47	1187	55	1191	57	1211	41	1293	48	1291
51	1174	64	1160	63	1191	45	1279	56	1266
60	1139	70	1140	70	1162	56	1238	67	1225
64	1124	78	1111	75	1148	69	1191	78	1187
76	1076	86	1081	79	1135	80	1155	82	1174
86	1040	96	1046	89	1097	92	1111	96	1123
96	1003	104	1014	100	1059	100	1087	110	1073
105	969	110	993	110	1020	110	1049	117	1046
117	924	119	959	119	987	120	1011	120	1038

Unit: T - Degree C, V - Meters/second.

Table 5

C_6H_{12}		C_7H_{14}		C_8H_{16}	
T (° C)	Vp	T (° C)	Vp	T (° C)	Vp
7	1337	-2	1456	...	...
12	1313	7	1416	...	...
17	1289	14	1390	14	1427
22	1265	23	1345	22	1395
27	1237	29	1311	27	1374
32	1213	31	1304	38	1328
37	1190	39	1267	47	1288
42	1166	45	1241	58	1243
47	1141	54	1200	67	1206
53	1111	64	1157	77	1163
60	1077	74	1111	87	1121
64	1064	86	1054	95	1086
72	1023	95	1017	101	1060
79	986	106	967	110	1023
80	982	108	959	120	984

Unit: V - Meters/second.

Table 6

Volume Fraction (%)		$V_{measured}$	$V_{calculated}$
$C_{10}H_{20}$	$C_{18}H_{36}$		
0	100	1369	1369
10	90	1358	1357
20	80	1348	1344
29.4	70.6	1336	1333
40	60	1321	1320
50	50	1307	1308
60	40	1298	1295
70	30	1286	1283
80	20	1275	1271
90	10	1260	1259
100	0	1247	1247

Unit: V - Meters/second. T = 20° C.

Table 7

50% $C_{10}H_{20}$, 50% $C_{16}H_{32}$ (by volume)			35% $C_{12}H_{24}$, 65% $C_{14}H_{28}$ (by volume)		
T ($^{\circ}C$)	$V_{measured}$	$V_{calculated}$	T ($^{\circ}C$)	$V_{measured}$	$V_{calculated}$
19	1307	1302	19	1319	1315
28	1266	1265	30	1275	1274
41	1218	1216	47	1210	1210
53	1173	1171	68	1128	1133
62	1138	1136	84	1071	1074
80	1068	1067	98	1018	1023
96	1008	1007	112	964	969
108	961	961	...	...	...
118	923	924	...	...	...

Unit: V - Meters/second.

Table 8

Composition	Vp at 20° C	Volume Fraction (%)					
C_8H_{18}	1194	...	...	20	...	...	4
$C_{10}H_{22}$	1247	20	...	20	...	...	8
$C_{12}H_{26}$	1294	20	...	20	...	...	8
$C_{14}H_{30}$	1333	20	...	20	...	...	8
$C_{16}H_{34}$	1354	40	...	20	...	...	12
C_8H_{16}	1188	...	...	...	10	...	2
$C_{10}H_{20}$	1247	...	...	...	10	10	6
$C_{12}H_{24}$	1290	...	30	...	20	...	10
$C_{14}H_{28}$	1321	...	30	...	10	10	10
$C_{16}H_{32}$	1349	...	40	...	50	20	20
C_6H_{12}	1276	...	...	...	...	10	2
C_7H_{14}	1358	...	...	...	...	20	4
C_8H_{16}	1402	...	...	...	...	30	6
$V_{calculated}$	...	1316	1323	1284	1308	1346	1313
$V_{measured}$	...	1319	1326	1286	1312	1343	1309

Unit: V - Meters/second.

Table 9

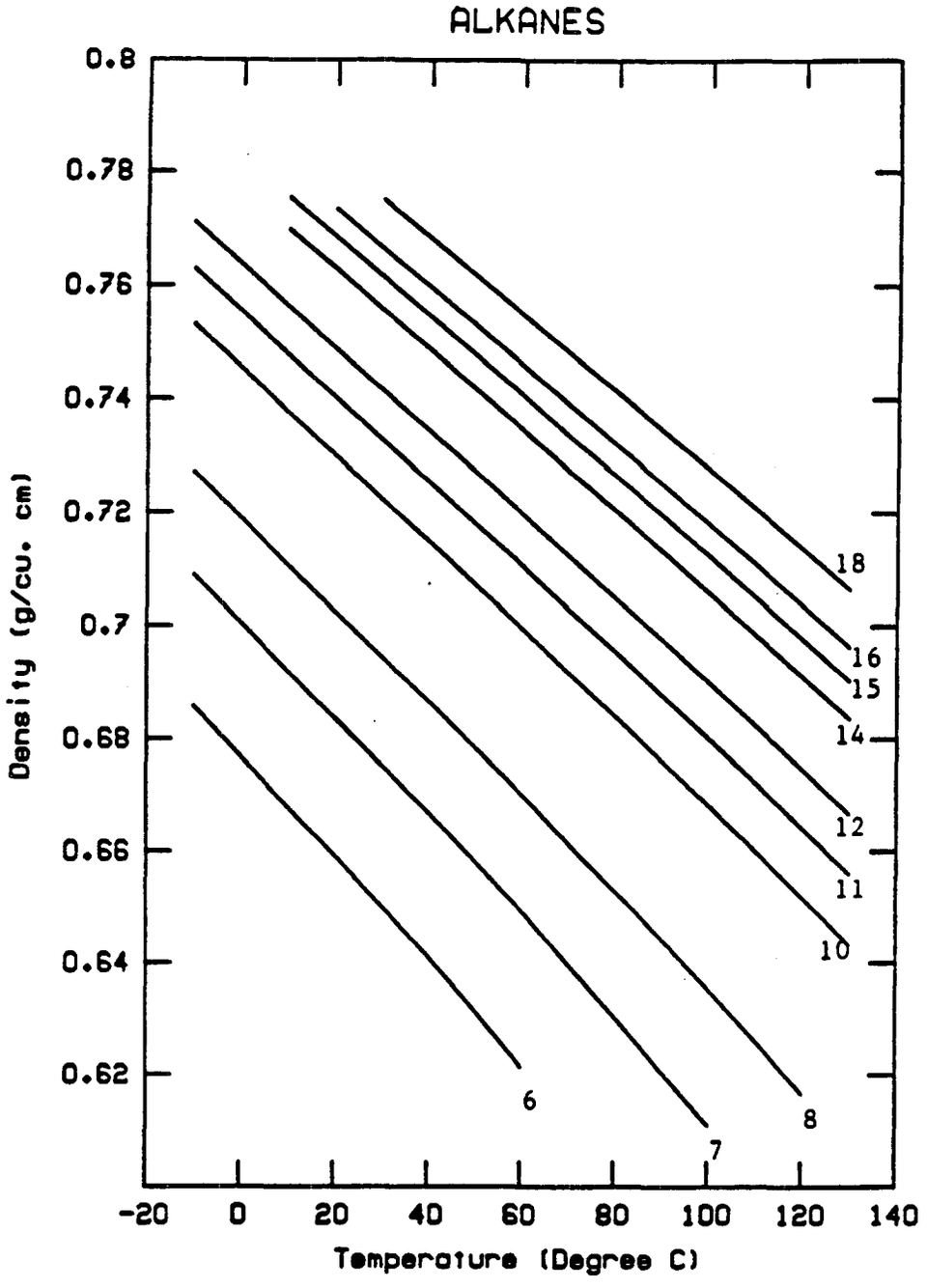
ALKANES
0.8
0.78
0.76
0.74
0.72
0.7
0.68
0.66
0.64
0.62
Density (g/cu. cm)
18
16
15
14
12
11
10
8
7
6
-20
0
20
40
60
80
100
120
140
Temperature (Degree C)

Fig. 1

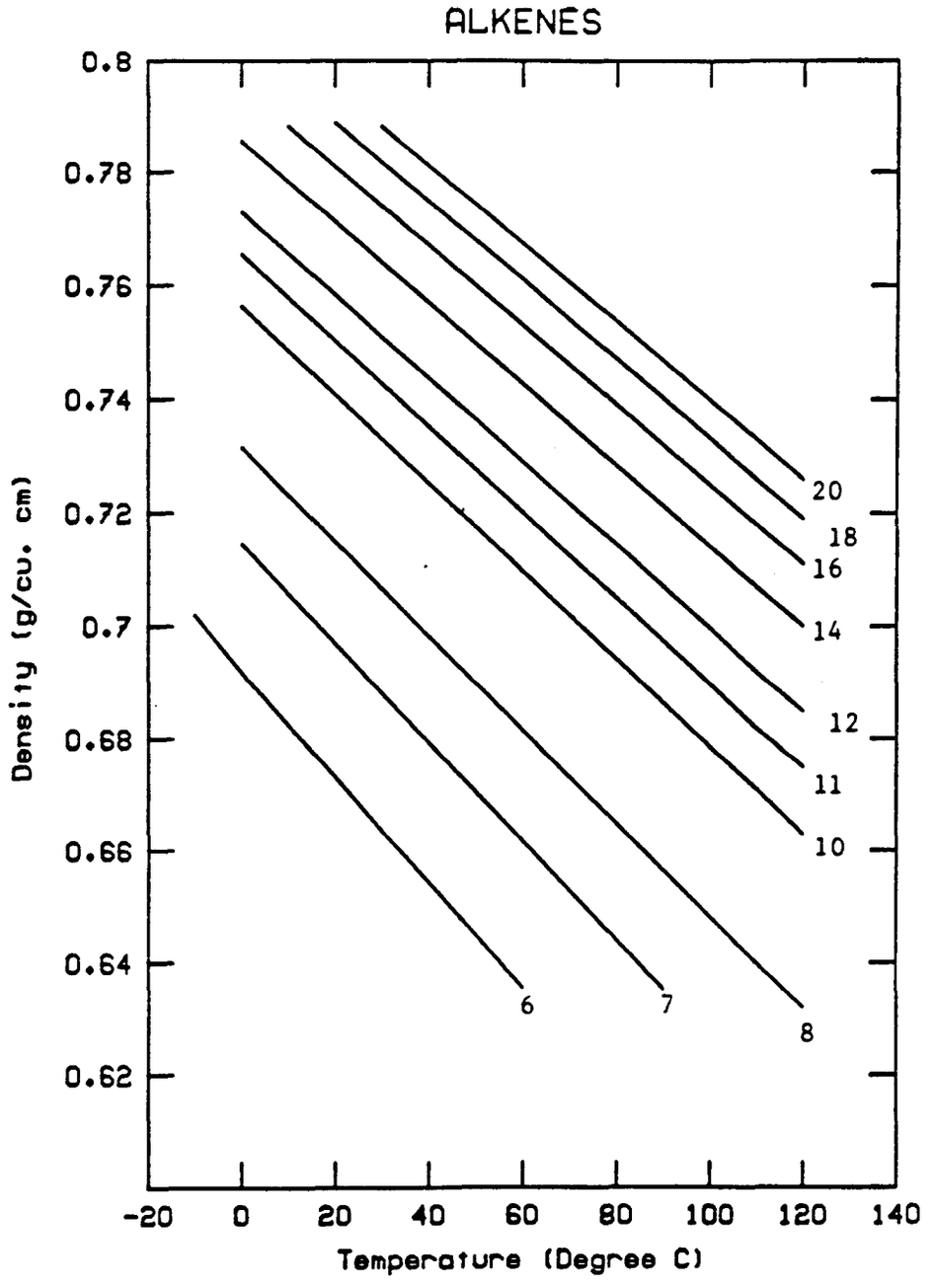
ALKENES
0.8
0.78
0.76
0.74
0.72
0.7
0.68
0.66
0.64
0.62
Density (g/cu. cm)
20
18
16
14
12
11
10
8
7
6
-20
0
20
40
60
80
100
120
140
Temperature (Degree C)

Fig. 2

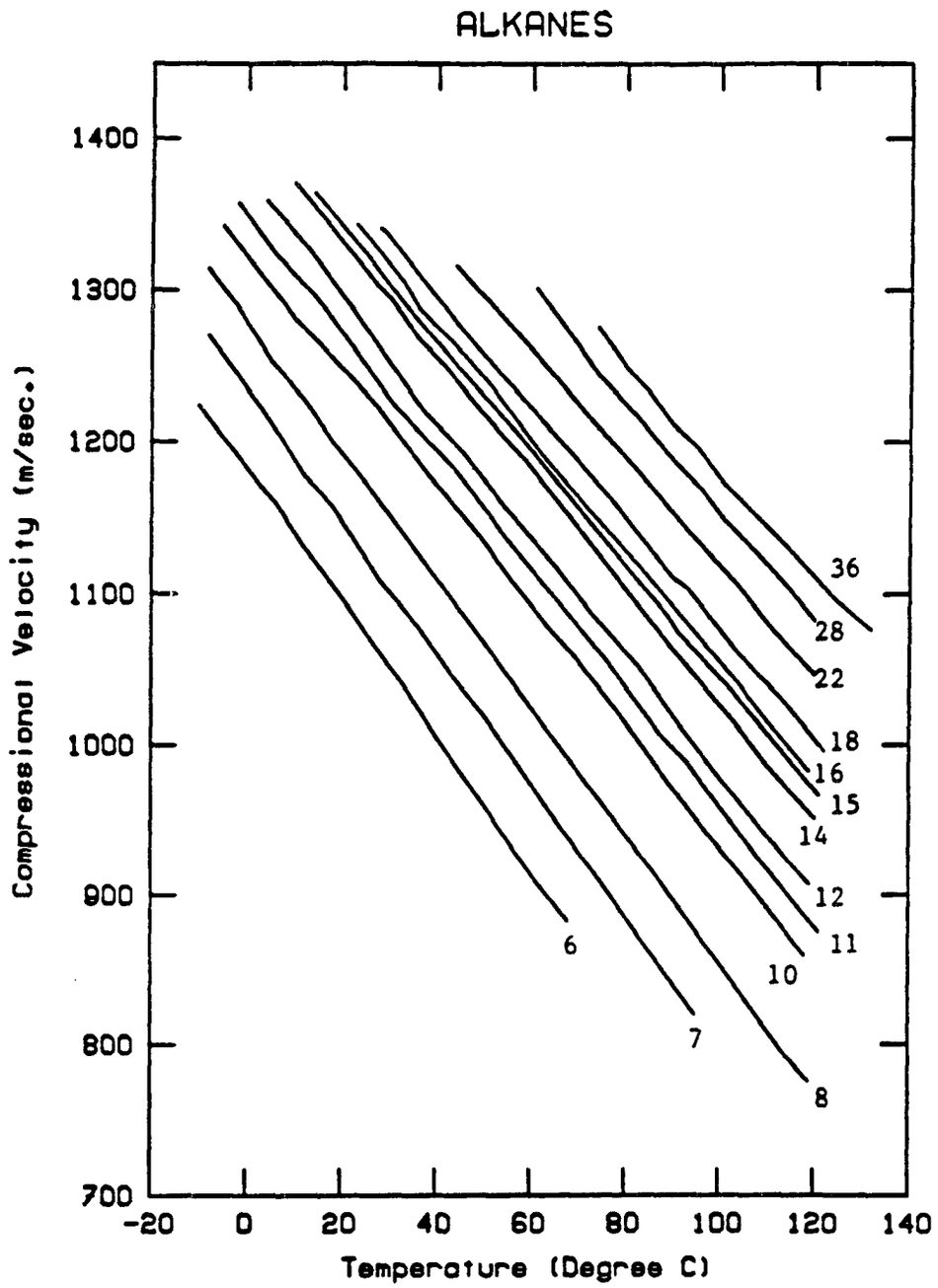
ALKANES
Compressional Velocity (m/sec.)
1400
1300
1200
1100
1000
900
800
700
-20
0
20
40
60
80
100
120
140
Temperature (Degree C)
36
28
22
18
16
15
14
12
11
10
7
6
8

Fig. 3

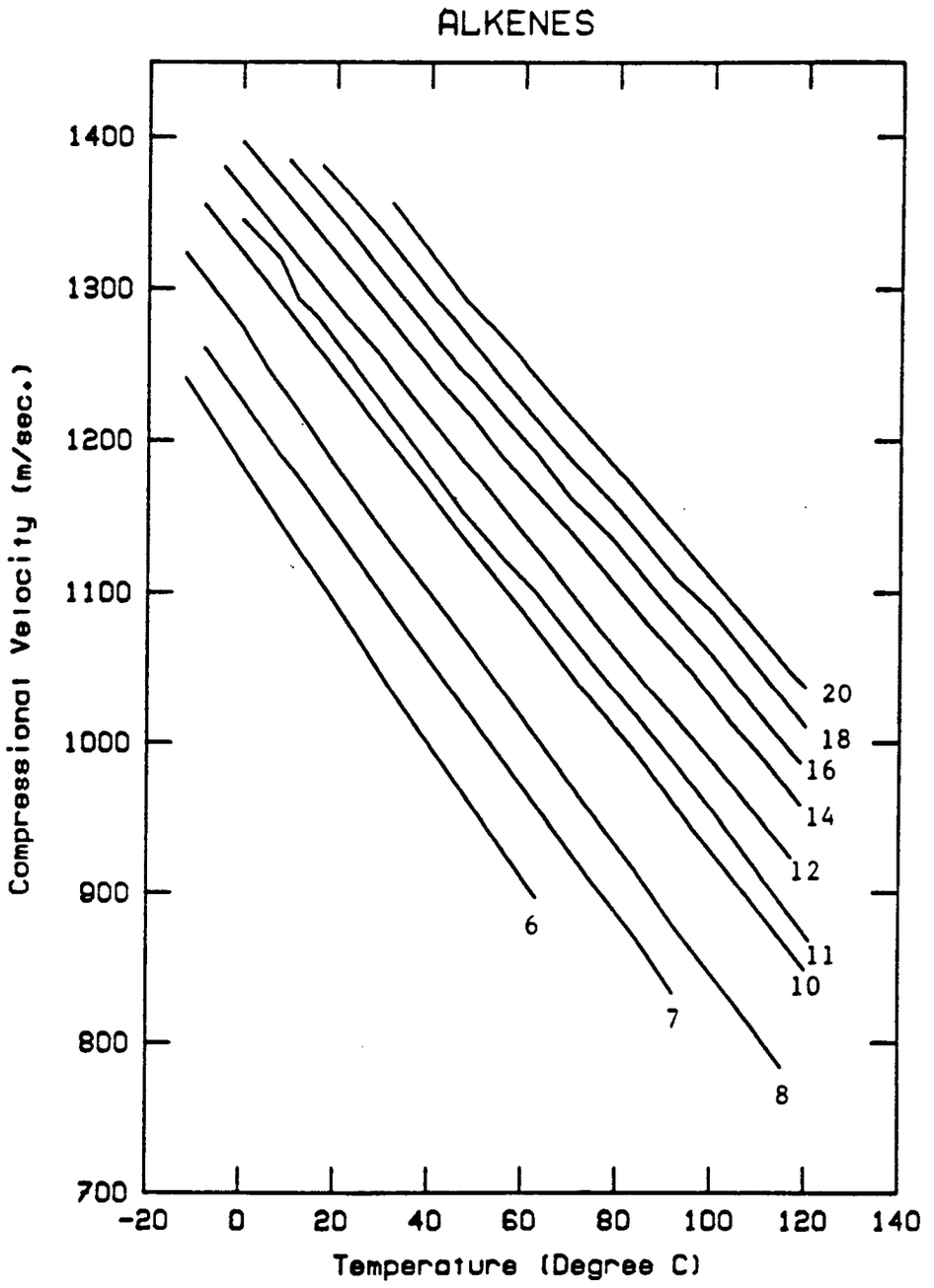
ALKENES
Compressional Velocity (m/sec.)
1400
1300
1200
1100
1000
900
800
700
-20
0
20
40
60
80
100
120
140
Temperature (Degree C)
20
18
16
14
12
11
10
6
7
8

Fig. 4

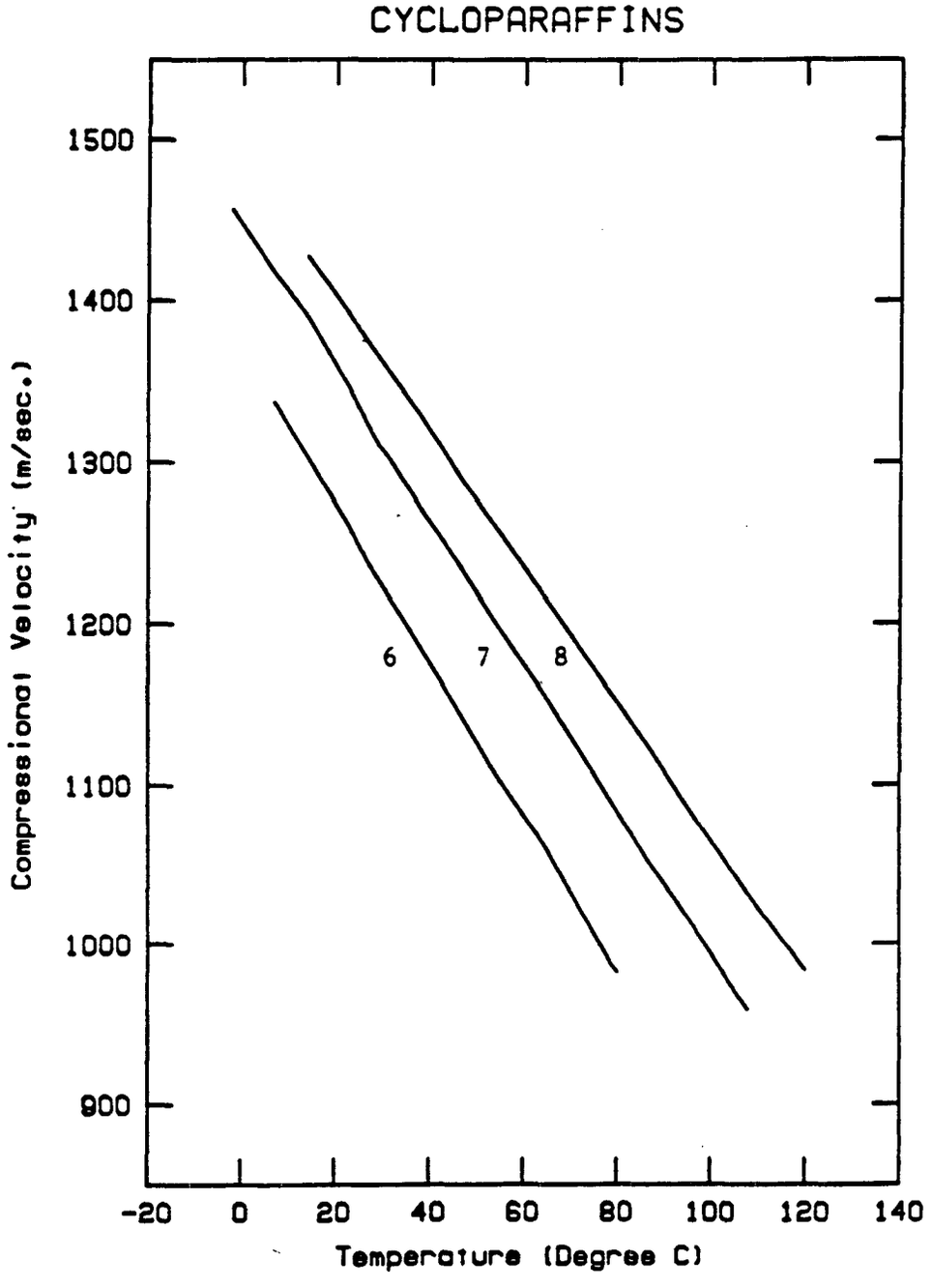
CYCLOPARAFFINS
1500
1400
1300
1200
1100
1000
900
Compressional Velocity (m/sec.)
6
7
8
-20
0
20
40
60
80
100
120
140
Temperature (Degree C)

Fig. 5

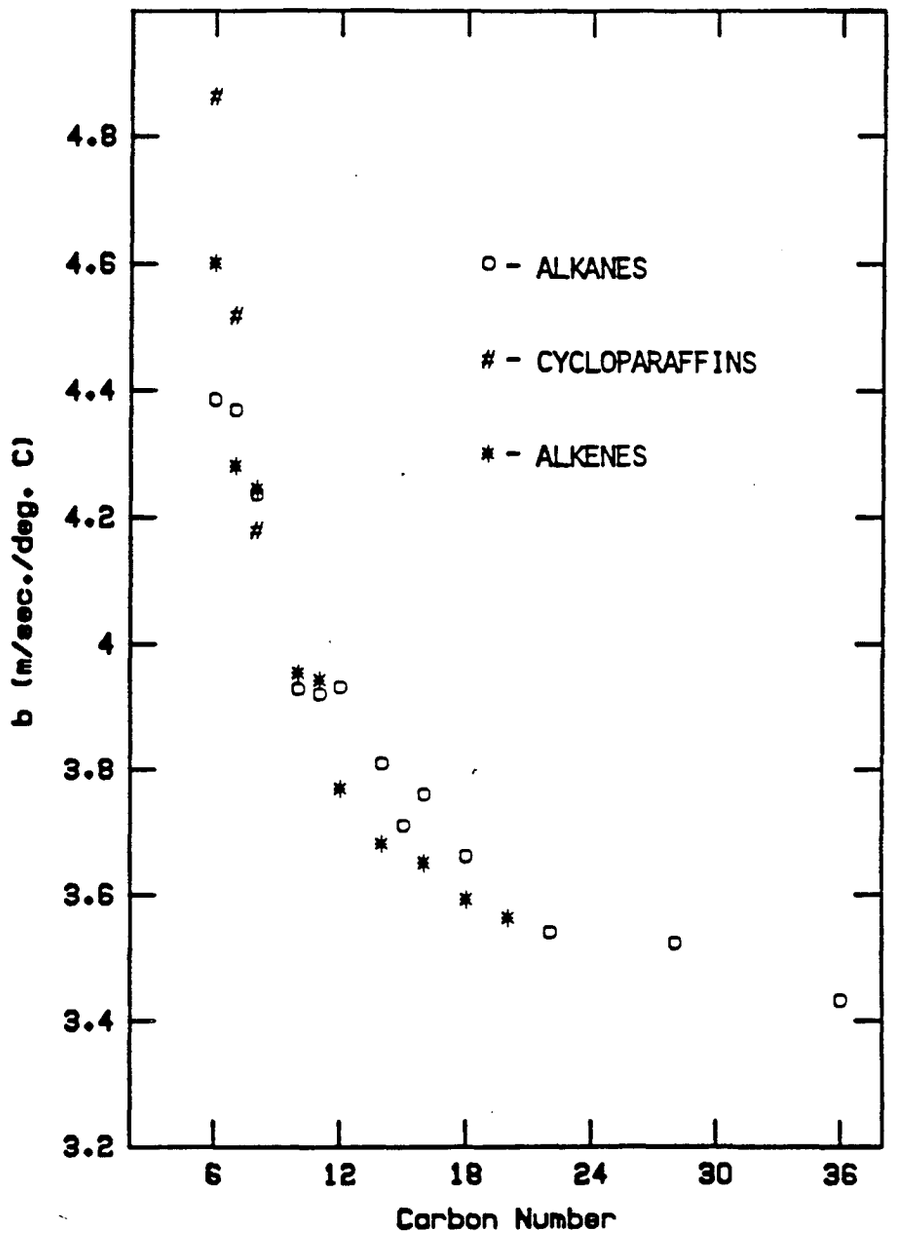
4.8
4.6
4.4
4.2
4
3.8
3.6
3.4
3.2
b (m/sec./deg. C)
6
12
18
24
30
36
Carbon Number
o - ALKANES
- CYCLOPARAFFINS
* - ALKENES

Fig. 6

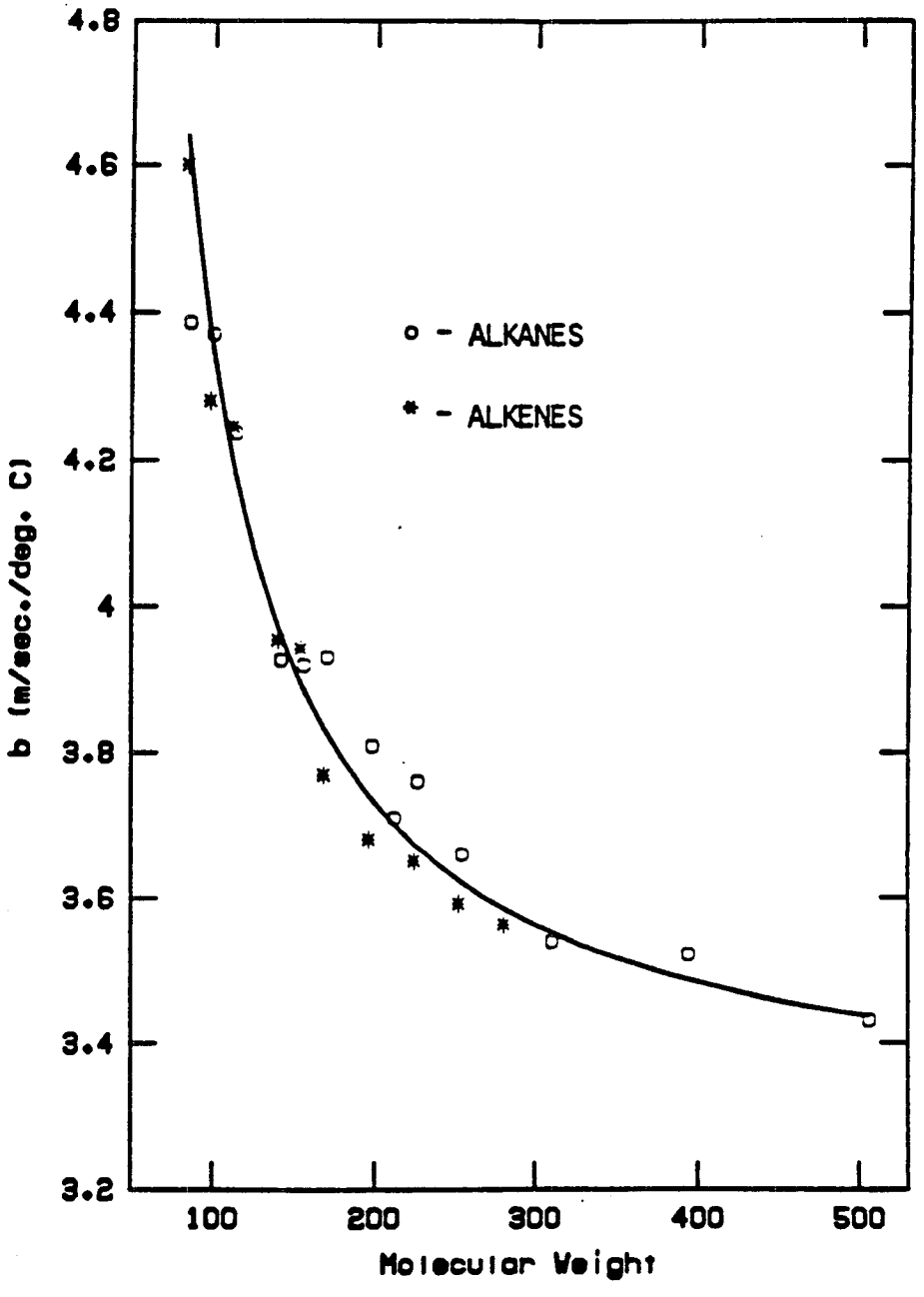
4.8
4.6
4.4
4.2
4
3.8
3.6
3.4
3.2
b (m/sec./deg. C)
o - ALKANES
* - ALKENES
100
200
300
400
500
Molecular Weight

Fig. 7

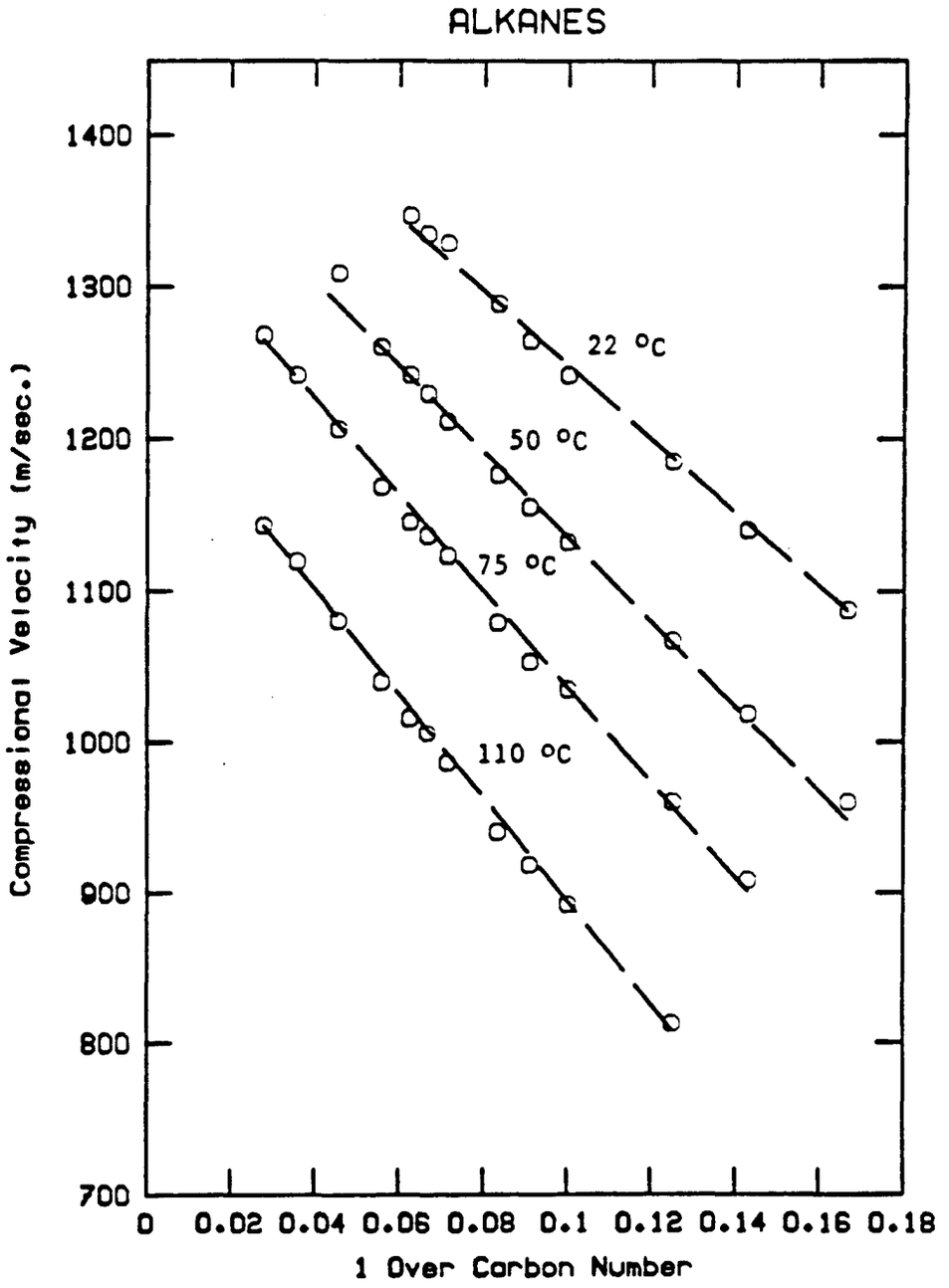
ALKANES
Compressional Velocity (m/sec.)
1400
1300
1200
1100
1000
900
800
700
0
0.02
0.04
0.06
0.08
0.1
0.12
0.14
0.16
0.18
1 Over Carbon Number
22 °C
50 °C
75 °C
110 °C

Fig. 8

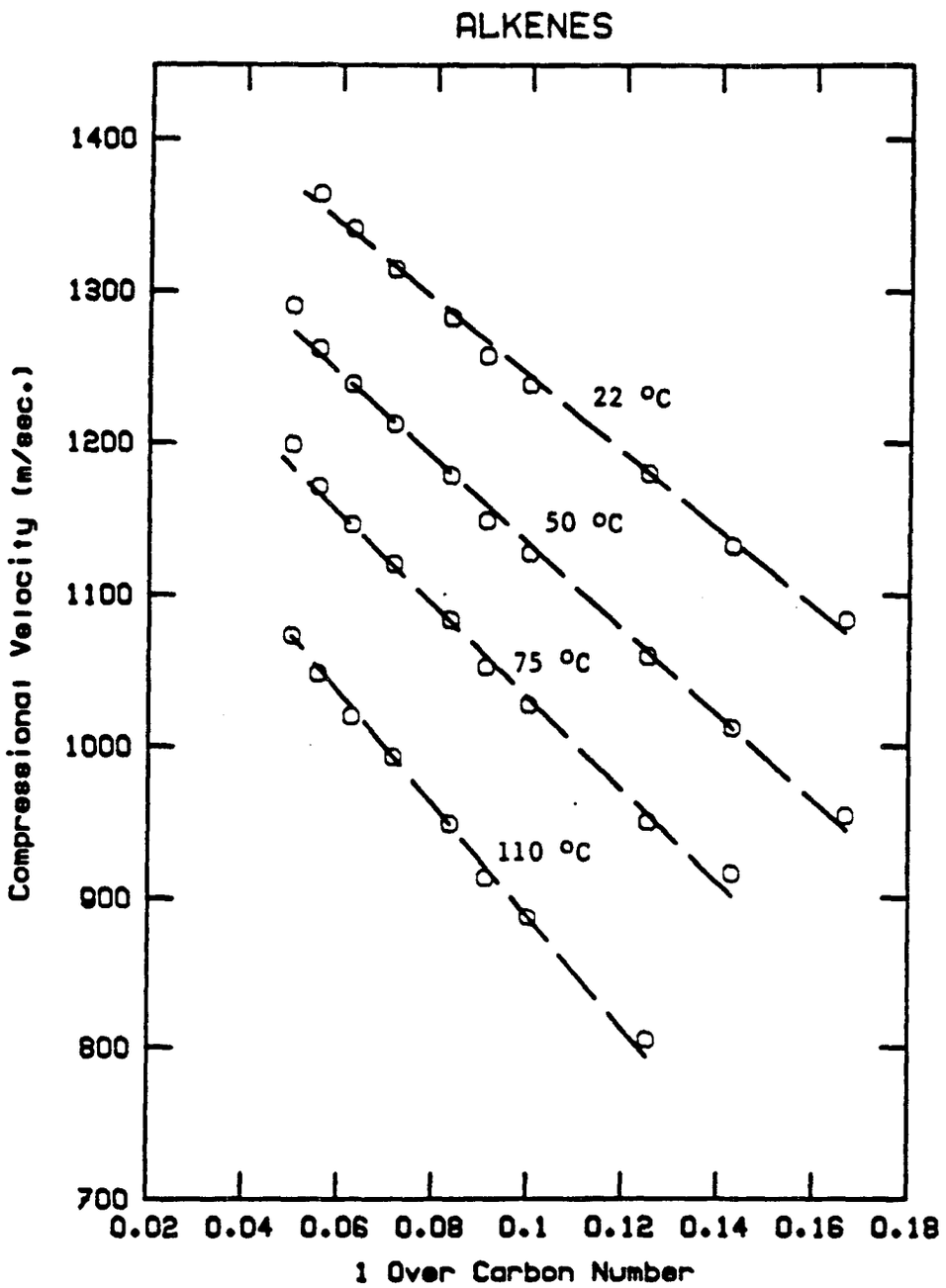
ALKENES
Compressional Velocity (m/sec.)
1400
1300
1200
1100
1000
900
800
700
22 °C
50 °C
75 °C
110 °C
0.02
0.04
0.06
0.08
0.1
0.12
0.14
0.16
0.18
1 Over Carbon Number

Fig. 9

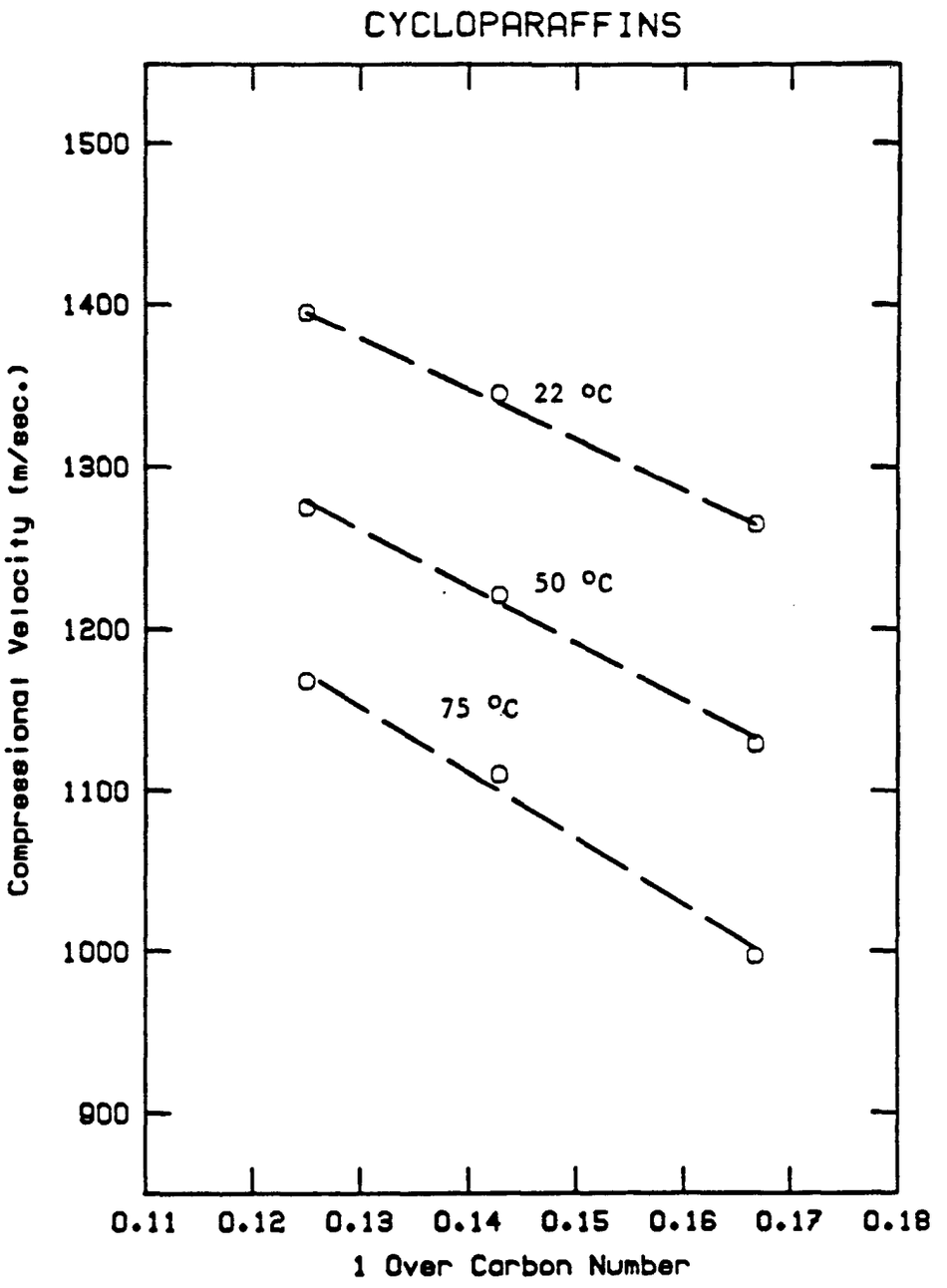
CYCLOPARAFFINS
1500
1400
1300
1200
1100
1000
900
Compressional Velocity (m/sec.)
22 °C
50 °C
75 °C
0.11
0.12
0.13
0.14
0.15
0.16
0.17
0.18
1 Over Carbon Number

Fig. 10

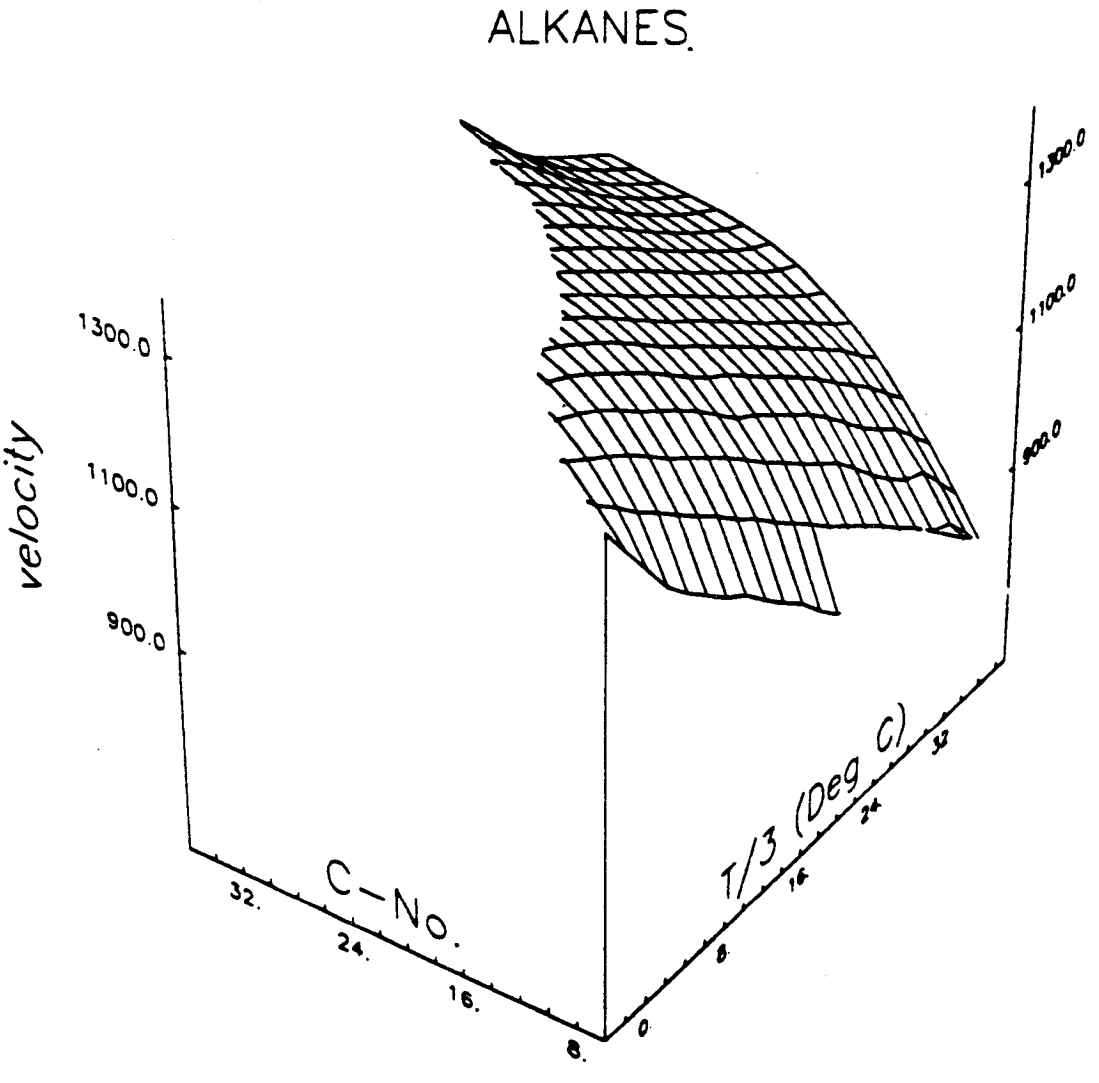
ALKANES.
velocity
1300.0
1100.0
900.0
C-No.
32.
24.
16.
8.
T/3 (Deg C)
0
8
16
24
32
1300.0
1100.0
900.0

Fig. 11

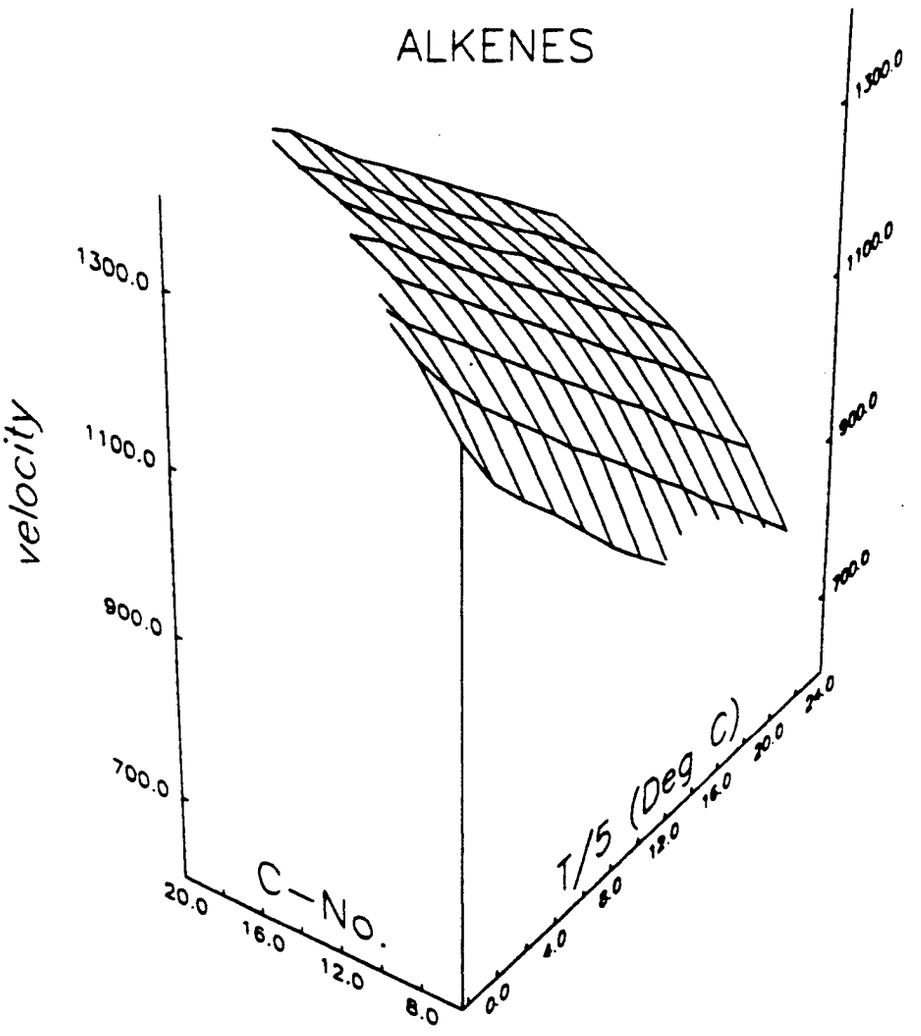
ALKENES
velocity
1300.0
1100.0
900.0
700.0
C-No.
20.0
16.0
12.0
8.0
T/5 (Deg C)
0.0
4.0
8.0
12.0
16.0
20.0
24.0
1300.0
1100.0
900.0
700.0

Fig. 12

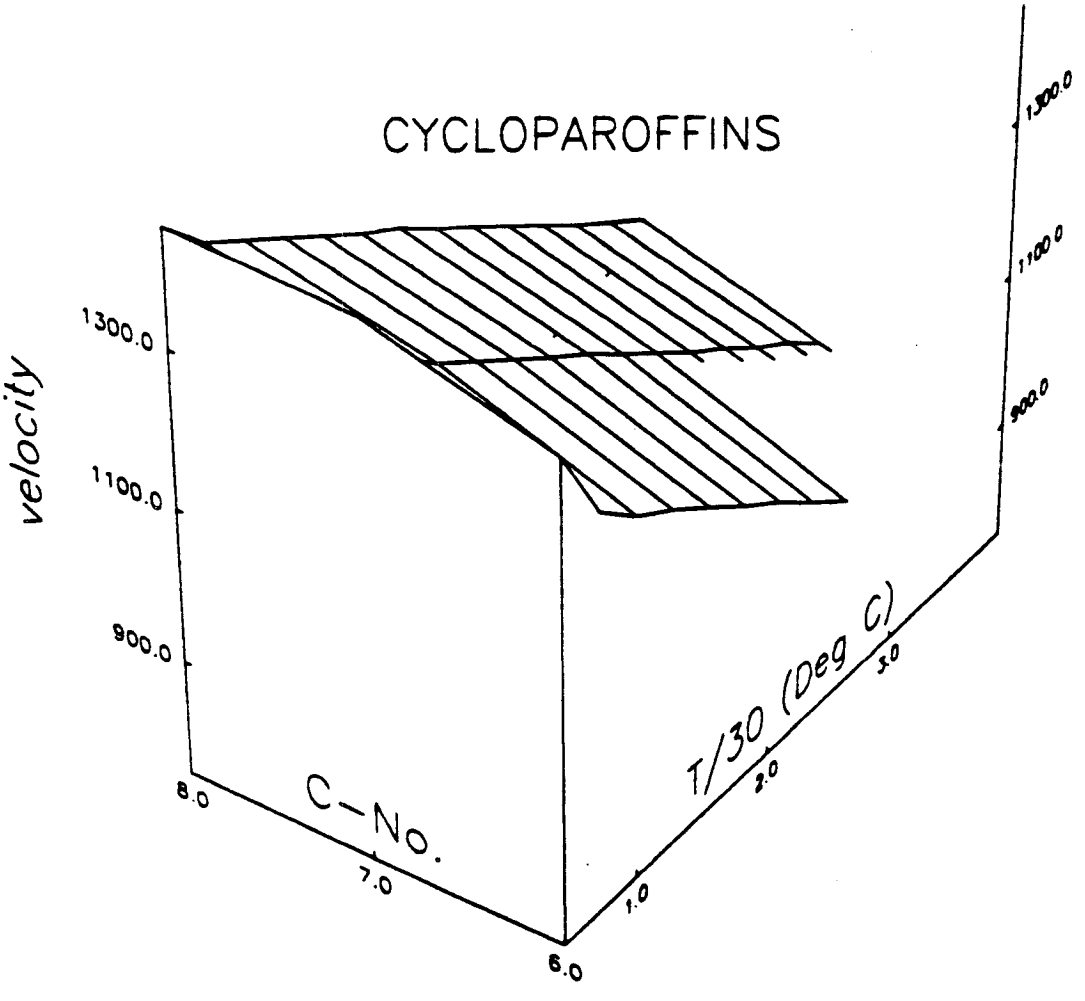
CYCLOPAROFFINS
velocity
1300.0
1100.0
900.0
C-No.
8.0
7.0
6.0
T/30 (Deg C)
1.0
2.0
3.0
1300.0
1100.0
900.0

Fig. 13

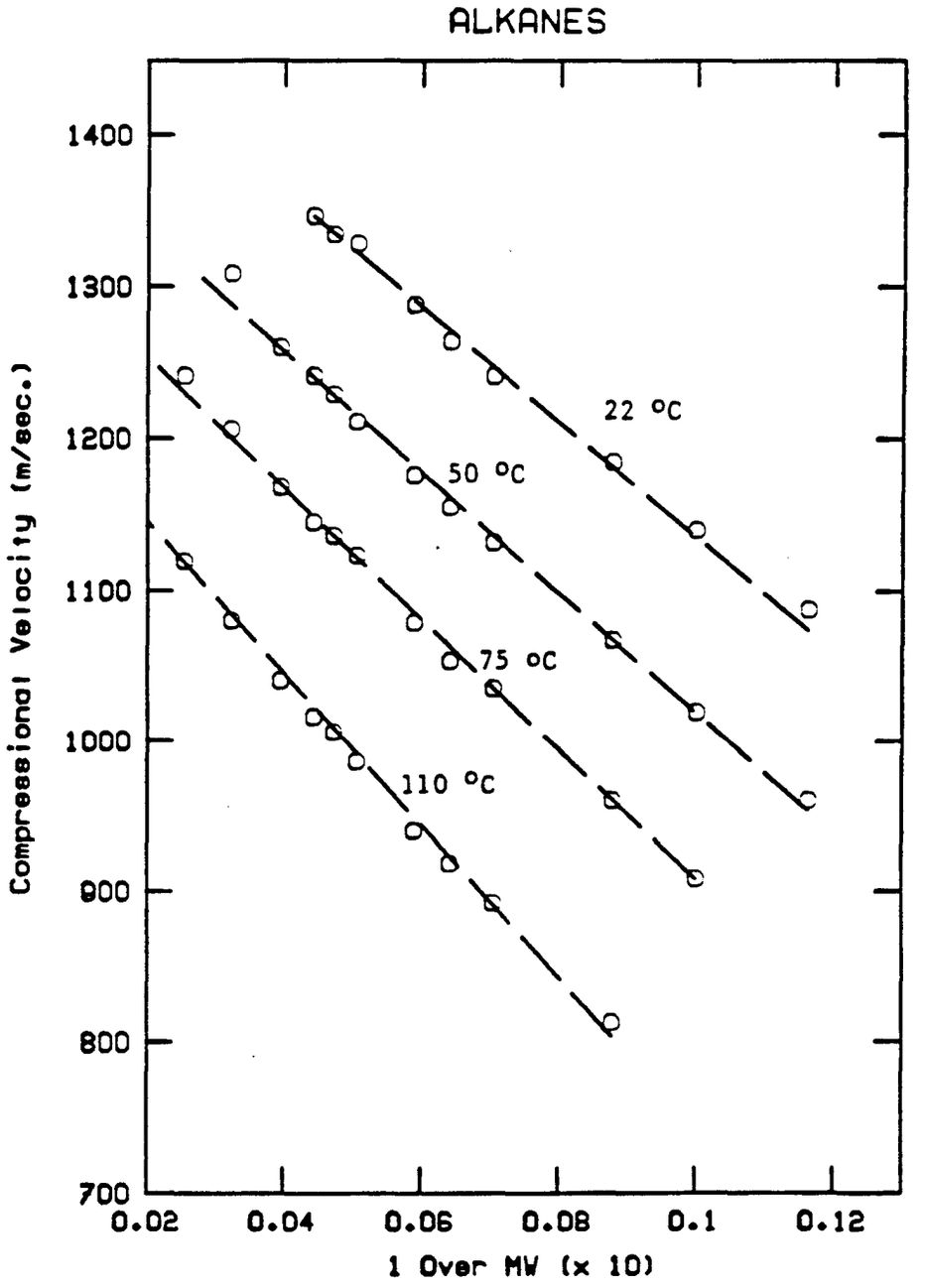
ALKANES
Compressional Velocity (m/sec.)
1400
1300
1200
1100
1000
900
800
700
0.02
0.04
0.06
0.08
0.1
0.12
1 Over MW (x 10)
22 °C
50 °C
75 °C
110 °C

Fig. 14

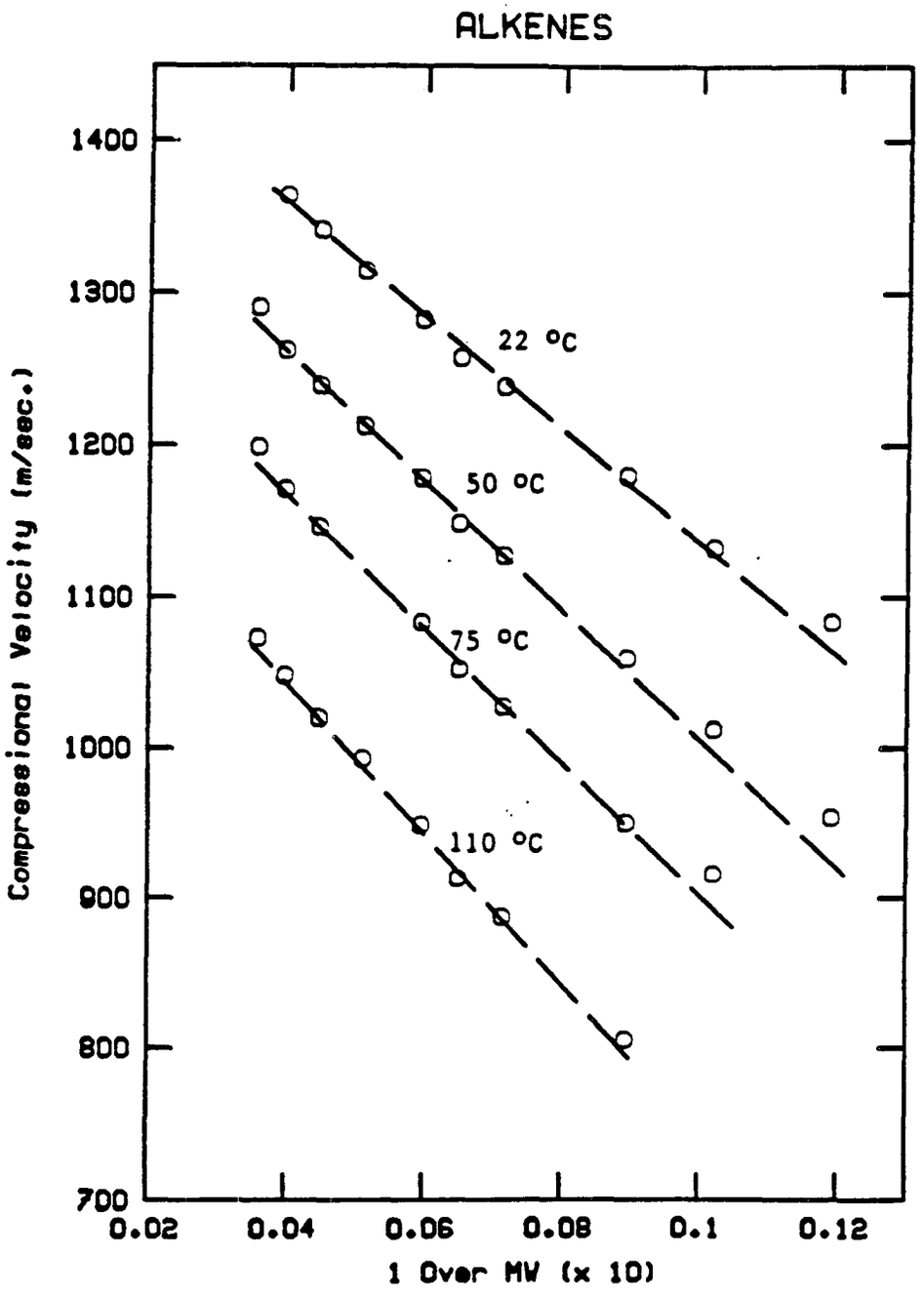
ALKENES
Compressional Velocity (m/sec.)
1400
1300
1200
1100
1000
900
800
700
22 °C
50 °C
75 °C
110 °C
0.02
0.04
0.06
0.08
0.1
0.12
1 Over MW (x 10)

Fig. 15

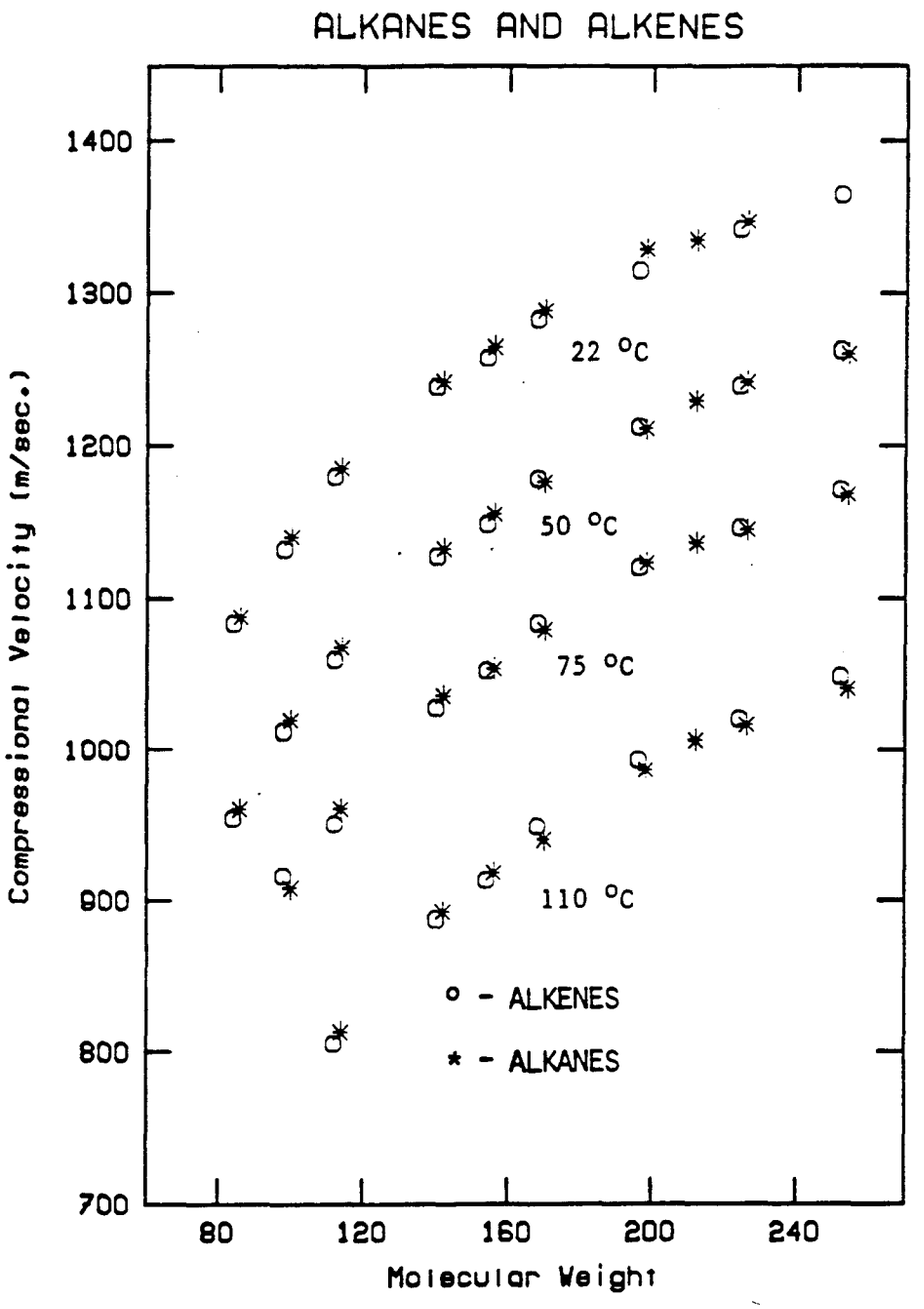
ALKANES AND ALKENES
Compressional Velocity (m/sec.)
1400
1300
1200
1100
1000
900
800
700
80
120
160
200
240
Molecular Weight
22 °C
50 °C
75 °C
110 °C
o - ALKENES
* - ALKANES

Fig. 16

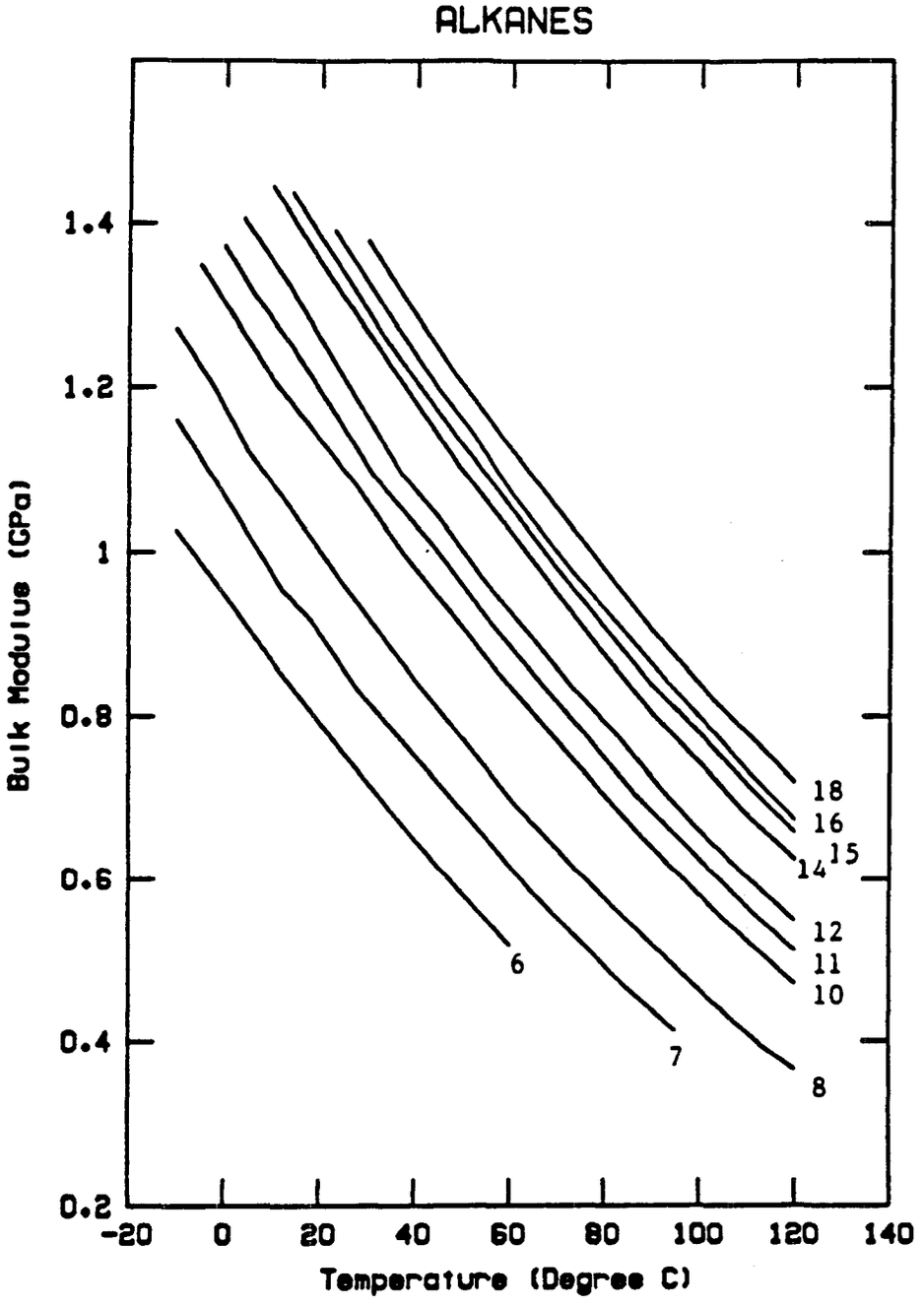
ALKANES
Bulk Modulue (GPa)
1.4
1.2
1
0.8
0.6
0.4
0.2
-20
0
20
40
60
80
100
120
140
Temperature (Degree C)
18
16
15
14
12
11
10
6
7
8

Fig. 17

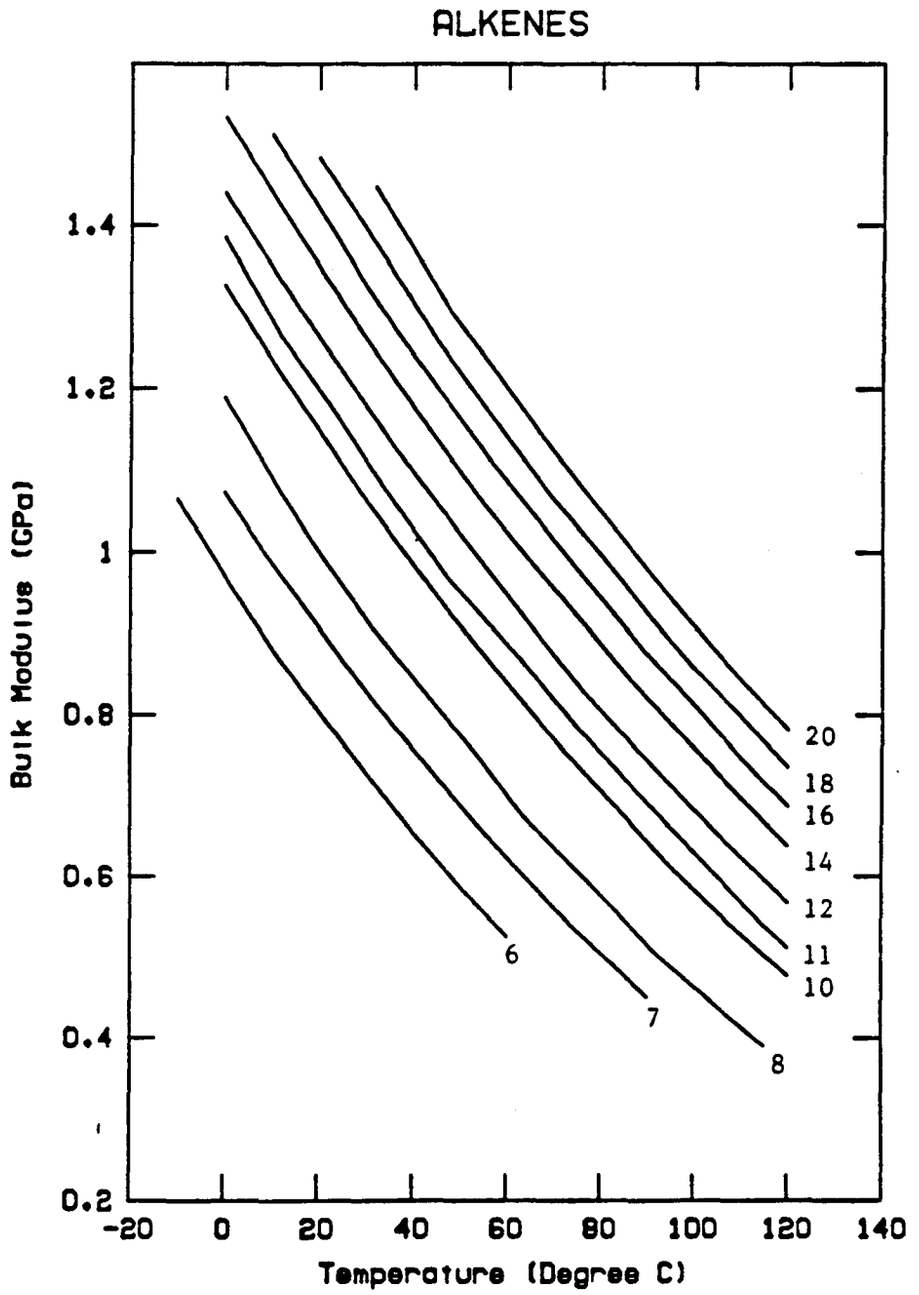
ALKENES
Bulk Modulus (GPa)
1.4
1.2
1
0.8
0.6
0.4
0.2
-20
0
20
40
60
80
100
120
140
Temperature (Degree C)
20
18
16
14
12
11
10
6
7
8

Fig. 18

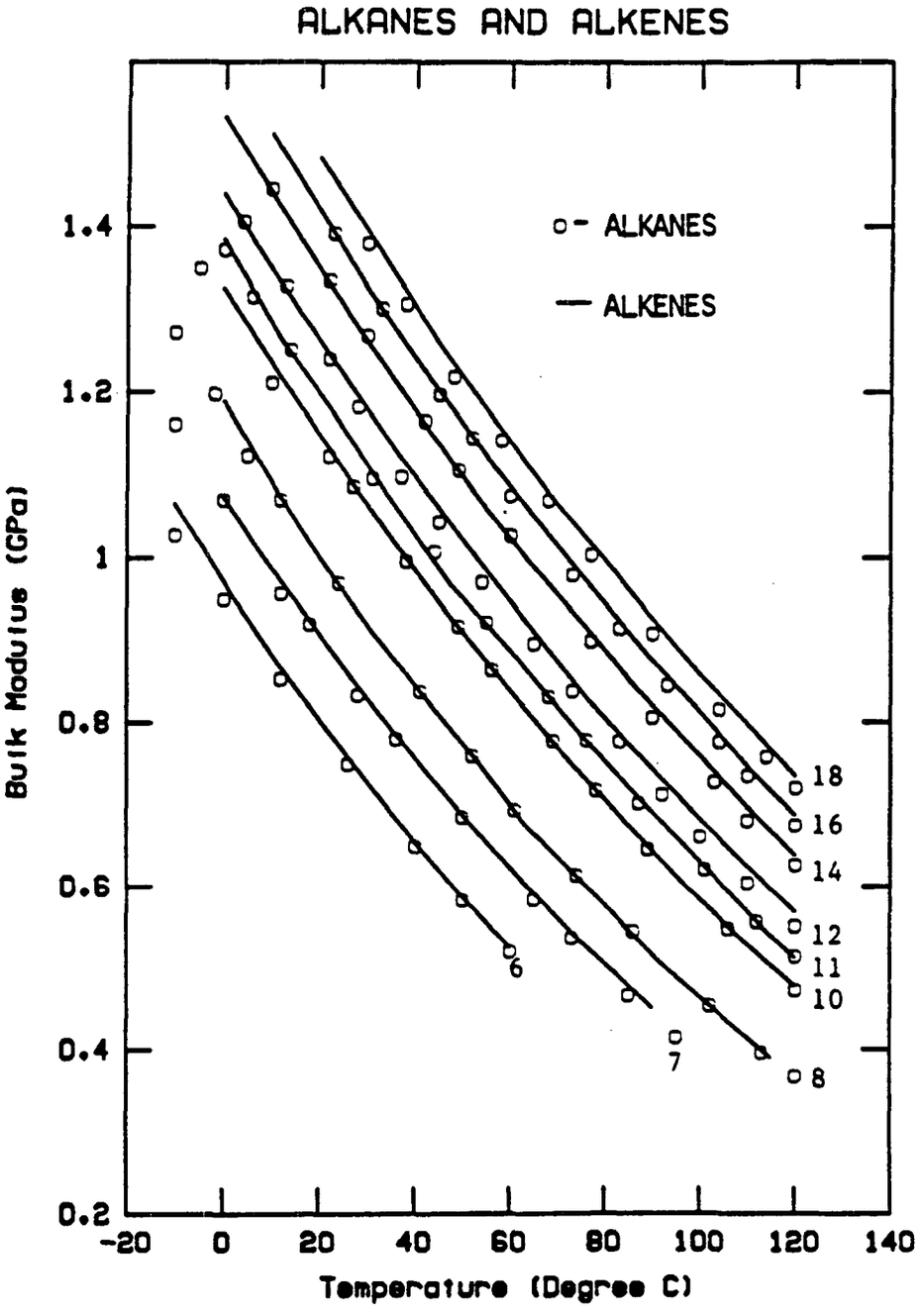
ALKANES AND ALKENES
o- ALKANES
— ALKENES
Bulk Modulus (GPa)
1.4
1.2
1
0.8
0.6
0.4
0.2
-20
0
20
40
60
80
100
120
140
Temperature (Degree C)
18
16
14
12
11
10
8
7
6

Fig. 19

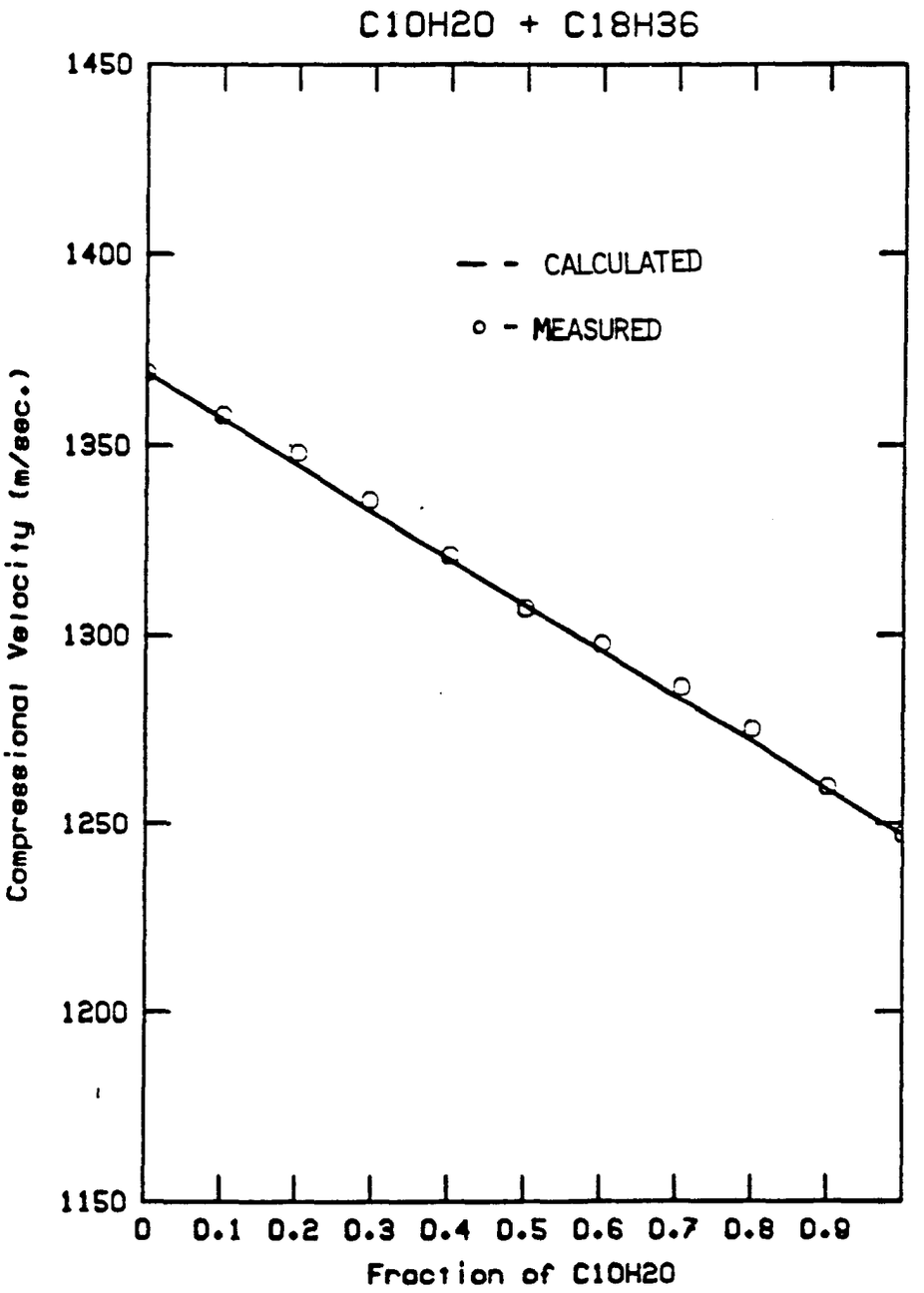
C10H20 + C18H36
1450
1400
1350
1300
1250
1200
1150
— - CALCULATED
o - MEASURED
Compressional Velocity (m/sec.)
0
0.1
0.2
0.3
0.4
0.5
0.6
0.7
0.8
0.9
Fraction of C10H20

Fig. 20

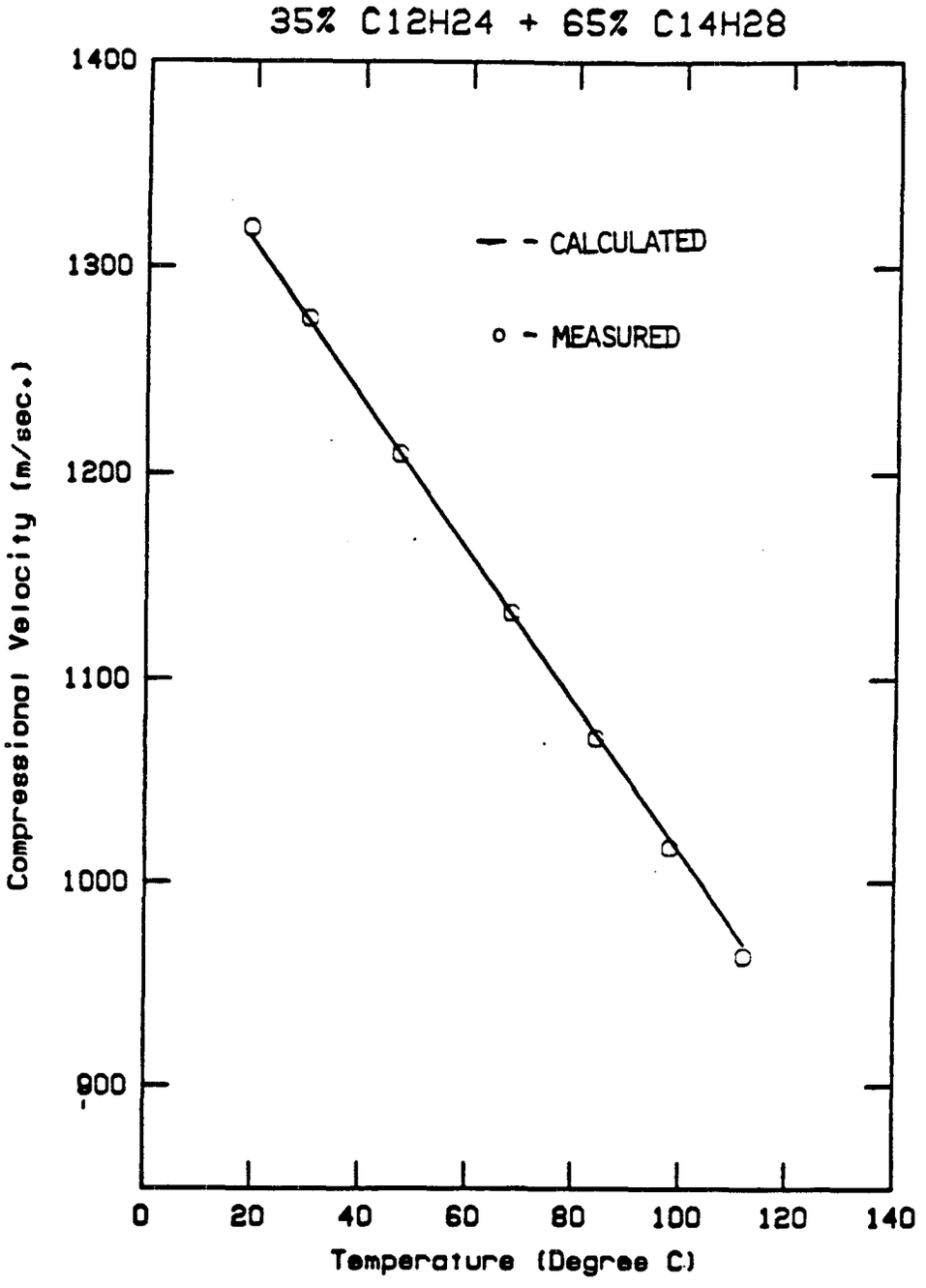
35% C12H24 + 65% C14H28
1400
1300
1200
1100
1000
900
— - CALCULATED
o - MEASURED
Compressional Velocity (m/sec.)
0
20
40
60
80
100
120
140
Temperature (Degree C)

Fig. 21

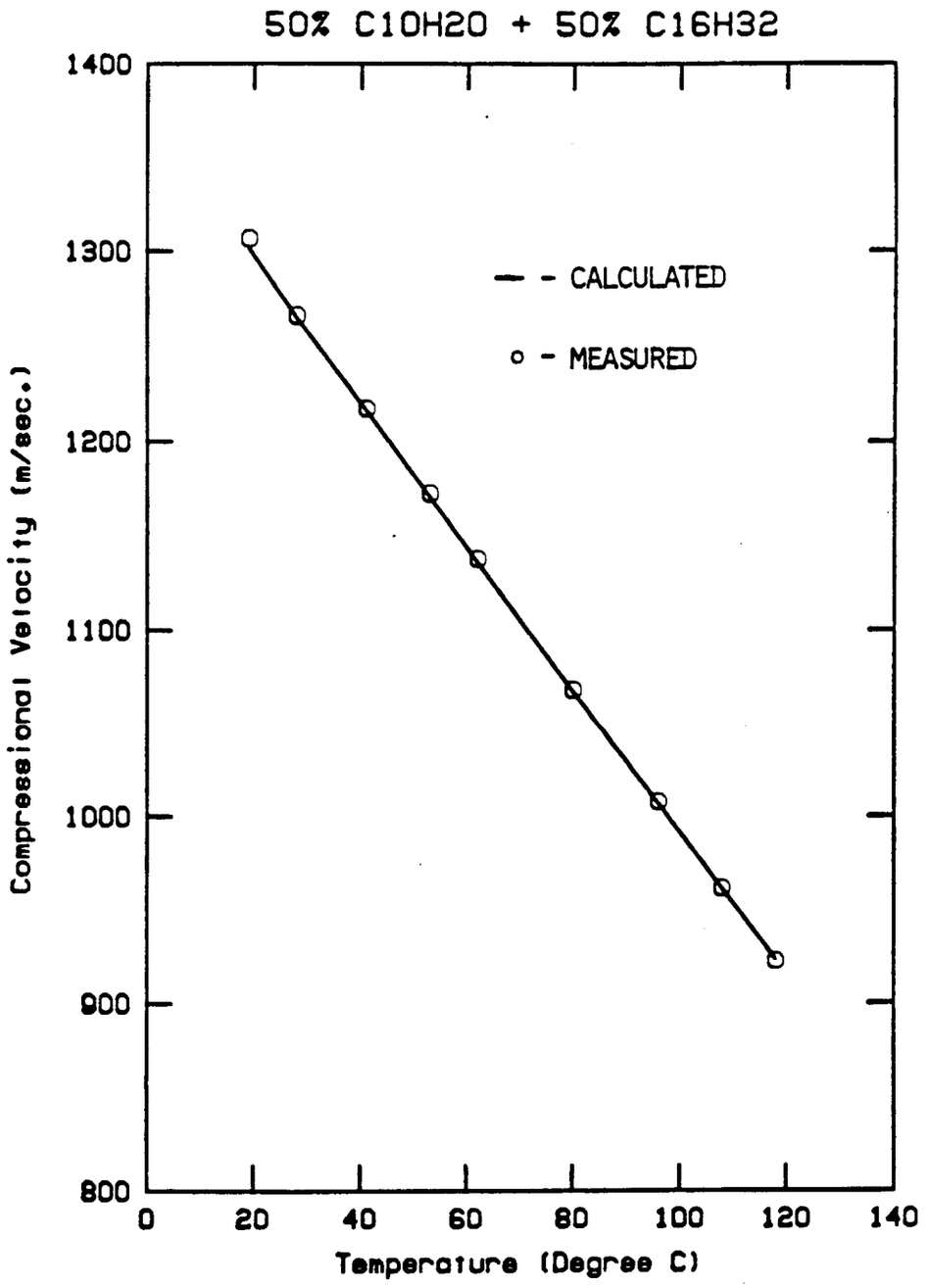
50% C10H20 + 50% C16H32
1400
1300
1200
1100
1000
900
800
Compressional Velocity (m/sec.)
— - CALCULATED
o - MEASURED
0
20
40
60
80
100
120
140
Temperature (Degree C)

Fig. 22

CHAPTER 3

ACOUSTIC VELOCITIES IN PETROLEUM OILS

ABSTRACT

A series of experiments were carried out in the laboratory on acoustic wave velocities in oils. The samples include 8 dead* crude oils, 2 refined petroleum hydrocarbons, and 1 live** oil.

In this chapter we first show the measured acoustic velocities in these oils as a function of both temperature and pressure; then discuss the experimental results in light of the various existing theories and models of the liquid state for the purpose of interpreting and understanding the acoustic velocity behaviors of the oils. Correlations are made between the acoustic velocity and temperature, pressure, API gravity, and molecular weight. Empirical equations are established which can be used to calculate the acoustic velocities in oils with known API gravities. Finally, various applications or potential applications of the experimental results are discussed.

INTRODUCTION

With the rapid developments in seismic and well logging technologies, more detailed studies on hydrocarbon reservoirs are getting more and more attention. In recent years, seismic borehole to borehole tomography, 3-D seismic reservoir imaging. seismic delineation of reservoir fluid saturations, seismic evaluation and characterization of hydrocarbon reservoirs, seismically monitoring production and enhanced oil

* Here "dead" oil refers to stock tank oil which does not contain dissolved gas
** "Live" oil refers to oil which has high content of dissolved gas.

recovery (EOR) processes in time, and detailed borehole sonic loggings have begun to emerge. There is little doubt that these technologies will become routine in the near future. However, acoustic properties of both reservoir fluids and rocks must be understood in order to utilize these new methods and interpret their results. Therefore, it is the main purpose of this chapter to provide acoustic wave velocity information on different kinds of oils.

As has been well known, the acoustic velocities in fluids are in fact pure thermodynamic quantities. From this point of view measurements of acoustic velocities in fluids can not give more information than that included in the data of the equation of state. However, the precision of the information on the fluids actually obtained by acoustic experiments is often one or two orders of magnitude higher than that of direct thermodynamic measurements (van Dael and van Itterbeek, 1965). For this reason, even if complete pressure-volume-temperature (P-V-T) data are available, acoustic velocity experiments are useful as an independent check of these data. If no complete P-V-T data are available, the interest of acoustic velocity measurements is of course obvious. On the other side, if acoustic velocity data are available, one can use these data to derive more accurate P-V-T properties of the fluids.

The importance of the acoustic properties of reservoir liquids have not gotten enough attention thus far. i.e., there are very few experimental data of acoustic velocities in crude oils, and no systematic studies. Therefore, the intention of this paper is to fill in this void.

In the experiments, we measured acoustic velocities in the ultrasonic frequency range (about 800 KHz) in 8 dead oils and 2 refined petroleum hydrocarbons which cover a wide range of API gravities (from 5 to 62 degrees). And acoustic velocities in a live oil which contains substantial amount of dissolved gases were also measured. The experimental results show that the velocities in oils all depend strongly on temperature and pressure. And dissolved gases lower the acoustic velocities in live oils substantially.

In this chapter, we first briefly describe the experimental method and procedures and the properties of the oil samples used in the experiments. Secondly, we show the experimental results of acoustic velocities in the dead and live oils, relations between acoustic velocities in and API gravities of the oils, and temperature and pressure derivatives of the velocities. Thirdly, discussions are made based on various theories and models of the liquid state to better understand and interpret the acoustic velocity behaviors of both the dead and the live oils, followed by discussions on the relations between acoustic velocities and P-V-T measurements. Fourthly, we correlate the acoustic velocities in the dead oils with temperature, pressure, API gravities and molecular weights of the oils, and establish empirical equations which can be used to calculate or estimate the acoustic velocities in oils if the API gravities are known. Finally, we discuss some applications or potential applications of our velocity results in both geophysical and petroleum engineering aspects, and draw some conclusions on this study.

EXPERIMENTS

Method

The pulse transmission method was employed in the experiments. The set-up basically consisted of a pulse generator/receiver, a digital oscilloscope, two acoustic transducers, and a pressure vessel.

The principle of the pulse transmission method is simple. In the experiments, electrical pulses which were generated by the pulse generator were sent to one of the transducers which converts electrical energy into mechanical vibration. Ultrasonic waves traveling through the fluid sample were picked up by the other transducer which converts mechanical energy back to electrical signal and sent to the oscilloscope for measurements.

Temperatures were controlled by a heating coil and a temperature controller, and measured by two thermocouples connected to a digital meter. The accuracy of the temperature measurements was approximately $0.5^{\circ}C$.

Pressures in the experiments were controlled by an automatic fluid pump and read through a digital pressure gauge. The accuracy was about 10 psi.

The frequency of the ultrasonic waves was around 800 KHz.

Travel times of the ultrasonic waves through the oil sample were measured on a digital oscilloscope with precision of 0.05 microseconds. Then, ultrasonic velocities were calculated by

$$C(P,T) = \frac{L(P,T)}{\Delta t(P,T)}$$

where L(P,T) is the pressure and temperature corrected distance between the two transducers, and $\Delta t(P,T)$ is the travel time of the ultrasonic waves which is a function of pressure and temperature.

Pressure and temperature corrections on the distance between the two transducers were made with ultrasonic measurements in distilled water (Fig. 1a, b), using Wilson's (1959) data as a reference. The deviation of our measured velocity data from Wilson's was assumed being caused by shortening (upon increasing pressure) and expansion (upon increasing temperature) of the spacers between the acoustic transducers.

We also compared our measured velocities (pressure and temperature corrected) in Soltrol 130 oil (oil H) with those measured by Katahara (1987, personal communication). The agreement was excellent (deviation within 0.2%). Furthermore, we also measured ultrasonic velocities in mercury (Figure 2). The deviation of our data from those measured by Hunter et al (1963) was only 0.5%. Therefore, we believe that the velocity data from the experiments have accuracy better than 1%.

Procedures

The experimental procedures for all the oils, except the "live" oil, were exactly the same. Acoustic transducers were put into a plastic tube with spacers. Then the oil to be measured was injected into the tube by syringe. The plastic tube was completely full of the oil sample without visible gas bubbles. Afterwards, the transducer-plastic tube assembly was put into the pressure vessel for test. Between measuring points of

different pressures and temperatures, we waited long enough to assure the pressure and temperature equilibrium inside the pressure vessel (usually 1 hour at one temperature point, about 10 to 15 minutes at one pressure point). The waveforms at each measuring point were stored on floppy disks.

The procedure for the live oil measurement was basically similar but a little different. First, the plastic tube with transducers was completely filled with mercury. Then after the transducer-plastic tube assembly was put into the pressure vessel, the pressure was increased to about 6,000 psig (about 414 bars). The "live" oil which was stored in a different vessel under a pressure (also about 6,000 psig) much higher than its critical pressure (2,994 psig or 206 bars at 160° F) was "transferred" to the plastic tube through pressure tubings connecting the two pressure vessels. Therefore, the mercury inside the plastic tube was gradually displaced out through another pressure tubing. During the transfer, we tried to keep the pressure gradient inside the plastic tubing as small as possible to assure that no dissolved gas could escape from the live oil. Usually, the transfer procedure took about 60 to 90 minutes for transferring about 35 cc live oil.

PROPERTIES AND DESCRIPTIONS OF SAMPLES

In the experiments, we measured acoustic velocities in 3 light oils, 2 refined oils (light oils), 5 heavy oils, and 1 live oil. The API gravity of the oils ranges from about 5 to 62 degrees (density at 60° F and 1 atmosphere ranges from 1.037 to 0.73 g/cc).

The API (American Petroleum Institute) gravity of an oil is related to the density ρ (g/cc) of the oil at 60° F (15.6° C) and at 1 atmosphere pressure (14.7 psig):

$$API\ Gravity\ (Degree) = \frac{141.5}{\rho} - 131.5$$

Obviously water has an API gravity of approximately 10 degree.

All the crude oils except the "live" oil used in the experiments were stock tank oils, which means that they are dead oils.

Oil G is from an offshore pilot. Its API gravity is approximately 43 degree. Similarly, oil F is a typical light oil and has API gravity of about 34 degree.

The refined petroleum fluids used in the experiments were Soltrol (Trade Mark) oil (oil H) and normal decane (oil I), respectively. The Soltrol oil is a petroleum solvent which is mainly composed of isoparaffins with carbon numbers ranging from 10 to 13 (similar to kerosene). It is a colorless liquid with mild odor, and has a boiling interval of $176^\circ - 208^\circ$ C ($349^\circ - 406^\circ$ F). Its density at 60° F and 1 atmosphere is 0.75 grams/cc or equivalent to API gravity of 57 degree. The normal decane is a pure hydrocarbon with a formula of $C_{10}H_{22}$. Its molecular weight is 142 and density is about 0.73 g/cc at 60° F and 1 atmosphere (equivalent to API gravity of 62 degree). Its boiling and melting points are 174° and -30° C, respectively. Like the Soltrol oil, normal decane is also a colorless liquid with mild odor.

Three of the 5 heavy oils are from the same formation of an offshore pilot, namely, oils A, B, and E. They all are of low API gravity, low quality, and low maturity level. Oil A has an API gravity of 5 degree and is the least mature one. Oil B has an API gravity of 7 degree and is a little more mature than oil A. The API gravity of oil E is about 12 degree, and is more mature than the other two heavy oils.

Oil C is from a heavy oil field, U.S.A.. It is severely biodegraded and has a low API gravity of 10.4 degree (its density at 60° F and 1 atmosphere is 0.997 g/cc). Its viscosity at 85° F (29.4° C) is 28,300 centipoise and decreases exponentially as temperature increases (1,920 centipoise at 130° F or 64.4° C). It is maily composed of saturates (36.9% weight), aromatics (32.5%), resins (21.6%), and asphaltenes (9.0%). with average molecular weight of 504. Figure 3 shows the temperature and pressure dependence of the density of the oil C.

Oil D is also biodegraded but much less severely than oil C. Its API gravity is about 10.5 degree (corresponding to density of 0.997 g/cc at 60° F and 1 atmosphere. its viscosity at 104° F (40° C) is about 5,450 centipoise. Its average molecular weight is 506.

Figures 4a to 4e are the chromatograms of oils A, B, C, D, and F, respectively. Figure 4c illustrates that heavy oil C is severely boidegraded so that it is very difficult to identify the carbon number distributions. Oil D is also biodegraded but less severely (figure 4d).

The live oil used in the experiments is a recombined research fluid. Its bubble point (the temperature and pressure point at which the dissolved gases begin to come out of solution) is 2994 psig (206.5 bar) at 160° F (71.1° C). Its average molecular weight (calculated) is 148.

EXPERIMENTAL RESULTS AND INTERPRETATIONS

Velocities in Light Oils

The measured velocities in normal decane (oil I) are plotted as a function of pressure at different temperatures in figure 5a. In figure 5b are the velocities plotted as a function of temperature at various pressures. The velocities increase with increasing pressure, and decrease as temperature increases. Approximately linear relationship exists between the velocity and pressure, especially at lower temperatures. At higher temperatures, this linear relationship breaks down, which, as shown in figure 5a, means that the velocities are more sensitive to pressure changes. In figure 5b, the experimental results show that the velocities in normal decane (oil I) basically have a linear response to temperature changes at any pressures. Also shown in figure 5b are the data reported by Wang and Nur (1987) at atmospheric condition (0 psig). It can be seen that the two measurements are very consistent.

The measured velocities in Soltrol oil (oil H), a petroleum solvent, are plotted as a function of pressure and temperature in figures 6a and 6b, respectively. The velocities show very similar responses to pressure and temperature changes as those in normal decane. Although the velocities in Soltrol oil slightly deviate from linear relationship with pressure, they still decrease approximately linearly as temperature increases.

As stated in the previous section, both normal decane and Soltrol oil are refined petroleum hydrocarbons. In light crude oils, the velocities essentially have the same relationship with pressure and temperature as in those two refined oils, although the absolute change in velocities as pressure or temperature changes varies among oils. Figures 7a and 7b show the measured velocity data in oil G (API gravity = 43 degree) as function of pressure and temperature, respectively. And plotted in figures 8a and 8b are the velocities measured in oil F (API gravity = 34 degree). The velocity - temperature relations in both light oils are essentially linear, with maximum deviation of less than 1% which is within the measurement uncertainty. Although the velocities in all these four light hydrocarbons do not seem to increase linearly with increasing pressure, the maximum deviation from the linear relationship is still less than 2% in the measurement range.

Velocities in Heavy Oils

Velocities in oil A (API gravity = 5 degree) are plotted as a function of pressure at various temperatures in figure 9a, and as a function of temperature at various pressures in figure 9b. Again, we see that the velocities are strongly dependent on both pressure and temperature: i.e., they increase with increasing pressure and decrease as temperature increases. The same behavior is found in oil B (API gravity = 7 degree) and oil E (API gravity = 12 degree) (figures 10a, 10b, 11a, 11b). However, in contrast to the light oils, the velocities in these heavy oils have approximately linear relationship with pressures (instead of temperature in light oils), with maximum deviation of less than 1%, while the linear relationship between velocity and temperature no longer exists (the deviation can be as high as 3%).

The velocities in heavy oils decrease faster as temperature increases in low temperature ranges (20 to 45° C), while at higher temperatures the decrease slows down. This phenomenon may be related to the composition of the oils. Since heavy oils usually contain some solid or semi-solid materials (e.g., asphaltenes, wax particle, etc.), the melting of these materials can cause substantial decreases in velocities (Wang and Nur.

1986). After the solid or semi-solid materials in the heavy oils are completely melted, the velocities tend to decrease linearly as temperature increases, as observed in light oils.

From the experimental data on the 3 heavy oils (oils A, B, E), we also found that the non-linearity between velocity and temperature is dependent on the API gravity (or heaviness) of the oil. The heavier the oil, the more severe the deviation. As figures 9b, 10b, and 11b show, the maximum deviation of the velocity from linear relationship with temperature in oil A (5 degree API) is about 3.0%, while in the lighter oil B (7 degree API) and oil E (12 degree API), such maximum deviations are around 2.2% and 1.4%, respectively. Intuitively, this phenomenon is reasonable since heavier oils usually contain more solid or semi-solid materials than lighter ones.

The velocities measured in oil C (API gravity = 10.4 degree) are plotted in figure 12a versus pressure at various temperatures and in figure 12b versus temperature at various pressures. As observed in the previous heavy oils (A, B, E), the linear relationship between velocity and pressure also applies to oil C. However, at low temperature (say 27.8° C), the velocity tends to increase faster in high pressure ranges (figure 12a), which is probably related to the glass transition phenomenon of the oil. This in fact can be seen more clearly in figure 12b. At low temperature and high pressure (say 6410 psig), decreasing temperature causes rapid increase in velocity. Since oil C is severely biodegraded as mentioned in the previous section and has abnormally high viscosity, its composition is very different from those of oils A, B, and E, as can be seen from the chromatography data (figures 4a, 4b, 4c). Under high pressures, lowering temperature might bring oil C to the glassy state due to the high viscosity. In the glassy state, the oil is virtually semi-solid, which will add shear modulus to the oil and in turn increase the compressional velocity. Unfortunately, we did not do further investigation on this phenomenon by further lowering the temperature due to the shortage of time. However, further work may be needed in order to prove or test such an interpretation.

Figures 13a and 13b plot the velocity data in oil D (API gravity = 10.5 degree) versus pressure and temperature, respectively. An approximately linear relationship between velocity and pressure is also observed, though the absolute dependence of the velocity on pressure is different from that in other heavy oils. Since oil D is also biodegraded (figure 4d), though not as severely as oil C, it is also very viscous. Therefore, stronger dependence of the velocity at low temperature and high pressure on temperature is also observed. However, oil D might have not reached the glass transition zone since the velocity does not change as fast as it does in oil C.

To summarize the velocities in dead oils, we see that the velocities in both light and heavy oils are strongly dependent on pressure and temperature. Typically, the velocities decrease by about 270 - 480 m/sec as temperature increases by 100° C, and increase by 28-50 m/sec as pressure increases by 1,000 psi. The rates of change are dependent upon the absolute pressure, temperature, and oil composition. From the experimental results, we also observed that in light oils velocities decrease approximately linearly as temperature increases while increase slightly non-linearly as pressure increases. However in heavy oils the opposite is true, i.e., velocities decrease non-linearly as temperature increases while increase linearly as pressure increases.

Velocities in Live Oil

Velocities in the recombined live oil were measured as a function of decreasing pressure at two temperatures. In figure 14, the velocities decrease approximately linearly as pressure decreases. When the pressure reaches the bubble point of the live oil (3,000 psig at 72° C)*, the measured velocity - pressure relation does not change much. Further lowering pressure only causes the velocity curve to wiggle slightly. As the pressure is decreased further (1,600 psig at 22.8° C, and 1,800 psig at 72.0° C), the acoustic signal dispears.

* Below about 3,000 psig at this temperature, gas in the live oil begins to come out of solution and we have a liquid-gas mixture. This pressure is termed the bubble point pressure of the oil. The bubble point depends on the amount of gas in solution, the composition of the oil, and temperature

The above observation on the velocities in the live oil at or below bubble point seems to be contradictory with theory. Intuitively, the velocities in a liquid - gas two phase mixture should have values of lower than those in the gas, since the mixture approximately has a compressibility of the gas but a density of the liquid. This means in our case when the pressure is at or below bubble point of the live oil, we should have seen abrupt decrease in the velocity. The simplest explanation for the phenomenon actually seen is that direct paths might still exist for the acoustic waves between the discrete bubbles. i.e., at ultrasonic frequency, the wave rays might be able to directly travel through the oil between bubbles.

The observed velocity behavior at and below bubble point pressure might also be explained in terms of experimental artifacts. As mentioned in the previous section, the live oil sample was transferred from the storage pressure vessel to the test vessel through pressure tubings. When the pressure is lowered to or below the bubble point pressure, the formed bubbles in the oil might rise into the pressure tubing. In this case, the transducers might not "see" the bubbles, and therefore there is no abrupt velocity change in the oil until enough gas bubbles formed stay between the two transducers. In this interval, the velocity may even increase as the density of the oil is lower.

The above observed phenomenon can also be explained by the surface tension effect of the gas bubbles. As the pressure is lowered to or below the bubble point, the gas bubbles formed in the live oil may be very small. Very small gas bubbles virtually can be as rigid as the surrounding liquid due to the increased internal pressure within the bubbles caused by the surface tension. Therefore the velocity can be even higher for the oil due to the lowered density. We will discuss this in more detail in a later section.

None of the above three explanations for the velocity behavior at or below bubble point pressure is experimentally or computationally examined in quantitative ways for the live oil. It is possible that all the three effects may be at work simultaneously. Further investigation is desirable.

After the measurements for the velocities in the live oil, the pressure was released to zero psig in the oil to let the dissolved gases out of solution, so that we could measure the velocity in the same oil without saturated gases. In figure 14, the velocity was measured again as a function of pressure at 72.0° C after the oil sample had stayed at zero psig for three hours. Similarly the velocity was measured at 22.8° C after the oil had remained at zero pressure for over 15 hours. Basically, the velocities in this now "dead" oil have very similar response to pressure and temperature changes as in other dead oils.

Dissolved gases significantly lowered the acoustic velocities in oils. As can be seen in figure 14, the velocity difference between the live oil and its "dead-end"* is 190 - 230 m/sec (or about 15 - 22% of the velocity value in the live oil) at both 22.8° C and 72.0° C, depending on the pressure. Theoretically, since gases are more compressible (even when they are in dense phase), the dissolved gas in the liquid oil substantially increase the compressibility, but only decrease the density very mildly, of the fluid. Therefore, we see pronounced decreases in the acoustic velocity. The amount of decrease is related to the composition of both the dissolved gases and the liquid oil.

Velocity -- API Gravity Relations

The experimental results of the velocities in oils showed that there might exist some simple relation between velocities and the API gravity. Figure 15 plots such a relation at pressure of 110 psig and two different temperatures, namely 23° C and 80° C. This figure shows that acoustic velocities in oils have very simple relationship with the API gravity (or the inverse of density): i.e., the velocity decreases systematically with increasing API gravity, both at lower and higher temperatures.

In figure 15, oils C and D deviate from the general trend of the velocity - API gravity curves, which might be again caused by the dramatic differences in composition

* Here "dead-end" refers to the live oil whose dissolved gases have been out of solution. e.g, after the live oil had been remained at zero pressure for over 15 hours, the gases were out of solution and the live oil became "dead". Such "dead" oil is defined as the "dead-end" of the live oil.

resulted from the biodegradation of the two oils.

The importance of figure 15 is that when the API gravity (or density at 60° F and 1 atmosphere) of an oil is known, one can estimate the acoustical velocities in the oil at pressures and temperatures. The details of such estimations will be shown in a later section.

Temperature and Pressure Derivatives of the Velocities

Temperature and pressure derivatives of the velocities in all the 9 dead oils (including the "dead-end" of the live oil) were taken assuming linear velocity-temperature and velocity-pressure relationships. i.e.,

$$(\frac{\partial C}{\partial T})_P = \frac{C_{T2} - C_{T1}}{T2 - T1} \quad [(m/sec)/^\circ C],$$

where C is the velocity (here we use C, but in figures 16-18, the notation for velocity is still V), T2 and T1 are the highest and lowest temperature, respectively, at which the velocity measurements were made. And accordingly,

$$(\frac{\partial C}{\partial P})_T = \frac{C_{P2} - C_{P1}}{P2 - P1} \quad [(m/sec)/1{,}000\ psi],$$

where P2 and P1 are the highest (usually 6,410 psig) and the lowest (usually 0 psig) pressures, respectively, at which the velocity measurements were made.

According to the above definitions, such temperature derivatives of the velocities are in fact averaged in the whole measurement temperature interval at constant pressure, and similarly such pressure derivatives are averaged in the whole measurement pressure interval at constant temperature. Therefore they do not represent the acoustic property of the oil at one temperature or pressure point, instead, they reflect the averaged acoustic property of the oil over a certain temperature or pressure range.

The temperature derivatives of the velocities in the 9 dead oils are plotted versus pressure in figures 16a and 16b. In oil C, $\frac{\partial C}{\partial T}$ increases as pressure increases, while in oil A, $\frac{\partial C}{\partial T}$ first does not change much at pressures lower than 3,300 psig, and increases

as pressure increases from 3,300 to 6,410 psig. In both oil B and oil D, $\frac{\partial C}{\partial T}$ is virtually independent of pressure in the measurement range. Starting from oil E to normal decane (oil I), $\frac{\partial C}{\partial T}$ decreases with increasing pressure.

In heavy oils, high pressure might create more solid or semi-solid materials in the oils. Therefore, the melting of these materials causes the velocities to decrease more rapidly. And hence we see higher (absolute value) temperature derivatives of the velocity.

In light oils, at high pressures the oils become very dense. Since dense materials usually have very small (absolute value) temperature derivatives of the ultrasonic velocities (e.g., in mercury (figure 2) and in solids), $\frac{\partial C}{\partial T}$ decreases with increasing pressure. We will also explain this in terms of free volume theories of the liquid state in the next section.

In other heavy oils (i.e., oils B, D, and E) the effects of density increase and of the creation of solid or semi-solid materials as pressure increases may cancel each other, so a more or less $\frac{\partial C}{\partial T}$ independence of pressure is observed.

The temperature derivatives of the velocities in all the 9 dead oils are plotted in figure 17 as a function of API gravity at various pressures. It shows that as the API gravity increases (density decreases), $\frac{\partial C}{\partial T}$ in oils first decreases then increases (oil C is certainly an exception). The importance of this figure is that one can easily estimate the acoustic velocity in an oil and its temperature dependence at various pressures if the API gravity or density is known, by assuming that linear relationship exists between velocity and temperature.

The pressure derivatives of the dead oils are shown in figures 18a and 18b. In oil C, $\frac{\partial C}{\partial P}$ is high at low temperature probably due to the glass transition effect. For all the heavy oils, $\frac{\partial C}{\partial P}$ first tends to decrease as temperature increases in 20° to 40° C

range, and slightly increases with increasing temperature. In light oils $\frac{\partial C}{\partial P}$ basically increases linearly as temperature increases, which means that at high temperatures the velocities are more sensitive to pressure changes. The intuitive explanation for this phenomenon is that at high temperatures the molecules are farther apart due to the thermal expansion, so that increasing pressure will decrease the compressibility (or put the molecules closer) substantially in oils.

It should be noted that all the above interpretations are qualitative in nature. We will also give more such interpretations in the next section in light of some existing theories or models of the liquid state. Owing to the lack of the needed data on other parameters or properties of the oils, numerical interpretations can not be made at this time.

DISCUSSION: THEORIES AND MODELS OF THE LIQUID STATE

There is at present no completely satisfactory theory or model of the liquid state. The intention of this section is not to provide a literature survey or review on the theories or models of the liquid state. Instead, we briefly summarize some of the existing theories and models and use them to interpret our experimental results. Due to the lack of other needed properties of the oils used in the experiments (such as thermal expansion, volume of the molecules, free volume of the oils, and specific heats, etc.), numerical examinations on the velocity results using these theories or models can not yet be done.

Specific Heats, Thermal Expansion, and Velocity

In thermodynamics, specific heat is defined as the energy needed to increase the temperature of a given material of unit mass by 1° C. There are two types of specific heats, one is called specific heat at constant volume, denoted by Cv, the other is specific heat at constant pressure, denoted by Cp. Cp is always greater than Cv since at constant pressure part of the energy used to increase the temperature is spent to

expand the volume (transferred to work).

Similarly, there are two types of acoustic velocities in fluids, one is adiabatic and the other is isothermal. The measured ultrasonic velocities are adiabatic since there is essentially no heat exchange between the fluid and the environment at ultrasonic frequencies.

In hydrodynamics,

$$\frac{Cp}{Cv} = \gamma = C^2 \rho \beta_T = \frac{\beta_T}{\beta_S} \tag{1}$$

and in thermodynamics,

$$Cp. - Cv = - \frac{T(\frac{\partial V}{\partial T})^2_P}{(\frac{\partial V}{\partial P})_T} \tag{2}$$

where γ is called specific heat ratio, T, V, P, C, ρ, β_S, and β_T are temperature, specific volume, pressure, adiabatic acoustic velocity, density, adiabatic compressibility, and isothermal compressibility, respectively.

Through some simple algebra, we have

$$Cv = \frac{T \alpha^2_P}{\beta_T \rho (\gamma - 1)} \tag{3}$$

or the acoustic velocity

$$C^2 = \frac{Cp(\gamma - 1)}{T \alpha^2_P}, \tag{4}$$

where $\alpha_P = (\frac{\partial V}{\partial T})_P$ is called the thermal expansivity at constant pressure.

Equation (4) allows one to calculate the acoustic velocity in fluids at a certain temperature and pressure point if the specific heats and thermal expansivity are known, or to calculate any parameter if all others are known. We do not have the specific heat and thermal expansivity data of the oils, so that we can not test the validity of this equation. However, equation (4) does provide some qualitative

interpretations on our experimental results.

The specific heats and the thermal expansivity are dependent upon temperature. If $T\alpha^2_P$ increases faster than $Cp(\gamma - 1)$ as temperature increases, equation (4) can predict the right trend of the velocities in all the oils.

Equation (4) also shows that the acoustic velocity squared is proportional to Cp and γ, and inversely proportional to the thermal expansivity squared of the fluid. Generally speaking, the specific heats and thermal expansivity are related to the API gravity (or density). In heavier oils (low API gravity or high density), Cp is higher and α_P is smaller, so that we have higher velocities. Theoretically, γ can never be less than or equal to 1 in any fluids (usually between 1.05 and 1.30 in liquids). However, lower γ usually means higher Cp and smaller α_P, hence although generally γ decreases as oil gravity (API) decreases (density increases), Cp may increases and α_P may decrease much faster than the γ change, so that we see increases in acoustic velocities.

Intermolecular Forces

As we have known, fluids are very complex systems. Both attractive and repulsive forces which are called intermolecular forces exist among molecules. Generally speaking attractive forces are dominant in gases since the molecules are far apart from one another, while in liquids, repulsive forces are dominant. When the distance between two molecules is r_o, the repulsive and attractive forces just cancel each other, then we say the two molecules are at equilibrium. r_o is usually in the order of 10^{-8} centimeters. When the distance r between two molecules is less than r_o, which is usually the case for liquids, the two molecules repel each other, otherwise they attract each other. As pressure increases, r_o decreases and the repulsive forces increase very rapidly, hence fluids can not be easily compressed.

The theory of intermolecular forces can qualitatively explain our experimental results of the temperature and pressure dependences of the acoustic velocities in oils. As temperature increases, the molecules in the oils become farther apart due to thermal expansion and the intermolecular repulsive forces between molecules decrease. Since the

intermolecular forces determines the compressibility of the oils, decrease in the repulsive forces means increase in compressibility. Therefore we see acoustic velocity decreases with increasing temperature.

As pressure increases, the molecules in the oils become closer due to compression, so the intermolecular repulsive forces increase, which causes the compressibility of the oils to decrease, and in turn, the acoustic velocity to increase.

Equation of State

Generally speaking, the methods of calculating the acoustic velocities in liquids can be divided into two groups. In the first group are those in which an estimate of the acoustic velocity is made on the basis of using some equation of state of the liquid, and in the second, those in which calculations of the acoustic velocities are governed by the choice of a corresponding model. In this sub-section, we discuss the estimation of the acoustic velocities in liquids using the equation of state. And in the following sub-sections, calculations of the acoustic velocities in liquids through some liquid theories and models will be discussed.

The van der Waals' equation of state expresses the pressure - volume - temperature (P-V-T) relation in a fluid,

$$(P + \frac{a}{V^2})(V - b) = RT$$

where a and b are two coefficients, and R and V are the universal gas constant and specific volume, respectively.

The definition of the acoustic velocity is

$$C^2 = -\gamma V^2 (\frac{\partial P}{\partial V})_T$$

where $\gamma = \frac{Cp}{Cv}$ is the specific heat ratio. And van der Waals' equation of state can also be written as

$$P = \frac{RT}{V - b} - \frac{a}{V^2}$$

Taking the partial derivative of the above equation and inserting it into the velocity definition, we have

$$C^2 = \gamma \left[\frac{RT}{(1 - b/V)^2} - \frac{2a}{V} \right]_T \tag{5}$$

or

$$C^2 = \gamma \left[\frac{PV^2 + a}{V - b} - \frac{2a}{V} \right]_T \tag{6}$$

Therefore, one can use these equations to calculate the acoustic velocities in fluids.

Equations (5) and (6) predict the right trends of changes in acoustic velocities as temperature and pressure change. As temperature increases, the specific volume of the liquid increases due to thermal expansion. While the velocity is very sensitive to the specific volume changes (V is squared) in liquids, the temperature term in (5) may not be dominant. Therefore, the effect of temperature on V may dominate the velocity change. In (6), both pressure and its effect on V cause the acoustic velocity to increase as pressure increases. However, this increase will diminish at very high pressures since when V is very small, the second term on the right side of (6) becomes more important.

From the above analysis, we see that equation (6) derived from the van der Waals' equation of state qualitatively explains the pressure and temperature dependences of the acoustic velocities in oils. However, we do not expect the calculated velocities from this equation to fit the experimental results numerically. Figures 19a and 19b are two examples given by Nozdrev (1965) on the velocities in normal hexane (C_6H_{14}) and ethyl alcohol. In these two figures, we see that only near the critical temperatures of the two liquids do the theoretical and the experimental velocity curves coincide. Below the critical temperatures, the calculated velocities are much higher than measured. This is not surprising since the van der Waals' equation of state was essentially derived for gases.

Besides equations (5) and (6), also known is an attempt to calculate the velocity of sound in liquids from an equation of state obtained by regarding the liquid as a highly

compressed gas (Kudryavtsev, 1954). This liquid model leads to an equation of state for N hard elastic spheres:

$$PV_a = 3NRT$$

where V_a is called available volume $= V - V_o$, and V_o is the closepacked volume of the molecules (we will discuss the available volume theory of the liquid state later). Experimental results (Kittel, 1946) showed that calculated velocities and their temperature coefficients from such a model treating a liquid as highly compressed gas and molecules as perfectly elastic spheres were correct only in order of magnitude and in sign.

The difficulty of using the van der Waals' equation of state to calculate the acoustic velocities in liquids is also coming from estimating the pressure and temperature dependences of the coefficients a and b. However, if a and b can be obtained accurately, fit between experimental and theoretically calculated velocities may improve.

As a conclusion, we see that the calculation of acoustic velocities in liquids using general equations of state is unsatisfactory. i.e., further modifications on or better equations of state are undoubtedly needed in order to make better fit between experimental and theoretical velocities.

Free Volume and Available Volume

Simplified Free Volume Theory

Kincaid and Eyring (1938), developing the idea of the free volume of liquid, put forward a scheme for the propagation of acoustic waves in a liquid which was very simple, although physically of little use. According to this idea a liquid is considered as an aggregate of perfectly elastic hard spheres (actually molecules) placed so that free spaces remain between them. In this theory, the acoustic wave front is propagated in the free spaces between molecules with the same finite velocity as in the ideal gas, but infinitely faster inside the molecules. Assuming a regular lattice structure with an intermolecular distance d, the path length for an acoustic wave is short-circuited for a

fraction of σ/d, where σ is the diameter of the molecules. The ratio of the distances covered in the same time by the wave in the liquid is $d/(d-\sigma)$, so that the acoustic velocity is then given by

$$C = C_{P=0}\frac{d}{d-\sigma} = C_{P=0}\frac{1}{1-\sigma/d} \tag{7}$$

where $C_{P=0}$ is the acoustic velocity in the ideal gas at zero pressure.

The basic drawbacks of this scheme are that no allowance is made for the interactions between molecules, and that the velocity of sound in a discontinuous medium consists of the sum of the velocity in the empty and dense spaces along the path of the sound beam. Furthermore, this crude theory has only sense if the repulsive forces are much larger than the attractive ones (which is actually true in liquids). The possibility of overlapping of the hard spheres is not taken into account and no direct temperature effect on velocity *at constant density* exists in this theory. Nevertheless, this simple theory expressed by equation (7) does predict the right signs of the acoustic velocity changes as temperature and pressure change. Since in (7) $C_{P=0}$ is temperature independent, increasing temperature increases the intermolecular distance d in (7) due to thermal expansion, so that the acoustic velocity decreases. And Accordingly, the intermolecular distance d decreases as pressure increases due to compression, so that the acoustic velocity increases.

Smeared Free Volume Theory

Hirschfelder et al (1954) derived an equation of state based on the assumption that using as elementary free volume the largest sphere can be included in a cell formed by the 12 nearest neighbors in a face-centered-cubic lattice. The equation of state is then

$$\frac{PV_M}{RT} = \frac{1}{1-\sigma/a}$$

where $a^3 = \sqrt{2}V_M/N$, V_M is the molar volume and N is the number of molecules.

From the definition of the acoustic velocity, we have

$$C^2 = \frac{\gamma RT}{M}\left[\frac{1-\frac{2}{3}(\sigma/a)}{(1-\sigma/a)^2}\right] \tag{8}$$

where M is the molecular weight.

Again, like the simplified free volume theory, equation (8) may only be able to predict the right sign of the temperature and pressure derivatives of the velocities. However, the calculated velocities by the smeared free volume theory can be much closer to the experimental data than those by the simplified free volume theory (van Dael and van Itterbeek, 1965).

Available Volume Theory

The available volume V_a of a liquid is defined as the difference between the actual volume V and the minimum possible volume V_o, and is given by

$$V_a = V(1-\theta)$$

where θ is the packing fraction with respect to the closest possible packing. The free volume is defined as the volume of possible motion of the center of a single molecule, and is given, per mole, by

$$V_f = V(1-\theta^{\frac{1}{3}})^3$$

For a classical three-dimensional gas of hard elastic spheres in the limit of close packing, Tonks (1936) gave the equation of state:

$$PV_M(1-\theta^{\frac{1}{3}}) = RT \tag{9}$$

where $\theta = 1 - V_a/V_M$.

The acoustic velocity corresponding to (9) is given by

$$C^2 = \frac{\gamma RT}{M}\left[\frac{1-\frac{2}{3}\theta^{\frac{1}{2}}}{(1-\theta^{\frac{1}{3}})^2}\right]$$

where R, T, and M are the universal gas constant, temperature, and molecular weight, respectively.

For high densities (in this model, the liquid is considered as highly compressed gas), θ is about equal to 1, and $1-\theta^{\frac{1}{3}}$ is approximately equal to $V_a/3V$. Kittel (1946) derived a formula for velocity in liquids:

$$C^2 = \frac{3\gamma RT}{M}(V_M/V_a)^2 = \frac{3\gamma RT}{M}(V_o/V_a + 1)^2 \qquad (10)$$

In equation (10), if we assume that V_o does not change with temperature and pressure, and V_a^2 changes faster than temperature as temperature changes, the temperature and pressure derivatives of the calculated velocities can have the same sign as those of the experimentally determined ones. However, as shown in Kittel's paper (Kittel, 1946), the detailed numerical agreement between the calculated (using this theory) and the measured velocities is usually unsatisfactory. Thus, we again do not expect this theory to fit our experimental results of oils numerically.

The free volume and available volume theories can also explain the temperature and pressure derivatives in the oils as pressure and temperature increases (figures 16 -18). Intuitively, at higher temperatures, changes in pressures will affect the available or free volume more since the oils are more compressible. As a result, we see higher pressure derivatives of the acoustic velocities (figures 18a and 18b). In light oils, higher pressures make the oils harder to compress or to expand, hence temperature change affects the available or free volume less. And consequently, the temperature derivatives of the velocities decrease as pressure increases (figure 16b). In heavy oils, the melting of solid and semi-solid materials may dominate the velocity changes with changing temperature. The higher the pressures the more solid and semi-solid materials are created. Therefore, at higher pressures, we see that the velocities decrease faster as temperature increases, due to the melting of the solid and semi-solid materials: i.e., the changes in available or free volumes in heavy oils as pressure changes may not dominate the temperature derivatives of velocities.

Cell Theory

Lennard-Jones and Devonshire (LJD) (1937) developed the cell theory by assuming the structure of the fluid being solid-like: the molecules spend most of their time near sites of a face centered cubic lattice. Each molecule is imprisoned in a cell formed by its 12 nearest neighbors, but it can move in this cell submitted to forces according the potential:

$$E(r) = \epsilon[(r_o/r)^{12} - 2(r_o/r)^6]$$

with a minimum energy $-\epsilon$ at $r = r_o$, and r_o is related to σ (molecule diameter) by $r_o^6 = 2\sigma^6$. For the sake of simplicity, the potential energy of a molecule at a distance d of the center of the cell is taken as its average energy over all the spheres of radius d.

In the cell model, if a is the distance from a central molecule to its 12 nearest neighbors in the lattice with $a^3 = \sqrt{2}(V_M/N)$, there is a second shell of 6 neighbors at a distance $\sqrt{2}a$ and a third one of 24 molecules at $\sqrt{3}a$ (Wentorf et al, 1950).

It is easy to see that the LJD cell theory is actually an extension of the smeared free volume theory: it includes the interaction between cells (molecule clusters).

Wentorf et al (1950) calculated the compressibility of hydrogen using a universal equation of state based on the LJD cell theory and showed that the calculated compressibility did not fit the experimental values numerically (about 25 - 30% higher). However it did predict much closer acoustic velocity values to the experimental ones than the free volume theories. David and Hamann (1961) calculated the acoustic velocities in liquid He, H_2, A, N_2, and O_2. The calculated velocities had the right trend of temperature dependences as measured, but the numerical agreement was not good. The lack of agreement evidently arose from the faults of the cell model rather than from the mathematical approximations of the LJD theory. Dahler and Hirschfelder's (1961) improved cell theory gave even worse agreement with experiment, the calculated values of the acoustic velocity being about 20% higher than those by the LJD theory.

Although the LJD cell theory improved the physical meaning compared to the free volume theories by including the interactions between molecules, the calculated velocities still deviate from the measured by substantial amount. Also the calculation is more complicated mathematically. Therefore we again do not expect that it can predict the right acoustic velocity values in oils.

Tunnel Theory

The cell theory described above is actually based on an ordered structure which does not permit density fluctuations, and is therefore more appropriate as a model for solids. One could consider large cells, containing many molecules, as the subsystems from which the fluid is built up to calculate the properties of the fluid. But in general this would require an enormous amount of computation to determine the properties of the individual cells (Barker, 1961). However, there is one case in which this calculation presents less difficulties, namely, the case of the tunnel theory.

Barker (1960, 1961) proposed the tunnel theory by imagining the structure of a liquid as formed by lines of molecules packed as closely as possible, but in such a way that the distribution of molecules in one line along that line bears no special relation to the distribution in another line; the relative positions of molecules in different lines are completely disordered. i.e., unlike the cell theory in which the subsystems are single molecules, the tunnel theory considers the subsystems as whole lines of molecules moving in tunnels.

Barker (1961) showed that predictions of the simplest form of the tunnel theory as to liquid densities and compressibilities were in excellent agreement with experimental values on liquid A, N_2, O_2, and CH_4. However, we do not know if the theory can still predict the right values of compressibilities and densities in denser liquids such as oils, since we do not have the data of the parameters in the theory.

Molecular-Kinetic Theory

Adkhamov (1954) investigated the phenomenon of acoustic wave propagation in liquids by using the molecular-kinetic theory. The idea behind his work was that the equilibrium values of the pressure (P) and internal energy (E) parameters obtained from the molecular-kinetic theory were used to solve approximately the equation (which can be obtained from general propositions of statistical physics) for the acoustic velocity:

$$C^2 = -\frac{V^2}{m}\left(\frac{\partial P}{\partial V}\right) + \frac{V^2 RT}{m\dfrac{\partial E}{\partial \Theta}}\left(\frac{\partial P}{\partial \Theta}\right)^2 \tag{12}$$

where V, m, R, T represent volume, mass of the molecule, universal gas constant, temperature, respectively; $\Theta = T/T_c$ is called reduced temperature, and T_c is the critical temperature. In this equation, P and E are determined from the radial distribution function g(r) and interaction potential $\Phi(r)$ of the molecules in the following way:

$$P = \frac{RT}{V} - \frac{2\pi}{3V^2}\int_0^\infty g(r)\Phi'(r)r^3 dr$$

$$E = \frac{3}{2}RT + \frac{2\pi}{V}\int_0^\infty g(r)\Phi'(r)r^2 dr$$

where r is the distance between molecules.

The calculated velocities using (12) in acetone, benzene, carbon disulphide, chloroform, ethyl alcohol, and carbon tetrachloride are always higher than the experimental values, generally by 11 - 37% (Adkhamov, 1954). We do not know how well the calculated velocities using this model would fit our experimental acoustic velocities in oils, since it is difficult to know the functions g(r) and $\Phi(r)$.

Summary

In this section, some of the existing theories and models of the liquid state were presented. Basically they all can only interpret our experimental results of the acoustic velocities in oils qualitatively. We did not use any of these theories or models to fit the

experimental results due to the lack of other required parameters of the oils. However, we do not expect the calculated velocity values to fit the measured ones numerically since in fact there is at present no perfectly satisfactory theory or model which can do so.

It should also point out that although we classified the theories and models of the liquid state into different categories, they are more or less related in one way or another. We hope that such classifications would not bring up much ambiguity.

DISCUSSION: VELOCITIES IN GAS-LIQUID TWO PHASE MEDIUM

Theoretically, the presence of gas bubbles in a liquid should dramatically decrease the acoustic velocity in the liquid (Barclay et al, 1969; McWilliam and Duggins, 1969). In particular, the acoustic velocity should be much lower in a gas-liquid two phase medium than in either the gas or the liquid component, since the two phase medium virtually has a compressibility of the gas but a density of the liquid. The experimental results of McWilliam and Duggins (1969) showed that the acoustic velocity in water was 1,440 - 1,480 m/sec and about 340 m/sec in air, but in air-water mixture fell to as low as 20 m/sec; and even very small concentrations of gas dramatically reduce the acoustic velocity: 1% (by volume) of air in water could reduce the acoustic velocity by 95%.

However, in our experiments, the acoustic velocities in the live oil did not decrease dramatically as the bubble point of the live oil was reached (figure 14). In this section we explain this phenomenon using some of the theoretical results (Kieffer, 1977; McWllim and Duggins, 1969; Nishihara and Michitoshi, 1979; Hanna et al, 1978), and analyze the possible experimental artifacts.

Kieffer (1977) used the equations of state and calculated the acoustic velocities in air-water two phase medium. In the first case in which the gas bubbles were assumed to be sufficiently large so that surface tension effect could be neglected (pressure in the gas bubbles is equal to that in the liquid), Kieffer's calculation showed that at low

pressures even very small amount of gas in the aggregate reduced the acoustic velocity dramatically. For instance, 2% by volume, or equivalently 10^{-5} of mass fraction, of air appearance in water reduces the velocity from 1,480 m/sec (in water) to about 100 m/sec (figures 20a and 20b). However at higher pressures, the velocity is basically unchanged as the mass fraction η of air increases (e.g., at 500 bars, from $\eta = 10^{-8}$ to 10^{-3}), which means that at higher pressures larger mass fractions are required to cause the velocity to decrease dramatically.

When the gas bubbles are sufficiently small, the surface tension effect becomes significant. In this case, the pressure in a gas bubble (P_G) exceeds the pressure in the surrounding liquid (P_L):

$$P_G = P_L + \frac{2\sigma}{r},$$

where r is the bubble radius and σ is the surface tension. Then the isothermal acoustic velocity in the gas-liquid mixture is related to the surface tension, mass fraction of the gas, bubble radius and other parameters (for the velocity expression, see Kieffer, 1977; McWilliam and Duggins, 1969).

When the surface tension is taken into account, both pressure and bubble size affect the acoustic velocity in a two phase medium. Figure 21, taken from Kieffer and assuming the surface tension of an air-water interface to be 72.2 dyne/cm, shows the calculated acoustic velocities in the air-water two phase mixture as a function of pressure, bubble radii, and the mass fraction of the air. Consider the figure in which $\eta = 10^{-1}$ (10% by weight of air in the mixture). The acoustic velocity at any pressure is close to that in pure liquid (water) if the bubble radius is smaller than about 4×10^{-8} cm. The velocity decreases rapidly as the bubble radius increases from 4×10^{-8} to about 10^{-6} cm. Afterwards, it is nearly constant at a given pressure, equal to the value obtained in the model in which the effect of surface tension is neglected, for bubble radii greater than 10^{-6} cm. Therefore figure 21 has basically three regions in which the acoustic velocity behaves distinctly: (1) A region in which at small bubble radii the

velocity is nearly independent of both pressure and bubble size; (2) A region in which at intermediate bubble radii the velocity decreases rapidly as bubble size increases; And (3) a region in which at large bubble radii the velocity is independent of bubble size but sensitive to pressure.

At smaller gas mass fractions, all the three regions move systematically to the larger bubble radii direction. Consider the figure in which $\eta = 10^{-4}$. At higher pressures of 300 and 500 bars, the acoustic velocity is virtually approximately independent of the bubble size in the air-water two phase medium. At lower pressures, the velocity is very sensitive to pressure when the bubble radius is greater than about 10^{-5} cm.

The calculated velocities in the air-water two phase mixture evidently can explain our experimental results of acoustic velocities in the live oil below bubble point. As the bubble point of the live oil is reached, gas bubbles become to form. At this stage, the bubbles may be very small and the surface tension effect can not be neglected, and the mass fraction of the gas bubbles is also very small. Therefore, at higher pressure (the bubble point pressure of the live oil is 2,994 psig or 206 bars at 71° C), the acoustic velocity is virtually approximately independent of the bubble size and bubble appearance, so that as observed in figure 14 the velocity is still high. Further lowering the pressure creates larger mass fraction of the gas, and consequently the velocity decreases. As the mass fraction of the gas in the live oil increases to a sufficiently large amount, the velocity decreases sharply. We do not know the exact mass fractions and bubble sizes of the gas at different pressures in our experiments since it is very difficult to measure them in a pressure vessel. However, a guess of $\eta = 10^{-3} - 10^{-2}$ and $r = 10^{-3} - 10^{-2}$ cm (bubble radii) at about 2,000 psig (138 bars) might be reasonable.

From the above discussions, we see that the calculated velocity behaviors in figure 21 can explain our experimental results of the velocities in the live oil well. However, the calculations by Kieffer (1977) were in fact based the assumptions given by McWilliam and Duggins (1969). i.e., the treatment of McWilliam and Duggins on velocity calculations in gas-liquid two phase medium assumes that: (1) The liquid and gas phases

are in equilibrium, and there is negligible mass transfer between the phases owing to gas becomes dissolved or liquefied; (2) There is no slip between the two phases; (3) The wavelength of the acoustic wave is much larger than the average dimension of non-uniformity of the mixture; (4) The gas is compressible and obeys the perfect gas law, and the liquid is elastic with a constant bulk modulus (or compressibility). The first three assumptions look more or less reasonable to us. However, the fourth assumption may not be a good one since at higher pressures the gas phase does not obey the perfect gas law, and furthermore the liquid compressibility varies with pressure. But nevertheless, as shown in Kieffer's paper, the calculated acoustic velocities are more or less in good agreement with the experimental data.

Although the theoretical treatment offers possible explanation for the experimental results, experimental artifacts might still exist in our experiments. As explained earlier, further lowering the pressure beyond the bubble point creates larger bubbles. These larger bubbles, due to the gravity effect and under excitation of the passing acoustic waves, might rise to the pressure tubings used to transfer the live oil to the testing pressure vessel, while the smaller bubbles still remain in between the two transducers. Therefore, as observed in the experiments, the acoustic velocities do not change much as further lowering the pressure to a certain point due to the out of the larger bubble. At this stage, the acoustic velocities may even increase a little due to the lowered density as a result of the larger bubbles' coming out of the live oil. This explains the wiggling of the velocity curves at pressures lower than the bubble point pressure (figure 14).

DISCUSSION: VELOCITIES AND P-V-T MEASUREMENTS

It is well known that one can derive the isothermal acoustic velocities from the pressure-volume-temperature (P-V-T) measurement on a fluid, since the isothermal acoustic velocity is defined as

$$C_T{}^2 = \frac{1}{\rho} \frac{\partial P}{(\frac{\partial V}{V})}.$$

If we know the initial density of the fluid at which the P-V-T measurement starts, we can calculate the numerical values of the isothermal acoustic velocities as a function of pressure at the temperature at which the P-V-T measurement is performed.

Figure 22 shows the measured adiabatic and the calculated isothermal acoustic velocities in 5 normal paraffins as functions of temperature at 0 psig. The P-V-T and the acoustic measurements were both performed by Boelhouwer (1960, 1961). In this figure $C7$ through $C16$ represent the carbon numbers of the normal paraffins and A, T represent adiabatic and isothermal, respectively.

From figure 22, one can see that the isothermal acoustic velocities are always lower than the adiabatic ones, and furthermore they are less temperature dependent. The lower isothermal velocity has actually been theoretically proven, since it is related to the adiabatic velocity by a factor of $\gamma^{\frac{1}{2}}$ and γ is always larger than 1. The phenomenon that the isothermal acoustic velocity is less temperature dependent suggests that γ may vary with changing temperature.

The following table gives the P-V data of the live oil at 71° C (160° F):

Pressure (psig)	Relative Volume	Pressure (psig)	Relative Volume
5000	0.9855	4600	0.9881
4200	0.9909	3800	0.9938
3400	0.9968	3200	0.9983
2994	1.0000	Bubble	Point

The initial density of the live oil at 2,994 psig can be calculated since the composition of the oil is known. The procedure for such a calculation is shown in the Appendix. Therefore, the calculated isothermal acoustic velocities, along with the measured adiabatic ones, are plotted in figure 23. Basically speaking, the calculated isothermal velocity curve is parallel to the adiabatic curve. The deviation of velocity points at 3,400 and 5,000 psig is believed to be caused by the inaccuracy of the P-V

measurement. Therefore we conclude here that in oder to get the accurate acoustic velocity calculation, the relative volume measurement should be accurate at least to the fifth digit.

The P-V-T measurement on oil C showed that the density of the oil can be treated as a linear function of temperature and pressure (figure 3) (Meyers, 1987):

$$\rho = \rho_o \ (1 - AT + BP + DPT),$$

where ρ_o, A, B, D are constants.

Taking the partial derivative of the above equation with respect to density at constant temperature, we have

$$C_T{}^2 = (\frac{\partial P}{\partial \rho})_T = \frac{1}{\rho_o \ (B + DT)},$$

which means that at a constant temperature, the calculated isothermal acoustic velocity is independent of pressure. Figure 24 shows the calculated isothermal velocities in oil C, along with the measured adiabatic velocity, at $27.8^\circ \ C$.

Figure 24 shows us that the calculation of the acoustic velocities in oils from the P-V-T measurements is certainly not accurate enough. One has to have very accurate P-V-T data in order to get the right velocity values. However, although the modern technology allows the P-V-T analysts to get the accuracy of the P-V-T measurement up to 0.0004 (Boelhouwer, 1960) or even better, the calculation of the acoustic velocity still needs better P-V-T accuracies. This fact on the other hand gives us some hint that it may be possible to use the acoustic measurements to derive the P-V-T data in oils, as has been done by Wang and Millero (1973) for pure water.

VELOCITY-TEMPERATURE-PRESSURE-API GRAVITY-MOLECULAR WEIGHT CORRELATIONS

Velocity-Temperature-Pressure-API Gravity Relations

In our experimental results, the acoustic velocities in 9 dead oils all show systematic relations with both temperature and pressure. In addition, the acoustic velocities in these oils are apparently related to their API gravities (figure 15). Therefore, we did regressions on all the velocity data to correlate the velocity-temperature-pressure-API gravity relations in oils.

First, linear (first order) regressions are applied to the velocity data with respect to temperature and pressure. i.e., in a given oil, the relation

$$C = b_o + b_1 T + b_2 P + b_3 PT \tag{13}$$

is assumed, where b_o, b_1, b_2, b_3 are regression coefficients. The correlation factors R^2 for all the dead oils except oil C are greater than 0.98. For oil C the correlation factors are around 0.96 ($R^2 = 1$ means the perfect fit between (13) and the measured data) probably due to the oil's severe biodegradation.

Table 1 shows the numerical data for the four coefficients in (13) in the 9 dead oils.

The four coefficients of table 1 are plotted versus the API gravity of the oils in figures 25a through 25d. These figures show that systematic relations do exist between the API gravity and the regression coefficients. In figures 25a and 25d, coefficient b_o decreases while b_3 increases monotonically with increasing API gravity. b_1 and b_2 show extremities as the API gravity increases (figures 25b and 25c). Figures 25a - 25d also show that the biodegradation of oils may not only affect the acoustic velocity values but also the coefficients in (13). The magnitude of such effect is dependent on the oil chemistry and hence probably on the degree of biodegradation, e.g., the biodegradation effect on the four coefficients is larger in oil C than in oil D.

Besides the linear (first order) regression, we also did a more complicated second order regression on the velocity data in all the dead oils with respect to both temperature and pressure. In the second order regression, we assumed that the acoustic velocities in a given oil are non-linearly related to temperatures and pressures, i.e.,

$$C = a_{00} + a_{01}T + a_{02}T^2 + (a_{10} + a_{11}T + a_{12}T^2)P + (a_{20} + a_{21}T + a_{22}T^2)P^2 \quad (14)$$

or in the matrix form

$$C = \mathbf{T}^T \mathbf{A} \mathbf{P}$$

where

$$\mathbf{T} = \begin{bmatrix} 1 \\ T \\ T^2 \end{bmatrix} \qquad \mathbf{A} = \begin{bmatrix} a_{00} & a_{10} & a_{20} \\ a_{01} & a_{11} & a_{21} \\ a_{02} & a_{12} & a_{22} \end{bmatrix} \qquad \mathbf{P} = \begin{bmatrix} 1 \\ P \\ P^2 \end{bmatrix}$$

All the coefficients in matrix **A** for the 9 dead oils are shown in table 2. The correlation factors R^2 for all the oils except the Ugnu are better than 0.99. For the Ugnu oil, the correlation factors are around 0.97.

The coefficients a_{00} through a_{22} are plotted in figures 26a through 26i versus the API gravities of the oils. Again, these coefficients all change systematically, though more complexly, with changing API gravities.

A very important feature in tables 1 and 2 and figures 25 and 26 is that when we know the API gravity of an oil, we can interpolate for the coefficients in (13) or (14) from theses tables or figures and use these coefficients to empirically calculate the acoustic velocities in this oil as a function of both temperature and pressure. To test this, we empirically calculated the acoustic velocities in 2 crude oils and 1 pure hydrocarbon and got very close fit with those measured experimentally.

Figure 27a plots the measured velocities in a 16 API degree oil measured by Han (1987, personal communication) at 725 psig (50 bars) and the calculated ones by linearly interpolating for the coefficients in equations (13) and (14). The plus and diamond signs represent the calculated velocity values by using equation (13) and (14).

respectively. One can see that the calculated velocities fit the measured ones very well, with deviations basically around 3% (figure 27b). Considering the different devices and methods used in the measurements, the uncertainties in velocity, temperature, pressure, and API gravity measurements, and error in the linear interpolation for the coefficients, etc., one should admit that the fit is extremely good.

Similar to figure 27a, shown in figure 28a are the calculated and measured velocities in the dead-end of the live oil as a function of pressure at 2 temperature points (22.8° and 72.0° C) (this oils did not participate in the regression). Again, the fittings are very satisfactory. The deviations of the calculated velocities from the measured ones are about 2.5% at 22.8° C and around 4.5% at 72.0° C (figure 28b). The slopes of the measured velocity curves versus pressure are essentially the same as those of the calculated velocities.

Figure 29a shows that the calculated velocities in cyclooctane (C_8H_{16}) at 0 psig as a function of temperature are very close to the velocity data measured by Wang and Nur (1987), with deviations of less than 3% (figure 29b).

One should notice that the coefficients in equations (13) and (14) used for calculating the acoustic velocities in the 16 API degree oil, the dead-end of the live oil, and the cyclooctane were interpolated linearly from figure 25 and 26. These linear interpolations may enlarge the deviations of the calculated velocities from those measured ones.

One may also have noticed that the calculated velocity curves using equation (13) and (14) are basically very close to each other, which means that for practical purposes, the first order (linear) regression results are essentially good enough in empirically predicting the acoustic velocities in oils with known API gravities.

To summarize, we see that our regression results shown in tables 1 and 2 and figures 25 and 26 are very useful and accurate in empirically calculating the acoustic velocities in oils with known API gravities. However, in order to improve the accuracy of such calculations, more experiments on a variety of oils may still be needed.

Velocity-Temperature-Molecular Weight Relations

Besides the velocity-temperature-pressure-API gravity correlations, we also fitted the measured acoustic velocities to the empirical relation between velocities and molecular weights of oils given by Wang and Nur (1987),

$$C = C_0 + \alpha\,(T - T_0) + \beta\,(\frac{1}{M} - \frac{1}{M_0}), \tag{15}$$

where M represents the molecular weight of the oil, and C_0, α, β are constants for a given oil.

First we interpolated for α and β from Wang and Nur's (1987) results for velocities in pure hydrocarbons, then calculated the acoustic velocities in 5 oils whose molecular weights (average) are known (the molecular weights of other oils used in the experiments are not known). The calculated results, along with those measured velocity values, at 0 psig and 3 different temperature points (22°, 50°, and 75° C) are shown in the table below.

Oil	API	Molecular	22° C		50° C		75° C	
Name	Gravity	Weight	$V_{meas.}$	$V_{cal.}$	$V_{meas.}$	$V_{cal.}$	$V_{meas.}$	$V_{cal.}$
Oil G	43	193	1315	1321	1212	1205	1123	1115
Oil F	34	243			1268	1253	1185	1159
Dead End	~ 23	~ 290			1308	1291	1214	1192
Oil C	10	504					1362	1265
Oil D	10.5	506					1340	1268

Pressure = 0 psig, Velocity Unit: m/sec..

From the above table, one can see that for light oils (oil G, oil F, and the dead-end of the live oil), the calculated velocities by equation (15) fit the measured ones

extremely well, basically within 2%. This 2% deviation may mainly be caused by the measurement and interpolation errors (uncertainties). However, for heavy oils (oils C and D), the fit between the calculated and measured velocities is apparently unsatisfactory, with deviations of about 7% for oil C and around 5% for oil D. These larger deviations may be caused by two factors: (1) The determination of the molecular weight for the heavy oils may not be accurate; (2) Heavy oils usually contain pronounced amount of asphaltenes, complex branched hydrocarbons, and non-hydrocarbons, while Wang and Nur's equation (15) was derived from the acoustic velocity measurements in pure relatively simple hydrocarbons (with less than 1% by weight impurities) and hence it was basically for light oils. We believe that the second factor plays a major role in the velocity discrepancies.

At low temperatures and high molecular weights of the oils, we can not get the values of coefficients α and β since in this range the pure hydrocarbons used in Wang and Nur's experiments are in the solid state.

Wang and Nur's equation (15) can predict the acoustic velocities in light oils (with API gravity higher than about 20 degree) of known molecular weights extremely well. Therefore, equation (15) works for lighter, more fluid-like oils, and breaks down for heavy, complex, and highly viscous oils: i.e., it generally under-predicts the acoustic velocities in heavy oils. To extend equation (15) to accurately calculate the velocities in heavy oils, further work is needed.

Waves propagating in viscous fluids are usually dispersive. The magnitude of such dispersion is dependent on viscosity. Therefore, the higher velocities in heavy oils may also be caused by the dispersion effect. Fit between equation (15) and the measured data might be better at lower frequencies.

APPLICATIONS

In this section, we briefly discuss some applications or potential applications of acoustic velocities in oils to sonic well log and seismic interpretations, P-V-T data determination, specific heat ratio derivation, and possible bubble point determination for live oils.

Sonic Log and Seismic Interpretations

With the rapid developments in acoustic well logging and seismic technologies, a better understanding of the acoustic properties of reservoir fluids are demanded. For example, seismic evaluations, delineations, and characterizations of hydrocarbon reservoirs are receiving more and more attention. Furthermore, more detailed sonic logging, borehole to borehole seismic tomography, 3-D surface imaging of hydrocarbon reservoirs, and seismically monitoring production and enhanced oil recovery processes are to become routine in the future. In all these technologies or potential technologies, without knowing and understanding the acoustic properties of the reservoir fluids and their variations with different processes, the interpretations of the field results would be very difficult, or even impossible.

Knowing the acoustic properties of the reservoir fluids, one can combine these properties with the field sonic or seismic results to delineate hydrocarbon saturations and adjust production strategy. One also can calculate the acoustic velocities in oils as function of depth by assuming a constant geothermal gradient. Figure 30 shows such a calculation for oil C and oil G. Such velocity-depth curves for oils can be used to empirically or theoretically estimate the acoustic velocities in reservoirs, supposing that the velocities in the dry rocks are known, by using the Gassmann relation or Biot theory or some other theories or models.

P-V-T Relation Determinations

As discussed previously, using the laboratory determined pressure-volume-temperature relations to calculate the acoustic velocities in oils requires that the numerical relative volume (normalized volume) data be accurate at least to the fifth

digit. But the highest accuracy for the directly measured P-V-T data can usually be up to the third or the fourth digit of the relative volume, so that we concluded that the determination of acoustic velocities from P-V-T measurements was not accurate enough (the case of oil C is an example). However, acoustic velocity measurements can easily get to high accuracy, and hence it is possible to use the acoustic velocity data to derive the P-V-T relations of crude oils.

As mentioned earlier, the acoustic velocity C is defined as

$$C^2 = \gamma \left(\frac{\partial P}{\partial \rho}\right)_T , \tag{16}$$

where γ, P , ρ represent the specific heat ratio, pressure, and density, respectively. For very small disturbance, equation (16) can be written as

$$C^2 = \gamma \left(\frac{P_1 - P_0}{\rho_1 - \rho_0}\right)_T , \tag{17}$$

where ρ_0 is an initial density of the oil at pressure P_0, and ρ_1 corresponds to the oil density at pressure P_1.

At temperature T, solving for ρ_1 from (17), we have

$$\frac{\rho_1}{\rho_0} = 1 + \frac{\gamma (P_1 - P_0)}{\rho_0 C^2} . \tag{18}$$

Since we are actually interested in the relative density, ρ_0 can be assumed to be equal to 1, then (18) becomes to

$$\rho_1 = 1 + \frac{\gamma (P_1 - P_0)}{C^2} . \tag{19}$$

In terms of specific volume, (19) can be written as:

$$V_1 = \frac{C^2}{C^2 + \gamma (P_1 - P_0)} . \tag{20}$$

Equations (19) and (20) show that one can easily calculate the pressure-density or pressure-volume relations at different constant temperature points if the acoustic velocities and γ values are known as functions of pressure at such temperature points. In

the calculation, a major problem is that there are generally no available γ values for crude oils. However, one may either estimate the γ values from some theories or empirical models or measure the Cp and Cv (or thermal expansivity α) simultaneously with the measurements of acoustic velocities. To do this, one just simply measures the heat required to increase the temperature by 1^{o} C in one mole of the oil. Also, to our knowledge, one can assume γ values of 1.1 for heavy oils and of 1.2 light oils and not to vary with temperature and pressure changes.

The following table lists the measured (V_M), along with those calculated by equation (20), P-V-T relation in the live oil at temperature of 71^{o} C. In the calculations, constant values of $\gamma = 1.1, 1.2, 1.3$ are assumed, respectively.

Pressure(psig)	V_M	$V\,\gamma$=1.1	$V\,\gamma$=1.2	$V\,\gamma$=1.3
5000	0.9855	0.98867	0.98764	0.98662
4600	0.9881	0.99078	0.98995	0.98912
4200	0.9909	0.99296	0.99232	0.99168
3800	0.9938	0.99521	0.99477	0.99434
3400	0.9968	0.99752	0.99730	0.99708
3200	0.9983	0.99873	0.99862	0.99850
3100	0.9991	0.99934	0.99928	0.99923
2994	1.0000	1.00000	1.00000	1.00000

Figure 31 plots the data shown in the above table. From this figure, one can see that the factor γ in equations (19) and (20) is not dominant in the relative volume calculations. i.e., uncertainties in the estimation of the γ values only change the calculated relative volume by very small amount. Figure 31b shows that about 10% uncertainties in γ only change the calculated relative volume by about 0.1% over the pressure range of 2,000 psi (140 bars). Therefore, if high accuracy acoustic velocity data are available, one can calculate or estimate the P-V-T relations in crude oils, even if the exact values

of γ are not known.

In the literature, Stallard et al (1968) used the measured acoustic velocities and calculated the isothermal compressibilities of liquids through the following equation:

$$\beta_T = \frac{1}{\rho C^2} + \frac{T\alpha^2}{\rho Cp} \tag{21}$$

where Cp, C, ρ, α, and T represent the specific heat at constant pressure, acoustic velocity (adiabatic), density, thermal expansivity, and temperature, respectively. The second term on the right side of equation (21) is approximately 10% of the total value of β_T for most liquids (Stallard et al, 1968). A 10% uncertainty in this term will lead to only 1% uncertainty in the value of β_T, while the uncertainties in β_T from direct measurement are usually larger than 5%.

Using (21) to calculate the isothermal compressibilities still requires one measure or estimate the values of Cp and α. Furthermore, both Cp and α are also functions of temperature and pressure. Nevertheless, this method is much simpler than direct measurements and the calculated compressibilities would be more accurate if the uncertainties in estimating the second term on the right side of equation (21) are not very high.

Another method used to calculate the P-V-T properties of liquids through acoustic results is to construct an equation of state using the acoustic velocity results. Wang and Millero (1973) iteratively generated the equation of state for water from the acoustic velocity, and used such equation of state to calculate the P-V-T properties of water and seawater. This method is very precise but less practical for oils since first it is a little complicated arithmetically and second it requires generating an equation of state for each oil under test.

In summary, we see that it is possible to use the acoustic velocity data to calculate the P-V-T properties of reservoir fluids. Such calculations would be more accurate than the direct measurements. However, much of the methodology still needs to be developed in this subject.

Cp/Cv Calculations

As discussed before, P-V-T data can be used to calculate the isothermal acoustic velocities in oils despite the inaccuracy of the data. On the other hand, if the acoustic velocity and P-V-T data are both available for an oil, one can use these data to calculate the specific heat ratio γ of the oil through the following equation:

$$\gamma = \frac{Cp}{Cv} = \frac{{C_M}^2}{{C_T}^2}, \tag{22}$$

where C_M and C_T are the measured adiabatic and calculated isothermal velocities, respectively.

Shown in figure 32 is the calculated specific heat ratio of the live oil over the pressure range of 3,200 to 5,000 psig. The deviations of the γ values at 3,400 and 5,000 psig are apparently caused by the inaccuracy of the P-V-T data. Generally speaking, the specific heat ratio of the live oil is more or less constant over the pressure range over which the calculations were made, with only a slight decrease with increasing pressure detectable.

Figure 33a shows that the calculated γ values for 5 normal alkanes all decrease slightly as temperature increases at atmospheric pressure. $C7$ through $C16$ in the figure represent the carbon numbers of the n-alkanes. Also, light n-alkanes have higher γ values.

Shown in figures 33b and 33c are the specific heat ratios in the 5 normal alkanes as a function of pressure up to 11,600 psig (800 bars) at two different temperature points (60° and 120° C), respectively. Again as observed in the case of the live oil, γ values in normal alkanes tend to decrease slightly with increasing pressure at both temperature points. This decrease might be also caused by the inaccuracy of the P-V-T data.

As a conclusion, we may say that reasonable values of the specific heat ratios can be obtained in oils when the acoustic velocity and accurate P-V-T data are both available.

Bubble Point Determination in Live Oils

Although the acoustic velocities in the live oil did not drop sharply when the bubble point pressure was reached, careful examinations of the velocity - pressure curves in figure 14 reveal that the slopes of the two curves for the live oil change slightly at the bubble point pressure, due to the appearance of the gas bubbles. Furthermore, during the experiments, we observed that when the bubble point pressure was reached, the acoustic signals on the oscilloscope became unstable and the amplitude started to decrease. Therefore, it is still possible to use the acoustic measurements to determine the bubble points of live oils by combining the slope change of the velocity - pressure curves and the amplitude change observations during the experiments.

SUMMARIES AND CONCLUSIONS

Acoustic velocity behaviors of 8 dead oils, 1 live oil, and 2 refined petroleum oils are well characterized in this study. The experimental results reveal that acoustic velocities in oils are systematically related to temperature, pressure, API gravities, and molecular weights of the oils. In all the oils studied, acoustic velocities increase as pressure or molecular weight increases, but decrease as temperature or API gravity increases.

Based on the experimental results, empirical equations are established which can be used to calculate the acoustic velocities in oils as a function of temperature and pressure if the API gravities are known. These empirical equations generally can predict the velocities in oils over wide ranges of temperatures and pressures very accurately, typically within 3-4%.

Acoustic velocities in live oils are lowered by the gas in solution, but the temperature and pressure behaviors remain very similar to those in dead oils without gas. At the bubble point, the velocities do not drop sharply as expected, instead they increase slightly as pressure further decreases. When the pressure is lowered to a certain point below the bubble point, the velocities drop sharply. These behaviors of live oils are

theoretically analyzed that they are controlled by the bubble size, content, and location.

There are at present no single theory or model of the liquid state which can predict the exact values of the acoustic velocities in oils (or in any liquids). Most theories and models of the liquid state we discussed in this paper can only predict the right direction of the velocity changes as temperature or pressure changes. Simpler theories such as the van der Waals' equation of state and the simplified free volume theory predict the acoustic velocities in liquids that deviate from the measured ones by one or two orders of magnitude at most reservoir conditions. The more complicated theories or models such as tunnel theory predict better values of the acoustic velocities but require too much mathematical manipulation and computational effort. Nevertheless, all the theories and models discussed in this paper can qualitatively be used to interpret our experimental results.

Pressure-Volume-Temperature data of oils can not replace acoustic velocity measurements, since the velocities calculated by P-V-T data are usually not accurate enough. On the other side, acoustic velocity data can well be used to check the accuracies of the P-V-T measurements, to calculate more accurate P-V-T data of reservoir fluids, and to calculate the specific heat ratio of oils when accurate P-V-T data are available. The acoustic velocity measurements in live oils can be potentially used to determine the bubble points of the live oils.

The empirical equation established by Wang and Nur (1987) which relates the acoustic velocity with temperature and molecular weight in hydrocarbons can also be used to calculate the velocities in light crude oils with API gravity higher than 20 degrees. But for heavy oils, this equation underpredicts the acoustic velocity values, which is apparently caused by the appearance of solid or semi-solid and non-hydrocarbon materials in heavy oils.

The acoustic velocities in reservoir fluids have wide applications in sonic log and seismic interpretations, particularly in interpretations of the results of 3-D seismic

imaging, seismic characterizations, evaluations, and delineations, of hydrocarbon reservoirs.

With the rapid developments in acoustic logging and seismic technologies, the acoustic velocities in reservoir fluids will certainly play important roles in interpreting the results gathered by such technologies.

APPENDIX : Density Calculation of the Live Oil at Bubble Point

When the composition of an oil is known, one can calculate the density of the oil (McCain, 1973). The calculation for the live oil is as following: First, calculate the pseudoliquid density of the oil under the assumption that it is all liquid at standard condition (60° F, 14.7 psia). Use a first trial density value of the oil of 0.79 g/cc which corresponds to 49.32 lb/cft. From Figure 4-1 of McCain (McCain, 1973, page 144), we get apparent liquid density (ρ_a) of methane = 22.47 lb/cft and apparent liquid density of ethane = 30.90 lb/cft.

Component	Mole%(Zi)	M.W.(Mi)	Zi.Mi	ρ_i*$(lb.cft^{-1})$	Liq. V*(cft)
Hydrogen Sulfide	0.00	34	0.0000	0.00	0.00000
Carbon Dioxide	0.59	44	0.2596	51.63	0.00503
Nitrogen	0.33	28	0.0924	50.44	0.00183
Methane	40.57	16	6.4912	22.47	0.28880
Ethane	5.04	30	1.5170	30.90	0.04910
Propane	3.43	44	1.5126	31.66	0.04780
iso-Butane	0.70	58	0.4067	35.15	0.01157
n-Butane	1.58	58	0.9180	36.48	0.02516
iso-Pentane	0.68	72	0.4910	38.94	0.01261
n-Pentane	0.85	72	0.6137	39.39	0.01558
Hexanes	2.33	86	2.0085	41.34	0.04858

Heptanes Plus	43.90	305	133.8950	58.52	2.28802
	100		148.21		2.79410

* - at standard condition (60° F /14.7 psia).

The first calculated pseudoliquid density of the live oil =

$$\frac{148.21}{2.7941} = 53.04 \ (lb/cft)$$

For a second trial value use 0.70 g/cc which corresponds to 43.70 lb/cft. ρ_a methane = 19.98 lb/cft, ρ_a ethane = 29.34 lb/cft.

Composition	. Zi.Mi	ρ_i (lb.cft^{-1})	liq. V (cft)
Methane	6.4912	19.98	0.3249
Ethane	1.5170	29.34	0.0517
Propane Plus	140.20		2.4562
	148.21		2.8328

At standard condition, the pseudoliquid density of the live oil =

$$\frac{148.21}{2.8328} = 52.32 \ lb/cft$$

Next, we construct a graph using trial values of pseudoliquid density and the resulting calculated values. The point at which a line through the calculated values crosses a line with slope of one is the correct value. Therefore, we get ρ = 53.5 lb/cft = 0.8578 g/cc at standard condition.

Correction of the density for pressure at 3000 psig: $\Delta\rho$ = +0.9 lb/cft. Correction for temperature at 160° F (71° C): $\Delta\rho$ = -2.2 lb/cft. Therefore density at 3000 psig and 160° F = 53.5 + 0.9 - 2.2 = 52.2 lb/cft = 0.8361 g/cc.

REFERENCES

Adhamov, A., 1954. Dissertation, Moscow State Univ..

Barclay, F. J., T. J. Ledwedge, and G. C. Cornfield, 1969. Proc. Inst. Mech. Eng., 184(3C), 185.

Barker, J. A., 1960. Austr. J. Chem., 13. 187-199.

Barker, J. A., 1961. Proc. Roy. Soc., A259, 442-457.

Boelhouwer, J. W. M., 1960. Physica, 26, 1021-1028.

Boelhouwer, J. W. M., 1967. Physica, 34, 484-492.

Dahler, J. S. and J. O Hirschfelder, 1961. J. Chem. Phys., 32, 330-338.

David H. G. and S. D. Hamann, 1961. Austr. I. Chem., 14, 1-7.

Han, D., 1987. Personal Communication.

Hanna, B. N., G. D. Raithby, and W. B. Nicoll, 1978. in ICMHT-1978, Int. Seminar. Dubrovnik. 33-59.

Hirschfelder, J. O., C. F. Curtiss, and R. B. Bird, 1954. Molecular theory of gases and liquids. John Wiley & Sons, New York.

Hunter, J. L., T. J. Welch, and C. J. Montrose, 1963. J. Acoust. Soc. Am., 35(10), 1568-1570.

Katahara, K., 1987. Personal Communication.

Kieffer, S. W., 1977. J. Geophys. Res., 82(20), 2895-2904.

Kincaid, J. F. and H. Eyring, 1938. J. Chem. Phys., 6, 620-629.

Kittel, C., 1946. J. Chem. Phys., 14(10), 614-624.

Kudryavtsev, B. B., 1954. Zh. fiz. chim. 28, 930-939.

Lennard-Jones, J. E. and A. F. Devonshire, 1937. Proc. Roy. Soc., A163, 53-66.

McCain, W. D., Jr., 1973. The properties of petroleum fluids. Petro. Publ. Co., Tulsa.

McWilliam, D. and R. K. Duggins, 1969. Proc. Inst. Mech. Engrs., 184(3C), 102-107.

Meyers, K. O., 1987. Personal Communication.

Nishihara, H. and I Michiyoshi, 1979. in Two Phase Flow Dynamics, U.S.-Japan seminar. Ed. A. E. Bergles and S. Ishigai. Hemisphere Publ. Co., Washington.

Nozdrev, V. F., 1965. The use of Ultrasonics in molecular physics. The MacMillanCo., New York.

Stallard, J. M., I. J. Rosenbaum and C. M. Davis, Jr., 1968. J Acoust. Soc. Am., 45(3), 583-586.

Tonks, L., 1936. Phys. Rev., 50, 955.

Wang, D. and F. J. Millero, 1973. J. Geophys. Res., 78(30), 7122-7128.

Wang, Z. and A. Nur, 1986. SPE Paper 15646.

Wang, Z. and A. Nur, 1987. SEG Expanded Abst., 1-4.

Wentorf, R. H., R. J. Buehler, J. O. Hirschfelder, and C. F. Curtiss, 1950. J. Chem.

Phys., 18(11), 1484-1500.

Wlison, W. D., 1959. J. Acoust. Soc. Am. 31(8), 1067-1072.

van Dael, W. and A. van Itterbeek, 1965. The velocity of sound in dense fluids. In: Physics of high pressure and the condensed phase. Ed. A van Itterbeek. North Holland Publ. Co., Amsterdam.

TABLE AND FIGURE CAPTIONS

Table Captions

Table 1. Regression results of the 4 coefficients in equation (13).

Table 2. Regression results of the 9 coefficients in equation (14).

Figure Captions

Figure 1. Comparisons between Wilson's and our measured velocity data in distilled water as a function of pressure (a) and a function of temperature (b). The differences between the two velocity curves are used in the velocity calibrations.

Figure 2. Acoustic velocity in Mercury measured in the experiments to test the accuracy of the velocity measurement.

Figure 3. Density of oil C as a function of temperature at different pressures (from Meyers, 1987).

Figure 4. X-ray chromatograms of five oils: (a) oil A, (b) oil B, (c) oil C, (d) oil D, (e) oil F.

Figure 5. Measured acoustic velocities in normal decane (oil I) plotted versus pressure (a) and temperature (b). The numbers in the figures represent temperature in degree Celcius and pressure in psig, respectively. The velocity curve at zero psig in (b) is taken from Wang and Nur (1987).

Figure 6. Measured acoustic velocities in Soltrol oil (oil H) plotted versus pressure (a) and temperature (b).

Figure 7. Measured acoustic velocities in oil (oil G) plotted versus pressure (a) and temperature (b).

Figure 8. Measured acoustic velocities in oil F plotted versus pressure (a) and temperature (b).

Figure 9. Measured acoustic velocities in oil A plotted versus pressure (a) and temperature (b).

Figure 10. Measured acoustic velocities in oil B plotted versus pressure (a) and temperature (b).

Figur› 11. Measured acoustic velocities in oil E plotted versus pressure (a) and temperature (b).

Figure 12. Measured acoustic velocities in oil C plotted versus pressure (a) and temperature (b).

Figure 13. Measured acoustic velocities in oil D plotted versus pressure (a) and temperature (b).

Figure 14. Measured acoustic velocities in the live oil as a function of decreasing pressure. The upper two velocity curves represent the acoustic velocities in the same oil after releasing pressure to zero psig for several hours.

Figure 15. Acoustic velocities plotted versus API gravity at two temperature points and pressure of 110 psig.

Figure 16. Temperature derivatives of the measured acoustic velocities in heavy (a) and light (b) oils plotted versus pressure.

Figure 17. Temperature derivatives of the measured acoustic velocities plotted as a function of API gravity at different pressures.

Figure 18. Pressure derivatives of the measured acoustic velocities in heavy (a) and light (b) oils plotted versus temperature.

Figure 19. Comparison of the acoustic velocity calculated from van der Waals' equation of state (curve 1) with that observed experimentally (curve 2) in ethyl alcohol (a) and n-hexane (b) (from Nozdrev, 1965).

Figure 20. Calculated dependence of adiabatic (a) and isothermal (b) acoustic velocity in water-air mixture on volume content of gas, and on mass fraction of gas (c) at different pressures. Surface tension is neglected (from Kieffer, 1977).

Figure 21. Calculated acoustic velocities in water-air mixture as a function of bubble radius and pressure for four mass fractions. Surface tension is considered (from Kieffer, 1977).

Figure 22. Comparison of the measured adiabatic acoustic velocities with the isothermal ones calculated from P-V-T data in 5 normal alkanes (data from

Boelhouwer, 1960 and 1967).

Figure 23. Comparison of the measured adiabatic acoustic velocities with the isothermal ones calculated from P-V-T data in the live oil.

Figure 24. Comparison of the measured adiabatic acoustic velocities with the isothermal ones calculated from P-V-T data in the Ugnu heavy oil.

Figure 25. The 4 coefficients in equation (13) plotted versus API gravity.

Figure 26. The 9 coefficients in equation (14) plotted versus API gravity.

Figure 27. Comparison of the measured acoustic velocities with those calculated from equations (13) and (14) in a 16 API degree oil (a). The deviations are plotted in (b).

Figure 28. Comparison of the measured acoustic velocities with those calculated from equations (13) and (14) in the dead-end of the live oil (a). The deviations are plotted in (b).

Figure 29. Comparison of the measured acoustic velocities with those calculated from equations (13) and (14) in cyclooctane (a). The deviations are plotted in (b).

Figure 30. Calculated acoustic velocities in light and heavy oils versus depth.

Figure 31. Comparison of the measured volume with those calculated from acoustic velocity measurements as a function of pressure in the live oil. The deviations caused by using different specific heat ratios are plotted in (b).

Figure 32. Calculated specific heat ratio in the live oil.

Figure 33. Calculated specific heat ratio in 5 normal alkanes versus temperature (a) and pressures (b, c).

First Order Regression

$$C = b_0 + b_1 T + b_2 P + b_3 TP$$

Oil	API Gravity	b_0	b_1	b_2	$b_3 \times 10^3$
A	5	1687.98	-3.8164	36.660	-29.47
B	7	1654.35	-3.5139	28.863	-8.37
C	10	1687.15	-4.0761	37.109	-70.12
D	10.5	1619.51	-3.5634	28.709	18.84
E	12	1593.41	-3.1685	26.277	37.19
F	34	1443.72	-3.3288	34.518	107.65
G	43	1398.86	-3.5332	35.565	127.029
H	57	1324.66	-3.6419	33.902	127.52
I	62	1333.16	-3.9139	32.146	136.62

Table 1

Second Order Regression

$$C = a_{00} + a_{01}T + a_{02}T^2 + (a_{10} + a_{11}T + a_{12}T^2)P + (a_{20} + a_{21}T + a_{22}T^2)P^2 = \mathbf{T}^T\mathbf{AP}$$

Oil	API Gravity	a_{00}	a_{01}	$a_{02}\times10^3$	a_{10}	$a_{11}\times10^3$	$a_{12}\times10^4$	$a_{20}\times10^3$	$a_{21}\times10^4$	$a_{22}\times10^5$
A	5	1772.58	-7.16662	25.335	36.797	114.209	6.66	387.061	-398.97	24.50
B	7	1694.96	-5.23585	13.723	37.086	-224.063	17.66	-647.008	69.41	-6.26
C	10	1765.38	-6.92836	20.366	48.621	-436.881	28.85	390.165	-213.24	11.77
D	10.5	1654.89	-5.07616	11.189	36.728	-146.980	11.95	-656.639	15.45	-0.70
E	12	1614.63	-3.96573	5.171	28.489	9.585	5.45	70.687	-115.40	2.79
F	34	1465.78	-4.31005	6.667	40.132	145.486	2.98	-1073.721	-13.84	-7.00
G	43	1402.24	-3.99833	3.412	50.457	-197.590	37.61	-2550.890	614.34	-68.20
H	57	1323.39	-3.74585	0.520	44.749	-109.962	27.33	-1218.753	143.50	-22.85
I	62	1328.87	-3.86261	0.837	36.984	121.462	7.48	-330.311	-156.36	1.51

Table 2

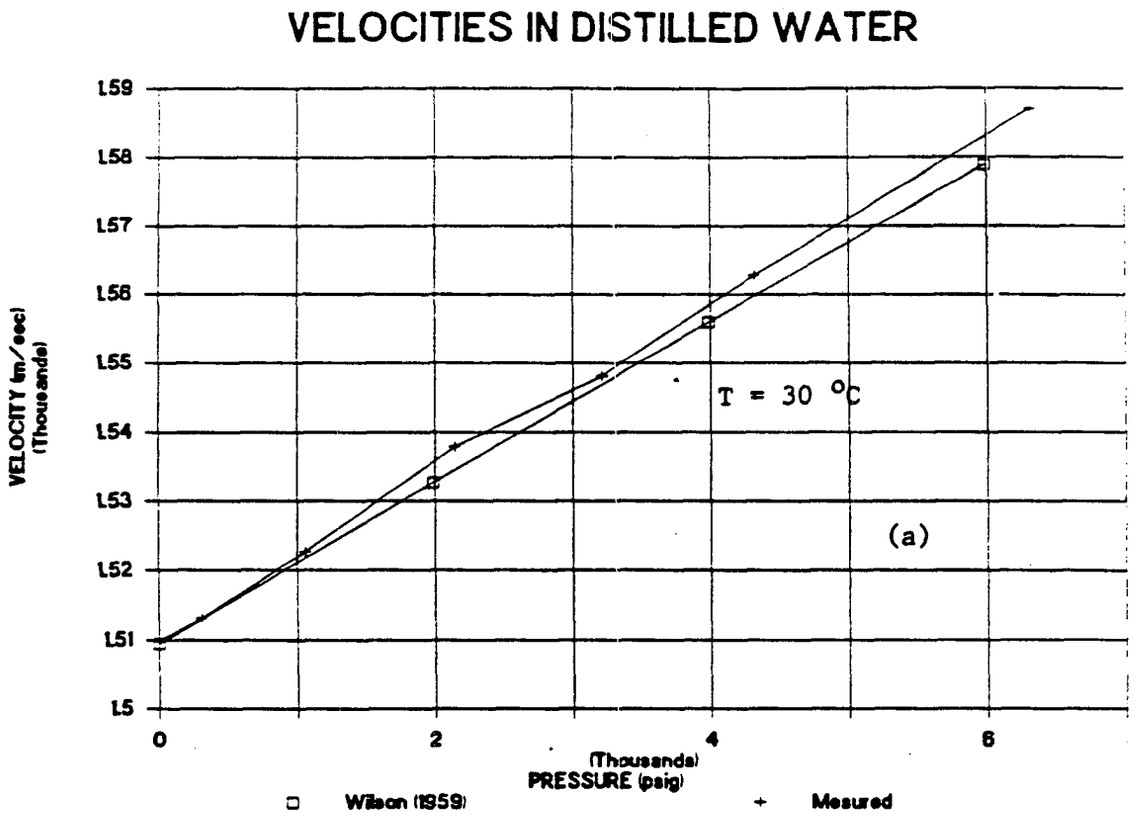
VELOCITIES IN DISTILLED WATER
1.59
1.58
1.57
1.56
1.55
1.54
1.53
1.52
1.51
1.5
VELOCITY (m/sec)
(Thousands)
T = 30 °C
(a)
0
2
4
6
(Thousands)
PRESSURE (psig)
Wilson (1959)
Measured

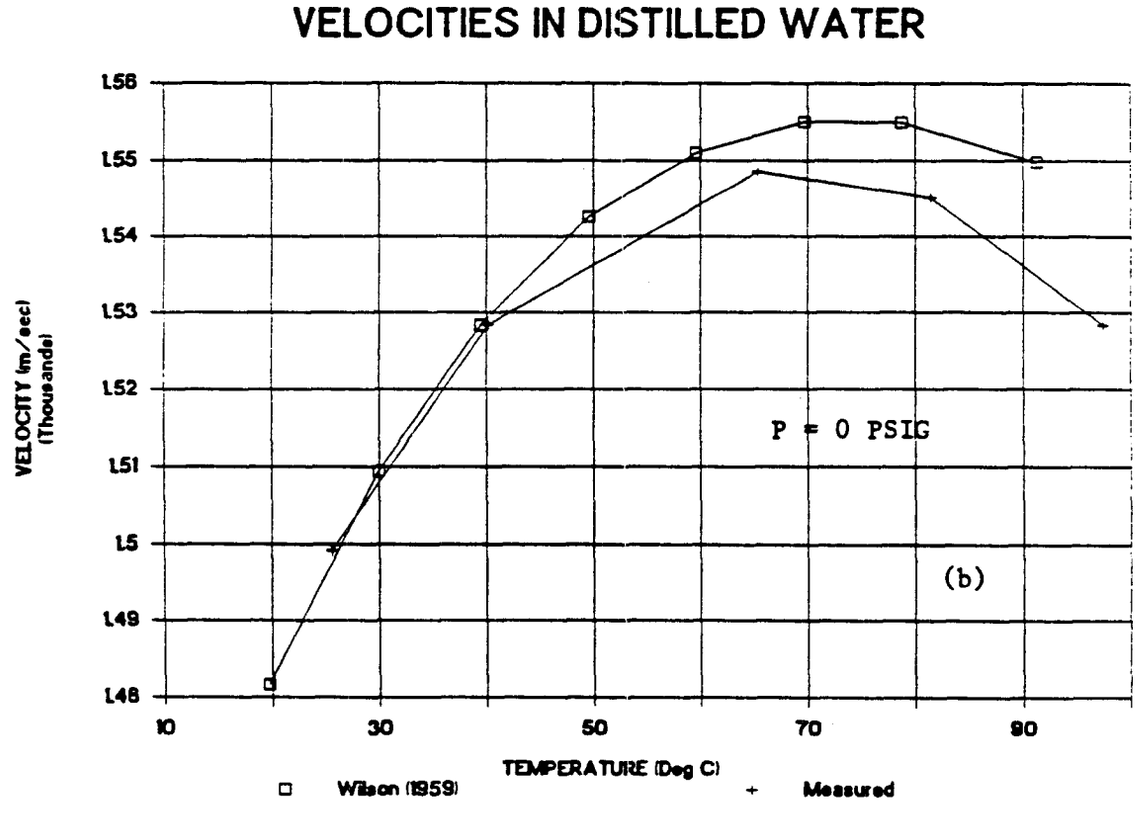
VELOCITIES IN DISTILLED WATER
1.56
1.55
1.54
1.53
1.52
1.51
1.5
1.49
1.48
VELOCITY (m/sec)
(Thousands)
P = 0 PSIG
(b)
10
30
50
70
90
TEMPERATURE (Deg C)
Wilson (1959)
Measured

fig. 1

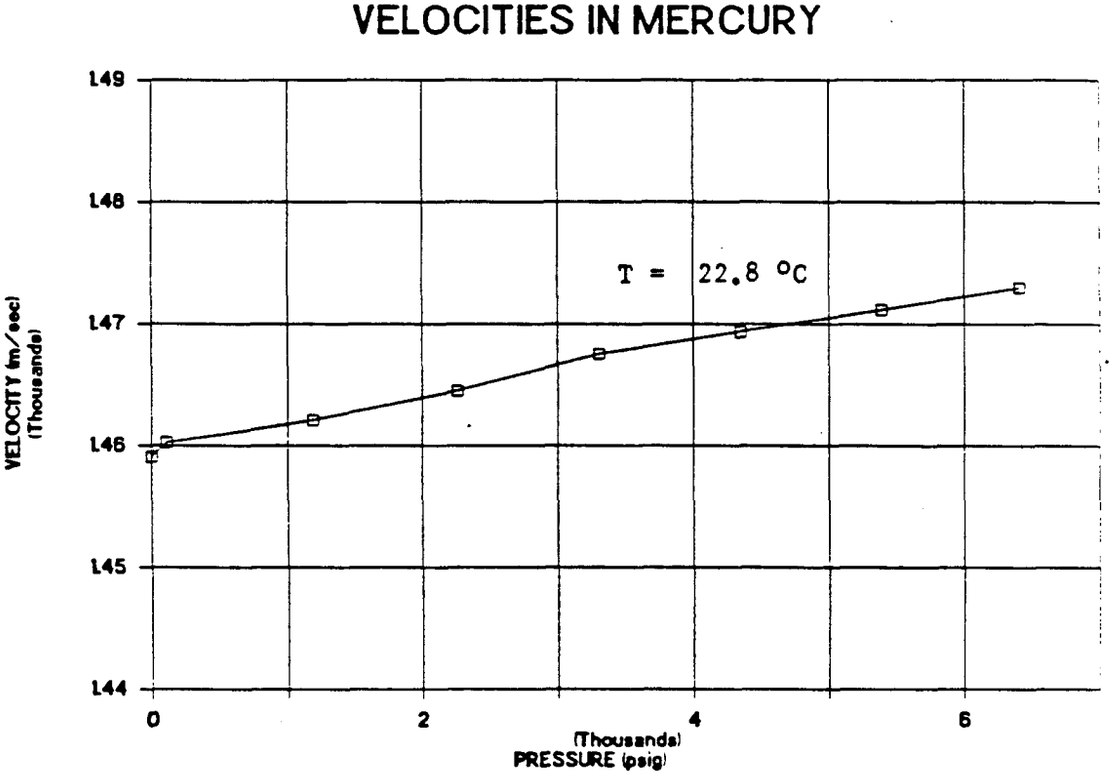
VELOCITIES IN MERCURY
149
148
147
146
145
144
T = 22.8 °C
VELOCITY (m/sec)
(Thousands)
0
2
4
6
(Thousands)
PRESSURE (psig)

Figure 2

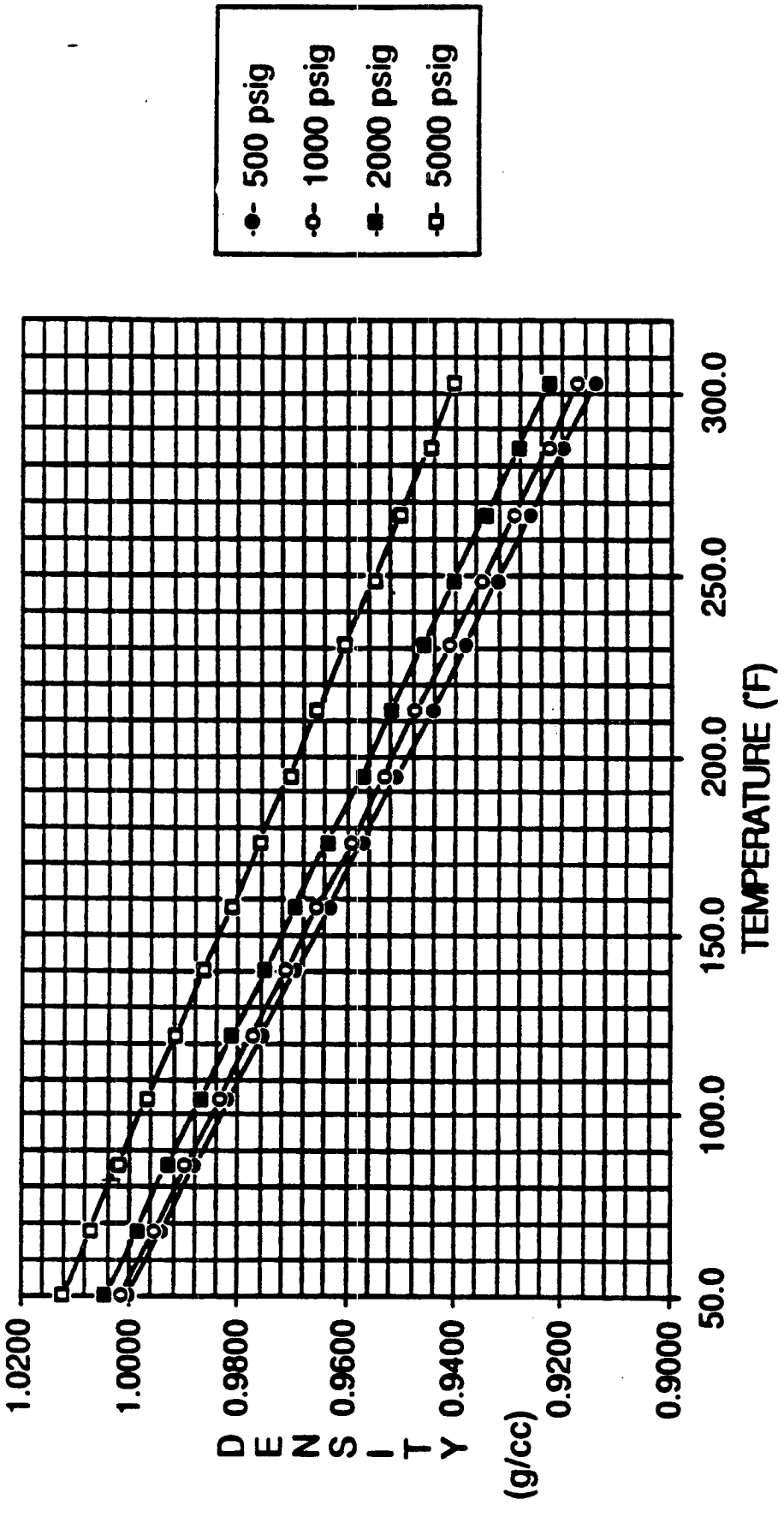
500 psig
1000 psig
2000 psig
5000 psig
1.0200
1.0000
0.9800
0.9600
0.9400
0.9200
0.9000
DENSITY (g/cc)
50.0
100.0
150.0
200.0
250.0
300.0
TEMPERATURE (°F)

fig. 3

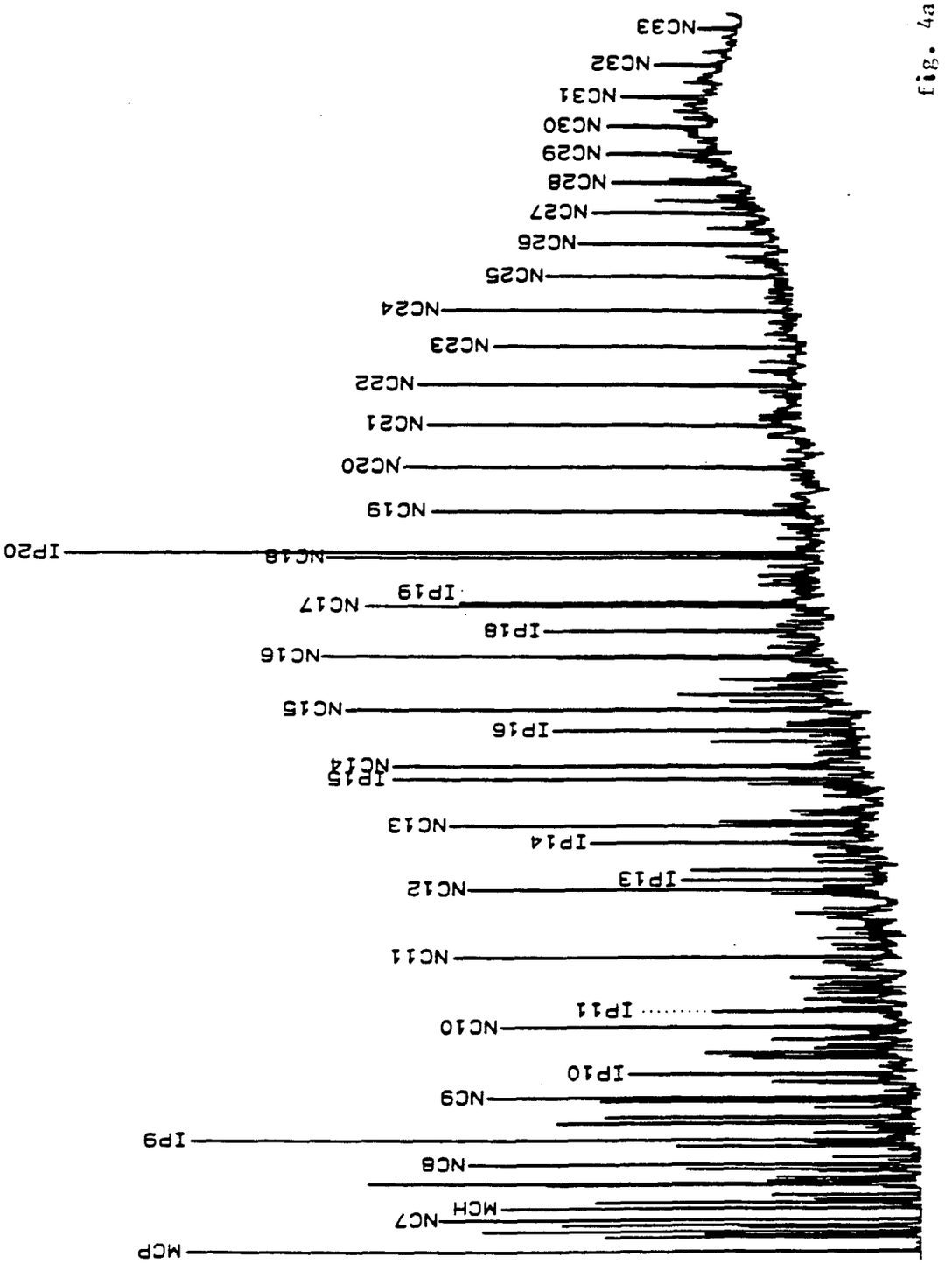
NC33
NC32
NC31
NC30
NC29
NC28
NC27
NC26
NC25
NC24
NC23
NC22
NC21
NC20
NC19
NC18
IP20
NC17
IP19
IP18
NC16
NC15
IP16
NC14
IP15
NC13
IP14
NC12
IP13
NC11
IP11
NC10
IP10
NC9
IP9
NC8
MCH
NC7
MCP

fig. 4a

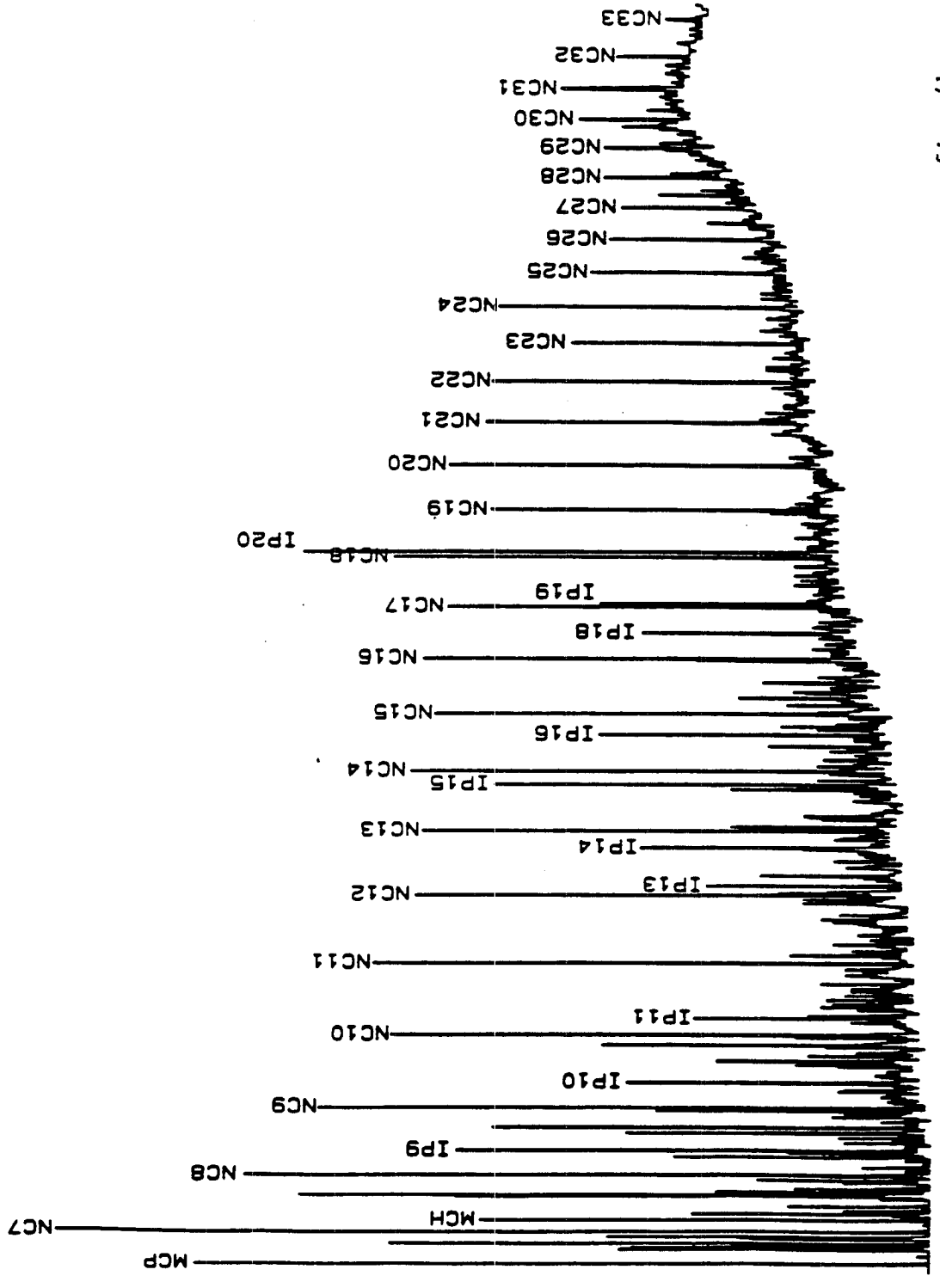
NC33
NC32
NC31
NC30
NC29
NC28
NC27
NC26
NC25
NC24
NC23
NC22
NC21
NC20
NC19
IP20
NC18
IP19
NC17
IP18
NC16
NC15
IP16
NC14
IP15
NC13
IP14
IP13
NC12
NC11
IP11
NC10
IP10
NC9
IP9
NC8
MCH
NC7
MCP

fig. 4b

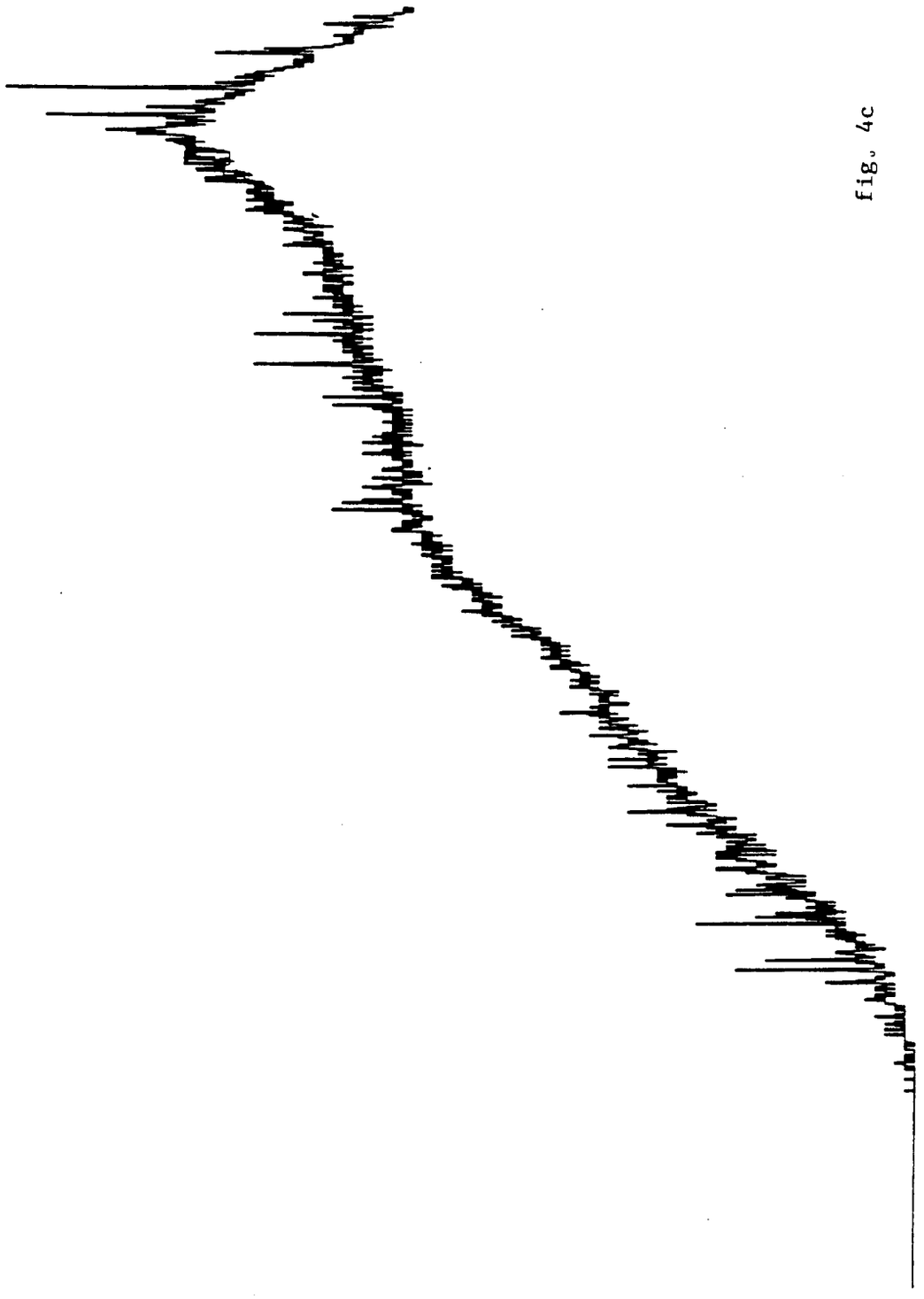

fig. 4c

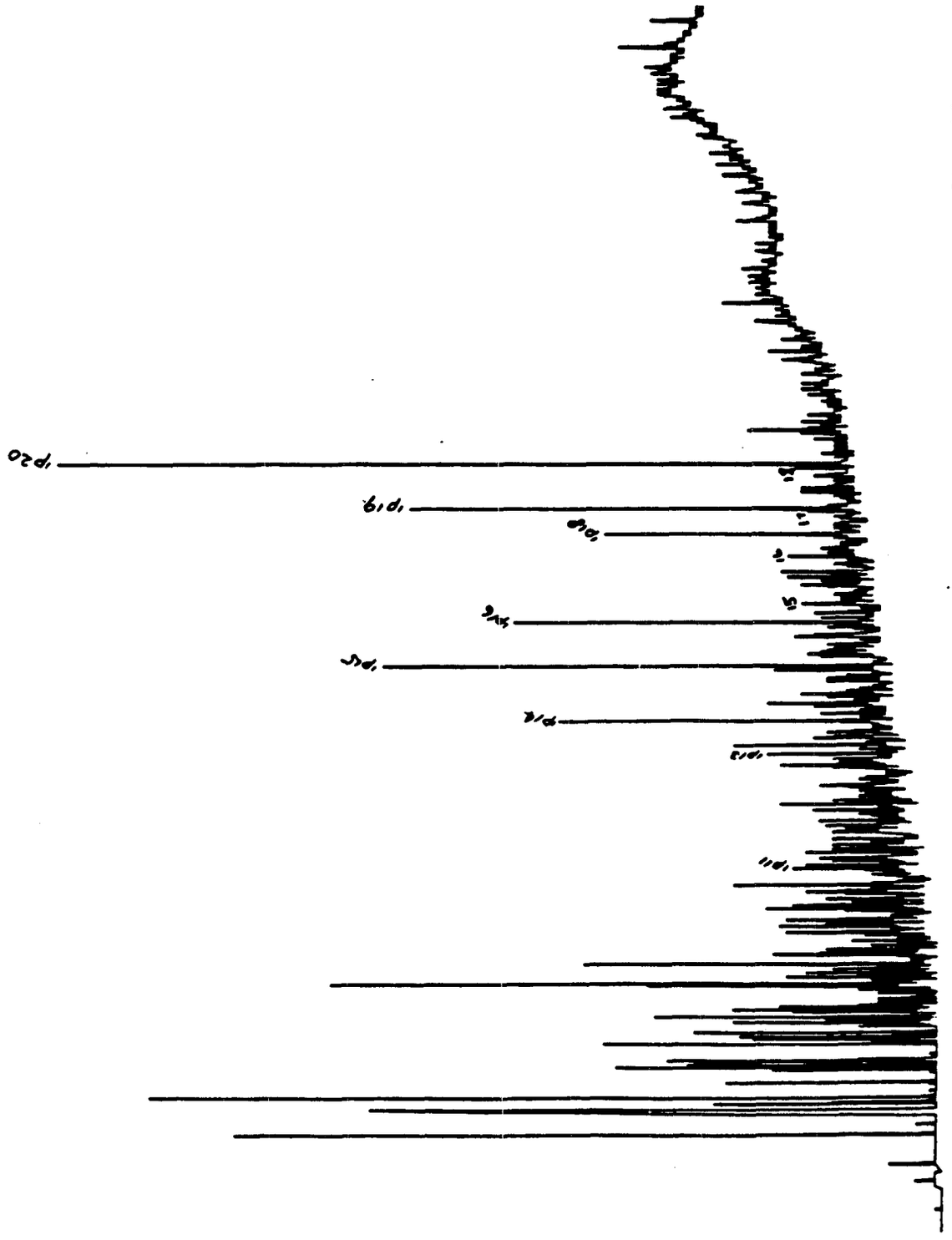

fig. 4d

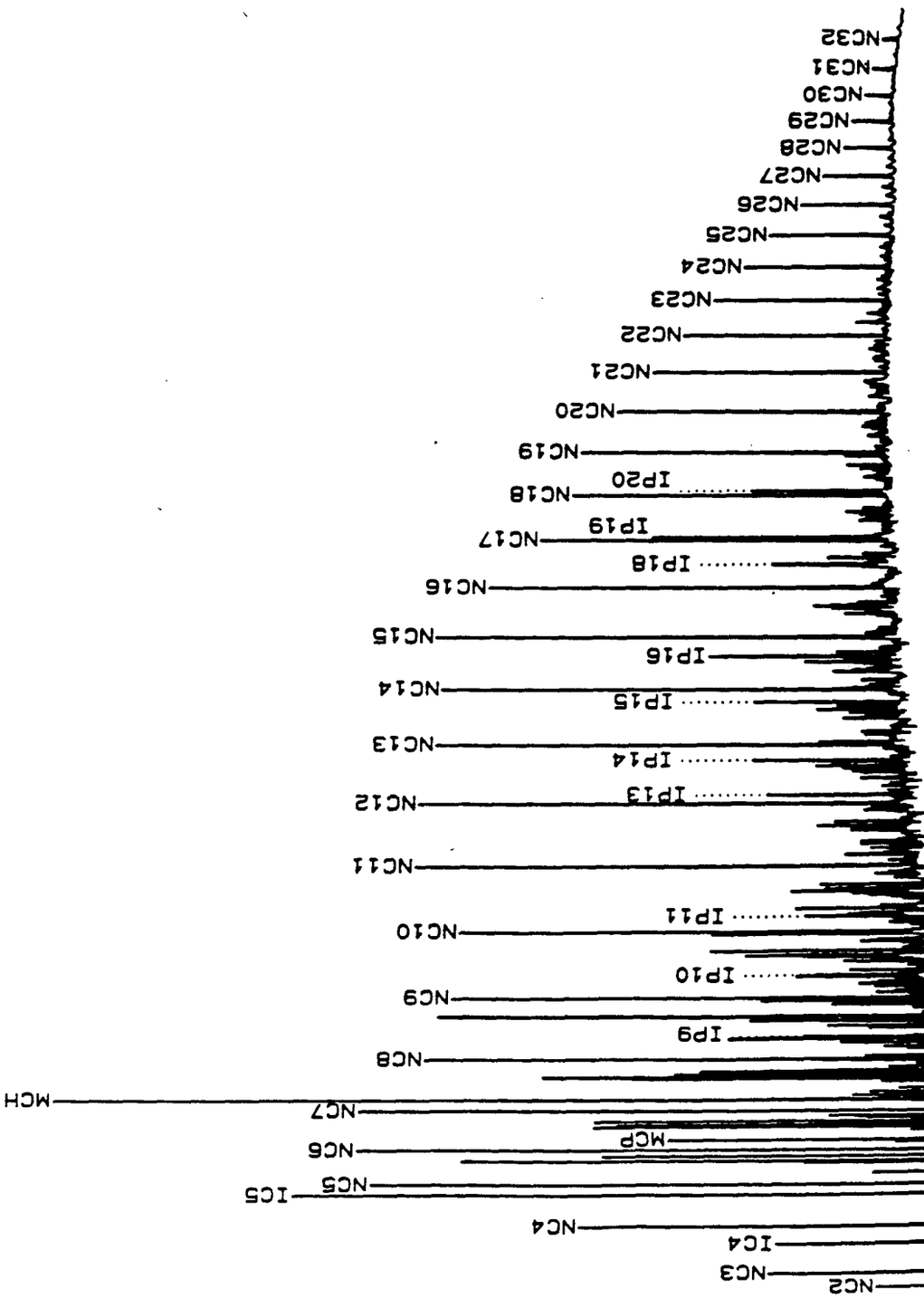
NC32
NC31
NC30
NC29
NC28
NC27
NC26
NC25
NC24
NC23
NC22
NC21
NC20
NC19
IP20
NC18
IP19
NC17
IP18
NC16
NC15
IP16
NC14
IP15
NC13
IP14
NC12
IP13
NC11
IP11
NC10
IP10
NC9
IP9
NC8
MCH
NC7
MCP
NC6
NC5
IC5
NC4
IC4
NC3
NC2

fig. 4e

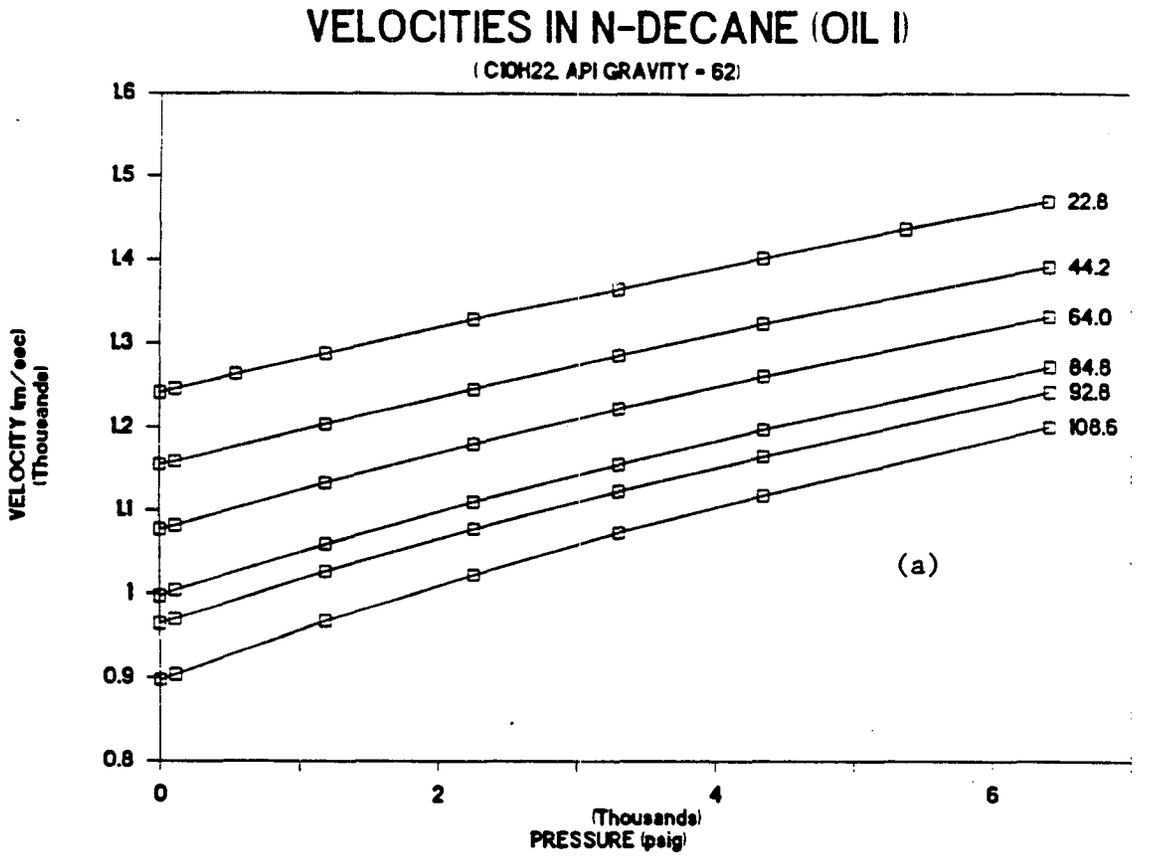
VELOCITIES IN N-DECANE (OIL I)
(C10H22, API GRAVITY = 62)
VELOCITY (m/sec)
(Thousands)
1.6
1.5
1.4
1.3
1.2
1.1
1
0.9
0.8
22.8
44.2
64.0
84.8
92.8
108.6
(a)
0
2
4
6
(Thousands)
PRESSURE (psig)

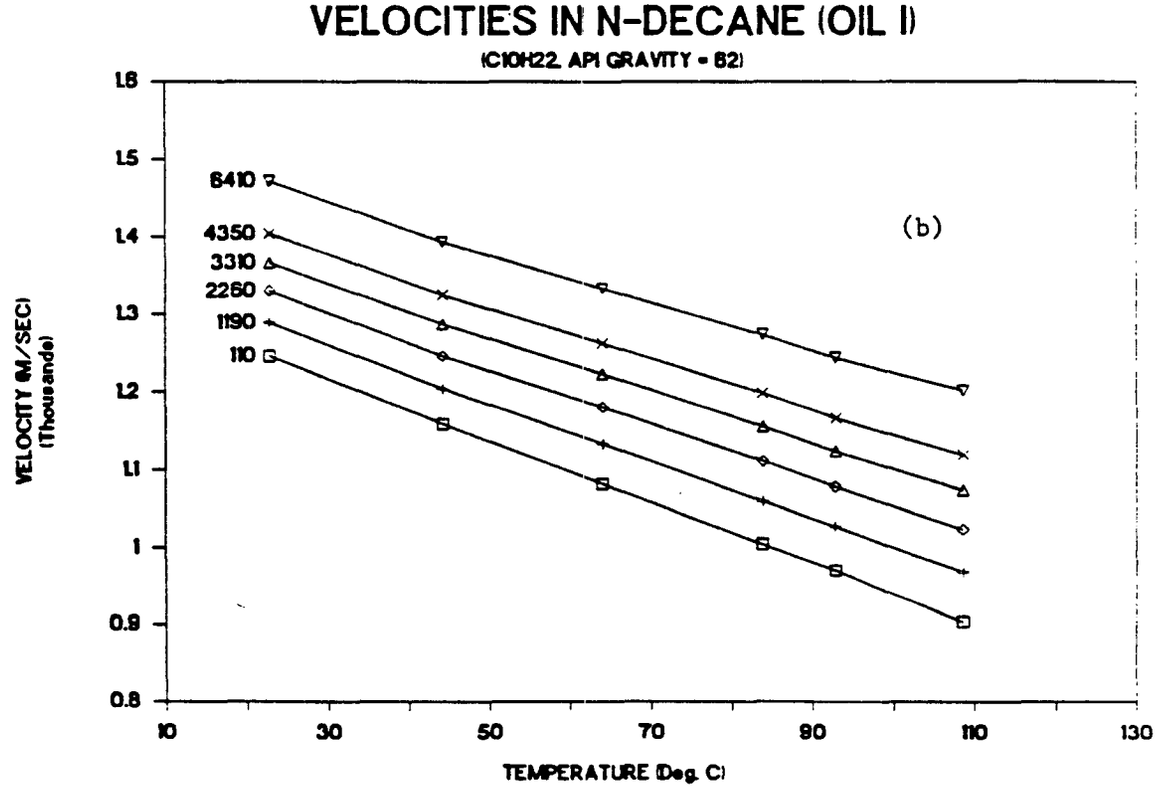
VELOCITIES IN N-DECANE (OIL I)
(C10H22, API GRAVITY = 62)
VELOCITY (M/SEC)
(Thousands)
1.6
1.5
1.4
1.3
1.2
1.1
1
0.9
0.8
6410
4350
3310
2260
1190
110
(b)
10
30
50
70
90
110
130
TEMPERATURE (Deg. C)

fig. 5

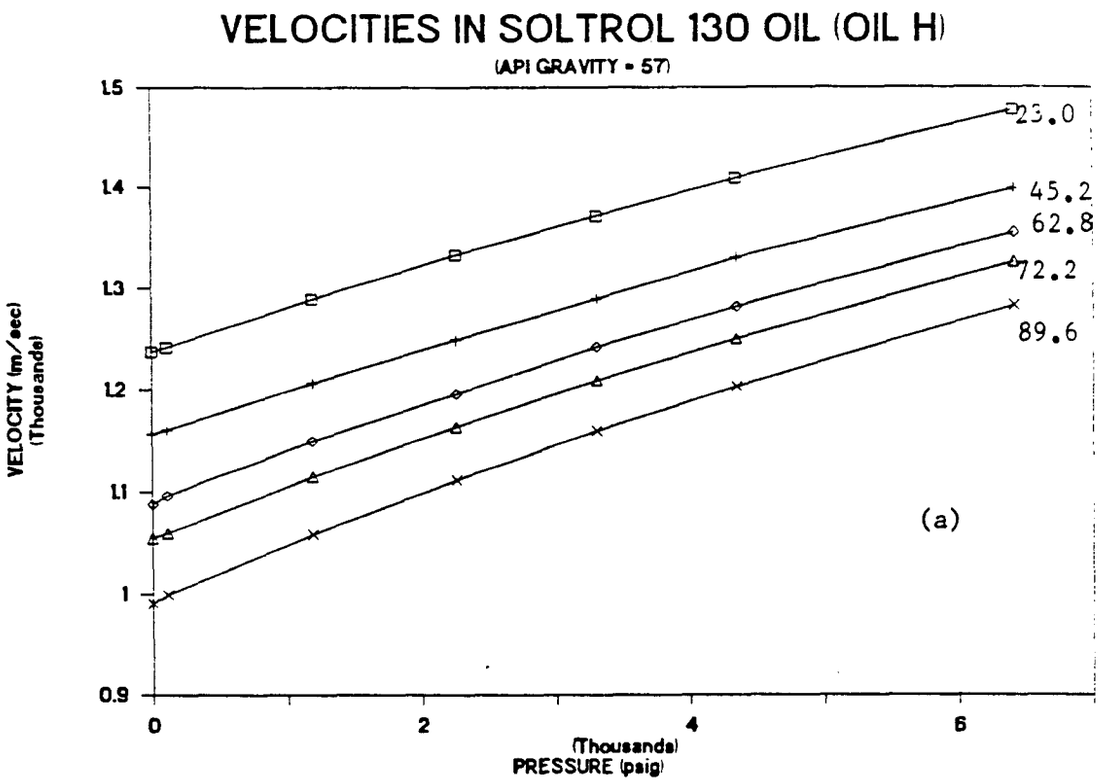
VELOCITIES IN SOLTROL 130 OIL (OIL H)
(API GRAVITY = 57)
VELOCITY (m/sec)
(Thousands)
1.5
1.4
1.3
1.2
1.1
1
0.9
23.0
45.2
62.8
72.2
89.6
(a)
0
2
4
6
(Thousands)
PRESSURE (psig)

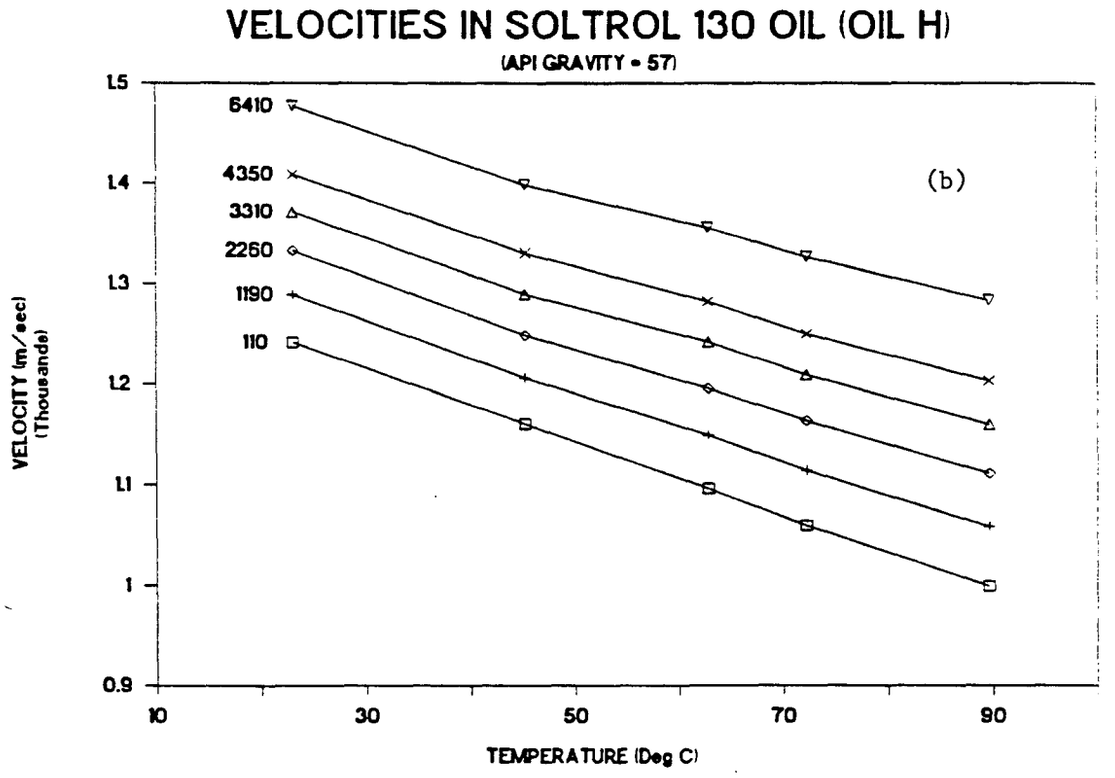
VELOCITIES IN SOLTROL 130 OIL (OIL H)
(API GRAVITY = 57)
VELOCITY (m/sec)
(Thousands)
1.5
1.4
1.3
1.2
1.1
1
0.9
6410
4350
3310
2260
1190
110
(b)
10
30
50
70
90
TEMPERATURE (Deg C)

fig. 6

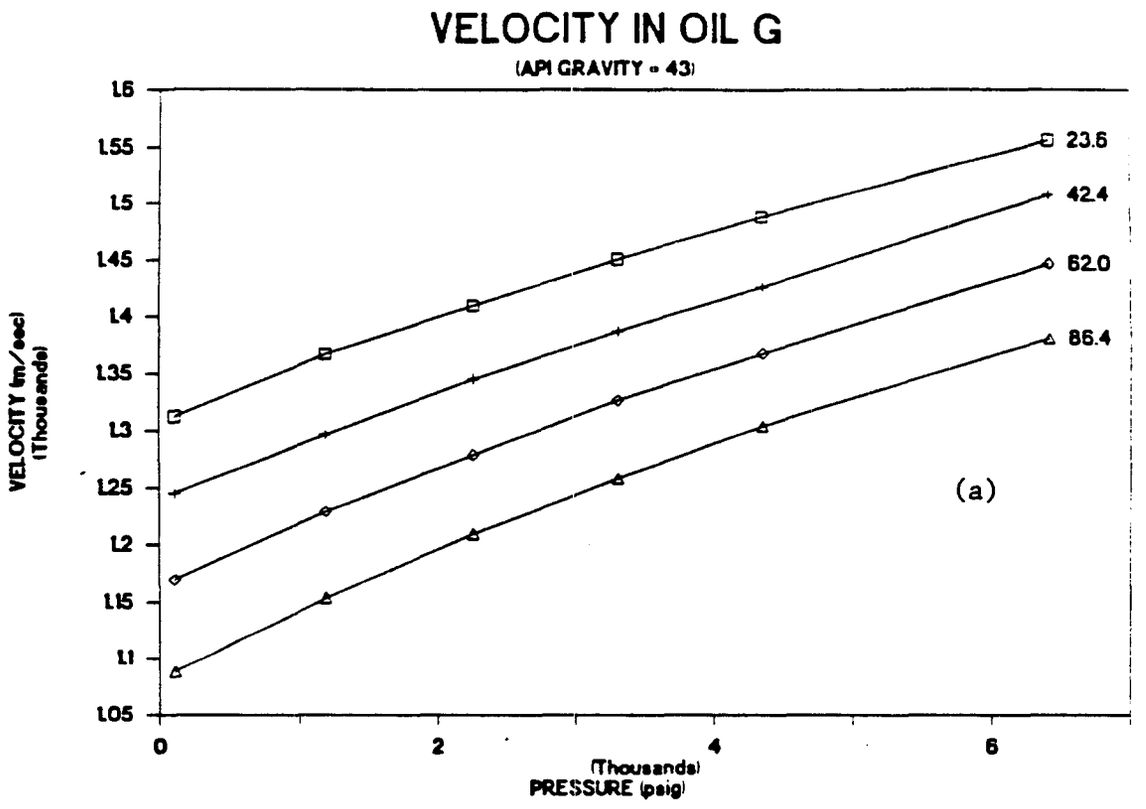
VELOCITY IN OIL G
(API GRAVITY = 43)
VELOCITY (m/sec)
(Thousands)
1.6
1.55
1.5
1.45
1.4
1.35
1.3
1.25
1.2
1.15
1.1
1.05
23.6
42.4
62.0
86.4
(a)
0
2
4
6
(Thousands)
PRESSURE (psig)

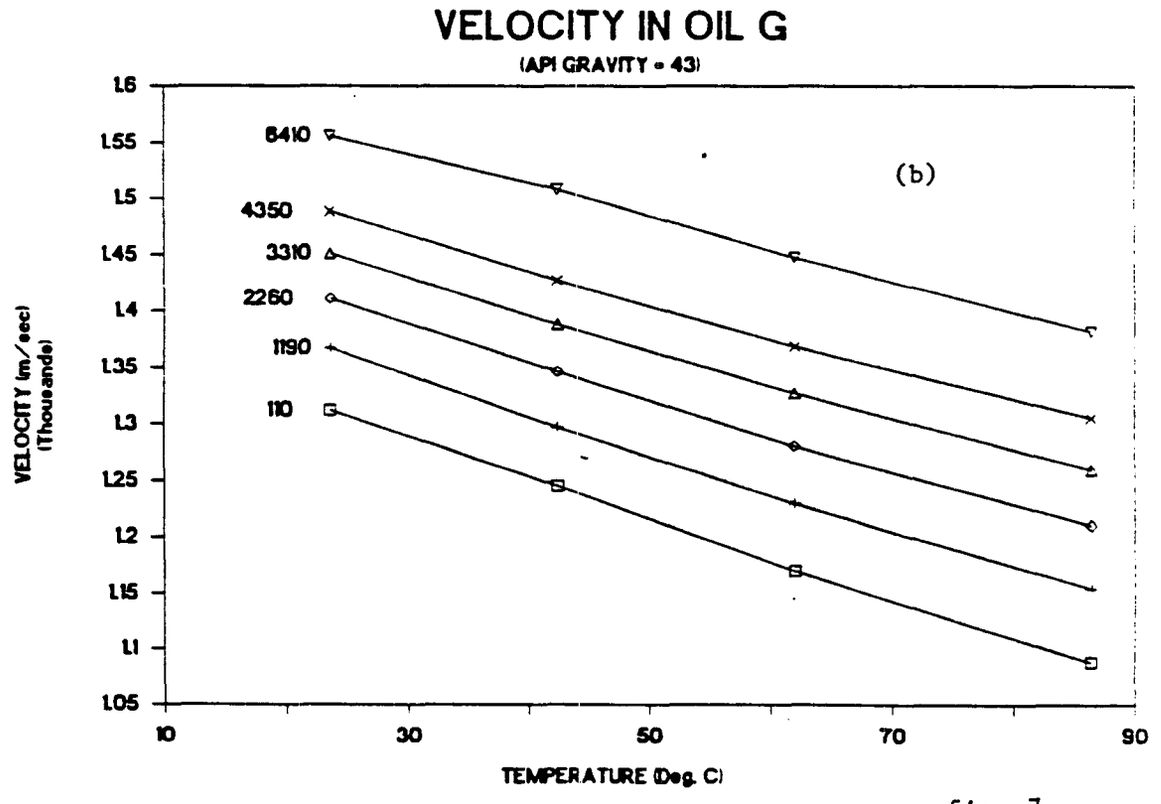
VELOCITY IN OIL G
(API GRAVITY = 43)
VELOCITY (m/sec)
(Thousands)
1.6
1.55
1.5
1.45
1.4
1.35
1.3
1.25
1.2
1.15
1.1
1.05
6410
4350
3310
2260
1190
110
(b)
10
30
50
70
90
TEMPERATURE (Deg. C)

fig. 7

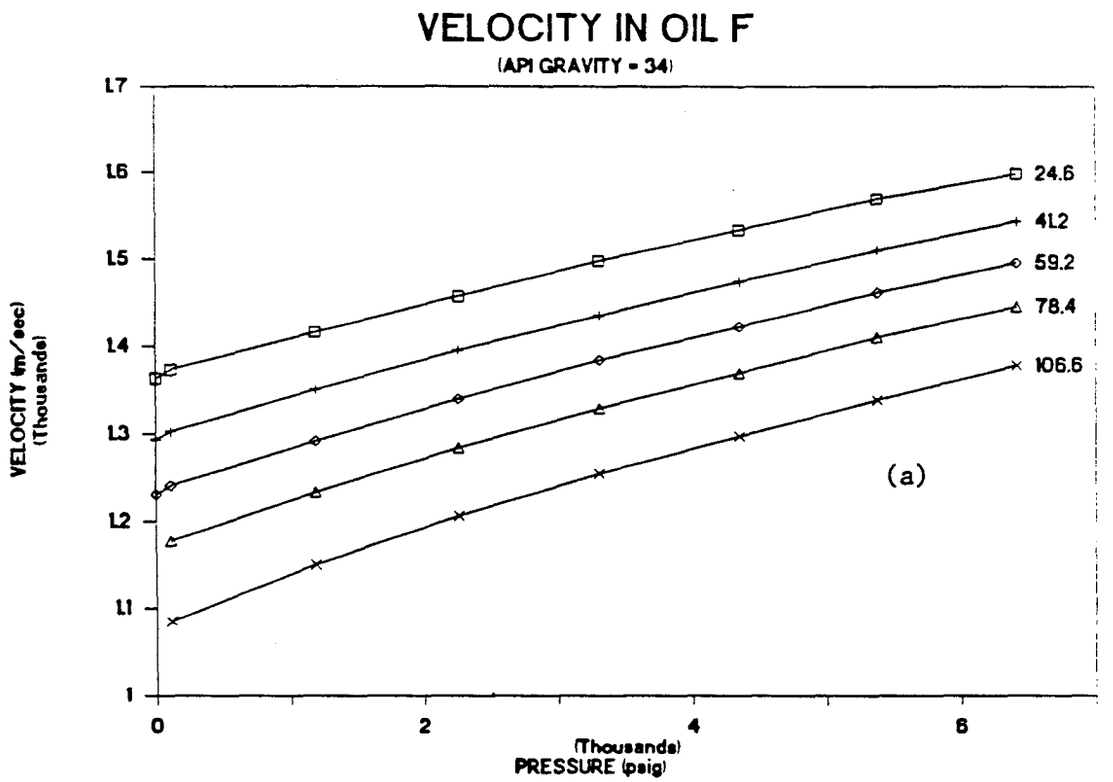
VELOCITY IN OIL F
(API GRAVITY = 34)
VELOCITY (m/sec)
(Thousands)
1.7
1.6
1.5
1.4
1.3
1.2
1.1
1
24.6
41.2
59.2
78.4
106.6
(a)
0
2
4
6
(Thousands)
PRESSURE (psig)

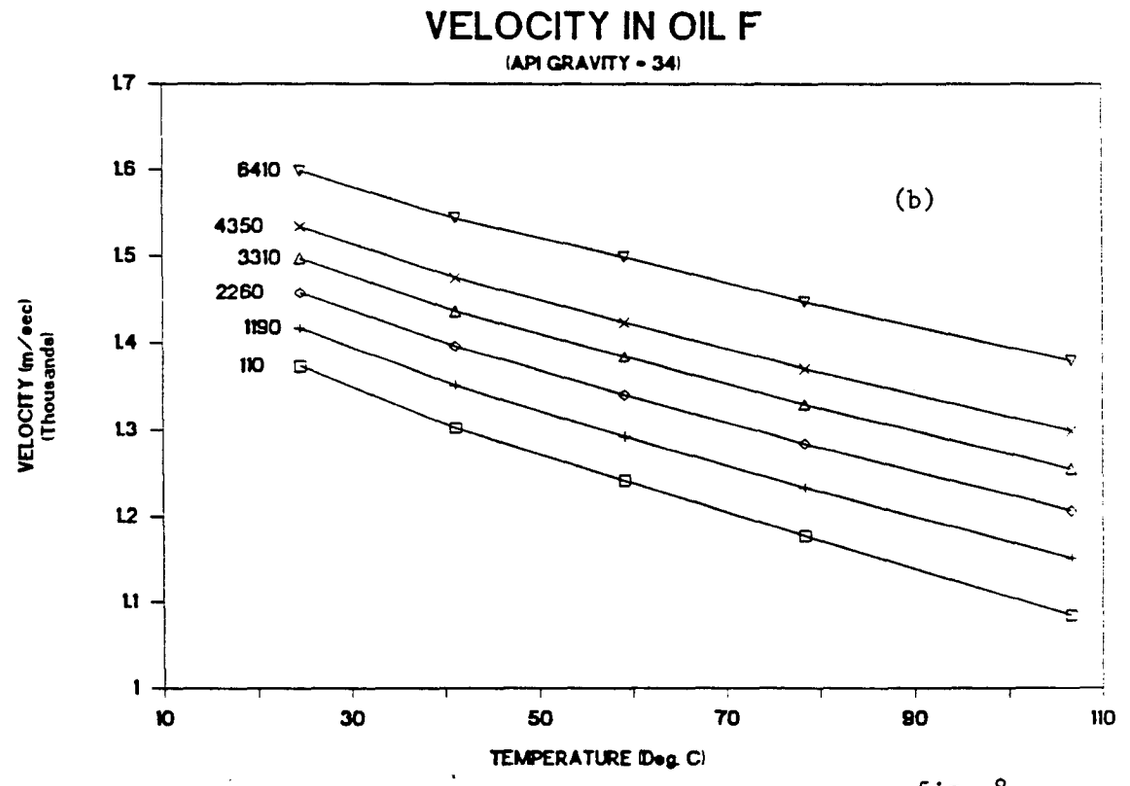
VELOCITY IN OIL F
(API GRAVITY = 34)
VELOCITY (m/sec)
(Thousands)
1.7
1.6
1.5
1.4
1.3
1.2
1.1
1
6410
4350
3310
2260
1190
110
(b)
10
30
50
70
90
110
TEMPERATURE (Deg. C)

fig. 8

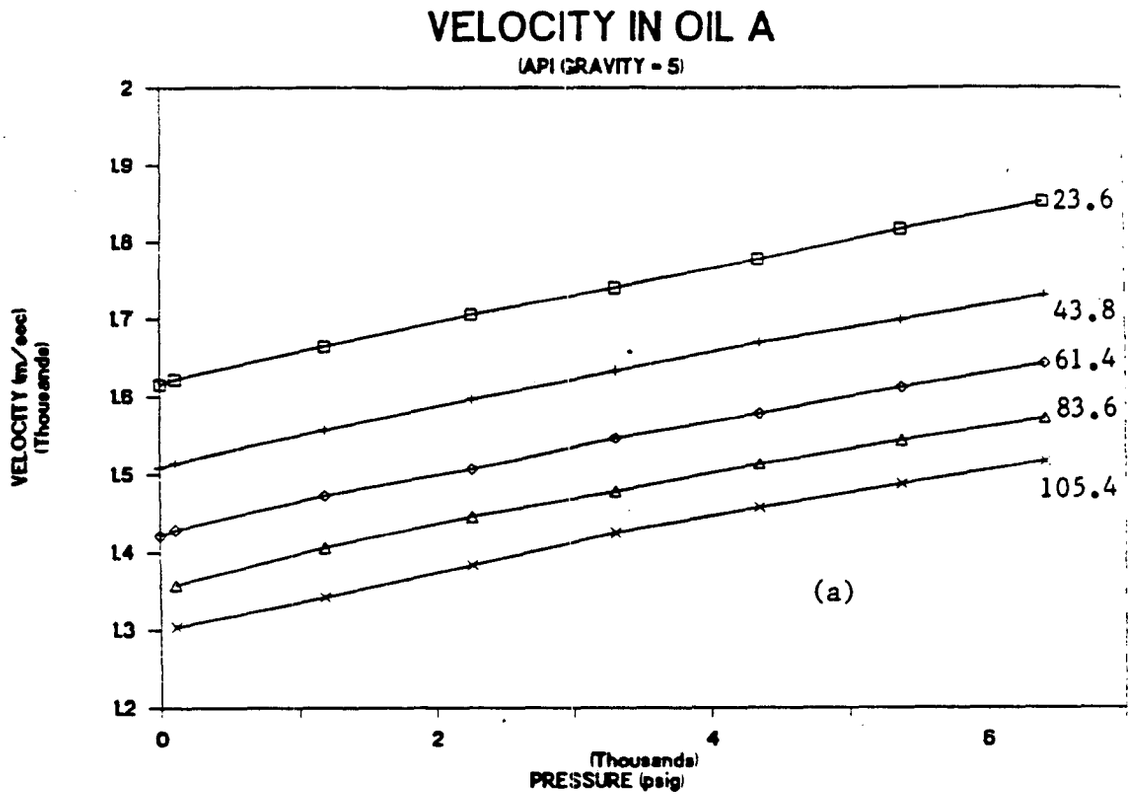
VELOCITY IN OIL A
(API GRAVITY = 5)
VELOCITY (m/sec)
(Thousands)
2
1.9
1.8
1.7
1.6
1.5
1.4
1.3
1.2
23.6
43.8
61.4
83.6
105.4
(a)
0
2
4
6
(Thousands)
PRESSURE (psig)

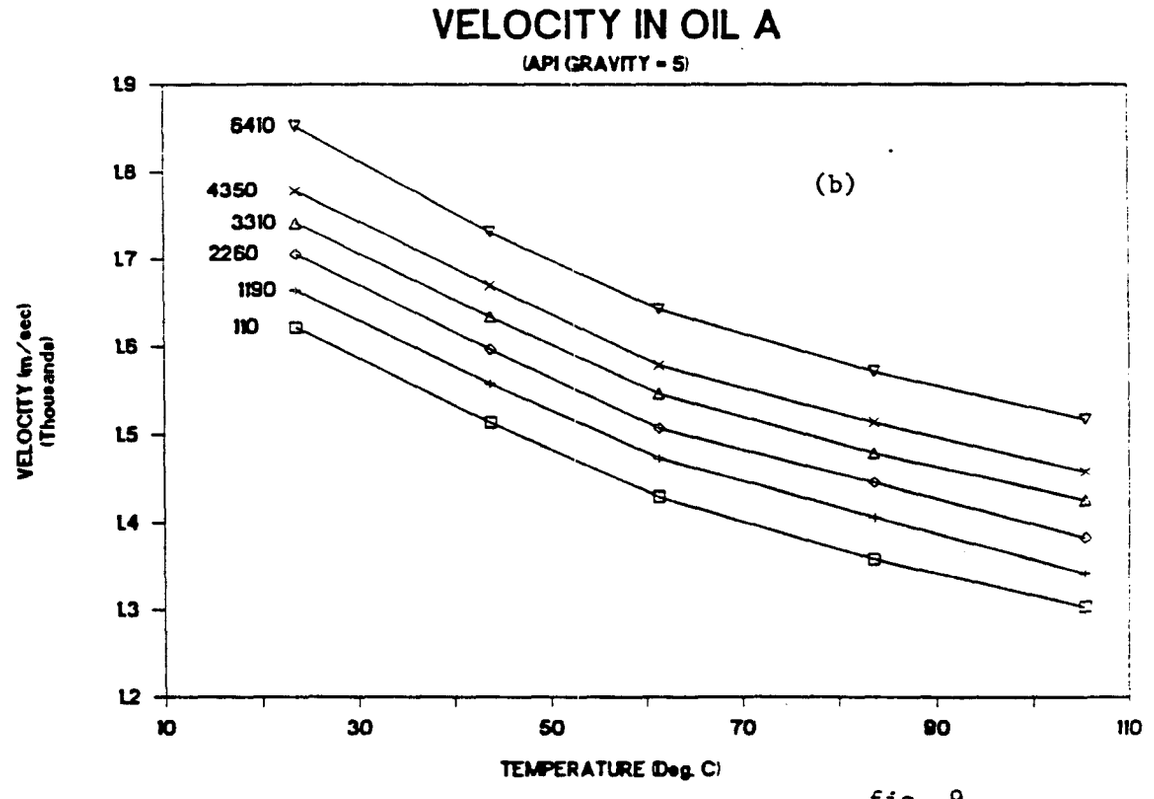
VELOCITY IN OIL A
(API GRAVITY = 5)
VELOCITY (m/sec)
(Thousands)
1.9
1.8
1.7
1.6
1.5
1.4
1.3
1.2
6410
4350
3310
2260
1190
110
(b)
10
30
50
70
90
110
TEMPERATURE (Deg. C)

fig. 9

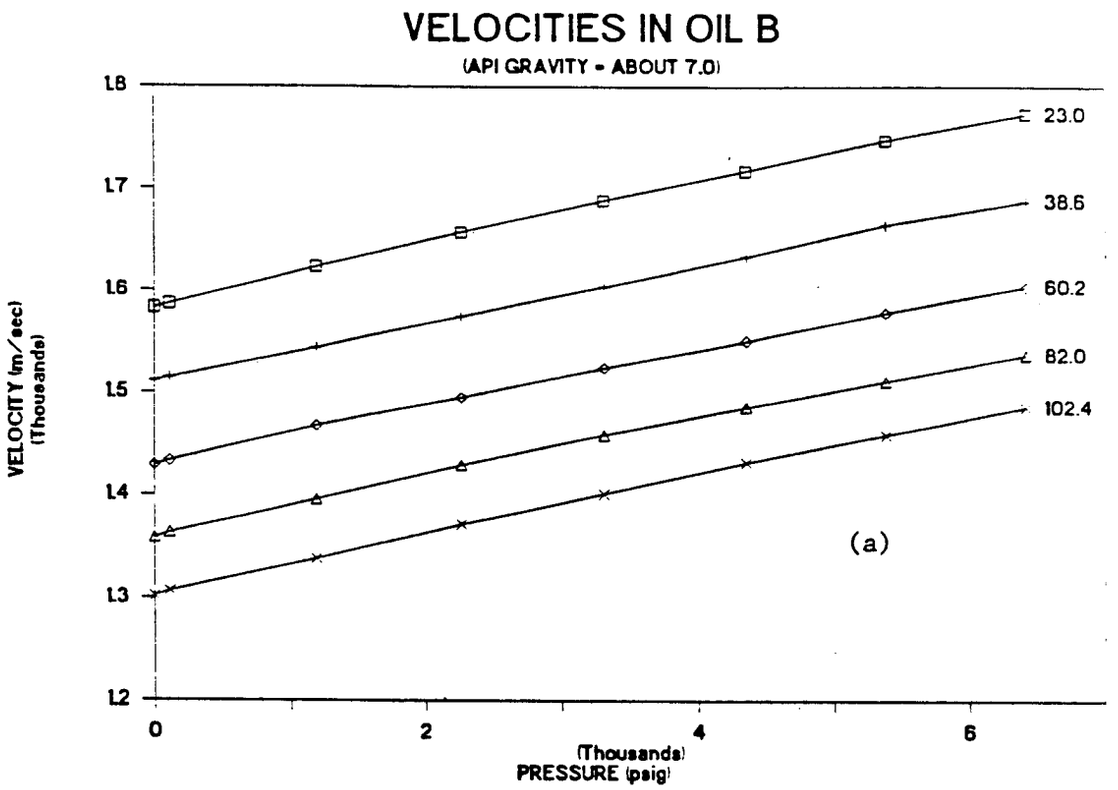
VELOCITIES IN OIL B
(API GRAVITY = ABOUT 7.0)
VELOCITY (m/sec)
(Thousands)
1.8
1.7
1.6
1.5
1.4
1.3
1.2
23.0
38.6
60.2
82.0
102.4
(a)
0
2
4
6
(Thousands)
PRESSURE (psig)

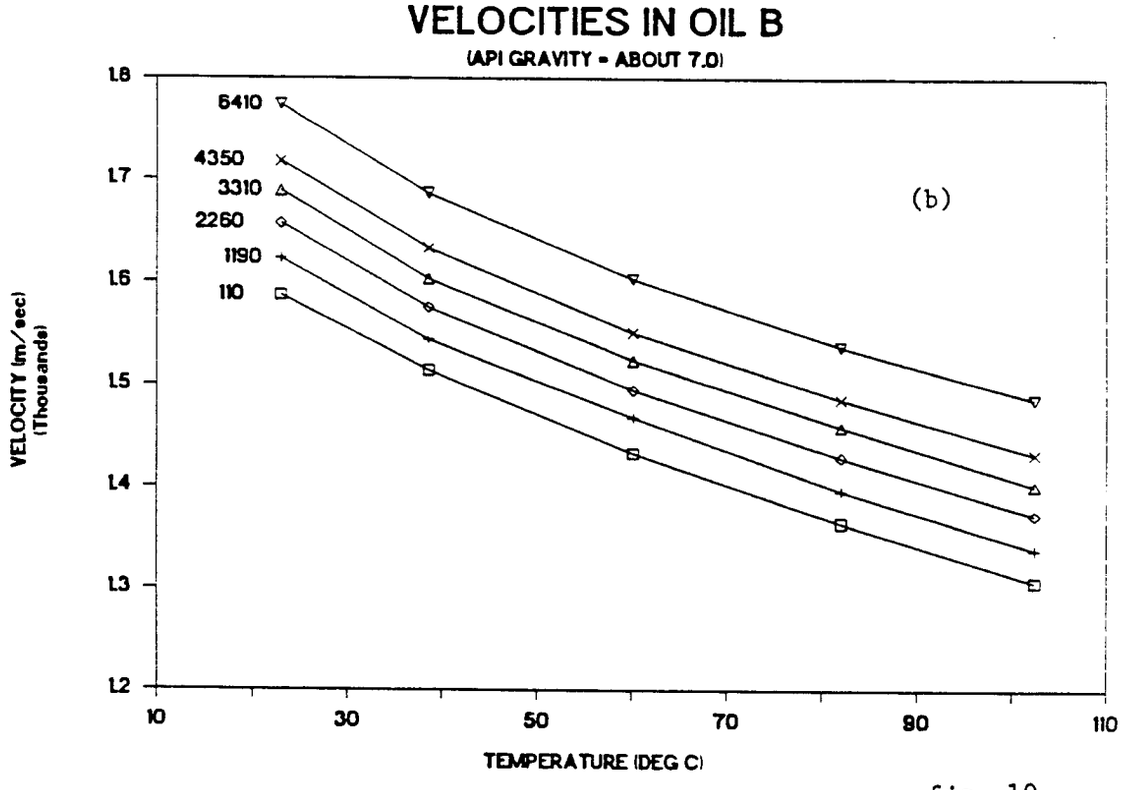
VELOCITIES IN OIL B
(API GRAVITY = ABOUT 7.0)
VELOCITY (m/sec)
(Thousands)
1.8
1.7
1.6
1.5
1.4
1.3
1.2
6410
4350
3310
2260
1190
110
(b)
10
30
50
70
90
110
TEMPERATURE (DEG C)

fig. 10

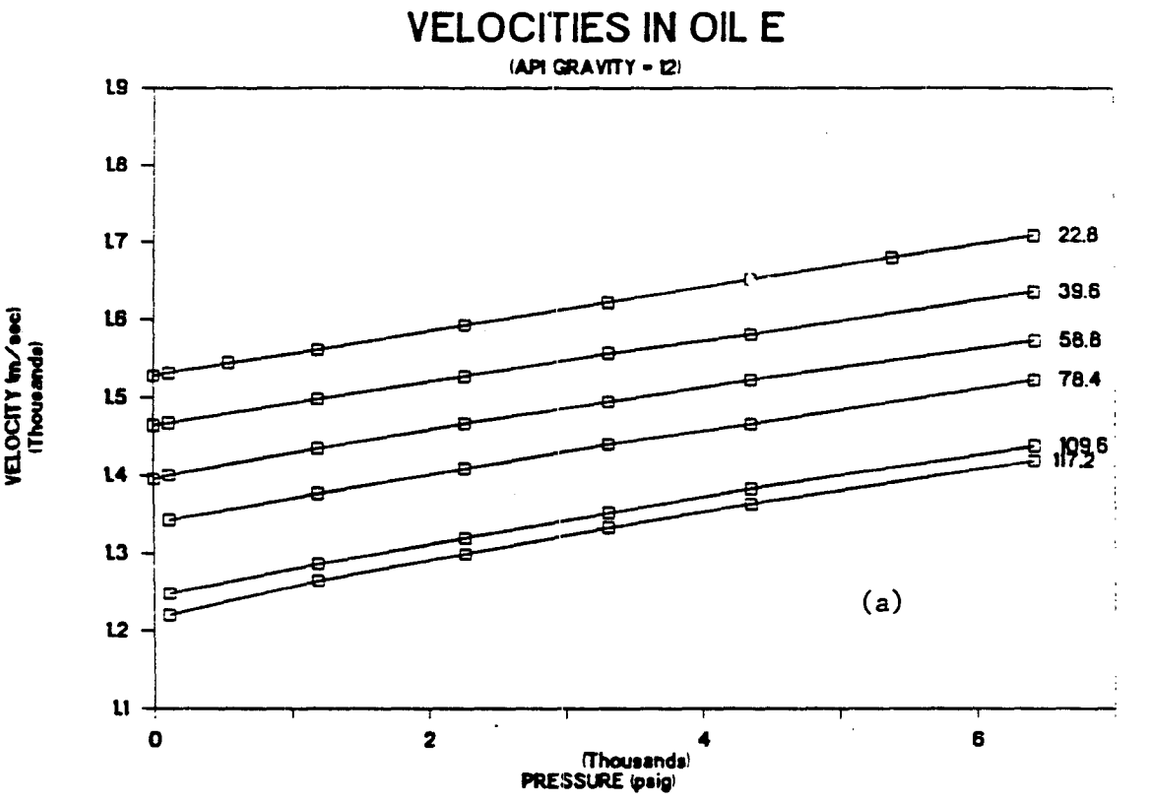
VELOCITIES IN OIL E
(API GRAVITY = 12)
VELOCITY (m/sec)
(Thousands)
1.9
1.8
1.7
1.6
1.5
1.4
1.3
1.2
1.1
22.8
39.6
58.8
78.4
109.6
117.2
(a)
0
2
4
6
(Thousands)
PRESSURE (psig)

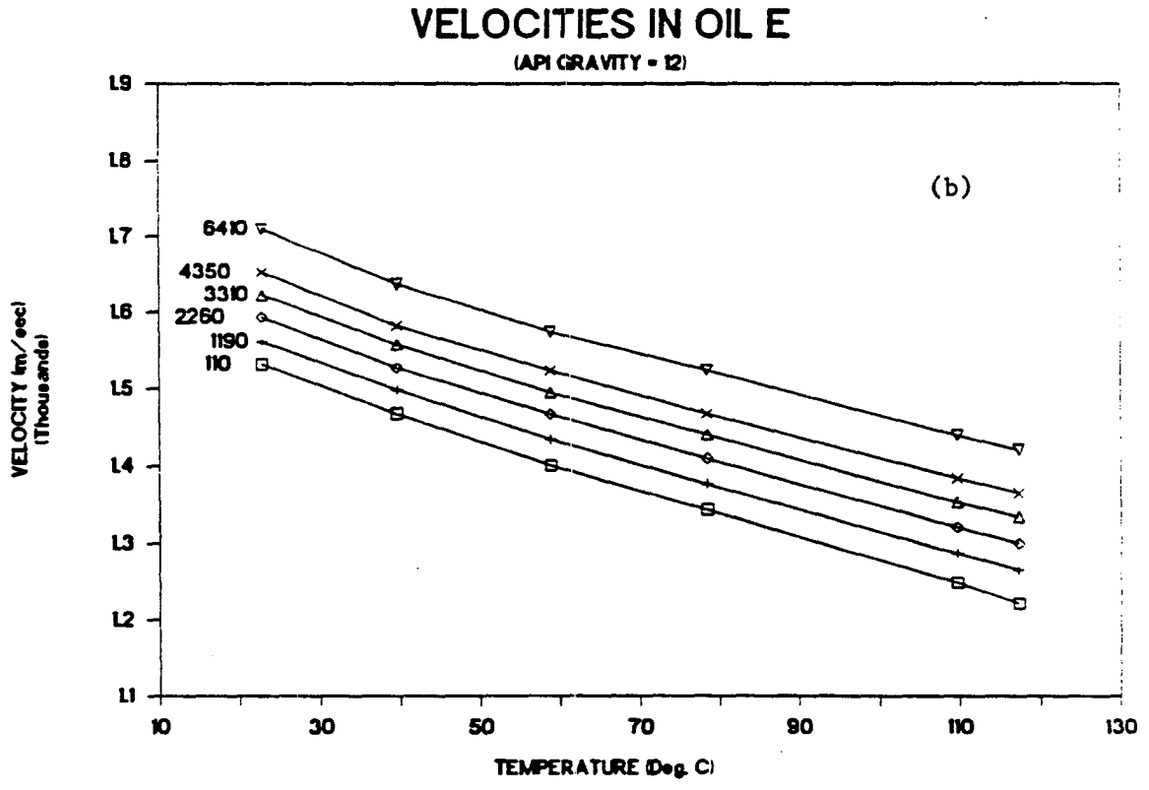
VELOCITIES IN OIL E
(API GRAVITY = 12)
VELOCITY (m/sec)
(Thousands)
1.9
1.8
1.7
1.6
1.5
1.4
1.3
1.2
1.1
(b)
6410
4350
3310
2260
1190
110
10
30
50
70
90
110
130
TEMPERATURE (Deg. C)

fig. 11

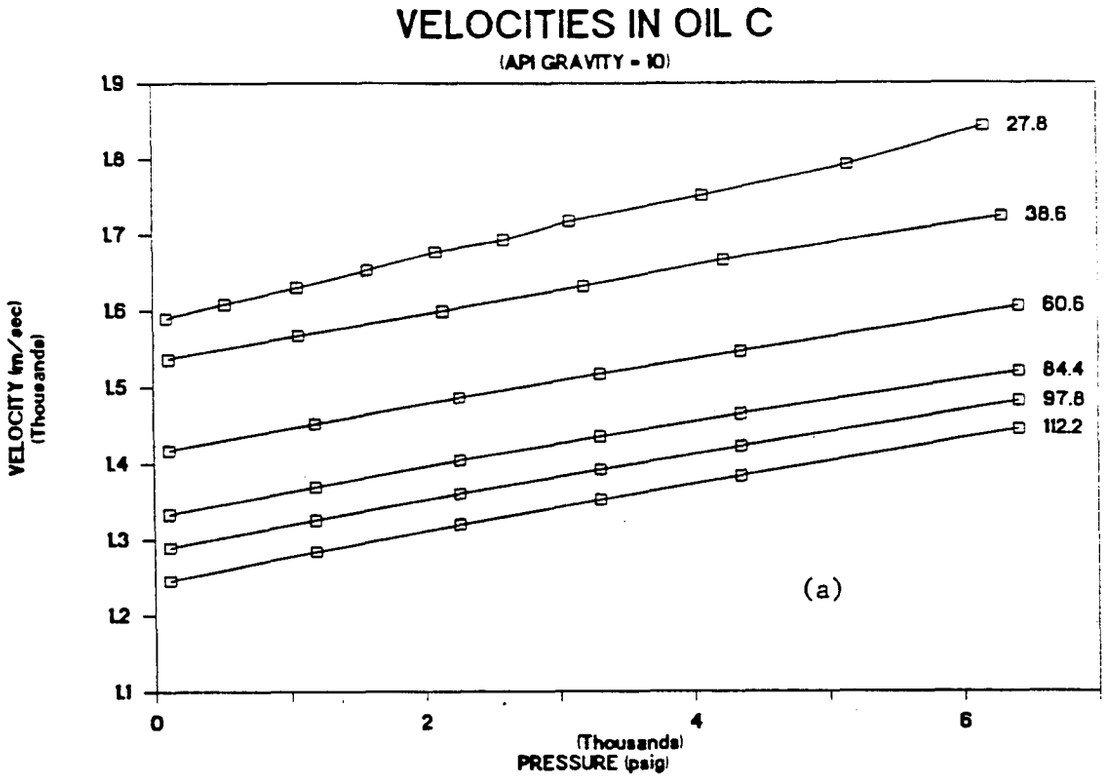
VELOCITIES IN OIL C
(API GRAVITY = 10)
VELOCITY (m/sec)
(Thousands)
1.9
1.8
1.7
1.6
1.5
1.4
1.3
1.2
1.1
27.8
38.6
60.6
84.4
97.8
112.2
(a)
0
2
4
6
(Thousands)
PRESSURE (psig)

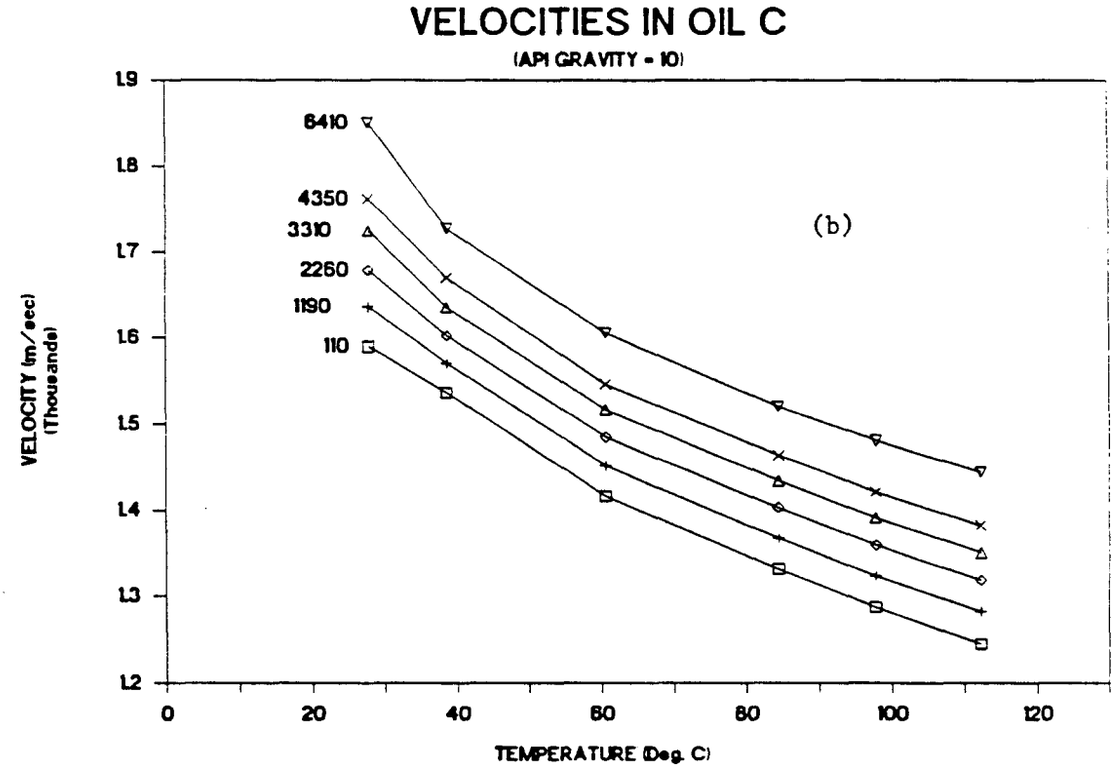
VELOCITIES IN OIL C
(API GRAVITY = 10)
VELOCITY (m/sec)
(Thousands)
1.9
1.8
1.7
1.6
1.5
1.4
1.3
1.2
8410
4350
3310
2260
1190
110
(b)
0
20
40
60
80
100
120
TEMPERATURE (Deg. C)

fig. 12

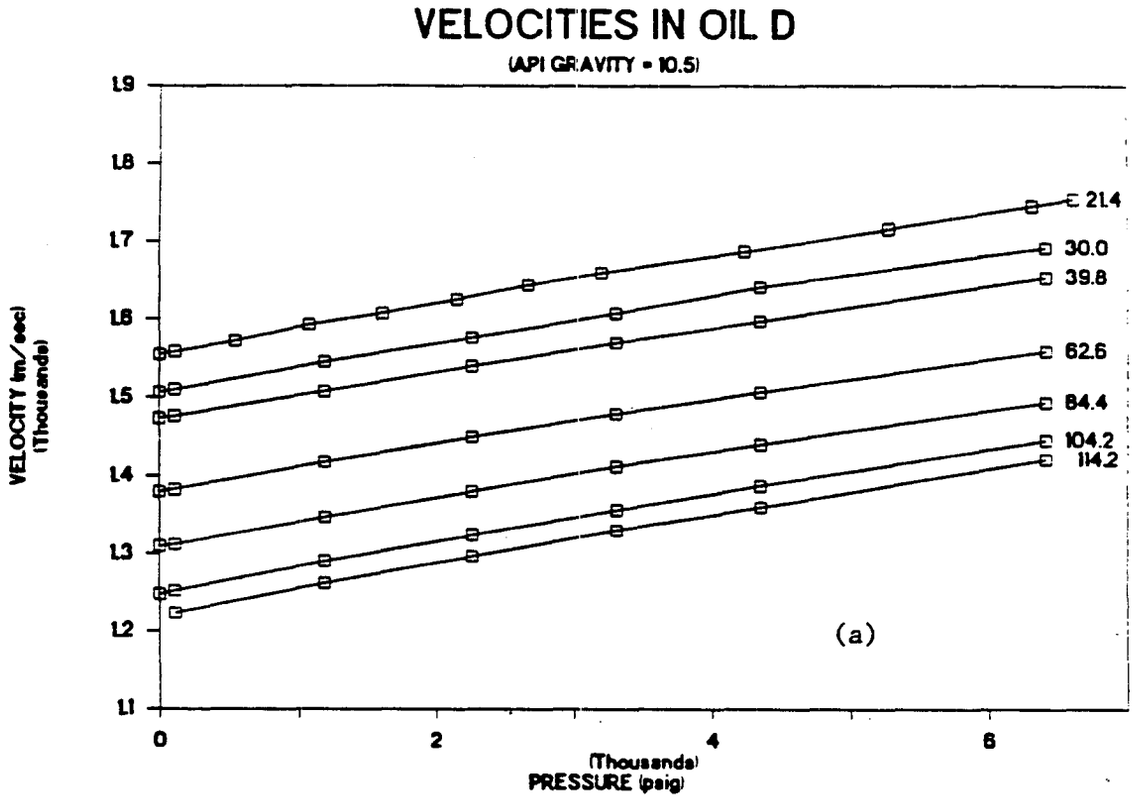
VELOCITIES IN OIL D
(API GRAVITY = 10.5)
VELOCITY (m/sec)
(Thousands)
1.9
1.8
1.7
1.6
1.5
1.4
1.3
1.2
1.1
21.4
30.0
39.8
62.6
84.4
104.2
114.2
(a)
0
2
4
6
(Thousands)
PRESSURE (psig)

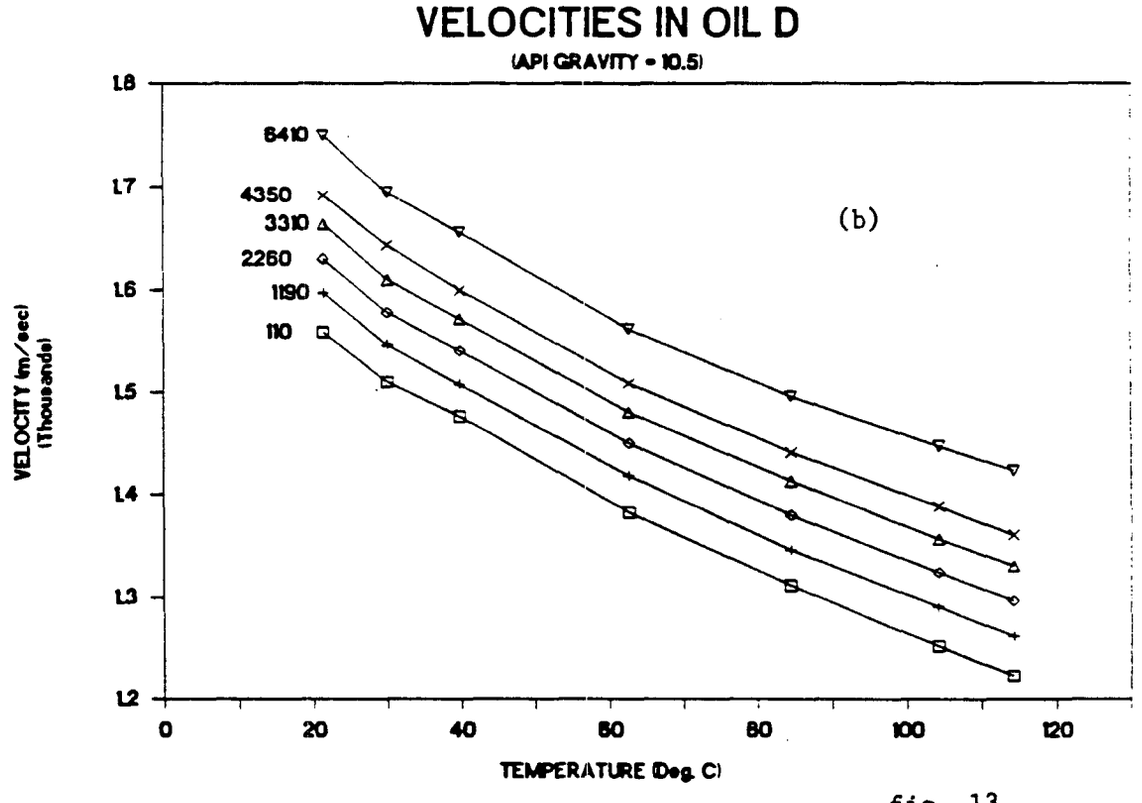
VELOCITIES IN OIL D
(API GRAVITY = 10.5)
VELOCITY (m/sec)
(Thousands)
1.8
1.7
1.6
1.5
1.4
1.3
1.2
6410
4350
3310
2260
1190
110
(b)
0
20
40
60
80
100
120
TEMPERATURE (Deg. C)

fig. 13

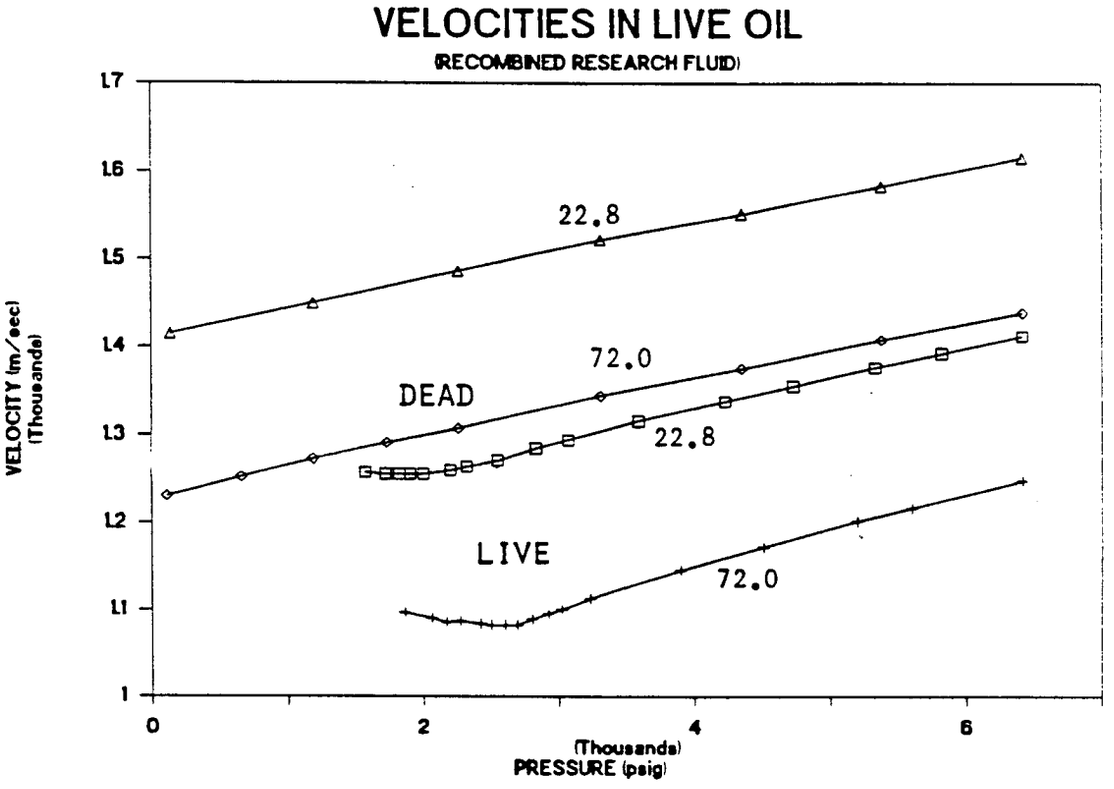
VELOCITIES IN LIVE OIL
(RECOMBINED RESEARCH FLUID)
VELOCITY (m/sec)
(Thousands)
1.7
1.6
1.5
1.4
1.3
1.2
1.1
1
22.8
72.0
DEAD
22.8
LIVE
72.0
0
2
4
6
(Thousands)
PRESSURE (psig)

fig. 14

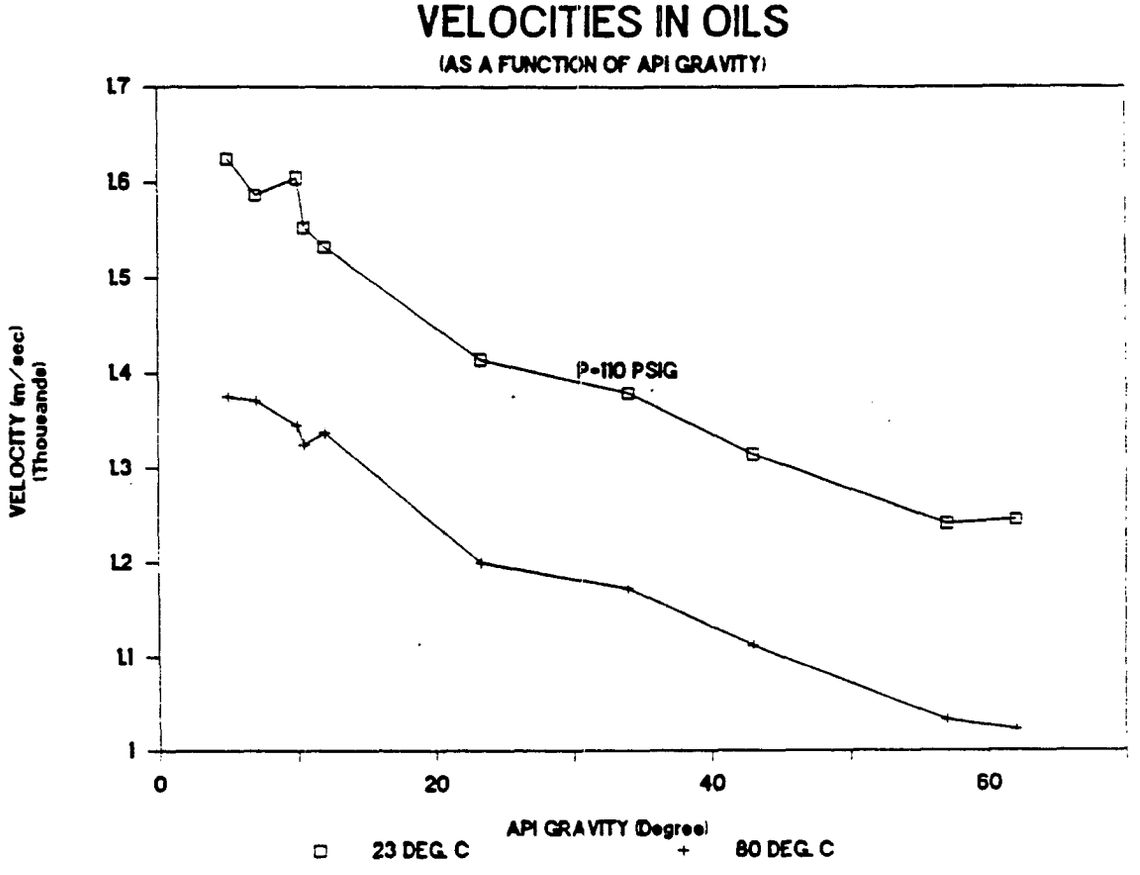
VELOCITIES IN OILS
(AS A FUNCTION OF API GRAVITY)
VELOCITY (m/sec)
(Thousands)
1.7
1.6
1.5
1.4
1.3
1.2
1.1
1
0
20
40
60
API GRAVITY (Degree)
P=110 PSIG
23 DEG. C
80 DEG. C

fig. 15

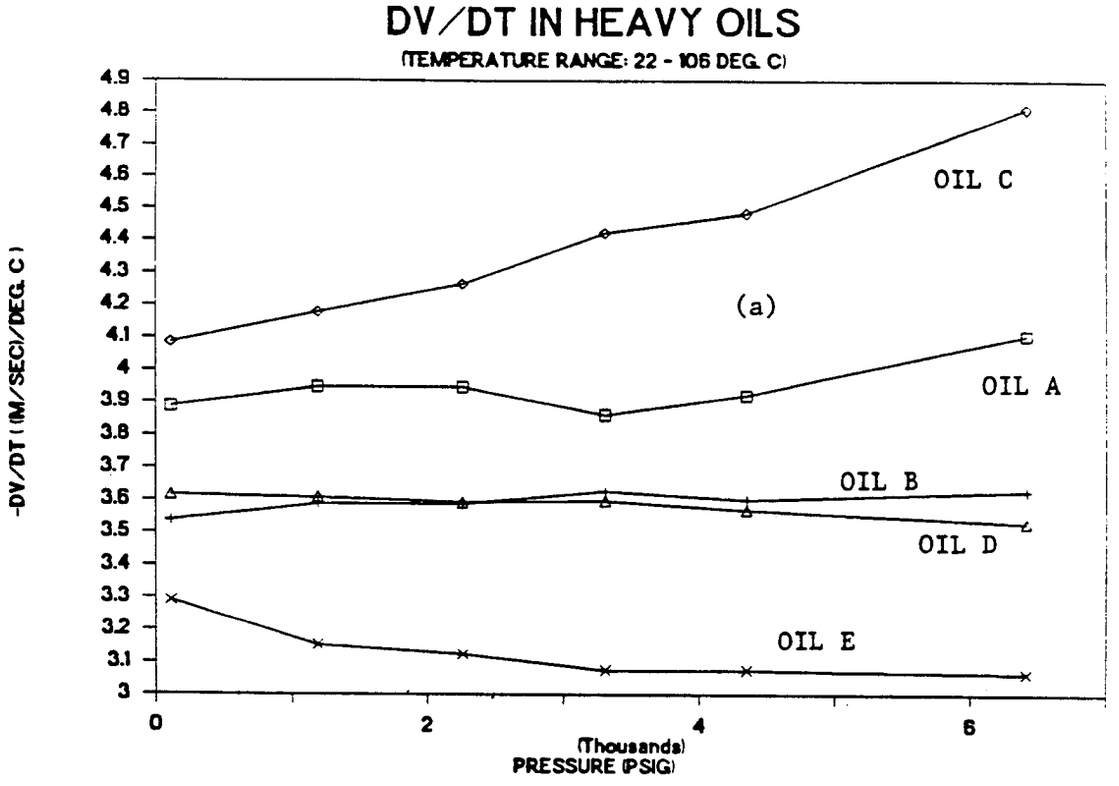
DV/DT IN HEAVY OILS
(TEMPERATURE RANGE: 22 - 106 DEG. C)
-DV/DT ((M/SEC)/DEG. C)
4.9
4.8
4.7
4.6
4.5
4.4
4.3
4.2
4.1
4
3.9
3.8
3.7
3.6
3.5
3.4
3.3
3.2
3.1
3
0
2
4
6
(Thousands)
PRESSURE (PSIG)
OIL C
(a)
OIL A
OIL B
OIL D
OIL E

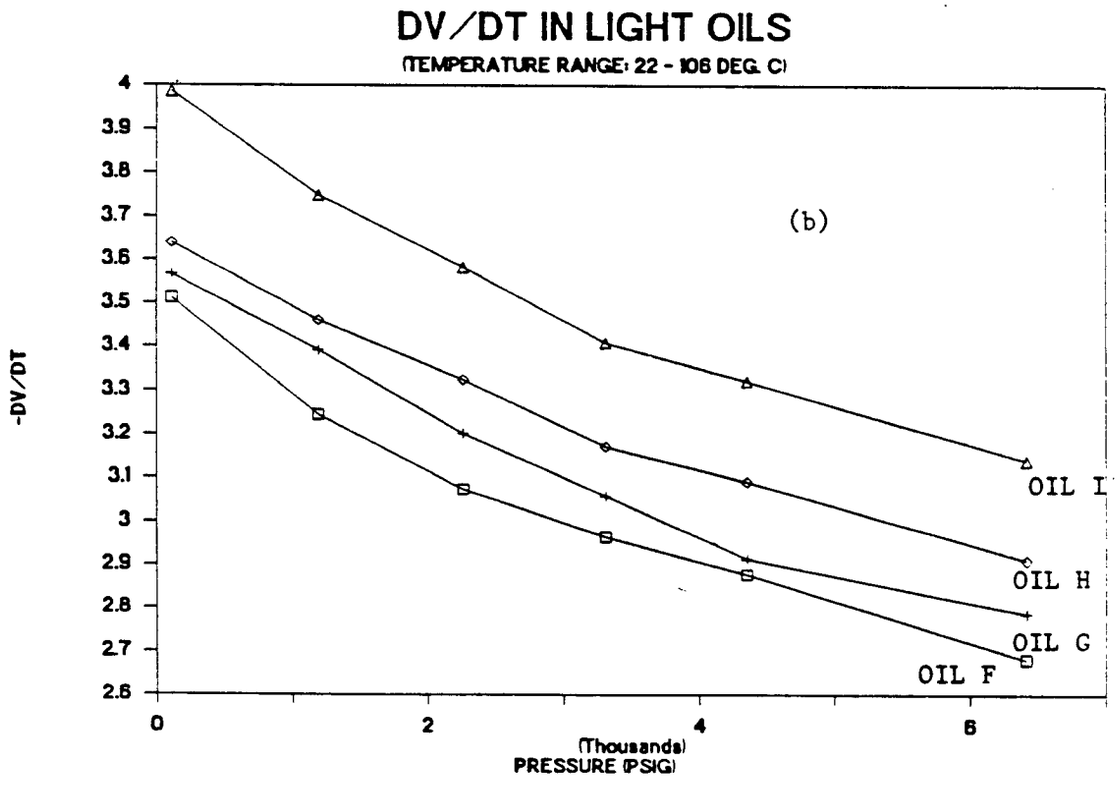
DV/DT IN LIGHT OILS
(TEMPERATURE RANGE: 22 - 106 DEG. C)
-DV/DT
4
3.9
3.8
3.7
3.6
3.5
3.4
3.3
3.2
3.1
3
2.9
2.8
2.7
2.6
0
2
4
6
(Thousands)
PRESSURE (PSIG)
(b)
OIL I
OIL H
OIL G
OIL F

fig. 16

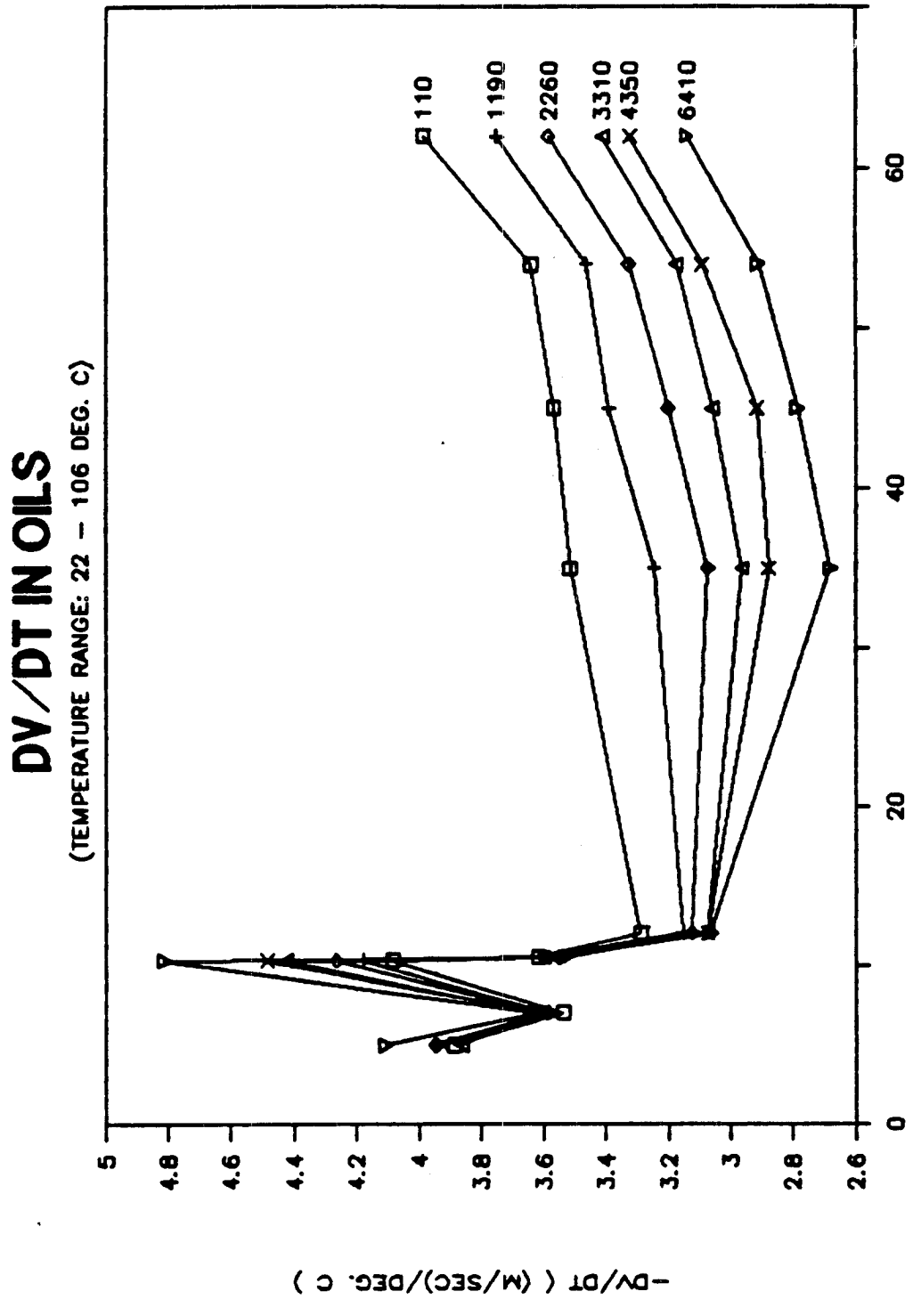
DV/DT IN OILS
(TEMPERATURE RANGE: 22 – 106 DEG. C)
110
1190
2260
3310
4350
6410
-DV/DT ((M/SEC)/DEG. C)
API GRAVITY (DEG.)
5
4.8
4.6
4.4
4.2
4
3.8
3.6
3.4
3.2
3
2.8
2.6
0
20
40
60

fig. 17

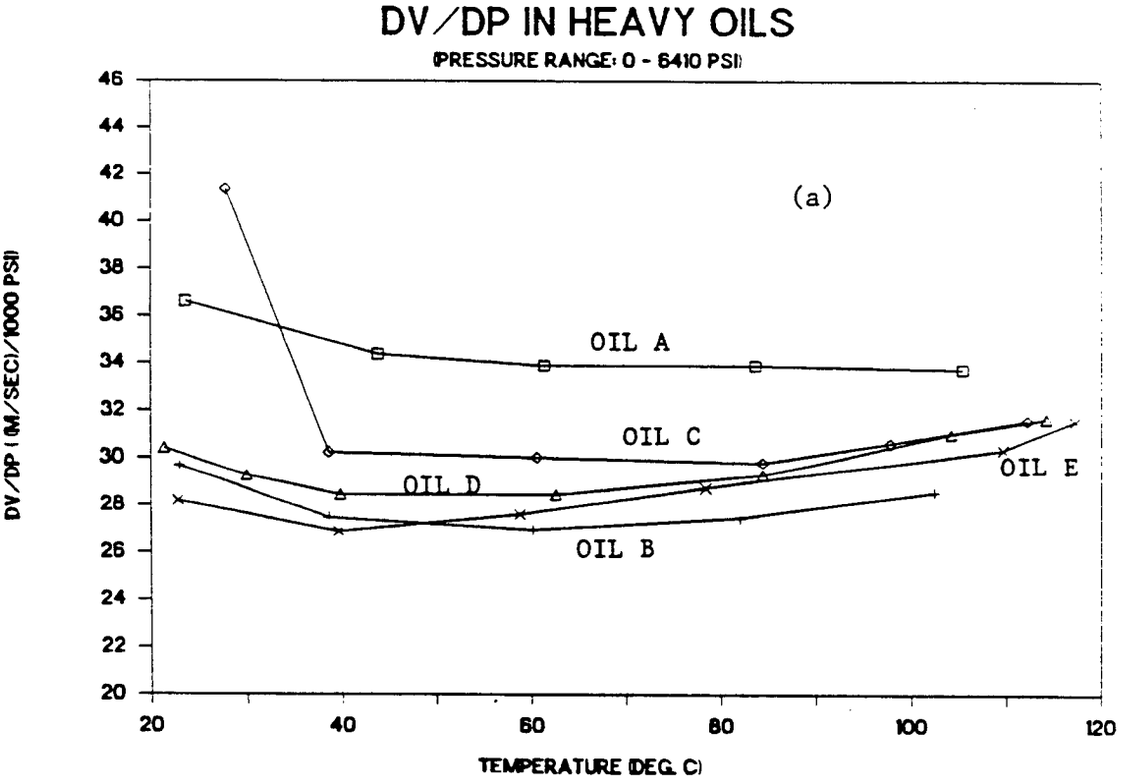
DV/DP IN HEAVY OILS
(PRESSURE RANGE: 0 - 6410 PSI)
DV/DP (M/SEC)/1000 PSI)
(a)
OIL A
OIL C
OIL D
OIL E
OIL B
TEMPERATURE (DEG. C)

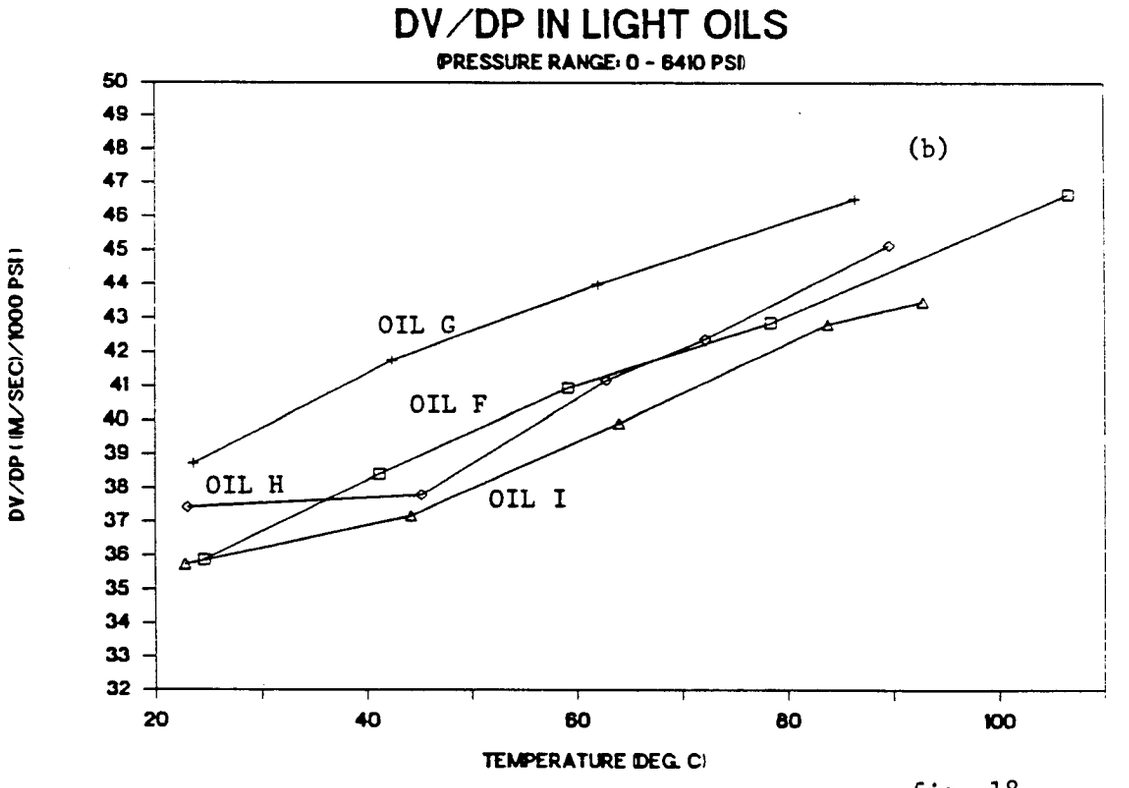
DV/DP IN LIGHT OILS
(PRESSURE RANGE: 0 - 6410 PSI)
DV/DP (M/SEC)/1000 PSI)
(b)
OIL G
OIL F
OIL H
OIL I
TEMPERATURE (DEG. C)

fig. 18

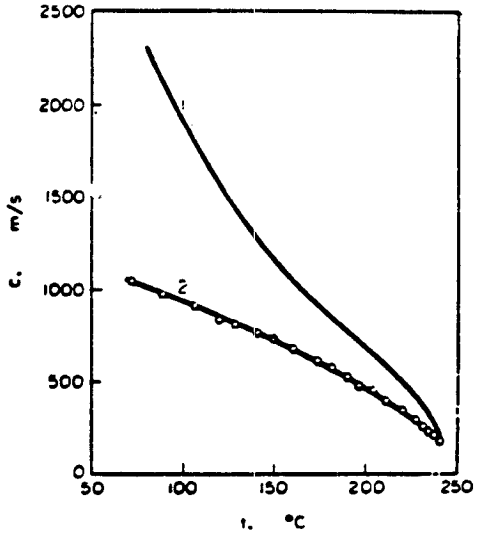

(a)

Comparison of the velocity of sound calculated from van der Waals' equation (1) with that observed experimentally in ethyl alcohol (2).

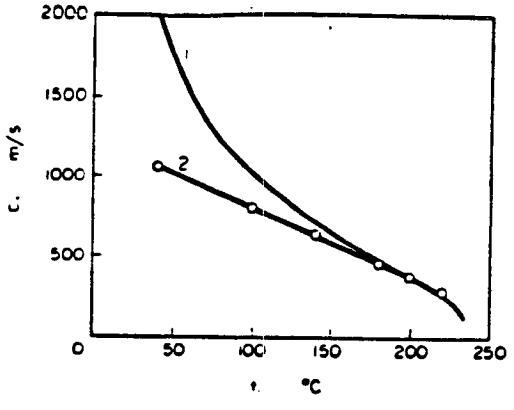

(b)

Comparison of the velocity of sound calculated from van der Waals equation (1) with that observed experimentally in n-Hexane (2).

fig. 19

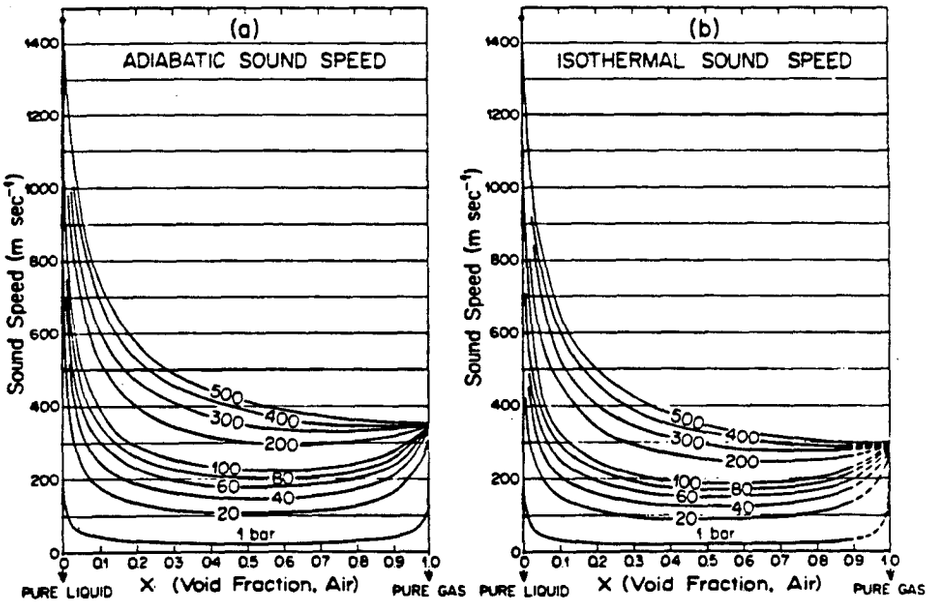

Calculated dependence of (*a*) adiabatic and (*b*) isothermal sound speed of water-air mixture on volume conte gas and on pressure. Surface tension is neglected.

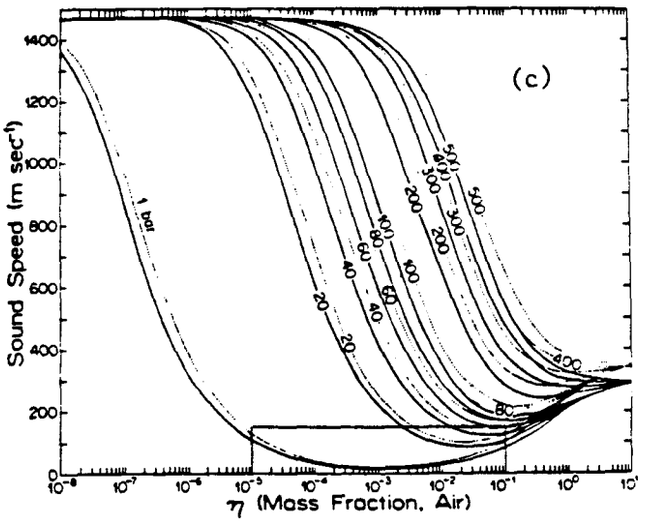

Calculated dependence of sound speed of water-air mixture on mass fraction of gas and on pressure, plotted on semilogarithmic paper to show the effect of small volume fractions of air. Surface tension is neglected. Solid curves indicate isothermal sound speed, and dotted curves indicate adiabatic sound speed.

fig. 20

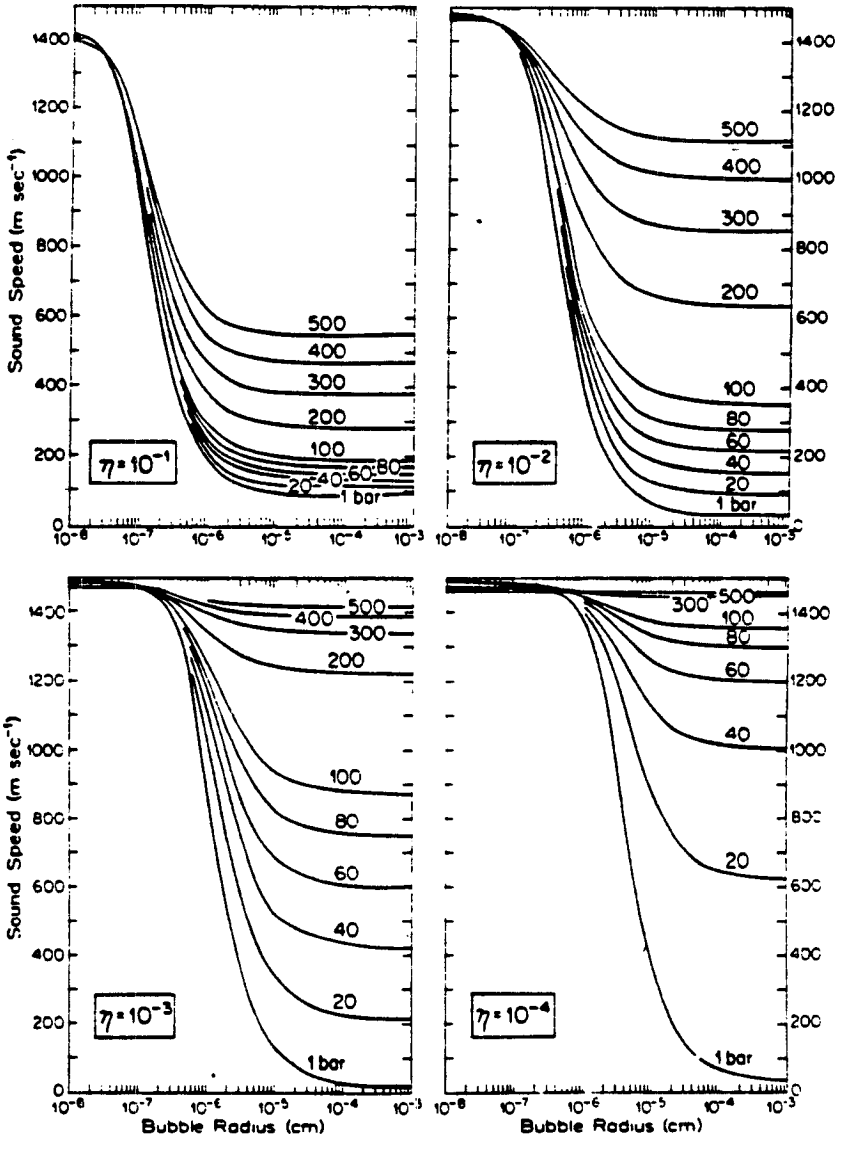

Calculated sound speed of water-air mixture as a function of bubble radius and pressure for four mass fractions. $\eta = 10^{-1}$, 10^{-2}, 10^{-3}, and 10^{-4}.

fig. 21

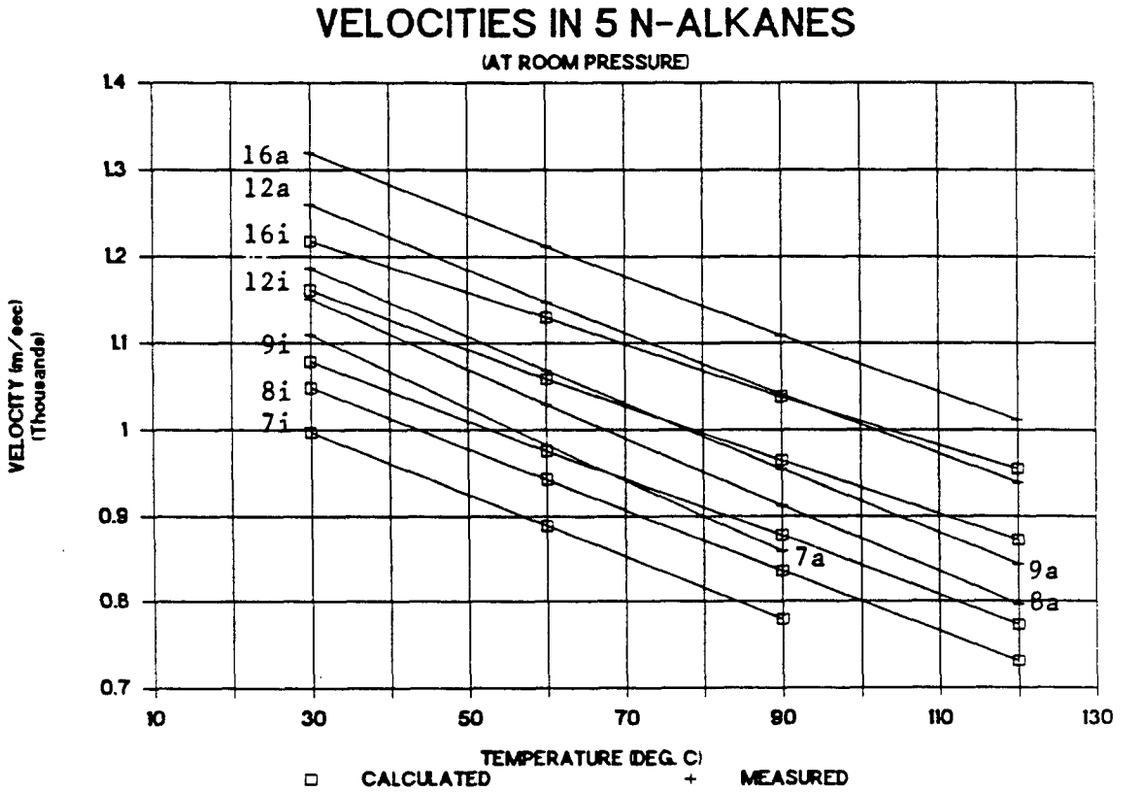
VELOCITIES IN 5 N-ALKANES
(AT ROOM PRESSURE)
VELOCITY (m/sec)
(Thousands)
1.4
1.3
1.2
1.1
1
0.9
0.8
0.7
16a
12a
16i
12i
9i
8i
7i
7a
9a
8a
10
30
50
70
90
110
130
TEMPERATURE (DEG. C)
□ CALCULATED
+ MEASURED

fig. 22

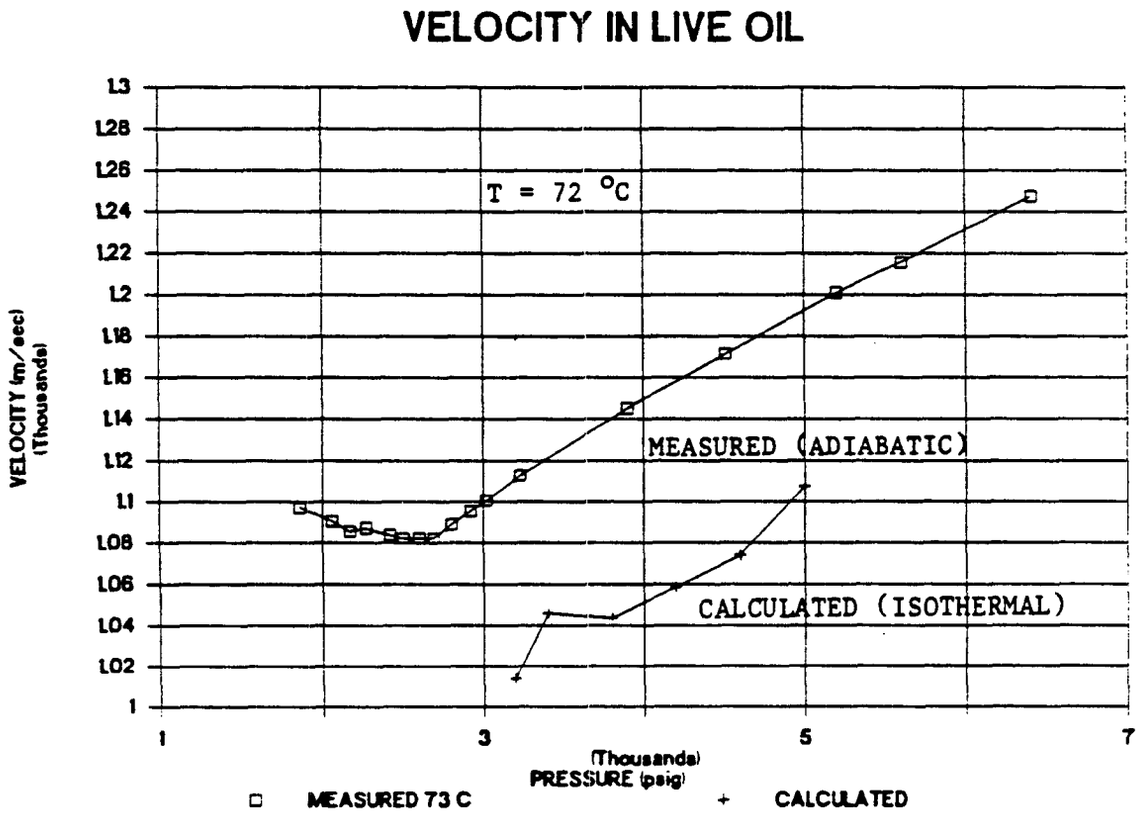
VELOCITY IN LIVE OIL
T = 72 °C
MEASURED (ADIABATIC)
CALCULATED (ISOTHERMAL)
VELOCITY (m/sec) (Thousands)
1.3
1.28
1.26
1.24
1.22
1.2
1.18
1.16
1.14
1.12
1.1
1.08
1.06
1.04
1.02
1
1
3
5
7
(Thousands)
PRESSURE (psig)
MEASURED 73 C
CALCULATED

fig. 23

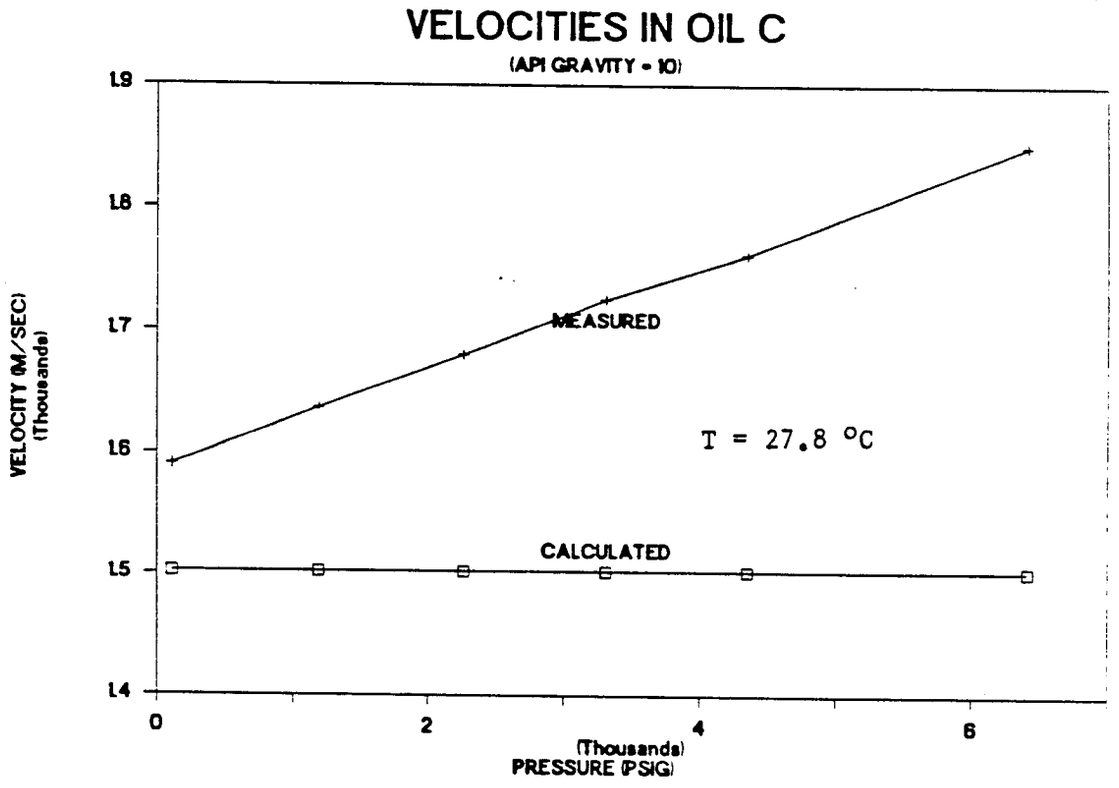
VELOCITIES IN OIL C
(API GRAVITY = 10)
VELOCITY (M/SEC)
(Thousands)
1.9
1.8
1.7
1.6
1.5
1.4
MEASURED
T = 27.8 °C
CALCULATED
0
2
4
6
(Thousands)
PRESSURE (PSIG)

fig. 24

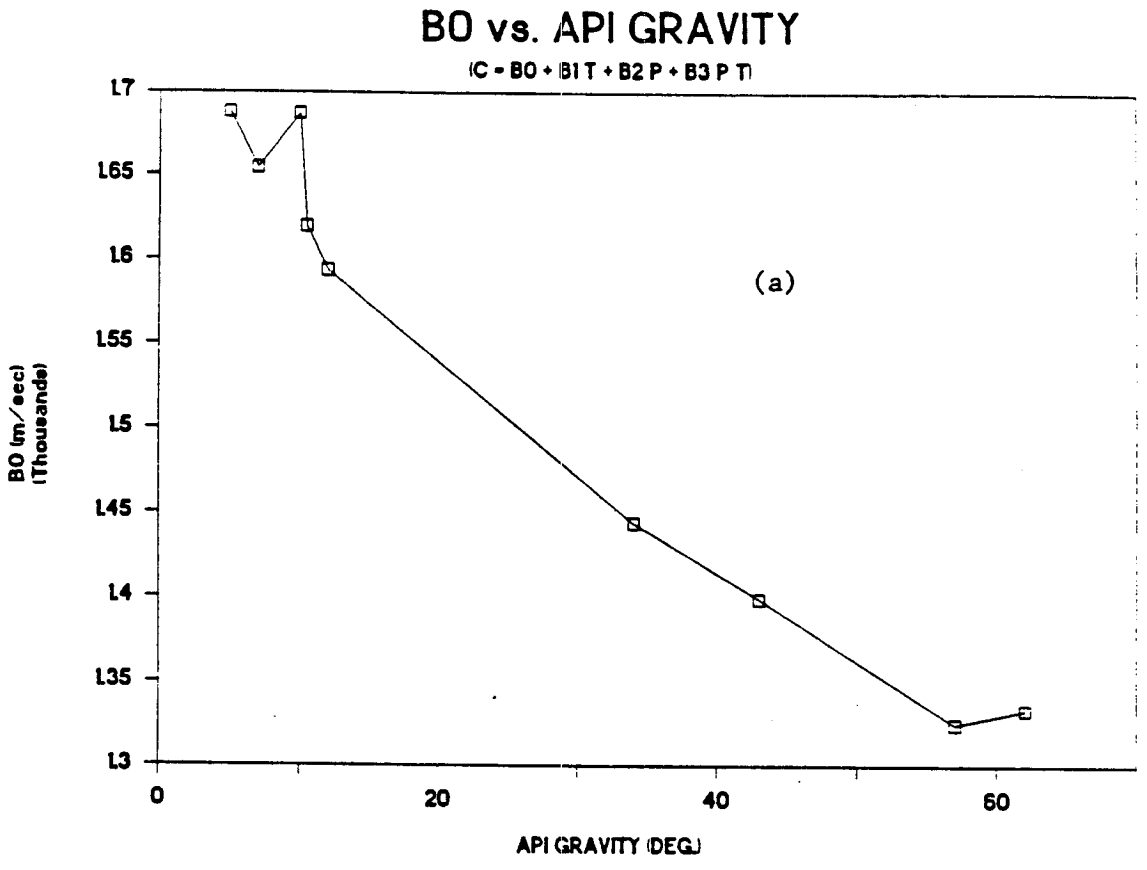
B0 vs. API GRAVITY
(C = B0 + B1 T + B2 P + B3 P T)
B0 (m/sec) (Thousands)
1.7
1.65
1.6
1.55
1.5
1.45
1.4
1.35
1.3
0
20
40
60
API GRAVITY (DEG.)
(a)

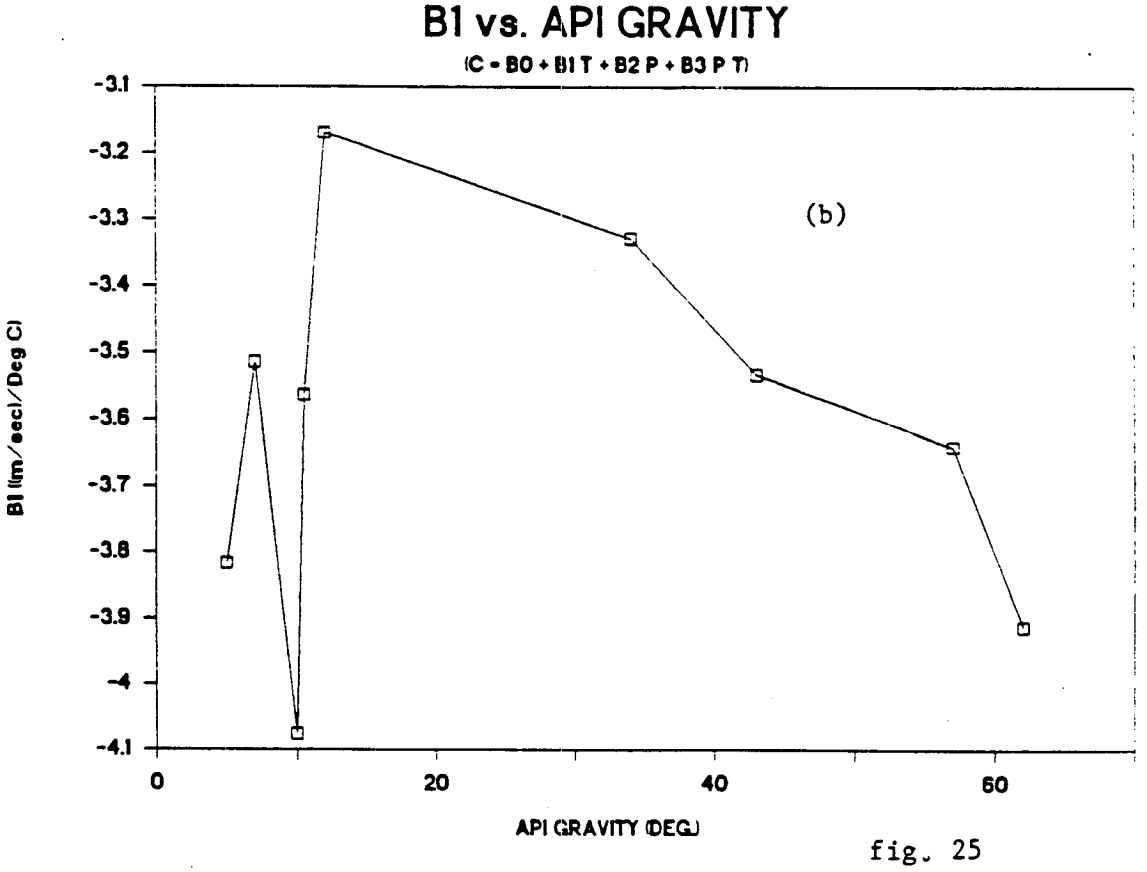
B1 vs. API GRAVITY
(C = B0 + B1 T + B2 P + B3 P T)
B1 ((m/sec)/Deg C)
-3.1
-3.2
-3.3
-3.4
-3.5
-3.6
-3.7
-3.8
-3.9
-4
-4.1
0
20
40
60
API GRAVITY (DEG.)
(b)

fig. 25

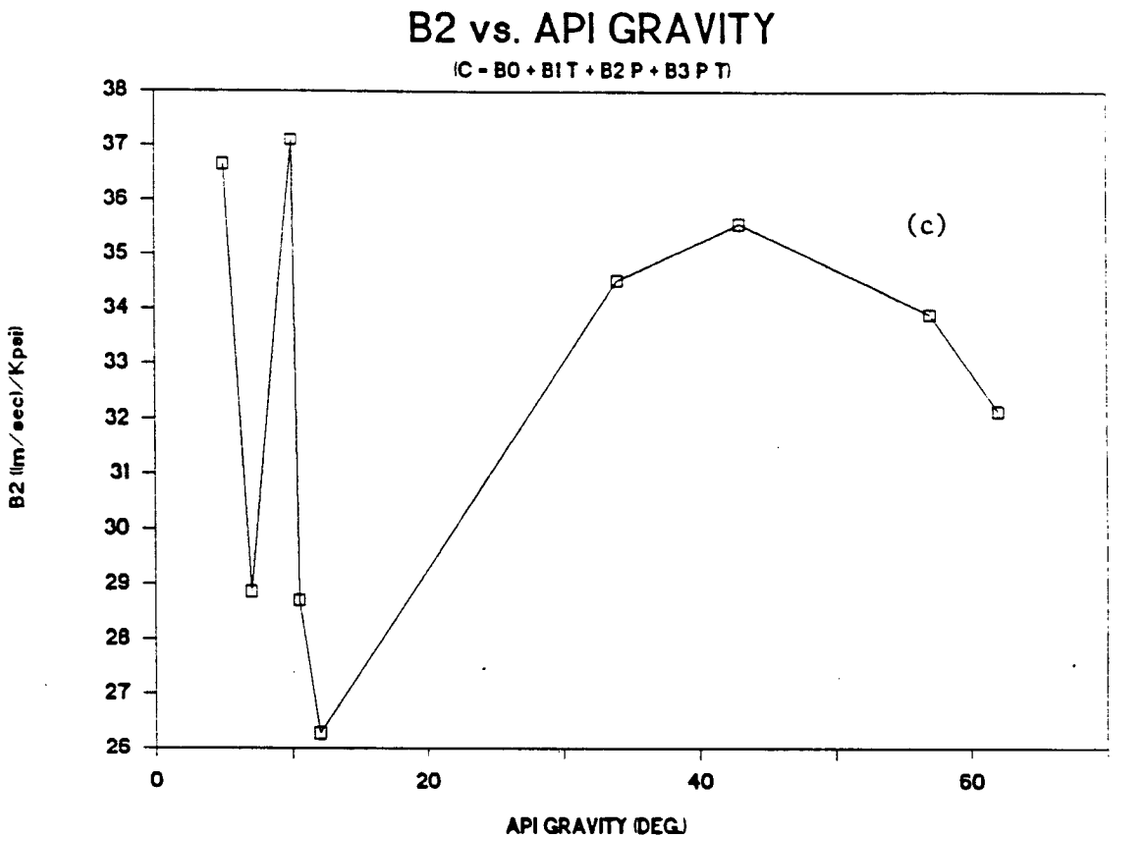
B2 vs. API GRAVITY
(C = B0 + B1 T + B2 P + B3 P T)
B2 (lm/ sec)/Kpsi)
38
37
36
35
34
33
32
31
30
29
28
27
26
0
20
40
60
API GRAVITY (DEG.)
(c)

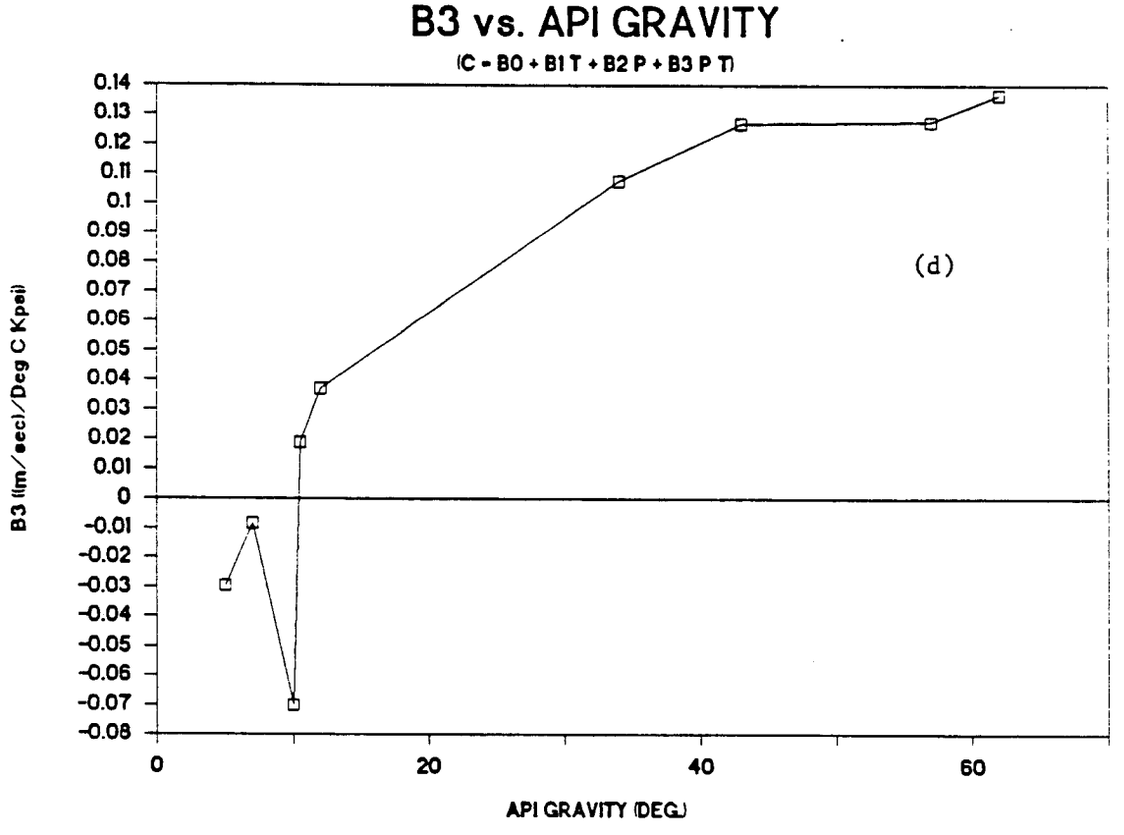
B3 vs. API GRAVITY
(C = B0 + B1 T + B2 P + B3 P T)
B3 (lm/ sec)/Deg C Kpsi)
0.14
0.13
0.12
0.11
0.1
0.09
0.08
0.07
0.06
0.05
0.04
0.03
0.02
0.01
0
-0.01
-0.02
-0.03
-0.04
-0.05
-0.06
-0.07
-0.08
0
20
40
60
API GRAVITY (DEG.)
(d)

fig. 25

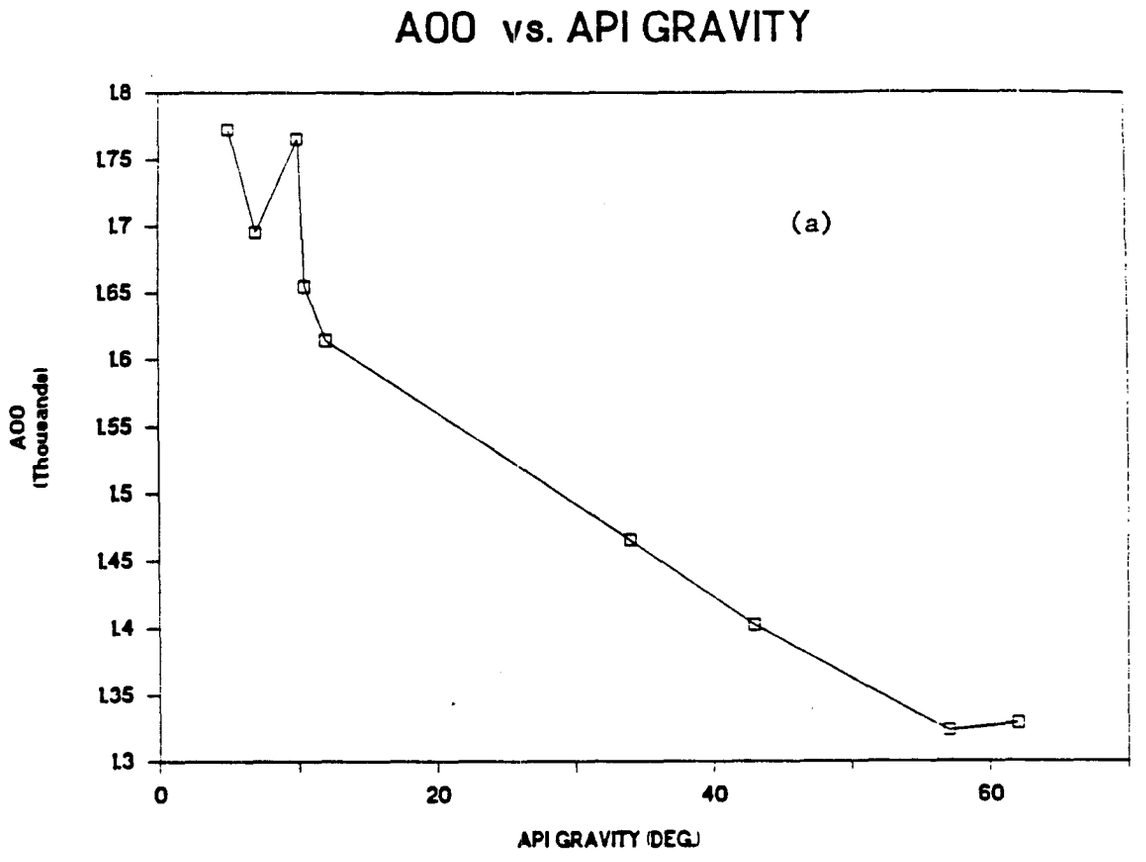
A00 vs. API GRAVITY
(a)
A00
(Thousands)
1.8
1.75
1.7
1.65
1.6
1.55
1.5
1.45
1.4
1.35
1.3
0
20
40
60
API GRAVITY (DEG)

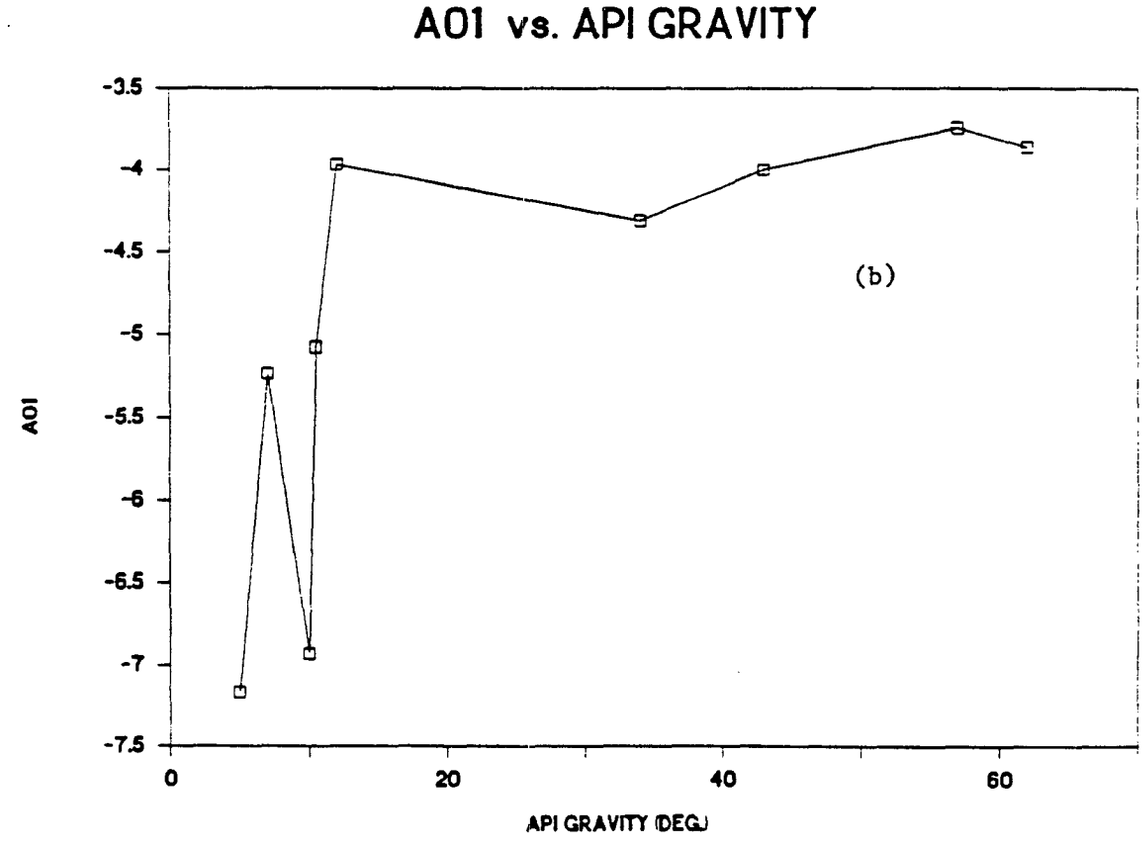
A01 vs. API GRAVITY
(b)
A01
-3.5
-4
-4.5
-5
-5.5
-6
-6.5
-7
-7.5
0
20
40
60
API GRAVITY (DEG)

fig. 26

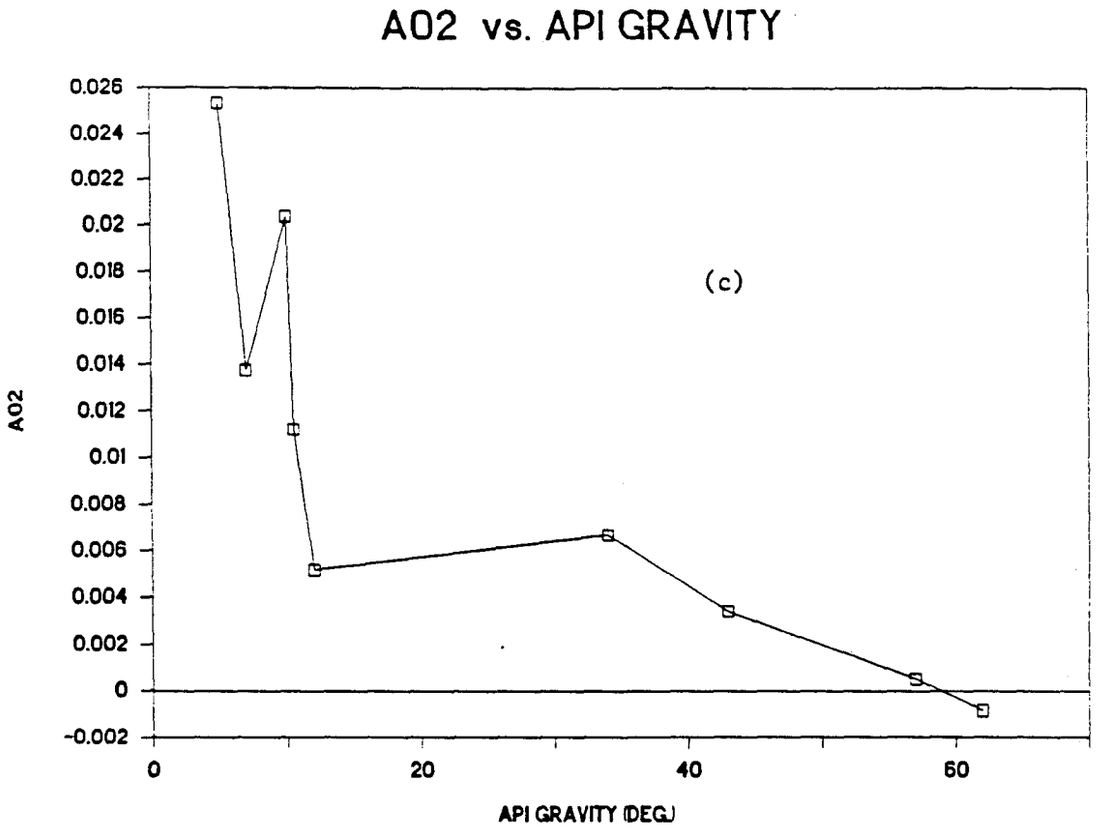
A02 vs. API GRAVITY
A02
0.026
0.024
0.022
0.02
0.018
0.016
0.014
0.012
0.01
0.008
0.006
0.004
0.002
0
-0.002
0
20
40
60
API GRAVITY (DEG.)
(c)

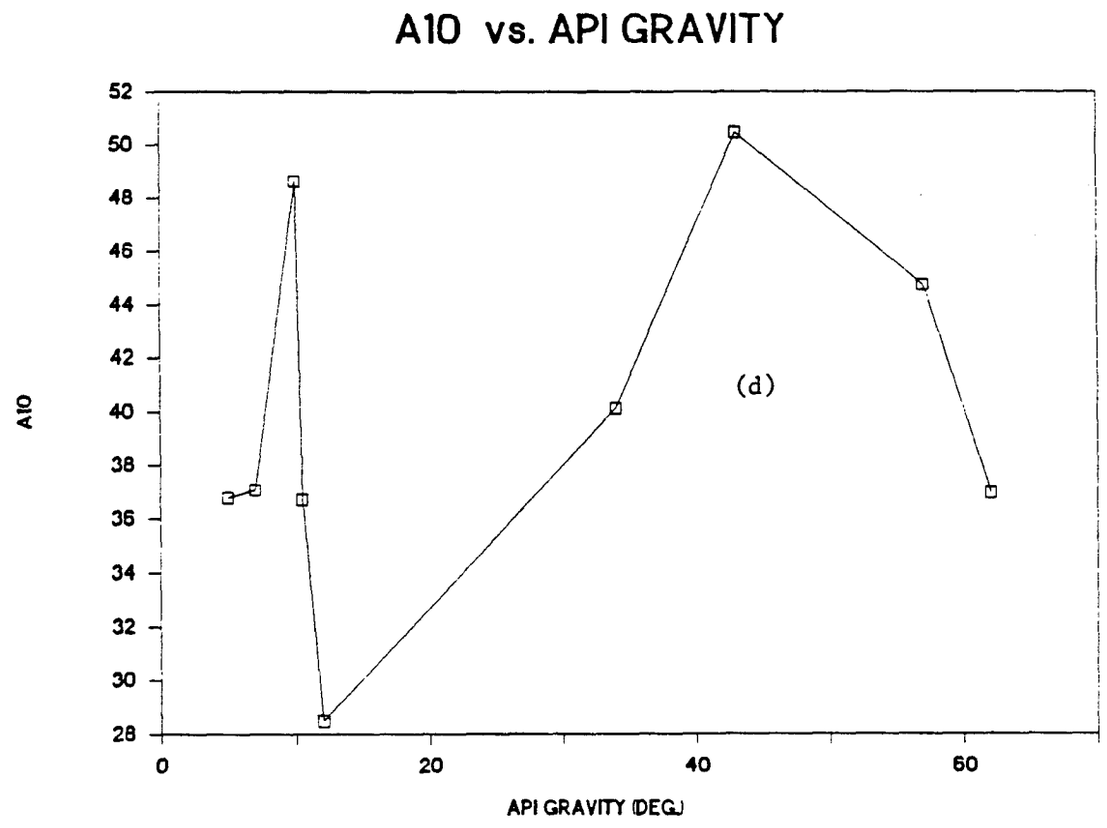
A10 vs. API GRAVITY
A10
52
50
48
46
44
42
40
38
36
34
32
30
28
0
20
40
60
API GRAVITY (DEG.)
(d)

fig. 26

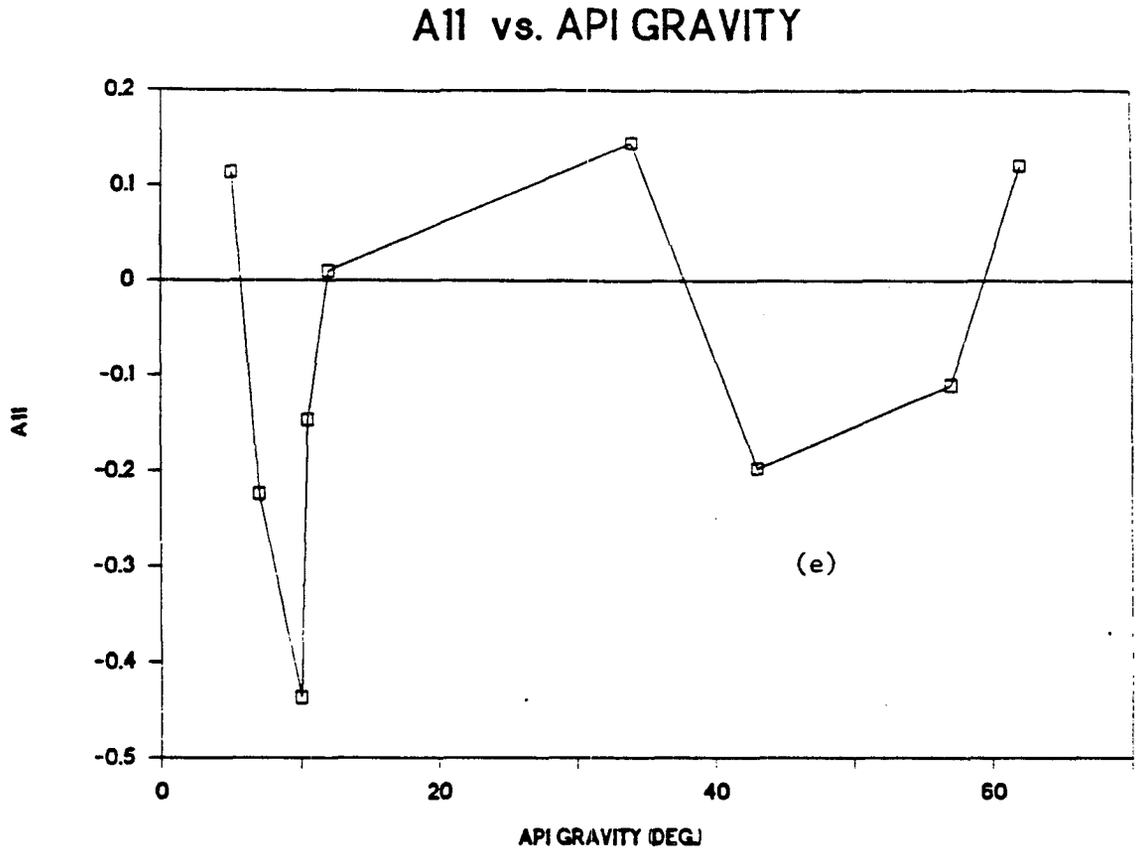
A11 vs. API GRAVITY
0.2
0.1
0
-0.1
-0.2
-0.3
-0.4
-0.5
A11
0
20
40
60
API GRAVITY (DEG.)
(e)

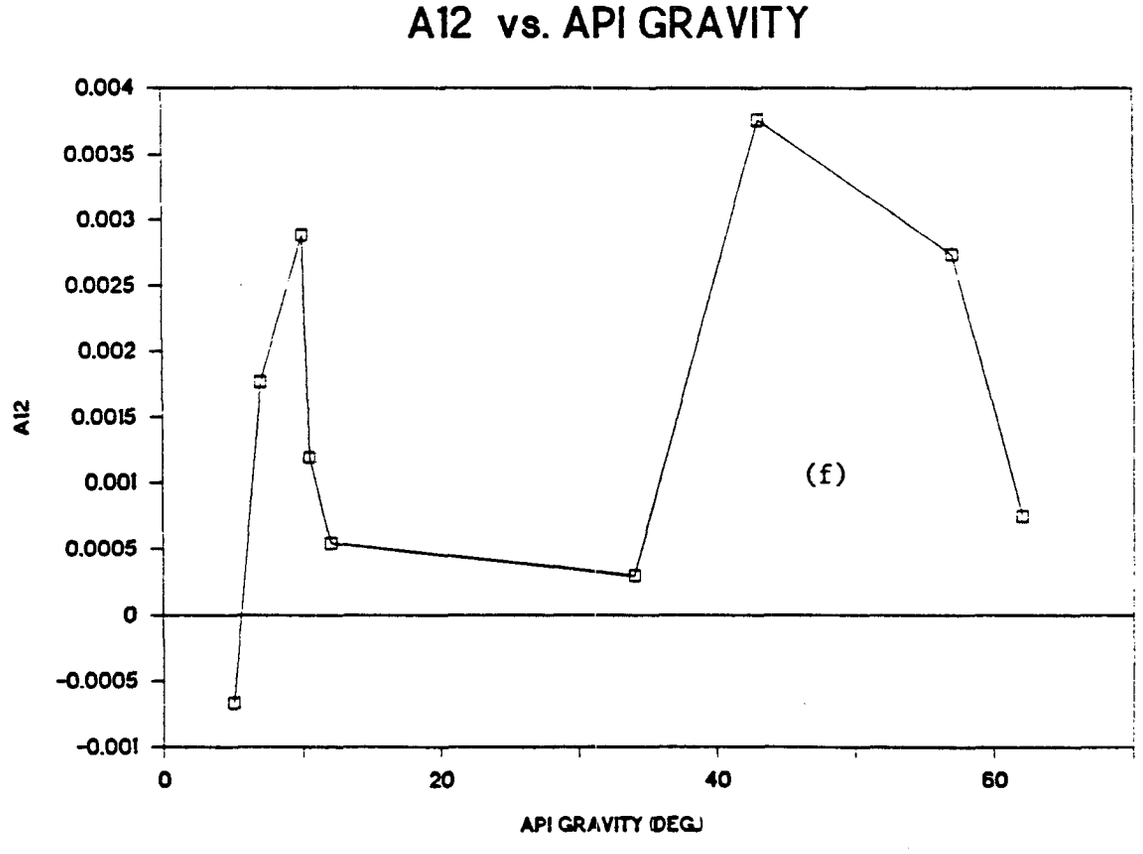
A12 vs. API GRAVITY
0.004
0.0035
0.003
0.0025
0.002
0.0015
0.001
0.0005
0
-0.0005
-0.001
A12
0
20
40
60
API GRAVITY (DEG.)
(f)

fig. 26

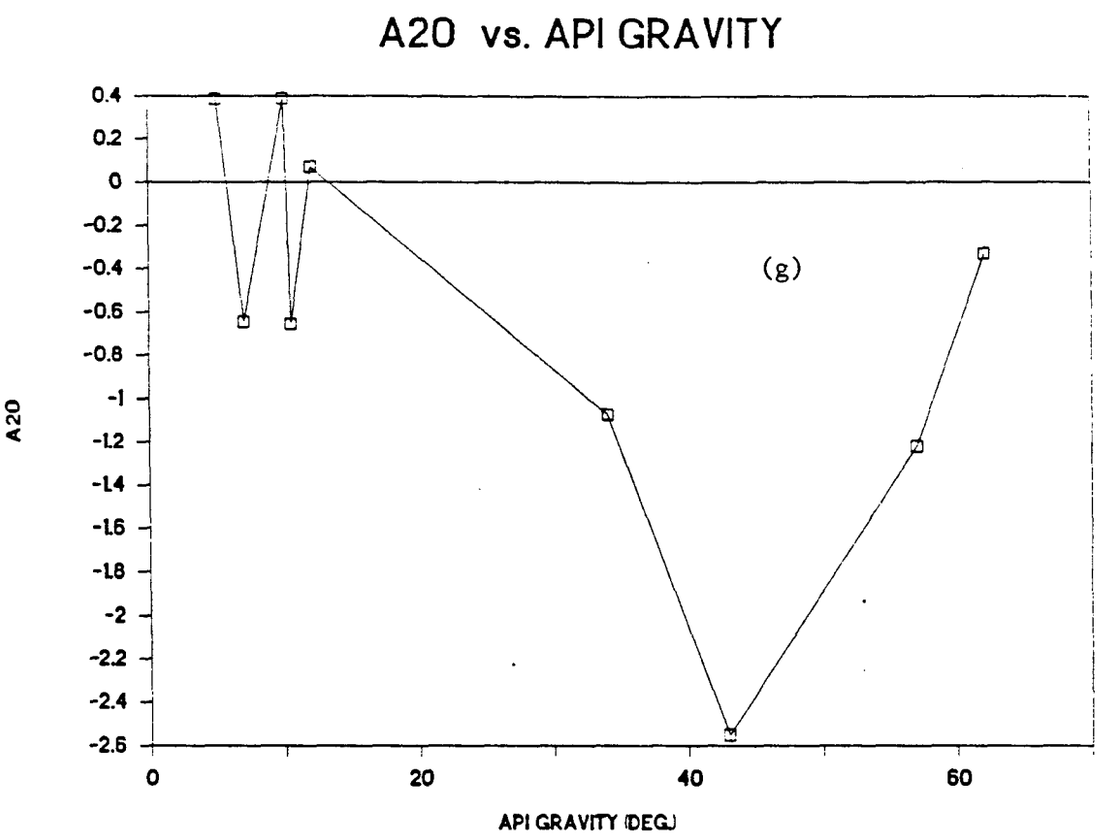
A20 vs. API GRAVITY
A20
0.4
0.2
0
-0.2
-0.4
-0.6
-0.8
-1
-1.2
-1.4
-1.6
-1.8
-2
-2.2
-2.4
-2.6
(g)
0
20
40
60
API GRAVITY (DEG)

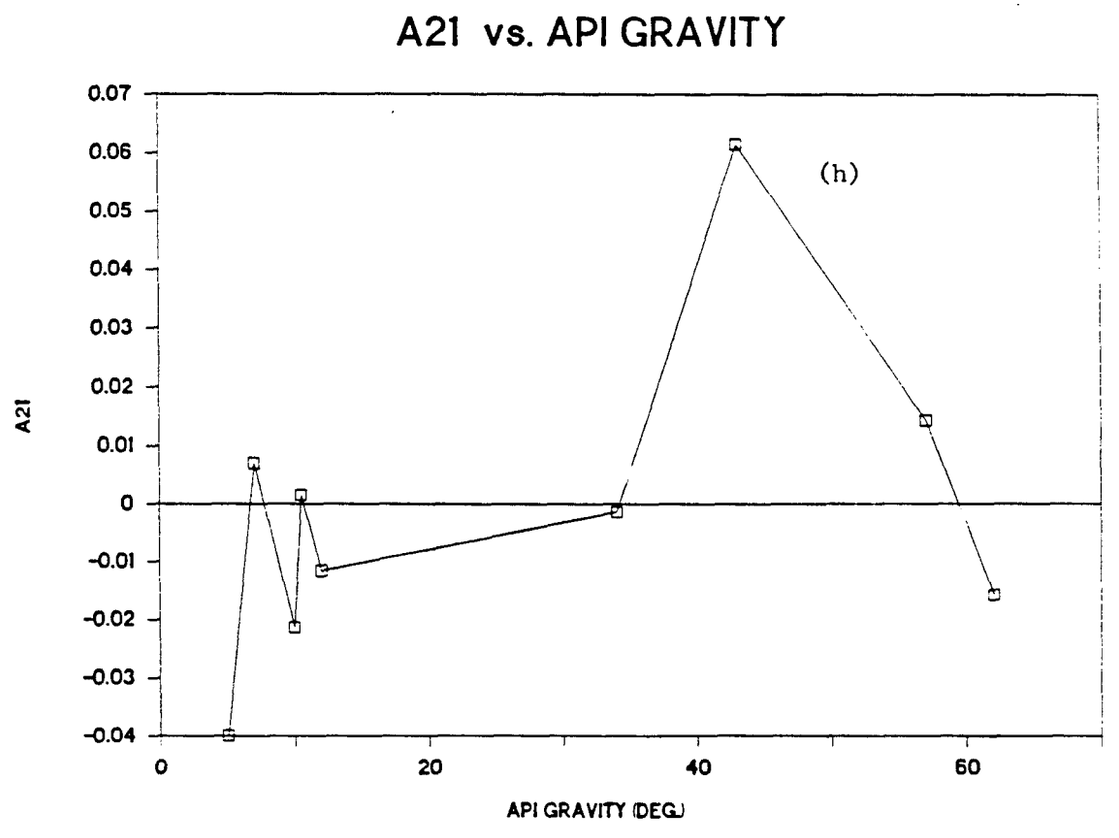
A21 vs. API GRAVITY
A21
0.07
0.06
0.05
0.04
0.03
0.02
0.01
0
-0.01
-0.02
-0.03
-0.04
(h)
0
20
40
60
API GRAVITY (DEG)

fig. 26

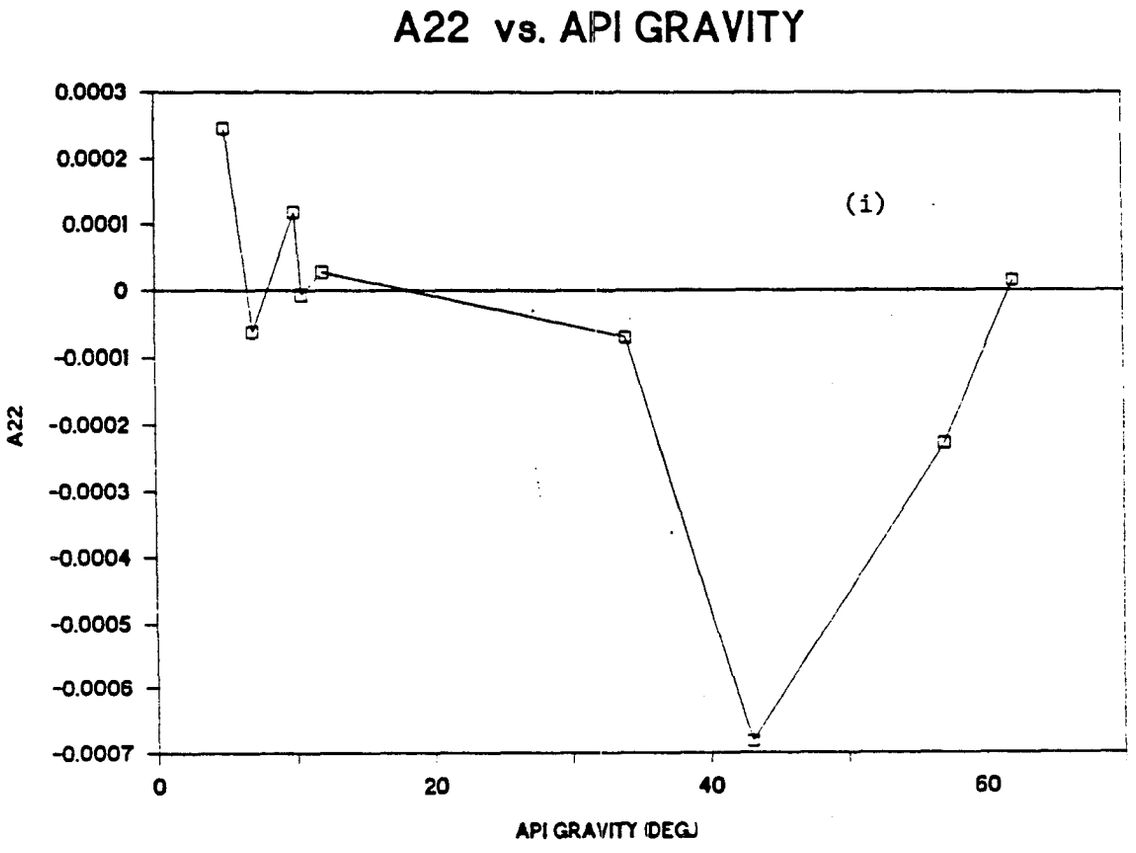
A22 vs. API GRAVITY
0.0003
0.0002
0.0001
0
-0.0001
-0.0002
-0.0003
-0.0004
-0.0005
-0.0006
-0.0007
A22
(i)
0
20
40
60
API GRAVITY (DEG)

fig. 26

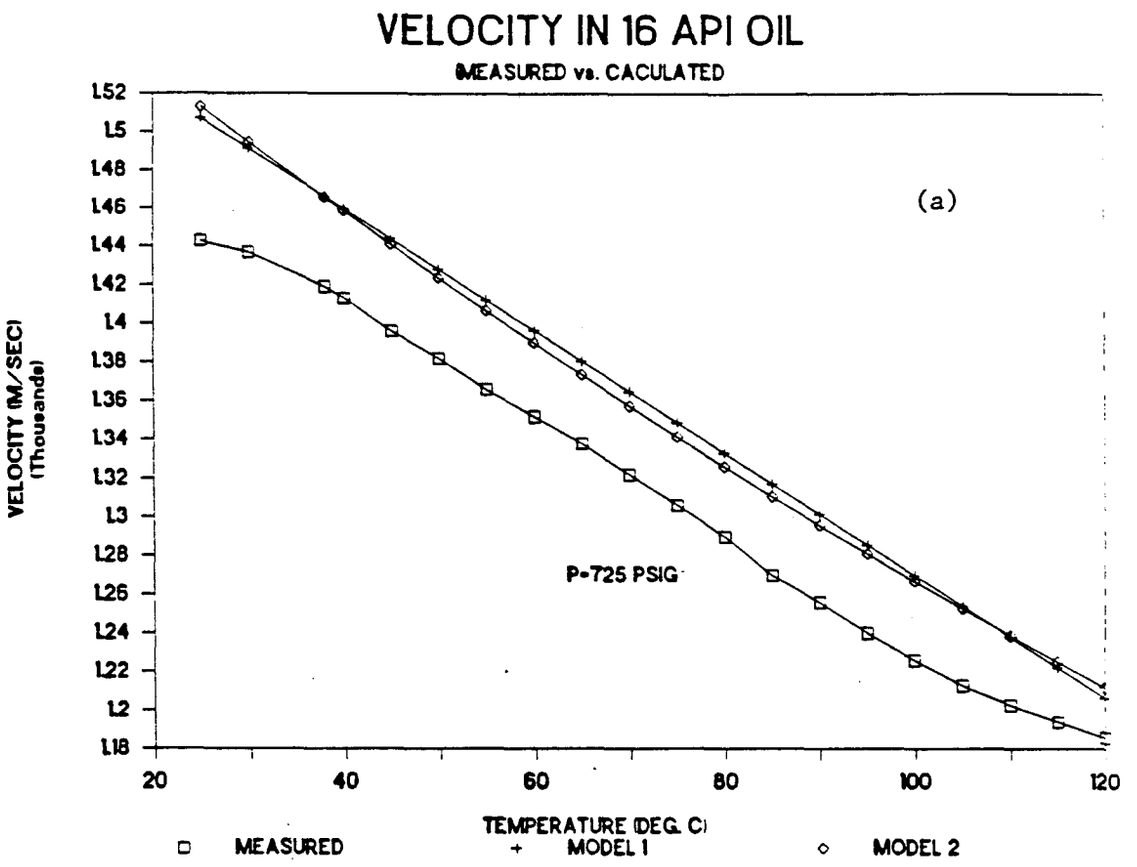
VELOCITY IN 16 API OIL
MEASURED vs. CACULATED
VELOCITY (M/SEC) (Thousands)
1.52
1.5
1.48
1.46
1.44
1.42
1.4
1.38
1.36
1.34
1.32
1.3
1.28
1.26
1.24
1.22
1.2
1.18
(a)
P=725 PSIG
20
40
60
80
100
120
TEMPERATURE (DEG. C)
MEASURED
MODEL 1
MODEL 2

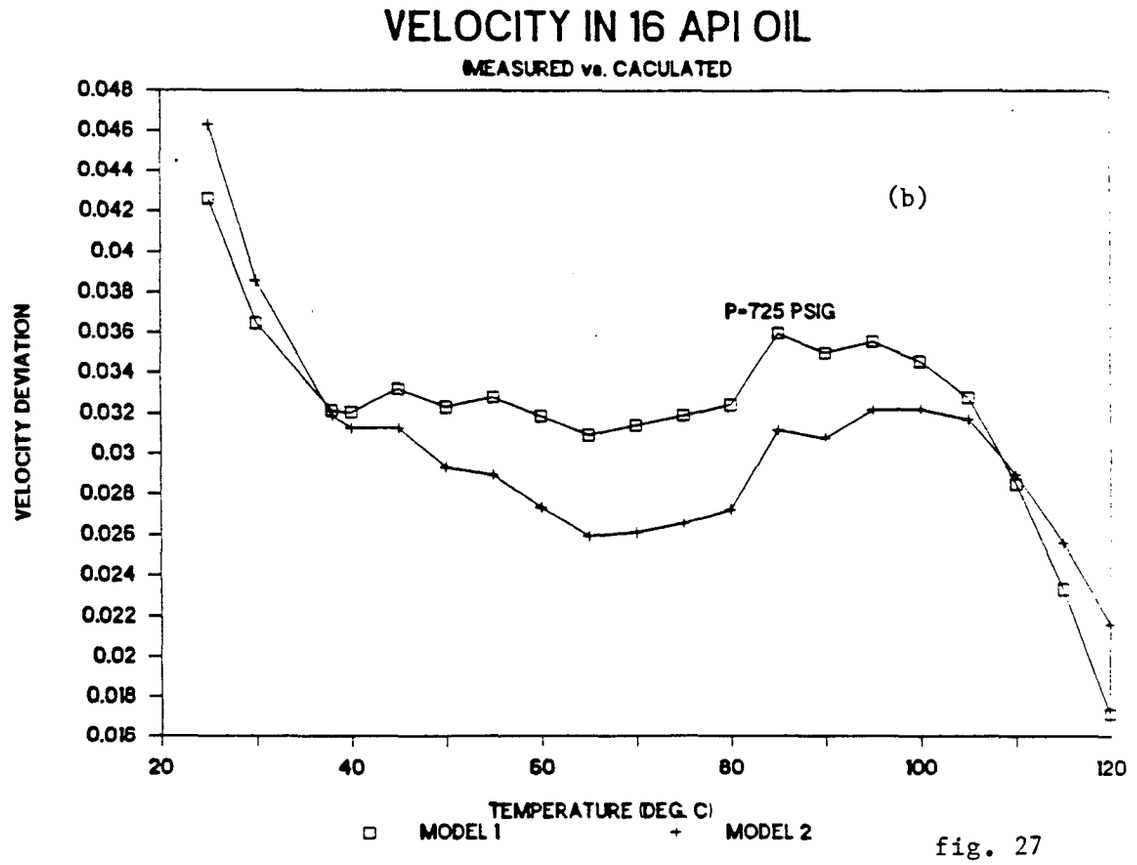
VELOCITY IN 16 API OIL
MEASURED vs. CACULATED
VELOCITY DEVIATION
0.048
0.046
0.044
0.042
0.04
0.038
0.036
0.034
0.032
0.03
0.028
0.026
0.024
0.022
0.02
0.018
0.016
(b)
P=725 PSIG
20
40
60
80
100
120
TEMPERATURE (DEG. C)
MODEL 1
MODEL 2

fig. 27

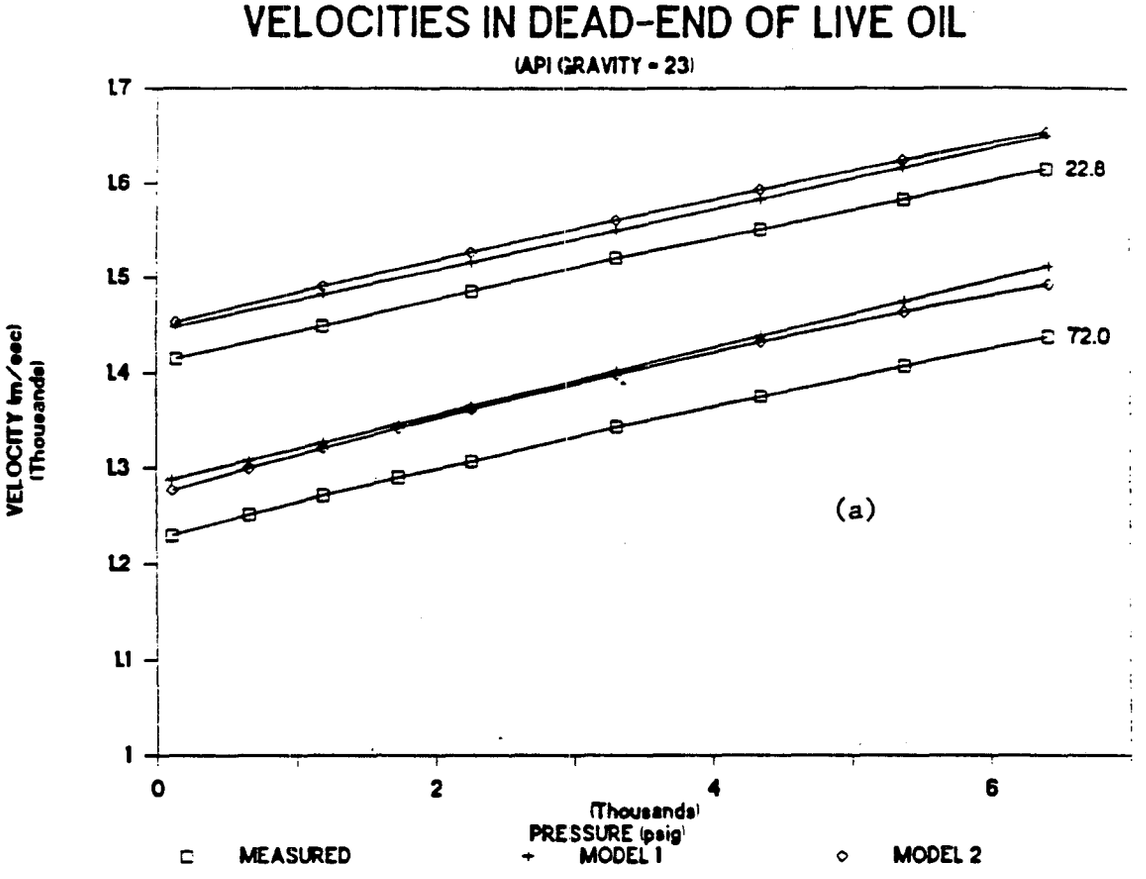
VELOCITIES IN DEAD-END OF LIVE OIL
(API GRAVITY = 23)
VELOCITY (m/sec)
(Thousands)
1.7
1.6
1.5
1.4
1.3
1.2
1.1
1
22.8
72.0
(a)
0
2
4
6
(Thousands)
PRESSURE (psig)
MEASURED
MODEL 1
MODEL 2

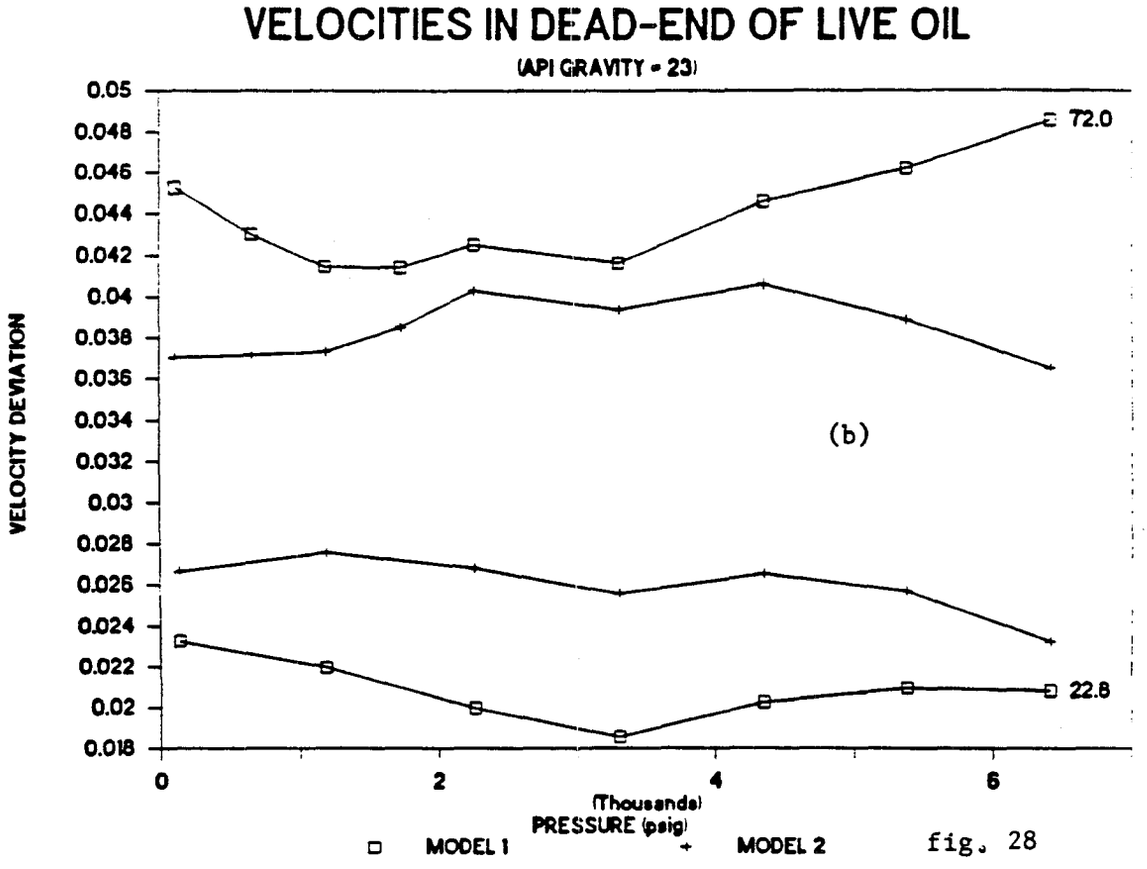
VELOCITIES IN DEAD-END OF LIVE OIL
(API GRAVITY = 23)
VELOCITY DEVIATION
0.05
0.048
0.046
0.044
0.042
0.04
0.038
0.036
0.034
0.032
0.03
0.028
0.026
0.024
0.022
0.02
0.018
72.0
22.8
(b)
0
2
4
6
(Thousands)
PRESSURE (psig)
MODEL 1
MODEL 2

fig. 28

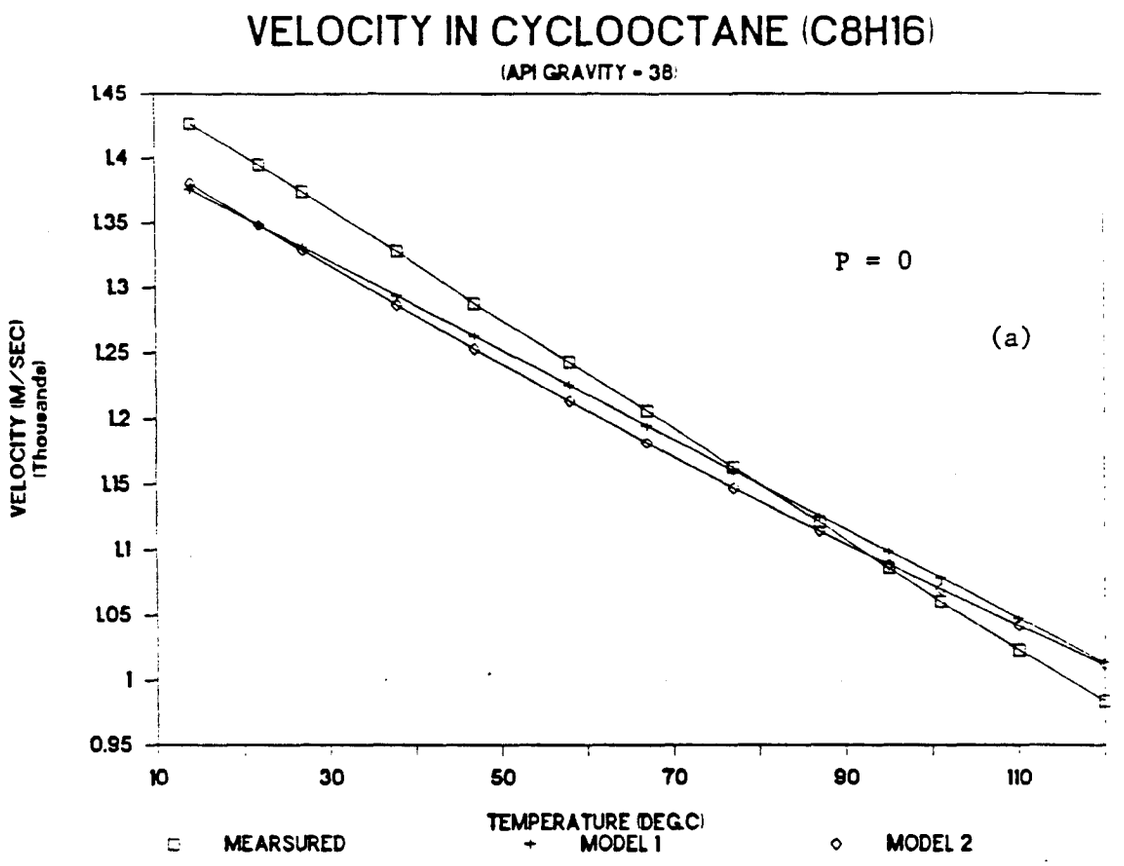
VELOCITY IN CYCLOOCTANE (C8H16)
(API GRAVITY = 38)
VELOCITY (M/SEC)
(Thousands)
1.45
1.4
1.35
1.3
1.25
1.2
1.15
1.1
1.05
1
0.95
P = 0
(a)
10
30
50
70
90
110
TEMPERATURE (DEG.C)
MEARSURED
MODEL 1
MODEL 2

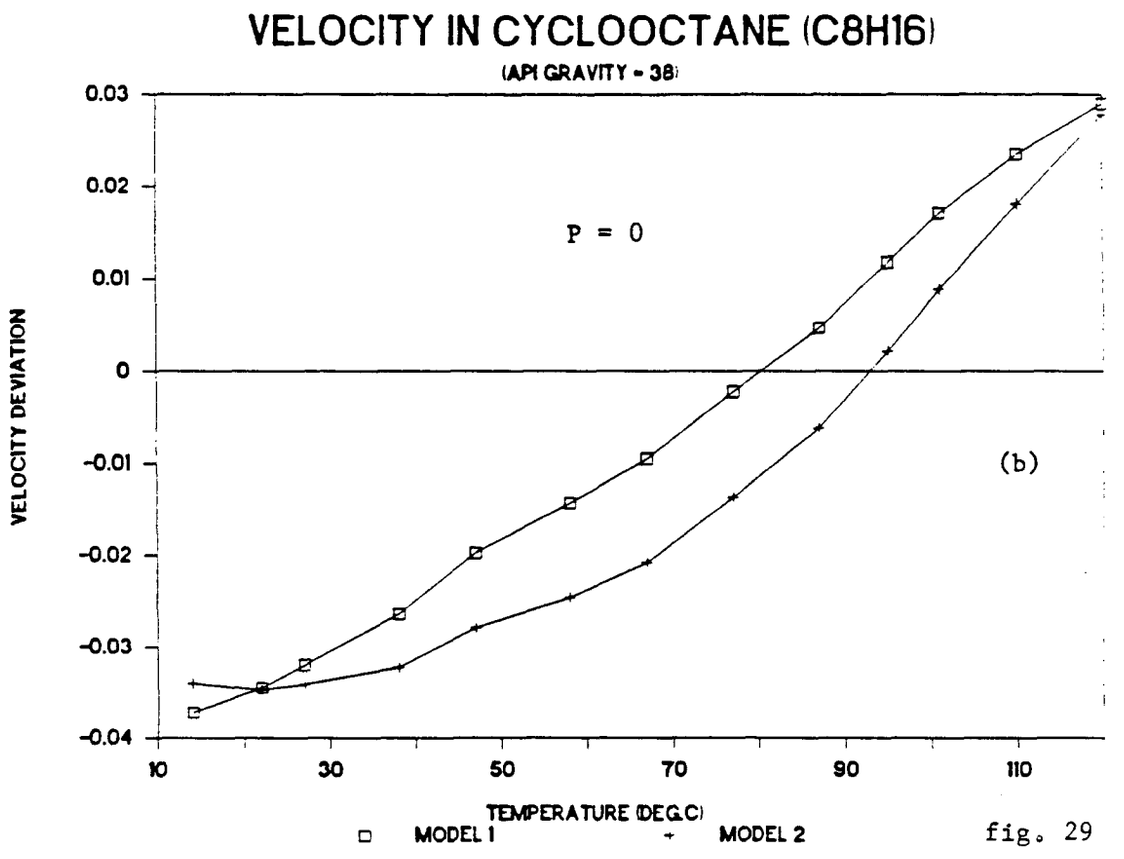
VELOCITY IN CYCLOOCTANE (C8H16)
(API GRAVITY = 38)
VELOCITY DEVIATION
0.03
0.02
0.01
0
-0.01
-0.02
-0.03
-0.04
P = 0
(b)
10
30
50
70
90
110
TEMPERATURE (DEG.C)
MODEL 1
MODEL 2

fig. 29

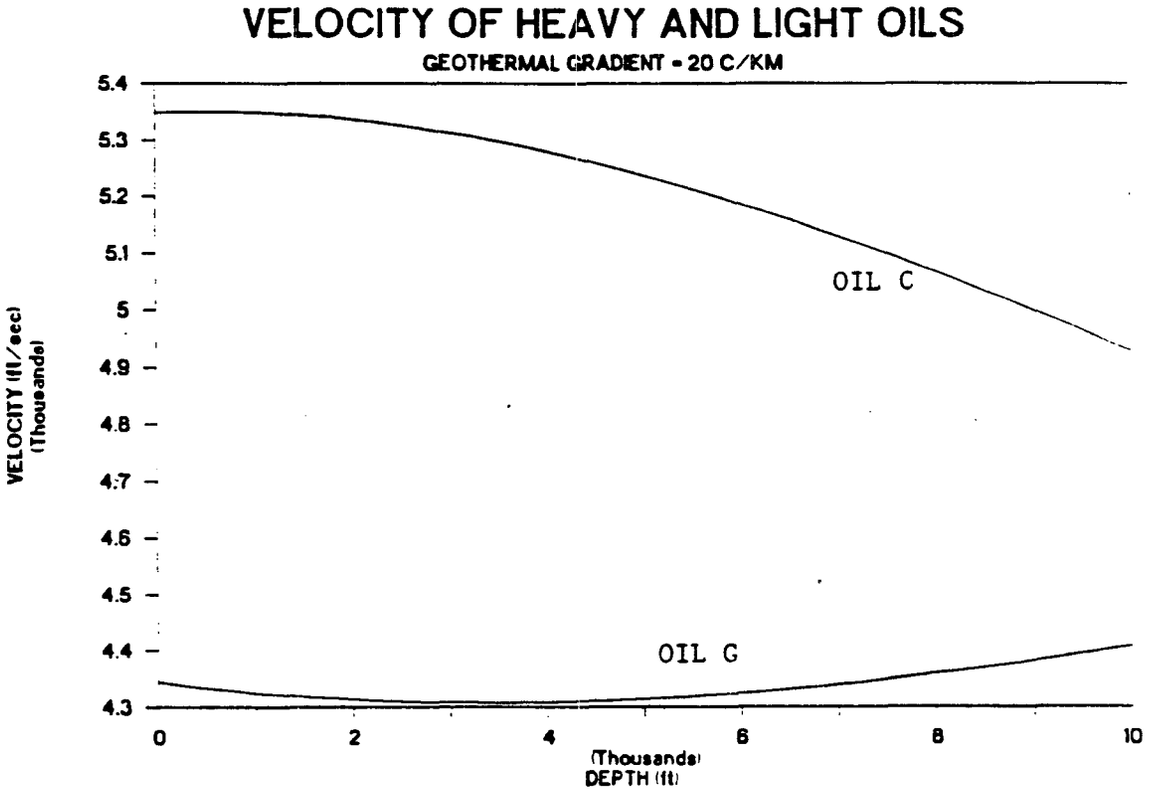
VELOCITY OF HEAVY AND LIGHT OILS
GEOTHERMAL GRADIENT = 20 C/KM
VELOCITY (ft/sec)
(Thousands)
5.4
5.3
5.2
5.1
5
4.9
4.8
4.7
4.6
4.5
4.4
4.3
OIL C
OIL G
0
2
4
6
8
10
(Thousands)
DEPTH (ft)

fig. 30

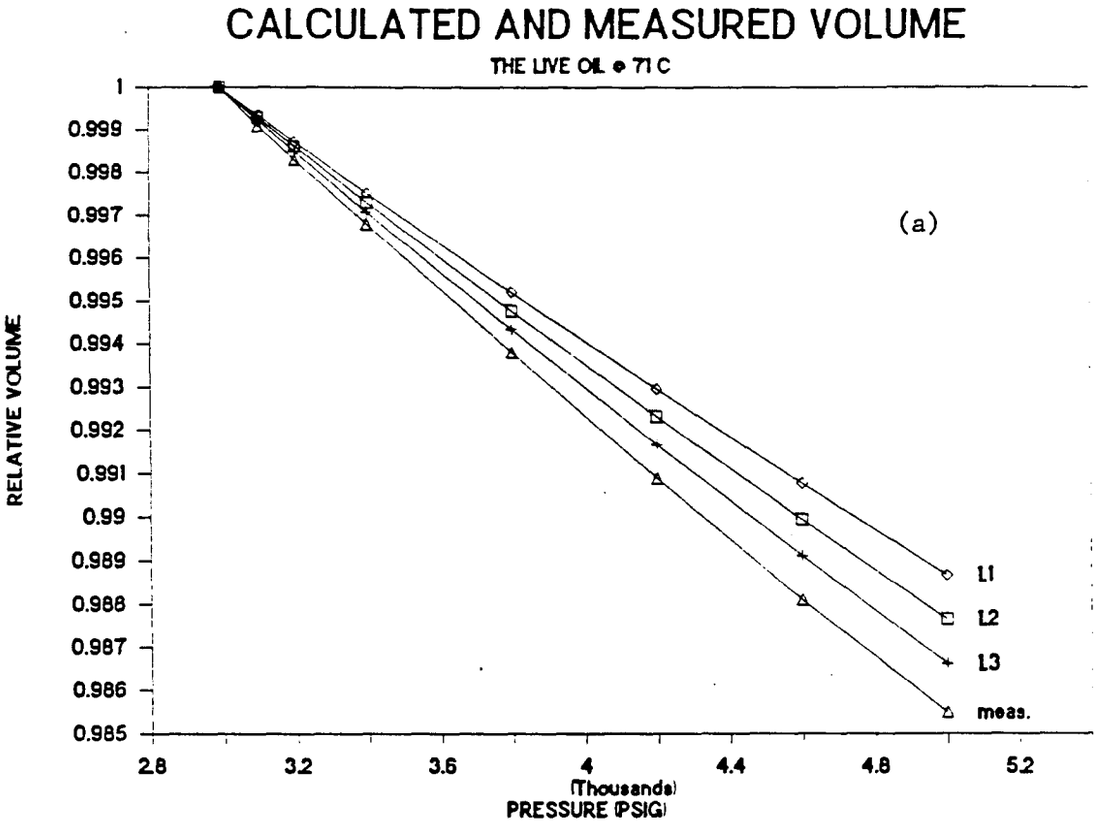
CALCULATED AND MEASURED VOLUME
THE LIVE OIL @ 71 C
RELATIVE VOLUME
1
0.999
0.998
0.997
0.996
0.995
0.994
0.993
0.992
0.991
0.99
0.989
0.988
0.987
0.986
0.985
(a)
L1
L2
L3
meas.
2.8
3.2
3.6
4
4.4
4.8
5.2
(Thousands)
PRESSURE (PSIG)

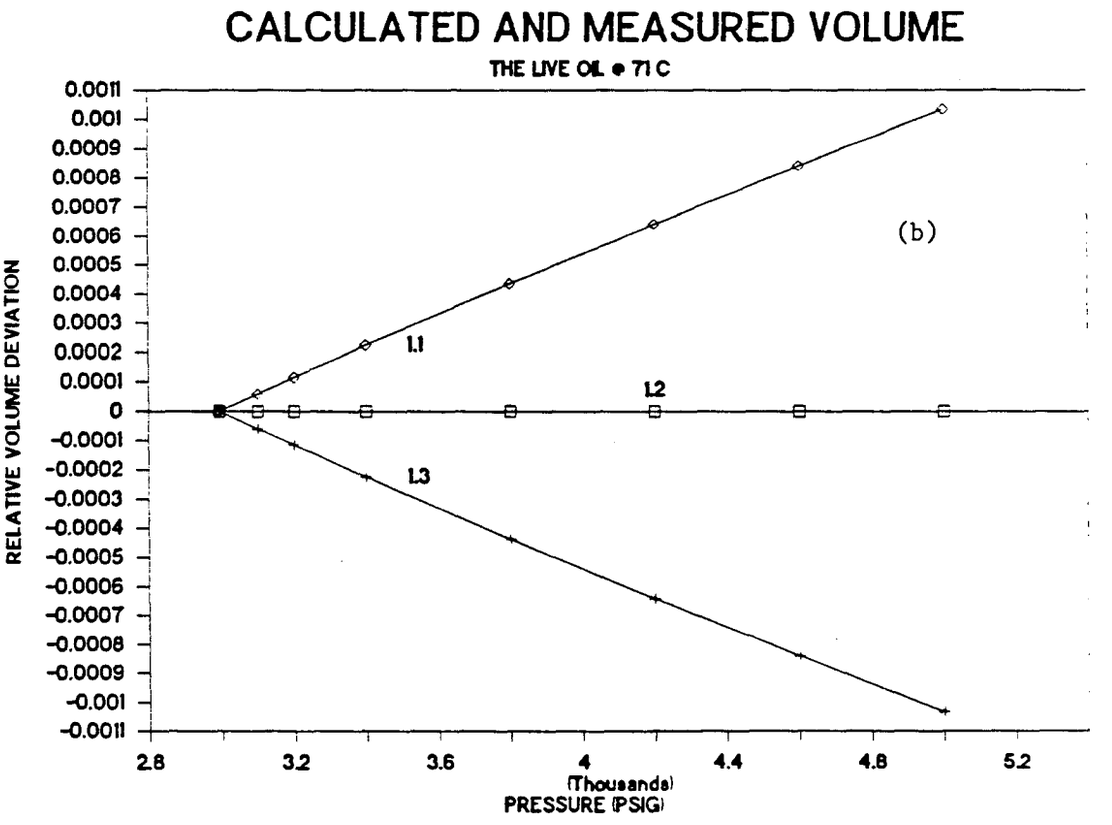
CALCULATED AND MEASURED VOLUME
THE LIVE OIL @ 71 C
RELATIVE VOLUME DEVIATION
0.0011
0.001
0.0009
0.0008
0.0007
0.0006
0.0005
0.0004
0.0003
0.0002
0.0001
0
-0.0001
-0.0002
-0.0003
-0.0004
-0.0005
-0.0006
-0.0007
-0.0008
-0.0009
-0.001
-0.0011
(b)
L1
L2
L3
2.8
3.2
3.6
4
4.4
4.8
5.2
(Thousands)
PRESSURE (PSIG)

fig. 31

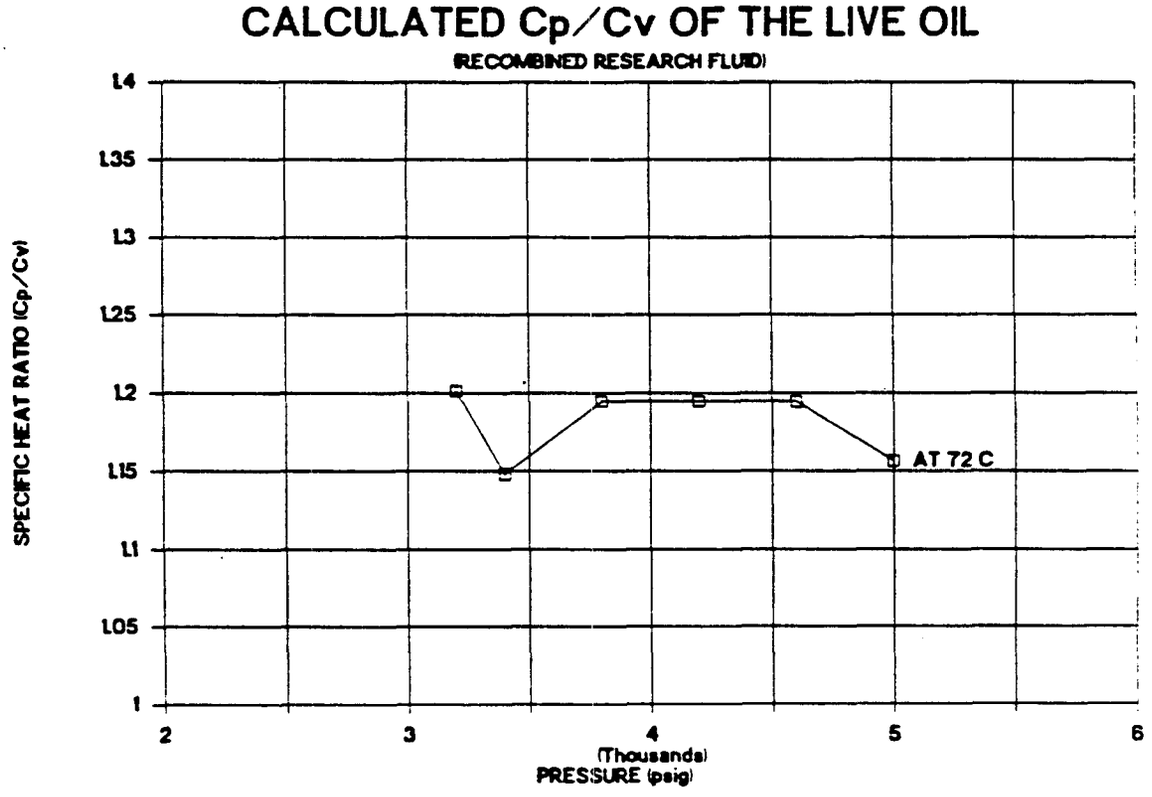
CALCULATED Cp/Cv OF THE LIVE OIL
(RECOMBINED RESEARCH FLUID)
SPECIFIC HEAT RATIO (Cp/Cv)
1.4
1.35
1.3
1.25
1.2
1.15
1.1
1.05
1
2
3
4
5
6
(Thousands)
PRESSURE (psig)
AT 72 C

fig. 32

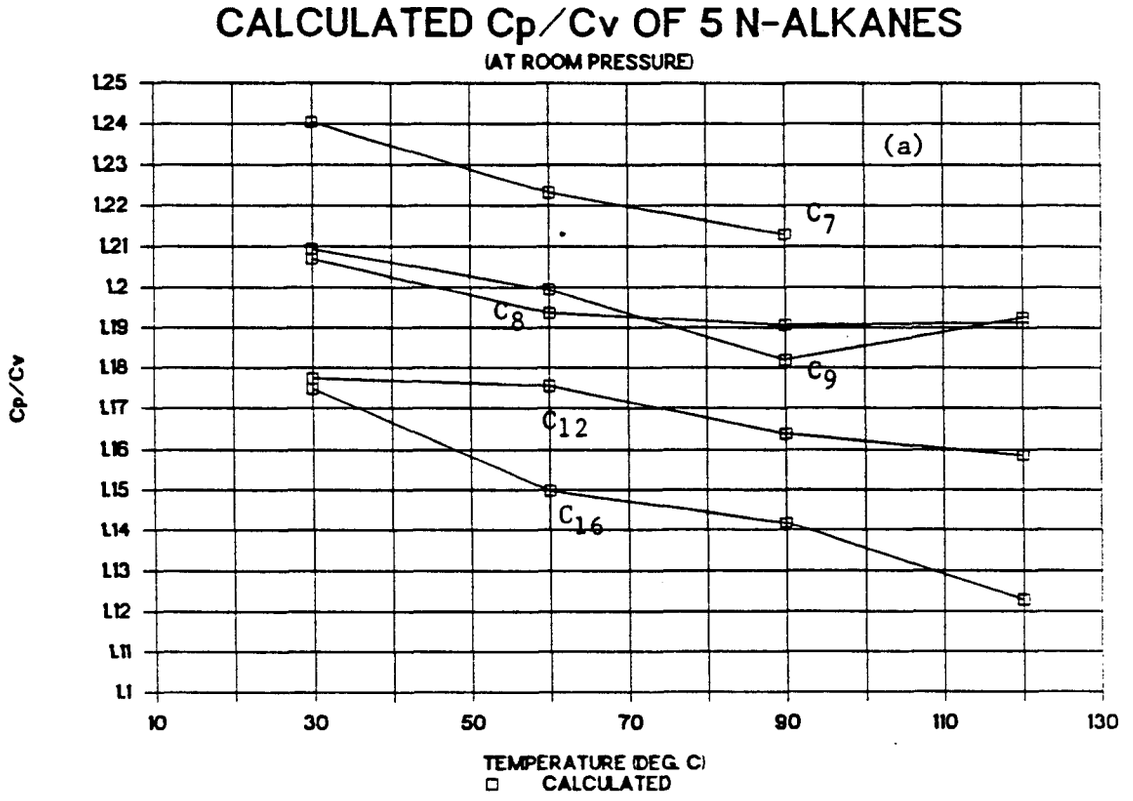
CALCULATED Cp/Cv OF 5 N-ALKANES
(AT ROOM PRESSURE)
Cp/Cv
1.25
1.24
1.23
1.22
1.21
1.2
1.19
1.18
1.17
1.16
1.15
1.14
1.13
1.12
1.11
1.1
(a)
C_7
C_8
C_9
C_{12}
C_{16}
10
30
50
70
90
110
130
TEMPERATURE (DEG. C)
□ CALCULATED

fig. 33

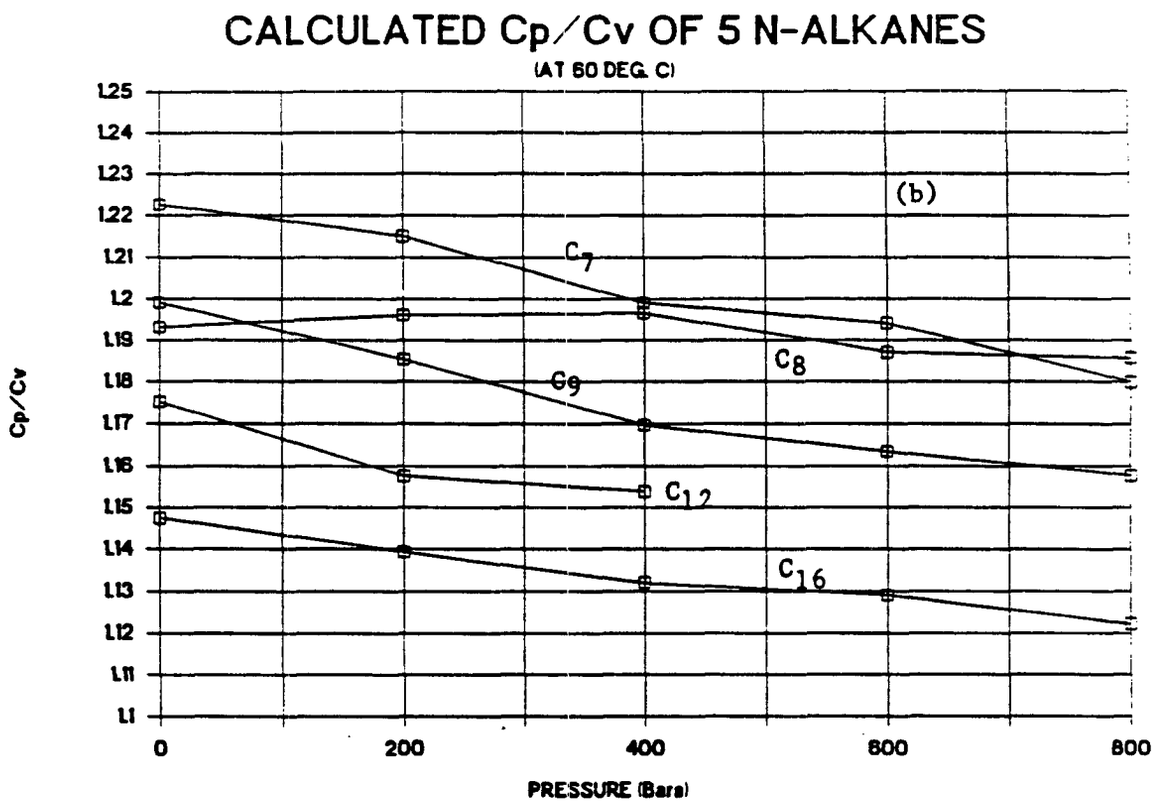
CALCULATED Cp/Cv OF 5 N-ALKANES
(AT 60 DEG. C)
Cp/Cv
1.25
1.24
1.23
1.22
1.21
1.2
1.19
1.18
1.17
1.16
1.15
1.14
1.13
1.12
1.11
1.1
0
200
400
600
800
PRESSURE (Bars)
(b)
C7
C8
C9
C12
C16

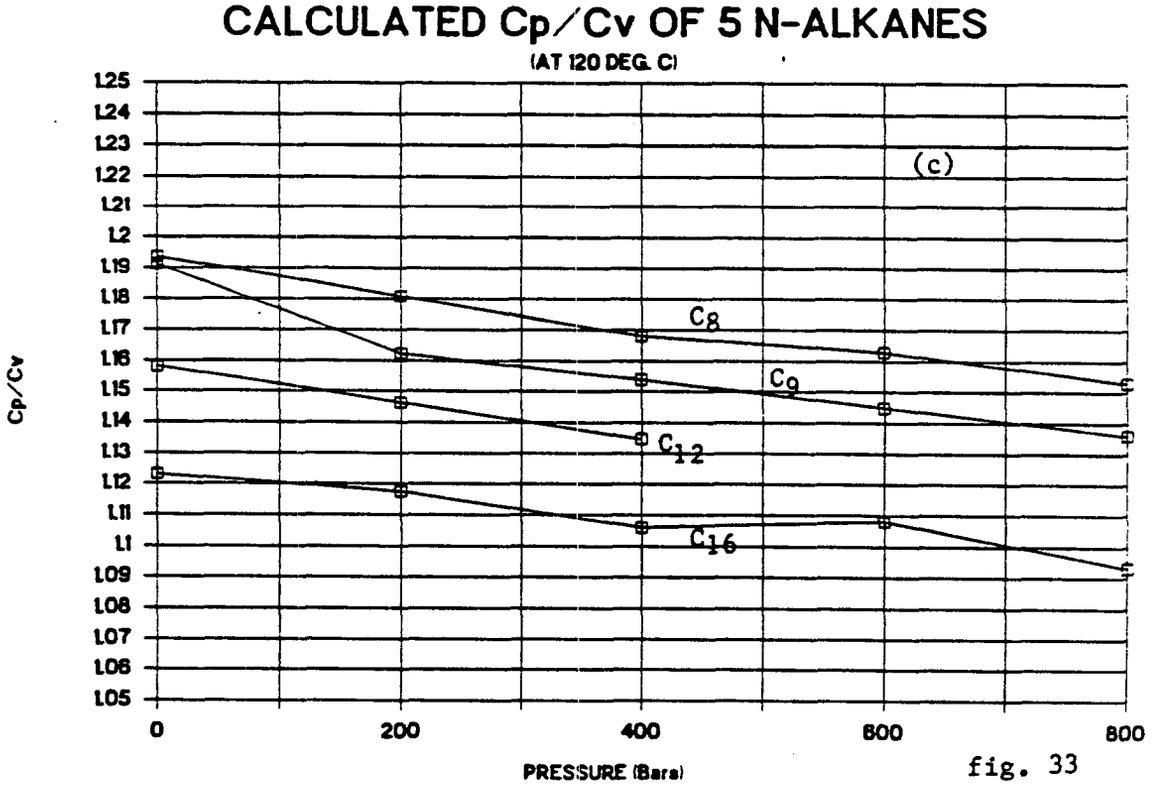
CALCULATED Cp/Cv OF 5 N-ALKANES
(AT 120 DEG. C)
Cp/Cv
1.25
1.24
1.23
1.22
1.21
1.2
1.19
1.18
1.17
1.16
1.15
1.14
1.13
1.12
1.11
1.1
1.09
1.08
1.07
1.06
1.05
0
200
400
600
800
PRESSURE (Bars)
(c)
C8
C9
C12
C16

fig. 33

CHAPTER 4

VELOCITIES IN PURE HYDROCARBON SATURATED ROCKS

ABSTRACT

Wave velocities were measured as a function of temperature in Beaver (porosity = 7%) and Boise (porosity = 27%) sandstones and the unconsolidated Ottawa sand (porosity = 37%) saturated with four pure hydrocarbons of successively increasing carbon numbers. It was found that the compressional wave velocities increased with the increase of the carbon numbers (or molecular weights) of the pore saturants, while the shear wave velocities were less affected.

The compressional wave velocities decreased by 6 to 8% in the sandstones and by 15 to 17% in the sand saturated with the hydrocarbons as the temperature increased from 22 to 122° C. This suggests that seismic, especially high frequency, high resolution seismic, methods are possibly applicable in detecting reservoir temperature changes caused by steam or fire floodings and in monitoring the processes of such floodings.

The effects of liquid saturation on the wave velocities in rocks and sand are also discussed.

INTRODUCTION

The capability of using seismic methods to monitor enhanced oil recovery (EOR) processes depends whether or not the seismic wave velocities or amplitudes are affected by the processes. If the seismic methods can resolve the travel time delay caused by the velocity decrease due to the EOR processes, they should be possible to be used in the

monitoring. Therefore, a series of experiments on the effects of temperature on wave velocities in rocks and sands saturated with hydrocarbons were carried out. In this chapter, it is assumed that the temperature increase in an oil reservoir is caused by the steam or fire floodings.

Four pure hydrocarbons with a successive carbon number increase, two sandstones of 7% and 27% porosity, and one unconsolidated sand of 37% porosity were used in the experiments. The results show that for the pure hydrocarbon saturated rocks, the compressional wave velocities decrease by around 7% as the temperature increases by 100° C, while the decrease in Vp in the sand is larger, by over 15%, in the same temperature range.

The effect of liquid saturation on the compressional wave velocities in the rocks and sand is also discussed. This effect is determined mainly by the properties of the liquid saturants, porosity, pore structures and geometries of the rocks, and possibly the chemical interactions between the rocks/sand and pore saturants.

Shear wave velocities do not always decrease in rocks upon liquid saturation, which disagrees with the Biot theory. Agreement with the theory is dependent on the presence of cracks in the rocks, pore fluid viscosity, porosity, pressure, and also possibly chemical interactions between the rock forming minerals and the pore fluid.

PROPERTIES OF THE ROCKS AND HYDROCARBONS

The rocks selected for the experiments are the Boise and Beaver sandstones. The Boise sandstone is fine to medium grained, well sorted, and with minor carbonate-clay cement. Both its porosity and its permeability are high (porosity = 27%, permeability = 910 mD). It is mainly composed of feldspar (about 44%) and quartz (about 27%).

The Beaver sandstone is fine to medium grained, well sorted, and cemented by quartz overgrowth. It is mainly composed of 7% porosity, 78% quartz, and quartz overgrowth as cement. Its permeability is unknown but believed to be much lower than

that of the Boise sandstone.

The Ottawa sand is unconsolidated and has porosity of 37% when well packed at room conditions. The size of the sand grains is mainly concentrated in the diameter range of 0.2 to 0.4 *mm* .

The hydrocarbons used as the pore saturants in the experiments were n-heptane (C_7H_{16}), 1-decene ($C_{10}H_{20}$), 1-tetradecene ($C_{14}H_{28}$), and 1-octadecene ($C_{18}H_{36}$). n-Heptane is a member of the homologous hydrocarbon series called alkanes or normal paraffins with a carbon number of 7. It is straight chained, single bonded, saturated, in molecular structure, and basically non-soluble in water. The other three hydrocarbons (1-decene, 1-tetradecene, and 1-octadecene) are all from a homologous hydrocarbon series called alkenes or olefins. The molecular structures of the alkenes are similar to those of alkanes, except that alkenes have a double bond between two of their carbon atoms (i.e., $-C=C-$), and therefore they are unsaturated. The alkenes are also basically non-soluble in water. The physical properties of the hydrocarbon saturants are listed in table 1.

EXPERIMENTS

Ultrasonic wave velocities were measured both in the hydrocarbon saturants and in the hydrocarbon saturated rocks, using two different apparatus based on the same pulse transmission principle. The apparatus for measuring the velocities in the hydrocarbons consists of a pair of transducers, a pulse generator/signal receiver, a signal amplifier, and a digital oscilloscope. The transducers are a pair of identical, wide band piezoelectric immersion transducers with a central frequency of 2.25 MHz and diameters of 19.05 mm (0.75 in.), and attached with two identical high-temperature buffers.

In the measurements, the two transducers, attached with high-temperature buffers, were built in and locked on a heat-conductive cylindrical container, and the distance (l) between them were precisely measured. The ultrasonic pulse of 1 MHz

frequency was sent to one of the transducers to generate ultrasonic waves traveling through the hydrocarbons under test. The waves were picked up by the other transducer and sent to the amplifier and then to the digital oscilloscope. The travel times of the waves therefore were measured on the oscilloscope, with precision of 0.05 *usec.*. Then the velocity V was calculated by

$$V = \frac{l}{\Delta t},$$

where l is the distance which the waves traveled in the hydrocarbon, and Δt is the travel time.

The hydrocarbons were pre-cooled in a refrigerator and heated up during the experiments by a heating tape which surrounded the heat-conducting container homogeneously.

The apparatus for measuring the velocities in fluid-saturated rocks is in principle similar to that for liquids. The system consists of basically a source/generator which generates ultrasonic pulses, a signal amplifier, an oscilloscope, an electronic microprocessor which measures the travel time of the wave through the sample, and a mechanical package which precisely controls the temperature and pore and confining pressures. (for more detailed descriptions of the apparatus, see Wang and Nur, 1985).

The rock samples were cut from a block into cylindrical shape of about 2.54 *cm* (1 *inch*) in both diameter and length. Then, they were well washed by distilled water and dried in a vacuum oven at 60° *C* for over 72 *hours*.

Once the rock sample was dried, it was jacketed with a high-temperature plastic tube and put into the pressure vessel for test. To saturated the sample with the hydrocarbons, the sample was evacuated up to 5 *microns* vacuum under confining pressure of 150 *bars*. Then the saturating hydrocarbon which was de-gased was injected into the sample by a pressure intensifier. After the pore pressure reached 50 *bars*, the confining pressure was increased to 200 *bars* to keep the effective pressure unchanged.

The temperature increase in the pressure vessel was controlled by an electrical heater which was attached inside to the pressure vessel. After an objective point of temperature was reached, the temperature was controlled at this point for about 45 *minutes* to assure good thermal equilibrium inside the sample.

The compressional and shear wave velocities in the rock samples were calculated by

$$V_p = \frac{l}{\Delta t_p},$$

$$V_s = \frac{l}{\Delta t_s},$$

respectively, where l is the length of the sample and Δt the travel time of the wave through the sample.

RESULTS AND DISCUSSIONS

Compressional wave velocities in the four hydrocarbon saturants were measured as a function of temperature ranging from -8 to 125° C, under the room pressure. The data are plotted in figure 1.

As discussed in chapter 2, the velocities in liquid hydrocarbons are approximately linearly related to the temperature changes and the changes of the inverse of the carbon numbers. The relation is expressed as

$$V_{T,C} = V_{T_o,C_o} - b\,(T - T_o) - a\,(\frac{1}{C} - \frac{1}{C_o}),$$

where $V_{T,C}$ is the velocity in the hydrocarbon of carbon number C at temperature T; T_o and C_o are the reference temperature and carbon number, respectively; b is the temperature coefficient which is a function of carbon number; and a is the carbon number coefficient which is a function of temperature.

Figure 1 shows that the velocities in the hydrocarbons decrease rapidly as the temperature increases. The temperature coefficient b ranges from -3.6 to -4.2 $[meters/sec]/^{\circ}C$. The velocity-temperature relation was discussed in chapters 2 and 3.

Both the compressional and shear wave velocities in air saturated (or "dry") Boise and Beaver sandstones were measured as a function of confining pressure (figures 2 and 3). The velocities (both Vp and Vs) all increased as the confining pressure increased up to 700 *bars* (10150 psi). These increases are caused by the closure of the thin cracks and thus the porosity reduction of the rocks and the better contact of the rock grains. The rate of these increases is determined by the pore structures, e.g., the crack content of the rocks.

At low confining pressures, both the compressional and shear wave velocities in Boise and Beaver sandstones are very sensitive to the pressure changes, while at higher confining pressures, the velocities increase with increasing pressures slowly. This behavior of rocks has been observed by many investigators (Nur and Simmons, 1969; Birch, 1961; King, 1966) and interpreted as caused by the closure of the thin cracks and the better contact of the rock grains. Generally, the confining pressure needed to close the cracks are moderate which is determined mainly by the aspect ratios of the cracks and pore structures, consolidation and cementation degrees, and grain packing patterns of the rock.

While the velocities in the air saturated Boise and Beaver sandstones increase with increasing confining pressures, they decrease with increasing temperatures. Figure 4 shows that the compressional and shear wave velocities in the Boise sandstone decreased by about the same amount (ΔVp = -141 m/sec, ΔVs = -130 m/sec) as the temperature increased from 21 to 124° C. The relative decrease for Vp and Vs in this temperature range are 4.1% and 5.9% respectively. In figure 5, the absolute decrease of Vp in the Beaver sandstone is smaller than that of Vs in the temperature range of 21 to 128° C (ΔVp = -129 m/sec, ΔVs = -183 m/sec): the relative decreases

are 2.7% and 5.6%, respectively. The decreases in the velocities as the temperature increases are mainly caused by the softening of the rock matrix and the thermal expansion of the rocks. From our data, it is believed that the increased temperature has a major contribution in reducing the shear modulus of the rocks: i.e., as the temperature increases, the softening of the rock matrix reduces the shear modulus of the rock, while the bulk modulus is less affected.

The temperature effect on the compressional wave velocities is smaller in the air saturated Ottawa sand than in the sandstones (figure 6). As the temperature rose from 22 to 123° C, the Vp in the Ottawa sand saturated with air decreased by only 81 m/sec, or by 5.4%.

Figures 7a and 7b show the compressional and shear wave velocities in the water saturated Boise sandstone. From these two figures, one can see that the water saturation enhanced the temperature effect on the compressional wave velocities. The absolute change for the velocities in the temperature range of 22 to 127° C are -229 m/sec for Vp and -143 m/sec for Vs, or by 6.5% and 6.7%, respectively.

In figure 8, the temperature effect on both the compressional and shear wave velocities in the Beaver sandstone is also enhanced by the water saturation. As the temperature increaseed from 22 to 124° C, the compressional and shear wave velocities decreased by 254 m/sec and 257 m/sec, or by 4.9% and 7.6%, respectively.

The compressional wave velocities in the Ottawa sand were increased by the water saturation. As seen in figure 9, the water saturation also enhanced the temperature effect on the velocities. In the temperature range of 22 to 124° C, the Vp in the water saturated sand decreased by 118 m/sec, or 6.1%.

It is also noticed that water saturation decreased the shear wave velocities in the Boise sandstone (figures 3b, 5b) but increased the shear wave velocity in the Beaver sandstone. This phenomenon will be discussed later along with the saturation effect of hydrocarbons on the shear wave velocities.

The compressional wave velocities in the Boise sandstone saturated with the hydrocarbons are shown in figure 10a. For the purpose of comparison, the compressional wave velocities in the same rock saturated with air and water are also plotted in the same figure. The compressional wave velocities all decrease as the temperature increases. The decreases are about the same for all the six velocity curves in the temperature range of 21 to 121° C (around -240 m/sec), though the relative decreases are slightly different (around 6.6 to 7.0%). This means that the temperature effect on the compressional wave velocities in pure hydrocarbon saturated rocks is basically similar.

Figure 10b shows the compressional wave velocities in the Beaver sandstone. Again, the velocity trends in the rock saturated with different pure hydrocarbons as the temperature increases are all similar. In Beaver sandstone, the absolute Vp decreases are all around 350 m/sec in the temperature range of 21 to 121° C, and the relative decreases are around 6.7 to 7.0%.

The compressional wave velocities in the Ottawa sand saturated with C_7H_{16}, $C_{18}H_{36}$, air and water are shown as a function of temperature in figure 11. In the temperature range of 21 to 126° C, the Vp decreased by 317 m/sec, or 17.2%, for the C_7H_{16} saturated sand, and by 283 m/sec, or 14.6%, for the $C_{18}H_{36}$ saturated sand.

The decreases of Vp in the hydrocarbon saturated rocks and sand are mainly caused by the decreases of the velocities in the "dry" rocks and sand and in the hydrocarbons, as the temperature increases, and possibly as well as the interactive effect between the rock frame and the pore saturants.

In figure 12, the shear wave velocities in all the pure hydrocarbon saturated Boise sandstone do not differ much from each other at the same temperature point. The $V_s - T$ curves for the hydrocarbon saturated Boise sandstone (figure 12a) lie between those for the same rock saturated with water and air. All the shear wave velocities in the Beaver sandstone saturated with the hydrocarbons decrease at about the same rate as the temperature increases (figure 12b). However, unlike that for the Boise

sandstone, this rate of Vs decrease is higher than that in the same rock saturated with air. Furthermore, the $Vs - T$ curve for the water saturated Beaver sandstone does not depart from other curves, instead, it is embedded in the cluster of the $Vs - T$ curves for the same sandstone saturated with the hydrocarbons.

From figures 10 and 12, one can see that the properties of the saturants also affect the wave velocities. In the same rock sample, Vp in the saturated rocks increase with increasing the pore hydrocarbon's carbon number (or molecular weight). This increase is essentially caused by the velocity increase in the hydrocarbons with increasing carbon numbers (or molecular weight) (figure 1). However, Vs in the hydrocarbon saturated sandstones are not much affected by the carbon number (or molecular weight) changes of the hydrocarbons, as long as the hydrocarbons are in the state of liquid. In figure 12a, all the Vs curves for the hydrocarbon saturated Boise sandstone are very close to each other, the difference between the neighbor curves is within the measurement precision. The similar situation occurs for the Beaver sandstone saturated with the hydrocarbons (figure 12b), except that the curves deviate from each other a little further.

Hydrocarbon (or water) saturation increased the compressional wave velocities in both Boise and Beaver sandstones (figures 10a, 10b). However, this saturation effect is different for the two sandstones. For the Boise sandstone, the hydrocarbon saturation increased the Vp by 86 (for C_7H_{16} saturation) to 178 m/sec (for $C_{18}H_{36}$ saturation) at $21^{\circ}C$, while at the same temperature point, the hydrocarbon saturation increased the Vp in the Beaver sandstone by 369 (for C_7H_{16} saturation) to 436 m/sec (for $C_{18}H_{36}$ saturation). This phenomenon has also been observed by Gregory (1976) who concluded that the fluid saturation effects on compressional wave velocities in rocks are much larger in low porosity than in high porosity rocks at elevated pressures.

Although the liquid saturation affects the compressional wave velocities more in low porosity than in high porosity rocks, the same phenomenon does not necessarily

also occur to unconsolidated sands. In our results, Vp in the Ottawa sand increased by 346 m/sec (for C_7H_{16} saturation) to 439 m/sec (for $C_{18}H_{36}$ saturation) at 21° C upon the hydrocarbon saturation, though the porosity of the sand is high (37%). One of the explanations to this phenomenon may be as follows: since the compressional wave velocities in the dry sand are very low, or in other words, the dry sand is highly compressible, full liquid saturation to the sand will greatly increase the bulk modulus of the aggregate, which in turn increases the compressional wave velocities.

Full saturation of a liquid to the pore space of a rock or sand always increases the compressional wave velocities, since the replacement of the gas by a liquid in the pores increases the bulk modulus of the rock or sand sample. However, the liquid saturation increases the bulk density of the rock sample as well, which in contrast reduces the compressional wave velocity. The higher the porosity of the rock, the more its bulk density will increase upon liquid saturation. Therefore, when the rock porosity is high, the liquid saturation effect on the Vp is smaller due to the bulk density increase. Besides the density increase, the liquid saturation effect is also contributed by the liquid properties, pore structure and wettability of the rock, and possibly chemical reactions between the pore fluid and the rock matrix.

The compressional wave velocity in the water saturated Boise sandstone is lower than that in $C_{18}H_{36}$ saturated one. This phenomenon does not agree with the Biot theory (Biot, 1956a, b) or the time average equation (Wyllie, et al., 1956)

$$\frac{1}{V_p} = \frac{1-\phi}{V_m} + \frac{\phi}{V_f}, \tag{1}$$

where V_p, V_m, and V_f are the velocities in the fluid saturated rock, the rock matrix, and the pore fluid, respectively, and ϕ is the porosity of the rock. According to the Biot theory or equation (1), increasing V_f should increase V_p. In our case, the velocity in water is higher than that in $C_{18}H_{36}$, but the Vp in the water saturated is lower than that in the $C_{18}H_{36}$ saturated Boise sandstone. This behavior of the Boise sandstone is

possibly caused by the chemical reaction between the water and the rock matrix and the wettability of the rock. Unfortunately, at this stage, no theory or quantitative interpretation has been proposed for this phenomenon.

At higher temperatures (above $110^{\circ}C$), the compressional wave velocities in the C_7H_{16} saturated rocks and sand decrease faster (figures 10a, 10b, 11). In the C_7H_{16} saturated Boise sandstone, the Vp even becomes lower than that in the air saturated sample. This is caused by the properties of the C_7H_{16} saturant. As seen in table 1, the boiling point of C_7H_{16} is $98^{\circ}C$ (and higher when under pressure). At higher temperatures, part of the C_7H_{16} in the pores of the sandstones or sand may become into the vapor phase, though the amount may be very small, which can dramatically decrease the compressional wave velocity (Biot, 1956a, b; Murphy, 1982), even to the degree that is lower than that in the "dry" rock due to the density effect.

In figure 12a, all the velocity curves for the hydrocarbon saturated lie between those for the water and air saturated Boise sandstone, which agrees with the Biot theory (Biot, 1956a,b). According to this theory, liquid saturation to the rock pores will decrease the shear wave velocities in the rock aggregate due to the density effect. i. e., the shear wave velocities in a liquid saturated rock should be lower than those in the dry rock. Theoretically, since both gas and liquid (not highly viscous) do not resist shear stress, replacing the gas in the rock pores by a liquid does not change the shear modulus, but does increase the density, of the rock aggregate. Therefore the shear wave velocity ($V_s = \sqrt{\mu/\rho}$, μ - shear modulus, ρ - density) is decreased by the increased density.

Although both the water and the hydrocarbon saturation to the Boise sandstone decreased the shear wave velocities, the same situation did not occur to the Beaver sandstone (figure 12b). In figure 12b, the shear wave velocities in the liquid (water, hydrocarbons) saturated Beaver sandstone are higher than those in the same sandstone saturated with air. This phenomenon can be explained as caused by the viscosity effect

of the liquids. According to the theory of wave propagations in viscous fluids (Thurston, 1964), shear waves can penetrate into liquids by a depth called skin depth which is proportional to the square root of the shear viscosity of the liquid. If a rock of low porosity has a high crack content, the density effect on the shear wave velocities is small and the shear wave can penetrate through the pore liquid in the cracks whose short axes are shorter than the skin depth of the wave. And hence, the shear wave velocity is increased (Wang and Nur, 1985).

In our case, the porosity of the Beaver sandstone is low (7%) and may have a high crack content (since the velocities are very sensitive to the pressure changes, figures 3a and 3b). Therefore the pore fluid viscosity plays a major role in the shear velocity increase in the rock upon liquid saturation. Furthermore, since the viscosities of the hydrocarbons increase systematically with increasing the carbon numbers (or molecular weight) (from 0.42 for C_7H_{16} to 4.32 cp for $C_{16}H_{36}$), the number of cracks through which the shear wave can penetrate also increases with the pore hydrocarbon carbon number (or molecular weight), which leads the shear wave velocities slightly to increase. Therefore, as also observed by Gregory (1976), at higher frequencies (1 MHz), the shear wave velocities do not always decrease when liquid pore saturants are added to rocks as theorized by Biot, agreement with the Biot theory is dependent upon the presence of cracks, porosity, pressure, and possibly chemical interactions between the rock forming minerals and the pore fluid.

SUMMARY AND CONCLUSION

As discussed in chapter 2, the compressional wave velocities in the hydrocarbon saturants are approximately linearly related to the changes of temperature and the inverse of the carbon numbers. These temperature and carbon number effects also contribute to the velocity changes in rocks saturated with hydrocarbons.

The compressional wave velocities decreased by around 6.6 to 7.0% in both the Beaver and Boise sandstones, and by 15 to 17% in the Ottawa sand, saturated with the pure hydrocarbons, as the temperature increased from 22 to 122° C. Theoretically, this amount of decrease in the compressional wave velocities could be detected in the field by high frequency, high resolution seismic methods. That is to say, in a reservoir subjecting steam or fire flooding, even if the reservoir rocks were saturated with light or pure hydrocarbons, it would still be possible to use seismic methods to monitor or map the flooding processes in the field. Furthermore, in the next chapter, we will show that the compressional wave velocities in the heavy hydrocarbon (e.g., heavy oil, tar) saturated rocks are much more affected by the temperature changes, usually decreasing by 15% or more for an increase in temperature by 100° C Therefore, seismic, especially high frequency, high resolution, methods are possible to be used in monitoring or mapping the steam or fire flooding processes.

The effect of the liquid saturation to porous rocks on the compressional wave velocities is mainly determined by the liquid properties, porosity, pore structure and geometries of the rocks, and possibly the chemical interactions between the rock frame and the saturant. In our experiments, the hydrocarbon or water saturation increased the compressional wave velocities in the rock aggregates, but this increase is much less in high porosity (Boise sandstone) than in low porosity (Beaver sandstone) rocks. However, this situation does not apply to high porosity unconsolidated sands.

The Biot theory predicts that the shear wave velocities always decrease when liquid pore saturants are added to rocks, due to the increase in the bulk density of the rocks. However, experimental results sometimes disagree with the prediction. The disagreement is mainly caused by the fact that the Biot theory did not consider the micro-structures of the rocks (e.g., the crack content). Generally speaking, the agreement of the experimental results with the Biot theory is mainly dependent upon the presence of thin cracks in the rocks, pore fluid viscosity, porosity, pressure, and

possibly chemical interactions between the rock forming minerals and the pore fluid.

REFERENCE

Biot, M. A., 1956a, b. Theory of propagation of elastic waves in a fluid saturated porous solid, I. low frequency range. II. higher frequency range. *Journal of Acoust. Soc. Am., Vol. 28, no.2, p168.*

Birch, F., 1961. The velocity of compressional waves in rocks to 10 Kb, part 2. *Journal of Geophy. Res., Vol. 66, p2199*

Gregory, A. R., 1976. Fluid saturation effects on dynamic elastic properties of sedimentary rocks. *Geophysics, Vol. 41, no.5, p895.*

Kincaid, J. F. and H. Eyring, 1938. *Journal of Chem. Phys., Vol. 6, p620.*

King, M. S., 1966, Wave velocities in rocks as a function of changes in overburden pressure and pore fluid saturants. *Geophysics, Vol 31, no.1, p50.*

Murphy, W, F, III, 1982. Effect of microstructure and pore fluids on the acoustic properties of granular sedimentary materials. Ph.D thesis, Stanford Univ., *Stanford Rock Physics Project, Vol. 16.*

Nur, A. and G. Simmons, 1969. The effect of saturation on velocity in low porosity rocks. *Earth Plan. Sci. Let., Vol. 7, p183.*

Wang, Z. and A. Nur, 1985. Effect of pore fluid viscosity on the acoustic wave velocities in porous rocks. *Journal Acoust. Soc. Am., Vol. 78(S1), p32.*

Wang Z. and A. Nur, 1986. The effect of temperature on the wave velocities in rocks and sands with heavy hydrocarbons. *Stanford Rock Physics Project, Vol. 27, p323.*

Wang, Z. and A. Nur, 1987. Ultrasonic wave velocities in hydrocarbons. *Stanford Rock Physics Project, Vol. 31, p59.*

Willie, M. R. J., A. R. Gregory, and L. W. Gardner, 1956. Elastic wave velocities in heterogeneous and porous media. *Geophysics, Vol. 21, p41.*

TABLE AND FIGURE CAPTIONS

Table 1. Properties of the hydrocarbon saturants.

Figure 1. Compressional wave velocities in the hydrocarbon saturants.

Figure 2. Compressional (a) and shear (b) wave velocities in the Boise sandstone with air, as a function of pressure.

Figure 3. Compressional (a) and shear (b) wave velocities in the Beaver sandstone with air, as a function of pressure.

Figure 4. Compressional (a) and shear (b) wave velocities in the Boise sandstone with air, as a function of temperature.

Figure 5. Compressional (a) and shear (b) wave velocities in the Beaver sandstone with air, as a function of temperature.

Figure 6. Compressional wave velocities in the Ottawa sand with air as a function temperature.

Figure 7. Compressional (a) and shear (b) wave velocities in the Boise sandstone with water, as a function of temperature.

Figure 8. Compressional (a) and shear (b) wave velocities in the Beaver sandstone with water, as a function of temperature.

Figure 9. Compressional wave velocities in the Ottawa sand with water as a function temperature.

Figure 10. Compressional wave velocities in the Boise (a) and Beaver (b) sandstones saturated with hydrocarbons, water, and air.

Figure 11. Compressional wave velocities in the Ottawa sand saturated with hydrocarbons, water, and air.

Figure 12. Shear wave velocities in the Boise (a) and Beaver (b) sandstones saturated with hydrocarbons, water, and air.

Properties of the Hydrocarbon Saturants

Name	Formula	Purity (%)	Molecular Weight	Melting Point (° C)*	Boiling Point (° C)*	Density at 20° C**
n-Heptane	C_7H_{16}	99+	100.07	-91	98	0.684
1-Decene	$C_{10}H_{20}$	96	140.10	-66	171	0.741
1-Tetradecene	$C_{14}H_{28}$	95	196.14	-13	251	0.775
1-Octadecene	$C_{18}H_{36}$	90	252.18	16	314	0.789

*: at 760 *mmHg*. **: at 760 *mmHg*, unit: *Grams* / cm^3.

Table 1

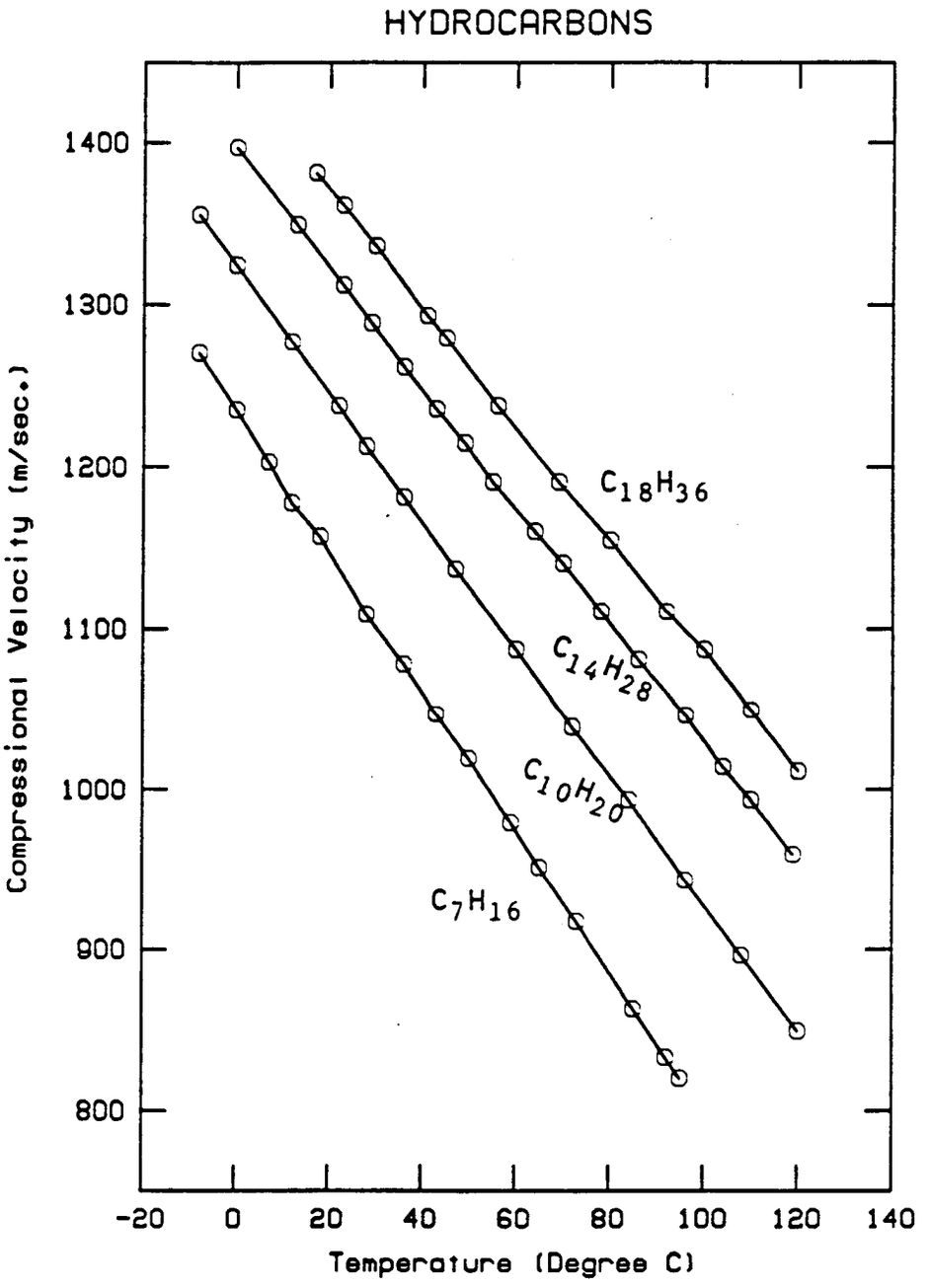
HYDROCARBONS
Compressional Velocity (m/sec.)
1400
1300
1200
1100
1000
900
800
-20
0
20
40
60
80
100
120
140
Temperature (Degree C)
$C_{18}H_{36}$
$C_{14}H_{28}$
$C_{10}H_{20}$
C_7H_{16}

Fig. 1

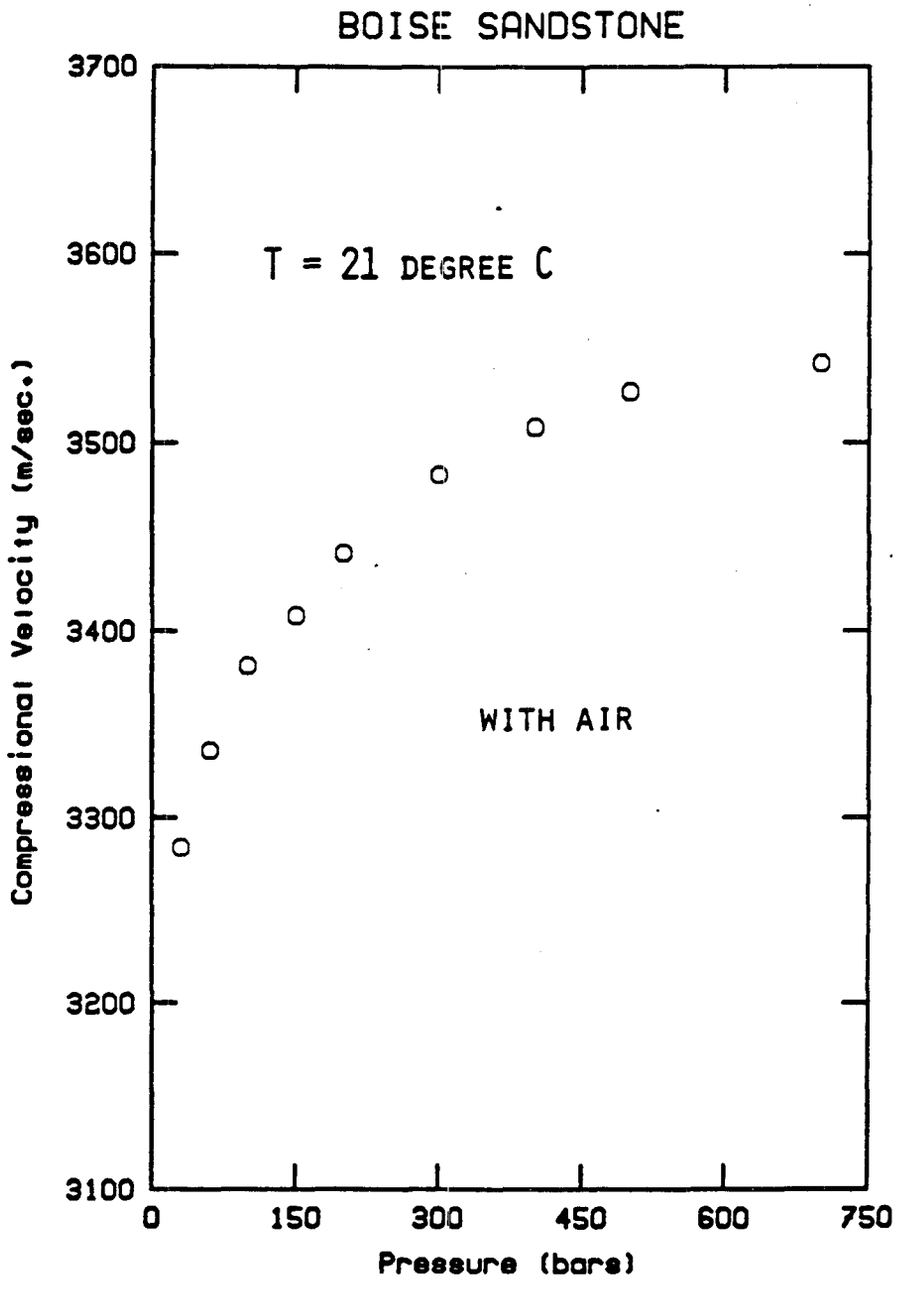
BOISE SANDSTONE
T = 21 DEGREE C
WITH AIR
Compressional Velocity (m/sec.)
3700
3600
3500
3400
3300
3200
3100
0
150
300
450
600
750
Pressure (bars)

Fig. 2a

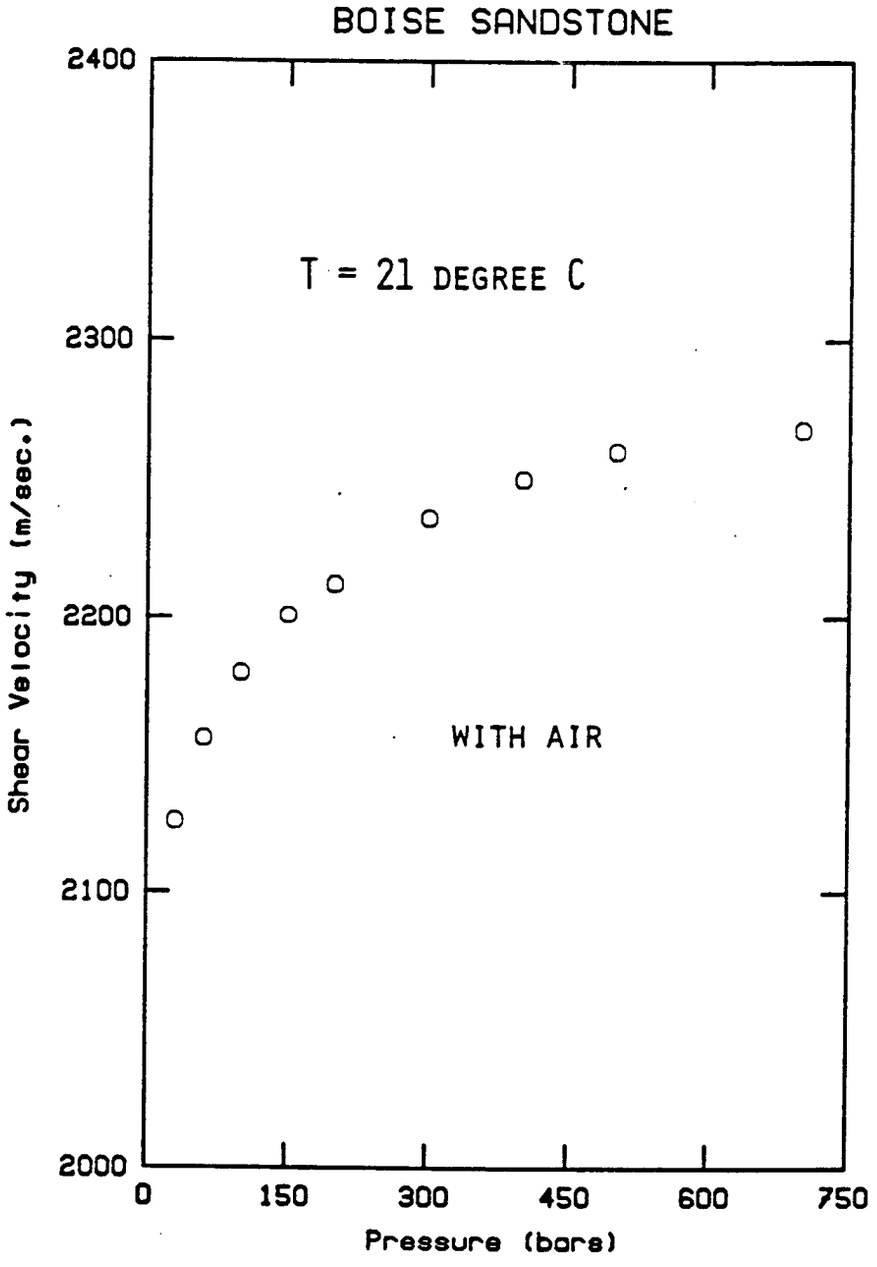
BOISE SANDSTONE
T = 21 DEGREE C
WITH AIR
Shear Velocity (m/sec.)
2400
2300
2200
2100
2000
0
150
300
450
600
750
Pressure (bars)

Fig. 2b

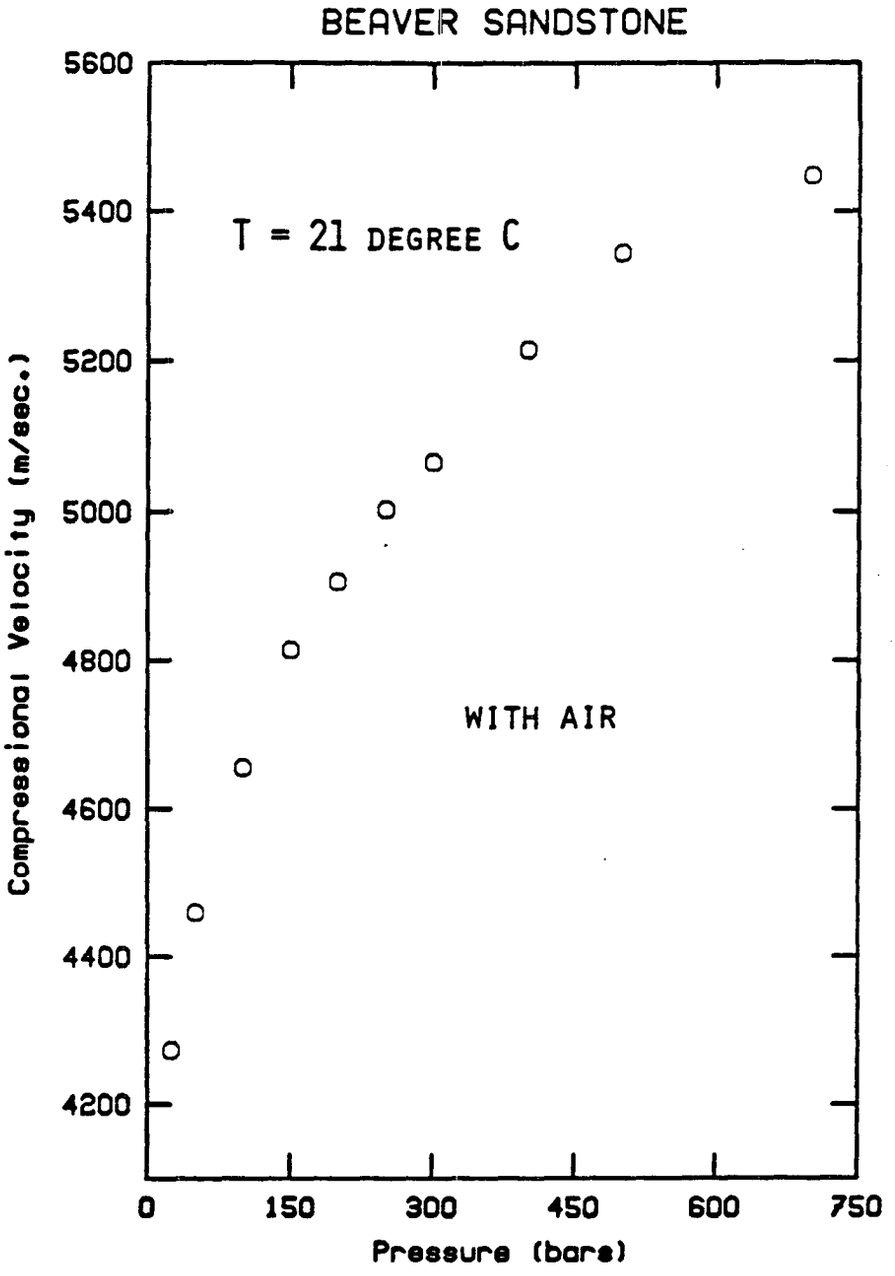
BEAVER SANDSTONE
T = 21 DEGREE C
WITH AIR
Compressional Velocity (m/sec.)
5600
5400
5200
5000
4800
4600
4400
4200
0
150
300
450
600
750
Pressure (bars)

Fig. 3a

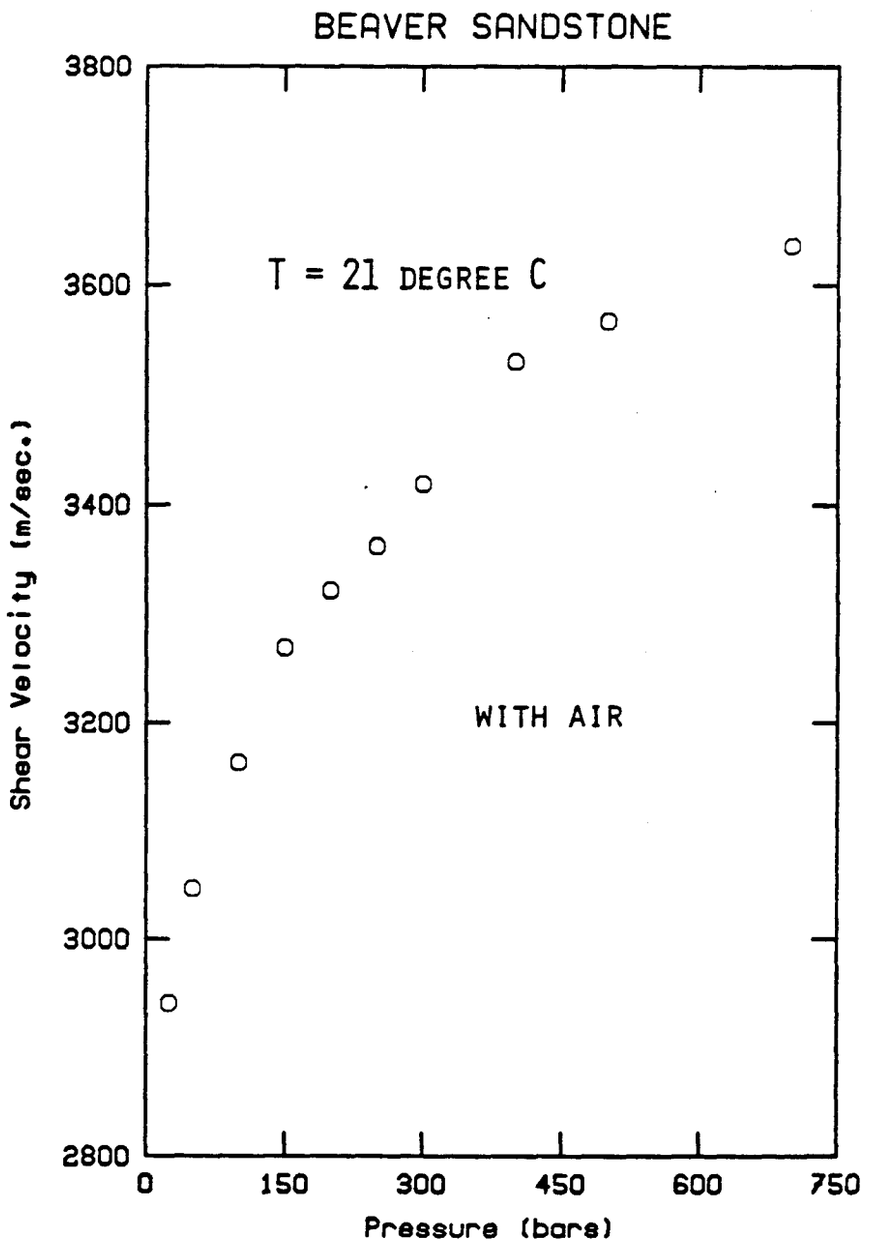
BEAVER SANDSTONE
T = 21 DEGREE C
WITH AIR
Shear Velocity (m/sec.)
Pressure (bars)
3800
3600
3400
3200
3000
2800
0
150
300
450
600
750

Fig. 3b

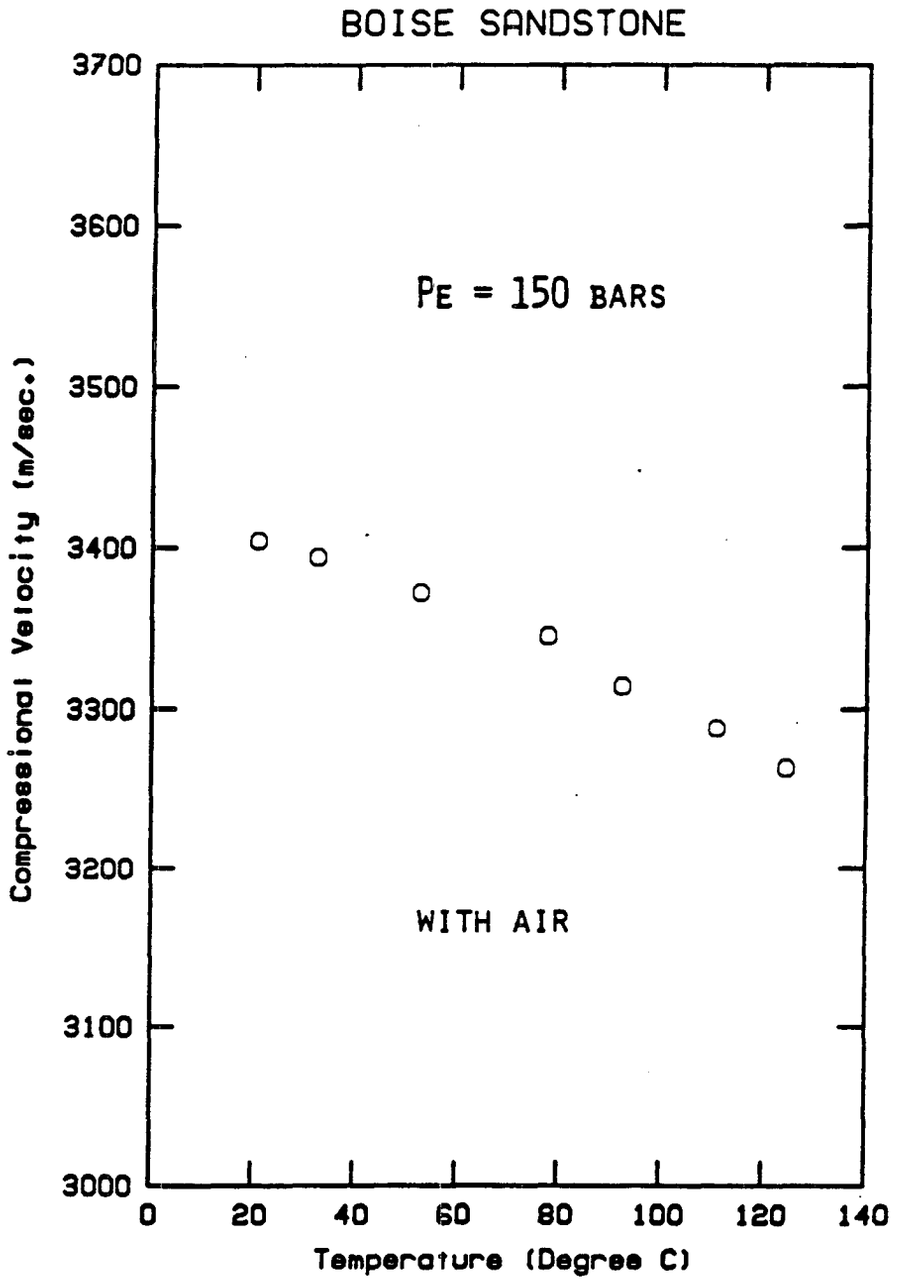
BOISE SANDSTONE
3700
3600
3500
3400
3300
3200
3100
3000
Compressional Velocity (m/sec.)
PE = 150 BARS
WITH AIR
0
20
40
60
80
100
120
140
Temperature (Degree C)

Fig. 4a

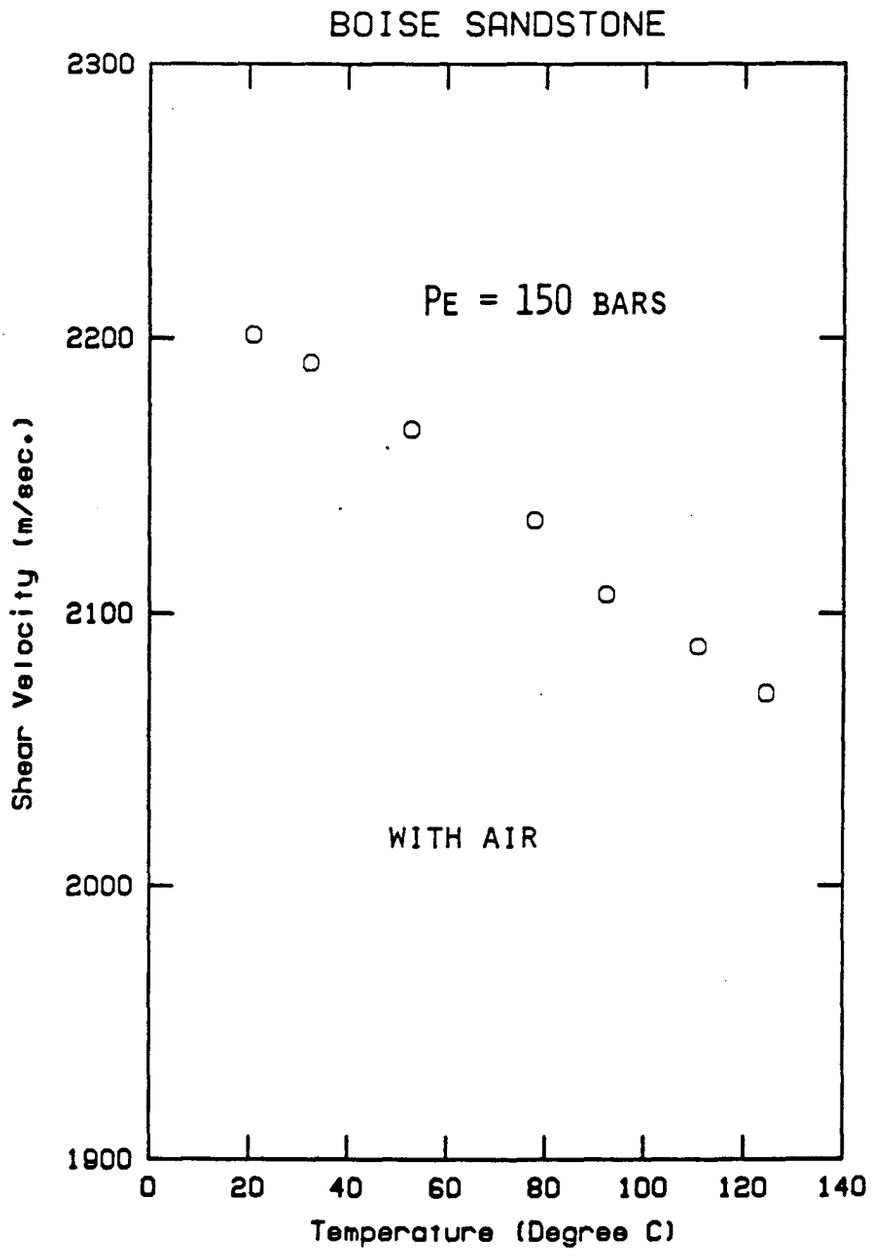
BOISE SANDSTONE
PE = 150 BARS
WITH AIR
Shear Velocity (m/sec.)
Temperature (Degree C)
2300
2200
2100
2000
1900
0
20
40
60
80
100
120
140

Fig. 4b

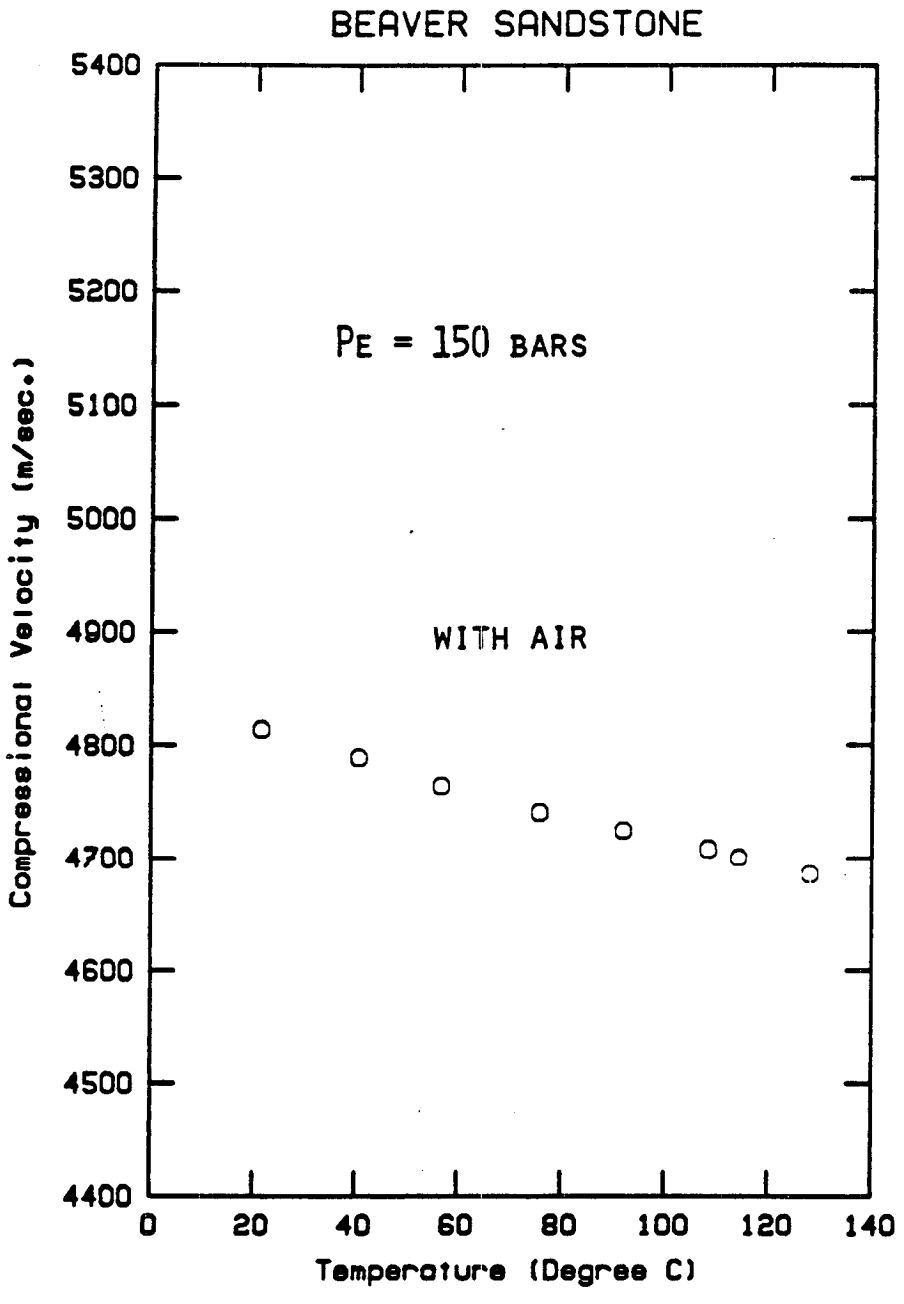
BEAVER SANDSTONE
PE = 150 BARS
WITH AIR
Compressional Velocity (m/sec.)
5400
5300
5200
5100
5000
4900
4800
4700
4600
4500
4400
0
20
40
60
80
100
120
140
Temperature (Degree C)

Fig. 5a

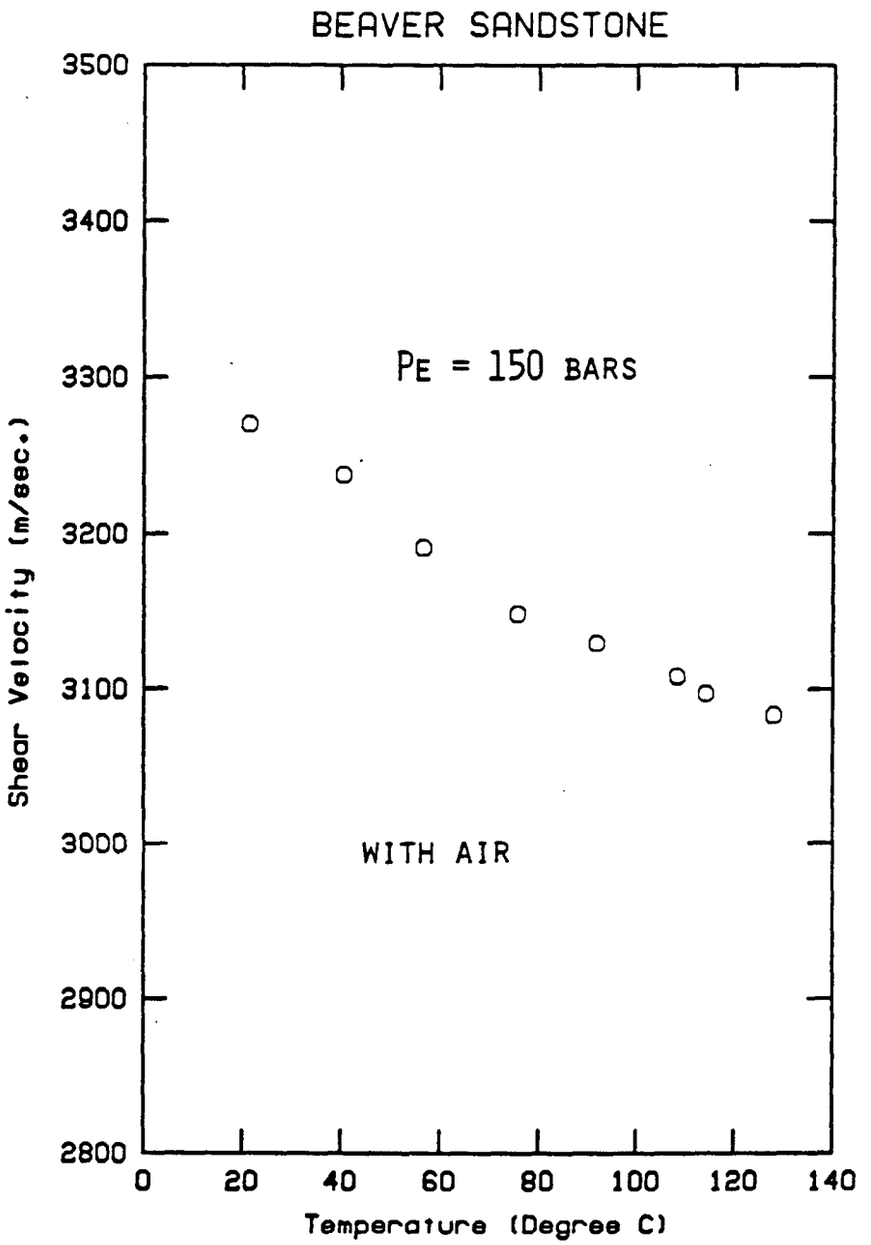
BEAVER SANDSTONE
PE = 150 BARS
WITH AIR
Shear Velocity (m/sec.)
Temperature (Degree C)
3500
3400
3300
3200
3100
3000
2900
2800
0
20
40
60
80
100
120
140

Fig. 5b

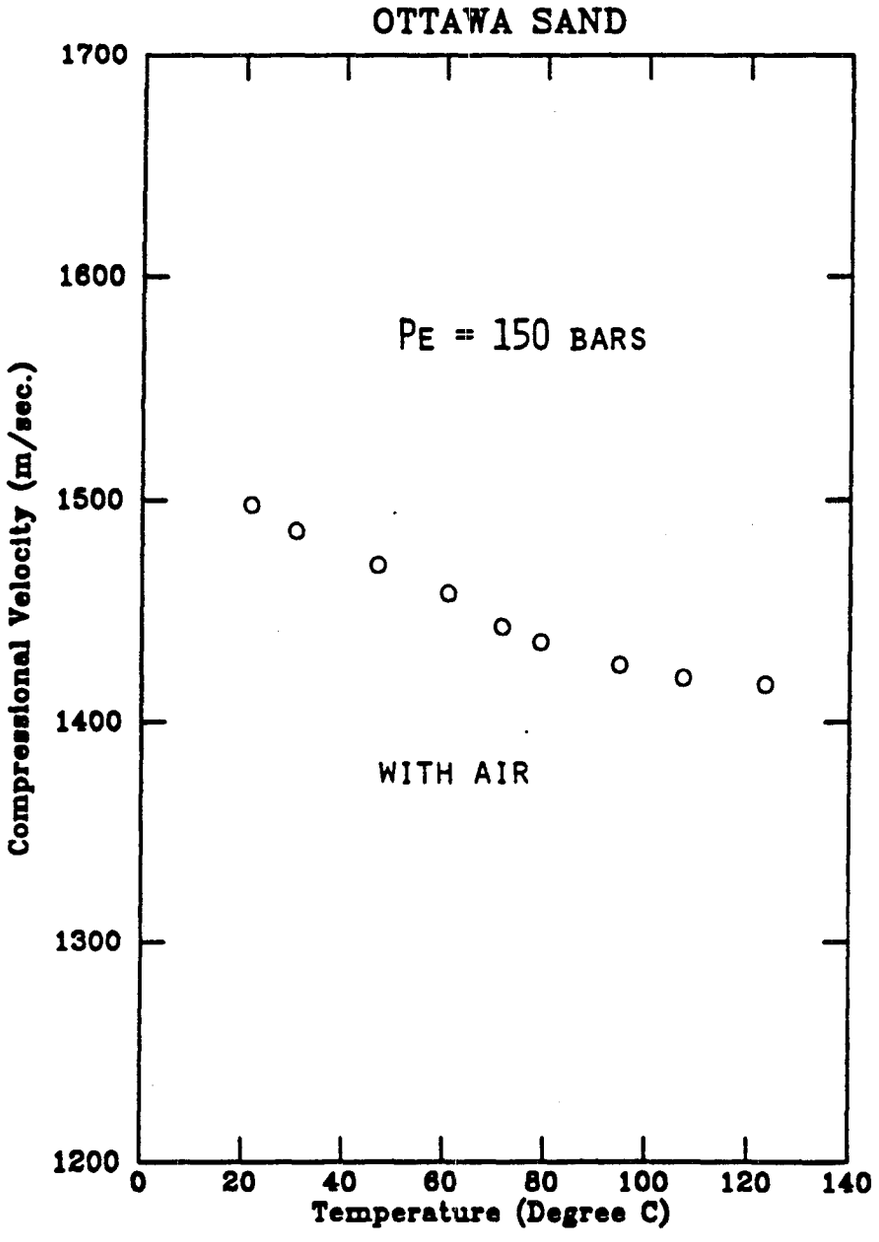
OTTAWA SAND
1700
1600
1500
1400
1300
1200
Compressional Velocity (m/sec.)
PE = 150 BARS
WITH AIR
0
20
40
60
80
100
120
140
Temperature (Degree C)

Fig. 6

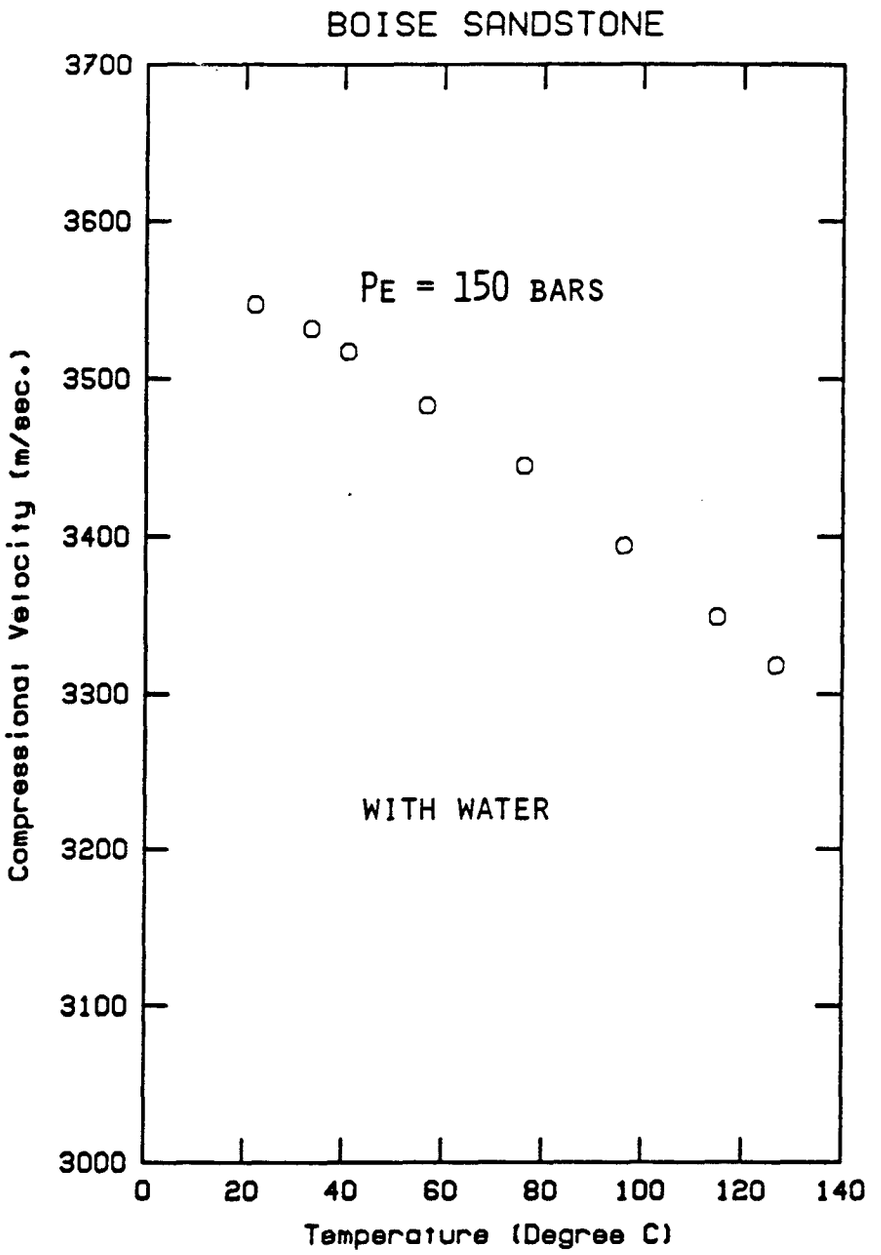
BOISE SANDSTONE
PE = 150 BARS
WITH WATER
Compressional Velocity (m/sec.)
3700
3600
3500
3400
3300
3200
3100
3000
0
20
40
60
80
100
120
140
Temperature (Degree C)

Fig. 7a

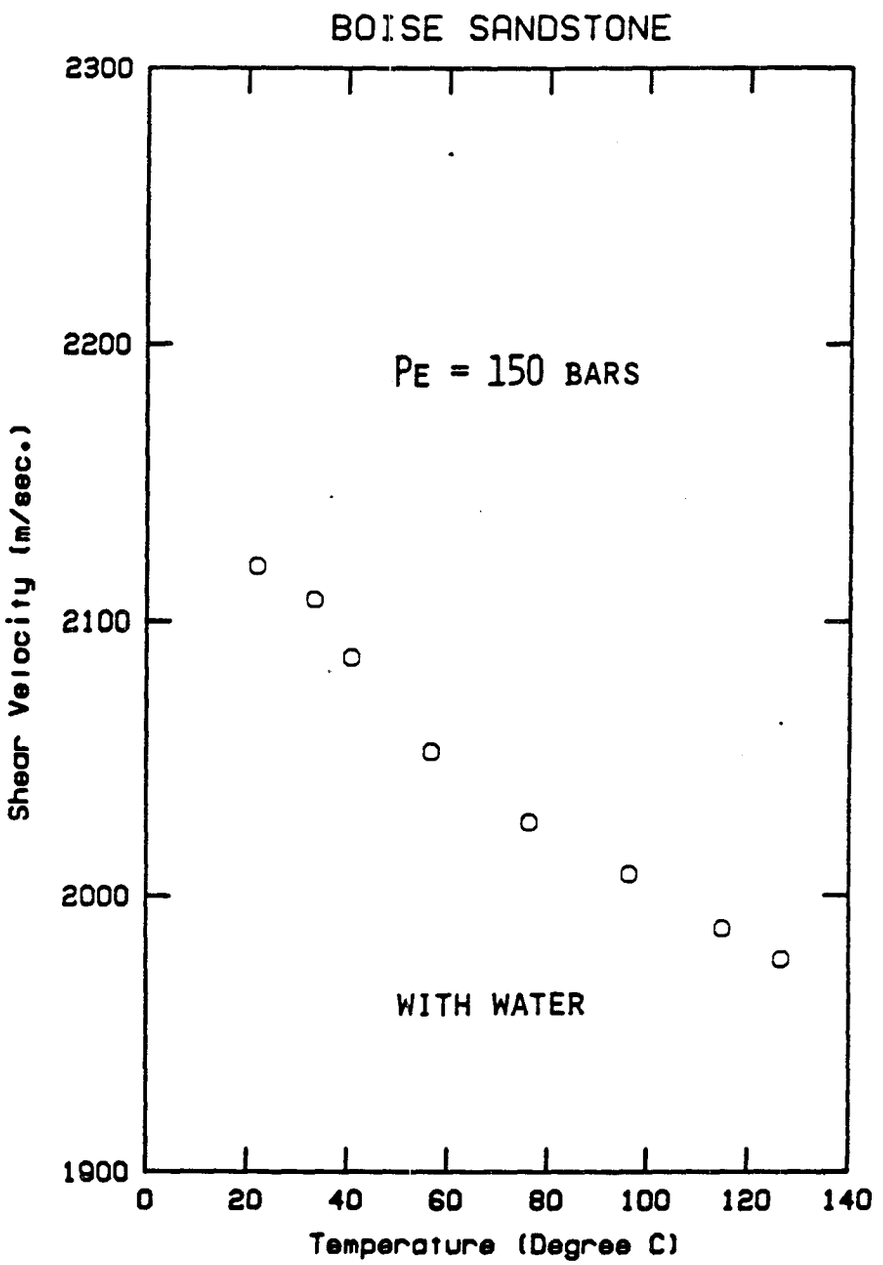
BOISE SANDSTONE
2300
2200
2100
2000
1900
Shear Velocity (m/sec.)
PE = 150 BARS
WITH WATER
0
20
40
60
80
100
120
140
Temperature (Degree C)

Fig. 7b

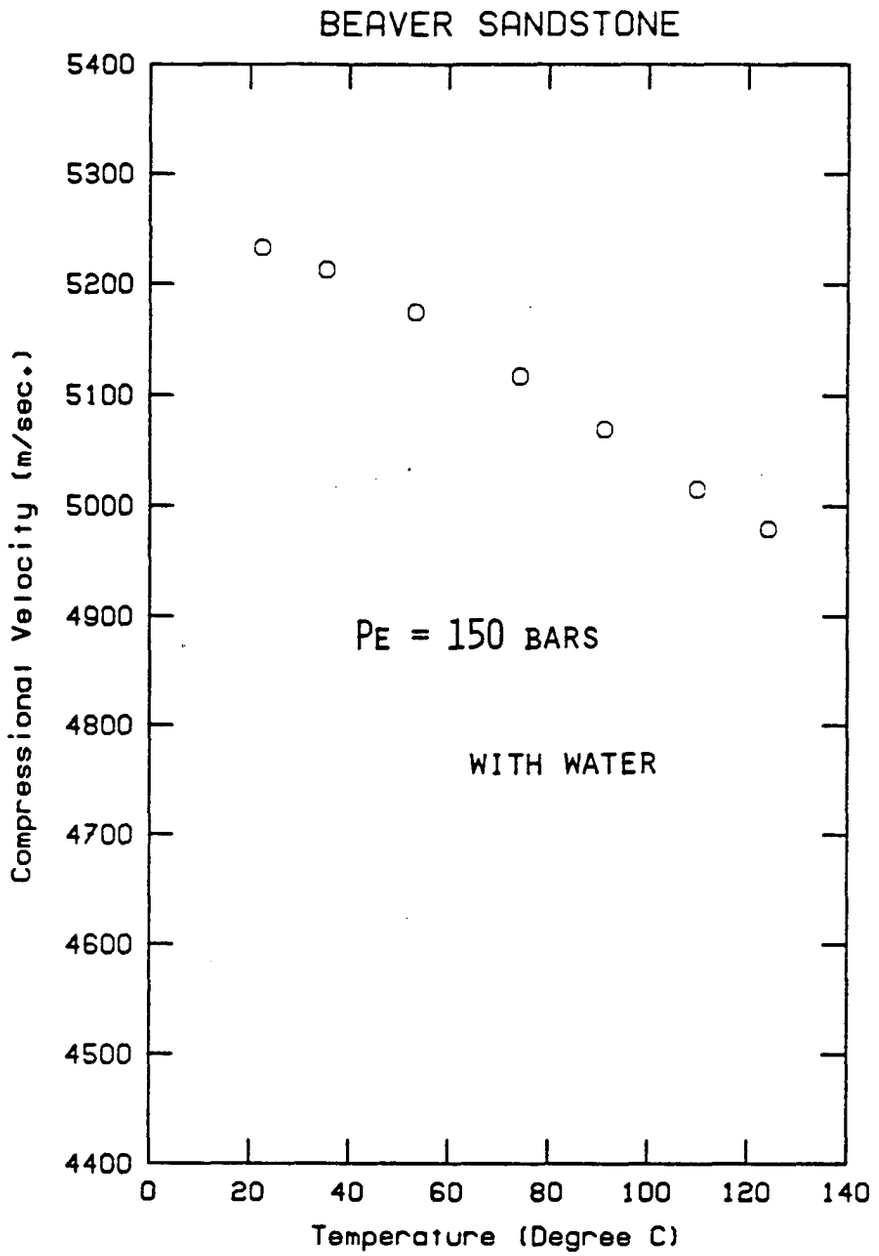
BEAVER SANDSTONE
5400
5300
5200
5100
5000
4900
4800
4700
4600
4500
4400
Compressional Velocity (m/sec.)
PE = 150 BARS
WITH WATER
0
20
40
60
80
100
120
140
Temperature (Degree C)

Fig. 8a

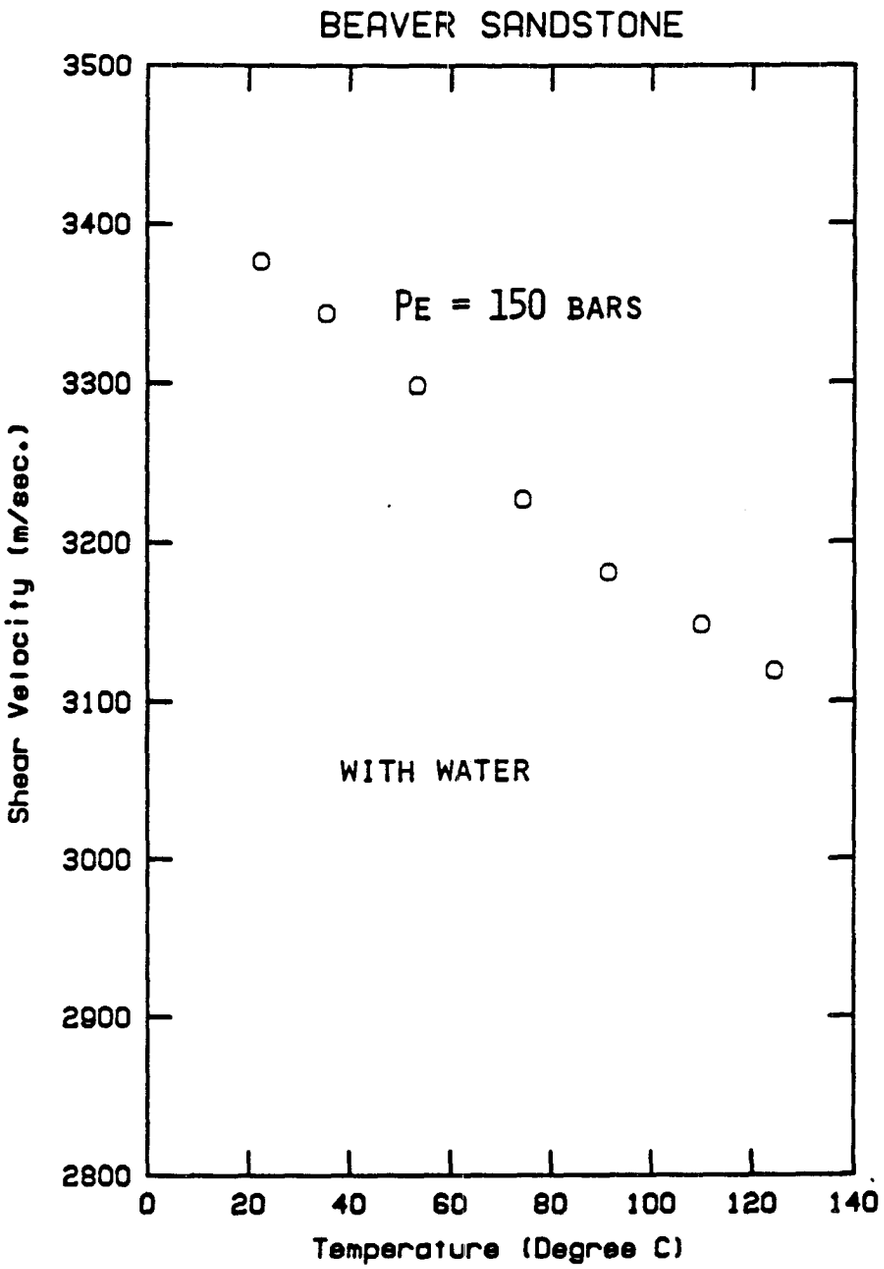
BEAVER SANDSTONE
3500
3400
3300
3200
3100
3000
2900
2800
Shear Velocity (m/sec.)
PE = 150 BARS
WITH WATER
0
20
40
60
80
100
120
140
Temperature (Degree C)

Fig. 8b

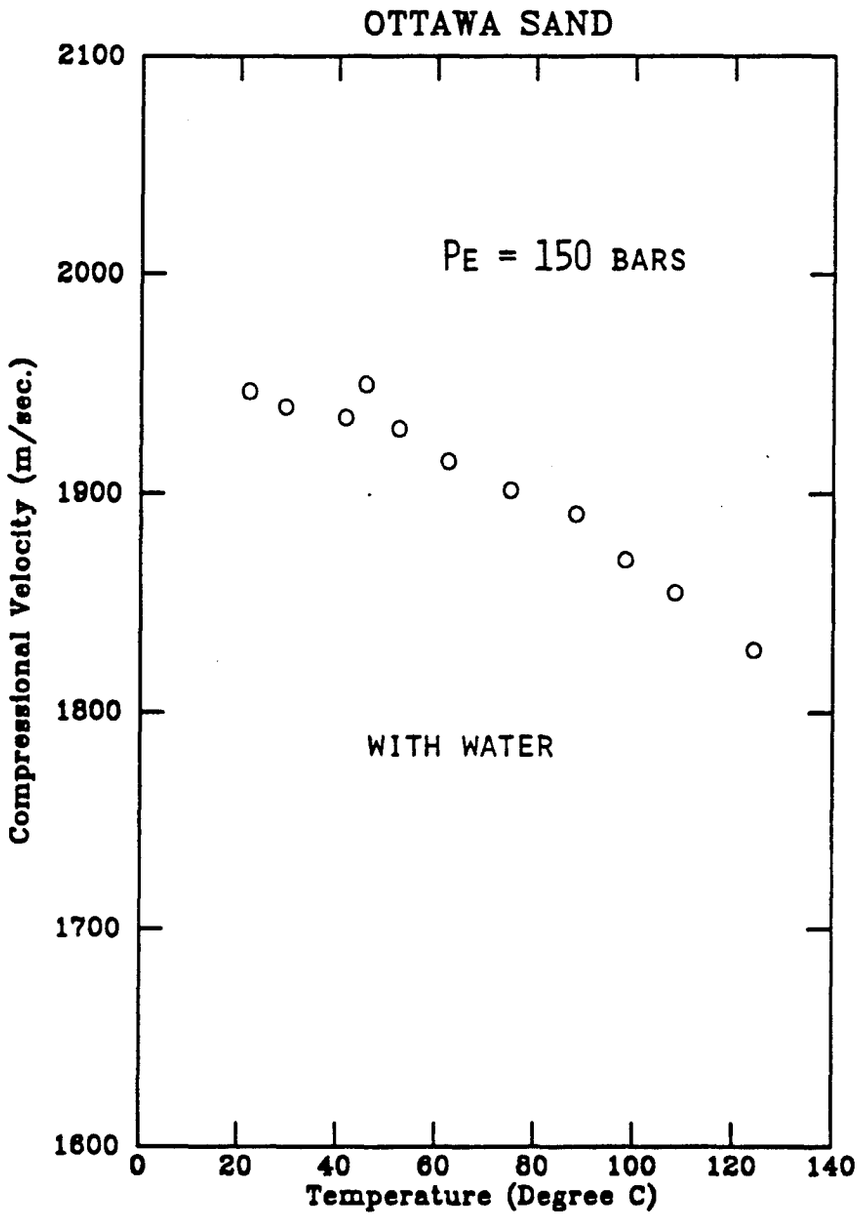
OTTAWA SAND
2100
2000
1900
1800
1700
1600
Compressional Velocity (m/sec.)
PE = 150 BARS
WITH WATER
0
20
40
60
80
100
120
140
Temperature (Degree C)

Fig. 9

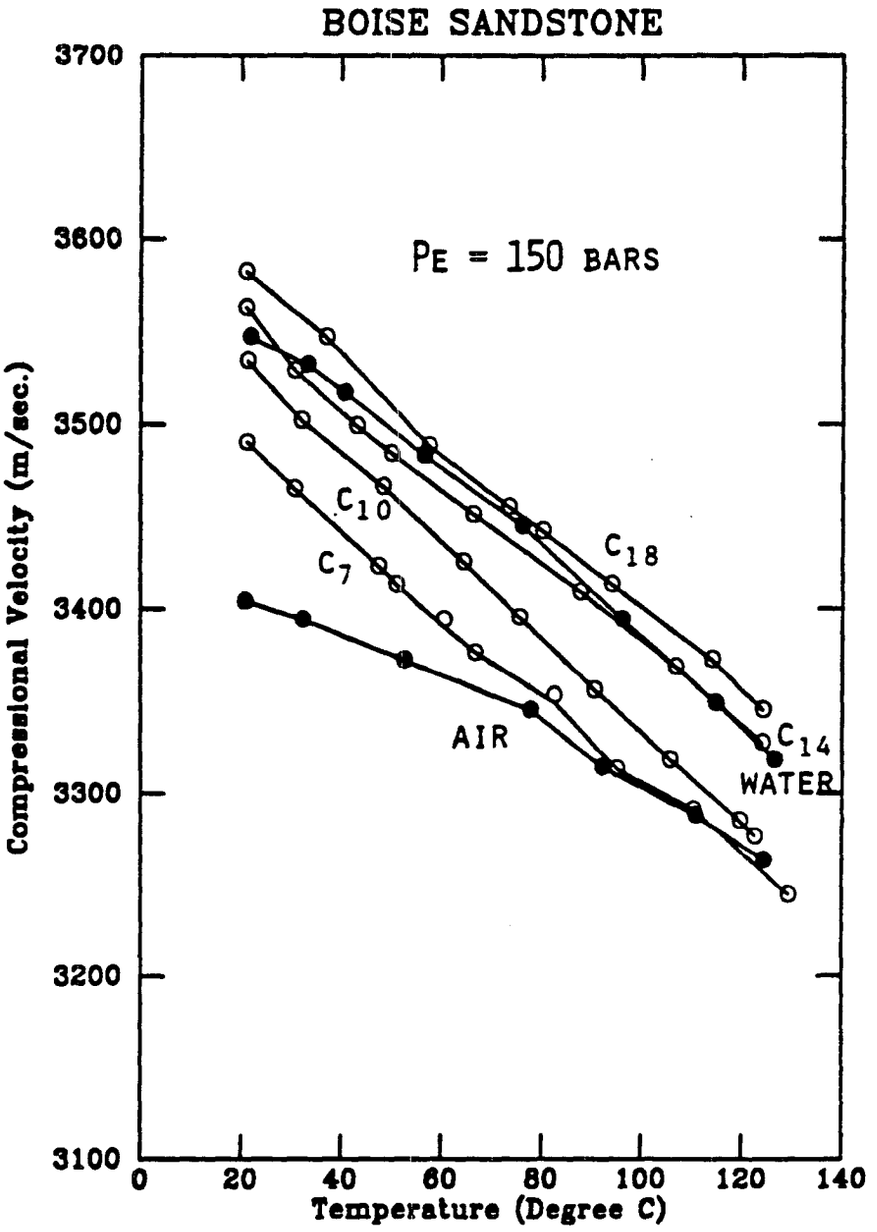
BOISE SANDSTONE
PE = 150 BARS
C18
C10
C7
C14
WATER
AIR
Compressional Velocity (m/sec.)
Temperature (Degree C)
3700
3600
3500
3400
3300
3200
3100
0
20
40
60
80
100
120
140

Fig. 10a

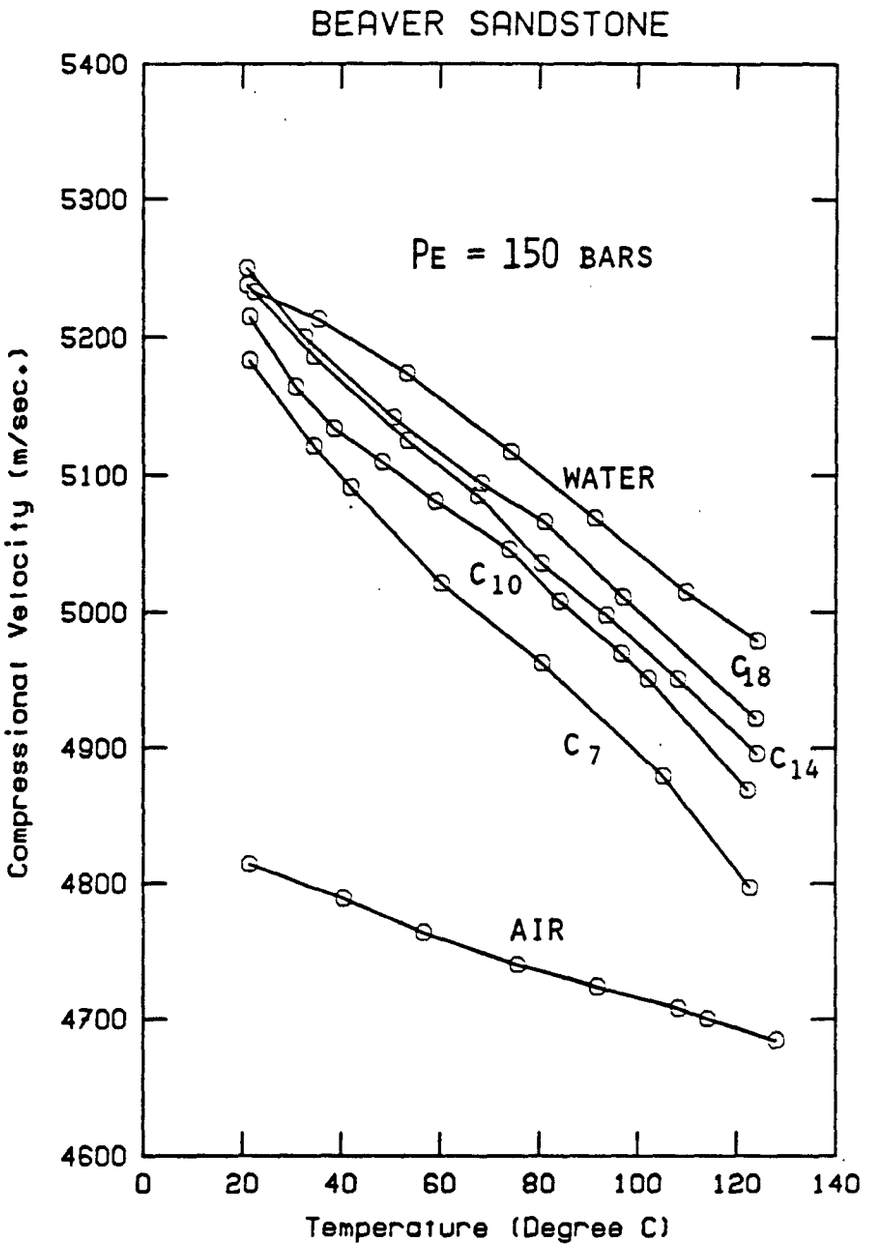
BEAVER SANDSTONE
PE = 150 BARS
WATER
C10
C18
C14
C7
AIR
Compressional Velocity (m/sec.)
Temperature (Degree C)
5400
5300
5200
5100
5000
4900
4800
4700
4600
0
20
40
60
80
100
120
140

Fig. 10b

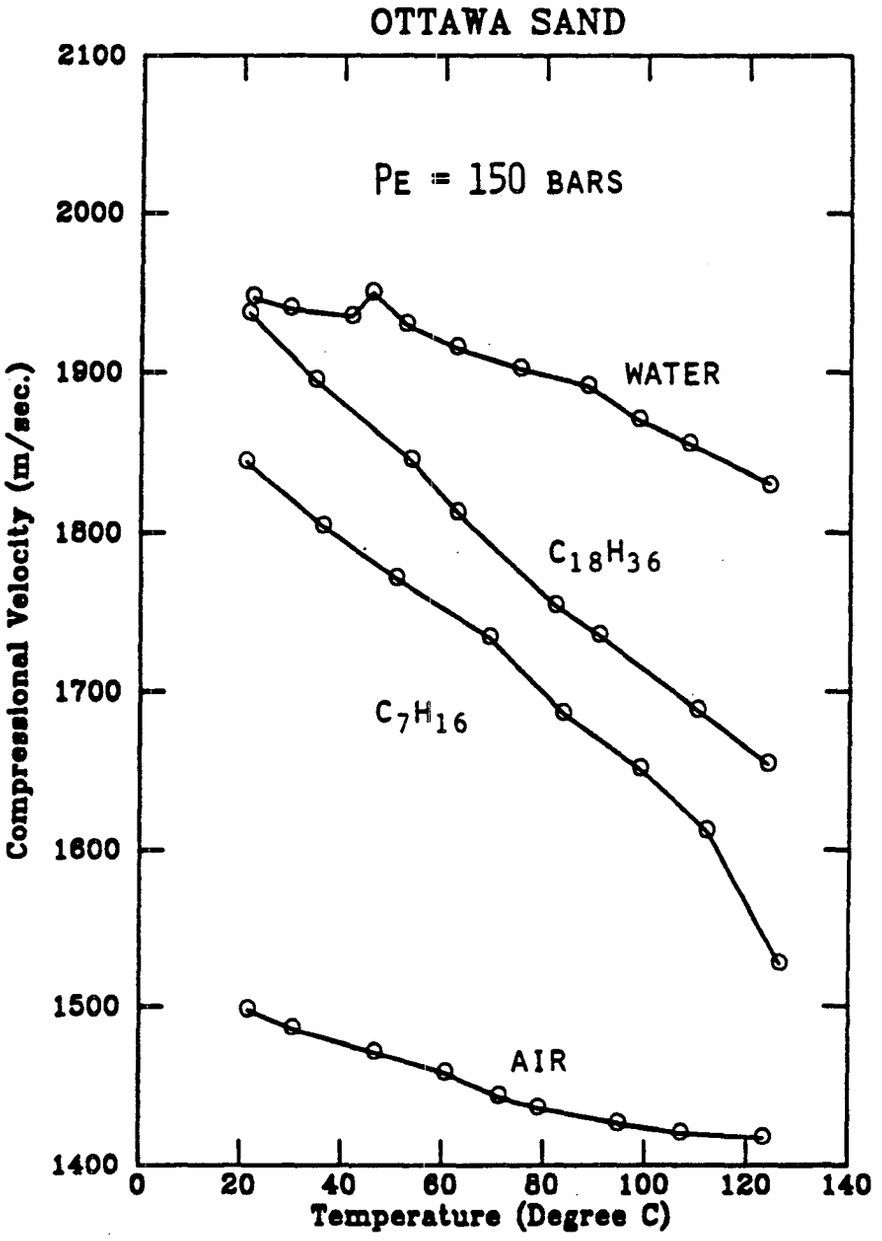
OTTAWA SAND
PE = 150 BARS
WATER
$C_{18}H_{36}$
C_7H_{16}
AIR
Compressional Velocity (m/sec.)
Temperature (Degree C)
2100
2000
1900
1800
1700
1600
1500
1400
0
20
40
60
80
100
120
140

Fig. 11

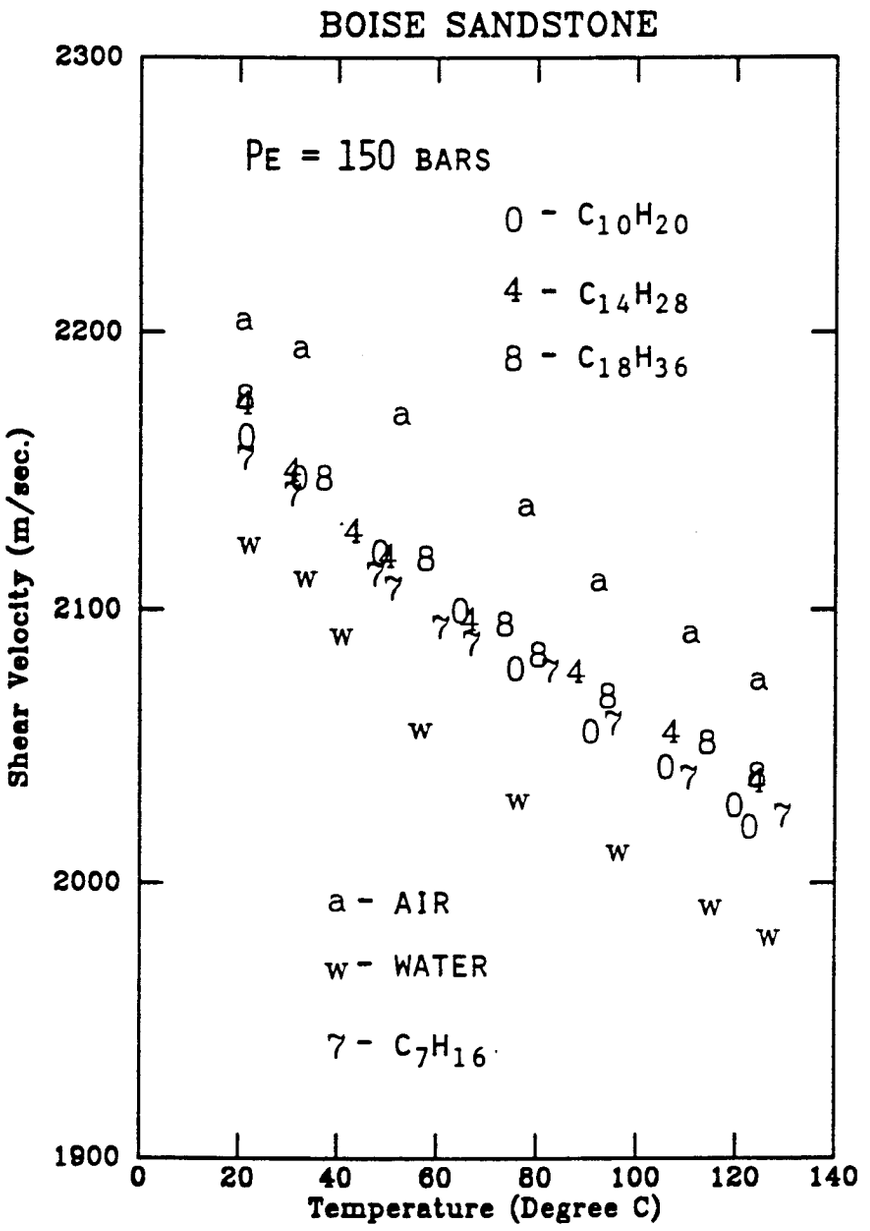
BOISE SANDSTONE
PE = 150 BARS
0 - C10H20
4 - C14H28
8 - C18H36
a - AIR
w - WATER
7 - C7H16
Shear Velocity (m/sec.)
Temperature (Degree C)
2300
2200
2100
2000
1900
0
20
40
60
80
100
120
140

Fig. 12a

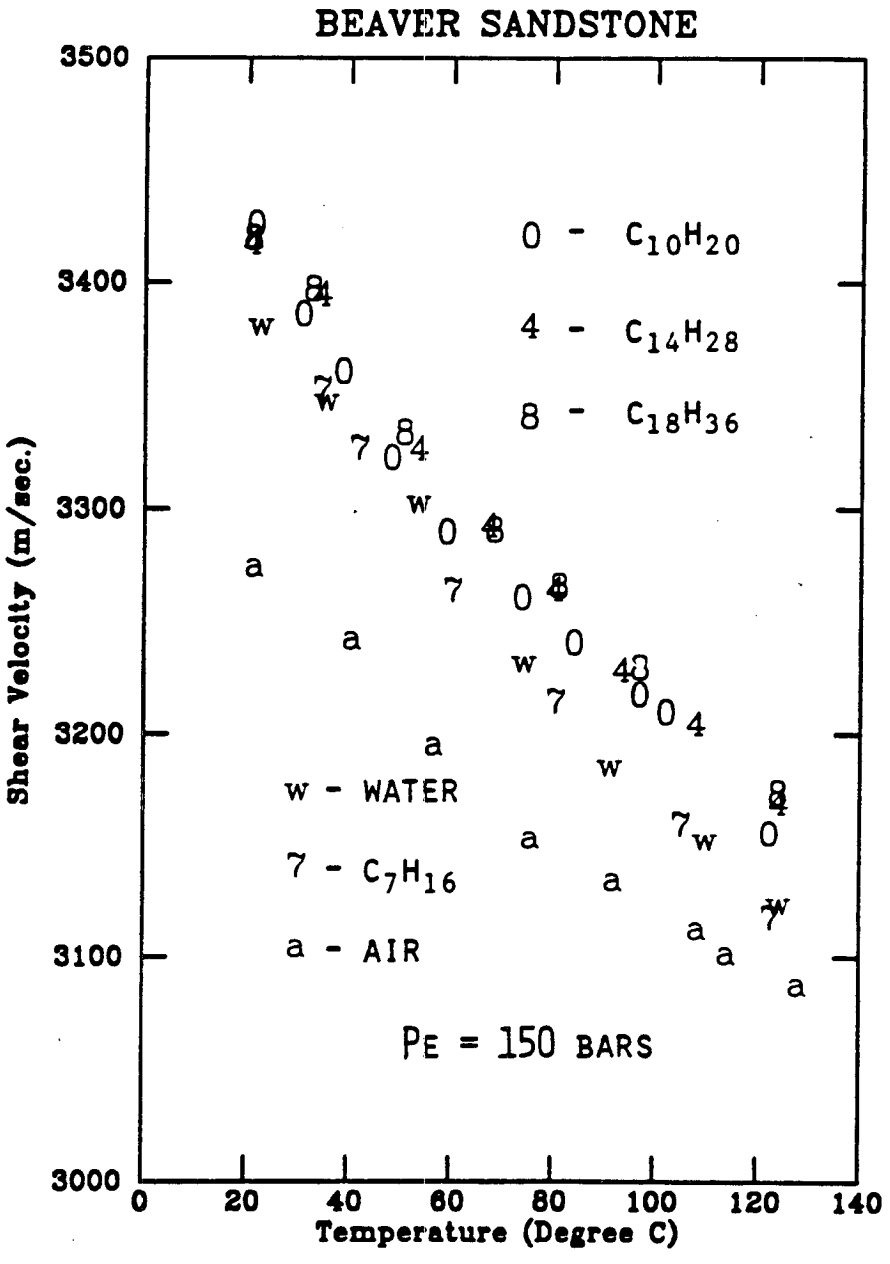
BEAVER SANDSTONE
Shear Velocity (m/sec.)
3500
3400
3300
3200
3100
3000
0
20
40
60
80
100
120
140
Temperature (Degree C)
0 - $C_{10}H_{20}$
4 - $C_{14}H_{28}$
8 - $C_{18}H_{36}$
w - WATER
7 - C_7H_{16}
a - AIR
PE = 150 BARS

Fig. 12b

CHAPTER 5

VELOCITIES IN HEAVY HYDROCARBON SATURATED ROCKS

ABSTRACT

Wave velocities in sandstones and unconsolidated sands saturated with heavy hydrocarbons were measured in the laboratory as a function of temperature and pressure. For the purpose of comparison, wave velocities in the heavy hydrocarbons were also measured versus temperature. It was found that increasing temperature dramatically decreased the velocities both in the heavy hydrocarbons and in the hydrocarbon-saturated rocks. Such decrease ranges from 15 to even 50% over the temperature interval from 22 to 122° C. In contrast, velocities in water- or air-saturated rocks are much less sensitive to the temperature changes.

The main causes for the large decrease of wave velocities in the heavy hydrocarbon saturated rocks are the melting of the solid or semi-solid hydrocarbons and the pore pressure generated by the thermal volume expansion of the heavy hydrocarbons. High pore pressure effect on the compressional wave velocities is particularly large in the tar-sand and heavy oil-sand, since it intends to push the sand grains apart. In the tar-sands, increasing the tar content in the interval of 10 to 20 percent (by weight) does not affect the compressional wave velocities much.

The compressional wave velocity decreases in the heavy hydrocarbon-saturated rocks as temperature increases provides a seismic thermometer, which makes it possible to use seismic methods to detect steam or fire fronts in heavy hydrocarbon reservoirs undergoing steam flooding or in-situ combustion processes.

INTRODUCTION

Velocities of acoustic waves traveling in rocks and unconsolidated sands have been a subject which interests many of investigators. As is known, acoustic wave velocities in porous rocks and unconsolidated sands are functions of many factors, such as porosity, confining and pore pressures, saturation, temperature, and etc.. Generally, the effect of temperature is small on wave velocities in dry rocks and considered to be of second order (Timur, 1977). However, laboratory measurements by Hughes and coworkers have shown that wave velocities in dry rocks can decrease by 10% or more as temperature increases by 100° *C* (Hughes and Cross, 1951; Hughes and Maurette, 1957). Similarly, Mobarak and Somerton (1971) reported a 10% decrease of the compressional wave velocities in sandstones saturated with silicone oils, corresponding to 100° *C* temperature increase.

Seismic wave velocities play important roles in geophysical explorations for hydrocarbon resources and in the assessment of hydrocarbon productions. In petroleum engineering, enhenced oil recovery (EOR) methods for hydrocarbons have been widely used, especially the steam flooding and in-situ combustion (fire flooding) methods. The injected hot steam or the burned in-situ oil greatly increases the reservoir temperature. Thus, seismic methods can be used in detecting the steam or combustion front, mapping the flooded zones, and continuously monitoring the thermal EOR processes, if the seismic wave velocities are affected by such temperature increase. Therefore, the effect of temperature on velocities in rocks saturated with heavy hydrocarbons is undoubtedly in demand.

In the recent studies of Tosaya *et al.* (1984) and Nur *et al.* (1984) it was discovered that heavy oil and tar sands experienced large (up to 60%) velocity decreases as temperature increased from to 25 to 150° *C* (figures 1 and 2). The magnitude of the velocity decrease, reported for heavy oil and tar sand samples from Venezuela, Canada and California, appeared to be primarily related to the presence

and concentration of the heavy hydrocarbons in the sands. In contrast, the velocities are insensitive to temperature changes in water- or gas-saturated sands.

In our investigations, we measured wave velocities in four heavy hydrocarbons and the heavy hydrocarbon-saturated Massillon light and Boise sandstones and the Ottawa unconsolidated sand. For the purpose of comparison, wave velocities in the air- and water-saturated sandstones and sand were also measured. The experimental results show that compressional wave velocities in both the hydrocarbons and hydrocarbon-saturated rocks decrease very rapidly as temperature increases. These rapid decreases, along with the effects of phase transition of the solid hydrocarbons and high pore pressure, are discussed in this chapter.

The fast decreases of the compressional wave velocities in the heavy hydrocarbon-saturated rocks and sand as temperature increases make it possible to use seismic methods to track the heat fronts, to map the heated zones, and to continuously monitor thermal EOR processes in heavy hydrocarbon reservoirs subject steam or fire floodings. A brief discussion on the applications of the experimental results is presented.

EXPERIMENTS

Apparatus and measurements

The apparatus employed in the experiments for rocks is an ultrasonic pulse transmission system which consists of an electronical package and a mechanical subsystem (fig. 2). A prepared sample, jacketed with a high-temperature plastic tube and coupled with two acoustic transducers, was sealed in a pressure vessel. A pulse generated by the pulse generator in the electronical package was sent through the sample by one transducer and picked up by the other. The travel time of the pulse through the sample was then measured on an oscilloscope by a digital electronic microprocessor.

Once the jacketed sample, coupled with the transducers, was sealed into the pressure vessel, it was evacuated by a vacuum pump connected to the pore pressure tubings. The confining pressure was raised to 200 *bars* (20 *MPa*, or 2900 psi) by pumping hydraulic fluid (confining medium) into the pressure vessel. The saturating fluid was injected into the sample by the pore pressure intensifiers. When the sample was completely saturated, the two pore pressure gauges connected to the two ends of the sample showed the same readings.

The temperature in the pressure vessel was increased by an electrical heater attached inside the vessel measured by a thermal couple with a digital thermometer. In all the experiments, once a temperature point was reached, we waited for at least 45 minutes at this point before taking measurement to assure that thermal equilibrium was established inside the vessel.

The device for measuring velocities in the heavy hydrocarbons (pore saturants) is similar to that discussed above, except that two immersion transducers were used. The hydrocarbon to be measured was filled in a container attached with the transducers. The container was surrounded by an electrical heating tape for increasing the temperature of the hydrocarbon. The temperature was also measured by a thermal couple with a digital thermometer. And the travel time of a pulse in the hydrocarbon was also measured on an oscilloscope by a digital microprocessor. The confining pressure to the hydrocarbon was 1 atmosphere (room pressure).

The compressional wave velocities traveling through a rock or a hydrocarbon sample was calculated by

$$V_p = \frac{L}{\Delta t_p},$$

and the shear wave velocities in a rock sample was calculated by

$$V_s = \frac{L}{\Delta t_s},$$

where L is the sample length and Δt the travel time. s and p represent shear and compressional waves, respectively.

Properties of the heavy hydrocarbons

In the experiments, we selected four different heavy hydrocarbons as the pore saturants. For the purpose of comparison, air and water were also used as pore fluids in the experiments. The properties of the heavy hydrocarbons are described in the following.

The parowax used in the experiments is solid at room condition and has a crystal structure. Its properties are listed below:

Major composition: $C_{18}H_{38}$ to $C_{30}H_{62}$ (normal paraffins),

Density at $22^{\circ}\,C$: 0.89 g/cm^3,

Melting temperature at room pressure: 45–65$^{\circ}\,C$.

The 1-eicosene (abbreviated as eicosene in the following text) has similar properties as the parowax. It is also solid at room condition and has also a crystal structure. However, unlike the parowax, eicosene is a pure material which belongs to the alkene family of hydrocarbons. Its chemical formula is $CH_3(CH_2)_{17}CH{=}CH_2$, its density at $70^{\circ}\,C$ is 0.76 g/cm^3, and its melting temperature at room pressure ranges from 27 to $29^{\circ}\,C$.

The heavy crude oil used in the experiments is obtained from a steam flooding pilot. It is a waxy heavy oil with gravity of 22° API (its density is 0.92 g/cm^3 at standard condition ($15.6^{\circ}\,C$ and 1 atmosphere)). Its pour point is about $4.4^{\circ}\,C$. It is composed of light to very heavy hydrocarbons. Figure 4 shows the viscosity of the crude we measured as a function of temperature . At $22^{\circ}\,C$, the viscosity is about 46,000 cp (46 $Pa.s$) and decreases very rapidly as the temperature increases. However, when the crude is cooled from high temperature back to $22^{\circ}\,C$, the viscosity at this point is only about 900 cp (0.9 $Pa.s$): big viscosity hysteresis is found. The viscosity hysteresis may be caused by the thermal cracking of some of the heavy hydrocarbons so that the

bonding forces among the hydrocarbon molecules may be decreased by the high temperature process.

The tar is also from a steam flooding pilot in a tar-sand field. It is mainly composed of heavy hydrocarbons. Its density is about 0.98 g/cm^3 and pour point is higher than $22^\circ C$. Its viscosity is about 7.6×10^5 cp (760 $Pa.s$) at $22^\circ C$ and 1,200 cp (1.2 $Pa.s$) at $83^\circ C$.

Properties of the rocks

The rock samples are from a block of Massillon light sandstone and a block of Boise sandstone. The Massillon light sandstone is mainly composed of well-sorted medium-sized quartz grains cemented by quartz overgrowths, chert, clay and Fe oxides. Its porosity is about 22% and permeability 740 mD.

The Boise sandstone has porosity of about 27% and permeability of 902 mD. It has a high feldspar content (44%) and a relatively low quartz content (28%).

The Ottawa sand is unconsolidated and has porosity of 37% when well-packed at room conditions. The size of the sand grains is mainly concentrated in the diameter range of 0.2 to 0.4 mm.

Sample preparation and saturation

The rock samples of the same kind were drilled from the same block and the two ends of the samples were finely ground. They were then washed thoroughly by water and dried in a vacuum oven at $45^\circ C$ for 5 days. All the samples are 2.54 cm (1 $inch$) both in length and in diameter.

To saturate the rock samples with parowax and eicosene, we first melted the parowax and eicosene in containers in an oven by raising the temperature up to $70^\circ C$. The rock samples to be saturated were vacuum dried for two days at $60^\circ C$ before immersed into the melted, also evacuated, saturants. The samples were kept in the saturants for over 240 $hours$ (10 $days$) at a constant temperature of $70^\circ C$ and then

cooled down for measurements.

The procedures for saturating the unconsolidated Ottawa sand with the parowax or eicosene were similar to that for saturating the rocks. After the dried sand were poured into the melted parowax or eicosene, the containers were well shaken for 20 minutes to get good packing of the sand and evacuated to 10 *microns* of vacuum. Afterwards, the samples were kept in an oven for over 72 hours at 70° *C*. Then, the saturated sand were cooled down and made up to cylindrical samples of about 2.54 *cm* (1.0 *in.*) both in diameter and length. The parowax-saturated sand samples were found to be very rigid and well-consolidated, while those eicosene-saturated appeared less-consolidated.

Saturating the heavy crude or water to the rock or sand samples was done by injection. A jacketed sample was first sealed inside the pressure vessel, and the saturant was contained in the pore pressure intensifiers. After both the sample and saturant were evacuated, the saturant was injected into the sample. Measurements were taken about 24 hours after the saturation.

In making the tar-sand samples, the tar was heated to 85° *C* in an oven and then mixed with the well-dried Ottawa sand. The tar-sand mixture was well stirred and then made up to cylindrical samples with diameter and length both of 2.54 *cm* (1 *in.*).

Two types of tar-sand samples were made. One of which contains 10.7%, and the other contains 20%, tar by weight. The porosities of these two samples are 16% and 0.7%, respectively.

In the experiments, the prepared rock-parowax, rock-eicosene, sand-parowax, sand-eicosene, and tar-sand samples were jacketed with high-temperature plastic tubes and sealed inside the pressure vessel with a pair of acoustic transducers. Since the rocks and the sands were saturated with solids or semi-solids at room temperature, the pore pressure could not be controlled. All the confining pressures for the above experiments were at 150 *bars* (15 *MPa*, or 2175 psi). However, for the water- and heavy

crude-saturated samples, the pore pressure was fixed at 50 *bars* (5 *MPa* , or 725 psi) and the confining pressure at 200 *bars* (20 *MPa* , or 2900 psi).

RESULTS AND DISCUSSIONS

Wave velocities were measured as a function of temperature and pressure for samples of sandstones and unconsolidated sands with parowax, eicosene, tar, and heavy crude, as well as for the heavy hydrocarbons alone. For the purpose of comparison, velocities were also measured for the sandstone and sand samples with air and water.

Wave velocities in the heavy hydrocarbons

Figures 5 and 6 show the compressional wave velocities (Vp) in the parowax and eicosene, respectively, as a function of temperature. In figure 5, the velocity decreases rapidly in the temperature interval of 20 to 65° *C*, which is caused by the softening and melting of the parowax as temperature increases. After the parowax is completely melted, Vp decreases slowly as temperature further increases. In figure 6, Vp in eicosene is also found to decrease rapidly in the melting interval of the sample (27 to 29° *C*). Beyond the melting interval, Vp decreases approximately linearly with increasing temperature, with an approximate slope of -4 meters per second per centigrade.

The observed sharp decreases in the compressional wave velocities in the melting intervals of the parowax and eicosene are theoretically predicted by Vaisnys (1968). In a paper on the propagation of acoustic waves through a system undergoing phase transformations, Vaisnys theoretically showed that as the temperature went across the phase boundaries of the system, sharp decreases in the velocities were expected. Knopoff (1959) showed experimentally that the compressional wave velocity decreased sharply in the melting interval of a two-component system.

Figure 5 and 6 show that temperature has large effects on the Vp in the parowax and eicosene, especially in their melting intervals. As temperature increases, these solid hydrocarbons are first softened and then melted. During this process, their moduli

(both bulk and shear, especially the shear moduli) decrease very rapidly. Such rapid modulus decreases in turn cause the Vp to decrease. As the solid hydrocarbons are completely melted, their shear moduli vanish and the compressional wave velocities are related only to the bulk moduli and densities. The velocities therefore decrease slower as temperature further increases.

The compressional wave velocities in the heavy crude and the tar are shown in figure 7. The compressional wave velocities also decrease with increasing temperature rapidly. The decreases are mainly caused by the increasing compressibility of, and the melting of the solid or semi-solid heavy hydrocarbons in, the crude and the tar, as temperature increases. In figure 7, the decrease of the compressional wave velocities in the heavy crude and the tar becomes slower at temperatures higher than $70^{\circ}\,C$ and $90^{\circ}\,C$, respectively, since most of the solid or semi-solid hydrocarbons are melted below these temperature points.

Wave velocities in the air-saturated rocks

Figures 8 and 9 show the compressional and shear wave velocities in the Massillon light sandstone and the Boise sandstone, respectively, with air in the pores. Vp in the Massillon light sandstone sample decreases by 4.6% and Vs by 4.5% (fig. 8), while Vp and Vs in the Boise sandstone sample decrease by 7.5% and 4.8%, respectively (fig. 9), as temperature increases from 20 to $120^{\circ}\,C$. These decreases are caused by the weakening of the rock frame and cements, and as well as the slight increase in the rock porosity due to different thermal expansions of the constituent minerals (Kern, 1982).

The compressional wave velocity in the Ottawa sand with air is shown in figure 10. The shear wave velocity in the sand could not be determined in the experiments. In figure 10, the Vp decreases by about 4.7% as temperature increases from 20 to $125^{\circ}\,C$. This decrease may also be caused by the thermal weakening of the sand grains.

The results shown in figures 8, 9, and 10 show that increasing temperature decreases the velocities in both the rocks and the sand with air. However, this temperature effect is not significant compared with the results shown in the following.

Wave velocities in rocks with parowax and eicosene

Wave velocities in the Massillon light sandstone and in the Ottawa unconsolidated sand with the parowax and eicosene, respectively, were measured in the experiments. For the purpose of comparison, velocities in the same sandstone and sand saturated with water were also measured. The results are shown in figures 11 to 16.

The compressional and shear wave velocities in Massillon light sandstone with parowax and water are shown in figures 11 and 12, respectively. Both Vp and Vs in the sandstone sample with parowax are much higher than those in the water-saturated sample in the temperature interval of 20 to 45° C. For example, at 22° C, the Vp and Vs in the water-saturated rock sample are 3418 and 2187 m/sec, respectively, while those in the parowax-saturated rock sample are 4028 and 2593 m/sec, respectively. The Vp increases by 17.9% and Vs by 18.6%, as the pore water is replaced by the parowax. These large increases are apparently caused by the large increases of the elastic moduli, especially the shear moduli, of the rocks. Since shear waves can not propagate in liquids, water saturation has very little effect on the shear moduli of rocks. However, the parowax is solid in the temperature interval of 20 to 45° C. Therefore the shear modulus of the rock with the solid parowax is much higher than that with water, which in turn increases both the compressional and shear wave velocities in the rock.

Another way to interpret the phenomenon in figure 11 which shows that the Vp in the parowax-saturated rock sample is higher than that in the sample with water in the temperature interval of 20 to 45° C is that the Vp in the parowax is higher than that in water in the same temperature range. For example, Vp in water is 1496 m/sec, while that in the parowax is 2010 m/sec, at 22° C. According to the Gassmann relation (Gassmann, 1951), Vp in a porous material with pore saturant of higher velocity is

also higher (Wyllie *et al.*, 1956; White, 1965). The Vp in the rock sample with parowax therefore should be higher than that in the water-saturated sample in the temperature interval of 20 to 45° *C*.

As the parowax in the rock pores is completely melted at temperatures higher than 65° *C*, both Vp and Vs in the rock sample with parowax are decreased. The decrease in the Vp is mainly caused by the lowered Vp in the parowax itself. As shown in figure 5, the Vp in the parowax is 1238 *m/sec* at 70° *C* which is lower than that in water at the same temperature. Therefore, the Vp in the parowax-saturated Massillon light sandstone sample is lower than that in the same sample with water at temperatures higher than 65° *C*.

Comparing figure 11 with figure 5, the two Vp curves have similar shape. This also shows that the decreases of Vp in the rock with parowax are mainly caused by the decreases of Vp in the parowax itself.

As the parowax in the rock pores becomes to liquid at temperatures higher than 65° *C*, the Vs in the rock sample with parowax becomes close to that in the sample with water. This comes from the fact that both the liquid parowax and water can not support shear stresses and therefore changing the pore fluid of the rocks does not affect the shear moduli of the rocks much (Murphy, 1982; King, 1966).

The compressional wave velocity in the sand-parowax sample, along with those in the same sample saturated with water and air, are shown in figure 13. As noticed during preparing the sand-parowax samples, the sand samples are very rigid at the room temperature when saturated with the parowax. Therefore the observed Vp in the sand-parowax sample at room temperature is much higher than that in the same sand saturated with either water or air (fig. 13). As the temperature increases from 20 to 65° *C*, the Vp in the sand-parowax sample decreases very fast due to the softening and melting of the parowax. In this temperature range, all the interpretations to the compressional wave velocity in the Massillon light sandstone with the parowax also

apply to that in the sand-parowax sample.

After the parowax in the sand sample is completely melted, the Vp decreases slowly as temperature increases. However, at temperatures higher than 100° C, the Vp is even lower than that in the dry sand. This situation is believed to be caused by the high pore pressure of the sand. As temperature increases, the parowax in the sand pores is melted, the thermal volume expansion of the parowax causes the pore pressure of the sand to increase. At higher temperatures, the pore pressure may be close to the confining pressure which is 150 *bars*. This pore pressure causes the Vp in the sand-parowax sample to decrease very rapidly. Since the high pore pressure intends to push the sand grains apart, the sand grains may become more or less suspended in the liquid parowax at high temperatures.

The high pore pressure can also occur in the rock-parowax measurements. However, unlike the unconsolidated sands, rocks are well-consolidated and hence the high pore pressure generated by the thermal volume expansion of the parowax can not push the rock grains apart.

The compressional and shear wave velocities in the Massillon light sandstone saturated with eicosene, along with those in the same rock saturated with water, are shown in figures 14 and 15, respectively. The Vp in the rock sample with eicosene decreases by 14.7% and the Vs by 13.4% as temperature increase from 22 to 122° C.

Both Vp and Vs shown in figures 14 and 15 decrease sharply as the melting interval of the eicosene in the rock pores is crossed. These results can be explained similar to those in parowax saturated sandstone samples.

Figure 16 shows the compressional wave velocities as a function of temperature in the Ottawa sand with eicosene, water, and air, respectively. Like that in the sand-parowax sample, the Vp in the sand with eicosene also decreases rapidly in the melting temperature interval of the eicosene. However, before the melting interval of the eicosene is reached, the Vp in the sand with eicosene is much lower than that in the

sand with parowax. This is apparently caused by the lower Vp in the eicosene.

At temperatures higher than $45^{\circ}C$, the compressional wave velocity in the sand with eicosene is lower than that in the air-saturated sand sample. As explained in the sand-parowax situation, this phenomenon is also caused by the high pore pressure due to the thermal expansion of the eicosene which intends to push the sand grains apart.

In figures 12 and 15, at temperatures beyond which the pore hydrocarbons are completely melted, the shear wave velocities in the rock samples with the parowax and eicosene are higher than those in the rock samples with water, although the difference is not significant. This phenomenon is probably caused by the viscous relaxation effect of the hydrocarbons and the density effect. According to the viscous relaxation theory, shear waves can exist in a viscous fluid by penetrating in the fluid to a certain depth which, as well as the shear wave velocity, is proportional to the square root of the viscosity (Thurston, 1964). The viscosities of the melted parowax and eicosene are about 7 times of that of water. Therefore the shear waves may penetrate through the liquid hydrocarbons in the thin cracks of the rocks, which causes the shear wave velocity in the rocks to increase slightly (Wang and Nur, 1985). Moreover, the densities of the melted parowax and eicosene are lower than that of water, which is also responsible for the slightly higher shear wave velocities in rocks with the hydrocarbons.

In summary, we see that replacing the pore fluid by the solid hydrocarbons in the rocks and sands increases both the compressional and shear wave velocities, since the solid pore saturants increase both the bulk and shear moduli of the rocks and sands dramatically. Upon the melting of the pore saturants as temperature increases, both Vp and Vs in the saturated rocks and sands decrease rapidly. Beyond the temperatures at which the pore saturants are completely melted, the velocities are less sensitive to the temperature changes. The high pore pressure in the saturated sands intends to push the sand grains apart and therefore decreases the compressional velocities.

Wave velocities in rocks with the heavy crude and tar

Shown in figures 17-20 are the compressional wave velocities measured in the Massillon light and Boise sandstone samples with the heavy crude at confining pressure of 200 *bars* and pore pressure of 50 *bars*. In figure 17, the Vp in the heavy crude-saturated Massillon light sandstone sample is slightly higher than that in the water-saturated sample at 22° *C*, because the Vp in the heavy crude is slightly higher at the same temperature. As the temperature increases up to 130° *C*, Vp in the heavy crude-saturated Massillon light sandstone decreases rapidly, while that in the water-saturated sample decreases slowly. The rapid decrease of the Vp is apparently caused by the rapid Vp decrease in the crude itself. At higher temperatures, the solid or semi-solid hydrocarbons in the crude are melted and hence the compressibility of the crude is increased, which in turn causes the Vp in the rock with the crude to decrease.

In figure 18, the two shear wave velocity curves measured from the heavy crude- and the water-saturated Massillon light sandstone samples are nearly parallel. As observed in the parowax- or eicosene-saturated samples, the Vs in the heavy crude-saturated rock is slightly higher than that in the water-saturated sample due to the higher viscosity and lower density of the crude. However, the difference between the two curves is very small (about 1.2%), which again shows that changing the liquid pore saturant of a rock does not change the shear modulus much.

Both Vp and Vs in the Boise sandstone saturated with the heavy crude, along with those in the same sandstone with water, were also measured (figs. 19, 20). The experimental results are similar to those from the Massillon light sandstone. In figure 19, the Vp in the heavy crude-saturated rock is much lower than that in the water-saturated sample at temperatures higher than 40° *C*. In figure 20, the two shear wave velocity curves for the heavy crude-saturated and the water-saturated Boise sandstone samples are nearly overlapped. There is almost no difference between the two shear wave velocities.

Figure 21 shows the compressional wave velocities in the Ottawa unconsolidated sand saturated with the heavy crude, water, and air, respectively. Like those in the sandstones saturated with the heavy crude, the Vp in the sand saturated with the crude is also affected by the melting of the solid or semi-solid heavy hydrocarbons.

The compressional wave velocities in the Ottawa sand mixed with 10.7% and 20% (by weight) tar, respectively, are shown in figure 22. They also decrease very rapidly as the temperature increases. These fast decreases of Vp are caused by both the fast Vp decrease in the tar itself and the high pore pressure created by the thermal volume expansion of the tar as the temperature increases. These two compressional wave velocity curves are very close to each other, which suggests that increasing the tar content of the unconsolidated sand in the interval of 10 to 20% does not affect the Vp much.

As mentioned earlier, the unconsolidated Ottawa sand sample still has porosity of 16% as it is mixed with 10.7% tar. When the pores of this sample are filled with water with controlled pore pressure, the compressional wave velocity increases (fig. 22). At temperatures below 70° C, the Vp in the sand-tar-water sample decreases also rapidly as the temperature increases. However, beyond this temperature point, the decrease with increasing temperature becomes slower. We interpret that in the sand mixed with different percentage of the tar, the decrease in the Vp at temperatures below 70° C is mainly caused by the Vp decrease of the tar caused by the melting of the solid or semi-solid hydrocarbons, and the high pore pressure caused by the thermal volume expansion of the tar at temperatures higher than 70° C also contributes to the Vp decrease.

In summary, we see that the compressional wave velocities in the sandstones and sand saturated with the heavy hydrocarbons are greatly affected by the temperature changes. Increase in temperature causes Vp to decrease, which is caused by the melting of the solid or semi-solid heavy hydrocarbons of the pore saturants and the high pore pressures. Large differences between the compressional wave velocities in the

hydrocarbon-saturated and the water-saturated sandstone or sand samples are found at high temperatures. In contrast, the shear wave velocities in the sandstones are less sensitive to the pore fluid changes.

APPLICATIONS

The experimental results show that the compressional wave velocities in both the sandstones and the unconsolidated sands with the heavy hydrocarbons decrease greatly as the temperature increases. Such rapid Vp decreases suggest that it be possible to use seismic methods to detect the heated zones of the sandstones or sands saturated with heavy hydrocarbons in thermal EOR processes. In this section, we first construct some idealized seismic stratigraphic models of heavy oil or tar-sand reservoirs using the compressional wave velocity data gathered from the experiments, and then discuss the properties of some synthetic seismograms obtained from these models.

Figure 23 shows an idealized sketch of a heavy oil-sand or a tar-sand reservoir sealed by shales undergoing steam floodings. Hot steam is injected into the injection well and increases the temperature of the reservoir. As the injection proceeds, the steam front moves toward the production well, and after some period of time, the displaced oil is produced at the production well.

Figure 24 shows an idealized stratigraphic model of a heavy oil-sand reservoir sealed by shales. The upper section of the reservoir is saturated with heavy oil with viscosity of 180 *cp* and density of 0.92 at the reservoir condition, and the lower section is saturated with water. The reservoir temperature before undergoing steam flooding is assumed to be $38^{\circ}C$, and to be $120^{\circ}C$ as the steam arrives. The compressional wave velocity in the sandstone of the uppermost section in figure 24 is taken as the value of the air-saturated Massillon light sandstone at $21^{\circ}C$, and that of the sealing shales is assumed according to the results of others (Tosaya, 1982; Jones, 1983). Both of these compressional wave velocities are also assumed to be not affected by the steam

injection. The compressional wave velocities in the sand saturated with heavy oil and water at temperatures of 38° C and 120° C are taken as those in the Ottawa sand with the heavy crude and water at these two temperature points, respectively.

A seismic pulse with an amplitude of 1 is sent downward to the reservoir and reflected back from the interfaces to the same point at the surface (vertical reflection). The reflection coefficients of the interfaces, both before and after the steam flooding, are shown in figure 25. The vertical axis in figure 25 represents the one-way travel time of the pulse, and the horizontal axis is the amplitude of the reflection coefficients.

Figure 26 shows the synthetic seismograms based on the model shown in figure 24. The vertical axis in this figure represents the two-way travel time, and the horizontal axis is the amplitude, of the pulse.

From figures 25 and 26, one can see that when the reservoir temperature increases from 38° C to 120° C as the steam arrives, the travel time of the pulse reflected from the interfaces of oil-sand--water-sand and water-sand--shale is delayed. The reflection coefficient and the wave pulse amplitude at the oil-sand--water-sand interface are both slightly increased. Both the travel time delay and the amplitude change are caused by the velocity changes. Therefore, one can tell from such surveys if the oil-sand in the reservoir has been steam flooded.

A similar idealized stratigraphic model of a tar-sand reservoir is constructed and shown in figure 27. The tar-sand reservoir temperature is assumed to be 21° C before steam injection and 120° C as the steam arrives. The compressional wave velocities in the tar-sand at these two temperature points are taken from those in the Ottawa sand saturated with 20% tar (by weight). The reflection coefficients of the interfaces and the synthetic seismograms obtained from this model are shown in figure 28 and 29, respectively.

In figure 28, the amplitude of the reflection coefficient at the tar-sand--water-sand interface is increased as the reservoir temperature is increased from 21 to 120° C by the

injected steam. Before the steam injection, the reflection coefficient at this interface is negative, while it becomes positive when the tar-sand is heated up by the hot steam. This polarity reverse is also found in the synthetic seismograms (fig. 29). The travel times of the pulses from the interfaces of the tar-sand--water-sand and the water-sand--shale are also found being delayed as the steam arrives.

The results in figures 23-29 show that it is possible to use seismic methods to detect the steam front and to map the flooded zones in the heavy oil and tar-sand reservoirs subject thermal floodings, since the arrival time of the reflected waves from the interfaces beneath the reservoir is delayed.

CONCLUSION

Wave velocities in four heavy hydrocarbons were measured as a function of temperature. Sharp velocity decreases were found as the parowax and eicosene were melted. The effect of the phase transition of the parowax and eicosene on the velocities is primarily caused by the changes of the compressibilities and the lost of the rigidity of the hydrocarbons. In the temperature range from $20^{\circ}C$ to the upper boundaries of the melting intervals of the hydrocarbons, the fast velocity decreases are caused by the softening and melting effects. The velocities in the tar and heavy crude decrease almost linearly as temperature increases, which is also caused by the increase of the compressibilities, as well as the melting of the solid or semi-solid heavy fractions.

Both the compressional wave velocities in the air-saturated sandstones and the unconsolidated sands decrease slowly with increasing temperatures. These decreases are mainly caused by the thermal weakening of the sand grains of the sandstones and the sands, as well as the slight increase in their porosities due to the thermal effects.

The solid hydrocarbons in the rocks and the sands increase both the compressional and shear wave velocities, which means that the solid hydrocarbons increase both the bulk and the shear moduli of rocks and the sands largely. As temperature

increases, the melting of the solid hydrocarbons in the pores decreases both the compressional and the shear wave velocities dramatically. The high pore pressure in the hydrocarbon-saturated sands intends to push the sand grains apart and therefore also decreases the compressional wave velocities.

The compressional wave velocities in the sandstones and sands saturated with the heavy crude and the tar decrease rapidly as temperature increases. Such Vp decreases are caused mainly by the melting of the heavy hydrocarbons and the high pore pressure created by the thermal volume expansion of the heavy hydrocarbons.

The experimental results show that it is possible to use seismic methods to detect the thermal front and the flooded zones in heavy oil- and tar-sand reservoirs subject thermal EOR processes.

REFERENCES

Dake, L. P., 1978; Fundamentals of reservoir engineering. Elsevier Sci. Pub. Co..

Domenico, S. N., 1976; Effect of brine-gas mixture on velocity in an unconsolidated sand reservoir. Geophysics, vol. 41, no. 5, pp. 882-894.

Interstate Oil Compact Commission, 1983; Improved oil recovery. Oklahoma.

Kern, H., 1982; Elastic-wave velocity in crustal and mantle rocks at high pressure and temperature: the role of the high-low quartz transition and of dehydration reactions. Phys. Earth Planet. Inter., vol. 29, pp. 12-23.

King, M. S., 1966; Wave velocities in rocks as a function of changes in overburden pressure and pore fluid saturants. Geophys., vol. 31, no. 1, pp. 50-73.

Kinghorn, R. R. F., 1983; An introduction to the physics and chemistry of petroleum. John Wiley & Sons.

Knopoff, L., 1959; Velocity of sound in two-component systems. J. Geophys. Res., vol. 64, no. 3, pp. 359-361.

Murphy, W. F., 1982; Effect of microstructure and pore fluids on the acoustic

properties of granular sedimentary materials. Ph.D thesis, Stanford Univ.. Stanford Rock Physics Project, vol. 16.

Nur, A, C. Tosaya and D. Vo-Thanh. Seismic monitoring of thermal enhenced oil recovery processes. Extended abstract, 1984 SEG meeting.

Thurston, R. N., 1964; Wave propagation in liquids. in: Physical Acoustics, vol. 1A, Ed. W. P. Mason. Academic Press, New York.

Tosaya, C. A., 1982; Acoustical properties of clay-bearing rocks. Ph.D thesis, Stanford Univ.. Stanford Rock Physics Project, vol. 15.

Tosaya, C., A. Nur, P. Aronstam. and G. Da Prat. Monitoring of thermal EOR fronts by seismic methods. SPE California regional meeting. pp. 12744. April, 1984.

Vaisnys, J. R., 1968; Propagation of acoustic waves through a system undergoing phase transformations. J. Geophys. Res., vol. 73, no. 24, pp. 7675-7683.

Wang, Z. and A. Nur, 1985; The effects of sample size on wave attenuations and velocities in the resonant bat technique. Stanford Rock Physics Project, vol. 25, pp. 331-367.

Wang, Z. and A. Nur, 1985; Effects of pore fluid viscosity on the acoustic wave velocities in porous rocks (abstract). Journal of Acoustic Society of America, vol. 78, suppl. 1, pp. p32-33.

White, J. E., 1965; Seismic radiation, transmission, and attenuation. McGraw Hill, New York. 302p.

Wyllie, M. R. J., A. R. Gregory, and L. W. Gardner, 1956; Elastic wave velocities in heterogeneous and porous media. Geophysics, vol. 21, pp. 41-70.

TABLE AND FIGURE CAPTIONS

Table 1. Selected data from the measurements -- compressional wave velocities in parowax, eicosene, tar, heavy crude, and sandstone and unconsolidated sands saturated with these heavy hydrocarbons, at 22° C and 122° C. Also shown are

the absolute and relative changes of the velocities in this temperature range.

Figure 1. Compressional wave velocities vs. temperature in Kern River oil sands (after Tosaya *et al.* , 1984).

Figure 2. Compressional wave velocities in Venezuelan oil sands as a function of temperature (after Tosaya *et al.* , 1984).

Figure 3. A sketch of the apparatus.

Figure 4. Logarithm of the viscosity and its hysteresis of the heavy crude as a function of temperature.

Figure 5. Compressional wave velocity in parowax as a function of temperature.

Figure 6. Compressional wave velocity in 1-eicosene as a function of temperature.

Figure 7. Compressional wave velocity in the heavy crude as a function of temperature.

Figure 8. Compressional and shear wave velocities in the air-saturated Massillon light sandstone as a function of temperature.

Figure 9. Compressional and shear wave velocities in the air-saturated Boise sandstone as a function of temperature.

Figure 10. Compressional wave velocity in the air-saturated Ottawa unconsolidated sand as a function of temperature.

Figure 11. Compressional wave velocities in Massillon light sandstone saturated with parowax and water as a function of temperature.

Figure 12. Shear wave velocities in Massillon light sandstone saturated with parowax and water as a function of temperature.

Figure 13. Compressional wave velocities in Ottawa unconsolidated sand saturated with parowax, water, and air as a function of temperature.

Figure 14. Compressional wave velocities in Massillon light sandstone saturated with eicosene and water as a function of temperature.

Figure 15. Shear wave velocities in Massillon light sandstone saturated with eicosene and water as a function of temperature.

Figure 16. Compressional wave velocities in Ottawa unconsolidated sand saturated with eicosene, water, and air as a function of temperature.

Figure 17. Compressional wave velocities in Massillon light sandstone saturated with the heavy crude and water as a function of temperature.

Figure 18. Shear wave velocities in Massillon light sandstone saturated with the heavy crude and water as a function of temperature.

Figure 19. Compressional wave velocities in Boise sandstone saturated with the heavy

Sample	V_p at 22° C*	V_p at 122° C*	ΔV_p *	$\frac{\Delta V_p}{V_p}$ (%)
Parowax	2.010	1.181	0.829	41.2
Parowax + Sand	3.044	1.387	1.657	54.4
Parowax + Sandstone	4.028	3.120	0.908	22.5
1-Eicosene	1.571	1.101	0.470	29.9
1-Eicosene + Sand	2.165	1.227	0.938	43.3
Duri Heavy Crude	1.502	1.235	0.267	17.8
Heavy Crude + Sand	1.994	1.691	0.303	15.2
Street Ranch Tar	1.676	1.312	0.364	21.7
Tar + Sand	2.252	1.531	0.721	32.0
10.7% Tar + 89.3% Sand	2.375	1.500	0.875	36.8
10.7% Tar + Sand + Water	2.436	1.780	0.656	26.9
Sand + Gas	1.494	1.414	0.080	5.4
Sand + Water	1.943	1.831	0.112	5.8

* Unit: kelometers per second.

Table 1

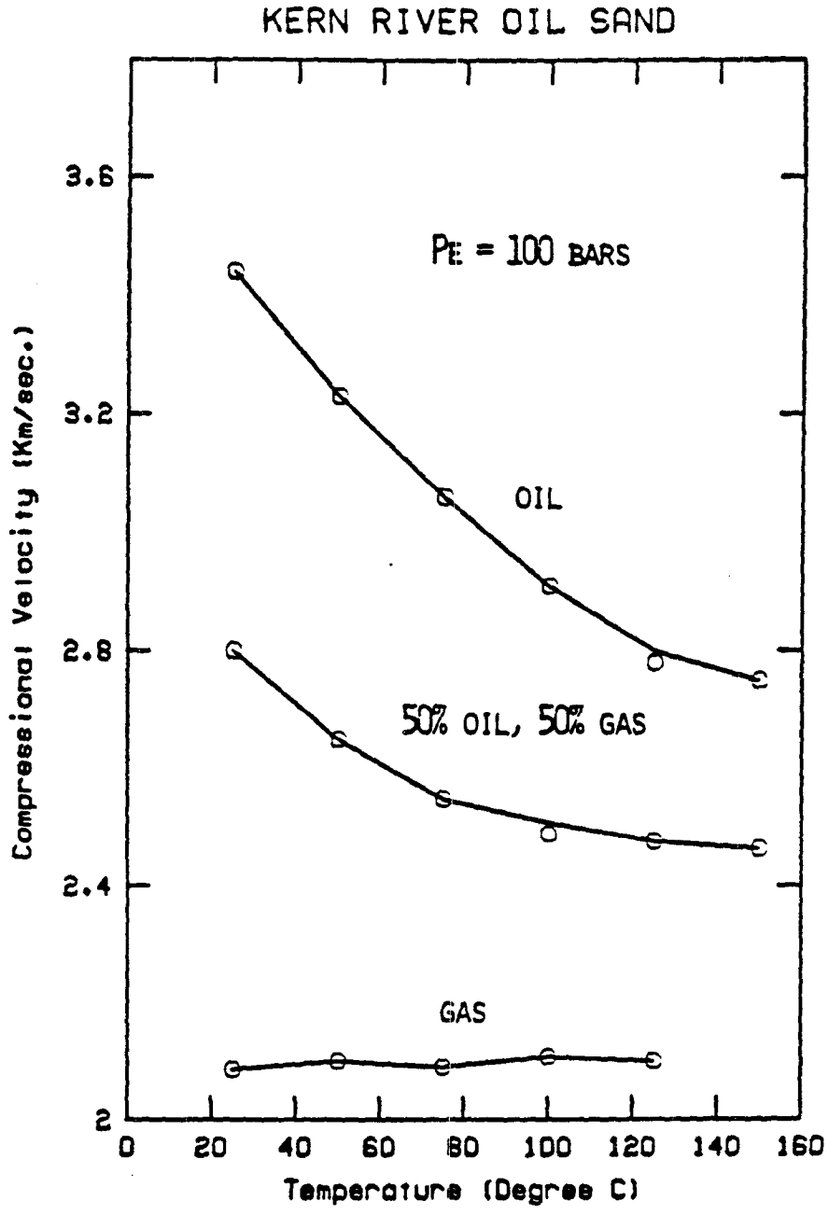
KERN RIVER OIL SAND
3.6
3.2
2.8
2.4
2
Compressional Velocity (Km/sec.)
Pe = 100 BARS
OIL
50% OIL, 50% GAS
GAS
0
20
40
60
80
100
120
140
160
Temperature (Degree C)

FIG. 1

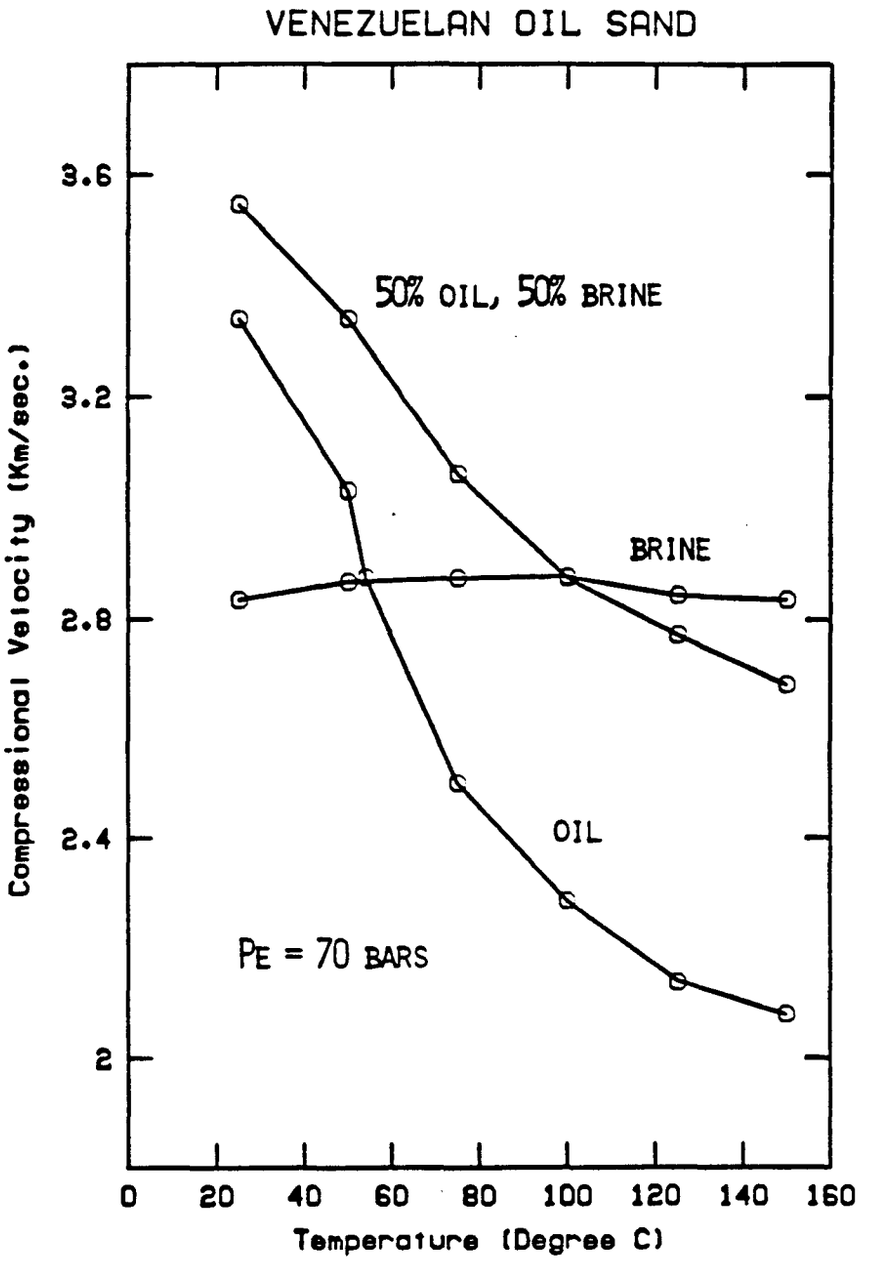
VENEZUELAN OIL SAND
Compressional Velocity (Km/sec.)
3.6
3.2
2.8
2.4
2
50% OIL, 50% BRINE
BRINE
OIL
PE = 70 BARS
0
20
40
60
80
100
120
140
160
Temperature (Degree C)

FIG. 2.

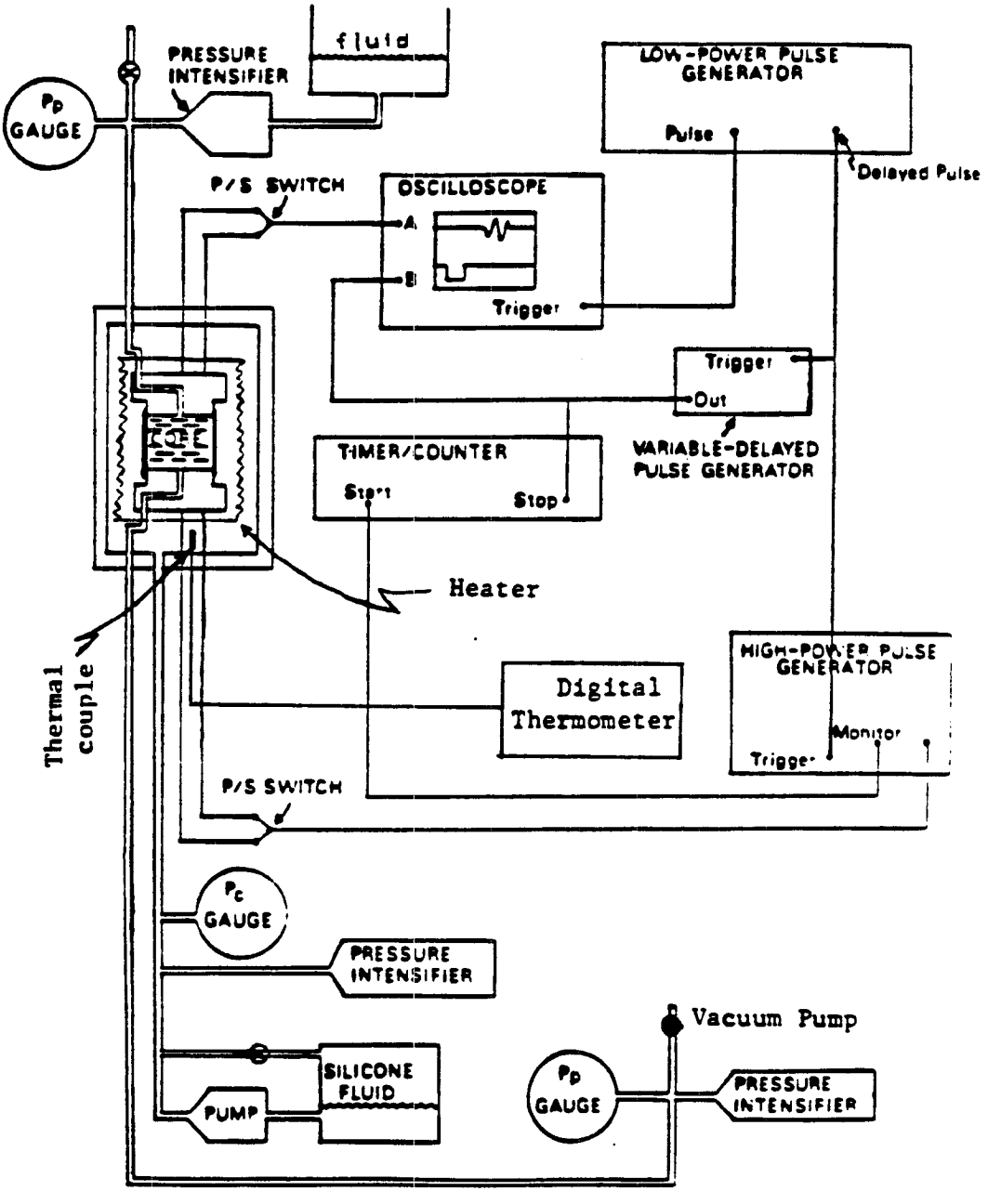
fluid
PRESSURE INTENSIFIER
P_p GAUGE
LOW-POWER PULSE GENERATOR
Pulse
Delayed Pulse
P/S SWITCH
OSCILLOSCOPE
A
B
Trigger
Trigger
Out
VARIABLE-DELAYED PULSE GENERATOR
TIMER/COUNTER
Start
Stop
Heater
Thermal couple
Digital Thermometer
HIGH-POWER PULSE GENERATOR
Monitor
Trigger
P/S SWITCH
P_c GAUGE
PRESSURE INTENSIFIER
Vacuum Pump
SILICONE FLUID
PUMP
P_p GAUGE
PRESSURE INTENSIFIER

FIG. 3

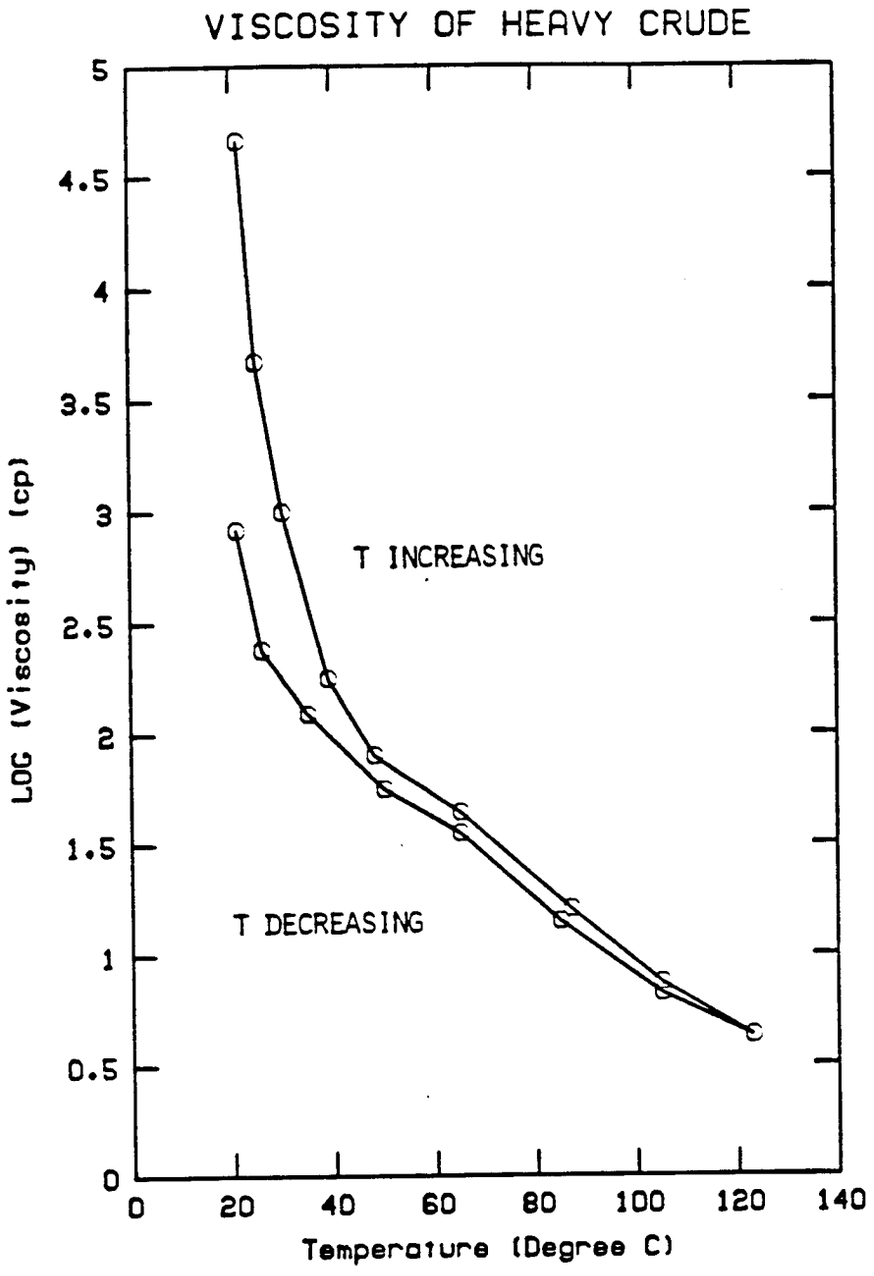
VISCOSITY OF HEAVY CRUDE
LOG (Viscosity) (cp)
Temperature (Degree C)
T INCREASING
T DECREASING
0
0.5
1
1.5
2
2.5
3
3.5
4
4.5
5
0
20
40
60
80
100
120
140

FIG. 4

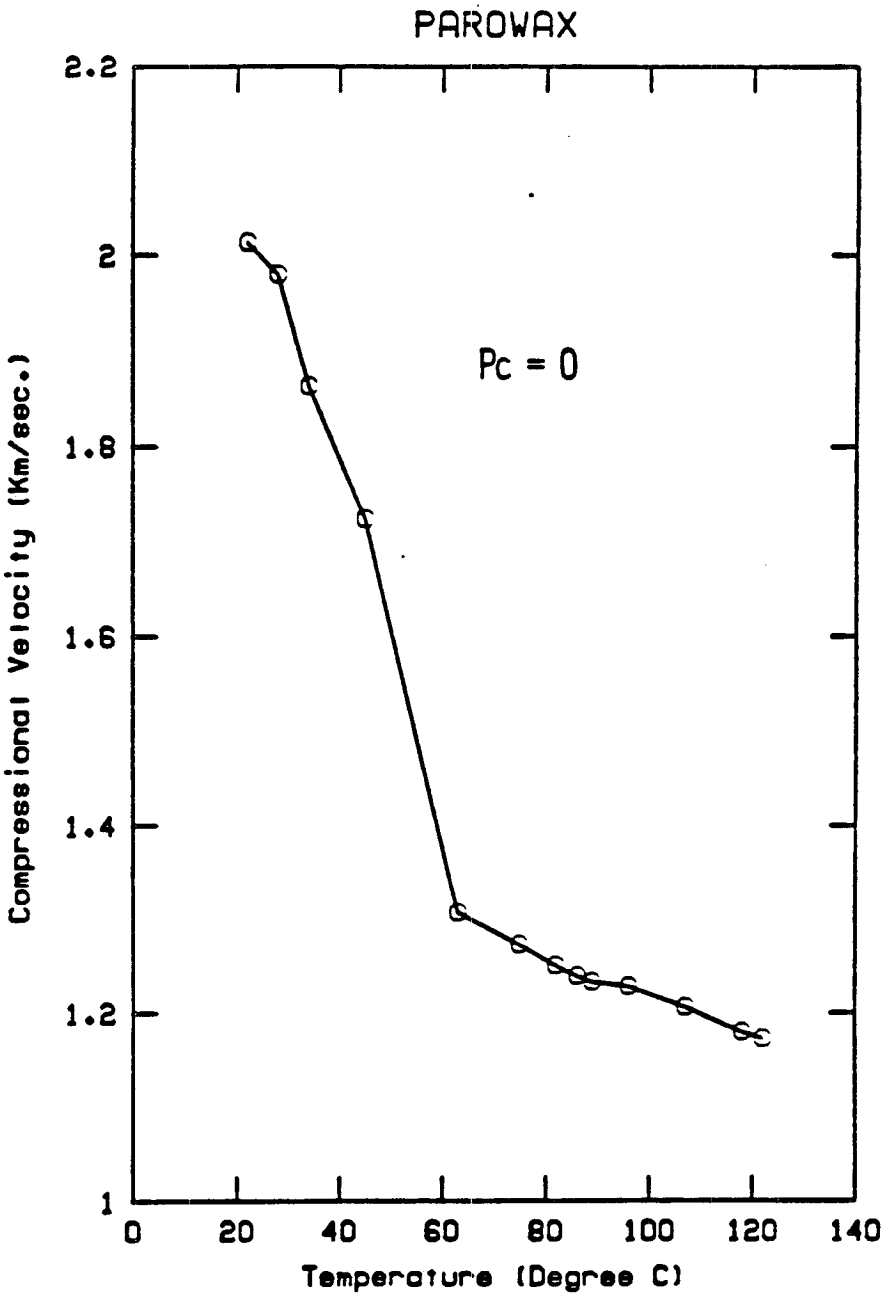
PAROWAX
Pc = 0
Compressional Velocity (Km/sec.)
Temperature (Degree C)
2.2
2
1.8
1.6
1.4
1.2
1
0
20
40
60
80
100
120
140

FIG. 5

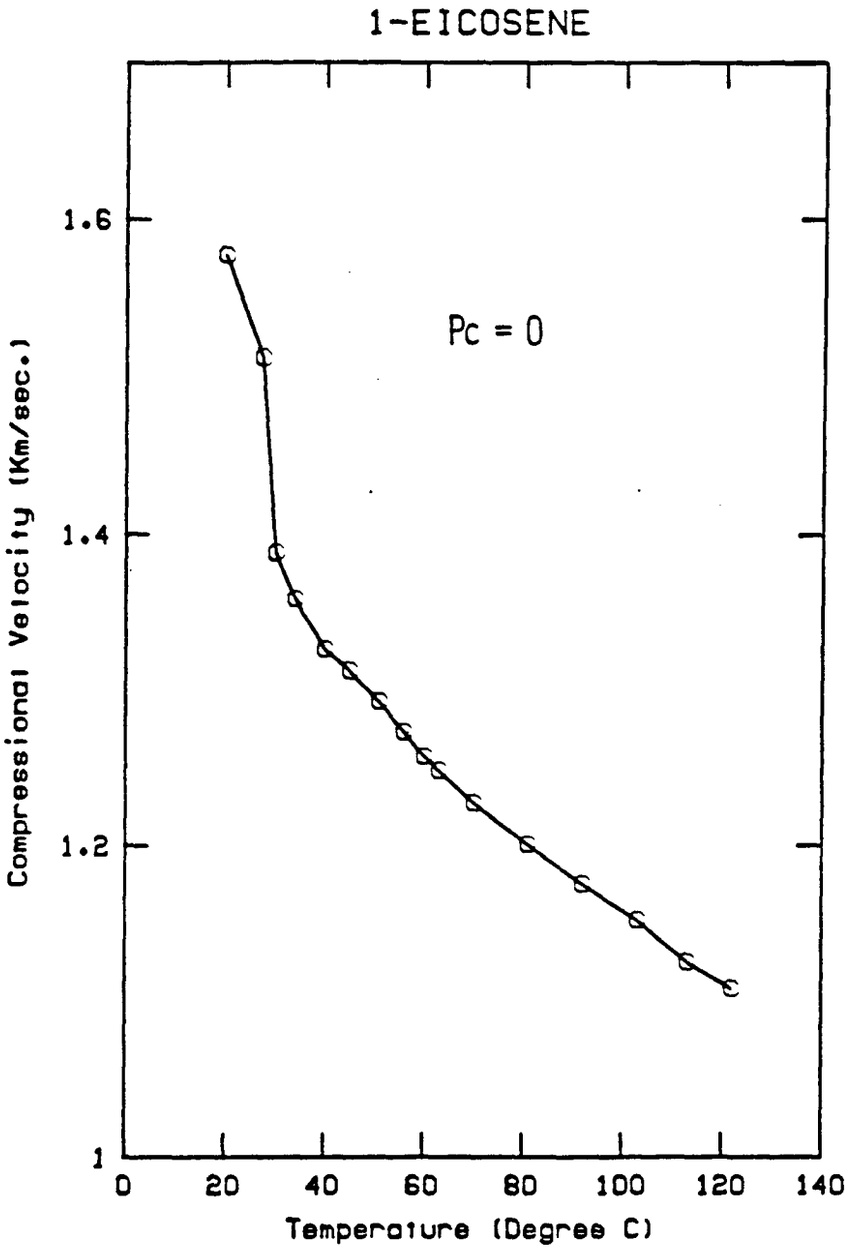
1-EICOSENE
Pc = 0
Compressional Velocity (Km/sec.)
1.6
1.4
1.2
1
0
20
40
60
80
100
120
140
Temperature (Degree C)

FIG. 6

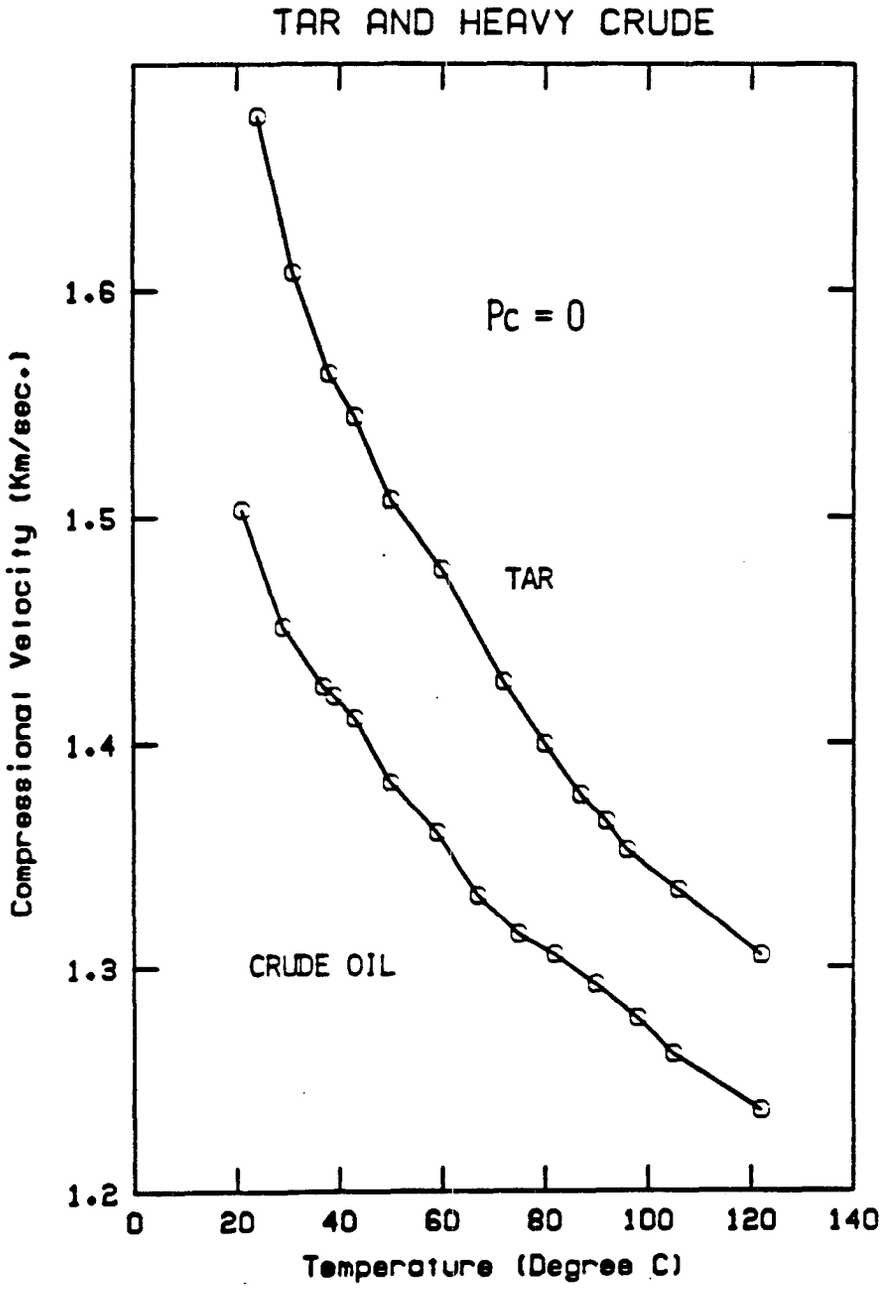
TAR AND HEAVY CRUDE
Pc = 0
TAR
CRUDE OIL
Compressional Velocity (Km/sec.)
1.6
1.5
1.4
1.3
1.2
0
20
40
60
80
100
120
140
Temperature (Degree C)

FIG. 7

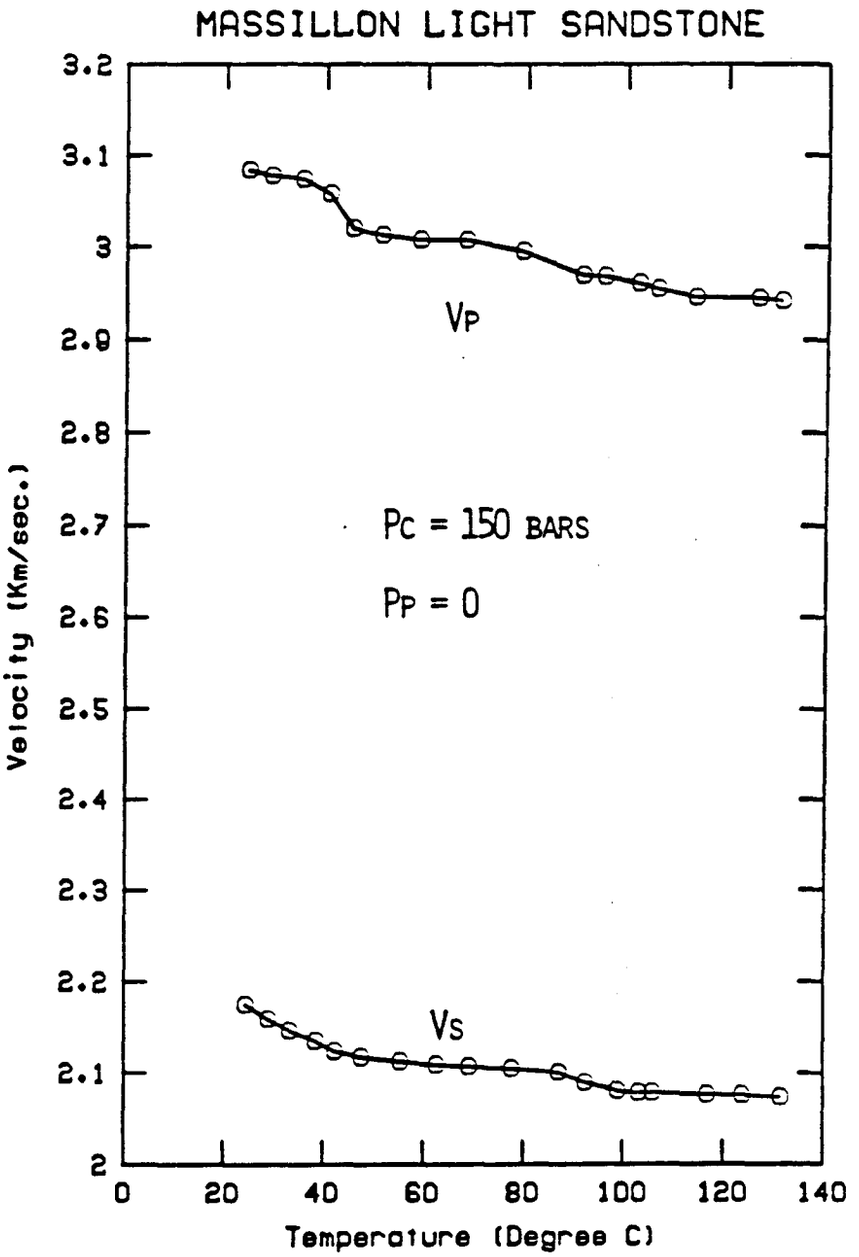
MASSILLON LIGHT SANDSTONE
Velocity (Km/sec.)
3.2
3.1
3
2.9
2.8
2.7
2.6
2.5
2.4
2.3
2.2
2.1
2
0
20
40
60
80
100
120
140
Temperature (Degree C)
VP
VS
PC = 150 BARS
PP = 0

FIG. 8

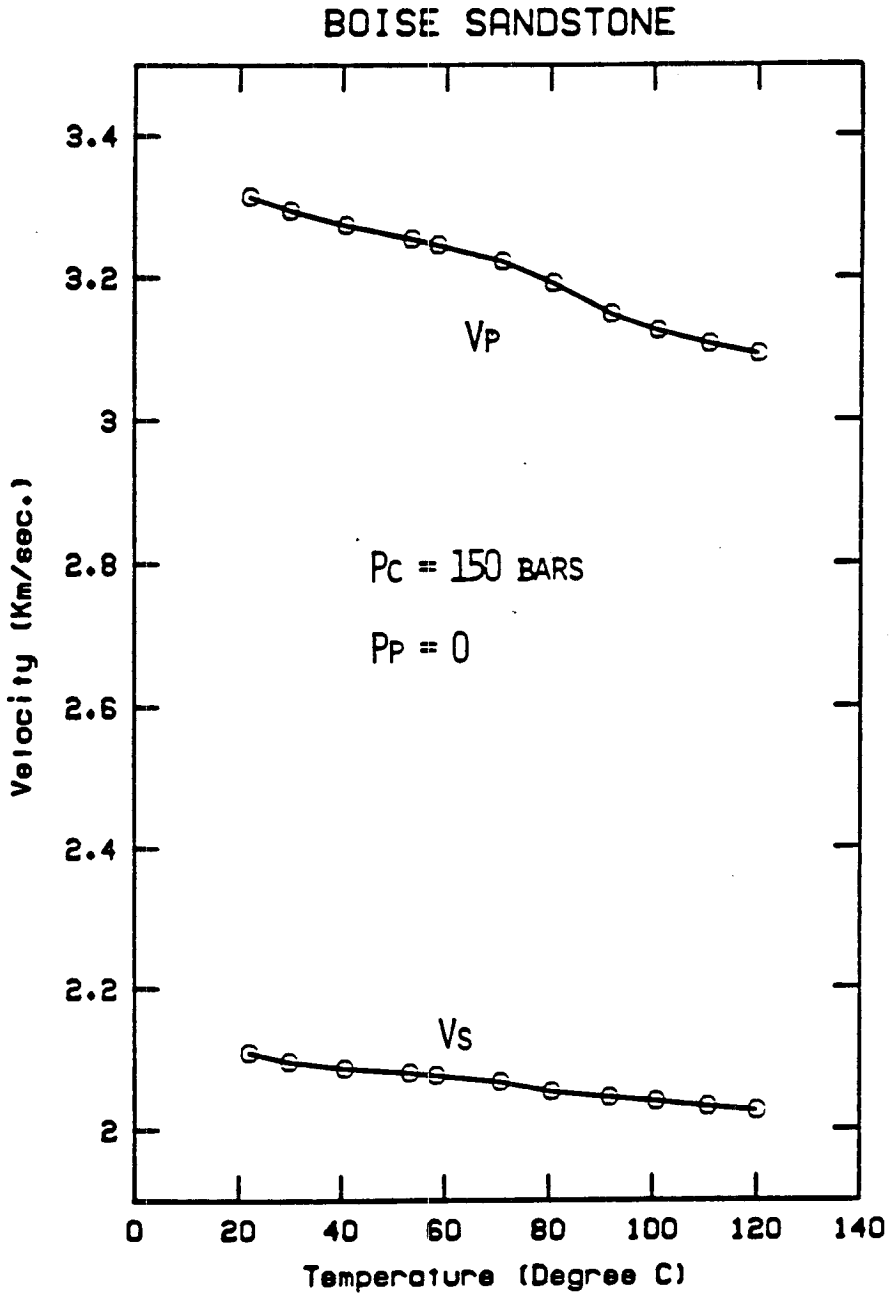
BOISE SANDSTONE
3.4
3.2
3
2.8
2.6
2.4
2.2
2
Velocity (Km/sec.)
Vp
Pc = 150 BARS
Pp = 0
Vs
0
20
40
60
80
100
120
140
Temperature (Degree C)

FIG. 9

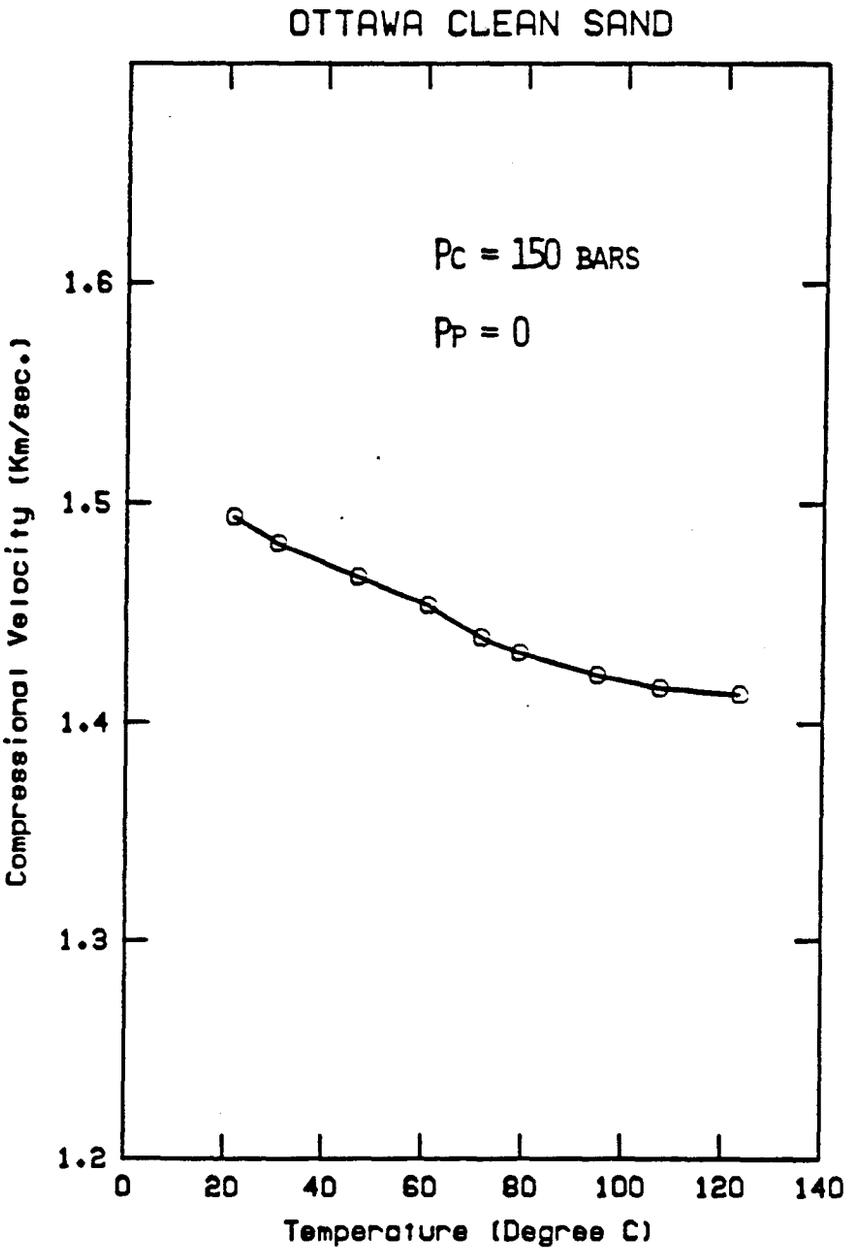
OTTAWA CLEAN SAND
Pc = 150 BARS
Pp = 0
Compressional Velocity (Km/sec.)
1.6
1.5
1.4
1.3
1.2
0
20
40
60
80
100
120
140
Temperature (Degree C)

FIG. 10

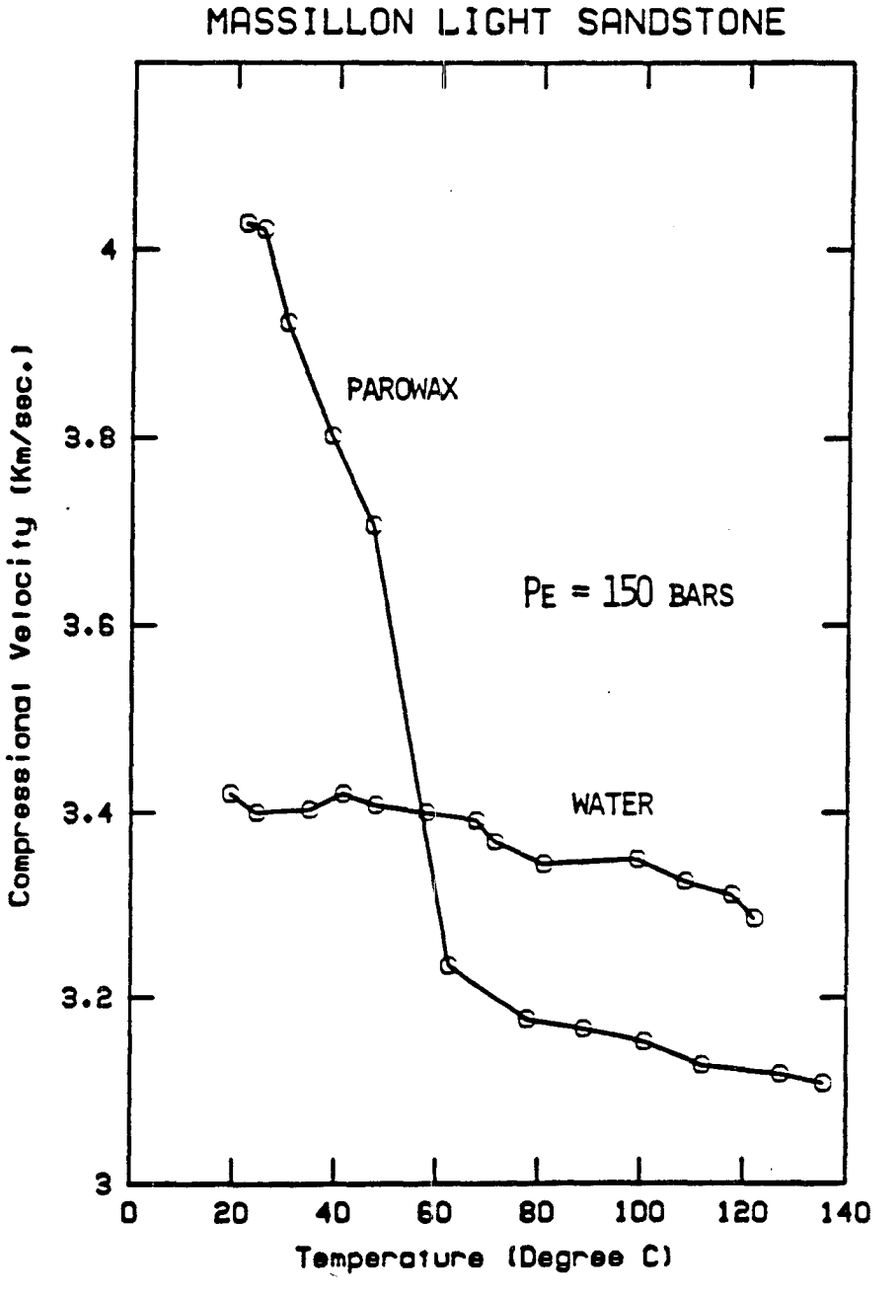
MASSILLON LIGHT SANDSTONE
Compressional Velocity (Km/sec.)
4
3.8
3.6
3.4
3.2
3
PAROWAX
PE = 150 BARS
WATER
0
20
40
60
80
100
120
140
Temperature (Degree C)

FIG. 11

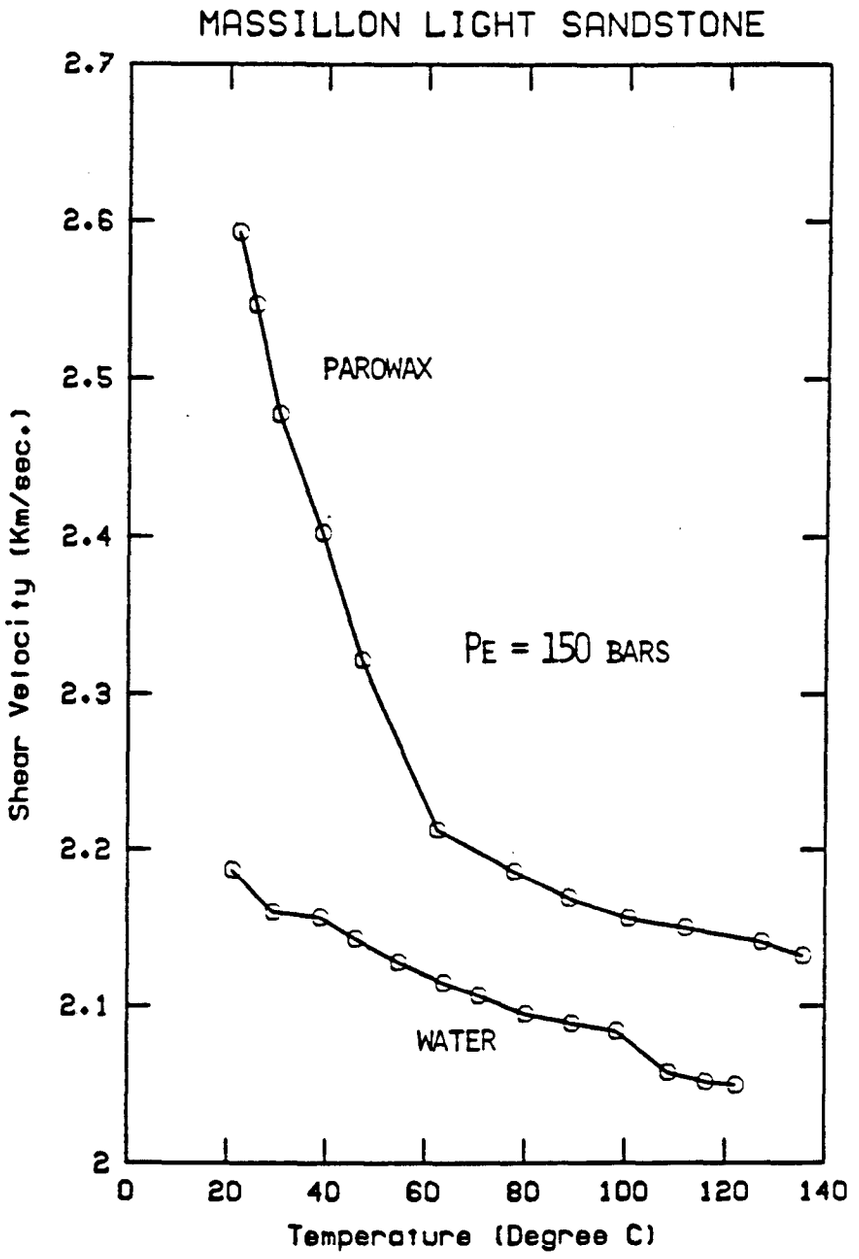
MASSILLON LIGHT SANDSTONE
Shear Velocity (Km/sec.)
2.7
2.6
2.5
2.4
2.3
2.2
2.1
2
PAROWAX
PE = 150 BARS
WATER
0
20
40
60
80
100
120
140
Temperature (Degree C)

FIG. 12

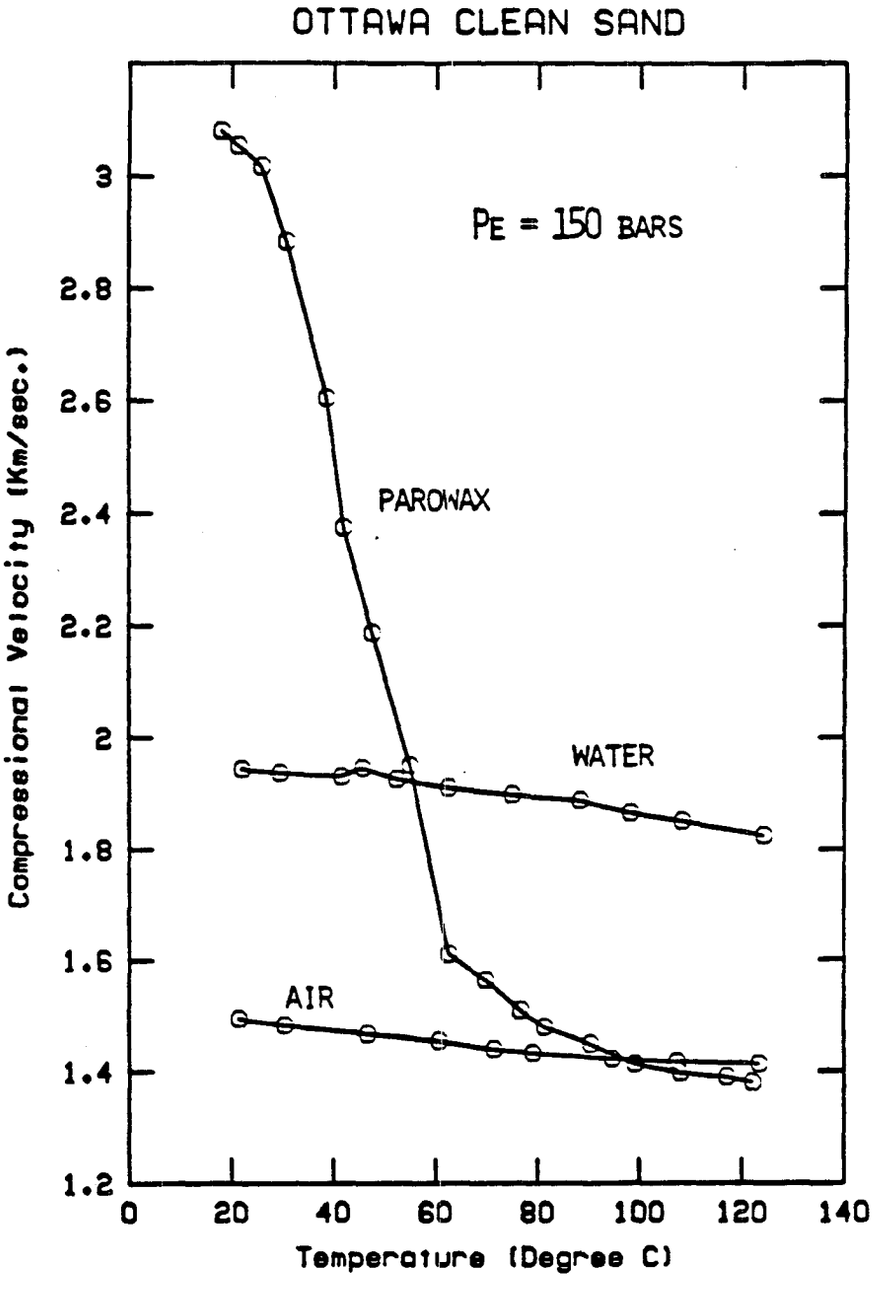
OTTAWA CLEAN SAND
PE = 150 BARS
PAROWAX
WATER
AIR
Compressional Velocity (Km/sec.)
Temperature (Degree C)
3
2.8
2.6
2.4
2.2
2
1.8
1.6
1.4
1.2
0
20
40
60
80
100
120
140

FIG. 13

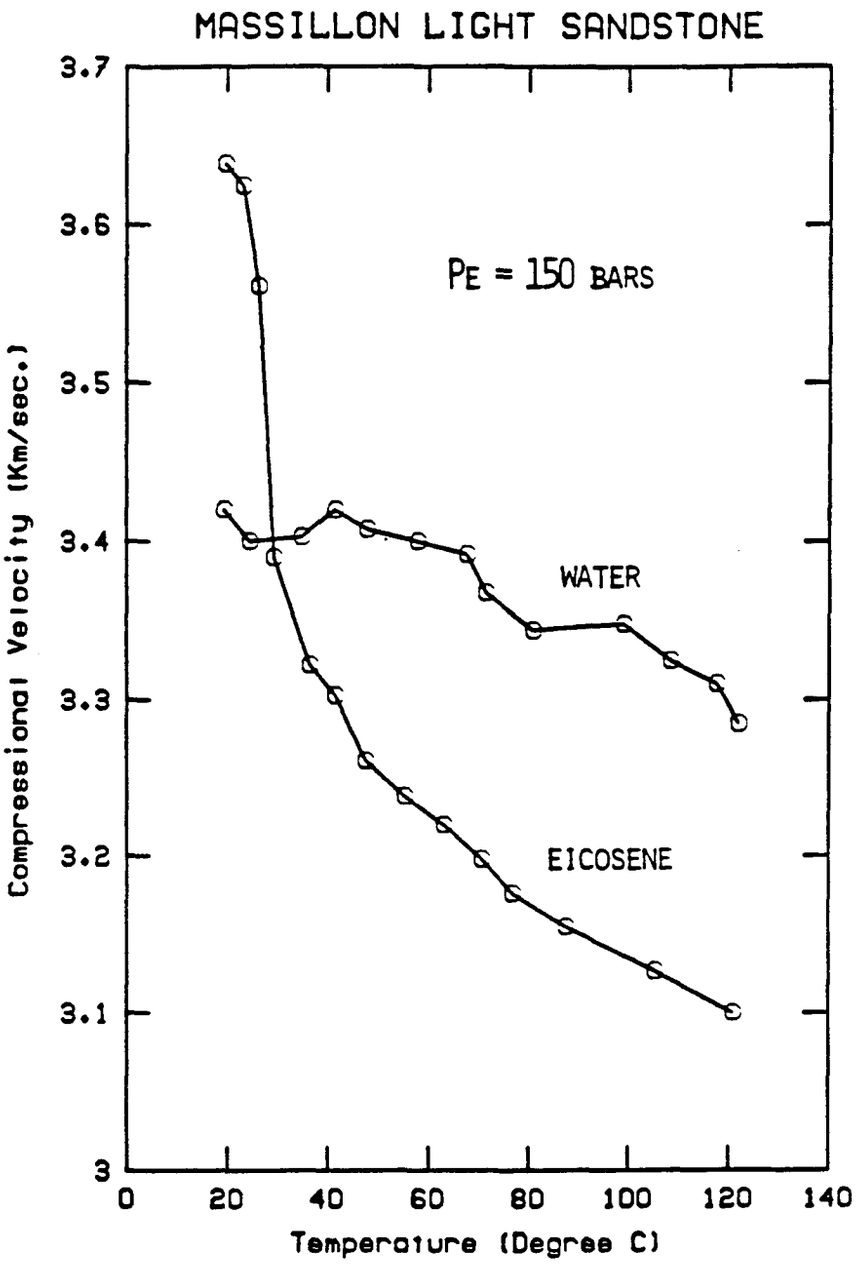
MASSILLON LIGHT SANDSTONE
Pe = 150 BARS
WATER
EICOSENE
Compressional Velocity (Km/sec.)
Temperature (Degree C)
3.7
3.6
3.5
3.4
3.3
3.2
3.1
3
0
20
40
60
80
100
120
140

FIG. 14

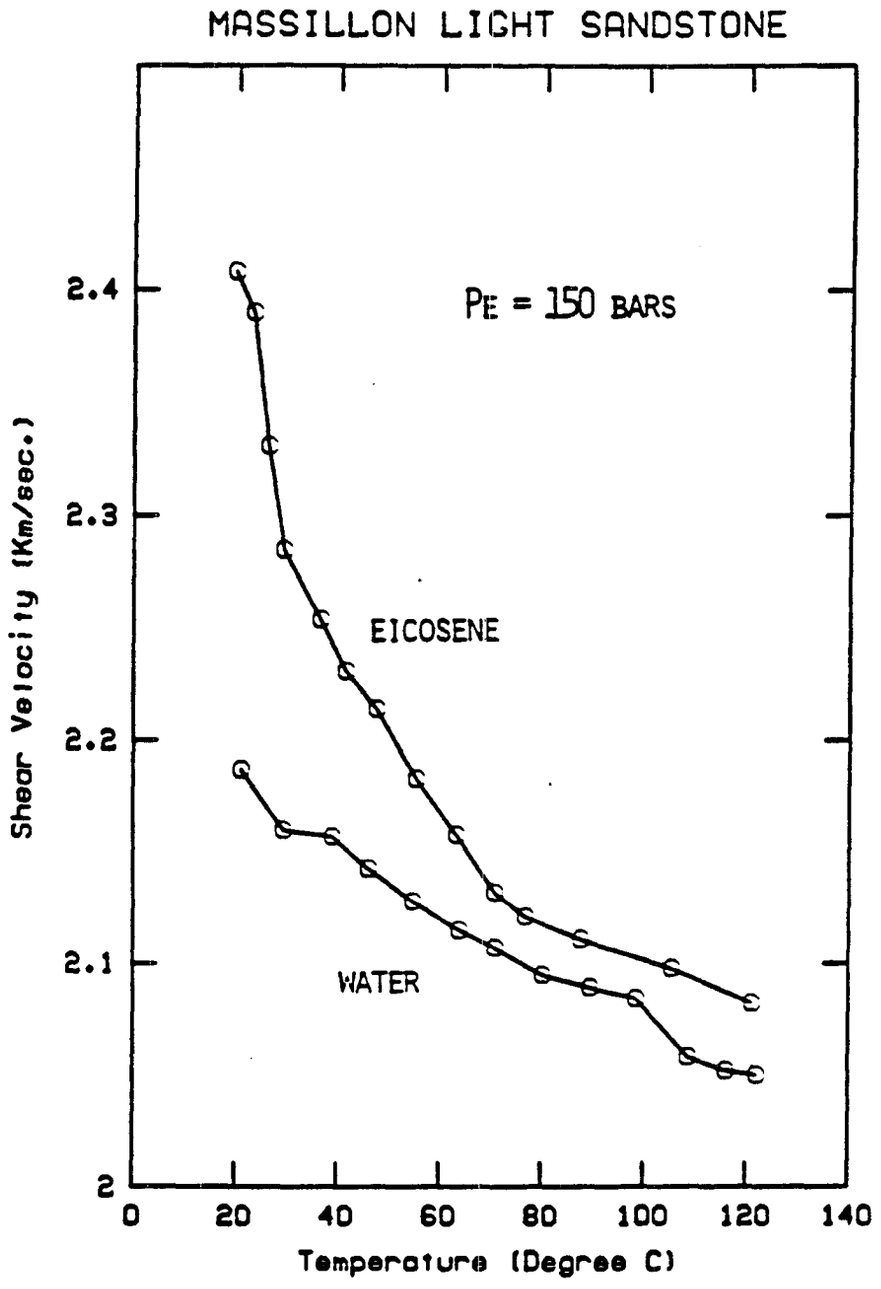
MASSILLON LIGHT SANDSTONE
PE = 150 BARS
EICOSENE
WATER
Shear Velocity (Km/sec.)
2.4
2.3
2.2
2.1
2
0
20
40
60
80
100
120
140
Temperature (Degree C)

FIG. 15

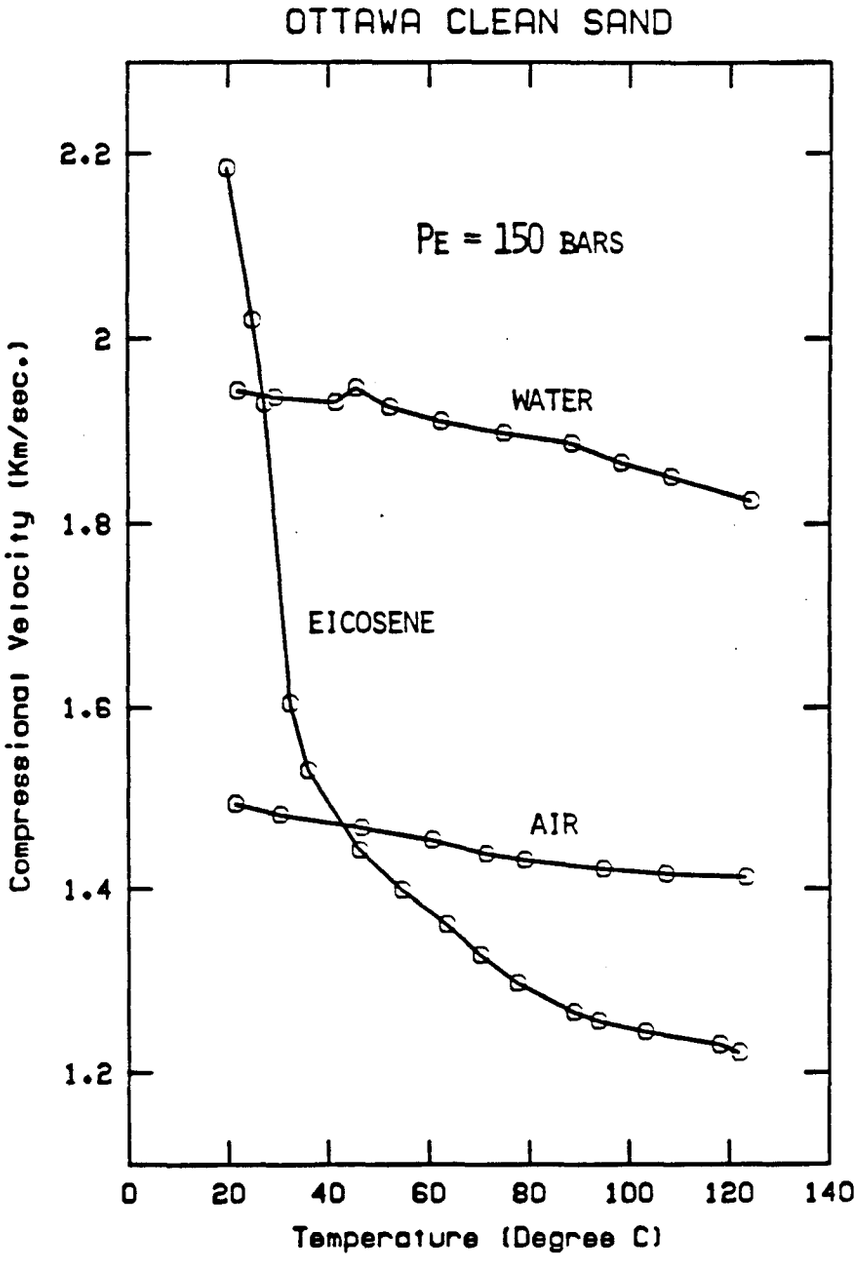
OTTAWA CLEAN SAND
PE = 150 BARS
WATER
EICOSENE
AIR
Compressional Velocity (Km/sec.)
2.2
2
1.8
1.6
1.4
1.2
0
20
40
60
80
100
120
140
Temperature (Degree C)

FIG. 16

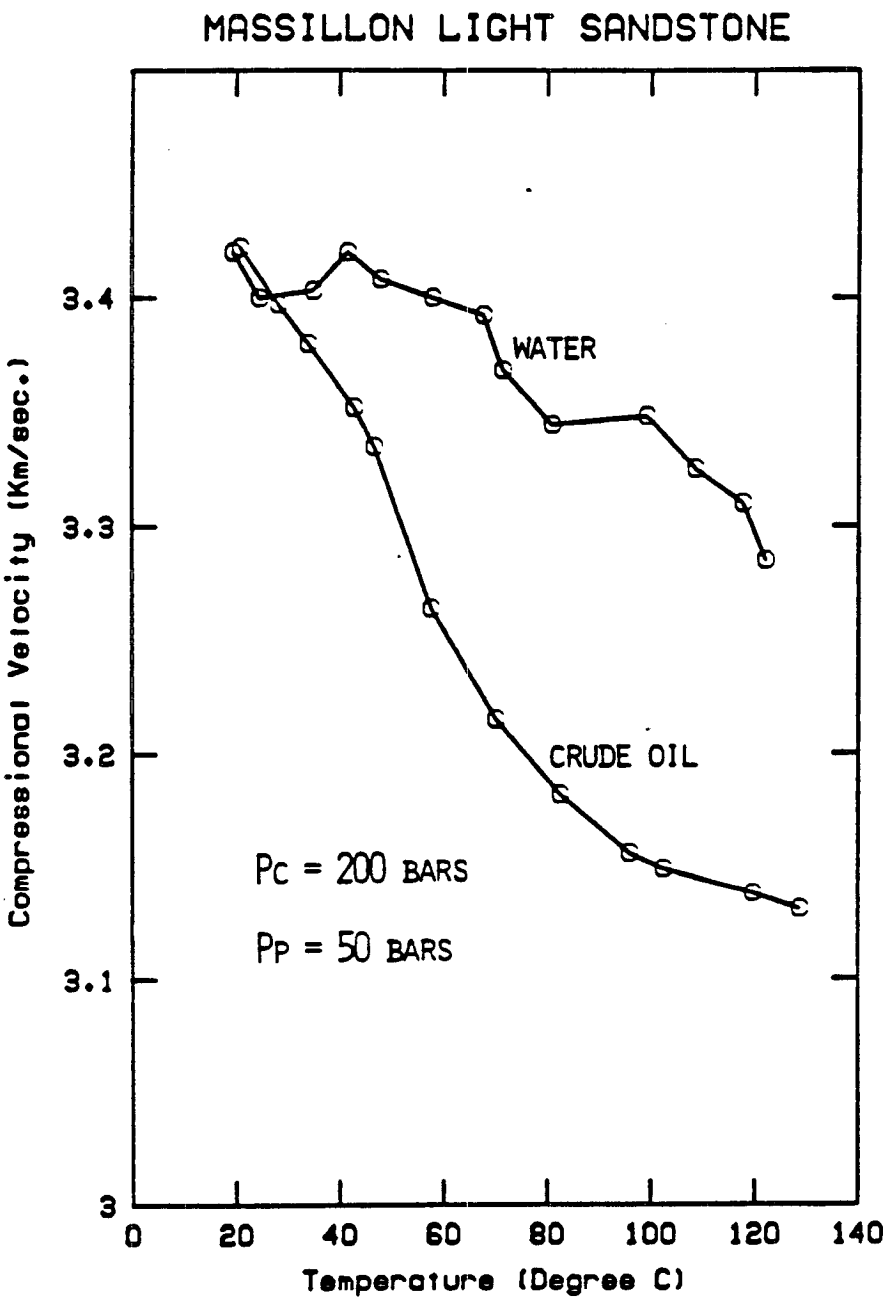
MASSILLON LIGHT SANDSTONE
Compressional Velocity (Km/sec.)
3.4
3.3
3.2
3.1
3
WATER
CRUDE OIL
Pc = 200 BARS
Pp = 50 BARS
0
20
40
60
80
100
120
140
Temperature (Degree C)

FIG. 17

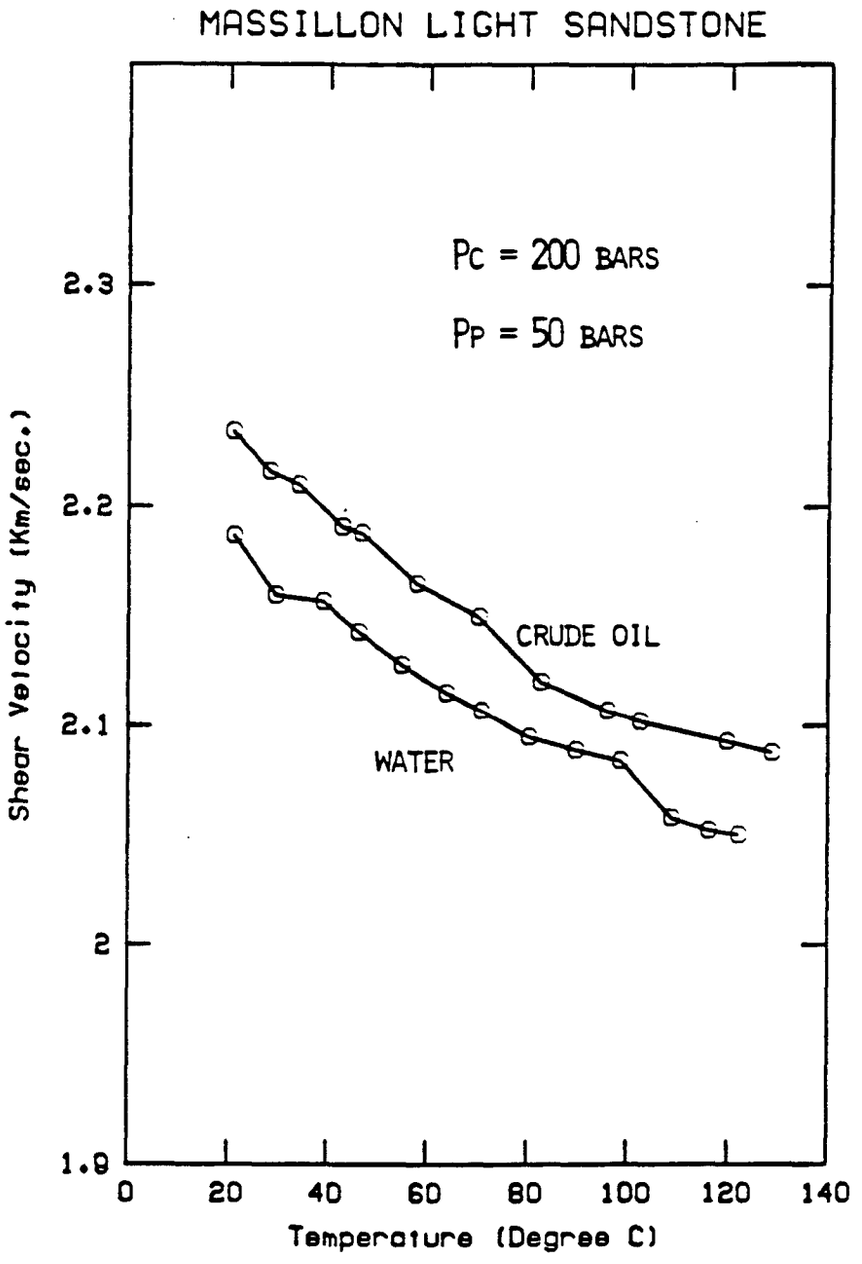
MASSILLON LIGHT SANDSTONE
Pc = 200 BARS
Pp = 50 BARS
CRUDE OIL
WATER
Shear Velocity (Km/sec.)
2.3
2.2
2.1
2
1.9
0
20
40
60
80
100
120
140
Temperature (Degree C)

FIG. 18

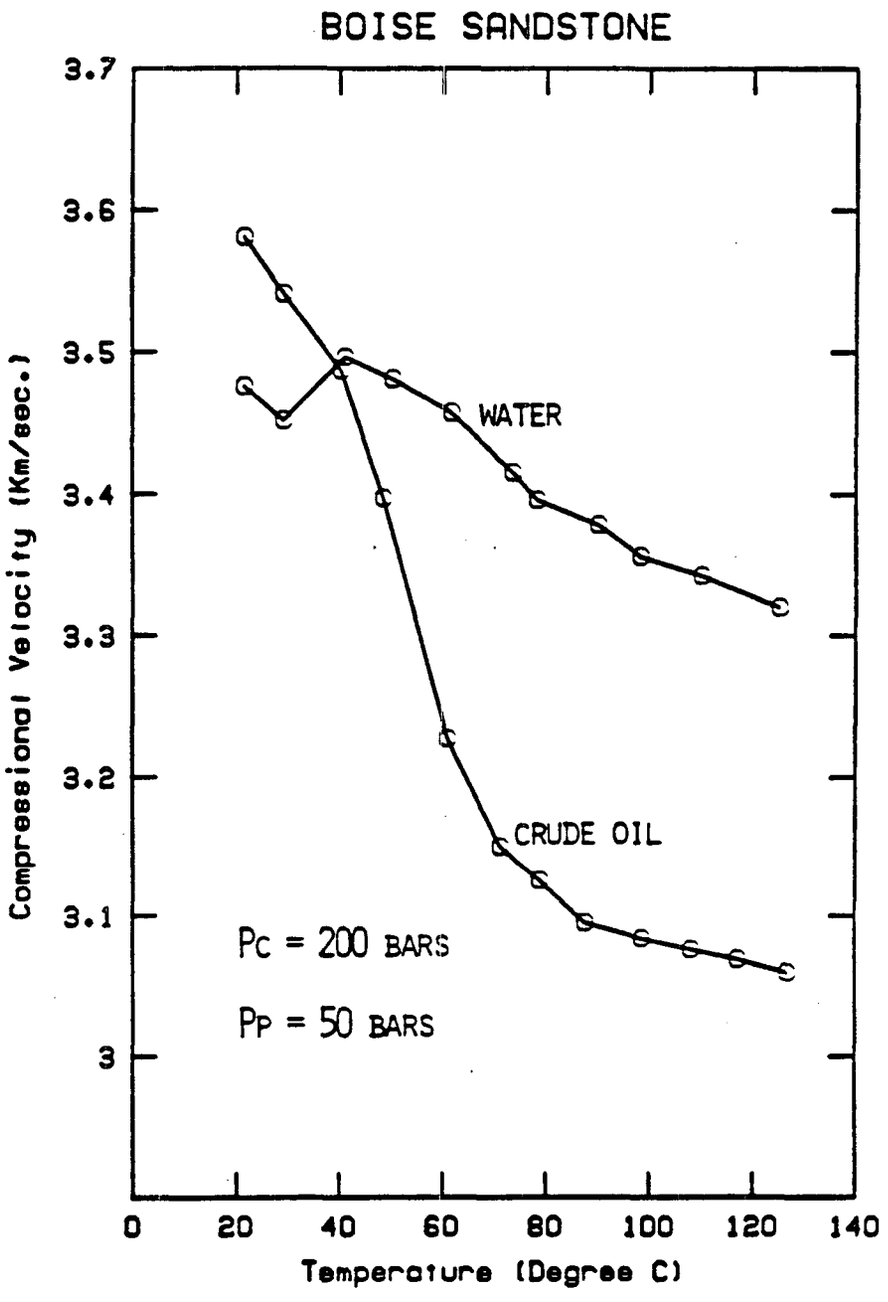
BOISE SANDSTONE
Compressional Velocity (Km/sec.)
3.7
3.6
3.5
3.4
3.3
3.2
3.1
3
WATER
CRUDE OIL
Pc = 200 BARS
Pp = 50 BARS
0
20
40
60
80
100
120
140
Temperature (Degree C)

FIG. 19

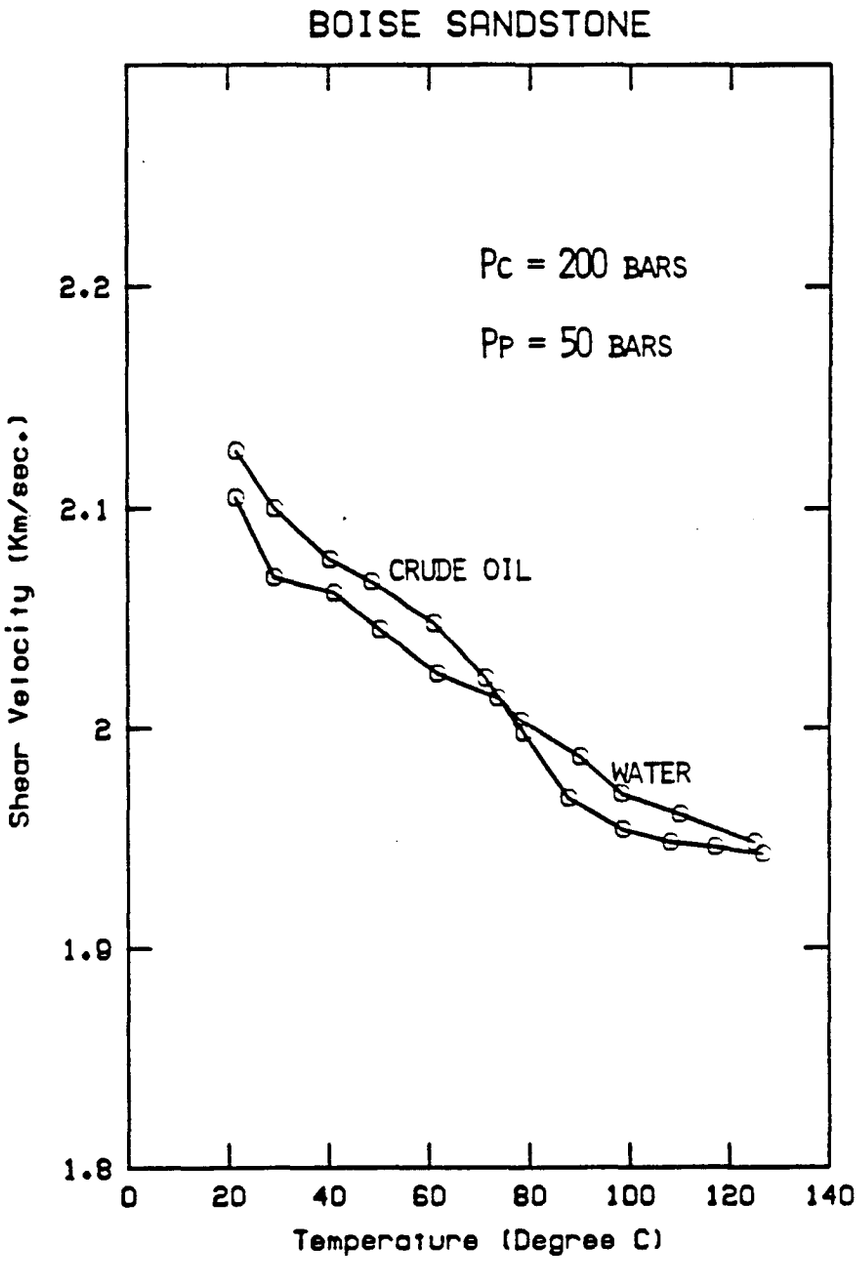
BOISE SANDSTONE
Pc = 200 BARS
Pp = 50 BARS
CRUDE OIL
WATER
Shear Velocity (Km/sec.)
2.2
2.1
2
1.9
1.8
0
20
40
60
80
100
120
140
Temperature (Degree C)

FIG. 20

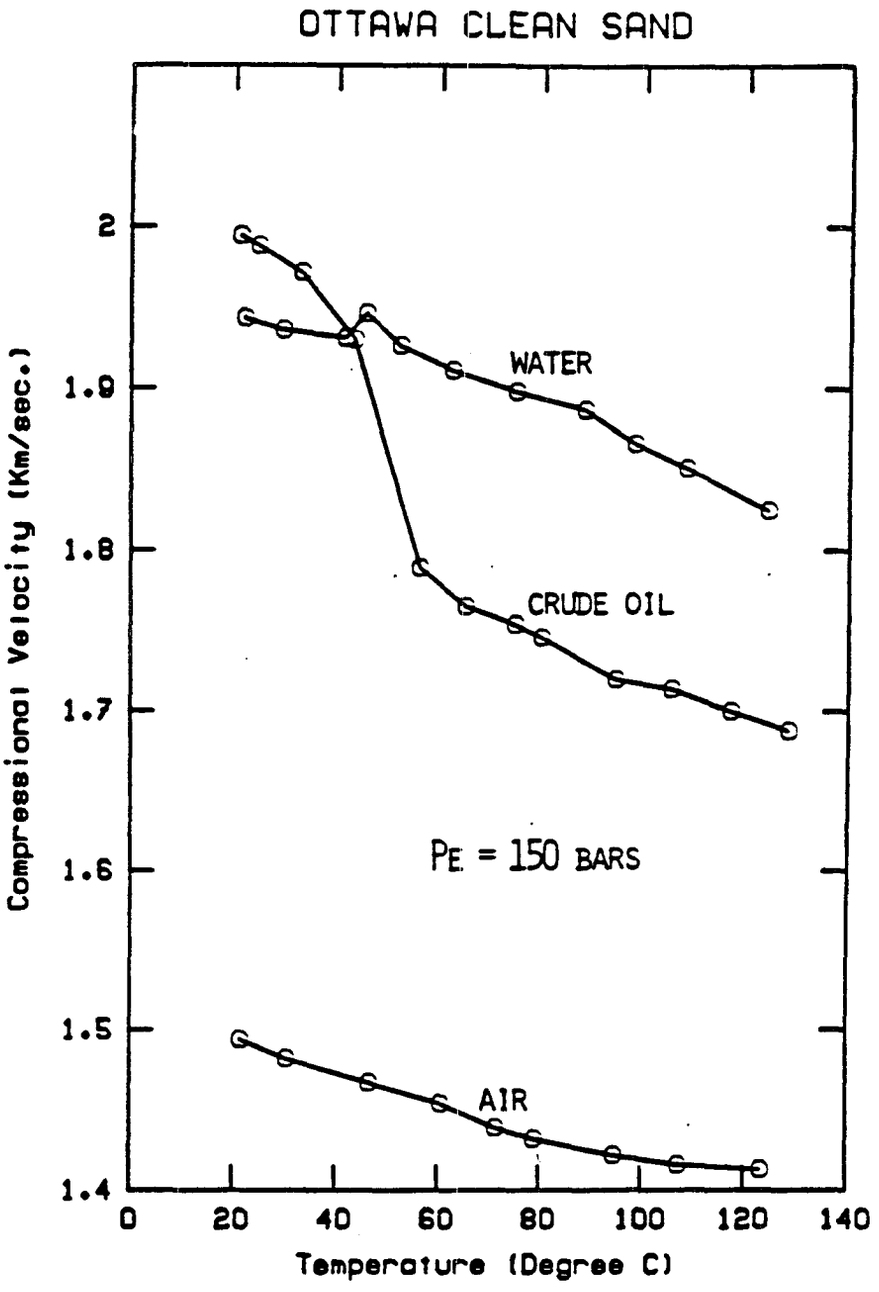
OTTAWA CLEAN SAND
Compressional Velocity (Km/sec.)
2
1.9
1.8
1.7
1.6
1.5
1.4
WATER
CRUDE OIL
AIR
PE = 150 BARS
0
20
40
60
80
100
120
140
Temperature (Degree C)

FIG. 21

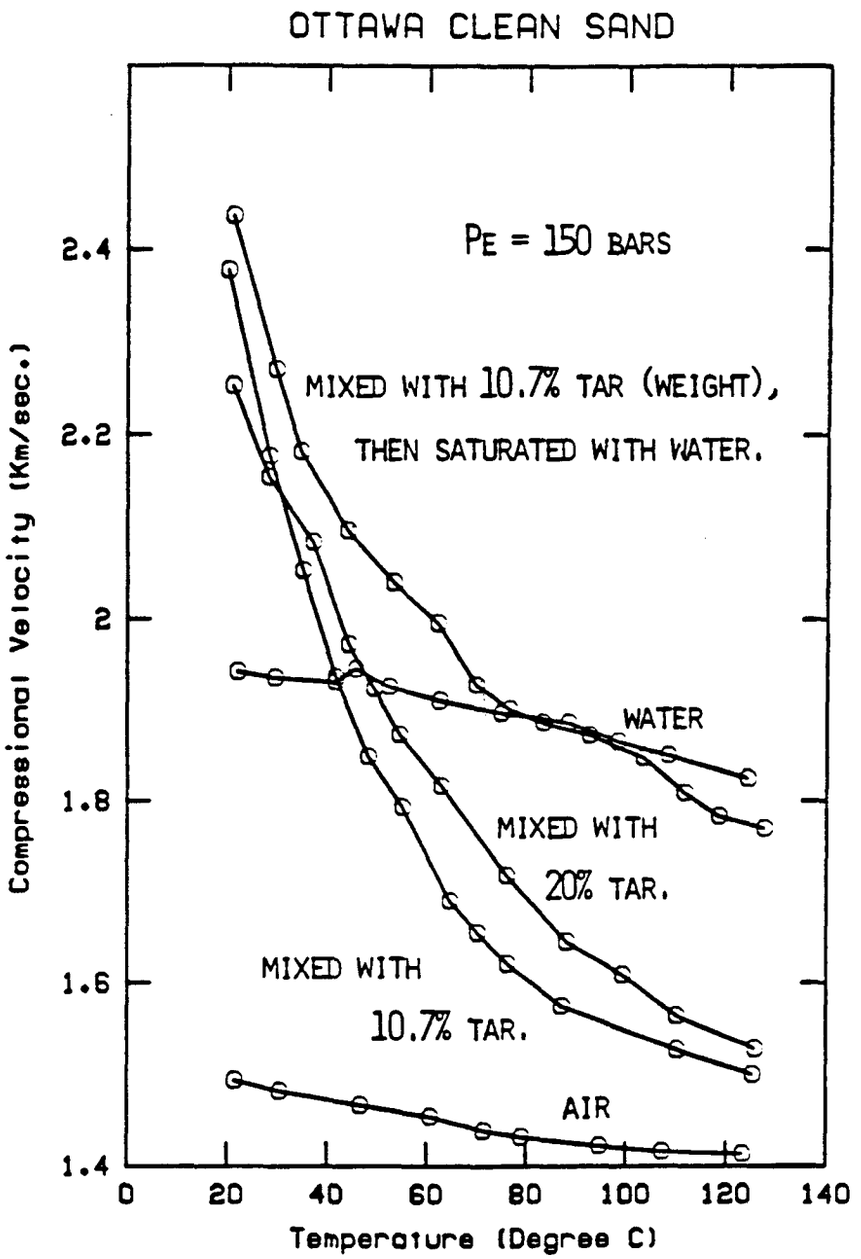
OTTAWA CLEAN SAND
PE = 150 BARS
MIXED WITH 10.7% TAR (WEIGHT),
THEN SATURATED WITH WATER.
WATER
MIXED WITH
20% TAR.
MIXED WITH
10.7% TAR.
AIR
Compressional Velocity (Km/sec.)
2.4
2.2
2
1.8
1.6
1.4
0
20
40
60
80
100
120
140
Temperature (Degree C)

FIG. 22

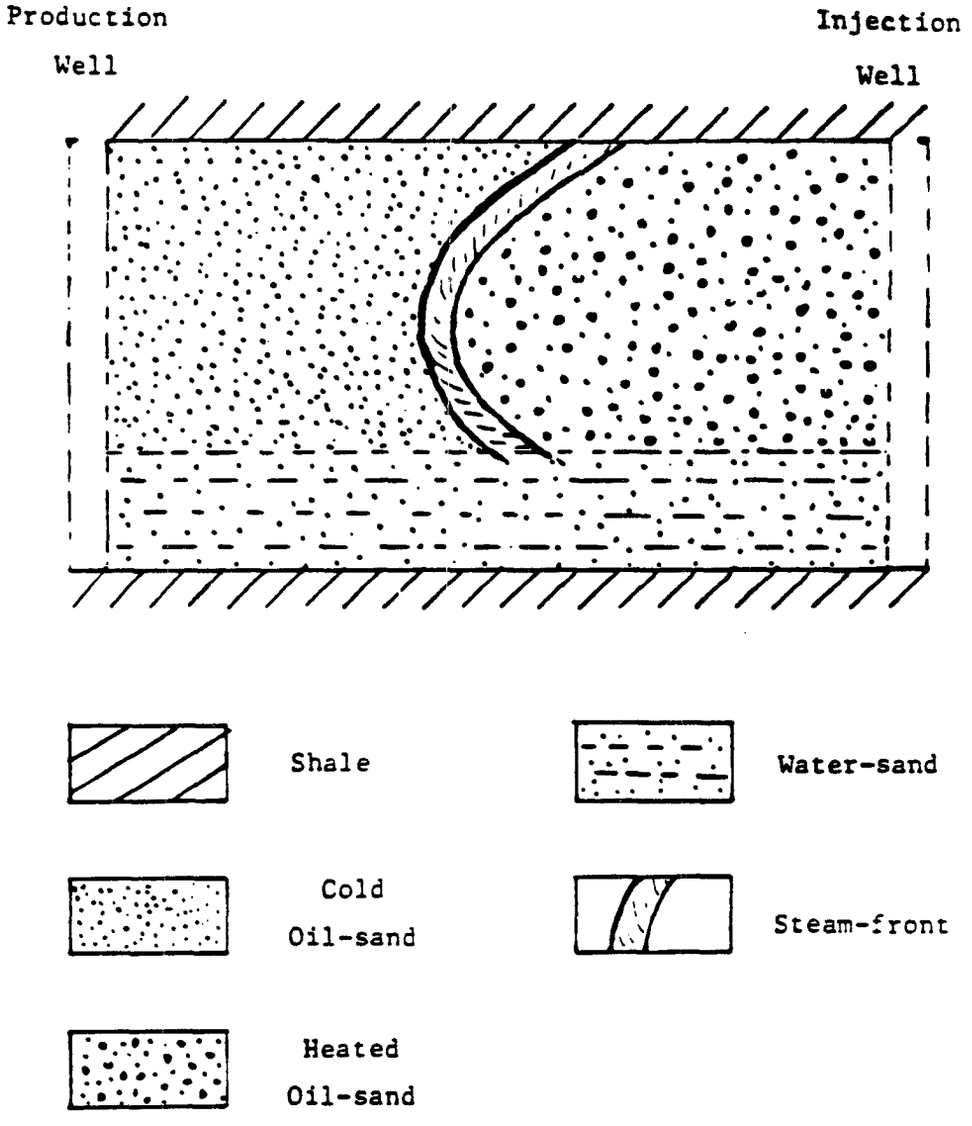
Production
Well
Injection
Well
Shale
Water-sand
Cold
Oil-sand
Steam-front
Heated
Oil-sand

FIG. 23

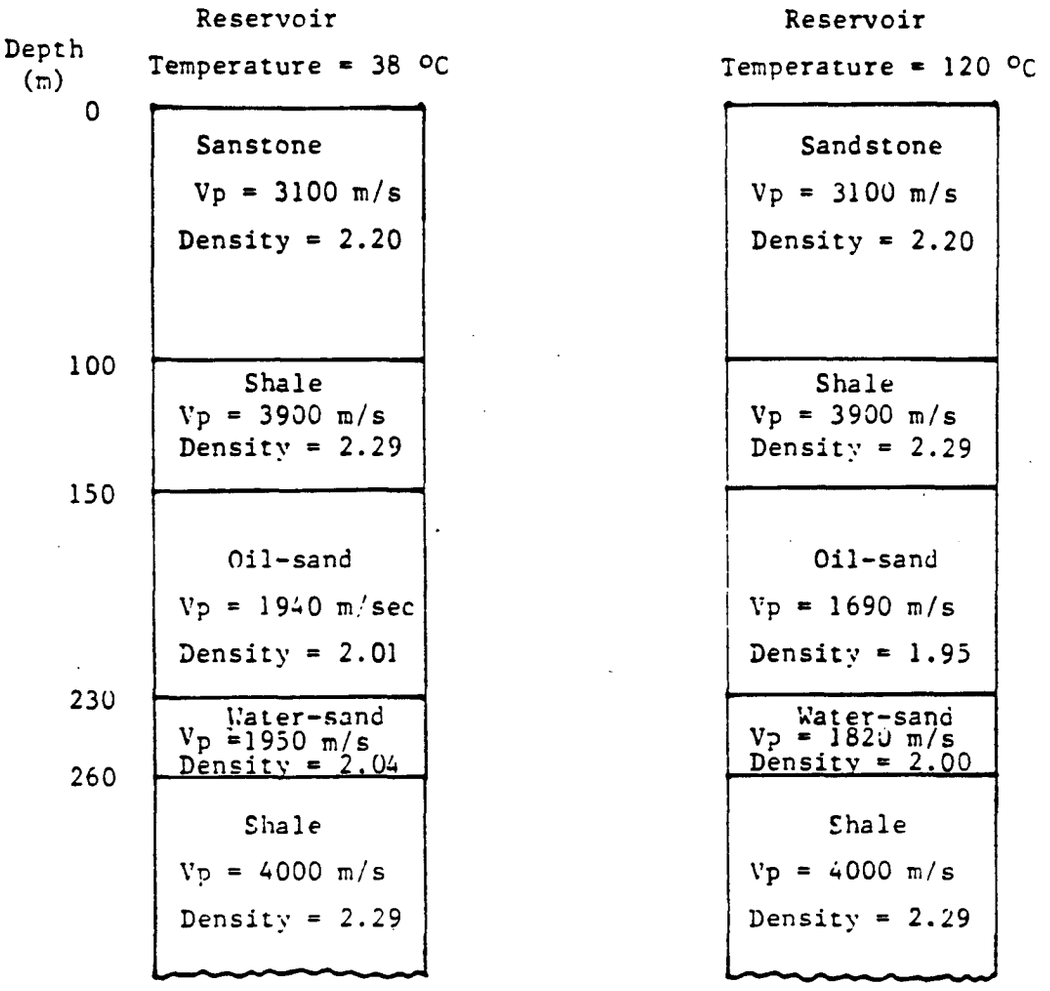
Depth (m)
Reservoir
Temperature = 38 °C
0
Sanstone
Vp = 3100 m/s
Density = 2.20
100
Shale
Vp = 3900 m/s
Density = 2.29
150
Oil-sand
Vp = 1940 m/sec
Density = 2.01
230
Water-sand
Vp =1950 m/s
Density = 2.04
260
Shale
Vp = 4000 m/s
Density = 2.29
Reservoir
Temperature = 120 °C
Sandstone
Vp = 3100 m/s
Density = 2.20
Shale
Vp = 3900 m/s
Density = 2.29
Oil-sand
Vp = 1690 m/s
Density = 1.95
Water-sand
Vp = 1820 m/s
Density = 2.00
Shale
Vp = 4000 m/s
Density = 2.29

FIG. 24

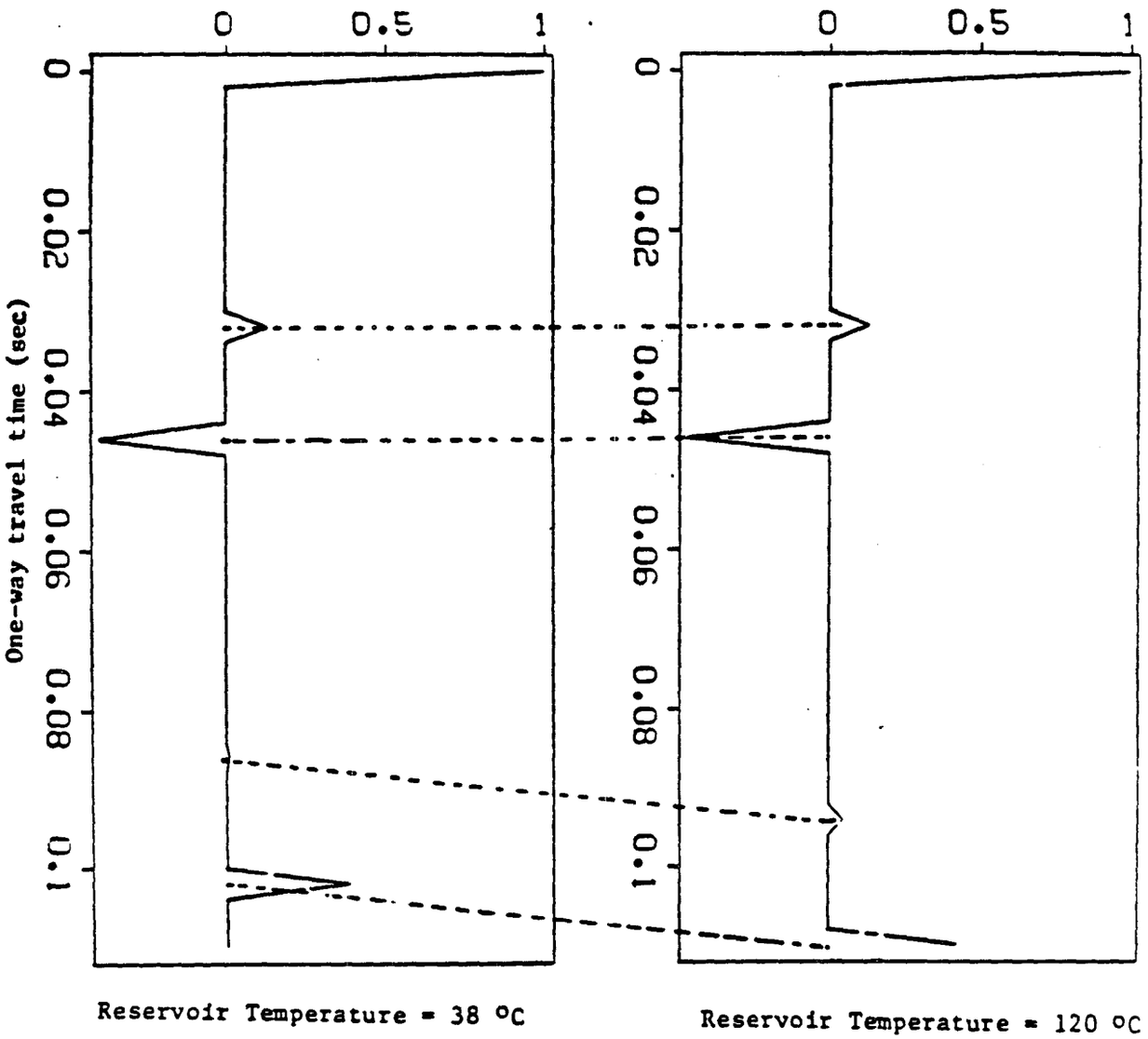
0
0.5
1
0
0.02
0.04
0.06
0.08
0.1
One-way travel time (sec)
Reservoir Temperature = 38 °C
Reservoir Temperature = 120 °C

FIG. 25

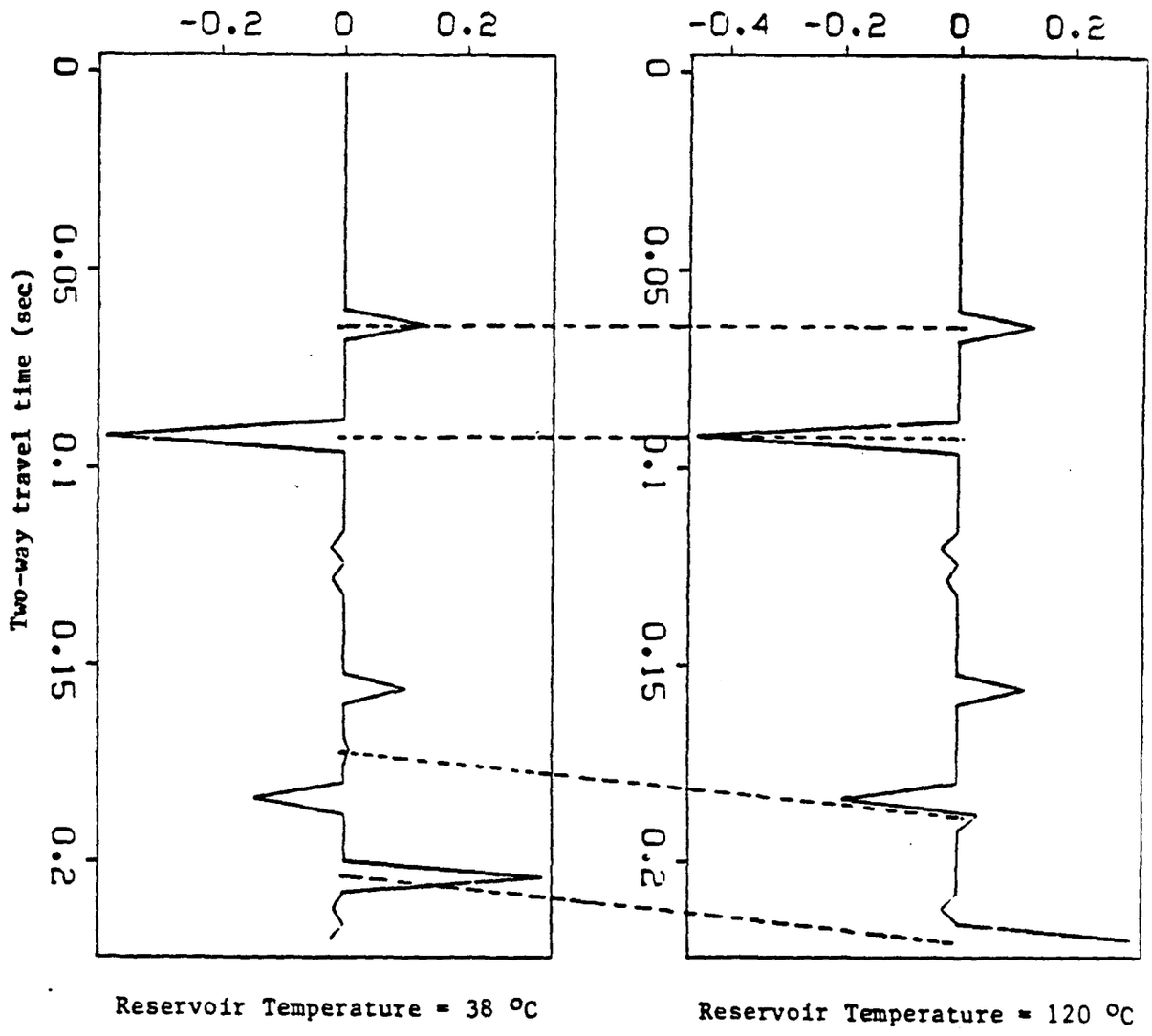
-0.2
0
0.2
-0.4
-0.2
0
0.2
0
0.05
0.1
0.15
0.2
Two-way travel time (sec)
Reservoir Temperature = 38 °C
Reservoir Temperature = 120 °C

FIG. 26

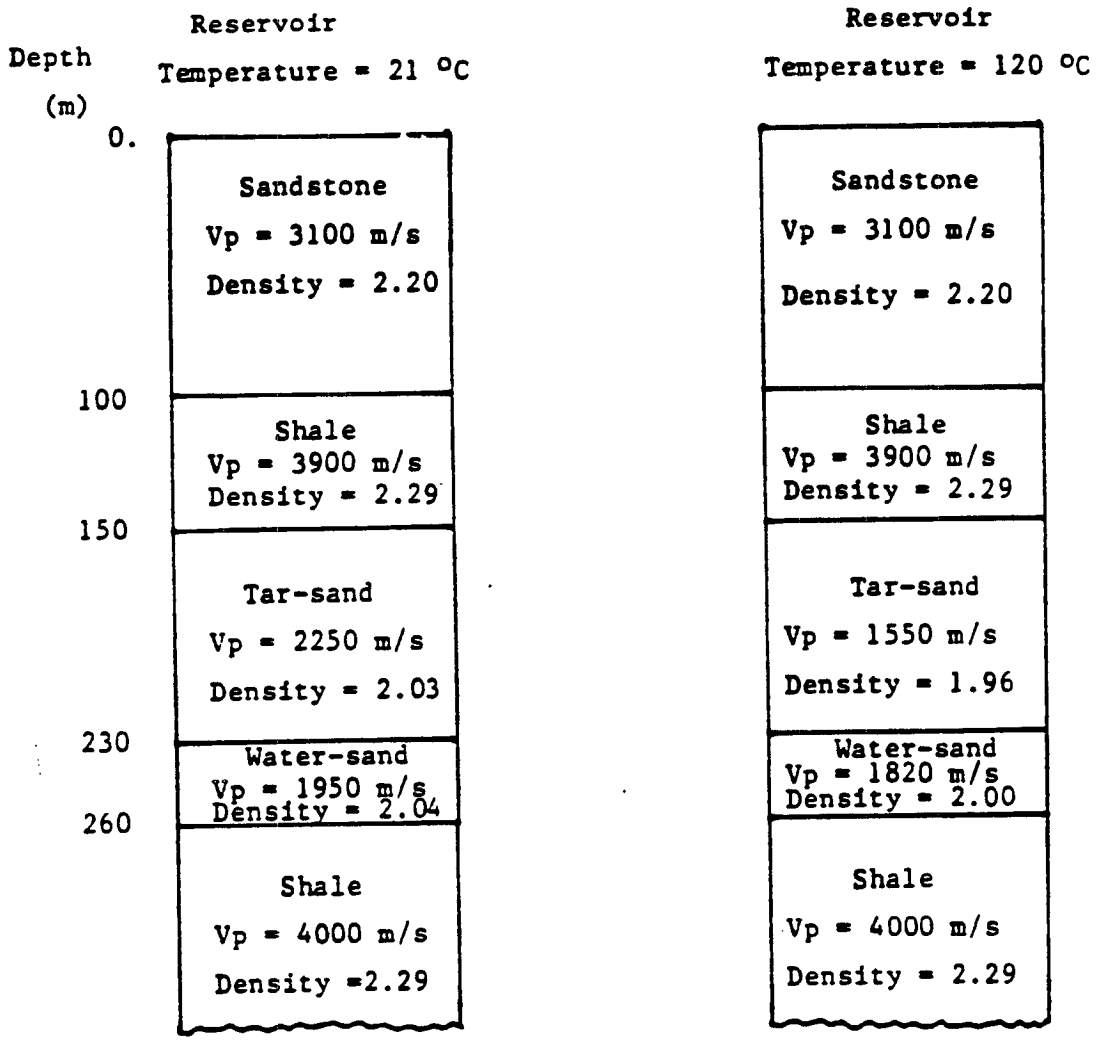
Depth
(m)
0.
100
150
230
260
Reservoir
Temperature = 21 °C
Sandstone
Vp = 3100 m/s
Density = 2.20
Shale
Vp = 3900 m/s
Density = 2.29
Tar-sand
Vp = 2250 m/s
Density = 2.03
Water-sand
Vp = 1950 m/s
Density = 2.04
Shale
Vp = 4000 m/s
Density =2.29
Reservoir
Temperature = 120 °C
Sandstone
Vp = 3100 m/s
Density = 2.20
Shale
Vp = 3900 m/s
Density = 2.29
Tar-sand
Vp = 1550 m/s
Density = 1.96
Water-sand
Vp = 1820 m/s
Density = 2.00
Shale
Vp = 4000 m/s
Density = 2.29

FIG. 27

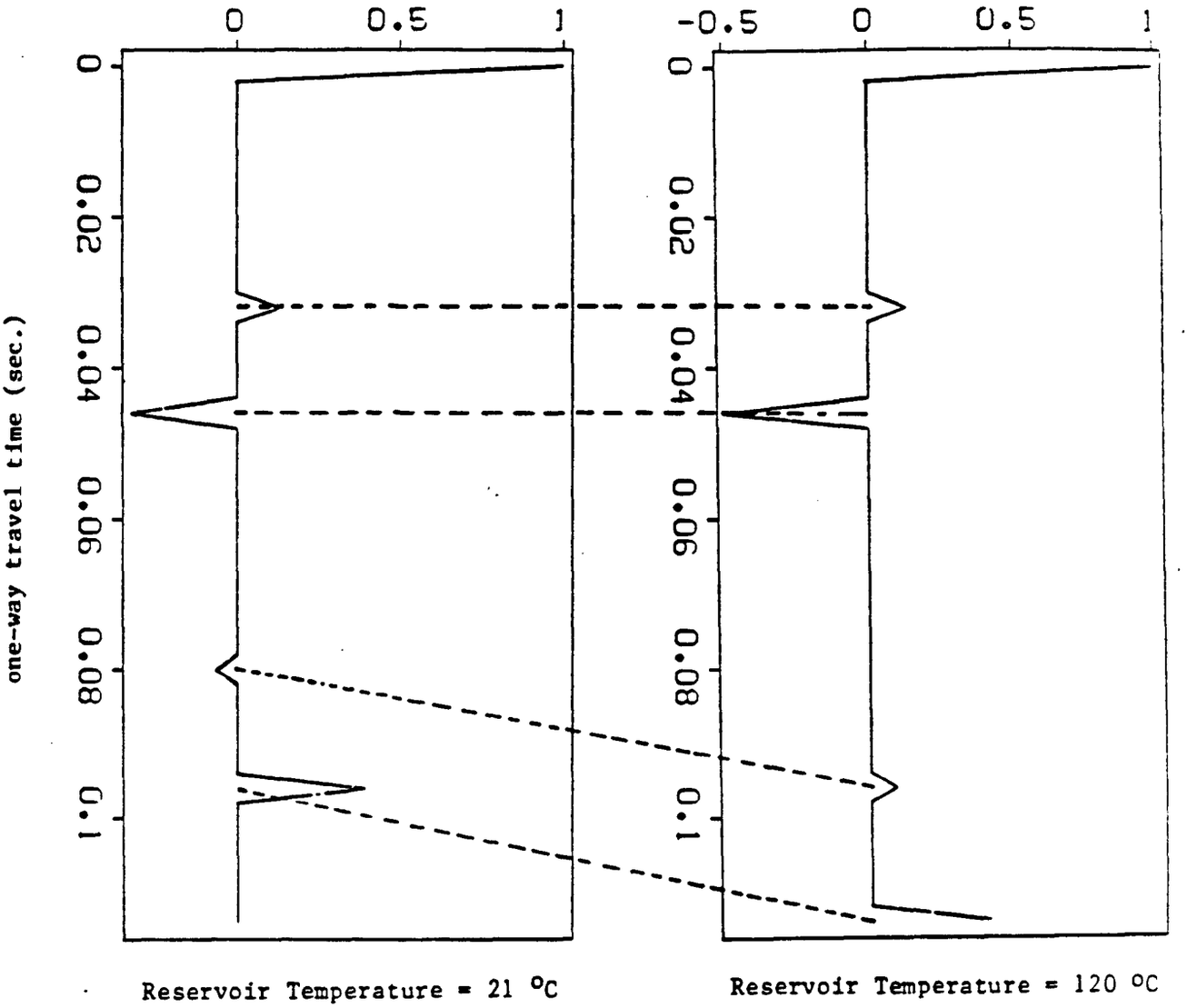
0
0.5
1
-0.5
0
0.5
1
0
0.02
0.04
0.06
0.08
0.1
one-way travel time (sec.)
Reservoir Temperature = 21 °C
Reservoir Temperature = 120 °C

FIG. 28

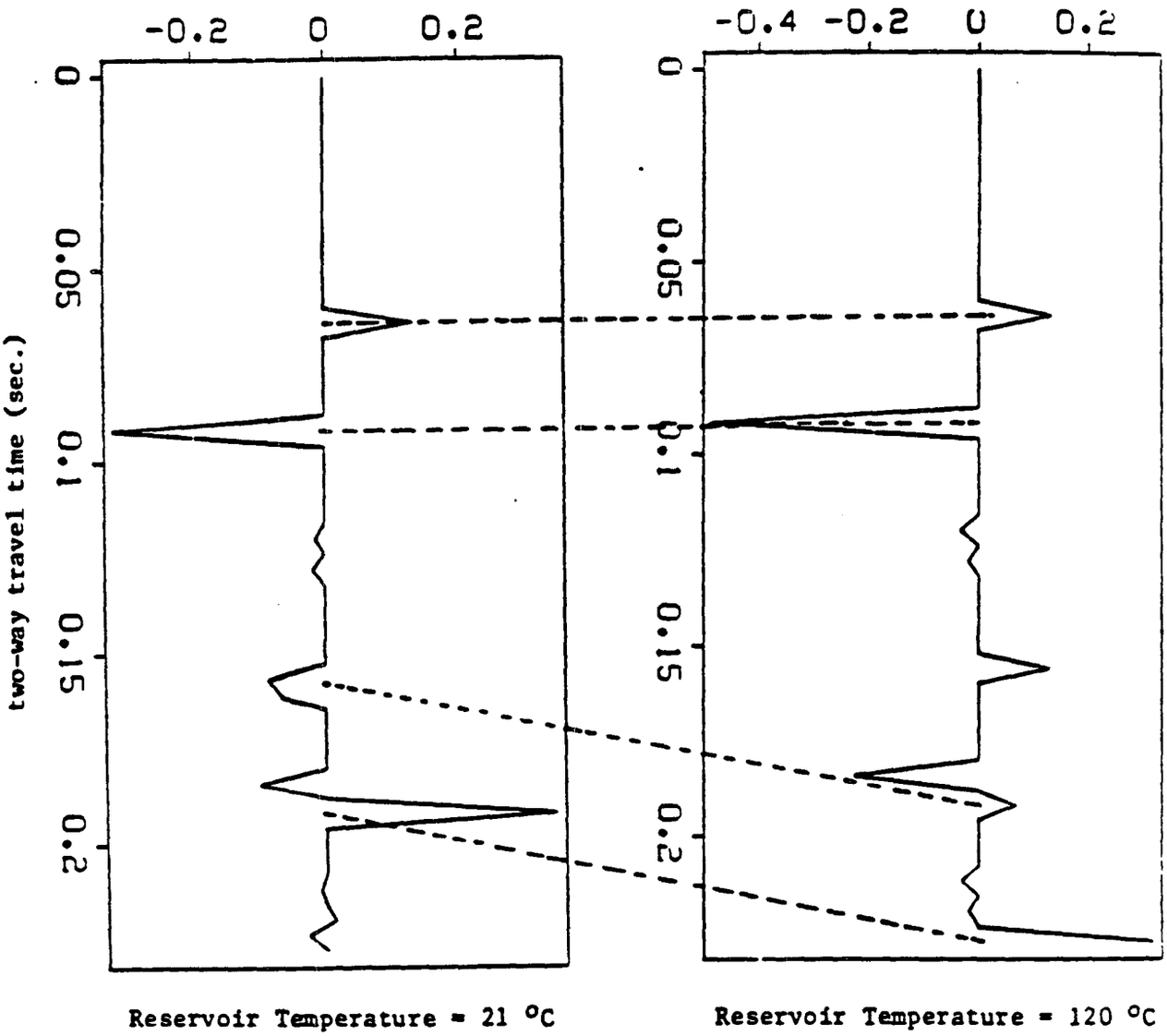
-0.2
0
0.2
-0.4
-0.2
0
0.2
0
0.05
0.1
0.15
0.2
two-way travel time (sec.)
Reservoir Temperature = 21 °C
Reservoir Temperature = 120 °C

FIG. 29

CHAPTER 6

EFFECTS OF CO_2 FLOODING ON WAVE VELOCITIES IN ROCKS WITH HYDROCARBONS

ABSTRACT

Compressional and shear wave velocities were measured in the laboratory in seven sandstones (porosities ranging from 6 to 29%) and one unconsolidated sand (porosity = 37%) saturated with n-hexadecane ($C_{16}H_{34}$) both before and after carbon dioxide (CO_2) floodings. It was found that CO_2 flooding decreased the compressional wave velocities significantly, while the shear wave velocities were less affected. The magnitude of these effects was found to be dependent on confining and pore pressures, temperature, and porosities of the rocks.

The experimental results as well as theoretical analysis shows that the decreases of compressional wave velocities caused by the CO_2 floodings may be seismically resolvable in-situ. Therefore, seismic, especially high-frequency high-resolution seismic methods may be useful in mapping and locating the CO_2 zones, tracking the movements of the CO_2 fronts, and monitoring the flooding processes in reservoirs undergoing CO_2 floodings.

INTRODUCTION

On average nearly three-quarters of hydrocarbons in place are not recoverable by conventional methods. Developments in new enhanced oil recovery (EOR) methods are becoming therefore more and more important to scientists and engineers. One of these EOR methods involves the use of high pressure carbon dioxide (CO_2) injection to

recover oils left behind by conventional recovery from reservoir rocks. Of course, not all reservoirs are suitable for CO_2 floodings or even for other EOR methods, but there is considerable current effort in the oil industry to implement large scale CO_2 injection projects, in addition to relatively smaller ongoing CO_2 injection pilots (Orr and Taber, 1984).

With the developments of better EOR methods, methods of monitoring EOR processes are also becoming important, because monitoring will open the door for the control and modification of the recovery processes as they go on. In our view, seismic methods are among the more promising monitoring methods. Seismic field survey are relatively economical and the acquisition and processing of field data are fairly routine. Furthermore, seismic monitoring does not generally require shutting in wells, does not disturb reservoir fluid flows (since seismic waves usually cause very small strains in the reservoir rocks), and does not cause precipitation chemicals in the reservoir.

The effectiveness of seismic methods in monitoring EOR processes depends on the velocity and amplitude changes of the seismic waves caused by these processes. Intuitively, the injected CO_2 will increase the compressibility and also change the density (either increase or decrease, depending on the pore pressure) of the reservoir rocks. These changes will in turn affect the propagation characteristics of the seismic waves. However, the quantitative effects of CO_2 flooding on wave characters are still not well known, and so far no laboratory or field experiments on such effects have been published. Before applying seismic methods in the field, it is necessary therefore to investigate the effects of CO_2 flooding on the seismic properties of reservoir rocks saturated with hydrocarbons in the laboratory, as reported in this paper.

Both compressional and shear wave velocities in seven sandstones of various porosities and compressional velocities in one unconsolidated sand saturated with n-hexadecane were measured both before and after CO_2 flooding, using the ultrasonic pulse transmission technique. It was found that the compressional wave velocities were

greatly decreased by the flooding with CO_2, especially when pore pressure was high. These decreases were also dependent on the porosity, temperature, effective pressure, and other properties of the rocks. The shear wave velocities were less affected by the CO_2 flooding.

The experimental results as well as theoretical analysis suggest that the decrease of the compressional wave velocity in hydrocarbon saturated rocks upon CO_2 flooding may be seismically resolvable in-situ. Therefore, it is possible that seismic methods can be used in mapping and locating the CO_2 zones, tracking the CO_2 front movement, and monitoring the CO_2 flooding processes in reservoirs undergoing such flooding processes.

EXPERIMENTS

Experimental Procedures. The ultrasonic pulse transmission method was employed in the experiments. The apparatus was basically the same as described by Wang and Nur (1986) except being modified for CO_2 injection (fig. 1).

The rock samples have a cylindrical shape of 1 in. both in diameter and in length. The cylinders' end surfaces were finely ground. The samples were jacketed by plastic tubes and sealed in the pressure vessel.

The sample under test was first subjected to confining pressure up to 20 MPa (2900 psi) to eliminate possible pressure hysteresis of the velocities. Both compressional and shear wave velocities were then measured versus confining pressure (from 0 to 20 MPa) in the dry rock sample. Afterwords, the same sample was subjected to vacuum and then saturated with de-gased n-hexadecane ($C_{16}H_{34}$). After measuring the velocities in the n-hexadecane saturated sample versus pore pressure as the confining pressure was kept constant at 20 MPa, the pore pressure was fixed at 4 MPa (580 psi) and the confining pressure at 20 MPa. The sample was then flooded with CO_2 at 7 MPa (1015 psi) through one of the two pore pressure tubings. A valve on the other pore pressure

tubing connected to the other end of the rock sample was released very gradually to let the displaced n-hexadecane out. After flooding, the pore pressure was increased by injecting CO_2 to 16 MPa (2320 psi), and the travel time of the pulse through the sample was measured as a function of decreasing pore pressure.

It was estimated that about 65 to 75 percent (volume) hydrocarbons in the pore space of the rock sample was displaced by the CO_2 flooding.

The temperature was controlled by a built-in electrical heater inside the pressure vessel and measured by a digital thermometer through a thermocouple. The travel time of the elastic wave pulse through the sample was measured with a digital oscilloscope, and the velocities (compressional and shear) were calculated by

$$V = \frac{L}{\Delta t},$$

where V and Δt are the respective velocity and travel time of the compressional or shear wave, and L is the temperature- and pressure-corrected sample length.

Properties of the Sandstones and Sand. Samples from seven different blocks of sandstones and one unconsolidated sand were used in the experiments, with porosities ranging from 6 to 37 percent. The porosities and major constituents of the rock samples are listed in table 1.

Properties of n-Hexadecane. The n-hexadecane is a normal paraffin with a formula $C_{16}H_{34}$. It is a saturated hydrocarbon with a straight-chain molecular structure. Its physical properties at room pressure are:

Molecular Weight: 226.16;

Melting Point: 18° C;

Boiling Point: 287° C;

Density: 0.773 g/cc (at 20° C);

Viscosity: 3.51 cp (at 20° C).

The compressional wave velocity in n-hexadecane as a function of temperature at room pressure is plotted in figure 2a (after Wang and Nur, 1987a). As temperature increases, the velocity decreases linearly. The slope is about -3.76 [m/sec]/ $^{\circ}C$. Figure 2b shows the pressure dependence of the velocity in n-hexadecane at various temperatures (data from Boelhouwer, 1967).

Properties of the Carbon Dioxide. The CO_2 was bought from a commercial source with a tank pressure of 5.5 MPa (800 psi). As is well known, CO_2 has a critical temperature of $31^{\circ}C$ $(87.8^{\circ}F)$ and a critical pressure of 7.4 MPa (1070 psi). Above the critical temperature, CO_2 behaves as a vapor whose density increases as pressure increases (fig. 3a). Figure 3a (from Holm and Josendal, 1982) shows the density of CO_2 as a function of both temperature and pressure. Note that at low temperature and high pressure, the density of CO_2 can be very high.

The viscosity of the CO_2 is a strong function of pressure and temperature, as shown in figure 3b (from Goodrich, 1980). However, even at high pressures, the viscosity of CO_2 is still much lower than those of most reservoir oils.

Figure 4 shows the compressional velocity in CO_2 as a function of both pressure and temperature (data from Hilsenrath, et al., 1955; Vargaftik, 1975). Above the critical temperature of CO_2, the velocity is very low and is a weak function of pressure. In contrast, below critical temperature, the velocity depends on the phase: With CO_2 in the liquid phase, the velocity is a strong function of pressure, increasing very fast as pressure increases. However, the velocity in liquid CO_2 is still much lower than that in water and most reservoir oils (fig. 2).

EXPERIMENTAL RESULTS

Both compressional (Vp) and shear (Vs) wave velocities were measured in dry (air-saturated) and n-hexadecane ($C_{16}H_{34}$) saturated rocks as a function of confining

pressure, and in the n-hexadecane saturated and CO_2-flooded rocks as a function of pore pressure.

Beaver Sandstone No. 9 (Porosity $\phi = 6\%$). Upon saturation by the hydrocarbon the Vp in Beaver sandstone No. 9 increased dramatically, especially at low effective pressures (which are approximately equal to the difference of confining and pore pressures). The increase is about 700 m/sec or 16 percent at effective pressure of 1 MPa (145 psi) and about 300 m/sec or 6 percent at 20 MPa (2900 psi) (figs. 5a, 5b).

The Vs in both dry and $C_{16}H_{34}$-saturated Beaver sandstone No. 9 sample increased as the confining pressure increased. It also increased upon hydrocarbon saturation, which is unexpected according to the Biot theory (Biot, 1956) which predicts shear velocities in porous materials should slightly decrease upon liquid saturation due to the increased overall density.

Figures 5c and 5d show the compressional and shear wave velocities, respectively, in $C_{16}H_{34}$-saturated and CO_2-flooded Beaver sandstone No. 9 sample at temperatures of 21° and 60° C. The Vp decreased markedly by the introduction of CO_2, especially at higher pore pressures, while at low pore pressures (below 6 MPa), the Vp in the CO_2-flooded rock sample is still rather high.

At temperature of 60° C, since the injected CO_2 is always in the vapor phase, there is no abrupt change in compressional wave velocities with pore pressure. At higher pore pressures, the Vp in the CO_2-flooded rock is much lower than that in the same rock saturated with $C_{16}H_{34}$. These lowered velocities are apparently caused by the presence of CO_2 in the rock pores.

The shear wave velocities at room temperature (21° C) decreased by as much as 240 m/sec or 7.3 percent at pore pressure of 16 MPa (2320 psi) upon the CO_2 flooding. Like the compressional wave case, the Vs also increased abruptly as the CO_2 in the pores transformed from liquid to vapor phase.

Beaver Sandstone No. 7 ($\phi = 9\%$). The compressional and shear wave velocities in air and in $C_{16}H_{34}$-saturated Beaver sandstone No. 7 sample were measured as a function of confining pressure. The results are very similar to the data for Beaver sandstone No. 9 sample. The saturation effect of the hydrocarbon on the Vp is also large, and the Vs is also increased by the liquid saturation (figs. 6a, 6b).

In figure 6c, the Vp in $C_{16}H_{34}$-saturated and CO_2-flooded Beaver No. 7 sample are plotted against pore pressure at 21° and 70° C, respectively. Like in the Beaver No. 9 sample, the velocities decreased uniformly with temperature increases. Injected CO_2 also decreased the Vp dramatically in the Beaver No. 7 sample, especially at higher pore pressures: At a pore pressure of 16 MPa, the decrease is 415 m/sec or 8.5 percent at room temperature (21° C), and 325 m/sec or 6.8 percent at 70° C.

At both room temperature and 70° C, the Vs in CO_2-flooded Beaver No. 7 sample is lower than that in the same sample saturated with $C_{16}H_{34}$ at higher pore pressures. While at low pore pressures (lower than 6 MPa), the Vs is higher in the CO_2-flooded sample (fig. 6d).

Beaver Sandstone No. 3 ($\phi = 14\%$). The effect of liquid hydrocarbon saturation on the Vp in Beaver No. 3 sandstone sample is smaller than that in the previous sandstones, e.g. at 21° C, hydrocarbon saturation increased the Vp by 390 m/sec or 9.0 percent at pore pressure of 14 MPa. The Vs in the $C_{16}H_{34}$-saturated Beaver No. 3 sample was still higher than those in the same sample which was CO_2-flooded (figs. 7a, 7b).

The compressional and shear wave velocities in the $C_{16}H_{34}$-saturated and CO_2-flooded Beaver No. 3 are shown in figures 7c and 7d, respectively. CO_2 flooding again decreased the Vp dramatically, especially at higher pore pressures, e.g. at pore pressure of 16 MPa, the CO_2 injection effect at room temperature deceased the Vp by 480 m/sec or 11 percent. The effect of CO_2-injection on the Vs in Beaver No. 3 sample is similar to that in Beaver No. 9 and No. 7 samples.

Berea Sandstones No. 6 (ϕ = 21%) and No. 4 (ϕ = 20%). The compressional and shear wave velocities in dry and $C_{16}H_{34}$-saturated Berea No. 6 were measured as a function of confining pressure (figs. 8a, 8b). The Vp is also very much pressure-dependent in the measured range, but the liquid saturation effect is smaller.

Figure 8c shows that the Vp at both 21° and 60° C has similar pore pressure response in $C_{16}H_{34}$-saturated Berea sandstone No. 6 sample. CO_2 flooding enhanced the pore pressure dependence of the velocities. The Vp is greatly affected by the CO_2 flooding: At 21° C, the CO_2 flooding decreased the Vp by 275 m/sec or 7.7 percent at pore pressure of 16 MPa.

All the Vs curves cluster together in figure 8d, which means that CO_2 flooding basically does not affect the shear velocities in this sandstone. However, temperature has a systematic, though small, effect on the shear velocities. Also note that at lower pore pressures (higher effective pressure), Vs is higher in the flooded than in the $C_{16}H_{34}$-saturated rock at the same temperature, and the opposite is true at higher pore pressures (lower effective pressures).

Figures 9a and 9b show the compressional and shear wave velocities, respectively, in Berea sandstone No. 4 sample after CO_2 flooding as a function of pore pressure. Basically, they are similar to figures 8a through 8d: Large decreases in Vp are caused by the effect of CO_2 flooding, while the Vs is not much affected.

Conotton Sandstone No. 5 (ϕ = 24%) and Boise Sandstone No. 3 (ϕ = 29%). Both Conotton and Boise sandstones have high porosity. The liquid saturation effect on the Vp is relatively small. The hydrocarbon saturation increased the Vp in both sandstones, and this increase became smaller as confining pressure increased (figs. 10a, 10b, 11a, 11b).

The Vs is again higher in $C_{16}H_{34}$-saturated than in air-saturated rocks at low confining pressures. At higher confining pressures, the opposite is true.

As observed in other sandstones, CO_2 flooding also decreased the Vp largely in the Conotton No. 5 sample (fig. 10c). Furthermore, pore pressure dependence of the Vp is enhanced by the flooding. The Vs behaves very similarly to those in the Berea sandstones, and the difference between the shear velocities in the hydrocarbon-saturated and in CO_2-flooded rock sample is small (fig. 10d).

Since the Boise sandstone has very high porosity, hydrocarbon saturation increased the Vp by only about 120 m/sec or 3.8 percent. The Vs is always lower in the $C_{16}H_{34}$-saturated than in the dry sample. The CO_2 flooding effect on the Vp in Boise sandstone is basically similar at all the pore pressures of the measured range (fig. 11c). The CO_2 flooding also decreased the Vp. However, the amount of decrease is rather small. The Vs in the Boise No. 3 sample plotted in figure 11d behaves similarly to those in the Berea sandstones.

Ottawa Unconsolidated Sand ($\phi = 37\%$). The compressional wave velocities in the Ottawa sand saturated with $C_{16}H_{34}$ are very inert to pore pressure changes (fig. 12). CO_2 flooding dramatically decreased the Vp, by about 470 m/sec or 24 percent at effective pressure of 20 MPa (zero pore pressure). This effect is even larger at lower effective pressures. We were unable to measure the Vs in the unconsolidated sand, but we believe that CO_2 flooding would have very little effect on it.

DISCUSSIONS

It was shown in the previous section that injecting CO_2 had large effects on decreasing the compressional wave velocities in sandstones and sand saturated with hydrocarbons. In this section, we discuss the influence of various factors such as porosity, saturation, temperature, and pressure on the velocities in rocks with CO_2 and hydrocarbons.

Basic Concepts. The compressional (Vp) and shear (Vs) wave velocities in a homogeneous and isotropic elastic material are defined respectively as

$$Vp = \sqrt{\frac{K + \frac{4}{3}\mu}{\rho}} \tag{1}$$

$$Vs = \sqrt{\frac{\mu}{\rho}}, \tag{2}$$

where K and μ are the bulk and shear moduli, respectively, and ρ is the density of the material.

The Gassmann equation (Gassmann, 1951) relates the bulk modulus of the saturated rock to the properties of the rock and the pore fluid:

$$K = K_d + \frac{(1 - K_d/K_s)^2}{\phi/K_f + (1 - \phi)/K_s - K_d/K_s^2} \tag{3}$$

where K_d, K_s, and K are the bulk moduli of the dry, solid frame of, and fluid-saturated rock, respectively; K_f is the bulk modulus of pore fluid; ϕ is porosity.

Effects of Saturation and Porosity. From equations (1) and (3), one can see that the Vp in a fluid saturated rock depends on the properties of both the rock and pore fluid. The Vp of a gas-saturated rock is usually close to that of the dry rock, because the bulk modulus (incompressibility) of gas is usually very low. While the bulk modulus of a liquid is often comparable to that of the rock frame, liquid saturation to a rock sample can increase Vp markedly, despite the overall density increase of the rock.

When a rock sample is partially liquid-saturated, the bulk modulus of the rock is about the same as that of the dry rock, but the overall density is higher, so that the Vp can be even lower than that of the dry (gas-saturated) rock. However, whether the Vp increases or decreases in a rock upon partial liquid saturation is dependent on the pore structure and porosity of the rock. In low porosity, high crack content rocks like the Beaver sandstone samples, the liquid in the partially saturated rocks usually

occupies the cracks and thin pores, while the gas occupies the larger pores. This pattern of pore fluid distribution causes the bulk moduli of the rocks to be higher. Furthermore the density increase due to the partial liquid saturation is smaller in low porosity rocks. These combined effects in turn yield higher compressional velocities (eq. 1). This is exactly the case for the Vp in CO_2 flooded Beaver sandstone samples at pore pressures below 6 MPa (figs. 5c, 6c, 7c).

The phase transition of the injected CO_2 affected both the Vp and Vs in the low porosity Beaver sandstone samples (figs. 5, 6, 7). When the injected CO_2 is in the liquid phase, its density is very high (fig. 4a), even higher than that of n-hexadecane, but its bulk modulus is still low (fig. 5). Therefore, the high density of the liquid CO_2 in the rock pores is responsible for the low Vp and Vs in the flooded rocks at pore pressures higher than 6 MPa. Above the critical temperature of the CO_2 (31° C), the density of CO_2 increases smoothly with pressure, and the velocities in turn also change smoothly with pore pressure, as shown in figures 5 through 9.

The shear wave velocities in the CO_2-flooded Beaver samples are lower than those in $C_{16}H_{34}$-saturated rocks at high pore pressures, but higher at low pore pressures (figs. 5d, 6d, 7d). This is caused by the combined effects of density, viscosity, and pore pressure. At low pore pressures, higher Vs is caused by the low density of the CO_2. At higher pore pressures, the higher Vs in the hydrocarbon saturated samples is caused by the higher viscosity and lower density of the n-hexadecane in the rock pores (Wang and Nur, 1986).

Upon CO_2 injection, the hydrocarbon-bearing rock sample is partially saturated with CO_2 with compressibility close to air. Therefore, the effect of CO_2 injection on the compressional velocities should be close to that of partial gas saturation, which is dependent on the porosity of the rocks (Gregory, 1976).

The effect of CO_2 flooding on the compressional wave velocities in the rocks at different pore pressures is plotted as a function of porosity in figures 13a, b. In

consolidated sandstones, increasing rock porosity decreases the CO_2 effect on the compressional velocities. In low-porosity sandstones such as the Beaver samples, CO_2 causes decreases of Vp by up to 440 m/sec (or 10.1%), while in high-porosity sandstones like the Boise sample, the decrease is only around 140 m/sec (or 4.4%). In the unconsolidated Ottawa sand, CO_2 decreased the Vp by up to 560 m/sec (or 30%), even though the porosity of the sand is high. According to the Gassmann equation (eq. 3), as the porosity increases, if the bulk modulus of the dry rock does not decrease dramatically fast (which is generally true; see Han, 1987), the difference between the compressional wave velocities in dry and fluid-saturated rocks will decrease due to the increased density and fluid content of the saturated rock. That is, for low-porosity rocks, full liquid saturation increases the bulk modulus of the rock greatly but not much the density, which in turn increases the Vp markedly. For high-porosity rocks, because the bulk modulus of the pore fluid is usually much lower than that of the rock frame, full liquid saturation has a lower effect on the increase of the bulk modulus of the liquid-saturated rock due to the increased liquid content, but a larger effect on the increase of the bulk density of the rock, which in turn does not increase the Vp as much.

Not only the fluid content and density contribute to the liquid saturation effect on compressional velocities, but also many other factors such as crack concentration, pore shapes, pore fluid properties, and so on. For instance, high crack content of the rock and high viscosity of the pore fluid may increase the shear modulus of the saturated rock which contributes to both Vp and Vs (Wang and Nur, 1986).

The unconsolidated dry Ottawa sand is highly compressible (low compressional velocity) in comparison with the consolidated sandstones. Liquid saturation will greatly increase its bulk modulus and hence the Vp (eq. 3). Although liquid saturation also increases the bulk density, the increase in bulk modulus plays a dominant role in unconsolidated sands.

Comparison of Flooding and Saturation Effects. The effects of CO_2 flooding and hydrocarbon saturation on compressional wave velocities at $21^\circ C$ are summarized in table 2. The effect of hydrocarbon saturation is about the same as that of CO_2 flooding on the compressional wave velocities in all the rock samples measured. After the rock is CO_2 flooded, it essentially becomes partially hydrocarbon saturated. Besides the porosity and crack concentration of the rock, the difference between the Vp in fully and partially hydrocarbon saturated rocks may also be dependent on the degree of partial saturation. The effect of CO_2 injection is in turn dependent on the amount of hydrocarbon displaced from the rock. In the experiments, it was estimated that around 65 to 75 percent oil in place had been displaced by the CO_2.

Effect of Temperature. The effect of temperature on wave velocities in both dry and hydrocarbon-saturated rocks were discussed elsewhere (Wang and Nur, 1986, 1987b). Generally speaking, increasing temperature by $100^\circ C$ in dry sandstones and sands will decrease the compressional wave velocities by about 2 to 8 percent, depending upon properties such as porosity, crack concentration, and clay content, of the rocks. The decrease in the velocities is believed to be caused by the softening of the rock frame and grains and increase in porosity as the result of different thermal expansions of the grains and cement (Kern, 1982; Wang and Nur, 1986).

The compressional wave velocities usually have larger decreases in liquid-saturated than in dry rocks as the temperature increases. That is, liquid saturation enhances the temperature dependence of Vp in rocks (Wang and Nur, 1987b). This enhancement may partly be caused by the fact that the Vp in the pore fluid alone is temperature dependent.

The temperature effect is usually larger on Vs than on Vp, which means that increasing temperature mainly decreases the shear modulus of the rock. This phenomenon can in fact be explained by the "lubrication" effect. As the temperature increases, the rock frame (or grains) softens and expands, which makes the sliding

between grains (or particles) easier (the friction decreases). This effect is analogous to that the grains (or particles) of the rock being "lubricated." In liquid-saturated rocks, additional decreases in shear velocities as temperature increases may be caused by the more pronounced lubrication effect caused by the pore fluid, the decreases of pore fluid viscosity, and probably some chemical and/or physical interactions between the rock frame and pore fluid. Such effects on the Vs also contribute to the Vp in the saturated rocks (eq. 1).

Pore pressure may also affect the temperature dependence of the velocities. Because the effect of pore pressure is to keep the pores and cracks open in rocks, higher pore pressure makes the porous rock contain more fluid and creates more contact areas between the rock frame and pore fluid, and in turn enhances the temperature dependence of the velocities. In contrast, the confining pressure has the opposite effect on the temperature dependence of the velocities.

As stated earlier, CO_2 has a critical temperature of about $31^\circ C$ beyond which it is always in vapor phase. At $21^\circ C$ (room temperature), there exists a pronounced effect of CO_2 phase transition on the velocities in low-porosity rocks, while this effect vanishes at temperatures higher than the critical temperature of CO_2. Therefore, temperature will affect the CO_2 flooding effect on the compressional wave velocities in rocks, especially in the pore pressure range of 6 to 10 MPa. The effect of temperature on the velocities in the CO_2-flooded rocks may be caused by the CO_2 properties, the temperature effect on the rock frame, and other factors, but we believe that the CO_2 density change with temperature may play the dominant role, especially in the pore pressure range of 6 to 10 MPa.

Effect of Pressures. The effect of confining pressure (at constant pore pressure) tends to close the thin cracks and penny-shaped pores and make better contact between particles (grains and cement) in the rock. Therefore both Vp and Vs increase as confining pressure increases. The degree of increase in the velocities is dependent

mainly on crack concentration, porosity, pore structure and geometry, mineral composition of the rock, pore fluid properties, and interactions between the rock frame and pore fluid.

Generally, the velocities are highly pressure-dependent in low-porosity rocks which usually have a large content of thin cracks. When the rock is liquid saturated, the pressure dependence of the velocities is lowered due to the resistance of the pore fluid to crack closures. Hence the liquid saturation effect, and further the CO_2 flooding-effect, on the compressional velocities is smaller at higher confining pressures.

For high porosity rocks, the confining pressure (at constant pore pressure) dependence of the velocities is smaller because high-porosity rocks usually contain very little amount of thin cracks but a lot of round pores and cavities. As confining pressure increases, the resistance of the pore fluid to pore closures in the saturated rock does not contribute to the velocity change much since the round pores or cavities in the dry rock are already hard to deform. Therefore, in most high porosity (usually higher than 25%) consolidated rocks, the velocity curves for dry and liquid saturated rocks are almost parallel in moderate pressure ranges (usually between 0 and 30 MPa) (figs. 10 and 11).

In contrast to confining pressure, pore pressure tends to keep the cracks and pores open, hence it has generally the opposite effect on velocities. In addition, pore pressure reinforces the effect of pore fluid properties on the velocities. In CO_2-bearing rocks, increasing pore pressure increases the density of CO_2 dramatically, which in turn greatly decreases the velocities. At temperatures lower than the critical temperature of CO_2 ($31^\circ C$), the phase transition of CO_2 caused by pore pressure changes greatly affects the velocities due to sudden changes in the density of CO_2.

Pore pressure also creates higher internal surface areas of the rock which will enhance the interactions (chemical and/or physical) between the rock frame and pore fluid. Also, high pore pressure would speed up the chemical interactions, if any,

between the rock and its pore fluid.

Theoretical Calculations. The Gassmann equation (eq. 3) is often used to calculate low-frequency wave velocities in porous materials saturated with fluids if the porosity and other parameters are known. The calculation results are generally fairly representative for velocities in sandstones saturated with light fluids at seismic wave frequencies. To further confirm the experimental results, we calculated the compressional wave velocities using the Gassmann equation in two sandstones (Beaver No. 9 and Berea No. 6) saturated with both $C_{16}H_{34}$ and CO_2 as a function of pore pressure.

Figure 14 shows that the calculated Vp in Beaver No. 9 sample saturated with CO_2 is about 9 percent lower than that saturated with $C_{16}H_{34}$ at pore pressures higher than 6 MPa (870 psi). In Berea No. 6 sample, such a velocity difference is about the same in percentage (fig. 15). The lower compressional velocities in CO_2-saturated sandstones are caused by both the low velocity and high density of CO_2.

The theoretically calculated effect of CO_2 injection on compressional wave velocities in hydrocarbon saturated sandstones is about the same as that measured in the experiments. Furthermore, both the experimental and theoretical results reveal that such a CO_2 effect may be seismically detectable. Therefore, seismic methods may be used in monitoring CO_2 flooding processes in-situ.

APPLICATION:

Seismic Monitoring of CO_2 Floodings

The capability of using seismic methods to monitor an enhanced oil recovery (EOR) process depends solely on the velocity and/or amplitude changes of the seismic waves caused by the process. The amplitude changes are usually difficult to measure accurately, either in the laboratory or in the field. In contrast, velocity changes can be easily detected with high accuracy.

The experimental results showed that Vp decreased dramatically as the rocks were flooded by CO_2 (figs. 13a, 13b), especially at high pore pressures. The decreased velocities in reservoir rocks upon CO_2 flooding may cause travel-time delay of seismic waves. Therefore, seismic methods, especially high-frequency high-resolution seismic methods, can be used in monitoring CO_2 flooding processes, or in detecting CO_2 zones in reservoirs subject to such floodings.

According to the experimental results, the injected CO_2 forms low velocity zones. Therefore, careful field survey using seismic methods such as reflection, vertical seismic profiling (VSP), and borehole seismic methods, can locate or map the CO_2 zones or fronts. And by such successive surveys, it is also possible to monitor the movement of the CO_2 zones as a function of time and hence to generate 4-D seismic profiles of the reservoir.

The experimental results show that the largest effect of CO_2 on the compressional wave velocities occurs at pore pressures higher than 6 MPa. In the field, the injection pressure of CO_2 is usually around or higher than 7 MPa (1015 psi), depending on the reservoir temperature, which suggests that seismic methods can be applied for monitoring purpose.

Velocities in liquid- or partially liquid-saturated rocks have been proven to be frequency dependent (dispersive) (Spencer, 1981; Murphy, 1982; Winkler, 1985; Han, 1987). However, for the purpose of monitoring, we are interested in the relative changes of the velocities caused by the flooding effect, not the absolute values. The results of the theoretical calculations using the Gassmann equation show dispersions of Vp are about the same in the sandstones before and after the CO_2 injection (figs. 14, 15). Therefore, the effect of CO_2 flooding on the velocities measured in the laboratory should also be seen in-situ at seismic and sonic frequencies.

SUMMARY AND CONCLUSIONS

Our laboratory investigations found that CO_2 flooding had a marked effect on compressional wave velocities in sandstones and sand saturated with hydrocarbons. CO_2 flooding decreased the compressional wave velocities by about 4 to 11 percent in well consolidated sandstones and by over 25 percent in unconsolidated sand at the conditions described in this paper. The absolute amount of Vp decrease caused by CO_2 floodings is close to, or even higher than, that caused by hydrocarbon saturation of the rocks.

Large decreases in compressional wave velocities in rocks upon CO_2 floodings are believed to be caused by lowered bulk modulus and increased density of the rock-hydrocarbon-CO_2 aggregate because CO_2 has very high compressibility and high density.

The decreases in compressional wave velocities are dependent on pore pressure, temperature, porosity, and other factors. Increasing pore pressure (at constant confining pressure) not only keeps the pores and cracks open and cancels out some of the confining pressure effect, but also increases the CO_2 density. Therefore, higher pore pressures cause larger decreases in both the compressional and shear wave velocities.

At room temperature (21° C), the CO_2 phase transition has pronounced effect on the velocities (both Vp and Vs), while at temperatures higher than the critical temperature (31° C) of CO_2, such effect vanishes due to the continuous change of the pore fluid properties with pressure.

In well-consolidated sandstones, increasing porosity tends to decrease the CO_2 effect. The decreased effect in high-porosity rocks is caused by the increased fluid content and overall density of the rocks. However, in the unconsolidated sand, the flooding effect is very large, even though the porosity of the sand is very high, because the bulk modulus of the sand frame is low.

Theoretical analysis on two of the sandstones showed that in the seismic frequency range, the decrease in compressional wave velocities caused by CO_2 floodings is about the same as that observed in the experiments, which means that the experimental results can be directly applied in-situ.

The dramatic decreases in compressional wave velocities caused by CO_2 floodings make it possible to use seismic methods in mapping the CO_2 zones, tracking the CO_2 front movements, and so monitoring the flooding processes in reservoirs subject to CO_2 flooding processes. A success in such exercises will allow the possibility for the field engineers to control and/or modify the flooding processes accordingly, and ultimately, to produce more oil. benefited from the discussions with Dr. F.M. Orr of Stanford University.

APPENDIX: DATA LISTING

Table A1 lists the measured compressional and shear wave velocities in $C_{16}H_{34}$-saturated and CO_2-flooded rocks as a function of pore pressure (confining pressure was fixed at 20 MPa) at 20° C. Shown in table A2 are the velocities in four of the rocks at higher temperatures.

REFERENCES

Biot, M. A., 1956. Theory of propagation of elastic waves in a fluid-saturated porous solid. I. Low frequency range, II. Higher frequency range. J. Acoust. Soc. Am., 28, 168-191.

Boelhouwer, J. W. M., 1967. Sound velocities in and adiabatic compressibilities of liquid alkanes at various temperatures and pressures. Phisica, 34, 484-492.

Gassmann, F., 1951. Elastic waves through a packing of spheres. Geophysics, 16, 673-685.

Goodrich, J. H., 1980. Review and analysis of past and ongoing carbon dioxide injection field tests. Paper SPE/DOE 8832, presented at the first joint DOE/SPE

Symposium on Enhanced Oil Recovery, Tulsa.

Gregory, A. R., 1976. Fluid saturation effects on dynamic elastic properties of sedimentary rocks. Geophysics, 41, 895-921.

Han, D., 1987. Effects of porosity and clay content on acoustic properties of sandstones and unconsolidated sediments. Ph.D. thesis, Stanford University.

Hilsenrath, J. et al, 1955. Tables of thermal properties of gases. National Bureau of Standards Circular 564.

Holm, L. W. and V. A. Josendal, 1982. Effect of oil composition on miscible-type displacement by carbon dioxide. SPEJ (Feb, 1982), 87-98.

Kern, H., 1982. Elastic wave velocity in crustal and mantle rocks at high pressure and temperature: the role of the high-low quartz transition and of dehydration reactions. Phys. Earth Plan. Inter., 29, 12-23.

Murphy, W. F., III, 1982. Effects of microstructure and pore fluids on the acoustic properties of granular sedimentary materials. Ph.D. thesis, Stanford University.

Orr, F. M. and J. J. Taber, 1984. Use of carbon dioxide in enhanced oil recovery. Science, 224, 563-569.

Spencer, J. W., 1981. Stress relaxations at low frequencies in fluid-saturated rocks: attenuation and modulus dispersion. J. Geophys. Res., 86, 1803-1812.

Vargaftik, N. B., 1975. Tables on the thermophysical properties of liquids and gases. Hemisphere Pub. Co., Washington.

Wang, Z. and A. Nur, 1986. Effect of temperature on wave velocities in sandstones and sand with heavy hydrocarbons. SEG expanded abstract, 3-5; presented at the 56th Annual Meetings and Expositions, Houston.

Wang, Z. and A. Nur, 1987a. Ultrasonic wave velocities in hydrocarbons. Stanford Rock Physics Project, 31, 59-118.

Wang, Z. and A. Nur, 1987b. Wave velocities in pure hydrocarbon saturated rocks and sand. Stanford Rock Physics Project, 31, 119-158.

Winkler, K. W., 1985. Dispersion analysis of velocity and attenuation in Berea sandstone. J. Geophys. Res., 90, 6793-6800.

FIGURE CAPTIONS

Figure 1. Sketch of the experimental apparatus.

Figure 2. Compressional wave velocities in n-hexadecane ($C_{16}H_{34}$) as a function of

temperature (a) and pressure (b).

Figure 3. Pressure and temperature dependences of the CO_2 density (a) and viscosity (b).

Figure 4. Compressional wave velocities in CO_2 as a function of pressure at various temperatures.

Figure 5. Compressional (a) and shear (b) velocities in dry and n-hexadecane saturated Beaver sandstone No. 9.
Compressional (c) and shear (d) velocities in n-hexadecane saturated and CO_2 flooded Beaver sandstone No. 9 vs. pore pressure.

Figure 6. Compressional (a) and shear (b) velocities in dry and n-hexadecane saturated Beaver sandstone No. 7.
Compressional (c) and shear (d) velocities in n-hexadecane saturated and CO_2 flooded Beaver sandstone No. 7 vs. pore pressure.

Figure 7. Compressional (a) and shear (b) velocities in dry and n-hexadecane saturated Beaver sandstone No. 3.
Compressional (c) and shear (d) velocities in n-hexadecane saturated and CO_2 flooded Beaver sandstone No. 3 vs. pore pressure.

Figure 8. Compressional (a) and shear (b) velocities in dry and n-hexadecane saturated Berea sandstone No. 6.
Compressional (c) and shear (d) velocities in n-hexadecane saturated and CO_2 flooded Berea sandstone No. 6 vs. pore pressure.

Figure 9. Compressional (a) and shear (b) velocities in n-hexadecane saturated and CO_2 flooded Berea sandstone No. 4 vs. pore pressure.

Figure 10. Compressional (a) and shear (b) velocities in dry and n-hexadecane saturated Conotton sandstone No. 5.
Compressional (c) and shear (d) velocities in n-hexadecane saturated and CO_2 flooded Conotton sandstone No. 5 vs. pore pressure.

Figure 11. Compressional (a) and shear (b) velocities in dry and n-hexadecane saturated Boise sandstone No. 3.
Compressional (c) and shear (d) velocities in n-hexadecane saturated and CO_2 flooded Boise sandstone No. 3 vs. pore pressure.

Figure 12. Compressional velocities in n-hexadecane saturated and CO_2 flooded Ottawa unconsolidated sand as a function of pore pressure.

Figure 13. Effect of CO_2 flooding on the compressional velocities in n-hexadecane saturated rocks as a function of porosity at different pore pressures. (a), absolute decreases; (b), in percentage.

Figure 14. Theoretically calculated compressional wave velocities using the Gassmann equation in Beaver No. 9 sandstone sample with CO_2 and n-hexadecane, respectively.

Figure 15. Theoretically calculated compressional wave velocities using the Gassmann equation in Berea No. 6 sandstone sample with CO_2 and n-hexadecane, respectively.

Table 1. Porosities and major compositions of the rocks.

Rock	ϕ	Composition	Rock	ϕ	Composition
Beaver No.9	6	mainly quartz	Beaver No.7	9	mainly quartz
Beaver No.3	14	mainly quartz	Berea No.4	20	quartz and 7% feldspar
Berea No.6	21	quartz and 7% feldspar	Conotton No.5	24	mainly quartz
Boise No.3	29	quartz and 44% feldspar	Ottawa sand	37	quartz grains

Table 2. Effects of CO_2 flooding and hydrocarbon saturation on compressional wave velocities at 21° C.

		Pd = 6 MPa				Pd = 10 MPa				Pd = 14 MPa			
		Flooding		Saturation		Flooding		Saturation		Flooding		Saturation	
Rock	ϕ	ΔV	-%	ΔV	+%	ΔV	-%	ΔV	+%	ΔV	-%	ΔV	+%
Be.9	6	405	8.0	454	9.0	368	7.2	394	7.8	364	7.1	351*	6.9
Be.7	9	405	8.2	496	10.0	398	8.0	458	9.2	384	7.7	430	8.6
Be.3	14	444	10.1	390	9.0	369	8.4	306	7.0	279	6.3	266	6.0
Ber.4	20	245	6.8	..	..	172	4.6	..	..	127	3.4	..	..
Ber.6	21	302	8.4	405	11.2	203	5.5	343	9.2	..	..	271	7.2
Con.5	24	231	7.1	..	..	173	5.3	210*	6.4	146	4.4	160	5.0
Boi.3	29	144	4.4	109	3.3	121	3.7	112*	3.4	110	3.3	120*	3.6
Ott.	37	553	29.4	..	..	513	27.1	..	..	496	26.0	..	..

* -- interpolated between two nearest data points.

ϕ -- porosity, ΔV -- velocity change, -% -- percent decrease, +% -- percent increase,
Pd -- differential pressure = confining pressure - pore pressure.

Units: ΔV -- Meters/second, ϕ -- percent.

Table A1. Compressional and shear velocities in $C_{16}H_{34}$ saturated and CO_2 flooded rocks and sand.

Beaver No. 9 ($\phi = 6\%$)						Beaver No. 7 ($\phi = 9\%$)					
$C_{16}H_{34}$ Saturated			CO_2 Flooded			$C_{16}H_{34}$ Saturated			CO_2 Flooded		
Pp	Vp	Vs	Pp	Vp	Vs	Pp	Vp	Vs	Pp	Vp	Vs
16	5021	3280	16	4579	3042	16	4886	3130	16	4471	2987
14	5041	3292	14	4636	3082	14	4914	3167	14	4509	3029
12	5060	3313	12	4686	3122	12	4942	3187	12	4548	3075
10	5080	3335	10	4712	3153	10	4970	3206	10	4572	3111
8	5100	3356	8	4729	3176	8	4979	3230	8	4588	3141
6	5110	3378	6	4746	3199	6	4988	3250	6	4604	3167
4	5120	3396	3.8	4992	3318	4	5007	3266	...	...	...
2	5130	3404	1.6	5041	3378	2	5017	3278	...	...	...
0	5140	3422	0	5060	3413	0	5024	3294	0.5	4859	3315

Units: Vp, Vs - Meters/second, Pp - MPa. Temperature = 21° C.

Table A1 (continued). Compressional and shear velocities in $C_{16}H_{34}$ saturated and CO_2 flooded rocks and sand.

Beaver No. 3 ($\phi = 14\%$)						Conotton No. 5 ($\phi = 24\%$)					
$C_{16}H_{34}$ Saturated			CO_2 Flooded			$C_{16}H_{34}$ Saturated			CO_2 Flooded		
Pp	Vp	Vs	Pp	Vp	Vs	Pp	Vp	Vs	Pp	Vp	Vs
16	4354	2787	16	3874	2688	16	3226	...	16	2982	2097
14	4375	2802	14	3931	2735	14	3245	...	14	3014	2105
12	4383	2832	12	3979	2787	12	3264	2189	12	3064	2130
10	4390	2863	10	4021	2817	10	3272	2198	10	3099	2163
8	4405	2879	8	4065	2848	8	3295	2215	8	3145	2180
6	4427	2898	5.8	4148	2872	6	3323	2233	6	3177	2209
4	4434	2910	4	4283	2904	4	3343	2251	4	3207	2242
2	4449	2927	2.3	4332	2930	2	3355	2270	1.6	3245	2289
0	4457	2936	0	4361	2960	0	3363	2285	0	3283	2308

Units: Vp, Vs - Meters/second, Pp - MPa. Temperature = 21° C.

Table A1 (continued). Compressional and shear velocities in $C_{16}H_{34}$ saturated and CO_2 flooded rocks and sand.

Berea No. 4 ($\phi = 20\%$)						Berea No.6 ($\phi = 21\%$)					
$C_{16}H_{34}$ Saturated			CO_2 Flooded			$C_{16}H_{34}$ Saturated			CO_2 Flooded		
Pp	Vp	Vs	Pp	Vp	Vs	Pp	Vp	Vs	Pp	Vp	Vs
16	...	...	16	3319	2011	16	3556	2080	16	3281	2026
14	3626	2199	14	3381	2113	14	3602	2136	14	3300	2080
12	3685	2236	12	3446	2190	12	3665	2214	12	3445	2153
10	3731	2264	10	3559	2236	10	3714	2259	10	3511	2231
8	3757	2292	8	3607	2264	7.5	3765	2298	7.5	3556	2278
6	3783	2322	6	3656	2292	5	3791	2336	6.5	3579	2297
4	3810	2352	4	...	...	4	...	...	5.1	3650	2336
2	3837	2373	2	...	...	2.5	3822	2362	3.2	3724	2372
1	3848	2383	1	...	...	1	...	...	1.1	3775	2407
0	...	...	0	3757	2405	0	3844	2382	0.1	3786	2417

Units: Vp, Vs - Meters/second, Pp - MPa. Temperature = 21° C.

Table A1 (continued). Compressional and shear velocities in $C_{16}H_{34}$ saturated and CO_2 flooded rocks and sand.

Boise No. 3 ($\phi = 29\%$)						Ottawa Sand ($\phi = 37\%$)			
$C_{16}H_{34}$ Saturated			CO_2 Flooded			$C_{16}H_{34}$ Saturated		CO_2 Flooded	
Pp	Vp	Vs	Pp	Vp	Vs	Pp	Vp	Pp	Vp
16	3278	2159	16	...	2117	16	1850	15	1276
14	3288	2171	14	3144	2133	14	1878	14	1325
12	3294	2185	12	3162	2159	12	1884	12	1353
10	3302	2200	10	3181	2177	10	1891	10	1378
8	3306	2212	8	3200	2194	8	1898	8	1397
6	3310	2221	6.8	3200	2194	6	1908	7	1404
4	3314	2231	5.2	3200	2221	4	1919	6	1412
2	3319	2240	2	3219	2259	2	1934	4	1456
0	3319	2247	0	3219	2288	0	1948	0	1472

Units: Vp, Vs - Meters/second, Pp - MPa. Temperature = 21° C.

Table A2. Compressional and shear velocities in $C_{16}H_{34}$ saturated and CO_2 flooded rocks and sand at higher temperatures.

Beaver No. 9 ($\phi = 6\%$) At 60° C						Beaver No. 7 ($\phi = 9\%$) At 70° C					
$C_{16}H_{34}$ Saturated			CO_2 Flooded			$C_{16}H_{34}$ Saturated			CO_2 Flooded		
Pp	Vp	Vs	Pp	Vp	Vs	Pp	Vp	Vs	Pp	Vp	Vs
16	4945	3141	16	4446	2956	16	4797	3022	16	4472	2921
14	4964	3172	14	4516	3007	14	4824	3057	14	4509	2971
12	4983	3191	12	4645	3096	12	4850	3093	12	4628	3027
10	5002	3211	10	4844	3172	10	4886	3122	10	4669	3075
8	5021	3231	8	4908	3199	8	4917	3148	8	4711	3111
6	5041	3251	6	4945	3231	6	4932	3167	6	4754	3167
4	5050	3268	4	4992	3272	...	...	...	...	...	...
2	5060	3284	2	5012	3292	3	4951	3194	...	...	...
0	5070	3301	0	5041	3326	0	4970	3226	5	4841	3246

Units: Vp, Vs - Meters/second, Pp - MPa.

Table A2 (continued). Compressional and shear velocities in $C_{16}H_{34}$ saturated and CO_2 flooded rocks and sand at higher temperatures.

Berea No. 4 ($\phi = 20\%$) At 58° C			Berea No.6 ($\phi = 21\%$) At 60° C					
CO_2 Flooded			$C_{16}H_{34}$ Saturated			CO_2 Flooded		
Pp	Vp	Vs	Pp	Vp	Vs	Pp	Vp	Vs
17	3259	1975	16	3480	1997	16	3223	1969
15	3312	1996	14	3520	2072	14	3242	2026
13	3381	2065	13	3556	2109	12	3281	2104
11	3468	2138	12	3602	2150	11	3466	2182
9	3513	2199	10	3650	2205	10	3458	2156
8	3536	2217	7.5	3709	2250	7.5	3511	2244
7	3583	2245	...	...	...	6.5	3533	2263
6	3607	2264	5	3739	2278	4	3675	2306
4	3631	2273	2.5	3765	2306	2.3	3699	2330
1	3731	2332	0	3791	2330	0	3734	2355

Units: Vp, Vs - Meters/second, Pp - MPa.

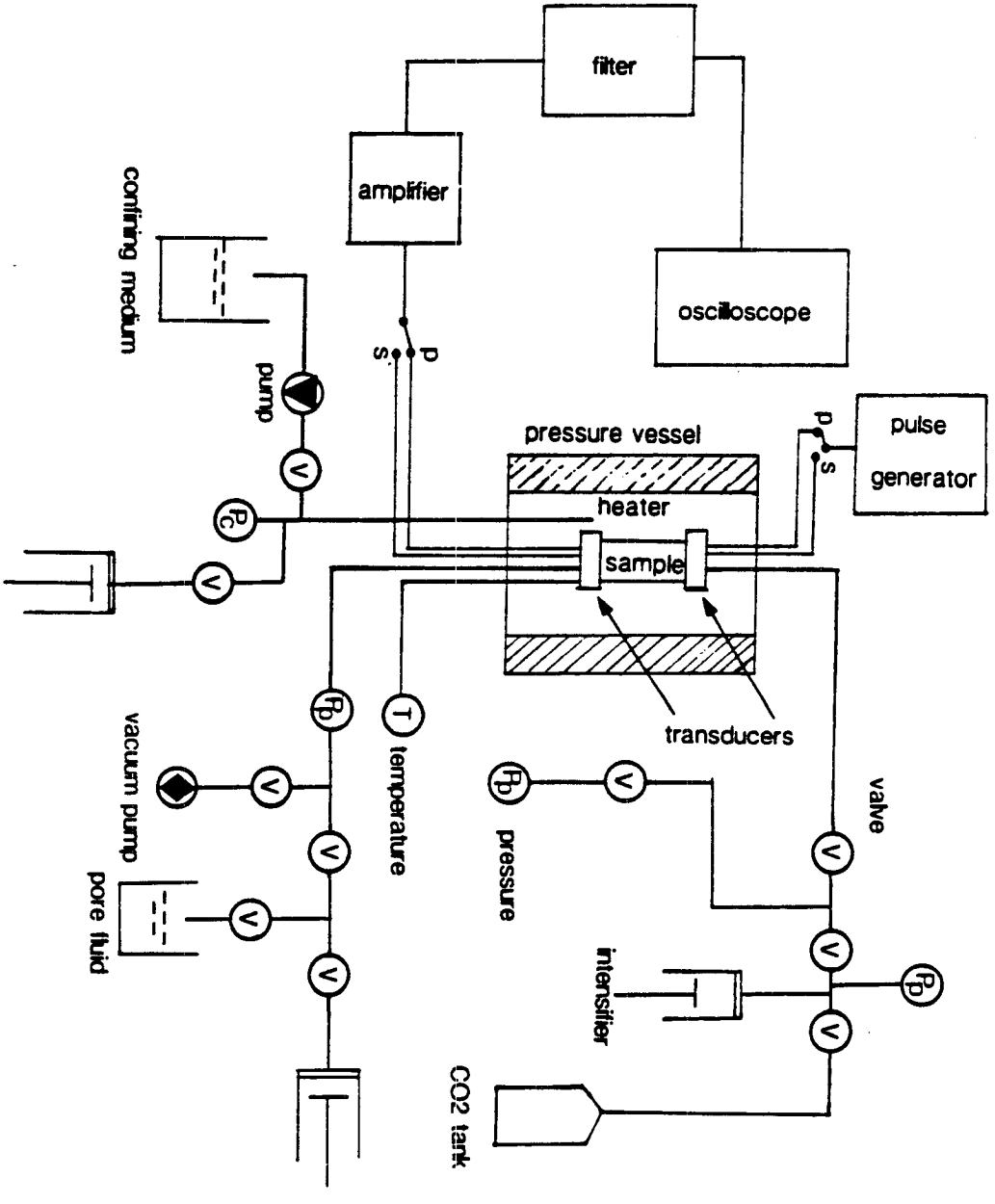
filter
amplifier
oscilloscope
confining medium
pump
pressure vessel
heater
sample
transducers
pulse generator
vacuum pump
pore fluid
temperature
pressure
valve
intensifier
CO2 tank

fig. 1

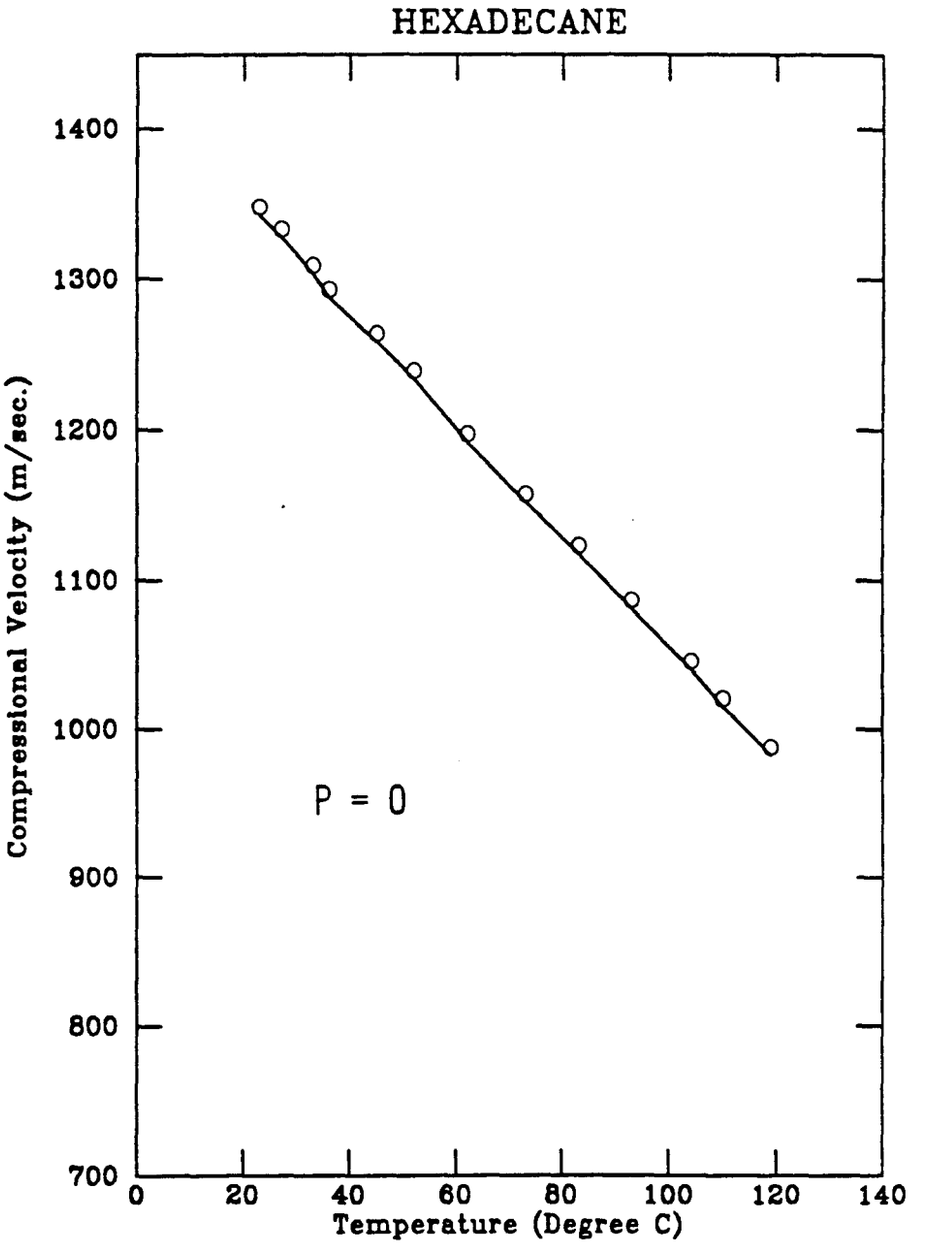
HEXADECANE
Compressional Velocity (m/sec.)
1400
1300
1200
1100
1000
900
800
700
P = 0
0
20
40
60
80
100
120
140
Temperature (Degree C)

fig. 2a

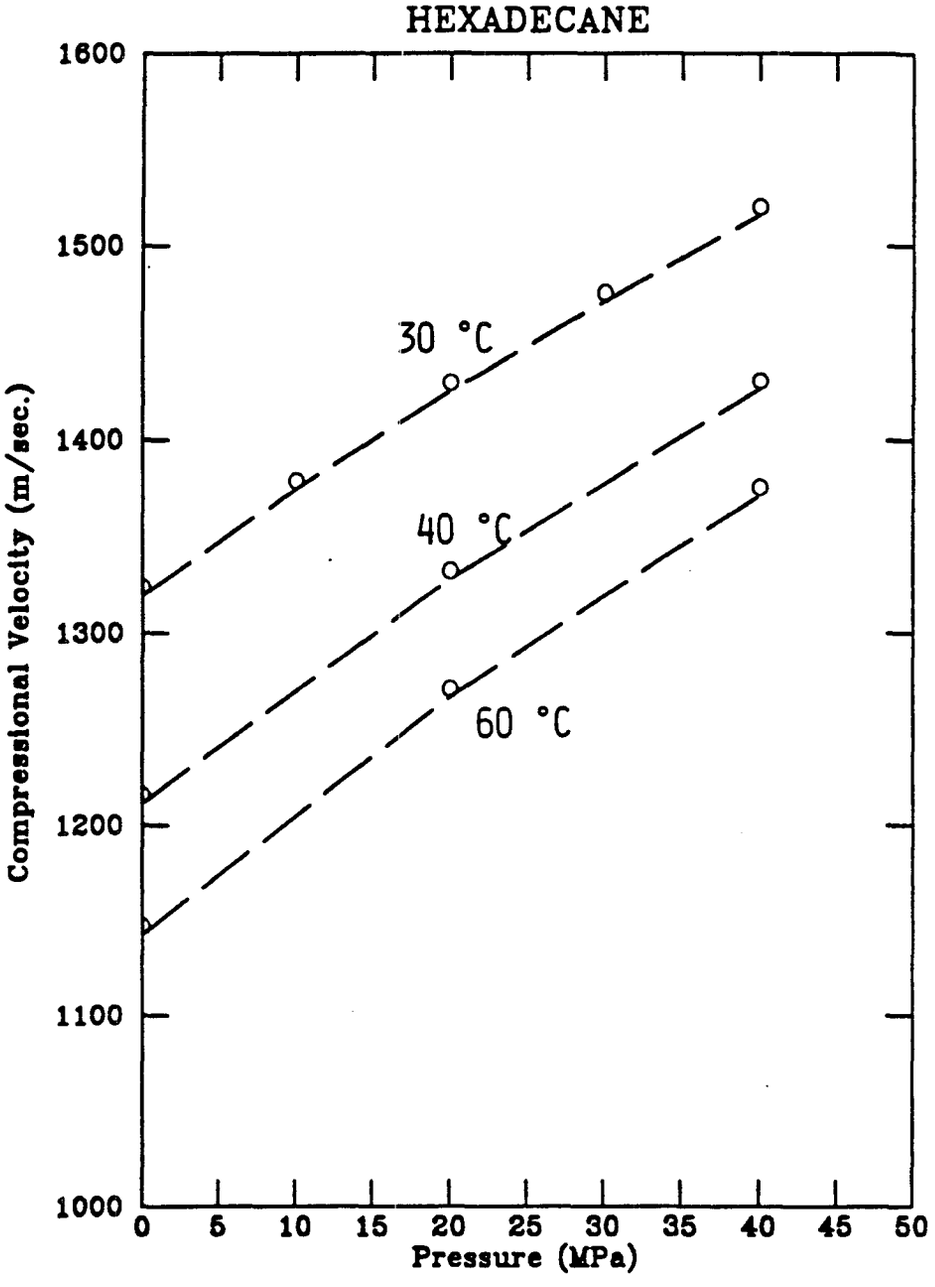
HEXADECANE
1600
1500
1400
1300
1200
1100
1000
Compressional Velocity (m/sec.)
30 °C
40 °C
60 °C
0
5
10
15
20
25
30
35
40
45
50
Pressure (MPa)

fig. 2b

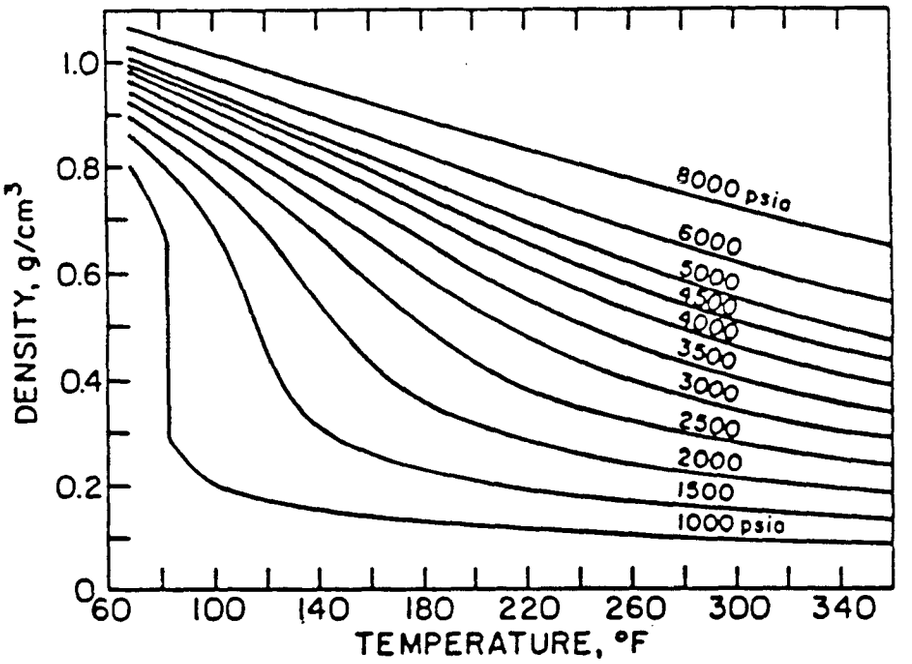
DENSITY, g/cm³
1.0
0.8
0.6
0.4
0.2
0
60
100
140
180
220
260
300
340
TEMPERATURE, °F
8000 psia
6000
5000
4500
4000
3500
3000
2500
2000
1500
1000 psia

fig. 3a

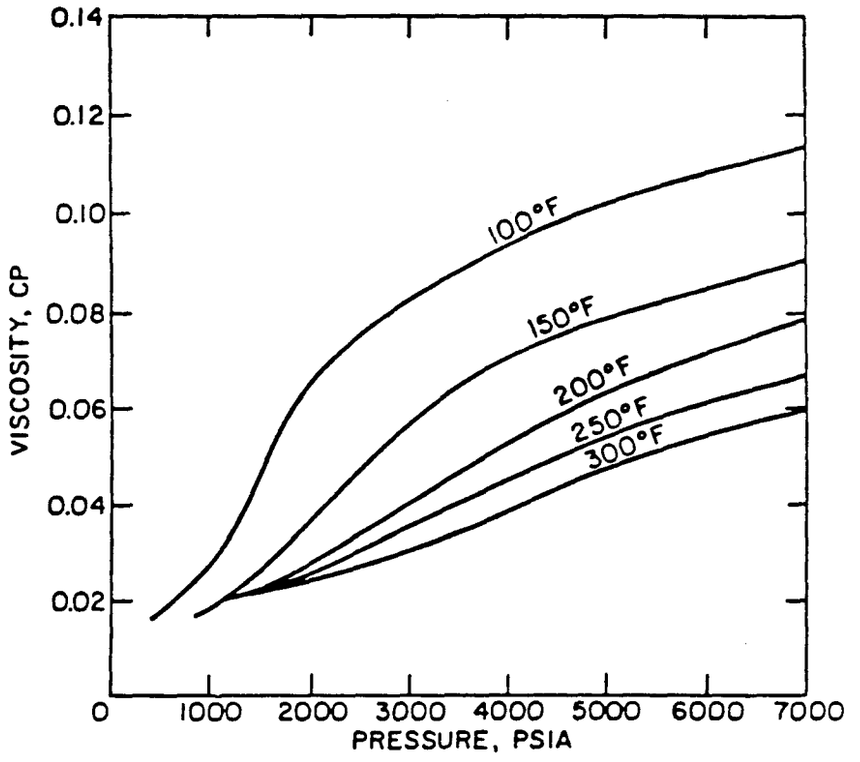
VISCOSITY, CP
0.14
0.12
0.10
0.08
0.06
0.04
0.02
0
1000
2000
3000
4000
5000
6000
7000
PRESSURE, PSIA
100°F
150°F
200°F
250°F
300°F

fig. 3b

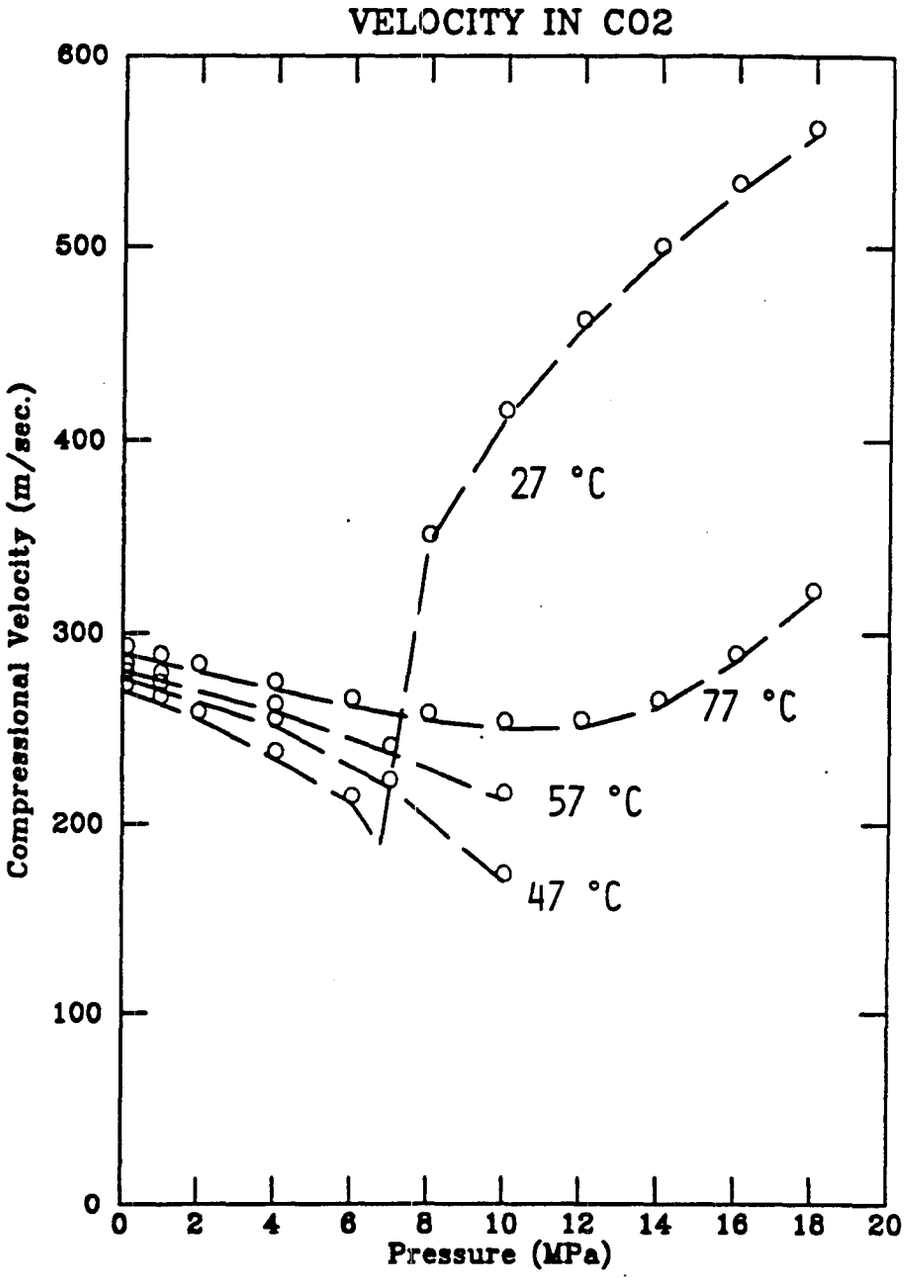
VELOCITY IN CO2
Compressional Velocity (m/sec.)
Pressure (MPa)
600
500
400
300
200
100
0
0
2
4
6
8
10
12
14
16
18
20
27 °C
77 °C
57 °C
47 °C

fig. 4

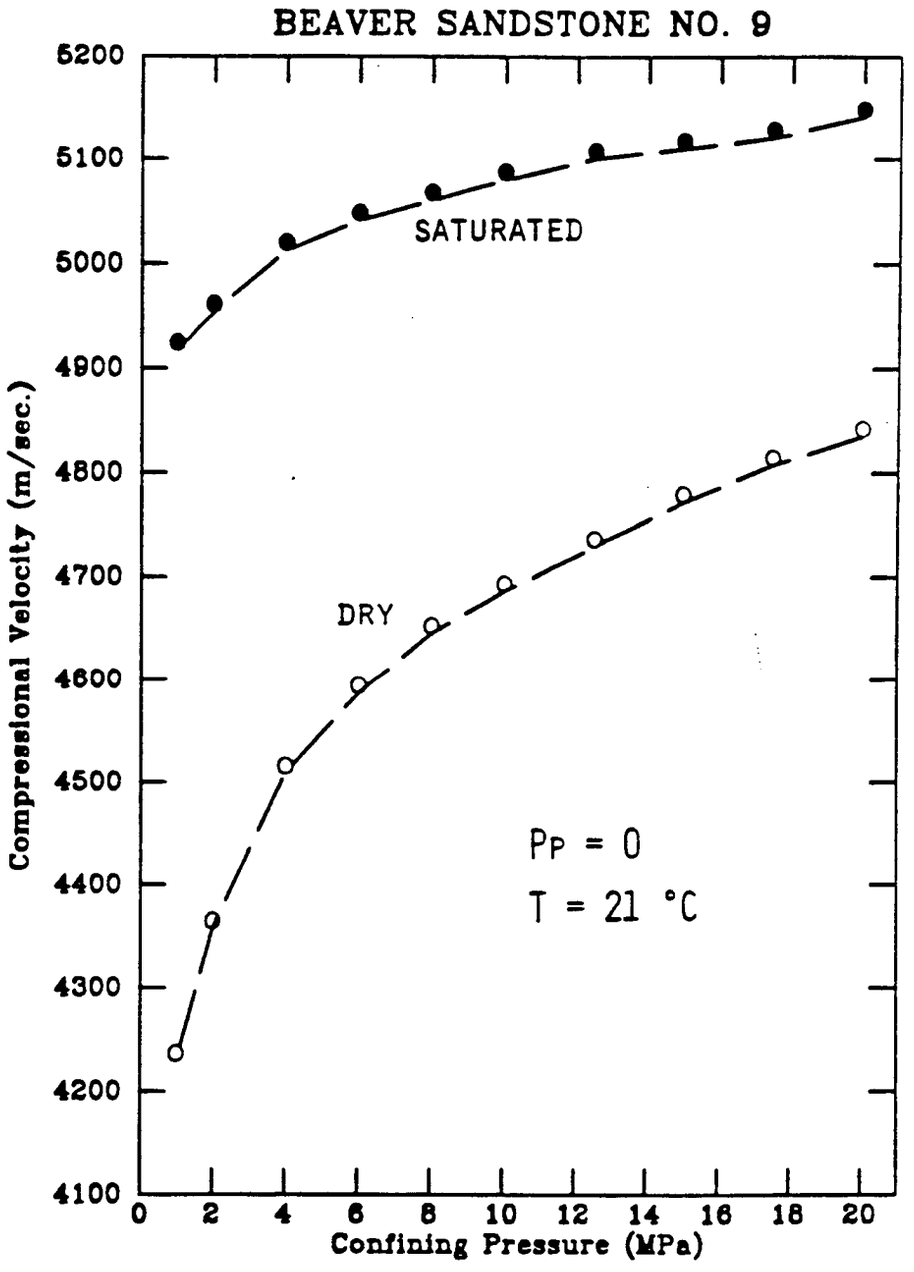
BEAVER SANDSTONE NO. 9
SATURATED
DRY
Pp = 0
T = 21 °C
Compressional Velocity (m/sec.)
Confining Pressure (MPa)
5200
5100
5000
4900
4800
4700
4600
4500
4400
4300
4200
4100
0
2
4
6
8
10
12
14
16
18
20

fig. 5a

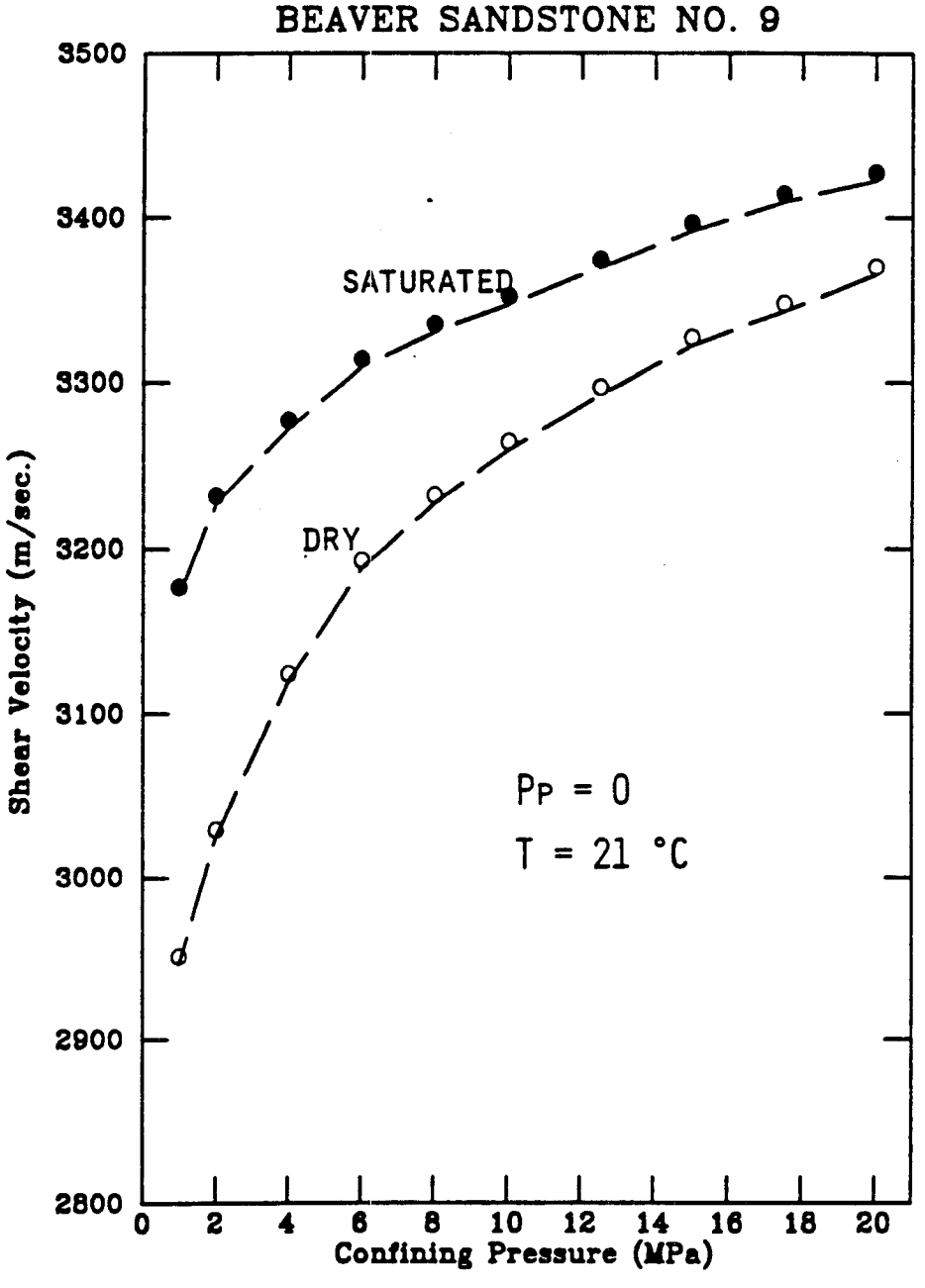
BEAVER SANDSTONE NO. 9
3500
3400
3300
3200
3100
3000
2900
2800
Shear Velocity (m/sec.)
SATURATED
DRY
Pp = 0
T = 21 °C
0
2
4
6
8
10
12
14
16
18
20
Confining Pressure (MPa)

fig. 5b

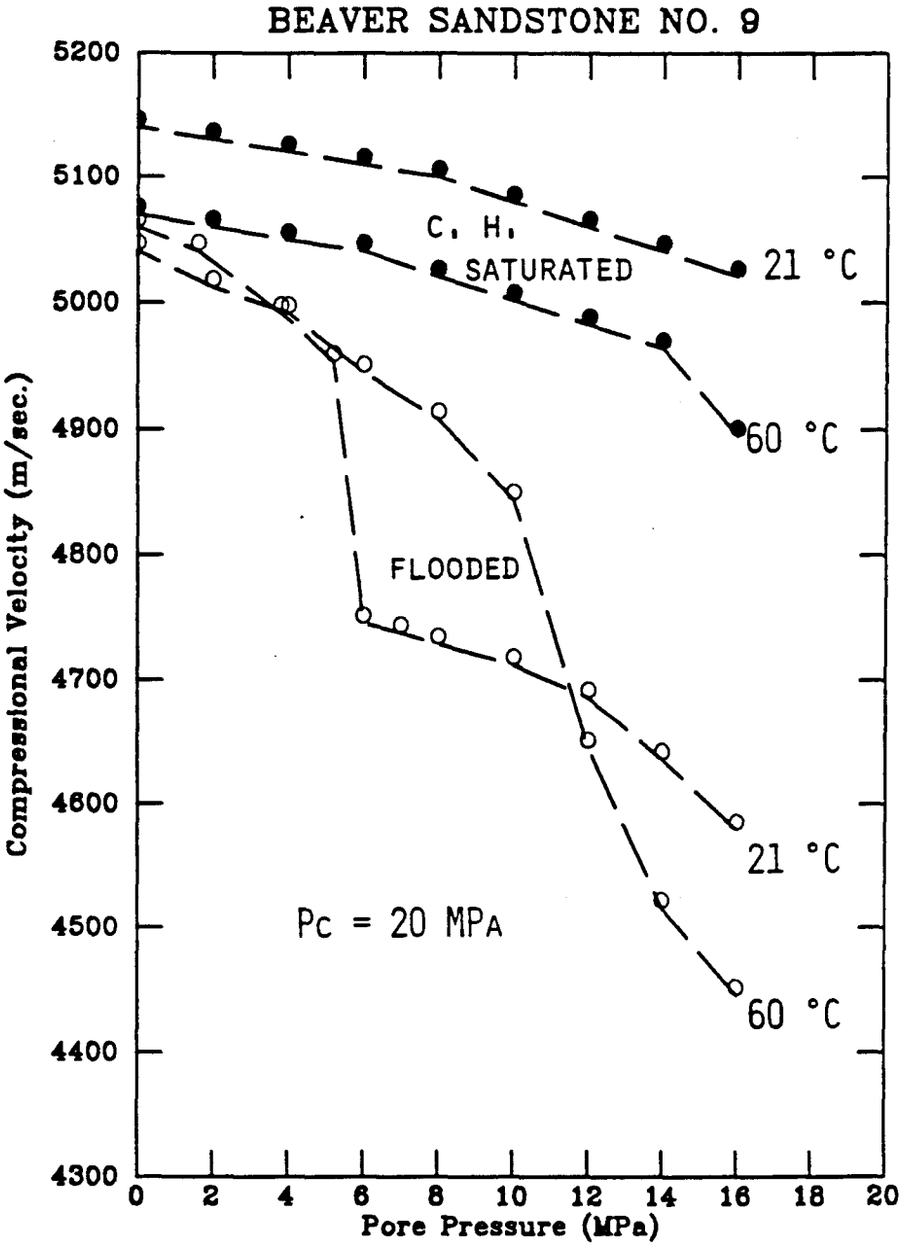
BEAVER SANDSTONE NO. 9
5200
5100
5000
4900
4800
4700
4600
4500
4400
4300
Compressional Velocity (m/sec.)
C. H.
SATURATED
21 °C
60 °C
FLOODED
21 °C
60 °C
Pc = 20 MPa
0
2
4
6
8
10
12
14
16
18
20
Pore Pressure (MPa)

fig. 5c

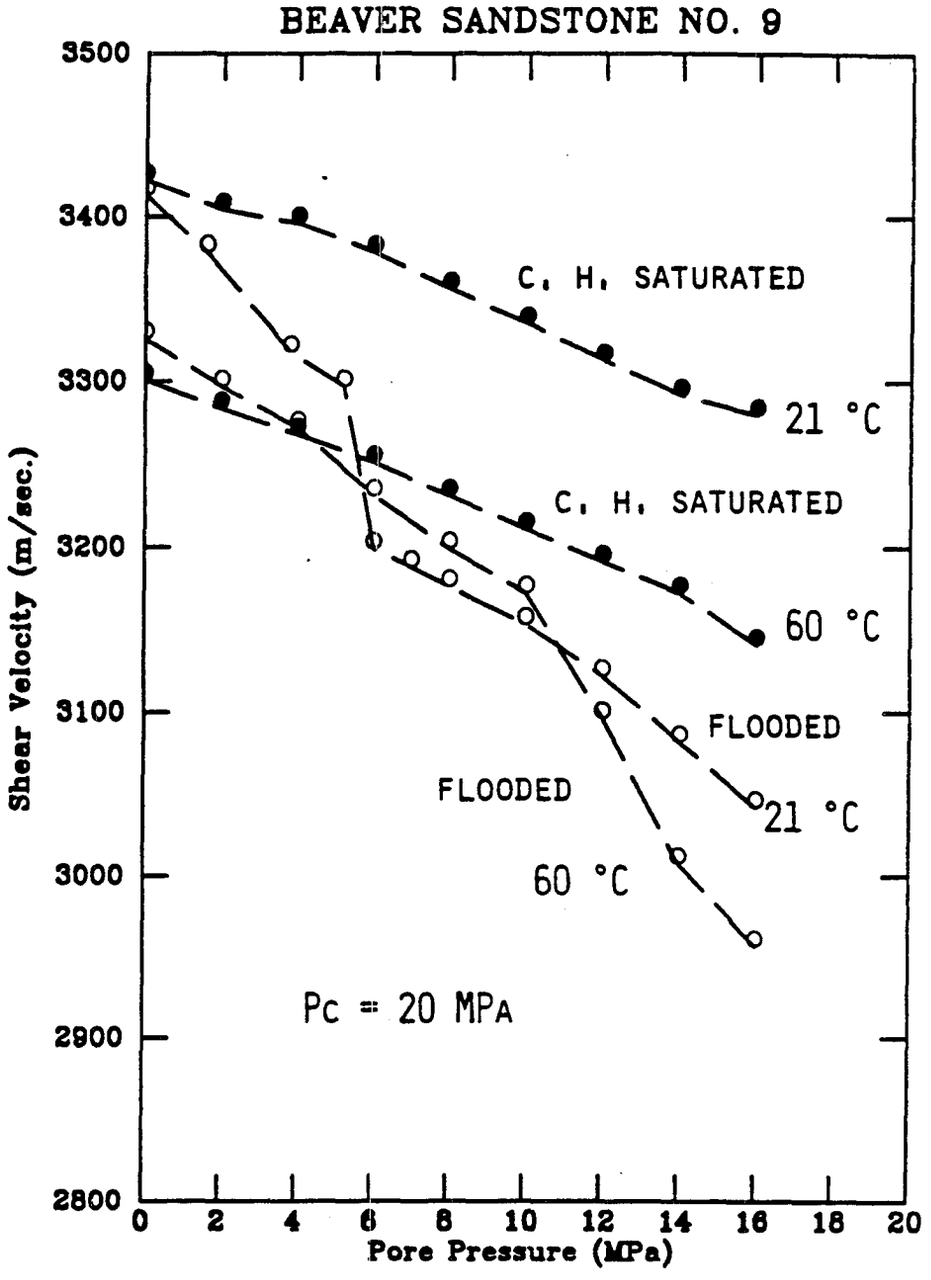
BEAVER SANDSTONE NO. 9
Shear Velocity (m/sec.)
3500
3400
3300
3200
3100
3000
2900
2800
0
2
4
6
8
10
12
14
16
18
20
Pore Pressure (MPa)
C. H. SATURATED
21 °C
C. H. SATURATED
60 °C
FLOODED
21 °C
FLOODED
60 °C
Pc = 20 MPA

fig. 5d

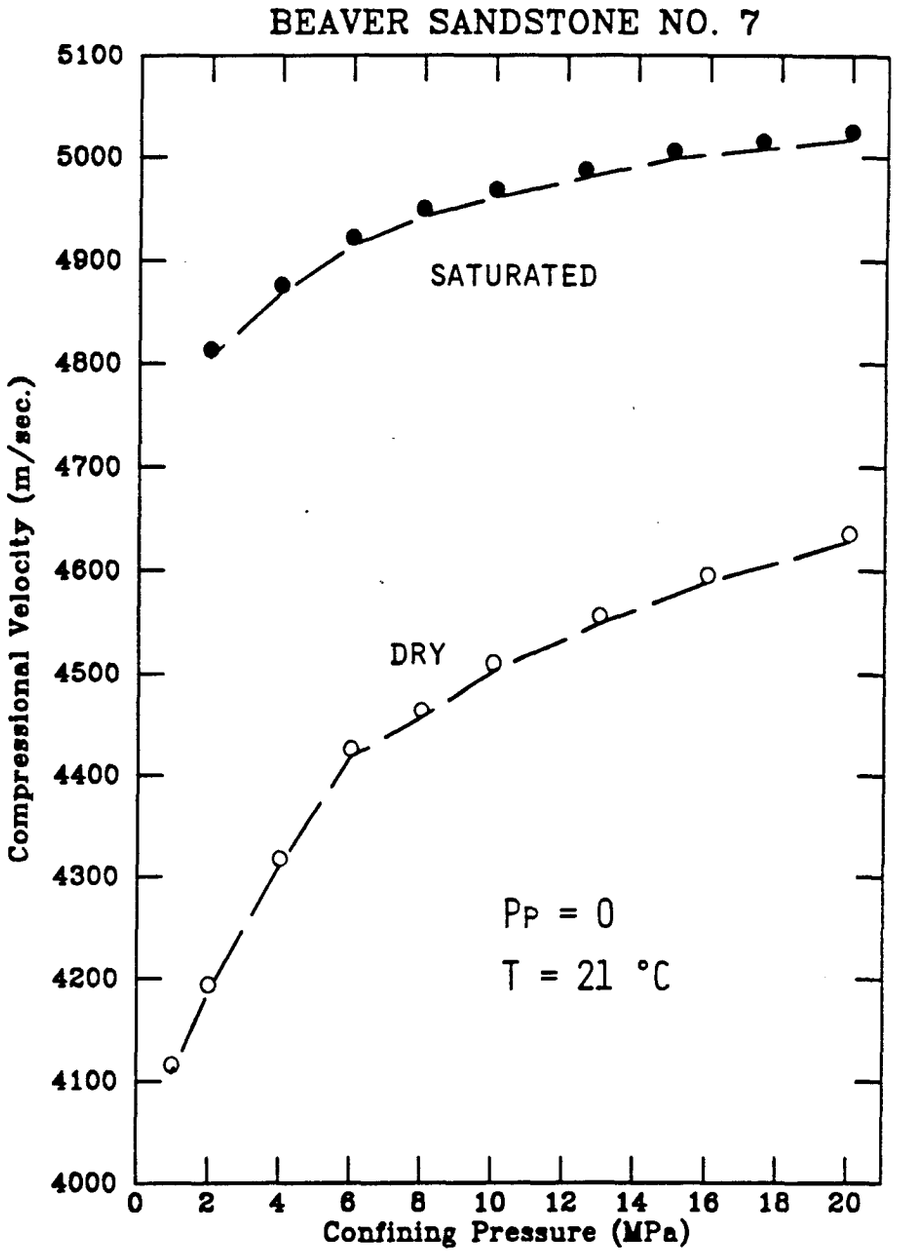
BEAVER SANDSTONE NO. 7
5100
5000
4900
4800
4700
4600
4500
4400
4300
4200
4100
4000
Compressional Velocity (m/sec.)
SATURATED
DRY
Pp = 0
T = 21 °C
0
2
4
6
8
10
12
14
16
18
20
Confining Pressure (MPa)

fig. 6a

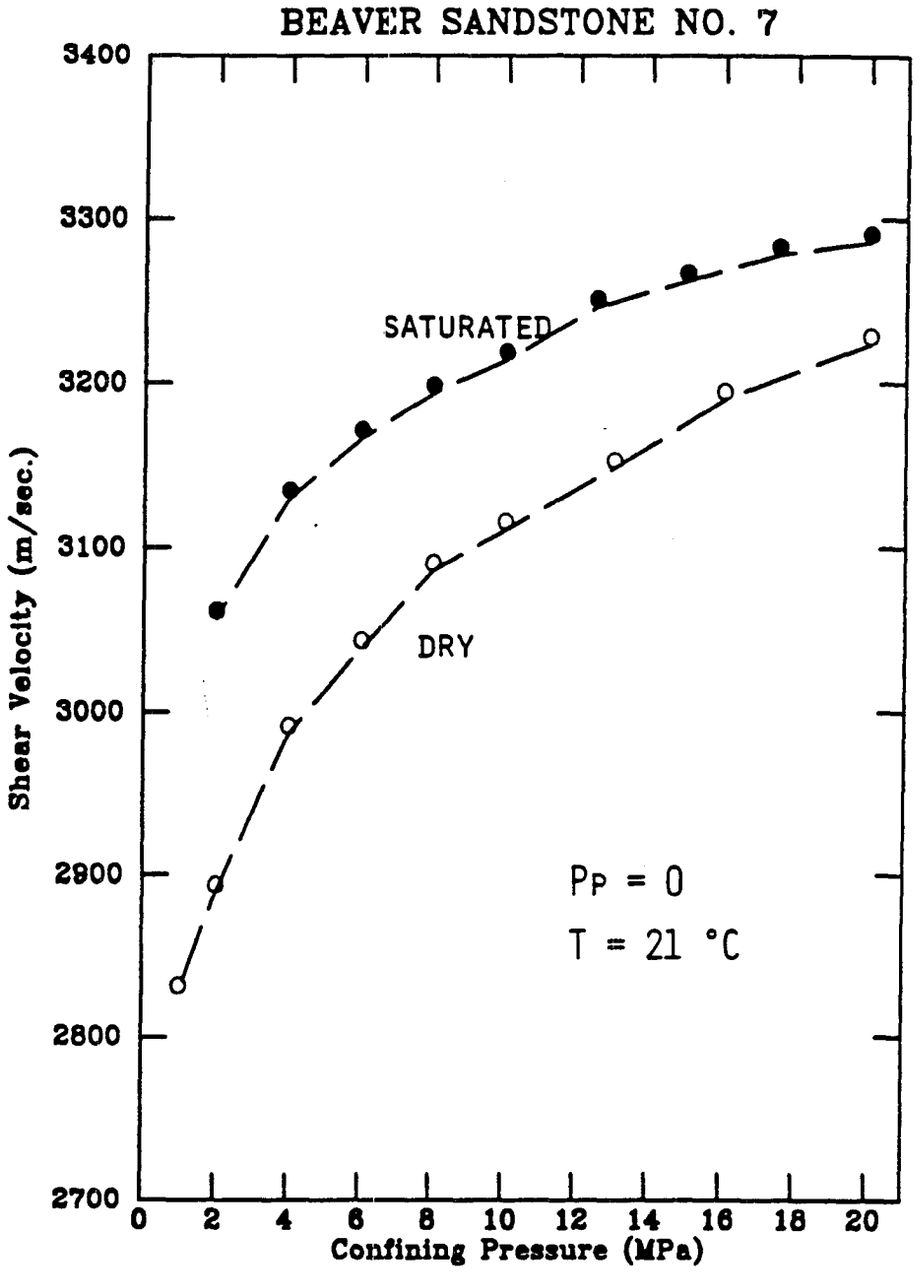
BEAVER SANDSTONE NO. 7
3400
3300
3200
3100
3000
2900
2800
2700
Shear Velocity (m/sec.)
SATURATED
DRY
Pp = 0
T = 21 °C
0
2
4
6
8
10
12
14
16
18
20
Confining Pressure (MPa)

fig. 6b

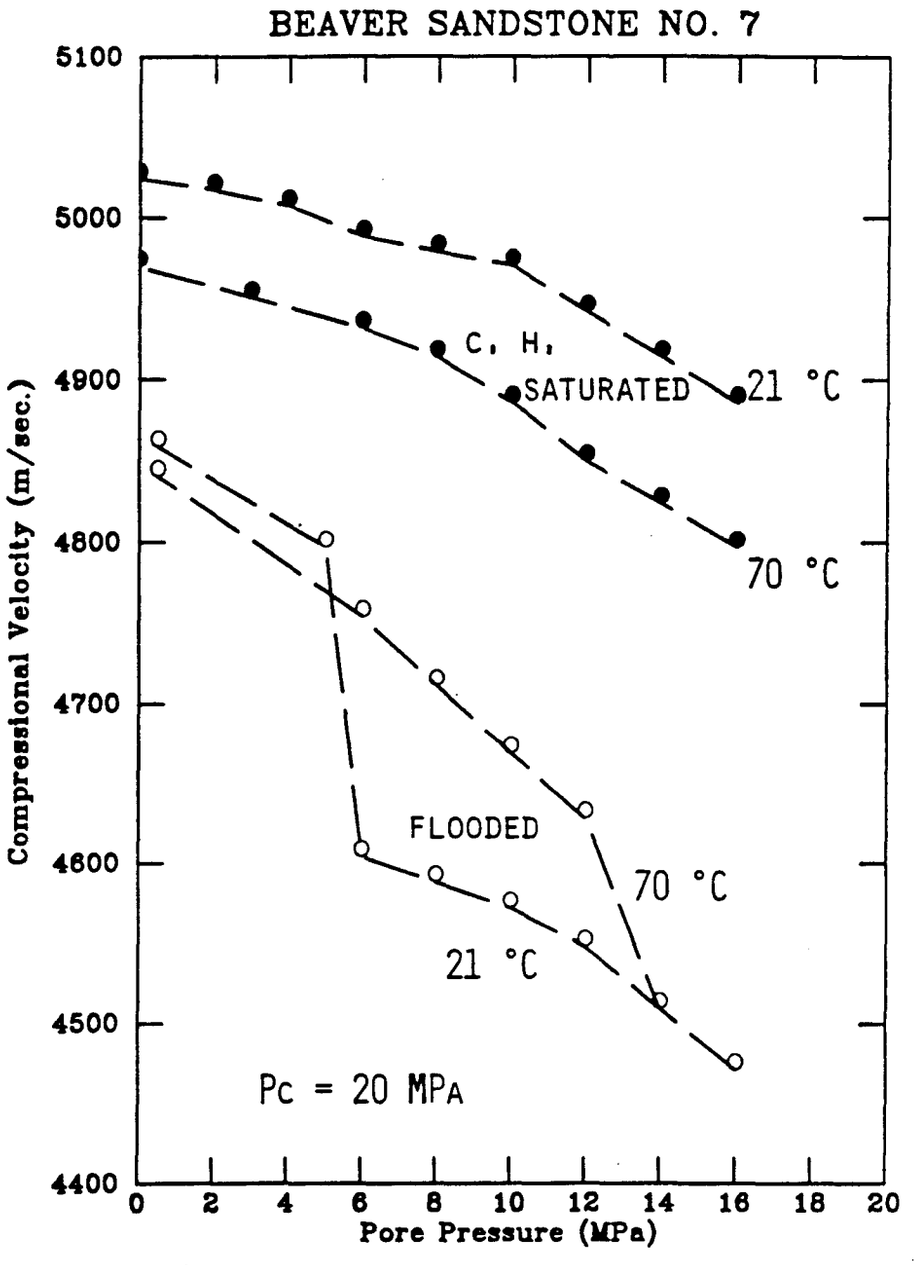
BEAVER SANDSTONE NO. 7
Compressional Velocity (m/sec.)
Pore Pressure (MPa)
5100
5000
4900
4800
4700
4600
4500
4400
0
2
4
6
8
10
12
14
16
18
20
C. H.
SATURATED
21 °C
70 °C
FLOODED
70 °C
21 °C
Pc = 20 MPA

fig. 6c

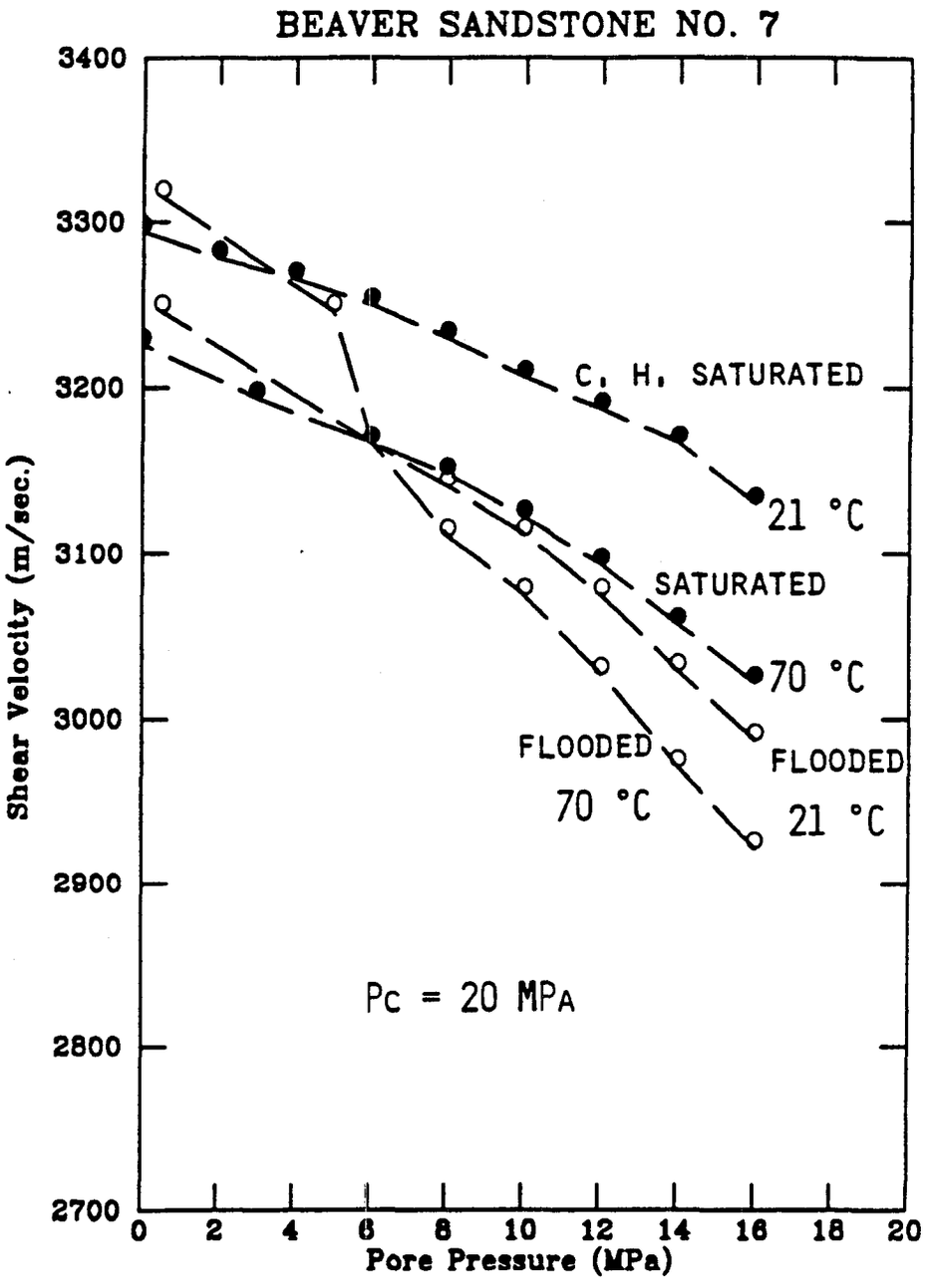
BEAVER SANDSTONE NO. 7
3400
3300
3200
3100
3000
2900
2800
2700
Shear Velocity (m/sec.)
0
2
4
6
8
10
12
14
16
18
20
Pore Pressure (MPa)
C. H. SATURATED
21 °C
SATURATED
70 °C
FLOODED
70 °C
FLOODED
21 °C
Pc = 20 MPA

fig. 6d

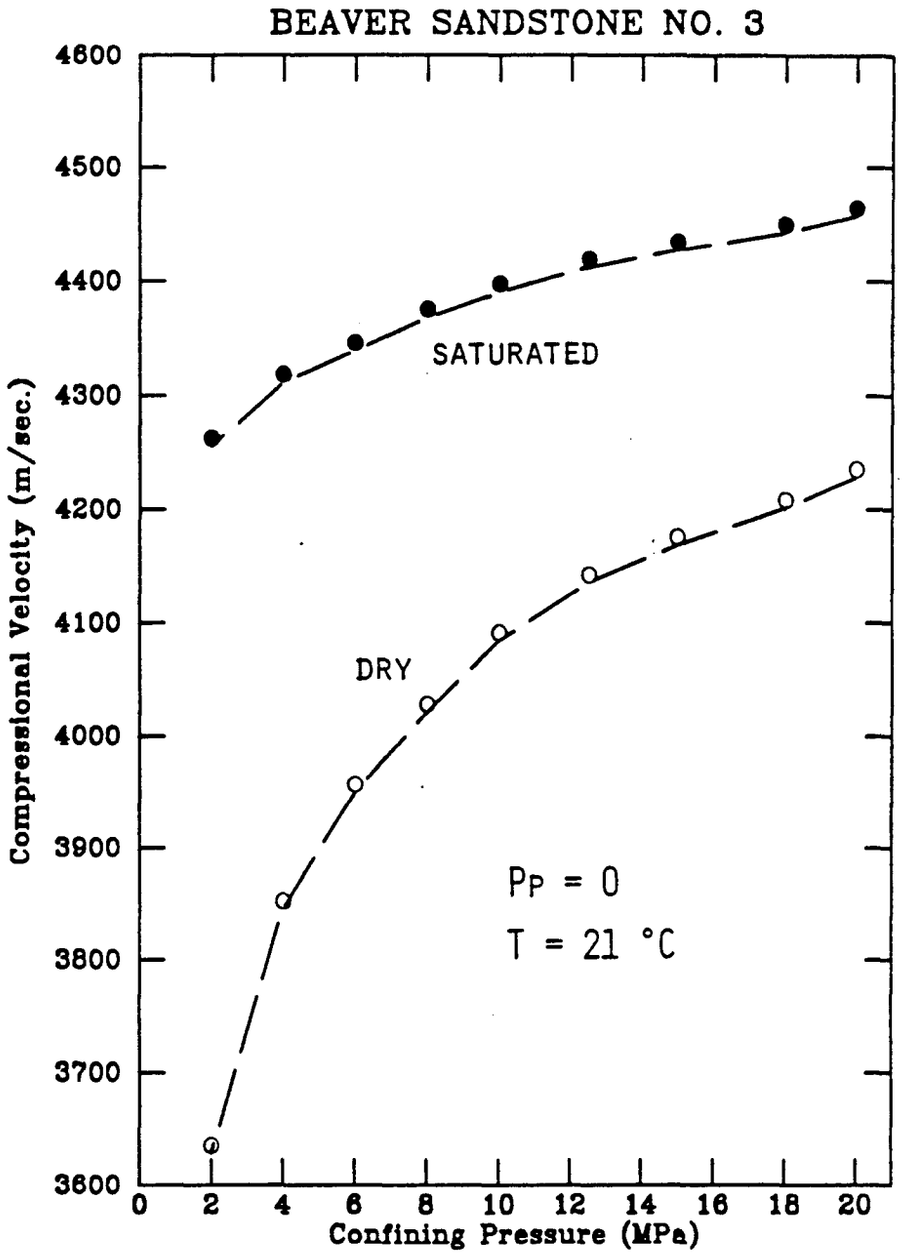
BEAVER SANDSTONE NO. 3
Compressional Velocity (m/sec.)
4600
4500
4400
4300
4200
4100
4000
3900
3800
3700
3600
SATURATED
DRY
Pp = 0
T = 21 °C
0
2
4
6
8
10
12
14
16
18
20
Confining Pressure (MPa)

fig. 7a

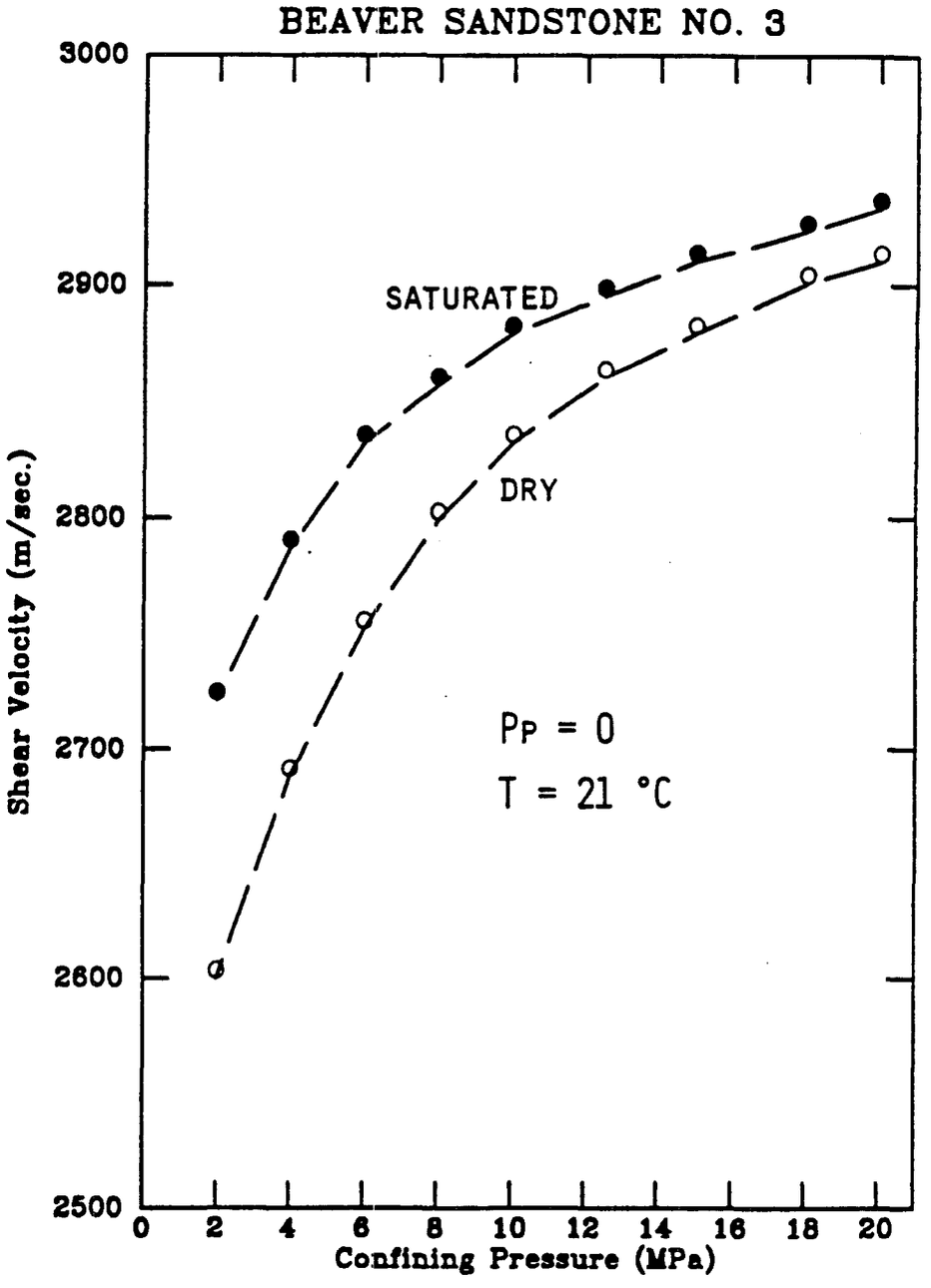
BEAVER SANDSTONE NO. 3
3000
2900
2800
2700
2600
2500
Shear Velocity (m/sec.)
SATURATED
DRY
Pp = 0
T = 21 °C
0
2
4
6
8
10
12
14
16
18
20
Confining Pressure (MPa)

fig. 7b

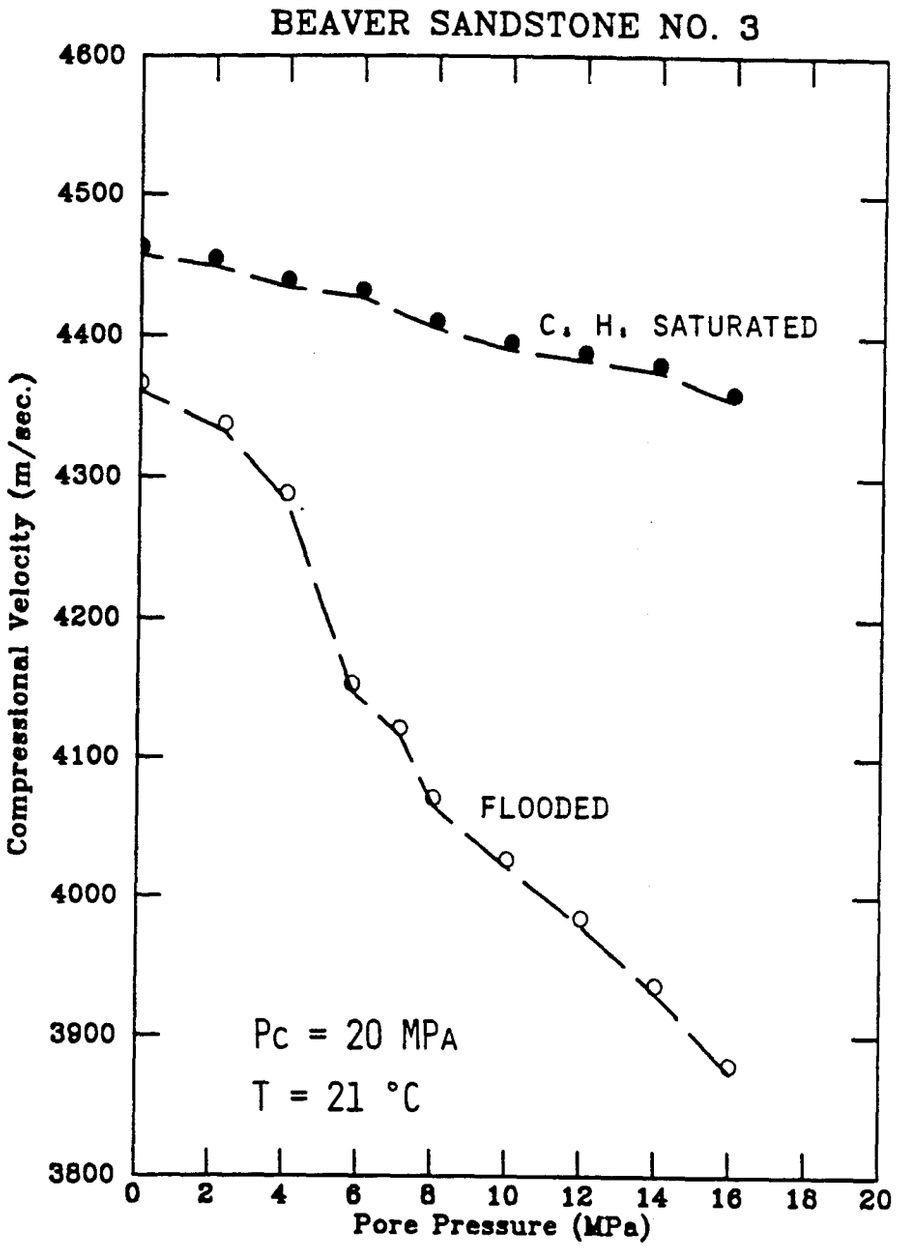
BEAVER SANDSTONE NO. 3
4600
4500
4400
4300
4200
4100
4000
3900
3800
Compressional Velocity (m/sec.)
C. H. SATURATED
FLOODED
Pc = 20 MPA
T = 21 °C
0
2
4
6
8
10
12
14
16
18
20
Pore Pressure (MPa)

fig. 7c

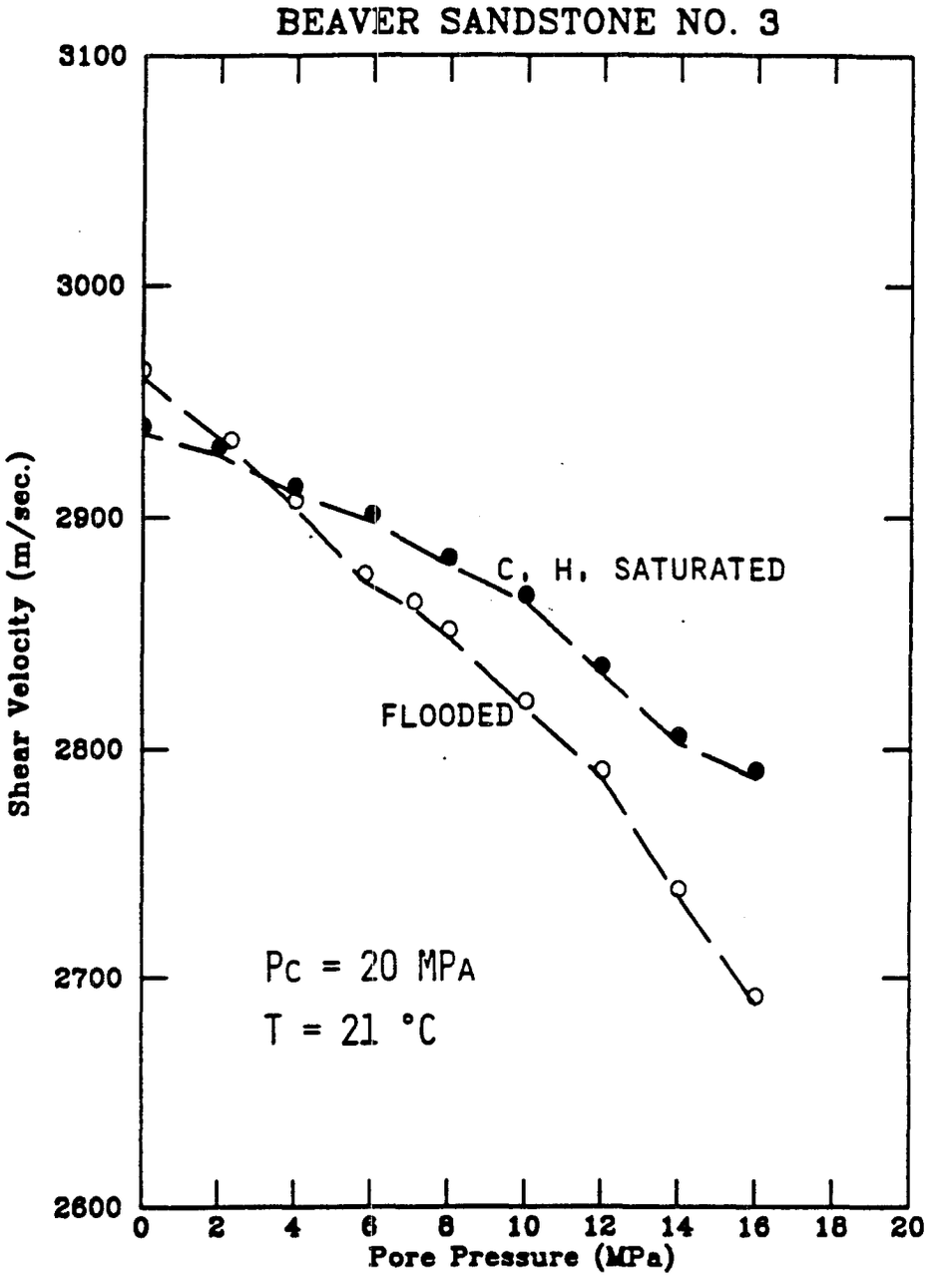
BEAVER SANDSTONE NO. 3
3100
3000
2900
2800
2700
2600
Shear Velocity (m/sec.)
C. H. SATURATED
FLOODED
Pc = 20 MPA
T = 21 °C
0
2
4
6
8
10
12
14
16
18
20
Pore Pressure (MPa)

fig. 7d

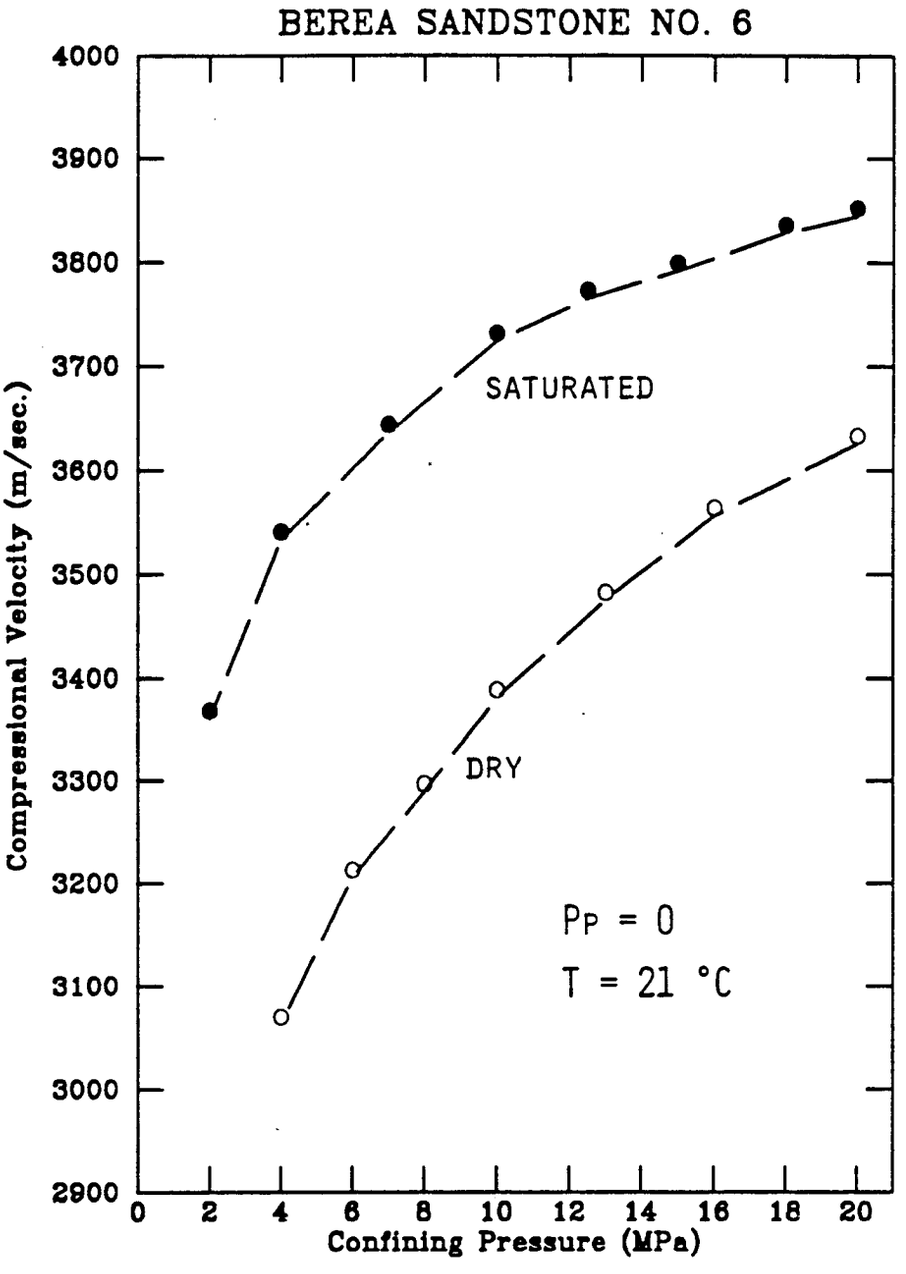
BEREA SANDSTONE NO. 6
Compressional Velocity (m/sec.)
4000
3900
3800
3700
3600
3500
3400
3300
3200
3100
3000
2900
0
2
4
6
8
10
12
14
16
18
20
Confining Pressure (MPa)
SATURATED
DRY
Pp = 0
T = 21 °C

fig. 8a

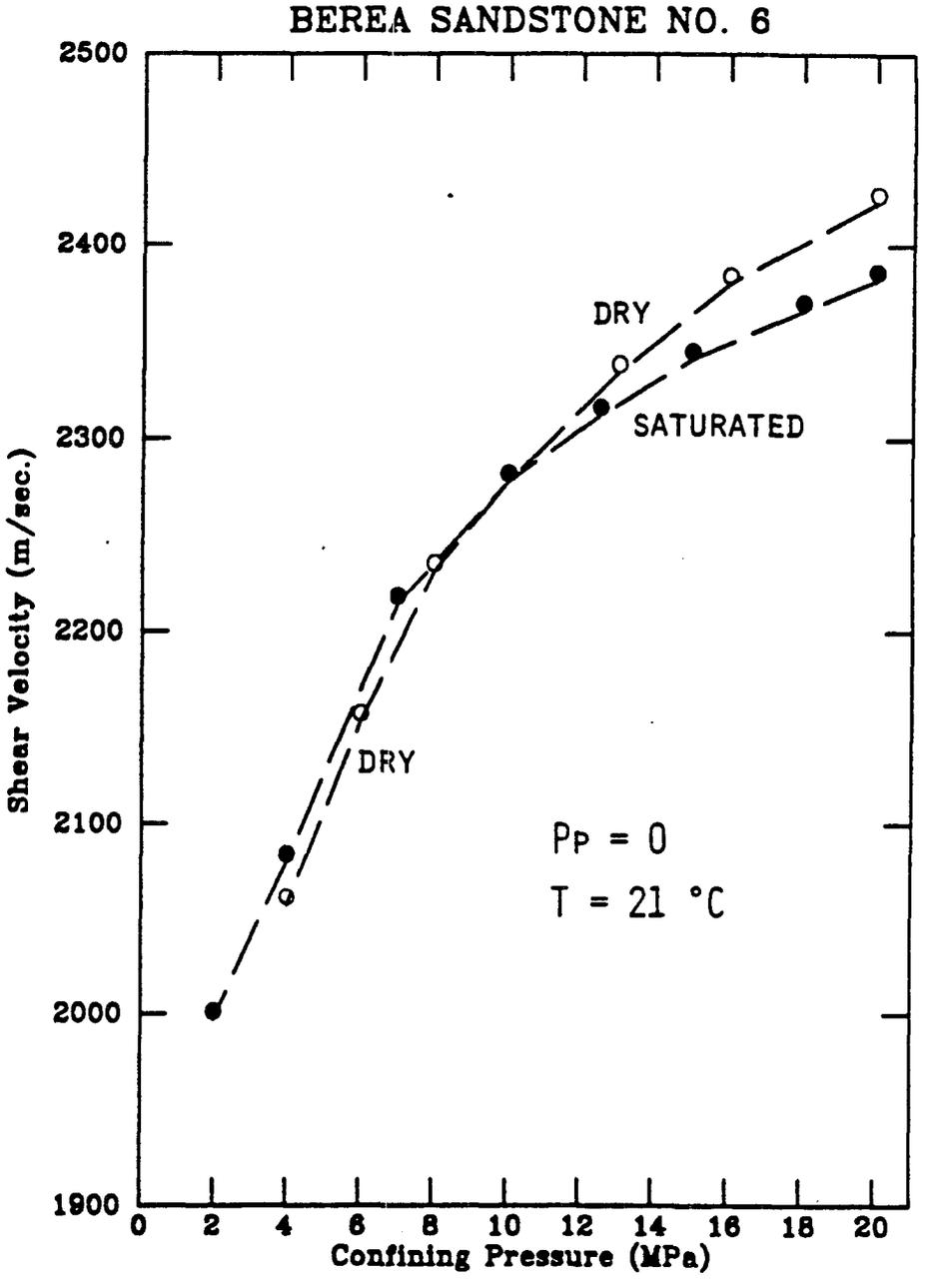
BEREA SANDSTONE NO. 6
2500
2400
2300
2200
2100
2000
1900
Shear Velocity (m/sec.)
DRY
SATURATED
DRY
Pp = 0
T = 21 °C
0
2
4
6
8
10
12
14
16
18
20
Confining Pressure (MPa)

fig. 8b

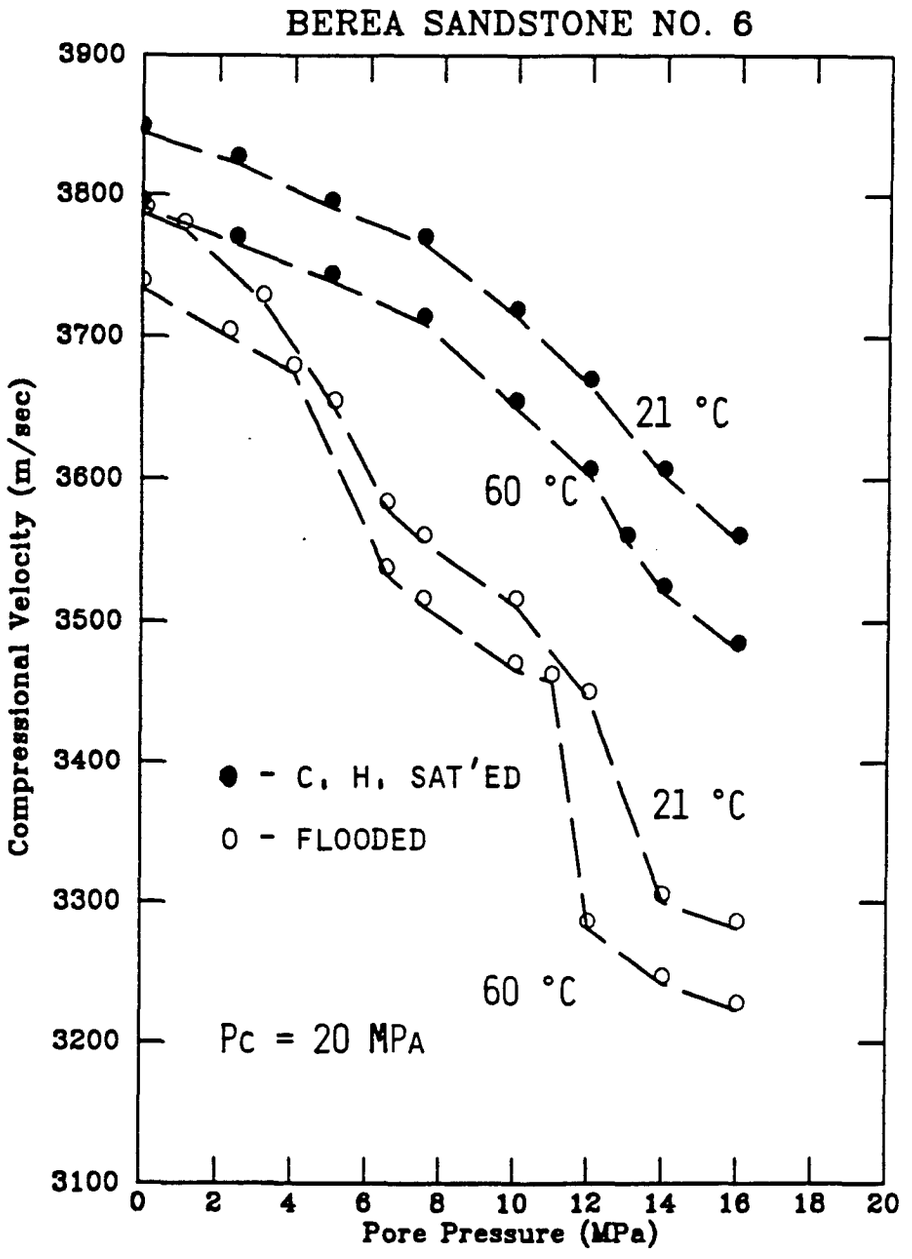
BEREA SANDSTONE NO. 6
Compressional Velocity (m/sec)
3900
3800
3700
3600
3500
3400
3300
3200
3100
0
2
4
6
8
10
12
14
16
18
20
Pore Pressure (MPa)
21 °C
60 °C
● - C. H. SAT'ED
O - FLOODED
21 °C
60 °C
Pc = 20 MPA

fig. 8c

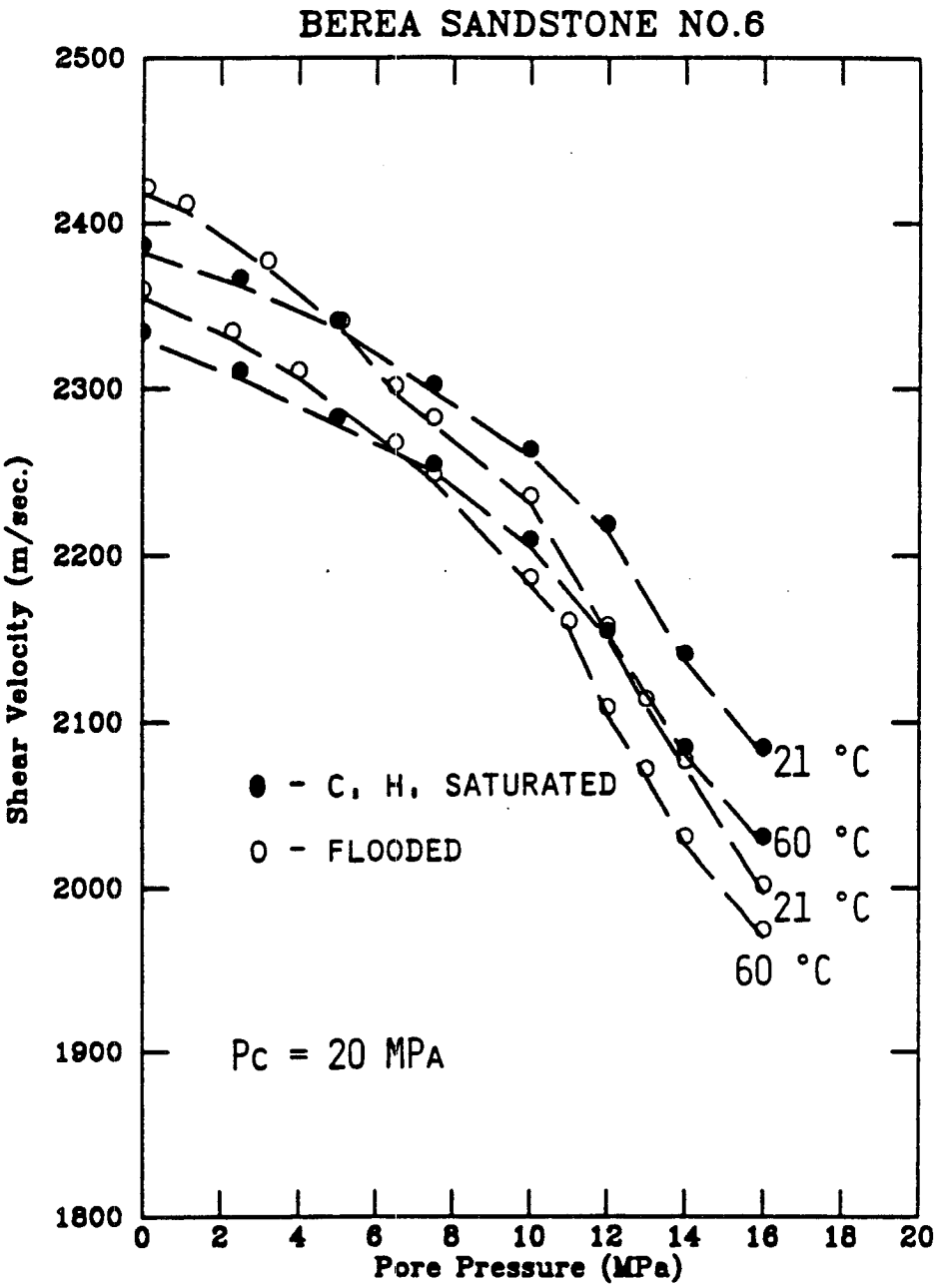
BEREA SANDSTONE NO.6
Shear Velocity (m/sec.)
2500
2400
2300
2200
2100
2000
1900
1800
0
2
4
6
8
10
12
14
16
18
20
Pore Pressure (MPa)
● - C. H. SATURATED
○ - FLOODED
21 °C
60 °C
21 °C
60 °C
Pc = 20 MPA

fig. 8d

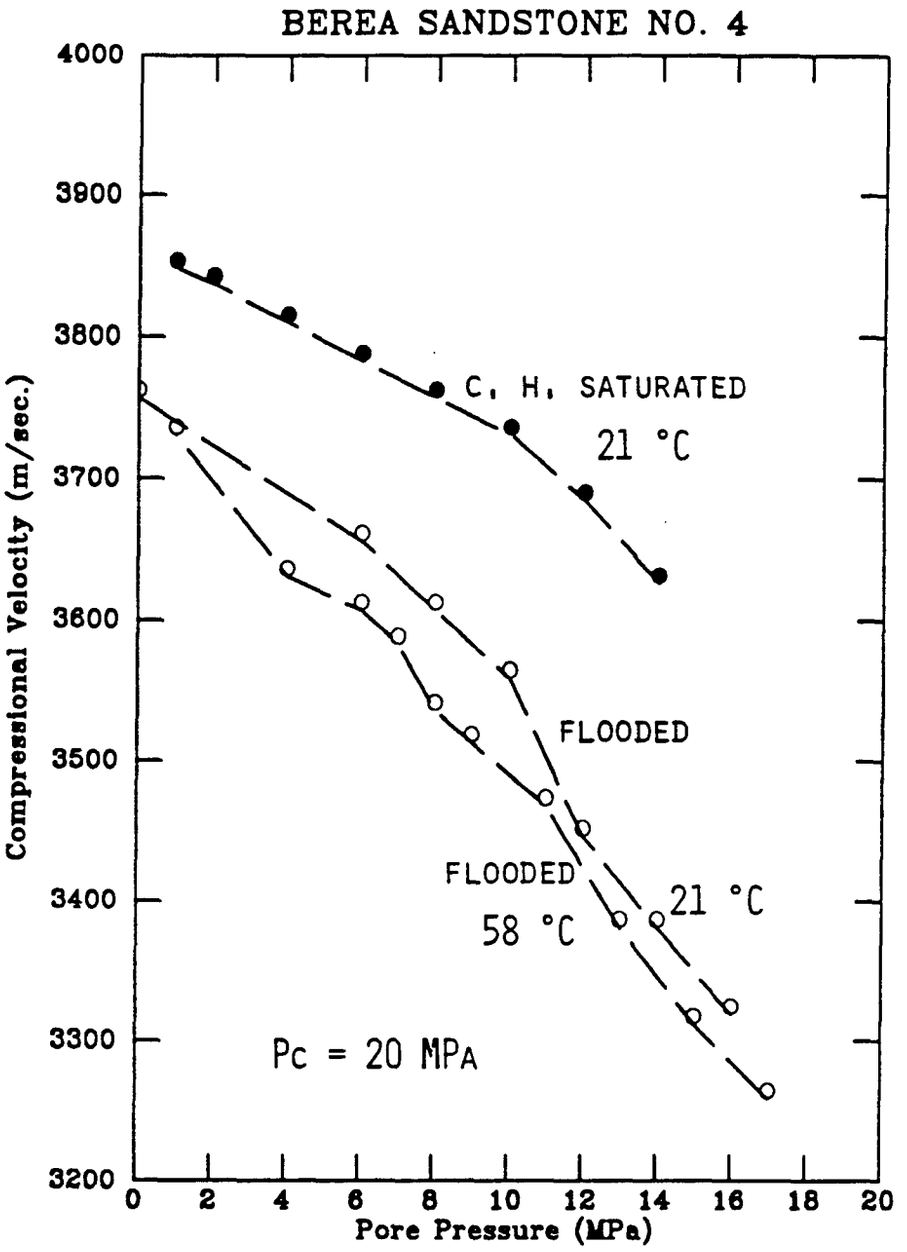
BEREA SANDSTONE NO. 4
Compressional Velocity (m/sec.)
4000
3900
3800
3700
3600
3500
3400
3300
3200
0
2
4
6
8
10
12
14
16
18
20
Pore Pressure (MPa)
C. H. SATURATED
21 °C
FLOODED
FLOODED
58 °C
21 °C
Pc = 20 MPA

fig. 9a

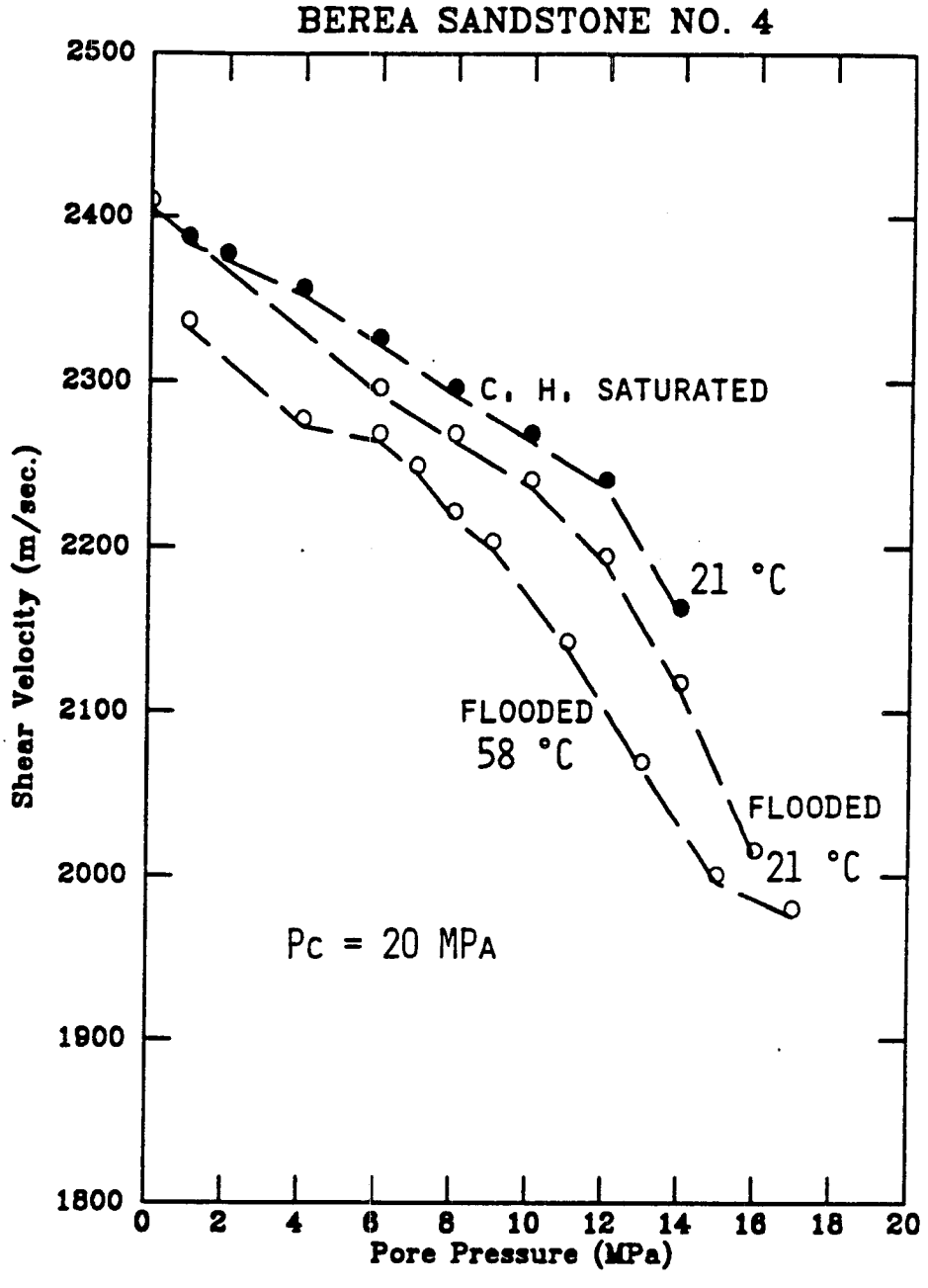
BEREA SANDSTONE NO. 4
2500
2400
2300
2200
2100
2000
1900
1800
Shear Velocity (m/sec.)
0
2
4
6
8
10
12
14
16
18
20
Pore Pressure (MPa)
C. H. SATURATED
21 °C
FLOODED
58 °C
FLOODED
21 °C
Pc = 20 MPA

fig. 9b

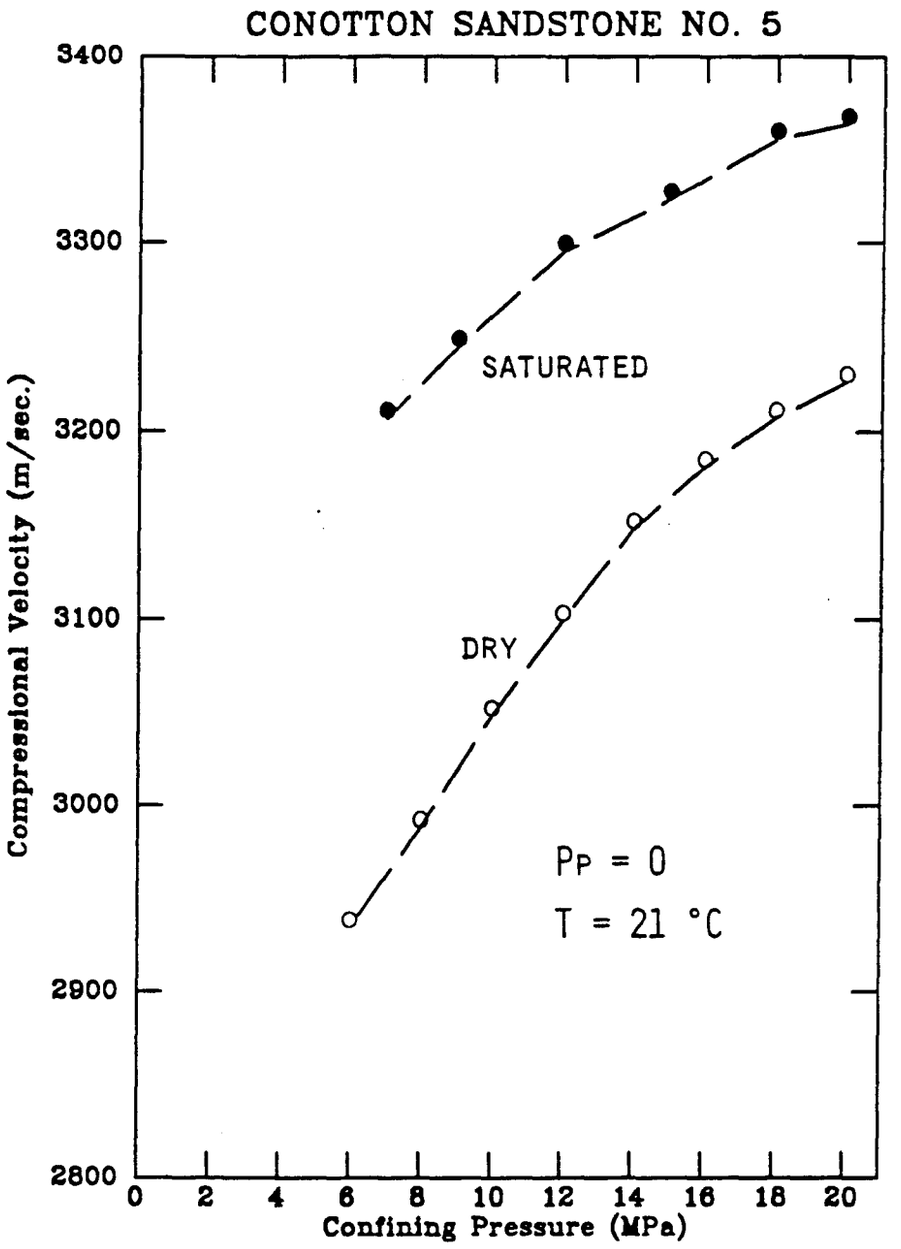
CONOTTON SANDSTONE NO. 5
Compressional Velocity (m/sec.)
3400
3300
3200
3100
3000
2900
2800
SATURATED
DRY
Pp = 0
T = 21 °C
0
2
4
6
8
10
12
14
16
18
20
Confining Pressure (MPa)

fig 10a

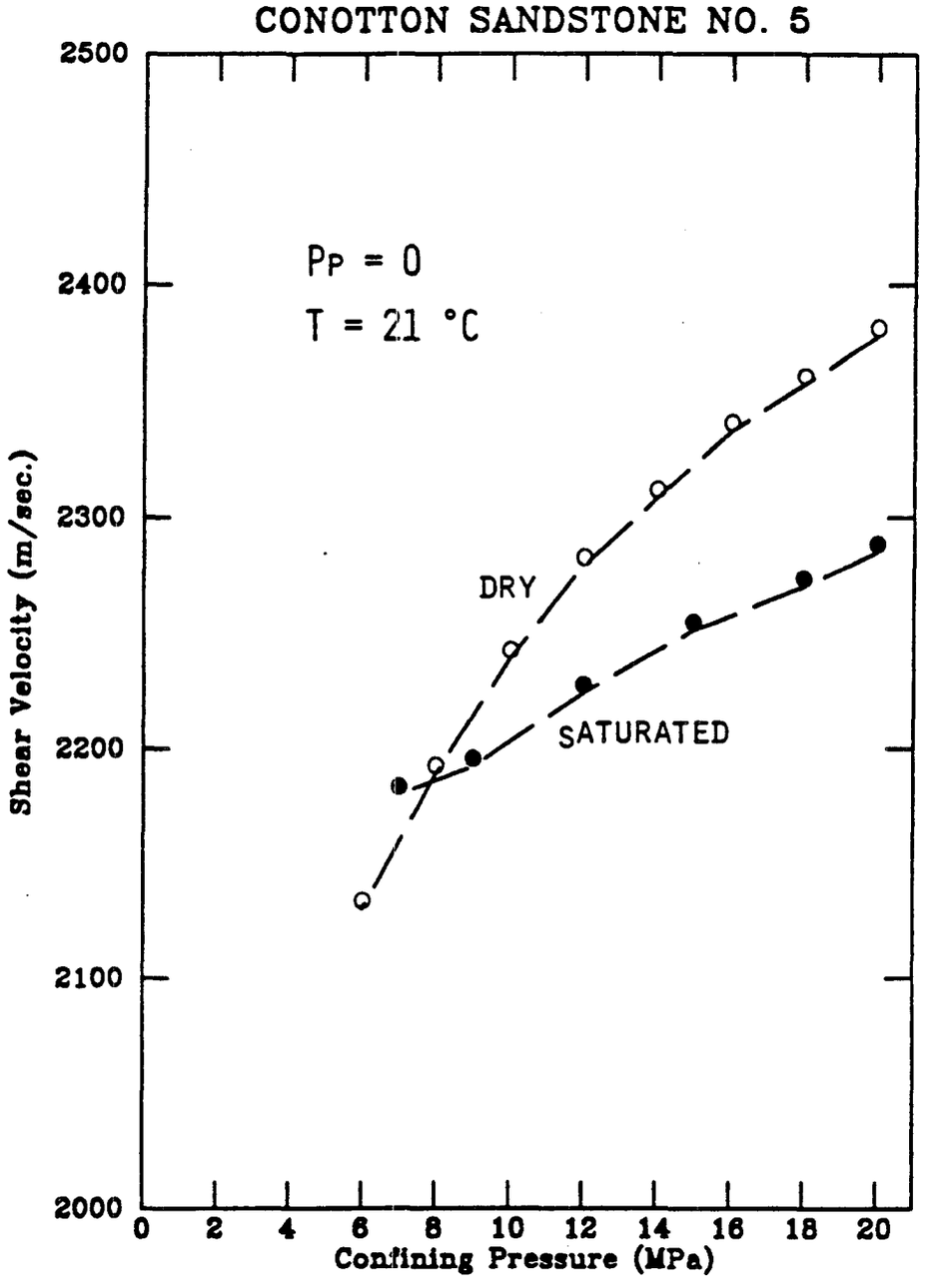
CONOTTON SANDSTONE NO. 5
Pp = 0
T = 21 °C
DRY
SATURATED
Shear Velocity (m/sec.)
2500
2400
2300
2200
2100
2000
0
2
4
6
8
10
12
14
16
18
20
Confining Pressure (MPa)

fig. 10b

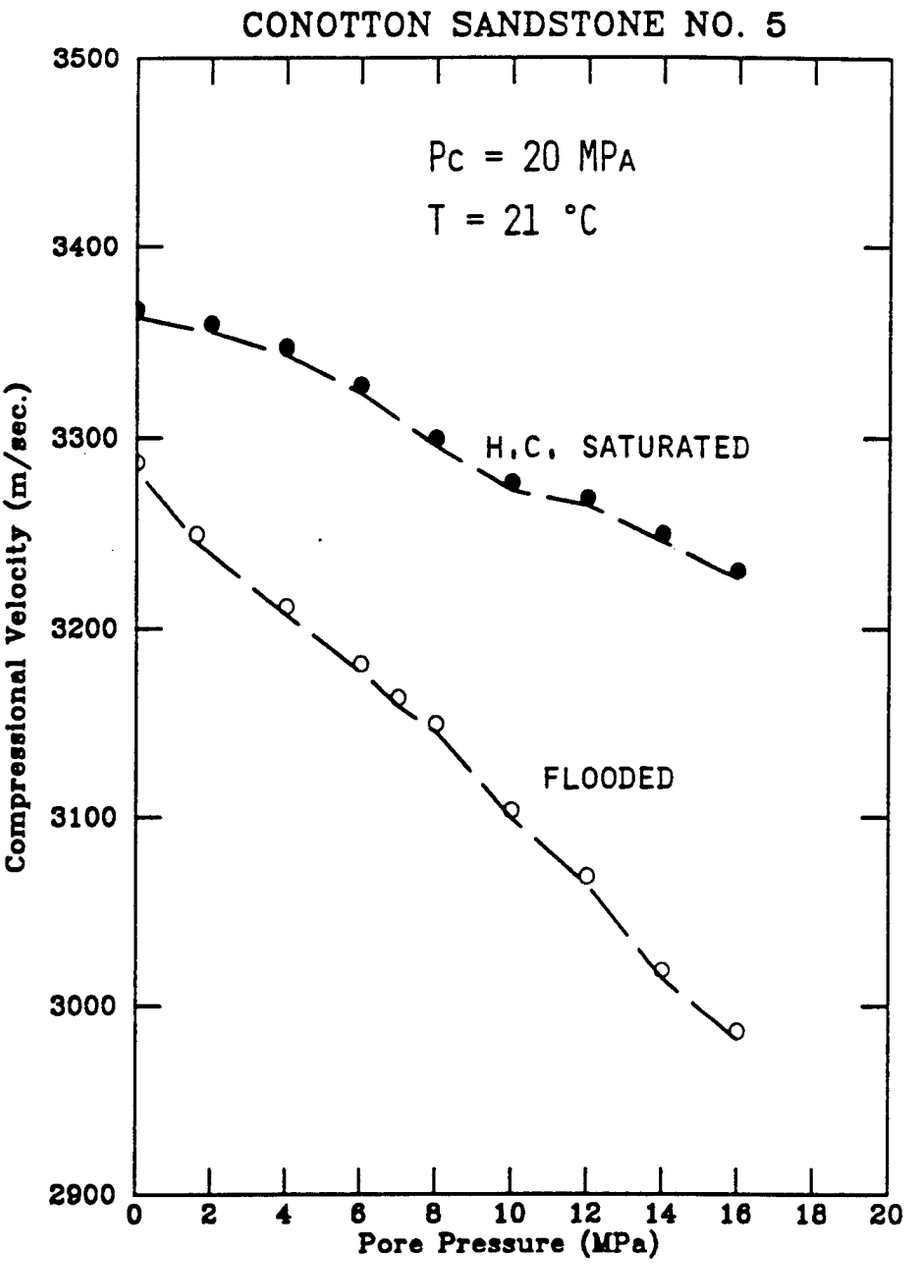
CONOTTON SANDSTONE NO. 5
Pc = 20 MPa
T = 21 °C
H.C. SATURATED
FLOODED
Compressional Velocity (m/sec.)
Pore Pressure (MPa)
3500
3400
3300
3200
3100
3000
2900
0
2
4
6
8
10
12
14
16
18
20

fig. 10c

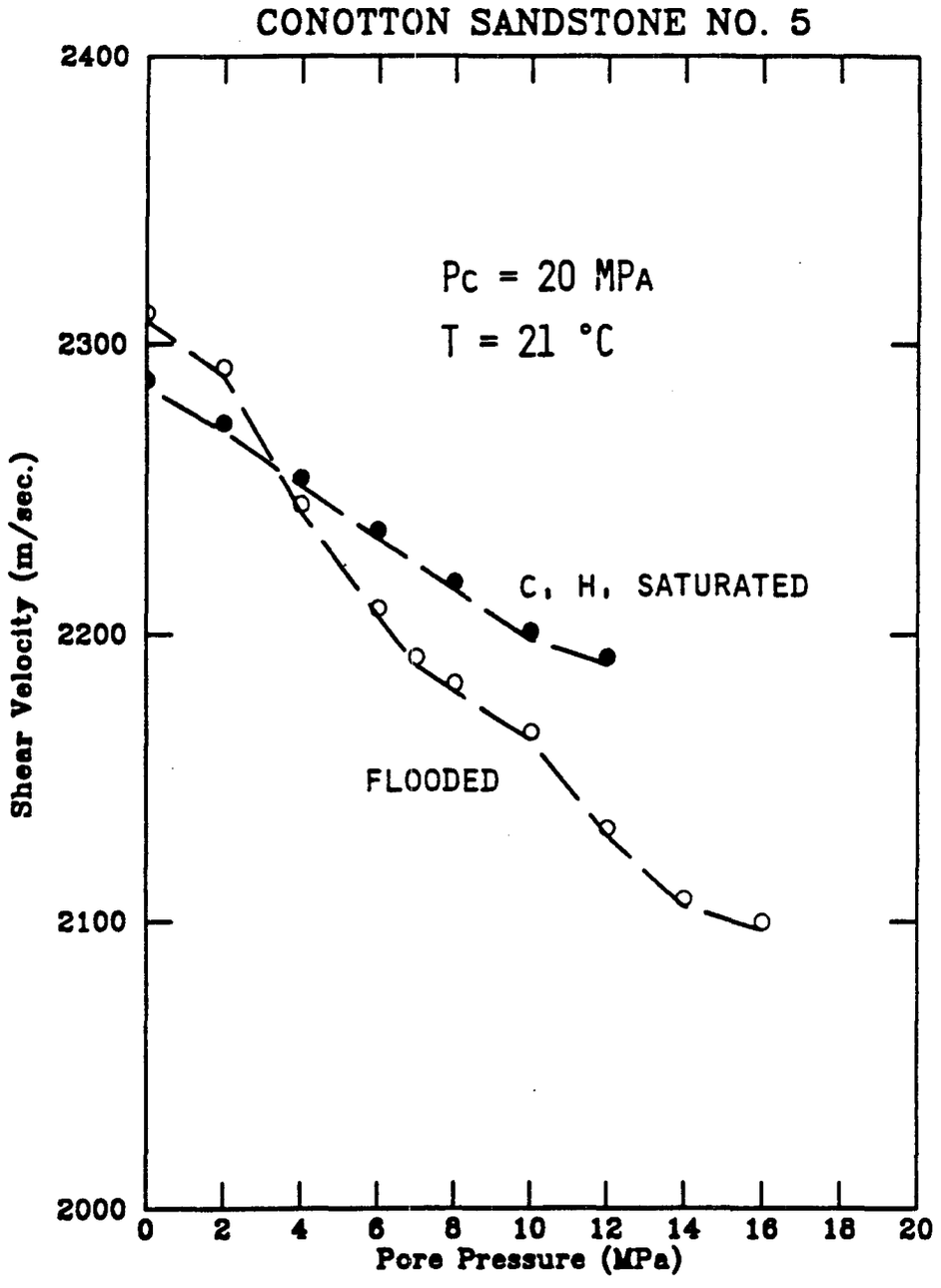
CONOTTON SANDSTONE NO. 5
Pc = 20 MPa
T = 21 °C
C. H. SATURATED
FLOODED
Shear Velocity (m/sec.)
Pore Pressure (MPa)
2400
2300
2200
2100
2000
0
2
4
6
8
10
12
14
16
18
20

fig. 10d

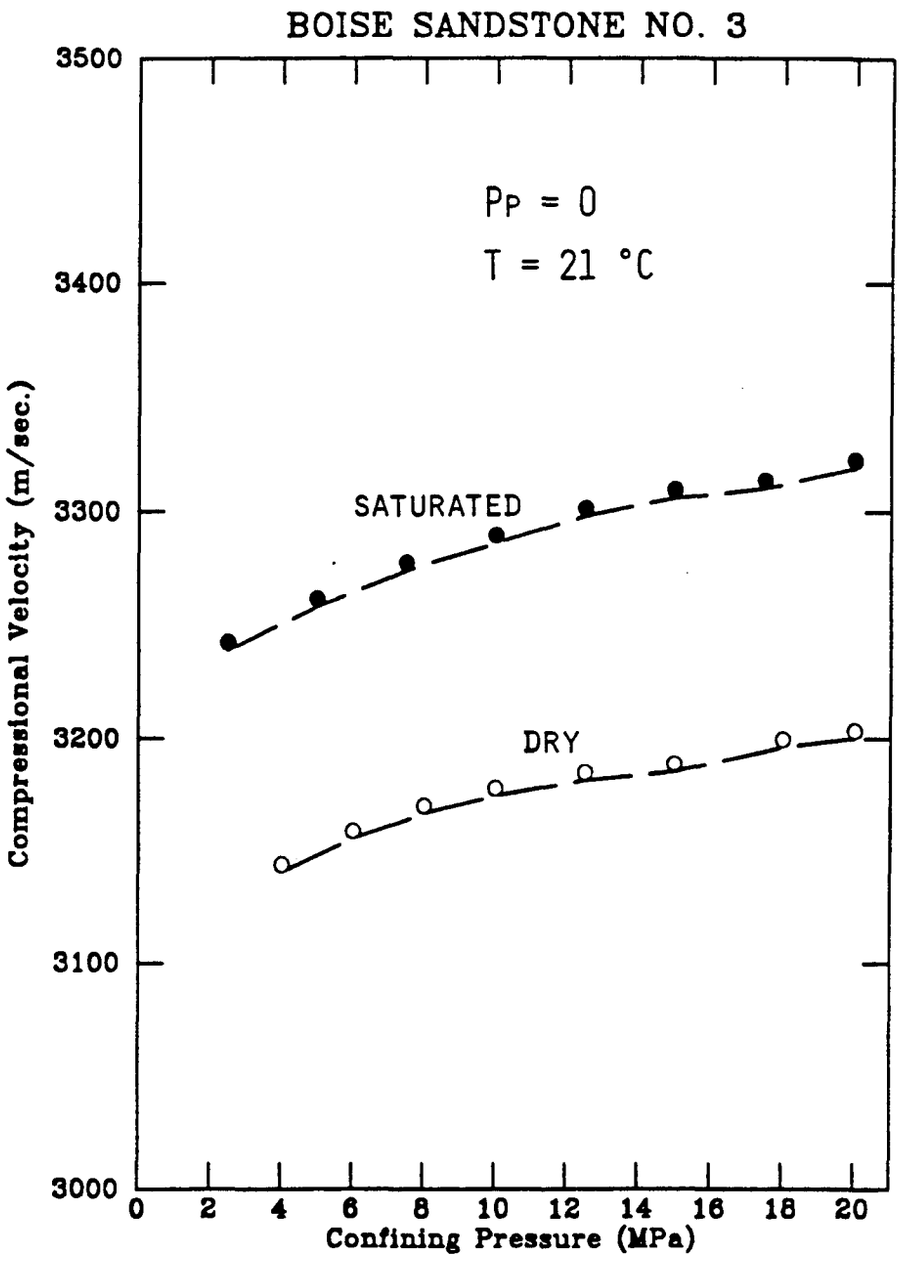
BOISE SANDSTONE NO. 3
Pp = 0
T = 21 °C
SATURATED
DRY
Compressional Velocity (m/sec.)
3500
3400
3300
3200
3100
3000
0
2
4
6
8
10
12
14
16
18
20
Confining Pressure (MPa)

fig. 11a

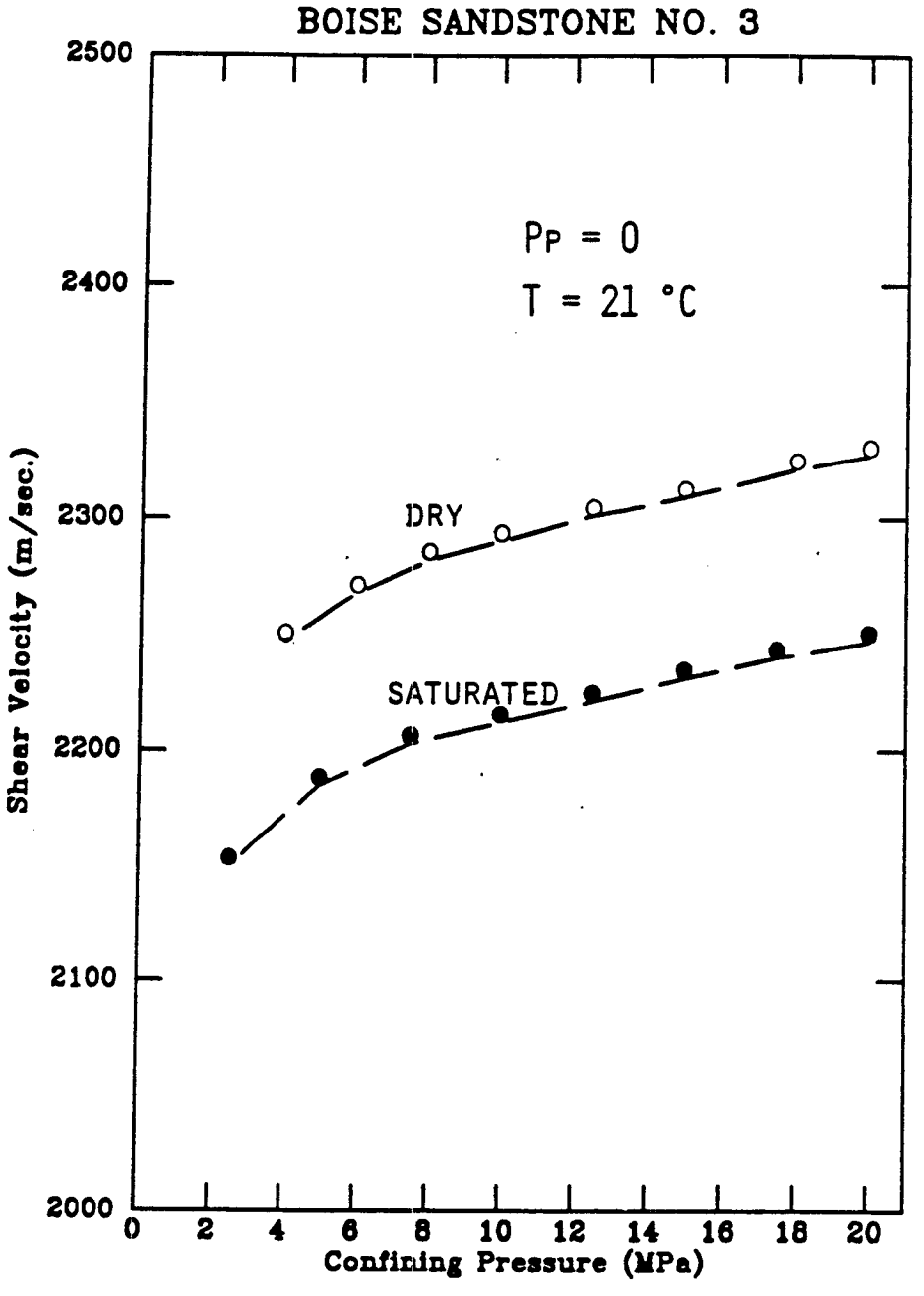
BOISE SANDSTONE NO. 3
Pp = 0
T = 21 °C
DRY
SATURATED
Shear Velocity (m/sec.)
2500
2400
2300
2200
2100
2000
0
2
4
6
8
10
12
14
16
18
20
Confining Pressure (MPa)

fig. 11b

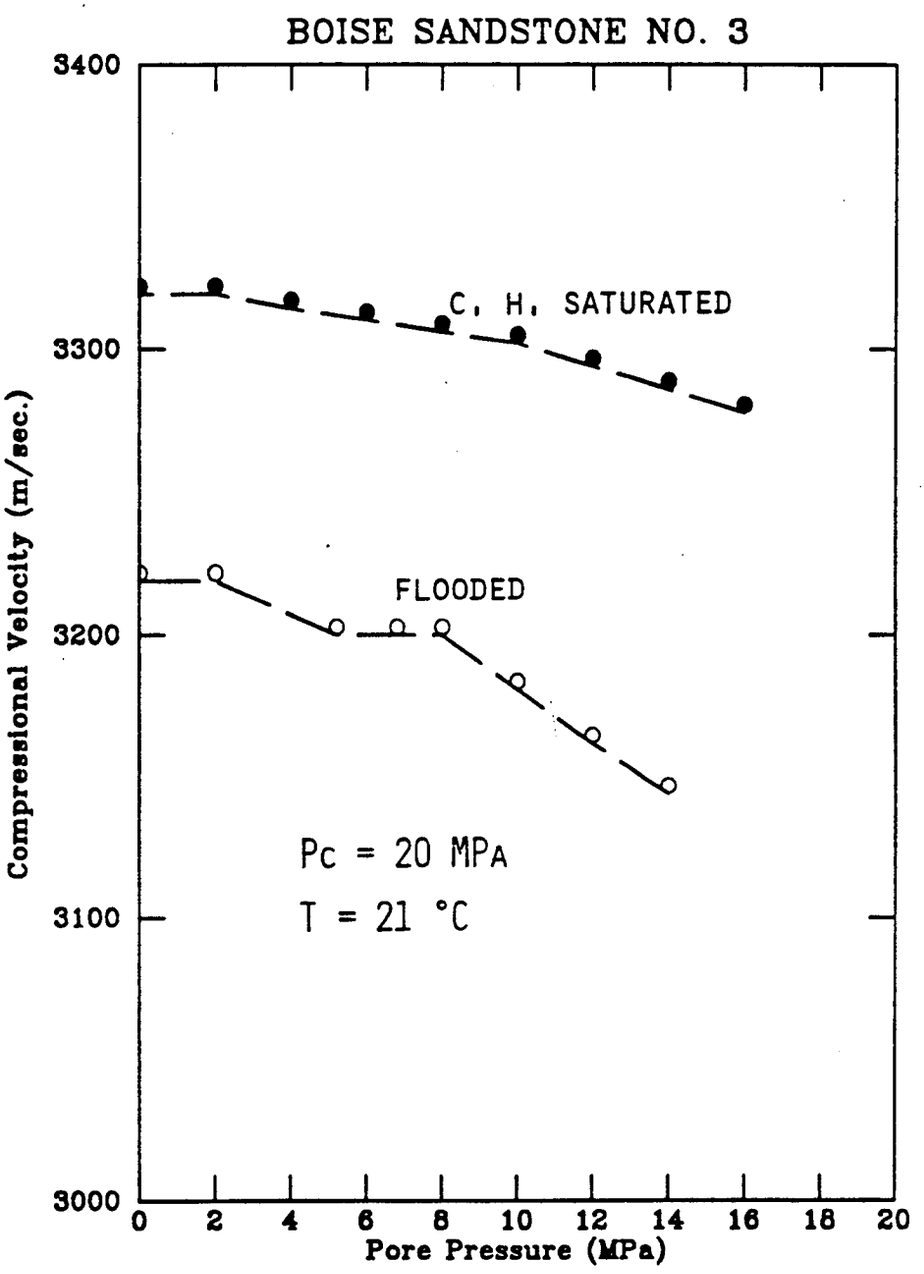
BOISE SANDSTONE NO. 3
3400
3300
3200
3100
3000
Compressional Velocity (m/sec.)
C. H. SATURATED
FLOODED
Pc = 20 MPA
T = 21 °C
0
2
4
6
8
10
12
14
16
18
20
Pore Pressure (MPa)

fig. 11c

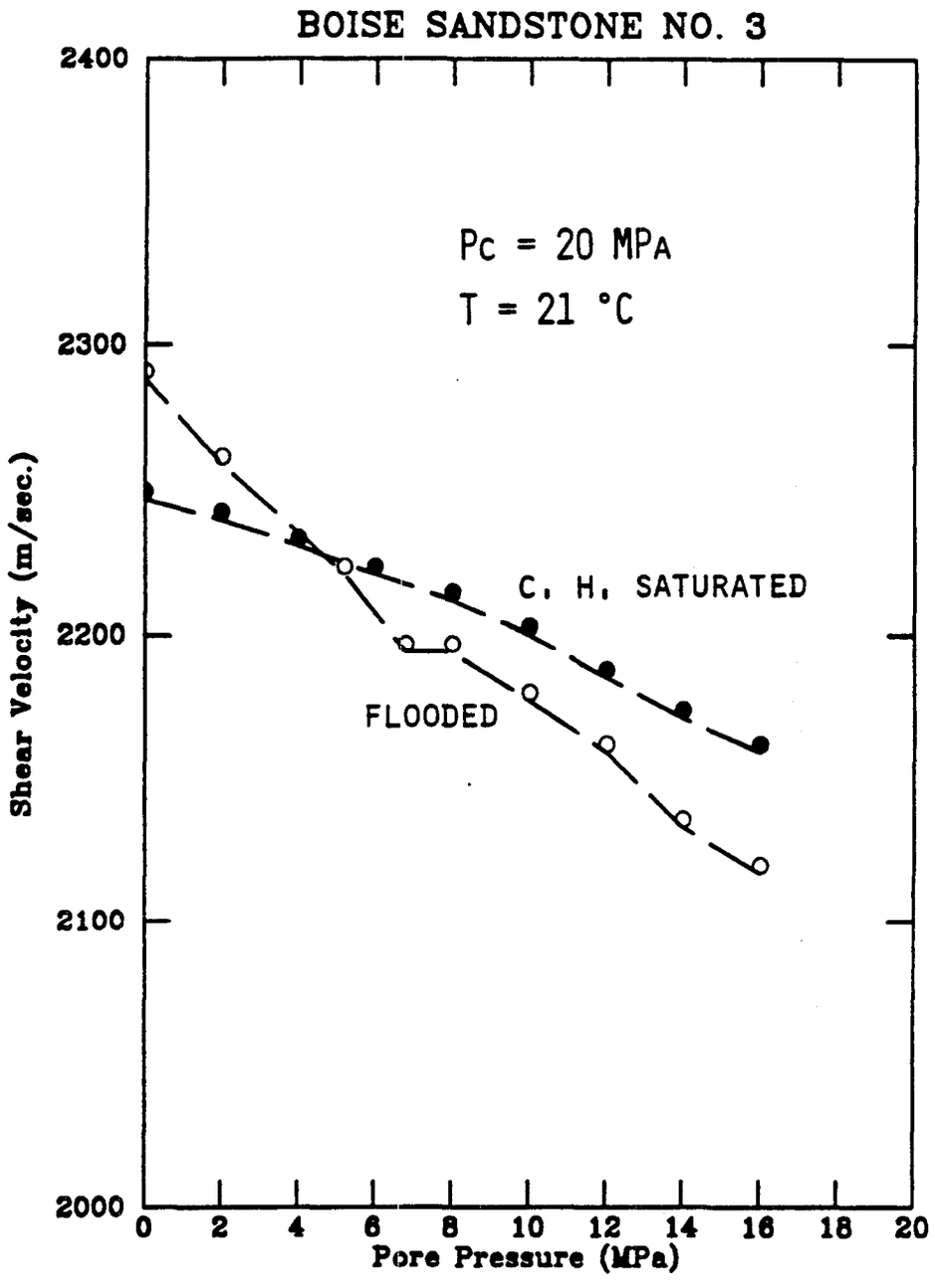
BOISE SANDSTONE NO. 3
Pc = 20 MPA
T = 21 °C
C. H. SATURATED
FLOODED
Shear Velocity (m/sec.)
Pore Pressure (MPa)
2400
2300
2200
2100
2000
0
2
4
6
8
10
12
14
16
18
20

fig. 11d

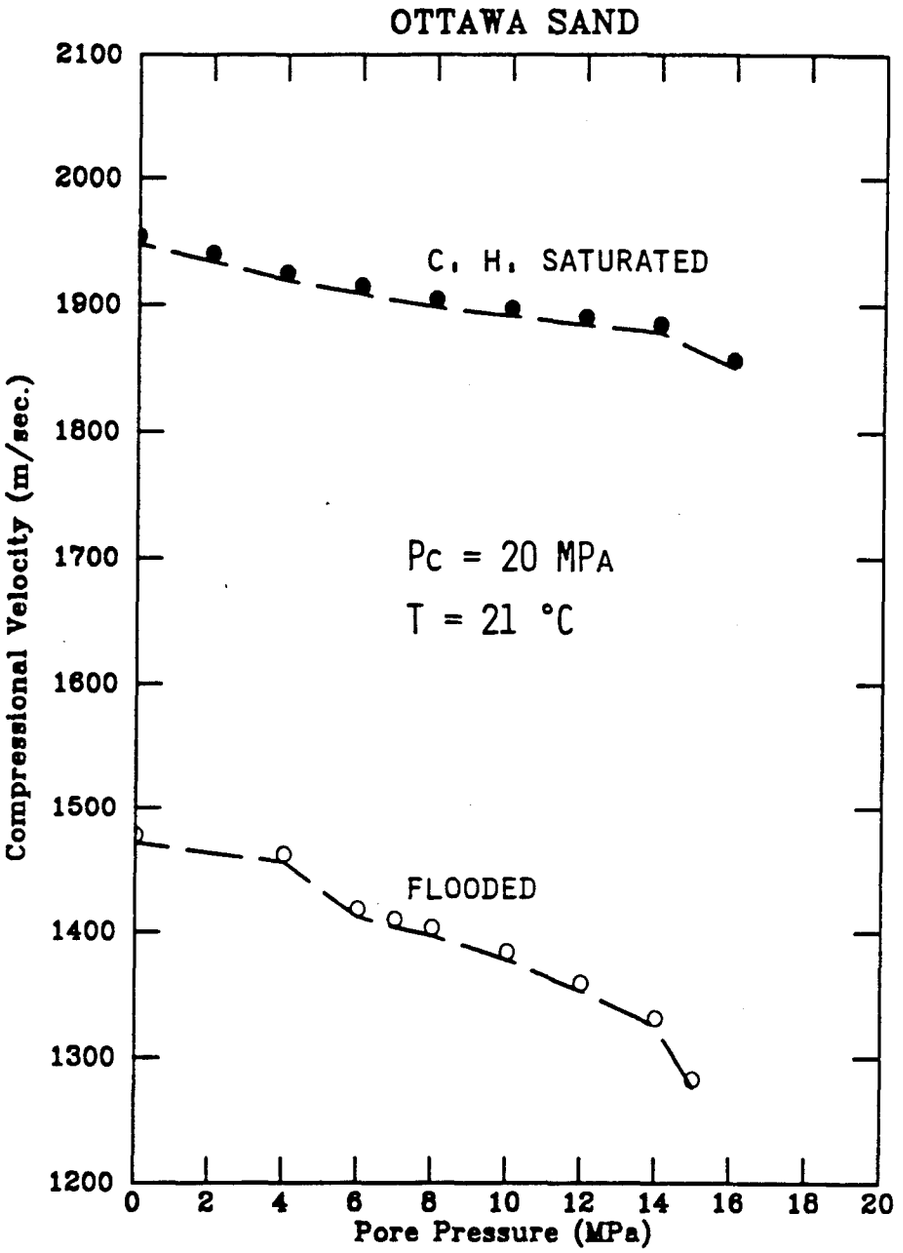
OTTAWA SAND
C. H. SATURATED
Pc = 20 MPA
T = 21 °C
FLOODED
Compressional Velocity (m/sec.)
Pore Pressure (MPa)
2100
2000
1900
1800
1700
1600
1500
1400
1300
1200
0
2
4
6
8
10
12
14
16
18
20

fig. 12

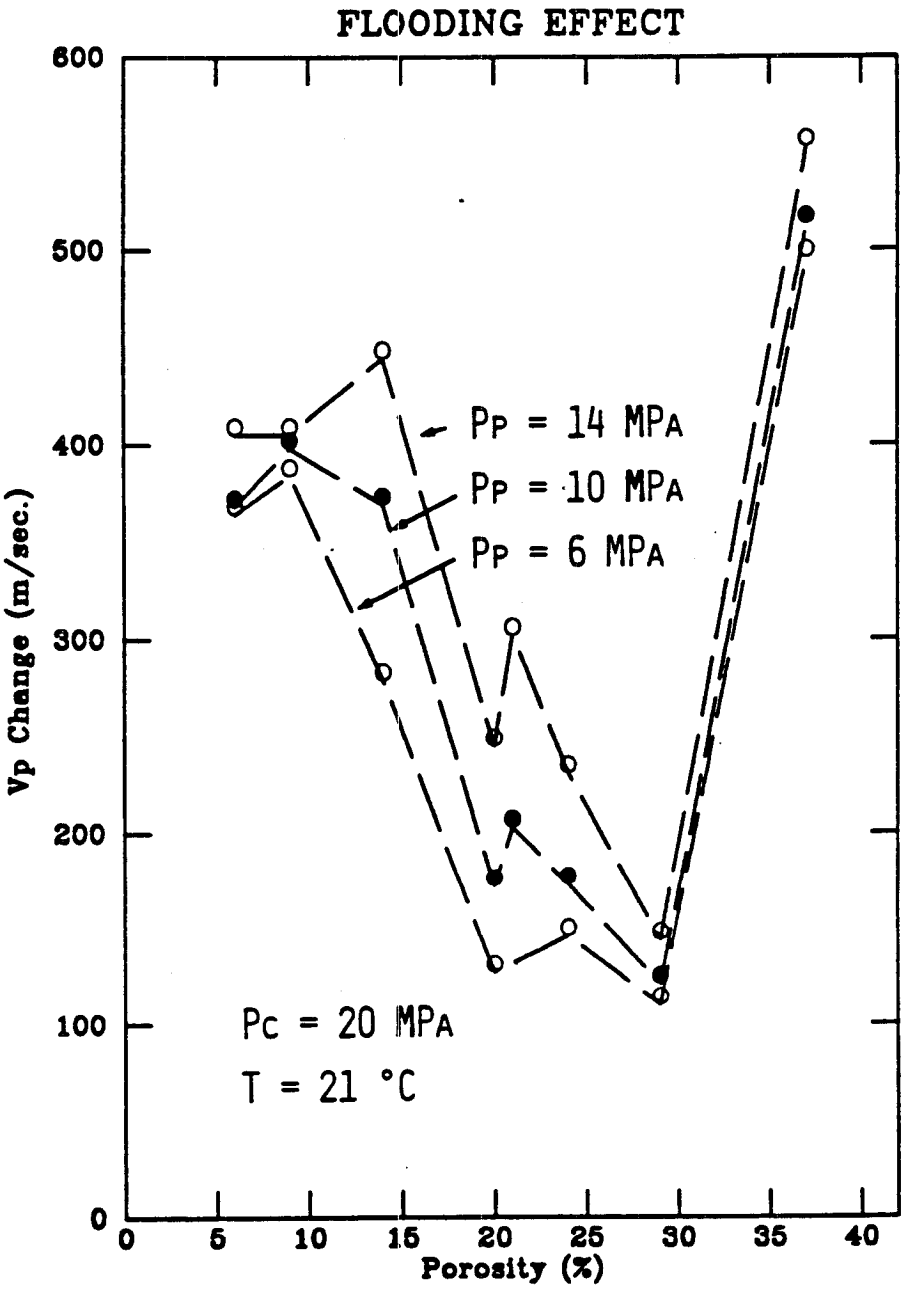
FLOODING EFFECT
600
500
400
300
200
100
0
Vp Change (m/sec.)
0
5
10
15
20
25
30
35
40
Porosity (%)
Pp = 14 MPa
Pp = 10 MPa
Pp = 6 MPa
Pc = 20 MPa
T = 21 °C

fig. 13a

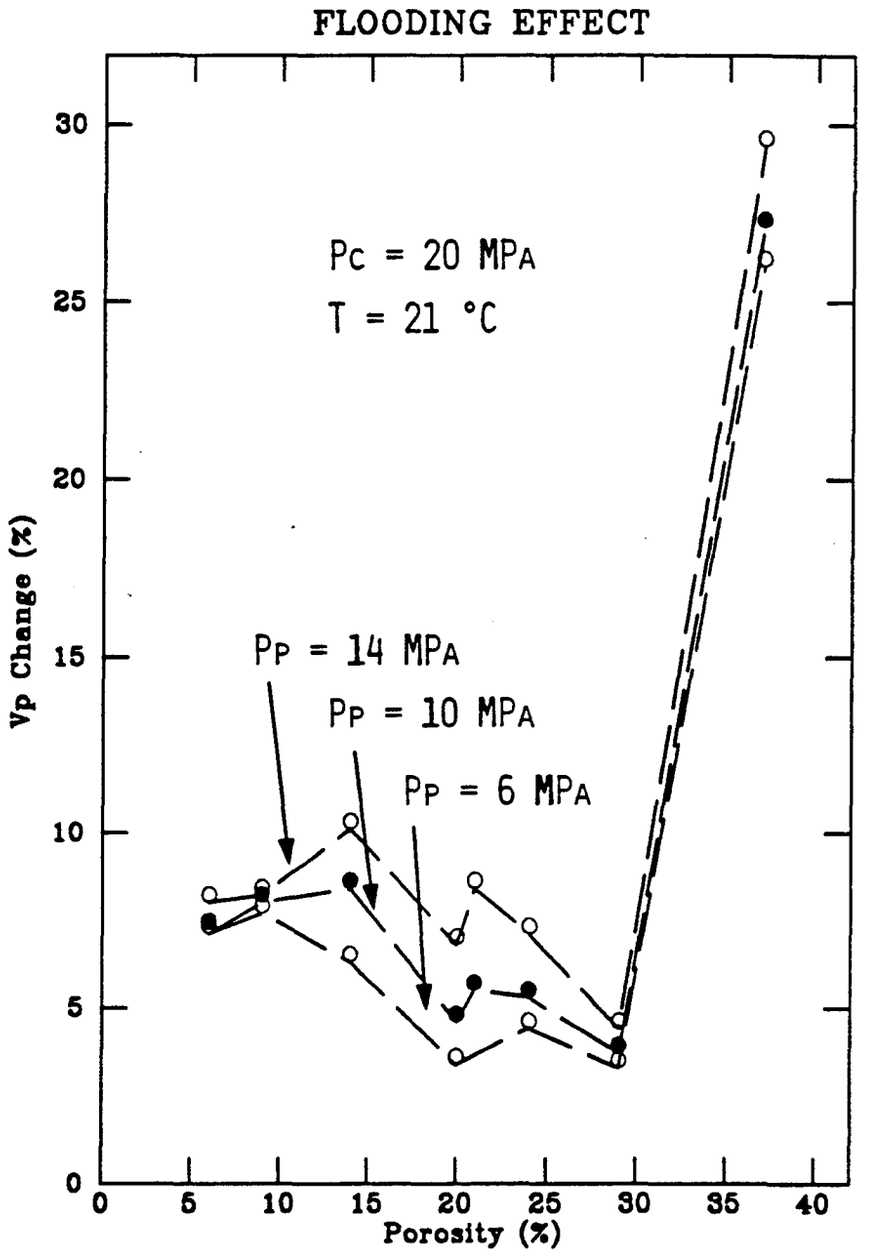
FLOODING EFFECT
Pc = 20 MPA
T = 21 °C
PP = 14 MPA
PP = 10 MPA
PP = 6 MPA
Vp Change (%)
Porosity (%)
0
5
10
15
20
25
30
35
40

fig. 13b

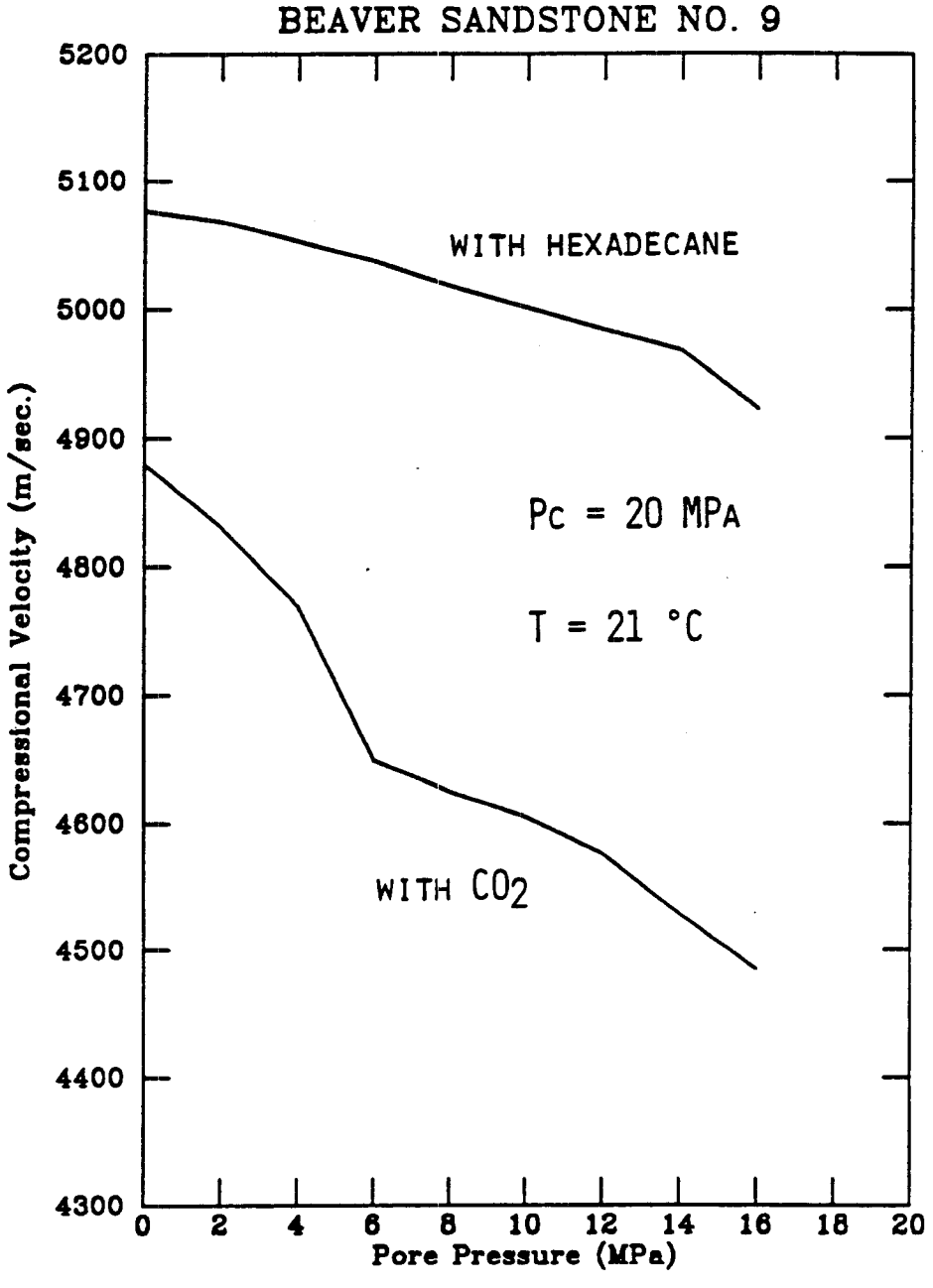
BEAVER SANDSTONE NO. 9
5200
5100
5000
4900
4800
4700
4600
4500
4400
4300
Compressional Velocity (m/sec.)
WITH HEXADECANE
Pc = 20 MPa
T = 21 °C
WITH CO2
0
2
4
6
8
10
12
14
16
18
20
Pore Pressure (MPa)

fig. 14

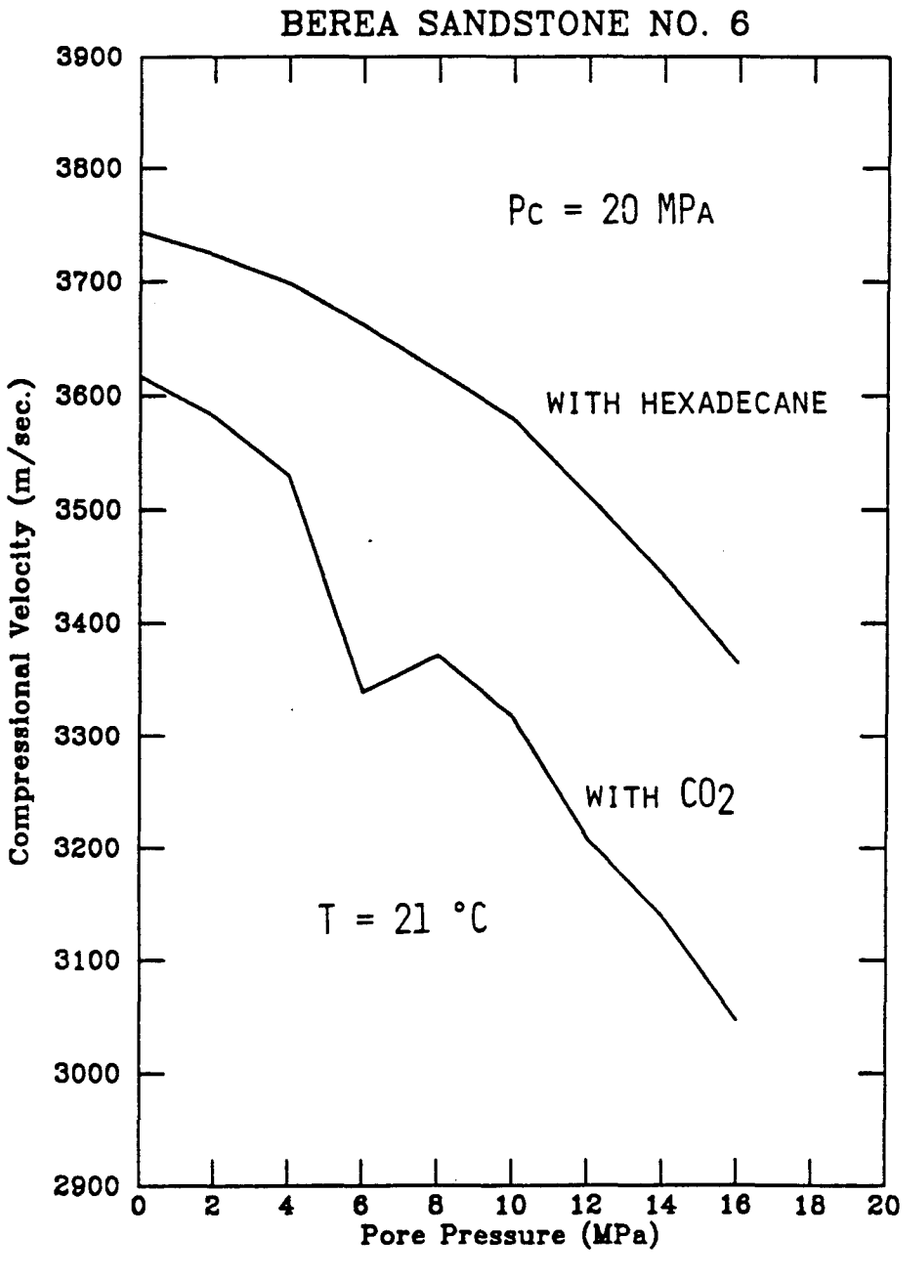
BEREA SANDSTONE NO. 6
Pc = 20 MPa
WITH HEXADECANE
WITH CO2
T = 21 °C
Compressional Velocity (m/sec.)
Pore Pressure (MPa)
3900
3800
3700
3600
3500
3400
3300
3200
3100
3000
2900
0
2
4
6
8
10
12
14
16
18
20

fig. 15

CHAPTER 7

EFFECT OF DIFFERENT PORE FLUIDS ON VELOCITIES IN ROCKS

ABSTRACT

This chapter provides some experimental results of the effects of different pore fluid saturations on wave velocities in rocks.

Compressional and shear wave velocities were measured in the laboratory in rocks saturated with air, water, light oil (normal decane), and heavy oil (oil C), respectively. It was found that the compressional wave velocities were different in the same rock sample with different pore fluids, while the shear wave velocities were not sensitive to the pore fluid changes.

Vp/Vs ratios and elastic moduli of the rocks with different pore fluids were also calculated and discussed in this chapter.

Our experimental results reveal that wave velocities and their temperature dependences in rocks saturated with heavy oils are pronouncedly different from those in the same rocks saturated with water or light oil; and it is highly possible that there exist reflection boundaries for seismic waves at the light-heavy oil saturation interfaces, and such reflections could be as strong as, or even stronger than, those at the air-water saturation interfaces. Therefore, it is suggested that the term "oil" used in seismic and acoustic logging interpretations is oversimplified: i.e., one should specify whether it is light or heavy oil when referring to oil saturations.

INTRODUCTION

During the past years, seismic methods have been playing a major role in the exploration for hydrocarbon reservoirs. However, little success would have been achieved without knowing and understanding seismic velocities and their behaviors with various parameters in various rocks. There is little doubt that seismic velocities and their variations with different parameters are the main cause of the success of seismic methods in explorations. Extended studies on velocities in various rocks have been done by numerous investigators. Unfortunately, most of these studies were done on rocks saturated with water or air, and very few experiments have been carried out on velocities and their behaviors with changing pressures and temperatures in rocks saturated with various hydrocarbons.

Furthermore, seismic methods have almost never been used in hydrocarbon recovery assessment, in spite of the growing need to better understand various recovery processes. A major problem in the area of reservoir evaluation and production is the realization of the complexity of most reservoirs, leading to large uncertainties in estimated total recovery, recovery rates, and recovery methods. There is little doubt that seismic methods will play, in the near future, a major role in helping to solve production and recovery problems. But we first need to understand what seismic waves can tell us about reservoir rocks, and how to extract the desired information. And, we also need to understand the seismic/acoustic properties of the reservoir fluids and rocks saturated with such fluids and their responses to the changes of reservoir conditions caused by the production or recovery processes.

Up to now, we still do not know if there exist reflection boundaries of seismic waves at the light-heavy oil saturation interfaces in reservoir rocks. In response to this problem and the problems described above, we carried out a series of experiments in the laboratory on wave velocities in two different reservoir rocks saturated with water, air, light and heavy oils, respectively, as a function of both pressure and temperature.

The experimental results show that velocities and their responses to temperature changes in the heavy oil saturated rock sample are different from those in water or light oil saturated samples; and it is highly possible that there exist reflections of seismic waves at the light-heavy oil saturation interfaces: Such reflections could be as strong as, or even stronger than, those at the air-water saturation interfaces, which means that "bright spots" could not only occur at the gas-water (or oil) but also at the light-heavy oil saturation interfaces on seismograms.

In this chapter, we first briefly describe the experimental method and apparatus used in the investigation and show the experimental results, then analyze the velocity data and their temperature and pressure behaviors, and finally discuss the applications of the experimental results and draw conclusions based on the results and analyses.

EXPERIMENTS AND SAMPLES

Method

As in the experiments described in the previous chapters, ultrasonic pulse transmission method was also employed in the experiments. The setup basically consisted an electronics panel and a mechanical package. The electronics panel was used for the pulse generation and data acquisition, while the mechanical package was for controlling the physical conditions (such as pore and confining pressures and temperature) of the rock samples.

The principle of the pulse transmission method was briefly described in the previous chapters. The pulses generated by the pulse generator were sent down to one of the two acoustic transducers attached to the rock sample which converts the electrical pulses to mechanical vibration. The mechanical waves were then picked up by the other transducer and converted back to electrical signals. These electrical signals were first amplified and then sent to a digital oscilloscope for the travel time measurements.

The velocities (both P and S) were calculated through

$$V_{p,s} = \frac{L(P,T)}{\Delta t(P,T)_{p,s}}, \tag{1}$$

where p,s represent compressional or shear waves, L(P,T) and $\Delta t(P,T)$ are the pressure and temperature calibrated sample length and travel time, respectively.

In the mechanical package, the confining pressure was controlled by pumping hydraulic fluid to the pressure vessel, and the pore pressure was by a digital fluid pump. Temperature was raised *via* a heating coil surrounded to the pressure vessel. The accuracies of the confining and pore pressures were around 50 psig (3 bars or 0.3 MPa) and 10 psig (1 bar or 0.1 MPa), respectively, while that of temperature was about 1° C.

Sample Preparation and Saturation

The rock samples used in the experiments were cut in cylindrical shape with diameters of 1.5 inches (3.81 cm) and length of about 2.5 inches (6.35 cm). The cross-section surfaces of the samples were finely ground to assure good contacts between the samples and the transducers.

After cut and ground, the rock samples were washed thoroughly with distilled water, and vacuum dried in an oven at about 60° C for several days. They were then ready to be saturated. The saturation of light pore fluids (i.e., n-decane and water) was done in the pressure vessel after the dry (air saturated) measurements, by injecting the pore fluid into the rock sample. However, the saturation of the heavy oil to the rocks was more complicated: We first jacketed the sample-transducers aggregate with high temperature plastic tubing with the heavy oil in between the sample and one of the transducers; then the aggregate was put in a vacuum oven under 60° C temperature and vacuum was applied to the aggregate in order to pull out the trapped air in the rock pores. The sample was evacuated for several hours. Afterwards, the rock-oil-transducers aggregate was put into the pressure vessel under pressure of 11500 psig

(793 bars or 79.3 MPa) and temperature of 60° C for 4 to 7 days to assure full saturations. We were unable to measure the degree of saturation since there was no way to do so. But we were confident that the rock sample was essentially fully saturated.

After the sample was believed to be fully saturated, the temperature was gradually brought down under high pressure. The leftover of the heavy oil was taken out by releasing the pore pressure line to room pressure. The sample was then ready for measurement.

Sample Descriptions

The rock samples used in the experiments were Berea sandstone and a Monterey formation rock. The composition of the Berea sandstone was analyzed by the point counting method and is listed in the following table.

Composition	Volume %	Composition	Volume %
Quartz	68	Clay	1.9
Mica	0.9	Opaque	2.3
Feldspar	3.2	Carbonate	0.9
Others	5.6	Porosity	18.2

The Monterey formation rock was from an oil-producing formation. It is a dolomitic chert with porosity of 15% (from saturation measurement), and mainly composed of quartz and dolomite. The composition result from X-ray analysis is listed in the table below.

The pore fluids used were distilled water, normal decane, air, and the heavy oil (oil C). The properties of water and air are well known, and those of normal decane and the heavy oil were described in chapter 3.

Composition	Weight %	Composition	Weight %
Quartz	67	Feldspar	2
Dolomite	19	Pyrite	3
Clay	7	Phosphate	2

Measurements

Measurements were made for travel times of the acoustic waves through the rock samples. Velocities were then calculated by equation (1) as a function of both pressure and temperature. In the measurements, pore pressures were controlled at 1450 psig (100 bars or 10 MPa) for water and n-decane saturated rocks and 0 psig for air and the heavy oil saturated samples.

The same rock sample was used for different pore fluid saturations: i.e., the rock sample was first used for air saturation. After the velocities were measured, it was evacuated and saturated with distilled water. After the velocity measurements on the water saturated sample, the sample was put in a vacuum oven at moderate temperature (60° C) to dry. Then it was saturated with normal decane for the velocity measurements. And accordingly, the sample was lastly saturated with the heavy oil after dried from decane saturation.

The potential problem of using the same rock sample for four measurements (air, water, n-decane, heavy oil saturations) was that there might exist velocity hysteresis since for each measurement process the rock was confined to about 12500 psig (862 bars or 86.2 MPa). However, we confined the rock sample first for several cycles before any measurement was made in order to eliminate or minimize such hysteresis. Therefore, if there was still some hysteresis, it would be small (less than 1%).

To assure temperature and pressure equilibrium inside the rock sample, we waited long enough between two measurement points. For example, once a temperature point

was reached, we kept this temperature point constant for at least 45 to 60 minutes before taking travel time measurements. For pressure, it took less time to equilibrate but 20 minutes was still allotted between two pressure points.

The measurements were essentially made in the ultrasonic frequency range, with central frequencies of about 1 MHz for compressional and about 0.6 MHz for shear waves.

Measurement errors might come from the precision of the digital oscilloscope readings, the uncertainties in picking the first break of the waveform train, uncertainties of the pressure and temperature measurements, and uncertainties in measuring the length of the sample. However we recorded waveforms at every measurement point onto floppy disks so that we could examine them later. Hence the error should be more or less systematic at every measurement point. The estimated total uncertainties were less than 2% for both compressional and shear wave velocities.

EXPERIMENTAL RESULTS AND INTERPRETATIONS

Acoustic wave velocities were measured in the Berea sandstone and Monterey dolomitic chert saturated with air ("dry"), distilled water, normal decane, and the heavy oil, respectively, as a function of both temperature and pressure. In this section, we show these experimental results and interpret the velocity behaviors of these two rocks.

Velocities in Air-saturated Rocks

Compressional wave velocities (Vp) in the air saturated ("dry") Berea sandstone are shown in figure 1a versus pressure, and the corresponding shear wave velocities (Vs) in the same rock sample are shown in figure 1b, at different temperatures. A common feature in these two figures is that both Vp and Vs are strongly dependent on confining pressures in the low pressure range, which suggests that the Berea sandstone may contain substantial amount of thin (low aspect ratio) cracks. At lower pressures, increasing

confining pressure tends to close the thin cracks and hence creates better contacts between the rock grains and grains and cements, since thin cracks are more compliant than pores. Such closures of thin cracks and better contacts in turn decrease the porosity and increase the moduli of the rock sample. Further increasing the confining pressure in the higher pressure range has less effect on the velocities owing to that the thin cracks are already closed.

The compressional and shear wave velocities in the "dry" Monterey dolomitic chert (saturated with air) are shown in figures 2a and 2b, respectively, as a function of pressure at different temperatures. Unlike those in the Berea sandstone, both Vp and Vs in the chert increase with increasing pressure consistently: there are no dramatic increases in low pressure ranges. This phenomenon apparently reflects that the dolomitic chert does not contain thin (low aspect ratio) cracks. Therefore, increasing confining pressure only decreases the porosity and makes better contacts between the rock grains and grains and cements.

Shown in figures 2c and 2d are respectively the compressional and shear wave velocities in the Monterey dolomitic chert versus temperature at different pressures. Similar to those in the Berea sandstone shown in figures 1a and 1b, both Vp and Vs decrease as temperature increases. Such decreases are mainly caused by the weakening and softening of the rock frame and possibly by different thermal expansions of the mineral constituents of the rock (Kern, 1982). However, the temperature dependence of both Vp and Vs is relatively small and different at different pressures. Basically the velocities decrease less than 5 to 6% at low pressures and about 2 to 3% at high pressures in the measurement temperature range.

Velocities in Water-saturated Rocks

The compressional and shear wave velocities in the Berea sandstone saturated with distilled water are shown in figures 3a and 3b, respectively, versus confining pressure at a constant pore pressure of 1450 psig (100 bars or 10 MPa) at different

temperatures. The confining pressure effect on the velocities (both Vp and Vs) is essentially the same as observed in the dry rock. However, water saturation increases the compressional wave velocities and decreases the shear wave velocities. The increase of the Vp is due to the fact that water is much less compressible than air and therefore substituting water for the air in the rock pores increases the bulk modulus of the rock. The decrease of the Vs is caused by the increased density of the rock upon water saturation. Since both air and water do not resist shear stresses, water saturation does not change the shear modulus (if not considering the wetting effect and other chemical and physical interactions between the water and the rock).

Like those in the air saturated rock, both Vp and Vs in the water saturated Berea sandstone decrease, but not strongly, as temperature increases. Again, this decrease becomes less significant at high pressures (figures 3c and 3d).

Velocities in Normal Decane-saturated Rocks

The compressional and shear wave velocities in the Berea sandstone saturated with normal decane are shown in figures 4a and 4b, respectively, versus confining pressure at different temperatures, and in figures 4c and 4d, respectively, versus temperature at various confining pressures. The velocities are very similar to those in the same rock sample saturated with water, except that the saturation effect is a little smaller since n-decane is more compressible and has a lower density than water. The increase in Vp and decrease in Vs upon n-decane saturation of the Berea sandstone are less significant.

Shown in figures 5a and 5b are the compressional and shear wave velocities, respectively, in the Monterey dolomitic chert as a function of confining pressure at various temperatures. The pressure response of both the Vp and Vs are essentially similar to that in the dry rock. i.e., there are no abrupt increases in either Vp or Vs as the confining pressure increases. Like that in the Berea sandstone, the n-decane saturation to the dolomitic chert also increases the Vp but decreases the Vs. The explanation

to the Berea sandstone also applies to this chert.

The compressional and shear wave velocities in the same chert are shown in figures 5c and 5d, respectively, versus temperature at different confining pressures. As observed before, both Vp and Vs decrease as temperature increases. And such decreases are leveled off at high pressures.

Both the compressional and shear wave velocities in the dry Berea sandstone and Monterey dolomitic chert decrease about 5 to 6% at low pressures and around 2 to 3% at high pressures, while in the water or n-decane saturated rocks, such decreases can be as high as 10% at low pressures and around 3 to 4% at high pressures, in the measurement temperature range (from 20 to 95° C). Therefore, liquid saturation enhances the temperature dependence of the velocities, which is especially true for the shear wave velocities. The possible explanation for this phenomenon is that the liquid in the pores serves as lubricant. As temperature increases, the minerals in the rock tends to expand, and the pore liquid makes such thermal expansion easier due to its lubrication effect. The lubrication effect of the pore liquid mainly contributes to the reduction of the shear friction between mineral grains. Therefore it mainly affects the shear modulus of the rock. At high pressures, such lubrication effect becomes less important since the grains are already confined together and relative slidings between them are highly restricted, so that even lubrication is put between grains, it does not reduce the shear friction much. Therefore, at high pressures, the temperature effect on the velocities is still small in liquid saturated rocks.

Velocities in Heavy Oil-saturated Rocks

Figures 6a and 6b show that both the compressional and shear wave velocities in the Berea sandstone sample saturated with the heavy oil are still strongly dependent on the confining pressures at various temperatures. However, the heavy oil saturation increases both the compressional and shear wave velocities. The increase in the compressional velocity is again caused mainly by the increased bulk modulus of the

pore fluid, and that in the shear velocity is caused by the viscous relaxation effect of the pore fluid. Furthermore, the dispersion effect also contributes to the Vp and Vs increases.

The compressional and shear wave velocities in the heavy oil saturated Berea sandstone are also plotted as a function of temperature at different pressures (figures 6c and 6d). The major difference of these two figures from those shown before is that both Vp and Vs decrease faster as temperature increases. For example, Vp decreases by 14% and Vs by 17% at low pressure (Pe = 550 psig or 38 bars), and Vp by 11% and Vs by 9% at high pressure (Pe = 10050 psig or 693 bars), in the measurement temperature range (from 22 to 92° C). These larger decreases are apparently related to the fast decrease of the Vp in and viscosity of the heavy oil as temperature increases.

For the Monterey dolomitic chert saturated with the heavy oil, the compressional and shear velocities are shown in figures 7a and 7b, respectively, as a function of confining pressure (pore pressure equals zero) at different temperatures, and in figures 7c and 7d, respectively, as a function of temperature at various pressures. The pressure responses of both the Vp and Vs are very similar to those in the same rock sample saturated with other fluids (air, water, n-decane). The heavy oil saturation increases the compressional velocity but still decreases the shear velocity, which again suggests that the dolomitic chert indeed does not contain thin cracks.

As observed in the Berea sandstone, both the compressional and shear wave velocities decrease faster in the heavy oil saturated chert than in the same sample saturated with other fluids (air, water, n-decane). As temperature increases from 22° to 88° C, both Vp and Vs decrease by about 8 to 9%. However, unlike that in the Berea sandstone, this amount of decrease is essentially the same at any pressures in the measurement range, which also suggests that the dolomitic chert basically contains only round pores which are still open at high pressures.

Effect of Different Pore Fluids

From the experimental results shown above, we see that fluid saturation to the rocks affects both the compressional and shear wave velocities. The magnitude of such effects is different for different pore fluids. In this section, we compare the effects of different pore fluid saturations on both Vp and Vs and provide some explanations on the possible causes. More quantitative analyses will appear in the next chapter.

Figure 8a shows the compressional wave velocities as a function of temperature at effective pressure of 2550 psig (176 bars or 17.6 MPa) in the Berea sandstone sample saturated with the four different pore fluids. A common feature in this figure is that liquid saturation increases the compressional wave velocities in the rock. Such increase is predicted by both the Gassmann relation (Gassmann, 1951) and the Biot theory (Biot, 1956) to be caused by the increase of the bulk modulus of the rock-fluid aggregate. The amount of such increase is mainly dependent on the pore fluid bulk modulus for the same rock sample.

The effect of the heavy oil saturation is much larger than expected. Since the bulk modulus and density (and hence compressional velocity) of the heavy oil are very close to those of water at room condition, we would expect, according to the Biot theory or Gassmann equation, similar compressional velocity in the heavy oil saturated rock sample as that in the same sample saturated with water. Such discrepancy of the measured Vp from that expected may be caused by several factors such as dispersion, chemical interaction and interfacial energy, and the contribution of the increased shear modulus due to the viscous relaxation of the pore fluid, etc..

Velocity dispersions usually always occur in liquid saturated rocks. That is, wave velocities increase with increasing frequency of the wave. Such a phenomenon is closely related to the inertial drag effect of the pore fluid (Biot mechanism), pore pressure gradients caused by the compliance heterogeneity of the pores ("local flow" mechanism), and pore fluid viscous relaxation effect. We will quantitatively analyze and discuss the

velocity dispersion effect in the next chapter.

The abnormally high Vp in the heavy oil saturated Berea sandstone may be partly contributed by the chemical effect. Generally speaking, liquid saturation tends to weaken the frame of the rock. When the rock sample is very dry, the compressional wave velocity may be 2-3% higher than that in the same sample which contains a small amount of liquid (say room dry condition) (Gregory, 1976; Murphy, 1982; Bacri and Salin, 1986). Oil is generally less reactive than water with the rock frame, therefore the chemical weakening effect in oil saturated rocks is smaller. In turn, we see higher Vp in oil saturated rocks.

The increased shear modulus of the rock with the heavy oil may also contribute to the increase in the compressional wave velocities. As seen in figure 8b, the shear wave velocities are systematically higher than those in the same Berea sandstone sample saturated with air, water, or n-decane, which is caused by the viscous skinning effect of the shear waves. Such higher shear velocities (i.e. higher shear modulus) also contribute to the compressional velocities since compressional velocities are related to both the bulk and shear moduli.

In figure 8b, both the water and n-decane saturations to the Berea sandstone sample decrease the shear velocities due to the increased density of the rock-fluid aggregate. Since water is denser than n-decane, its saturation effect is larger. The higher shear wave velocities in the same sandstone sample saturated with the heavy oil are apparently caused by the viscous skinning effect. According to the theory of wave propagation in fluids, shear waves can penetrate into viscous fluids by a depth called "skin depth" which is expressed as (Thurston, 1964)

$$\delta = \sqrt{\frac{\eta}{\rho \pi f}},$$

where η and ρ are the shear viscosity and density of the fluid, respectively, and f is the frequency of the shear wave.

According to the above expression, the shear wave traveling in a rock sample saturated with viscous fluids can penetrate through those cracks and pores with axis in the direction of wave propagation shorter than the "skin depth" of the wave. Therefore, the shear modulus of the rock is increased. For the heavy oil saturated Berea sandstone, the skin depth at 85° F (29.4° C) ($\eta = 28300$ cp or 28.3 Pa.s) is about 0.012 cm which may be longer than the diameter of many pores in this sandstone (assuming $\rho = 1{,}000\ Kg/m^3$ and $f = 0.6\ MHz$). For the water saturated Berea sandstone, the viscous skin depth is only about 0.73 μm which is obviously shorter than the diameter of most pores in this rock. Therefore, according to such a theory, the shear waves can travel through the heavy oils inside the thin cracks of the rock but not the water, hence we see higher shear wave velocities.

As temperature increases, the viscosity of the heavy oil decreases very fast (exponentially), so that the shear velocity in the heavy oil saturated rock becomes closer to those in the same rock saturated with other liquids.

The viscous skinning effect on shear wave velocities is only secondary. The primary factor is still the density of the pore fluid. Therefore, even though the viscous skinning effect increases the shear modulus of the rock-oil aggregate, the shear velocity is still not greatly increased due to the added density to the rock sample.

Figure 8c shows that the saturation effect on the compressional wave velocities in the Berea sandstone is decreased at higher effective pressure (6550 psig or 452 bars), due to the closure of the thin cracks. Since at high pressures, thin cracks are closed and the velocity in the dry rock is high, so that the velocity difference caused by the different fluid saturations becomes smaller. At higher effective pressures, the shear viscous skinning effect is also smaller due to the closure of the thin cracks and since only the round pores are open. Furthermore, the fast viscosity decrease of the heavy oil caused by the temperature increase causes the viscous skin depth to rapidly drop to the value of less than the diameter of these round pores.

Figure 9a shows the compressional wave velocities in the Monterey dolomitic chert saturated with different pore fluids (air, n-decane, and the heavy oil) at 22° C. All the compressional wave velocities have similar response to the effective pressure changes, except that when the sample is saturated with the heavy oil at low pressures. This phenomenon is apparently caused by the creation of thinner pores or cracks by the effective pressure increase, so that the viscous skinning effect is added. This explanation is also supported by figure 9b which shows that the shear wave velocity is increasing faster as the effective pressure increases in the low pressure range. Also shown in figure 9b is that the shear wave velocities are basically not affected by the heavy oil saturation, which may suggest that the effects of increased density due to saturation and of the viscous skinning just cancel each other.

Shown in figure 10a and 10b are the compressional and shear wave velocities, respectively, in the same Monterey dolomitic chert saturated with the three different pore fluids (namely, air, n-decane, and the heavy oil) as a function of temperature at effective pressure of 2000 psig (138 bars). The compressional wave velocities are increased, while the shear wave velocities are decreased, systematically by the liquid saturations. The slight decrease of the shear wave velocity in the chert upon the heavy oil saturation indicates that the density effect, but not the viscous skinning effect, is dominant, due to the fact that the chert contains mainly round pores.

At effective pressure of 6000 psig (414 bars, or 41.4 MPa) and lower temperatures, the difference between the compressional wave velocities in the n-decane and heavy oil saturated chert is slightly increased, owing to that at higher effective pressures, more thin cracks or pores are created, so that more viscous skinning effect is added (figure 10c). This explanation is apparently supported by figure 10d which shows that the difference between the shear wave velocities is larger at higher effective pressures.

Vp/Vs Ratios

The Vp/Vs ratios in the air-saturated Berea sandstone and the Monterey dolomitic chert are plotted in figure 11a and 11b, respectively. The Vp/Vs in both of these two rocks increase rapidly with increasing confining pressures, but slightly decrease with increasing temperature. Since Vp is related to both the bulk and shear moduli while Vs is only related to the shear modulus, the results suggest that increasing confining pressure increases, and increasing temperature decreases, both the bulk and shear moduli of the rocks (the moduli are shown later).

While the Vp/Vs ratios increase with increasing effective pressure in the air-saturated Berea sandstone, they decrease with increasing effective pressure when the rock is saturated with liquids (water, n-decane, and the heavy oil). The results are shown in figures 12a, 12b, and 12c, respectively.

The Vp/Vs is defined as

$$Vp/Vs = \sqrt{\frac{K}{\mu} + \frac{4}{3}},$$

where K and μ are the bulk and shear moduli, respectively. Our Vp/Vs results reveal that as the effective pressure increases, the bulk modulus increases faster than the shear modulus in dry rocks, while in the Berea sandstone fully saturated with liquids, μ increases faster than K in low pressure ranges. In a gas-saturated rock, increasing the effective pressure deforms the pores of the rock, so that both K and μ of the rock increase. In a liquid saturated rock, since the pore liquid is also highly incompressible, the bulk modulus of the rock is less sensitive to the pressure change; while the closure of the thin cracks in the rock increases the shear modulus greatly in the low pressure range, which results the Vp/Vs decrease.

In the Monterey dolomitic chert saturated with liquids (n-decane and heavy oil), the Vp/Vs ratios hardly change with pressure: i.e., both K and μ increase in the same rate as the effective pressure increases, which again confirms the previous statement

that the chert does not contain thin cracks or low aspect ratio pores.

Different liquid saturation also affects the Vp/Vs ratios slightly, which is mainly caused by the density and viscous skinning effects on the shear wave velocities.

At shallower depth, say less than 1000 meters (3050 feet) (equivalent to confining pressure of 3840 psig or 265 bar), the Vp/Vs ratio in the air-saturated Berea sandstone is around 1.55, while it is about 1.9 or 1.7 when the rock is water or oil saturated. In the dolomitic chert, the Vp/Vs ratio of the gas-saturated rock sample is also obviously different from those of the liquid-saturated sample.

From the experimental results, we see that the Vp/Vs ratios may well be an indicator which can be useful in delineating gas from liquid saturations in reservoir rocks, since the Vp/Vs ratios in gas-saturated rocks are lower than those in liquid saturated rocks.

Elastic Moduli of the Rocks

The bulk and shear moduli of the rocks with different pore fluids were calculated using the velocity data. The bulk modulus

$$K = \rho \left(Vp^2 - \frac{4}{3} Vs^2 \right),$$

and the shear modulus

$$\mu = \rho \, Vs^2,$$

where ρ is the density of the rock.

Figure 14a shows that the bulk modulus of the air-saturated Berea sandstone increases faster than the shear modulus as the confining pressure increases. However, in figures 14b, 14c, and 14d, the shear moduli of the same Berea sandstone sample saturated with water, n-decane, and the heavy oil, respectively, increase faster than the bulk moduli in the low effective pressure range (below 5000 psig or 345 bars), while at higher pressures, the shear and bulk modulus curves are essentially parallel as the

effective pressure increases. Theses modulus responses to the pressure changes also provide explanations to the Vp/Vs results shown in figures 11 to 13.

In figure 15a, the bulk modulus of the air-saturated Monterey dolomitic chert also increases faster than the shear modulus as the confining pressure increases. In the same chert sample saturated with n-decane and the heavy oil, the bulk and shear moduli increase with about the same rate as the confining pressure increases.

Figures 16 and 17 show the bulk and shear moduli of the Berea sandstone sample saturated with water and n-decane, respectively. At high confining pressures, the bulk moduli of both the water- and n-decane-saturated rock are insensitive to the temperature changes. However, at low confining pressures, the bulk moduli are affected by the pore fluid properties: For example, at confining pressure of 2000 psi (138 bar, or 13.8 MPa) (effective pressure = 550 psi or 38 bars), the bulk moduli of the water-saturated sample increases slightly as temperature increases below $75^{\circ}C$, which is correspondent to the bulk modulus increase of the pore water. The shear moduli of the Berea sandstone sample always decrease with increasing temperature, although at high confining pressures, such decrease is slower.

In figure 18, both the bulk and shear moduli of the same Berea sandstone sample saturated with the heavy oil decrease rapidly at any pressure level as temperature increases. Such rapid decreases are directly related to the properties of the heavy oil, since both the bulk modulus and the viscosity of the heavy oil decrease very rapidly with increasing temperature.

As observed in the Berea sandstone sample, the bulk moduli of both the air- and n-decane-saturated Monterey dolomitic chert sample are insensitive to the temperature changes at high effective pressures (figures 19 and 20). The shear moduli decrease consistently as temperature increases.

Both the bulk and shear moduli of the same chert saturated with the heavy oil decrease rather rapidly as temperature increases (figure 21), as also observed in the

Berea sandstone.

The effect of different pore fluid saturation on the bulk and shear moduli of the Berea sandstone sample and of the Monterey dolomitic chert sample are shown in figures 22 and 23, respectively. The liquid (water, n-decane, and the heavy oil) saturation increases the bulk moduli of the rocks, since the pore liquids are much less compressible than air. The magnitude of such bulk modulus increase is dependent on the bulk modulus of the pore fluid. However, the bulk modulus of the heavy oil-saturated Berea sandstone is much higher than that of the same sandstone sample saturated with water, although the bulk modulus of the heavy oil is about the same as that of water. This bulk modulus anomaly is caused by the dispersion of the wave velocities which will be discussed and analyzed in the next chapter.

The shear moduli of the Berea sandstone sample saturated with different pore fluids are very close to each other, except that of the same sample saturated with the heavy oil. The higher shear modulus of the heavy oil-saturated sandstone is caused by the viscous skinning effect of the heavy oil, as discussed previously. Figure 22b also shows that the water saturation does not change the shear modulus of the Berea sandstone. However, the n-decane saturation increases the shear modulus slightly, which may be caused by that n-decane is a non-wetting fluid to the Berea sandstone so that the surface energy at the rock grain-n-decane interfaces is higher (Murphy, *et al.*, 1984).

As observed in the Berea sandstone sample, the shear modulus of the Monterey dolomitic chert saturated with the heavy oil is also higher than that of the same sample saturated with air. In contrast, however, the n-decane saturation decreases the shear modulus of the same chert sample, which may be caused by the interactions of the pore fluid with the mineral constituents of the rock.

From the experimental results, we see that the pore fluid difference affects not only the velocities in, but also the moduli of, the rocks. The effects are caused by the

compressibility and viscosity differences of the pore fluids and the velocity dispersions which will be discussed in the next chapter.

APPLICATION:

Reflection Coefficients at Light-Heavy Oil Saturation Interfaces

Our experimental results show that there exists pronounced difference between the measured compressional wave velocities in light oil (normal decane) and heavy oil (oil C) saturated rocks, especially in the Berea sandstone sample, which suggests that saturation interfaces between light and heavy oils might be also the reflection boundaries of seismic waves. Therefore we calculated the reflection coefficients at the normal decane-heavy oil saturation interface in the Berea sandstone, and as a comparison, the reflection coefficients at the air-water saturation interface in the same sandstone were also calculated. The calculated results are listed in the following table.

Berea Sandstone	Reflection Coefficients			
	$T = 23°\ C$		$T = 91°\ C$	
Saturation	Effective P (psig)		Effective P (psig)	
Interface	2550	6550	2550	6550
N-Decane --- Oil C	0.0636	0.0598	0.0346	0.0201
Air --- Water	0.0742	0.0573	0.0889	0.0609

From the above table, we see that at low temperatures (most heavy oil reservoirs have low reservoir temperatures), the reflection coefficients of the acoustic waves at the light-heavy oil saturation interface could be as large as, or even larger than, those at the air-water saturation interface in the same rock, which means "bright spots" may exist not only at the gas-water saturation interfaces, but also at the light-heavy oil

interfaces. Hence, such light-heavy oil saturation interfaces can be detected by conventional seismic and acoustic logging methods.

The dispersion analysis which will be shown in the next chapter shows that the wave velocities are dispersive even at seismic frequencies in heavy oil saturated rocks, which means that in the seismic frequency band the velocities are about equal to the values measured at 1 MHz frequency in the laboratory. This suggests that the seismic wave reflection would be stronger at the light-heavy oil interfaces in the seismic frequency band since the velocities in light oil saturated rocks are a little lower at seismic frequencies due to dispersion.

The reflection coefficients at the light-heavy oil saturation interfaces are dependent on both the effective pressure and temperature. At higher effective pressures, the effect of different pore fluids is decreased due to the closure of the cracks and thin pores, so that the reflection coefficients are decreased. As temperature increases, the compressional wave velocity in heavy oil saturated rocks decreases faster due to the dramatic decreasing in the Vp and viscosity of the heavy oil, so that the reflection coefficients at the light-heavy oil saturation interface decrease.

The light-heavy oil interfaces may exist in the field. Figure 24 is a map of part of the Lagunillas field, Venezuela, showing the API gravity of the the oil (after Dickey and Hunt, 1972). In this map, the shallowest oil has an API gravity of 12°. The oil becomes gradually lighter downdip. At a depth of 1500 m (4921 feet), the API gravity of the oil is 20°. In this reservoir, the heavier oil overlies the lighter oil, which is physically impossible if there is continuity of the vertical permeability and if the fluid is Newtonian. The explanation of Dickey and Hunt (1972) for this situation is that the shallow oil has become highly asphaltic as a result of loss of its light ends in water solution. Asphalts, which are non-Newtonian, may have formed a gel which prevented the gravitational adjustment of the fluids and the leakage of the oil at the outcrop.

SUMMARY AND CONCLUSION

Our experimental results show that the velocities in fluid saturated rocks are related to the pore fluid type. Generally speaking, besides the effect of the bulk modulus of the pore fluid, the viscosity and the chemical effect of the fluid on the surface of the rock grains also play important roles on the velocities in the rock-fluid aggregate.

The viscosity of the pore fluid affects both the compressional and shear wave velocities in rocks, especially in those crack-rich rocks. Our analyses show that when the viscosity of the pore fluid is high, the pore fluid does not have enough time to get relaxed during a half period of the acoustic wave passing through, so that the measured velocities (both Vp and Vs) are higher. Such a phenomenon is especially very common in thin crack-rich rocks such as granites and many sandstones.

Another effect of the pore fluid viscosity is that it also increases the measured shear wave velocities in thin crack-rich rocks through the viscous skinning effect. However, such viscous skinning effect is only secondary, the primary factor on the shear wave velocity is still the density of the pore fluid.

The Vp/Vs ratio of a rock basically can not tell if the rock is light oil, or heavy oil, or water saturated. But there does exist pronounced difference between the Vp/Vs ratios of a gas-saturated and a liquid-saturated rock: the Vp/Vs ratio in gas-saturated rocks is always lower. Therefore, Vp/Vs ratios may be useful in delineating gas from liquid saturations in reservoir rocks.

Both the Bulk and shear moduli of the rocks are affected by the pore fluid difference. The bulk modulus of a saturated rock is directly related to the bulk modulus of the pore fluid and the velocity (or modulus) dispersions. The shear modulus of a saturated rock is related to the viscosity of the pore fluid and the thin crack content of the rock. Furthermore, both the bulk and shear moduli may be also related to the pore geometry and structure of the rock and to the interactions of the

pore fluid with the rock frame.

The experimental results show that it is highly possible that there exist wave reflections at the light-heavy oil saturation interfaces in rocks. Such reflections could be as strong as, or even stronger than, the reflections at the air-water saturation interfaces in the same rocks. Therefore, it is suggested that the term "oil" is oversimplified in the interpretations of seismic and acoustic logging results, and one should specify whether it is light or heavy oil when referring to oil saturations.

REFERENCES

Bacri, J. and Salin, D. 1986. Sound velocity of a sandstone saturated with oil and brine at different concentrations. Geophys. Res. Let., vol. 13, no. 4, 326-328.

Biot, M. A., 1956. Theory of propagation of elastic waves in a fluid saturated porous solid, I, Low frequency range. J. Acoust. Soc. Am., vol. 28, 168-178. II, high frequency range. J. Acoust. Soc. Am., vol. 28, 179-191.

Dickey, P. A. and Hunt, J. M, 1972. Geochemical and hydrogeologic methods of prospecting for stratigraphic traps. AAPG Memoir, 16, 136-167.

Gassmann, F., 1951. Uber die elastizitat poroser medien, Vierteljahrsschr. Naturforsh. Ges. Zuerich, vol. 96, 1-23.

Gregory, A. R., 1976. Fluid saturation effects on dynamic elastic properties of sedimentary rocks. Geophysics, vol. 41, 895-921.

Kern, H., 1982. Elastic wave velocity in crustal and mantle rocks at high pressure and temperature: the role of the high-low quartz transition and of dehydration reactions. Phys. Earth Plan. Inter., vol. 29, 12-23.

Murphy, W. F., 1982. Effects of partial water saturation on attenuation in Massillon sandstone and Vycor porous glass. J. Acoust. Soc. Am., vol. 71, 1458-1468.

Murphy, W. F., K. W. Winkler and R. L. Kleinberg, 1984. Contact microphysics and viscous relaxation in sandstones. In: Physics and chemistry of porous media. edited by D. L. Johnson and P. N. Sen. Am. Inst. Phys., New York, 176-190.

Nur, A. M. and Wang, Z., 1987. In-situ seismic monitoring EOR: The petrophysical basis. SPE paper 16865.

Thurston, R. N., 1964. Wave propagation in liquids. In: Physical acoustics, vol. 1A.

Edited by W. Mason. Academic Press.

Wang, Z., 1987. Acoustic velocities in oils and the effects on velocities in rocks, Part I: Acoustic velocities in oils. 120pp.

Wang, Z. and A. M. Nur, 1986. Effect of temperature on wave velocities in sands and sandstones with heavy hydrocarbons. SEG Expanded Abs., 3-5.

Wang, Z. and Nur, A. M., 1987. Velocities in hydrocarbons and hydrocarbon-saturated rocks and sands. SEG Expanded Abs., 1-4.

FIGURE CAPTIONS

Figure 1. Compressional (a) and shear (b) wave velocities in the Berea sandstone saturated with air.

Figure 2. Compressional and shear wave velocities in the Monterey dolomitic chert saturated with air versus confining pressure (a, b) and temperature (c, d).

Figure 3. Compressional and shear wave velocities in the Berea sandstone saturated with water versus confining pressure (a, b) and temperature (c, d).

Figure 4. Compressional and shear wave velocities in the Berea sandstone saturated with normal decane versus confining pressure (a, b) and temperature (c, d).

Figure 5. Compressional and shear wave velocities in the Monterey dolomitic chert saturated with normal decane versus confining pressure (a, b) and temperature (c, d).

Figure 6. Compressional and shear wave velocities in the Berea sandstone saturated with the heavy oil versus confining pressure (a, b) and temperature (c, d).

Figure 7. Compressional and shear wave velocities in the Monterey dolomitic chert saturated with the heavy oil versus confining pressure (a, b) and temperature (c, d).

Figure 8. Compressional and shear wave velocities in the Berea sandstone saturated with different fluids as function of temperature at effective pressures of 2,550 psig (a, b) and 6,550 psig (c, d).

Figure 9. Compressional (a) and shear (b) wave velocities in the Monterey dolomitic chert saturated with different fluids versus effective pressure at 22° C.

Figure 10. Compressional and shear wave velocities in the Monterey dolomitic chert saturated with different fluids as function of temperature at effective pressures of 2,000 psig (a, b) and 6,000 psig (c, d).

Figure 11. Vp/Vs ratios in the air-saturated Berea sandstone (a) and Monterey dolomitic chert (b) as a function of confining pressure.

Figure 12. Vp/Vs ratios in the Berea sandstone saturated with water (a), normal decane (b), and the heavy oil (c), respectively, versus confining pressure at various temperatures.

Figure 13. Vp/Vs ratios in the Monterey dolomitic chert saturated with normal decane (a) and the heavy oil (b), respectively, versus pressure at various temperatures.

Figure 14. Bulk and shear moduli of the Berea sandstone saturated with air (a), water (b), n-decane (c), and the heavy oil (d), respectively.

Figure 15. Bulk and shear moduli of the Monterey dolomitic chert saturated with air (a), n-decane (b), and the heavy oil (c), respectively.

Figure 16. Bulk (a) and shear (b) moduli of the Berea sandstone saturated with water, versus temperature at different confining pressures.

Figure 17. Bulk (a) and shear (b) moduli of the Berea sandstone saturated with n-decane, versus temperature at different confining pressures.

Figure 18. Bulk (a) and shear (b) moduli of the Berea sandstone saturated with the heavy oil, versus temperature at different confining pressures.

Figure 19. Bulk (a) and shear (b) moduli of the Monterey dolomitic chert saturated with air, versus temperature at different confining pressures.

Figure 20. Bulk (a) and shear (b) moduli of the Monterey dolomitic chert saturated with n-decane, versus temperature at different confining pressures.

Figure 21. Bulk (a) and shear (b) moduli of the Monterey dolomitic chert saturated with the heavy oil, versus temperature at different confining pressures.

Figure 22. Effect of different pore fluids on the bulk (a) and shear (b) moduli of the Berea sandstone at $22^{\circ}\,C$.

Figure 23. Effect of different pore fluids on the bulk (a) and shear (b) moduli of the Monterey dolomitic chert at $22^{\circ}\,C$.

Figure 24. A map of part of the Lagunillas field, Venezuela, showing the API gravity of the oil (after Dickey and Hunt, 1972).

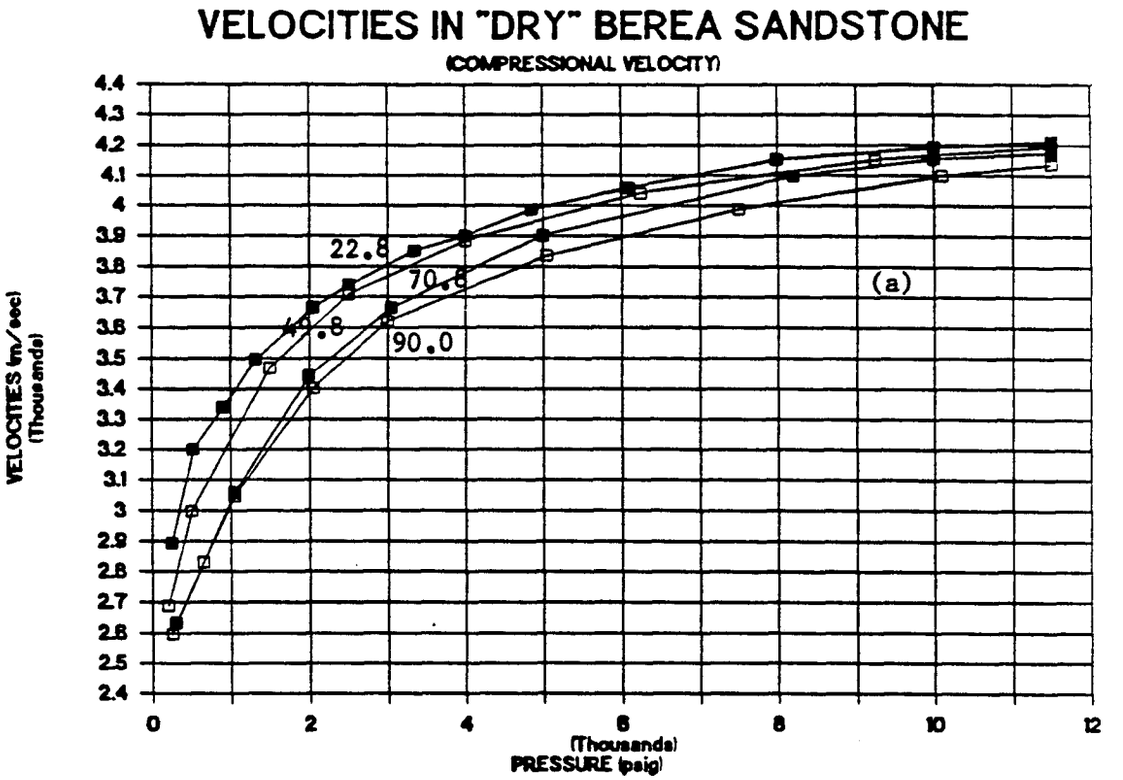
VELOCITIES IN "DRY" BEREA SANDSTONE
(COMPRESSIONAL VELOCITY)
VELOCITIES (m/sec)
(Thousands)
4.4
4.3
4.2
4.1
4
3.9
3.8
3.7
3.6
3.5
3.4
3.3
3.2
3.1
3
2.9
2.8
2.7
2.6
2.5
2.4
22.8
70.8
49.8
90.0
(a)
0
2
4
6
8
10
12
(Thousands)
PRESSURE (psig)

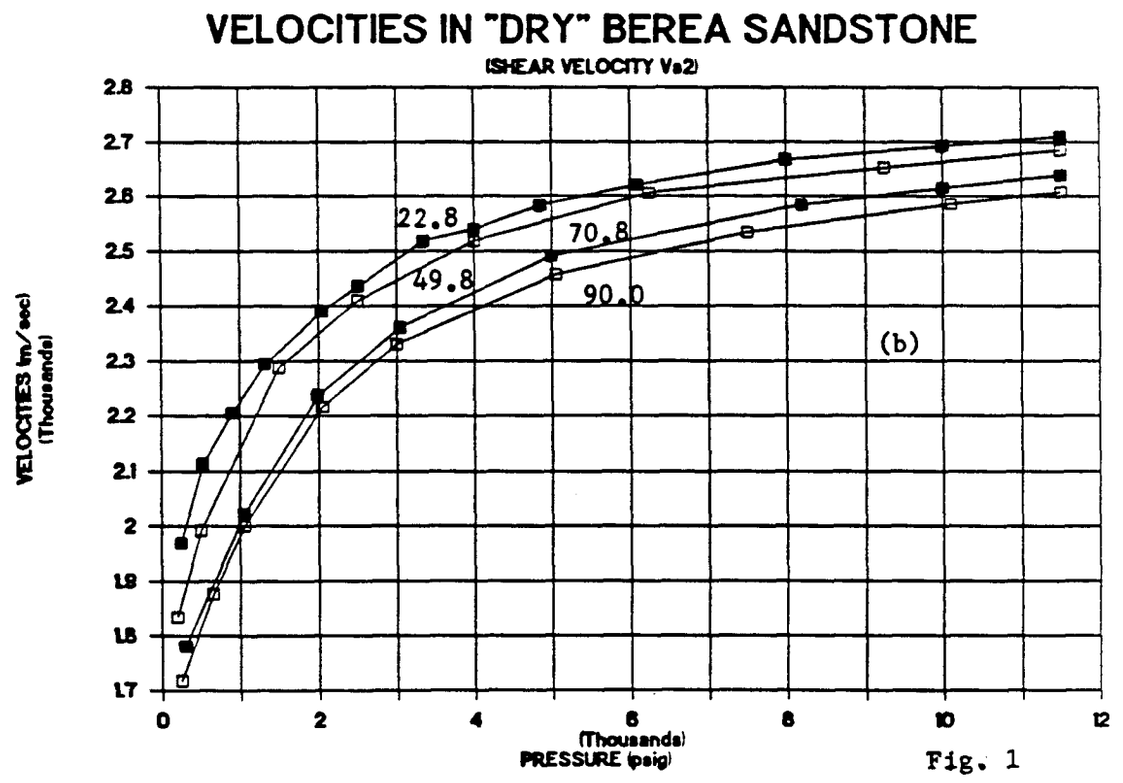
VELOCITIES IN "DRY" BEREA SANDSTONE
(SHEAR VELOCITY Vs2)
VELOCITIES (m/sec)
(Thousands)
2.8
2.7
2.6
2.5
2.4
2.3
2.2
2.1
2
1.9
1.8
1.7
22.8
70.8
49.8
90.0
(b)
0
2
4
6
8
10
12
(Thousands)
PRESSURE (psig)

Fig. 1

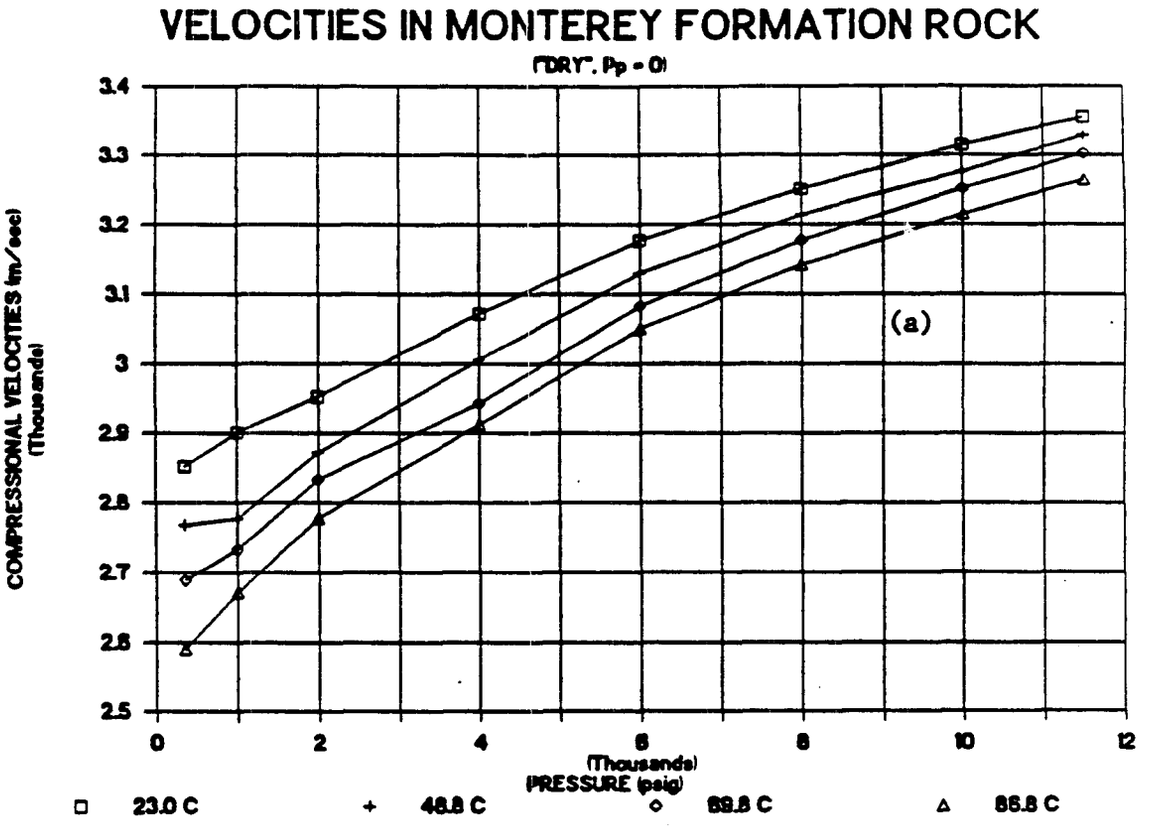
VELOCITIES IN MONTEREY FORMATION ROCK
("DRY", Pp = 0)
COMPRESSIONAL VELOCITIES (m/sec)
(Thousands)
3.4
3.3
3.2
3.1
3
2.9
2.8
2.7
2.6
2.5
0
2
4
6
8
10
12
(Thousands)
PRESSURE (psig)
(a)
□ 23.0 C
+ 46.8 C
◇ 69.8 C
△ 86.8 C

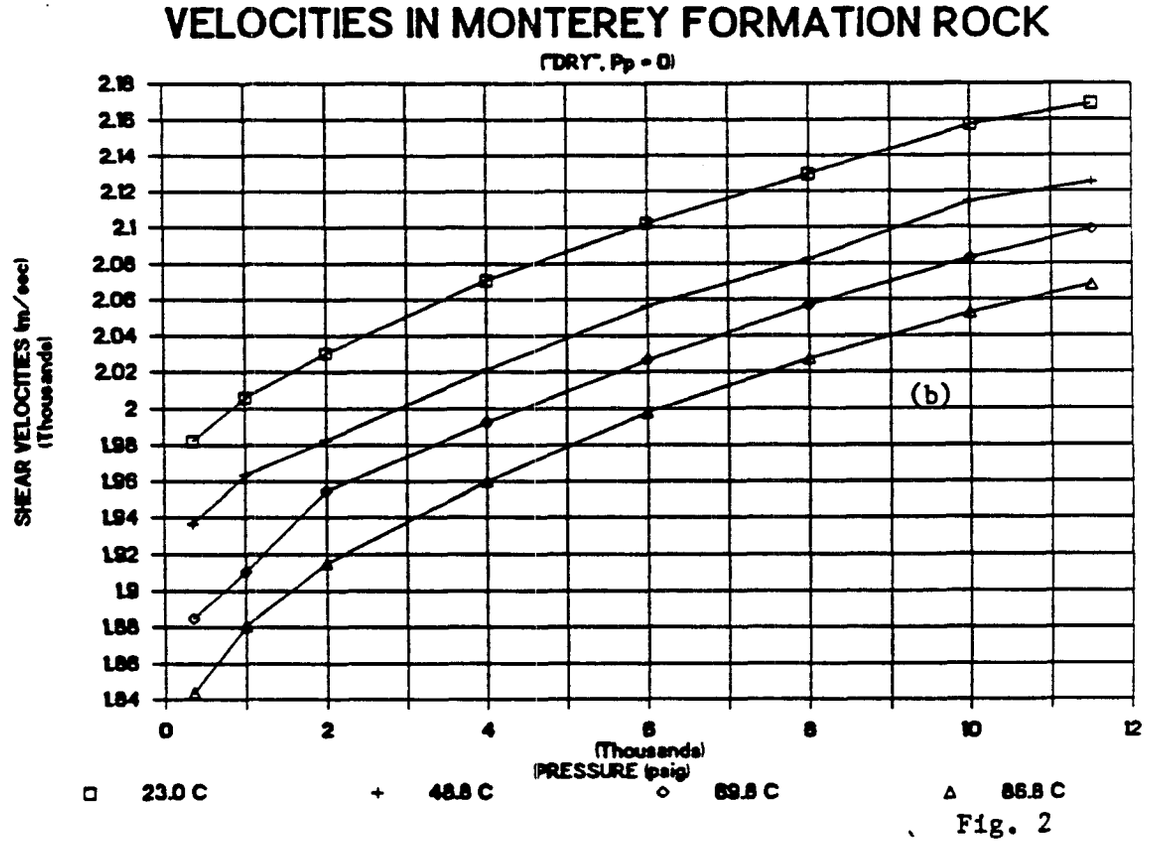
VELOCITIES IN MONTEREY FORMATION ROCK
("DRY", Pp = 0)
SHEAR VELOCITIES (m/sec)
(Thousands)
2.18
2.16
2.14
2.12
2.1
2.08
2.06
2.04
2.02
2
1.98
1.96
1.94
1.92
1.9
1.88
1.86
1.84
0
2
4
6
8
10
12
(Thousands)
PRESSURE (psig)
(b)
□ 23.0 C
+ 46.8 C
◇ 69.8 C
△ 86.8 C

Fig. 2

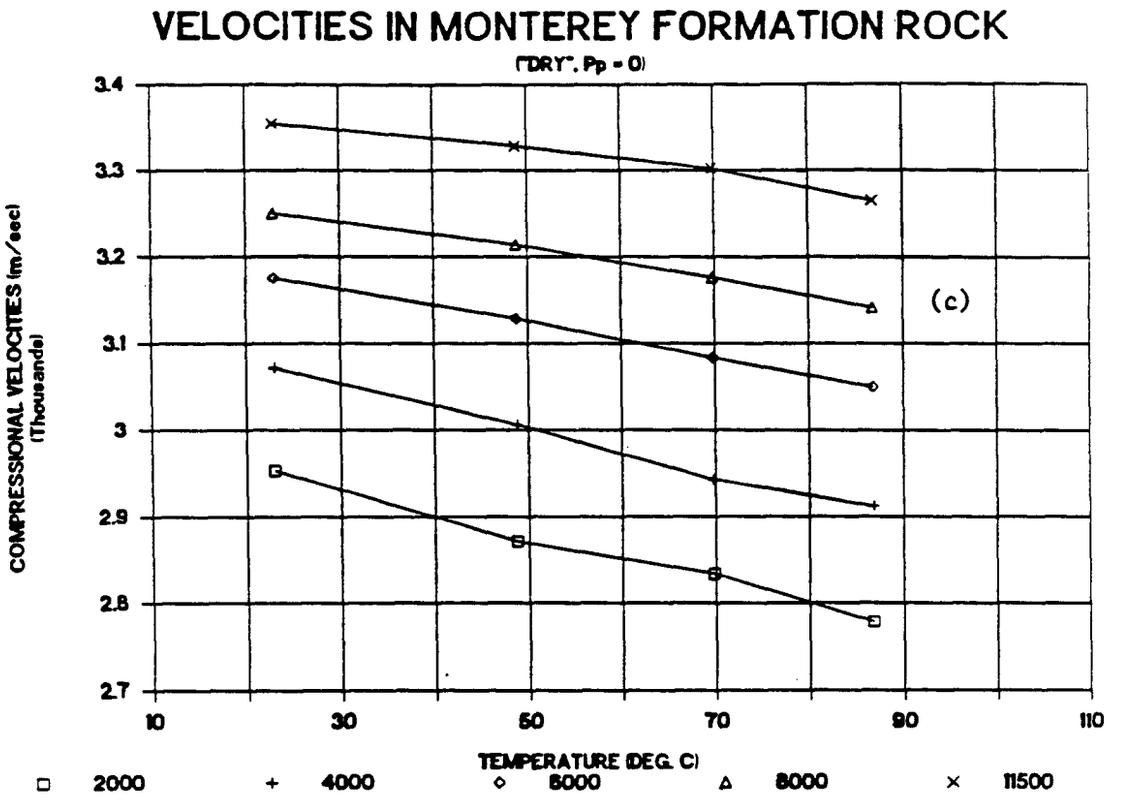
VELOCITIES IN MONTEREY FORMATION ROCK
("DRY", Pp = 0)
COMPRESSIONAL VELOCITIES (m/sec)
(Thousands)
3.4
3.3
3.2
3.1
3
2.9
2.8
2.7
10
30
50
70
90
110
TEMPERATURE (DEG. C)
(c)
□ 2000
+ 4000
◇ 6000
△ 8000
× 11500

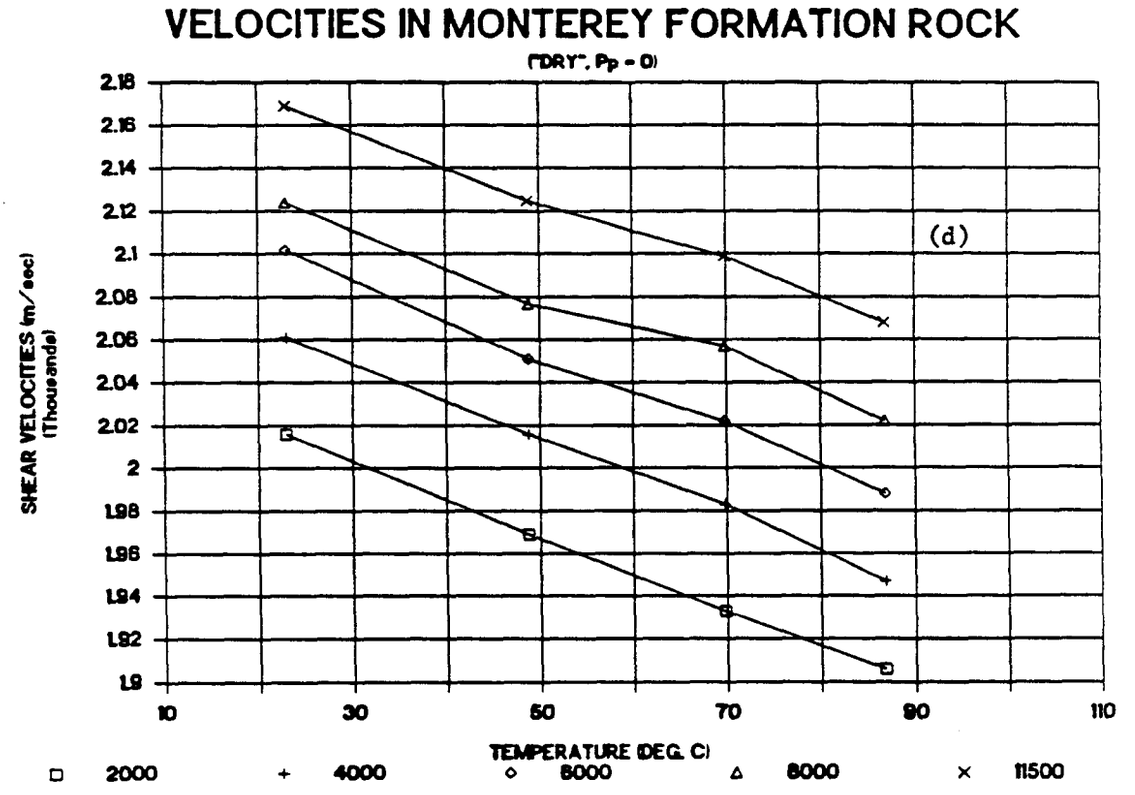
VELOCITIES IN MONTEREY FORMATION ROCK
("DRY", Pp = 0)
SHEAR VELOCITIES (m/sec)
(Thousands)
2.18
2.16
2.14
2.12
2.1
2.08
2.06
2.04
2.02
2
1.98
1.96
1.94
1.92
1.9
10
30
50
70
90
110
TEMPERATURE (DEG. C)
(d)
□ 2000
+ 4000
◇ 6000
△ 8000
× 11500

Fig. 2

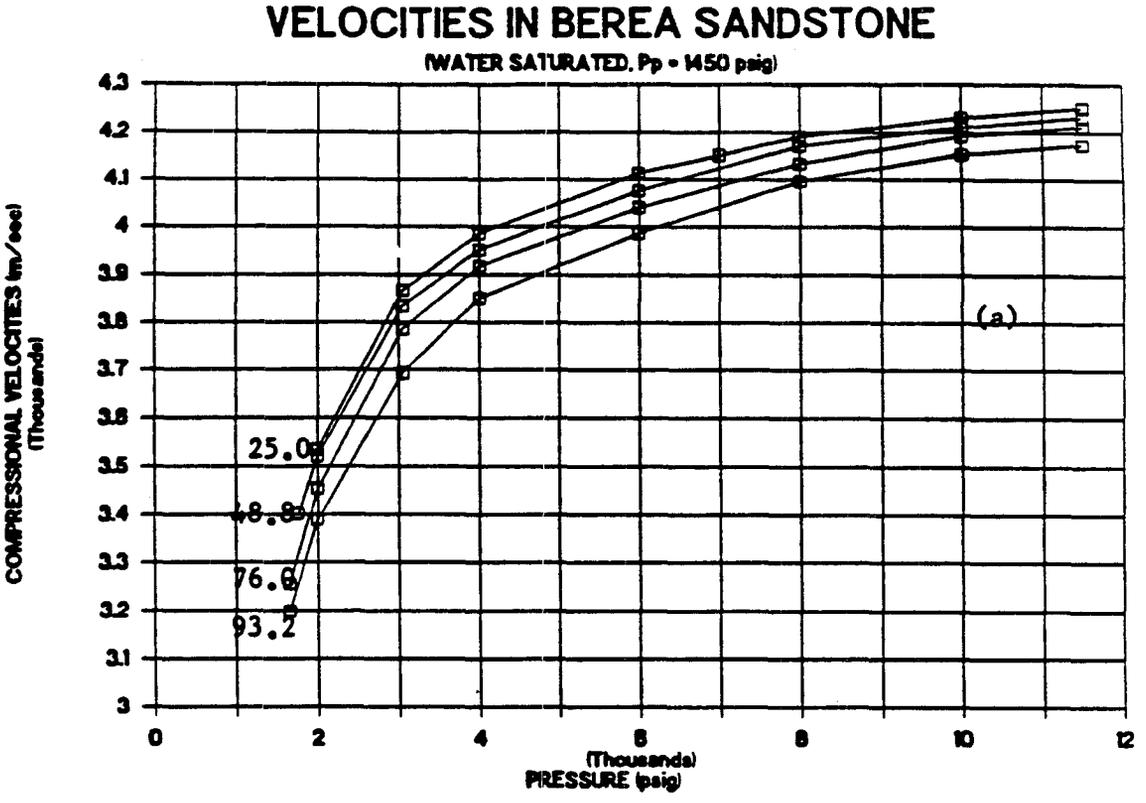
VELOCITIES IN BEREA SANDSTONE
(WATER SATURATED, Pp = 1450 psig)
COMPRESSIONAL VELOCITIES (m/sec)
(Thousands)
4.3
4.2
4.1
4
3.9
3.8
3.7
3.6
3.5
3.4
3.3
3.2
3.1
3
25.0
48.8
76.6
93.2
(a)
0
2
4
6
8
10
12
(Thousands)
PRESSURE (psig)

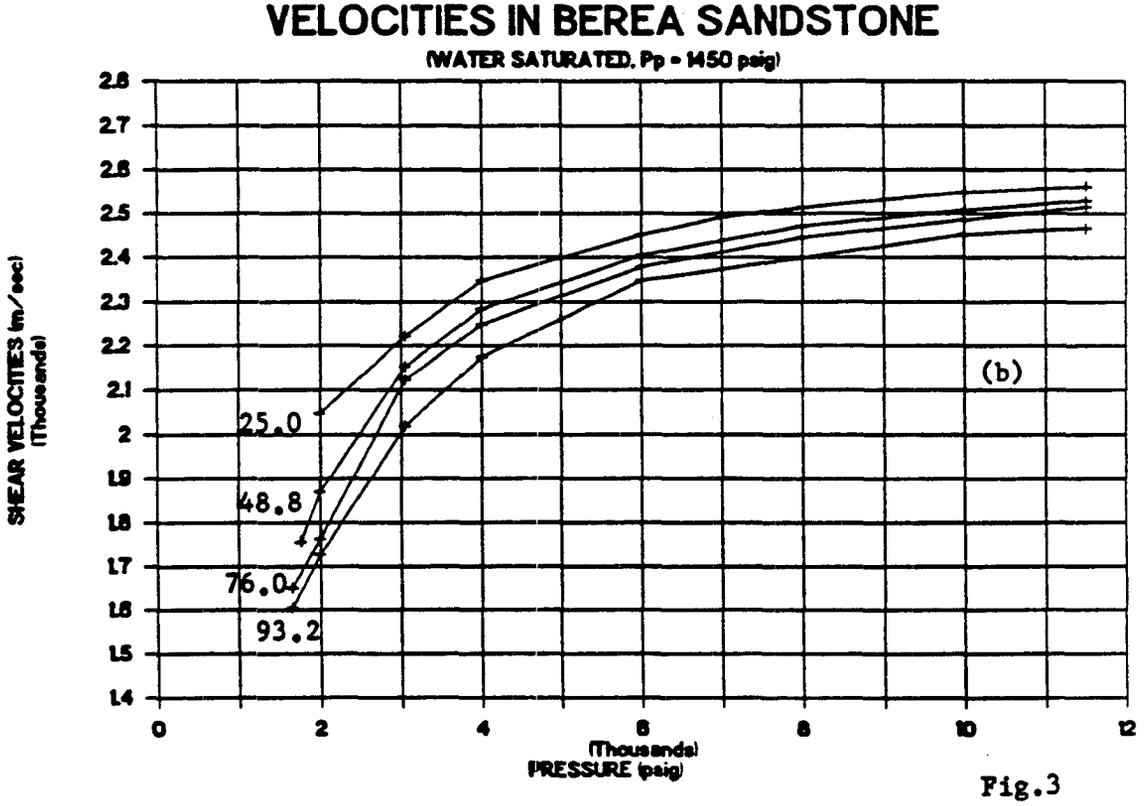
VELOCITIES IN BEREA SANDSTONE
(WATER SATURATED, Pp = 1450 psig)
SHEAR VELOCITIES (m/sec)
(Thousands)
2.8
2.7
2.6
2.5
2.4
2.3
2.2
2.1
2
1.9
1.8
1.7
1.6
1.5
1.4
25.0
48.8
76.0
93.2
(b)
0
2
4
6
8
10
12
(Thousands)
PRESSURE (psig)

Fig.3

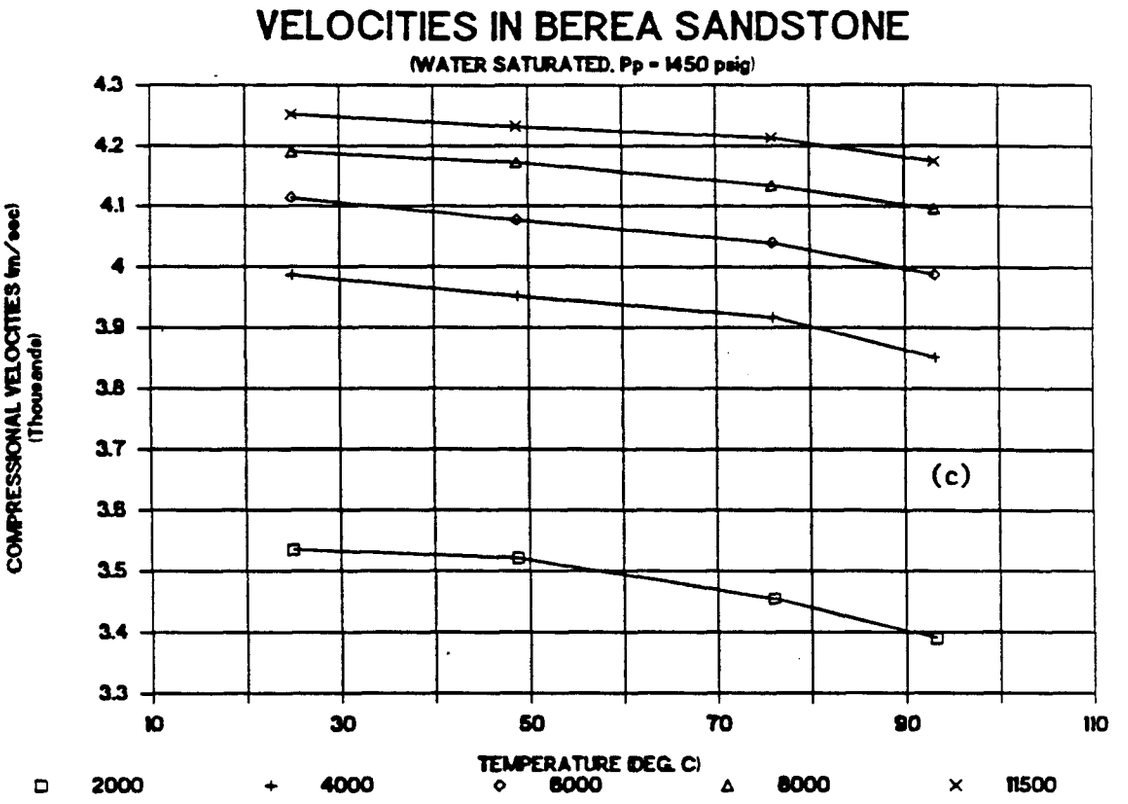
VELOCITIES IN BEREA SANDSTONE
(WATER SATURATED, Pp = 1450 psig)
COMPRESSIONAL VELOCITIES (m/sec) (Thousands)
4.3
4.2
4.1
4
3.9
3.8
3.7
3.6
3.5
3.4
3.3
10
30
50
70
90
110
(c)
TEMPERATURE (DEG. C)
□ 2000
+ 4000
◇ 6000
△ 8000
× 11500

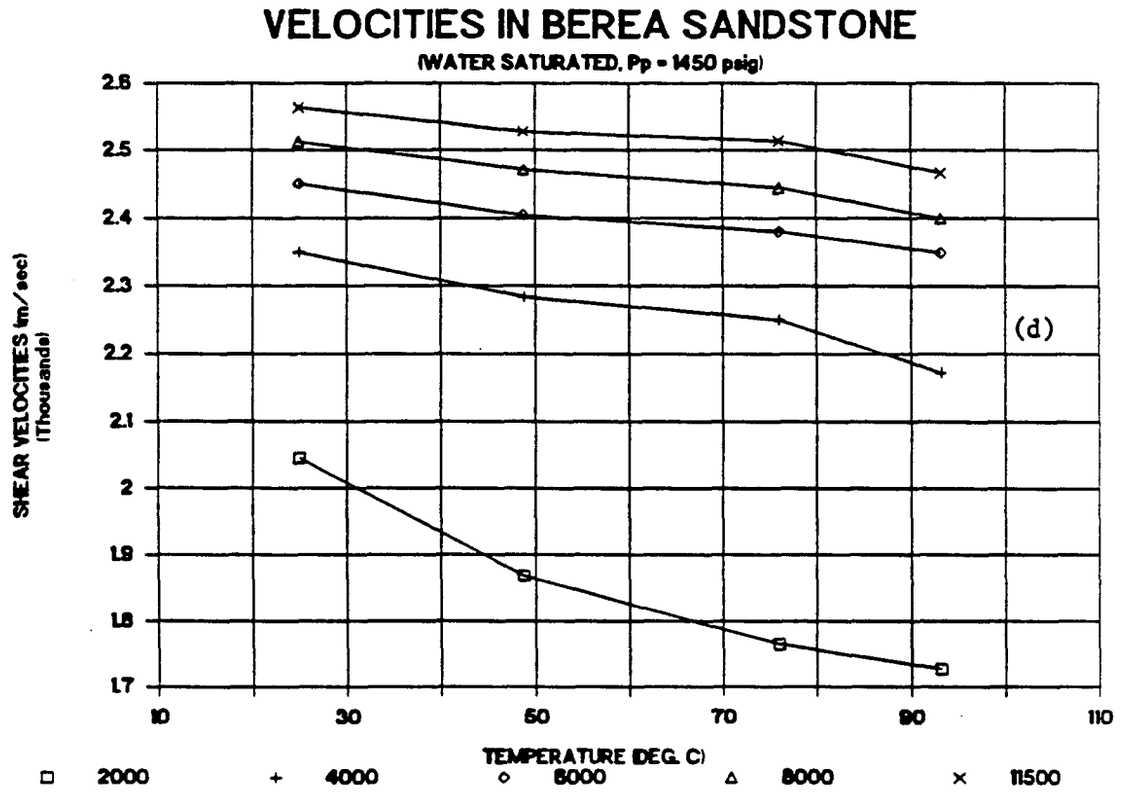
VELOCITIES IN BEREA SANDSTONE
(WATER SATURATED, Pp = 1450 psig)
SHEAR VELOCITIES (m/sec) (Thousands)
2.6
2.5
2.4
2.3
2.2
2.1
2
1.9
1.8
1.7
10
30
50
70
90
110
(d)
TEMPERATURE (DEG. C)
□ 2000
+ 4000
◇ 6000
△ 8000
× 11500

Fig.3

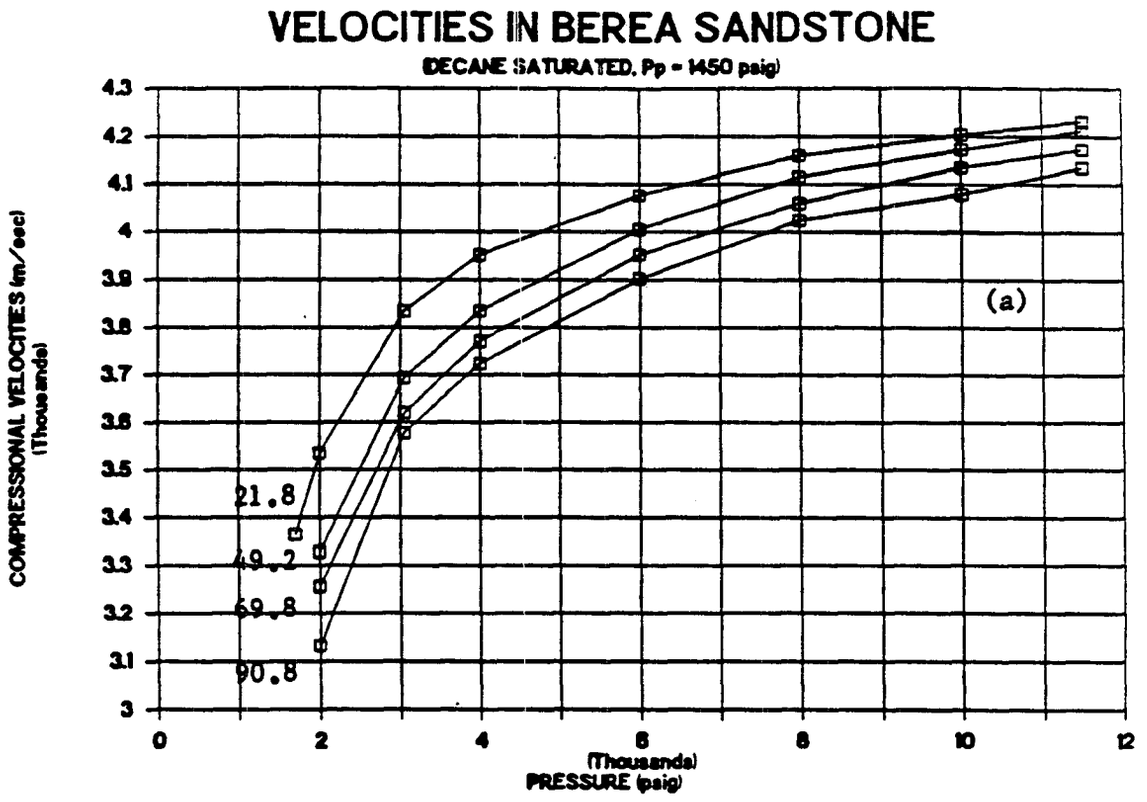
VELOCITIES IN BEREA SANDSTONE
(DECANE SATURATED, Pp = 1450 psig)
COMPRESSIONAL VELOCITIES (m/sec)
(Thousands)
4.3
4.2
4.1
4
3.9
3.8
3.7
3.6
3.5
3.4
3.3
3.2
3.1
3
0
2
4
6
8
10
12
(Thousands)
PRESSURE (psig)
21.8
49.2
69.8
90.8
(a)

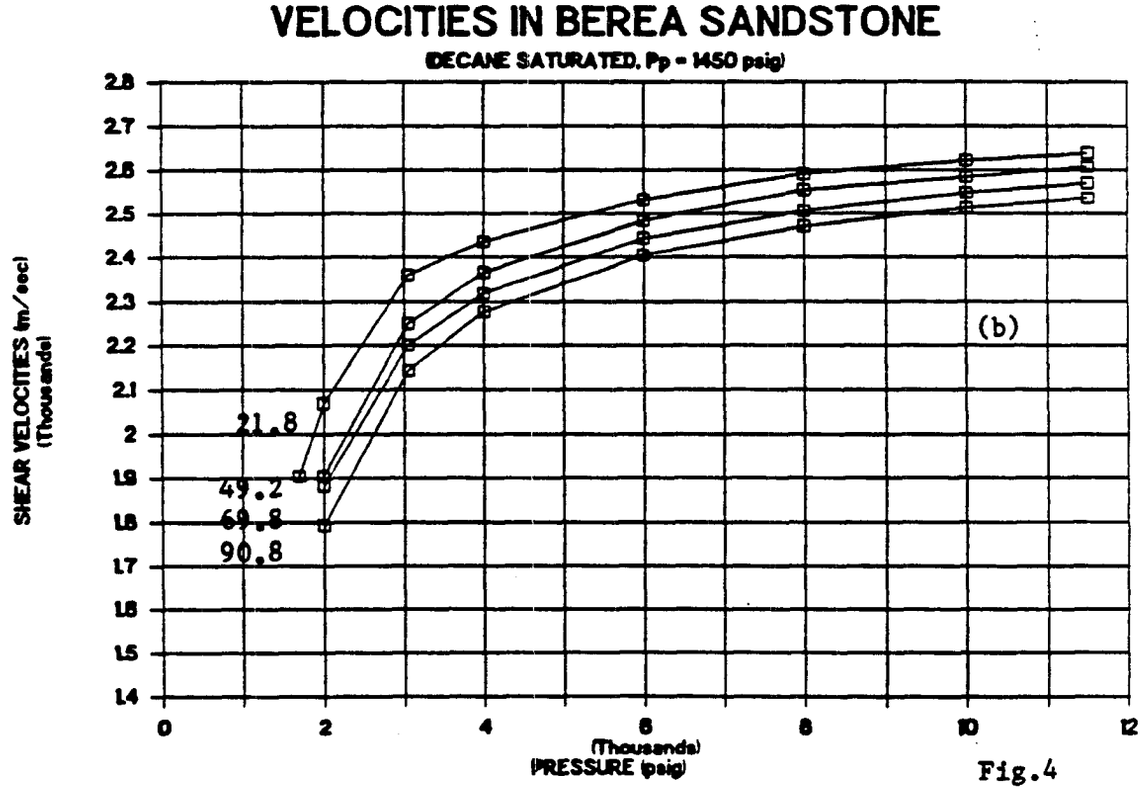
VELOCITIES IN BEREA SANDSTONE
(DECANE SATURATED, Pp = 1450 psig)
SHEAR VELOCITIES (m/sec)
(Thousands)
2.8
2.7
2.6
2.5
2.4
2.3
2.2
2.1
2
1.9
1.8
1.7
1.6
1.5
1.4
0
2
4
6
8
10
12
(Thousands)
PRESSURE (psig)
21.8
49.2
69.8
90.8
(b)

Fig.4

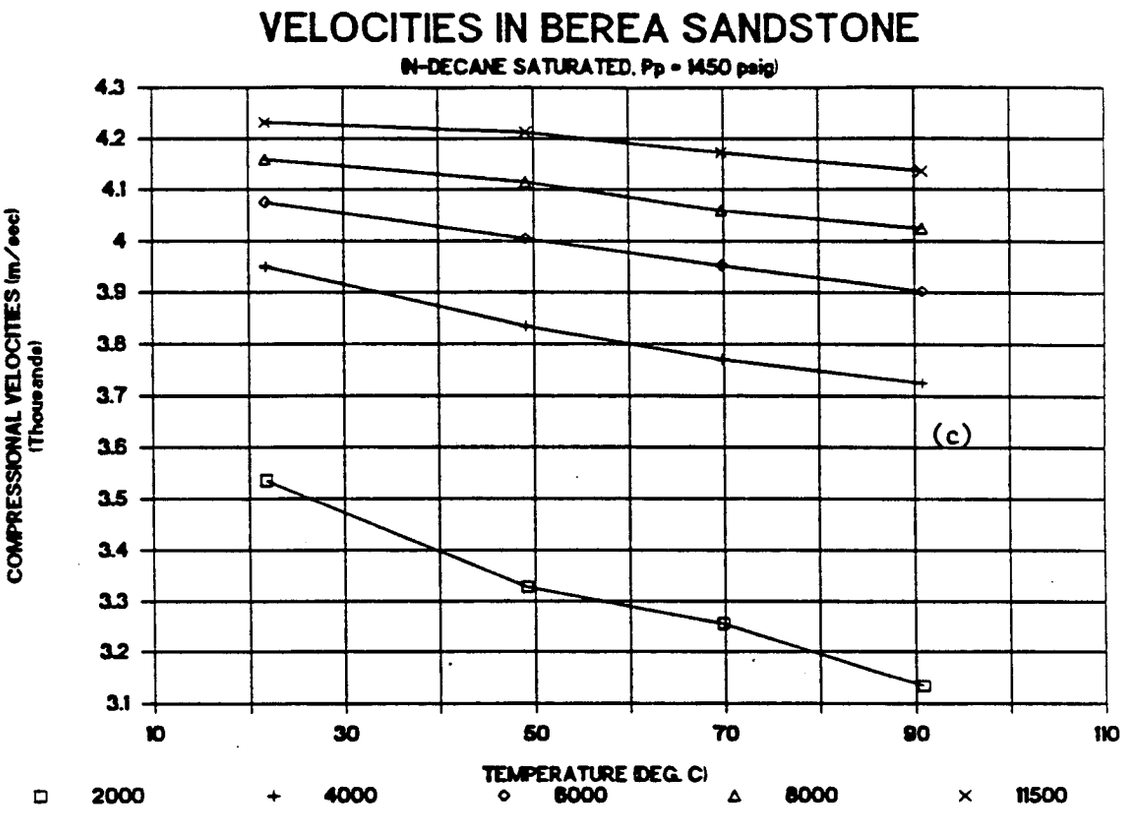
VELOCITIES IN BEREA SANDSTONE
(N-DECANE SATURATED, Pp = 1450 psig)
COMPRESSIONAL VELOCITIES (m/sec)
(Thousands)
4.3
4.2
4.1
4
3.9
3.8
3.7
3.6
3.5
3.4
3.3
3.2
3.1
10
30
50
70
90
110
TEMPERATURE (DEG. C)
(c)
□ 2000
+ 4000
◇ 6000
△ 8000
× 11500

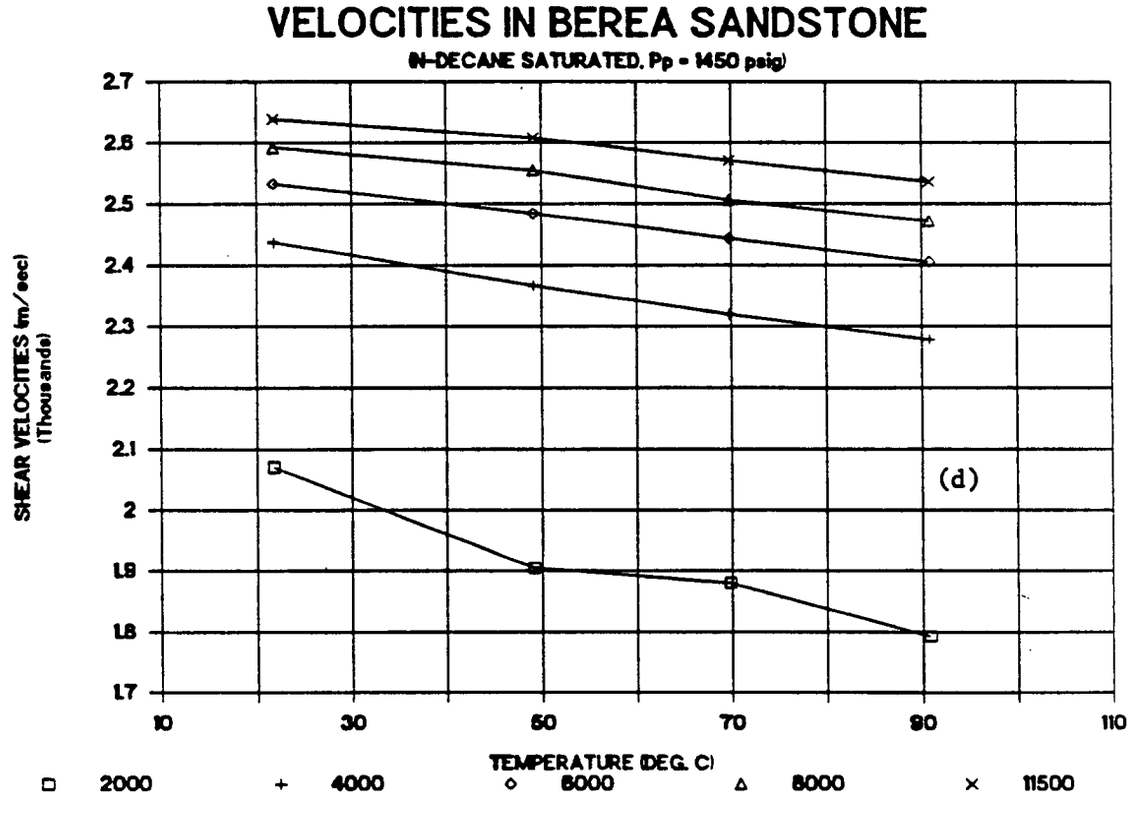
VELOCITIES IN BEREA SANDSTONE
(N-DECANE SATURATED, Pp = 1450 psig)
SHEAR VELOCITIES (m/sec)
(Thousands)
2.7
2.6
2.5
2.4
2.3
2.2
2.1
2
1.9
1.8
1.7
10
30
50
70
90
110
TEMPERATURE (DEG. C)
(d)
□ 2000
+ 4000
◇ 6000
△ 8000
× 11500

Fig.4

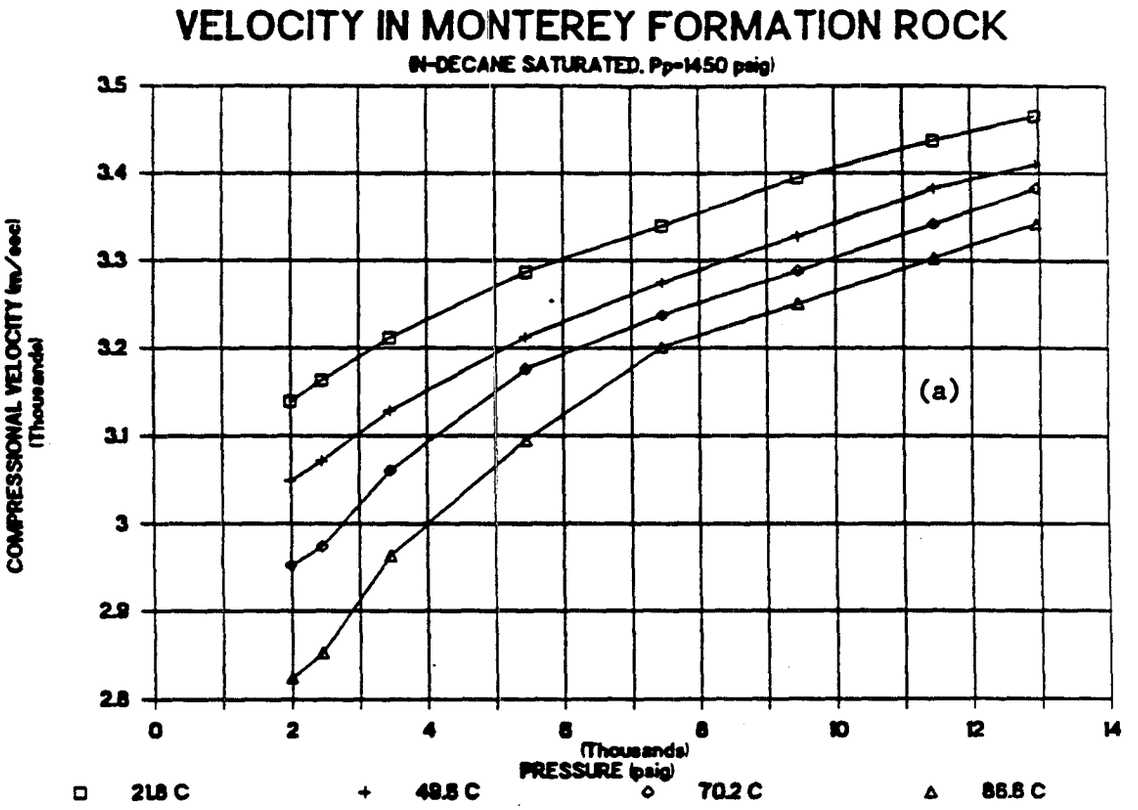
VELOCITY IN MONTEREY FORMATION ROCK
IN-DECANE SATURATED. Pp=1450 psig)
COMPRESSIONAL VELOCITY (m/sec)
(Thousands)
3.5
3.4
3.3
3.2
3.1
3
2.9
2.8
0
2
4
6
8
10
12
14
(Thousands)
PRESSURE (psig)
(a)
21.8 C
49.8 C
70.2 C
86.8 C

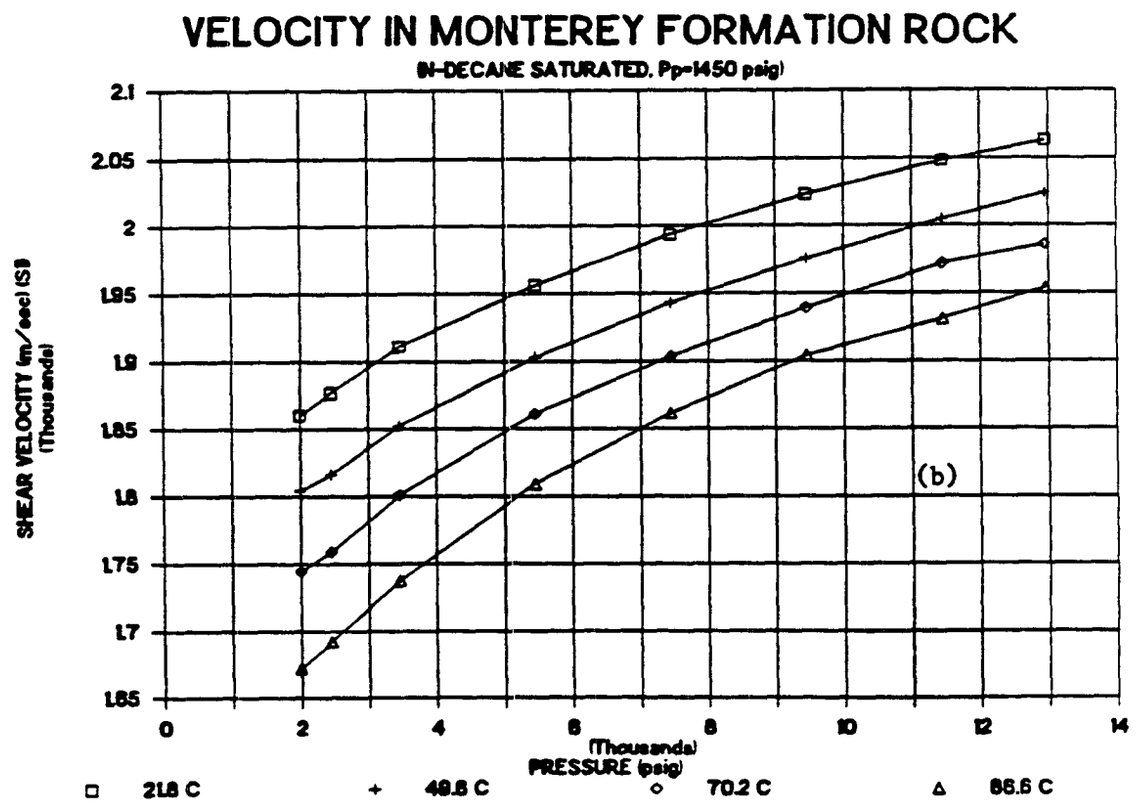
VELOCITY IN MONTEREY FORMATION ROCK
IN-DECANE SATURATED. Pp=1450 psig)
SHEAR VELOCITY (m/sec) (S)
(Thousands)
2.1
2.05
2
1.95
1.9
1.85
1.8
1.75
1.7
1.65
0
2
4
6
8
10
12
14
(Thousands)
PRESSURE (psig)
(b)
21.8 C
49.8 C
70.2 C
86.6 C

Fig.5

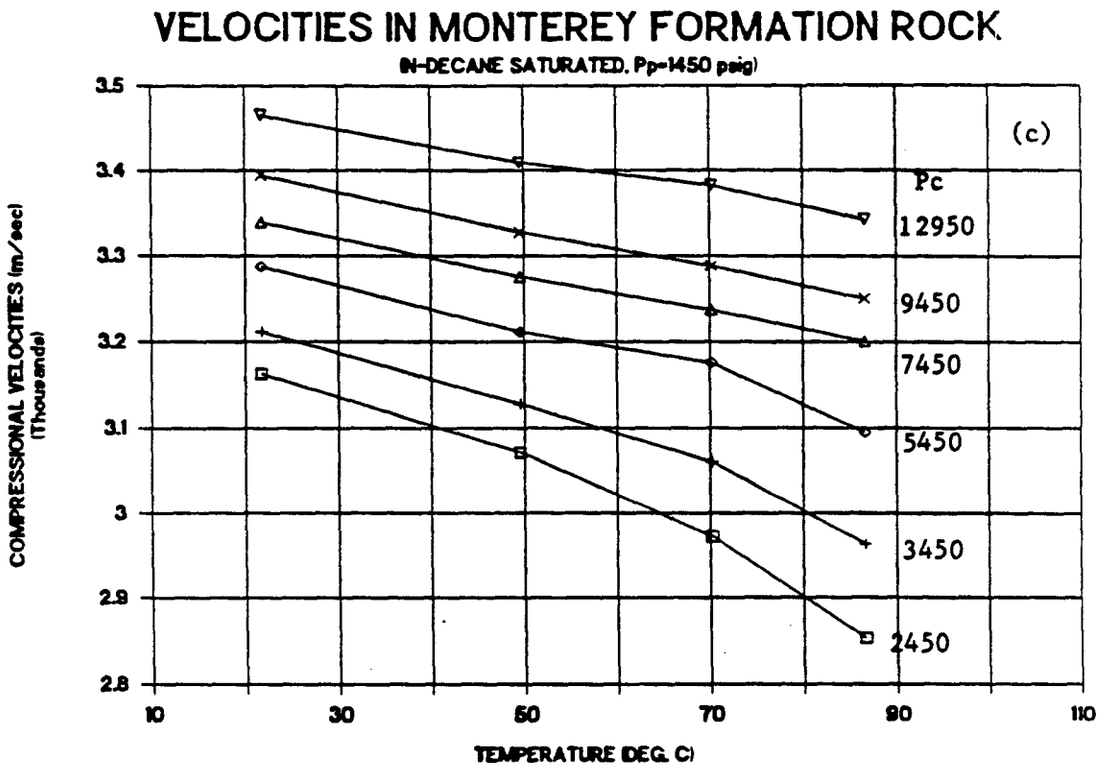
VELOCITIES IN MONTEREY FORMATION ROCK
(N-DECANE SATURATED, Pp=1450 psig)
COMPRESSIONAL VELOCITIES (m/sec)
(Thousands)
3.5
3.4
3.3
3.2
3.1
3
2.9
2.8
10
30
50
70
90
110
TEMPERATURE (DEG. C)
(c)
Pc
12950
9450
7450
5450
3450
2450

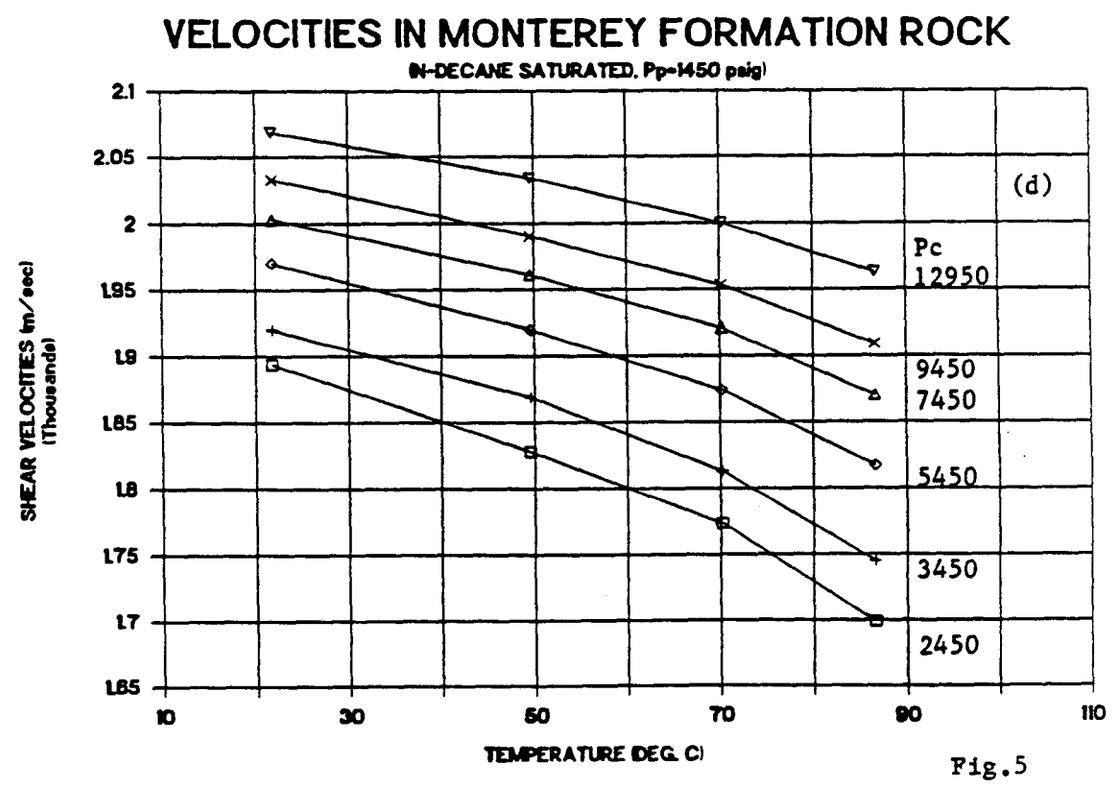
VELOCITIES IN MONTEREY FORMATION ROCK
(N-DECANE SATURATED, Pp=1450 psig)
SHEAR VELOCITIES (m/sec)
(Thousands)
2.1
2.05
2
1.95
1.9
1.85
1.8
1.75
1.7
1.65
10
30
50
70
90
110
TEMPERATURE (DEG. C)
(d)
Pc
12950
9450
7450
5450
3450
2450

Fig.5

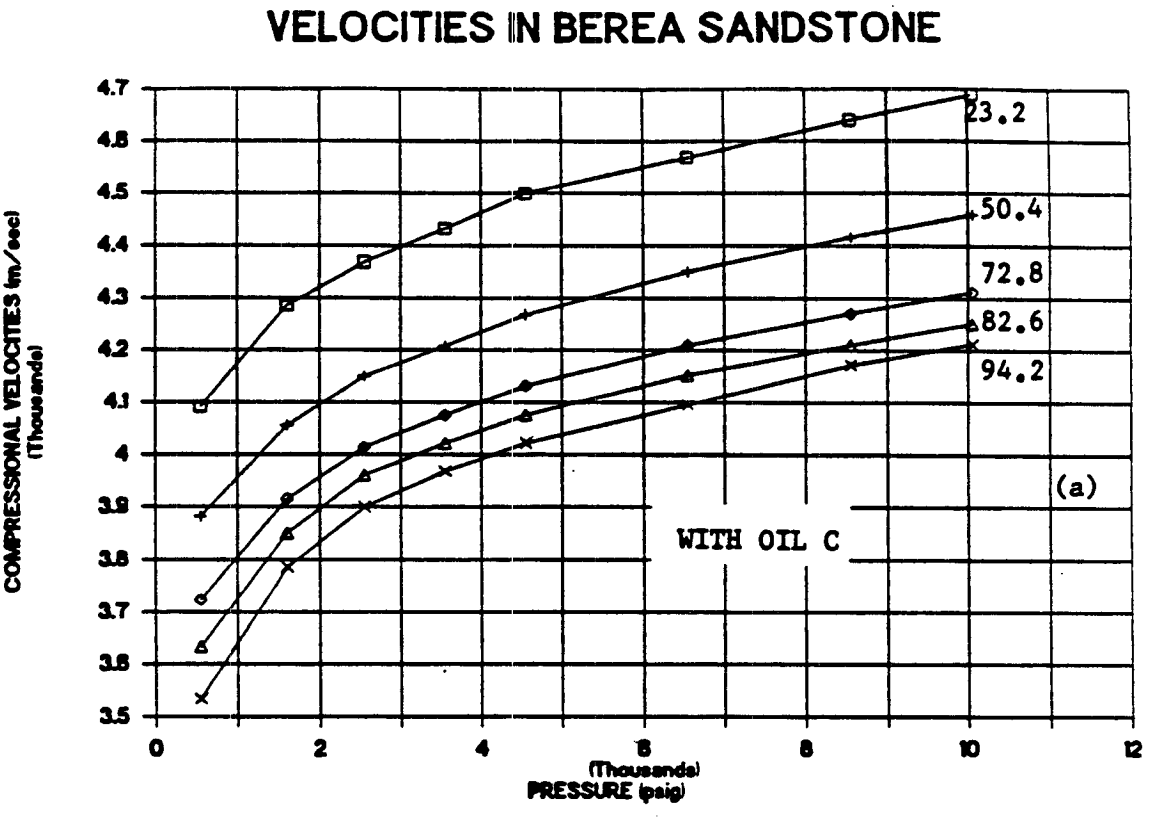
VELOCITIES IN BEREA SANDSTONE
COMPRESSIONAL VELOCITIES (m/sec)
(Thousands)
4.7
4.6
4.5
4.4
4.3
4.2
4.1
4
3.9
3.8
3.7
3.6
3.5
0
2
4
6
8
10
12
(Thousands)
PRESSURE (psig)
23.2
50.4
72.8
82.6
94.2
(a)
WITH OIL C

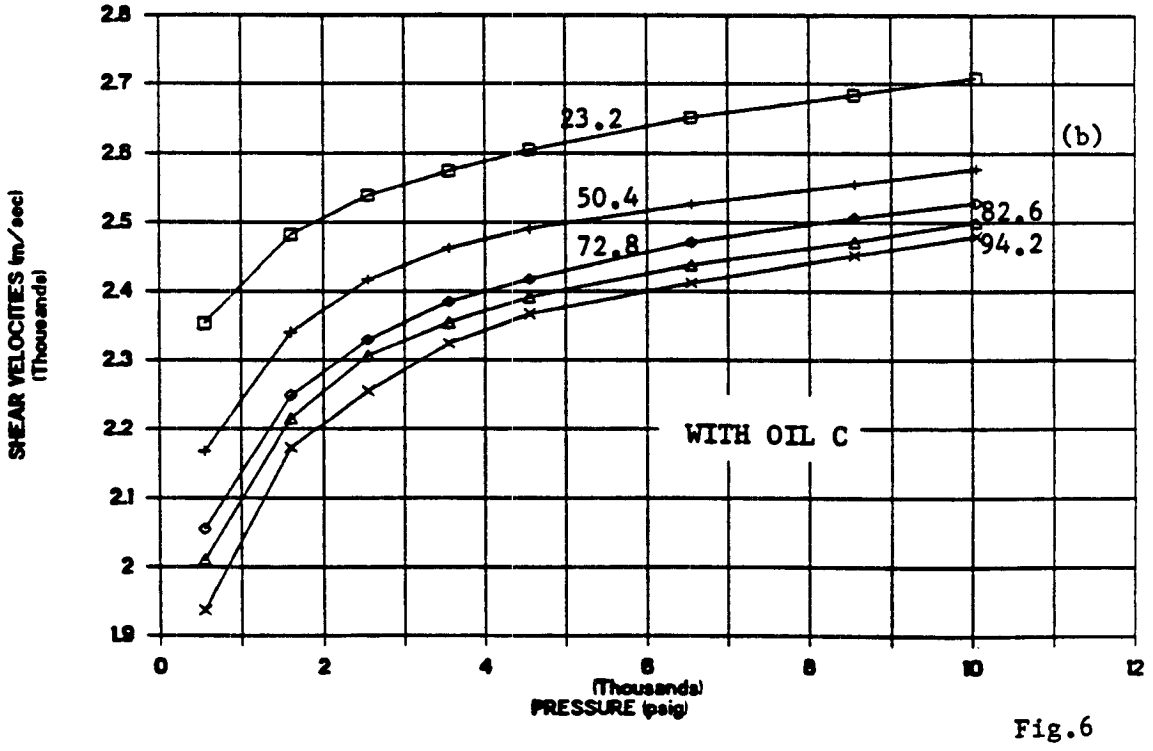
VELOCITIES IN BEREA SANDSTONE
SHEAR VELOCITIES (m/sec)
(Thousands)
2.8
2.7
2.6
2.5
2.4
2.3
2.2
2.1
2
1.9
0
2
4
6
8
10
12
(Thousands)
PRESSURE (psig)
23.2
50.4
72.8
82.6
94.2
(b)
WITH OIL C

Fig.6

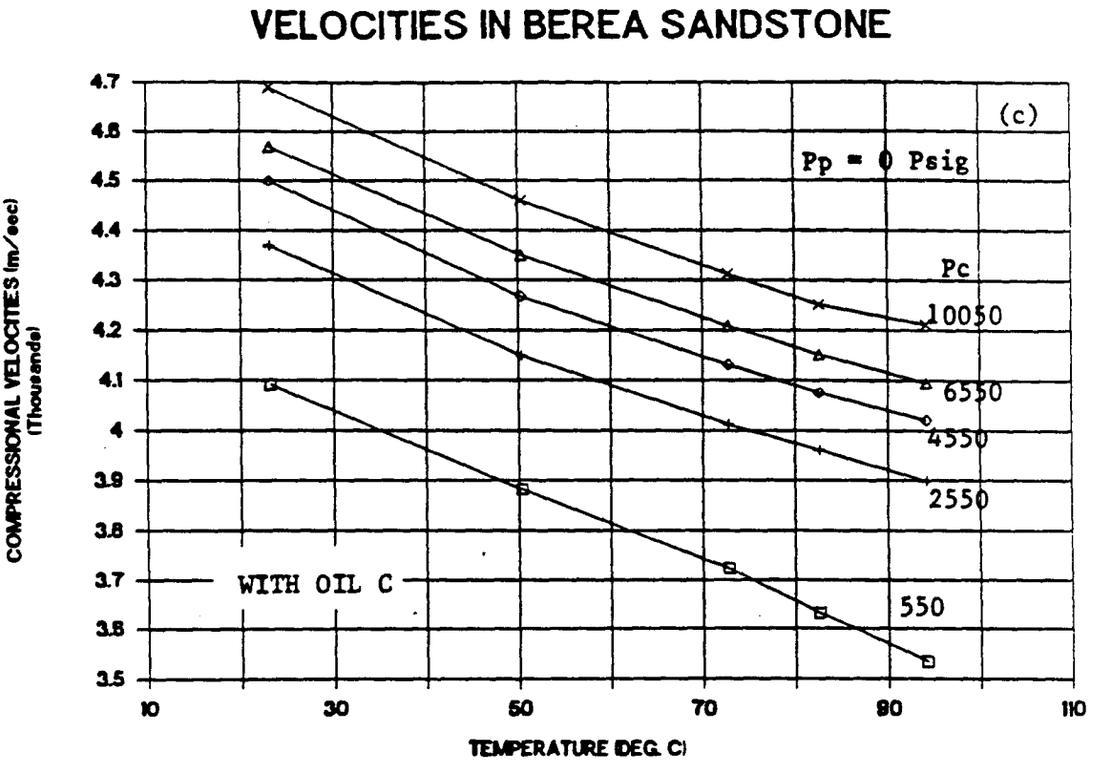
VELOCITIES IN BEREA SANDSTONE
(c)
Pp = 0 Psig
Pc
10050
6550
4550
2550
550
WITH OIL C
COMPRESSIONAL VELOCITIES (m/sec)
(Thousands)
4.7
4.6
4.5
4.4
4.3
4.2
4.1
4
3.9
3.8
3.7
3.6
3.5
10
30
50
70
90
110
TEMPERATURE (DEG. C)

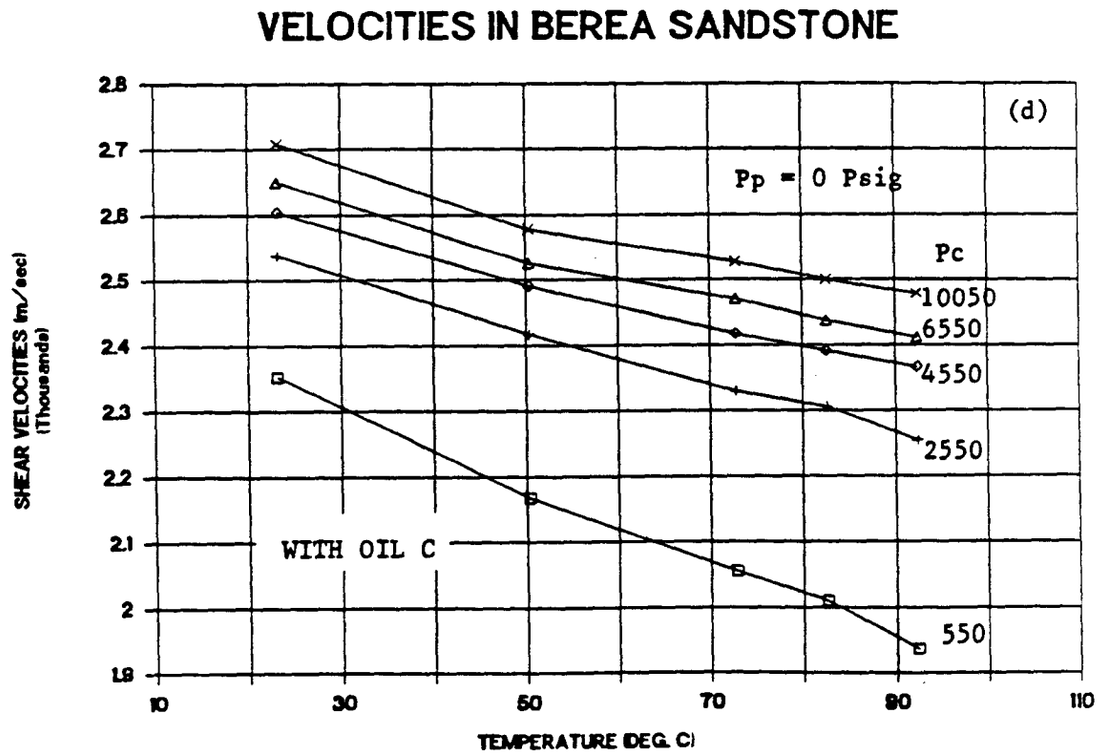
VELOCITIES IN BEREA SANDSTONE
(d)
Pp = 0 Psig
Pc
10050
6550
4550
2550
550
WITH OIL C
SHEAR VELOCITIES (m/sec)
(Thousands)
2.8
2.7
2.6
2.5
2.4
2.3
2.2
2.1
2
1.9
10
30
50
70
90
110
TEMPERATURE (DEG. C)

Fig.6

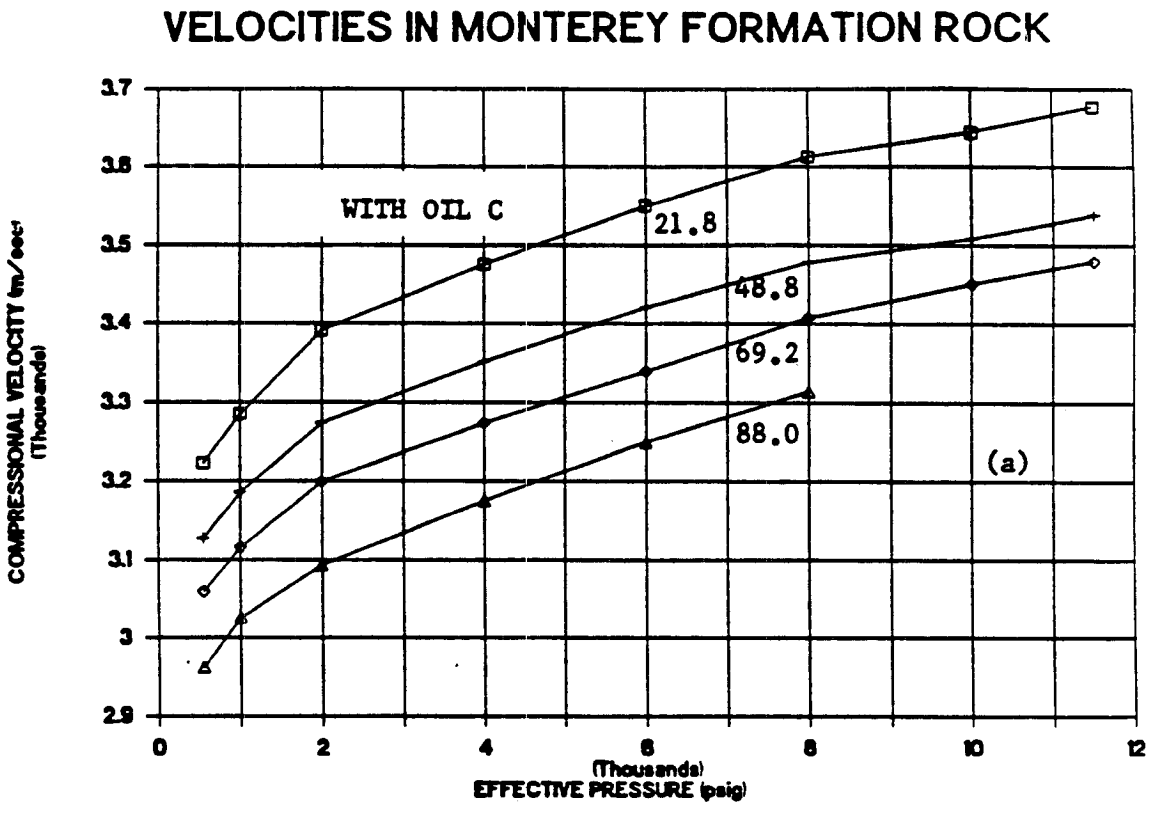
VELOCITIES IN MONTEREY FORMATION ROCK
WITH OIL C
21.8
48.8
69.2
88.0
(a)
COMPRESSIONAL VELOCITY (m/sec)
(Thousands)
EFFECTIVE PRESSURE (psig)
(Thousands)
3.7
3.6
3.5
3.4
3.3
3.2
3.1
3
2.9
0
2
4
6
8
10
12

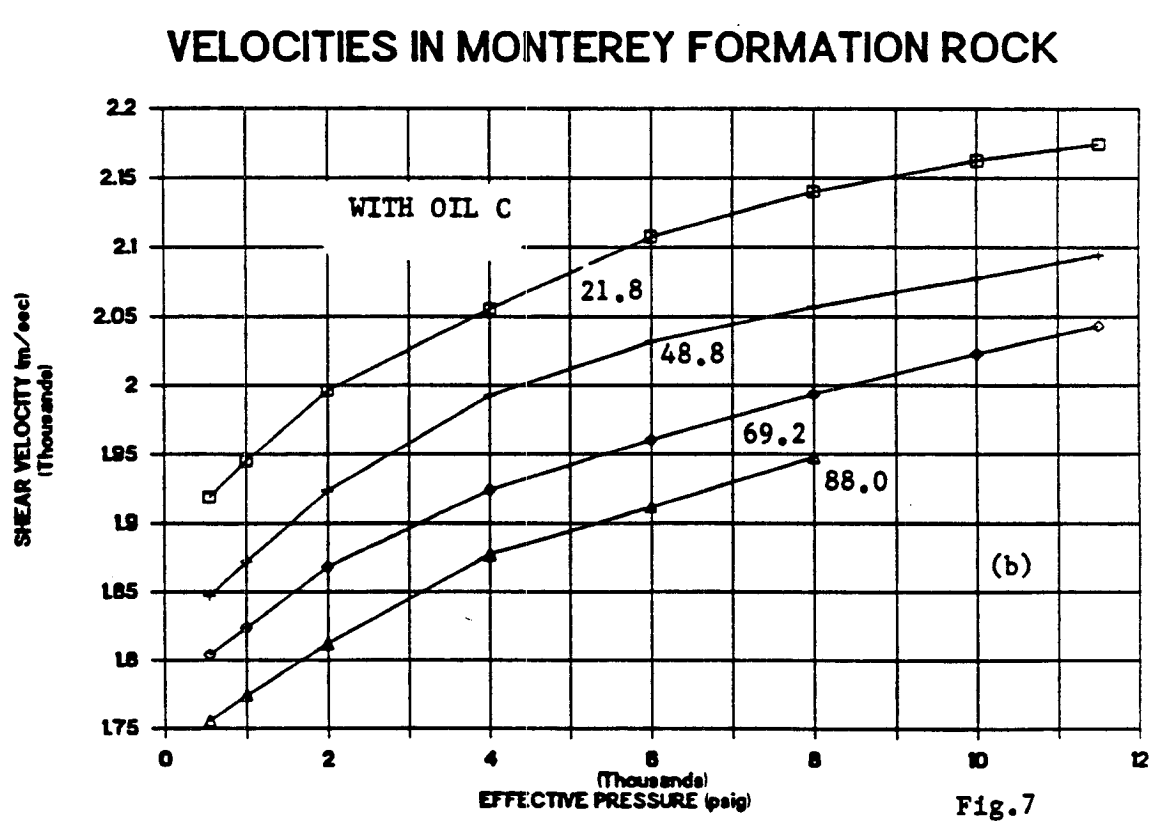
VELOCITIES IN MONTEREY FORMATION ROCK
WITH OIL C
21.8
48.8
69.2
88.0
(b)
SHEAR VELOCITY (m/sec)
(Thousands)
EFFECTIVE PRESSURE (psig)
(Thousands)
2.2
2.15
2.1
2.05
2
1.95
1.9
1.85
1.8
1.75
0
2
4
6
8
10
12

Fig.7

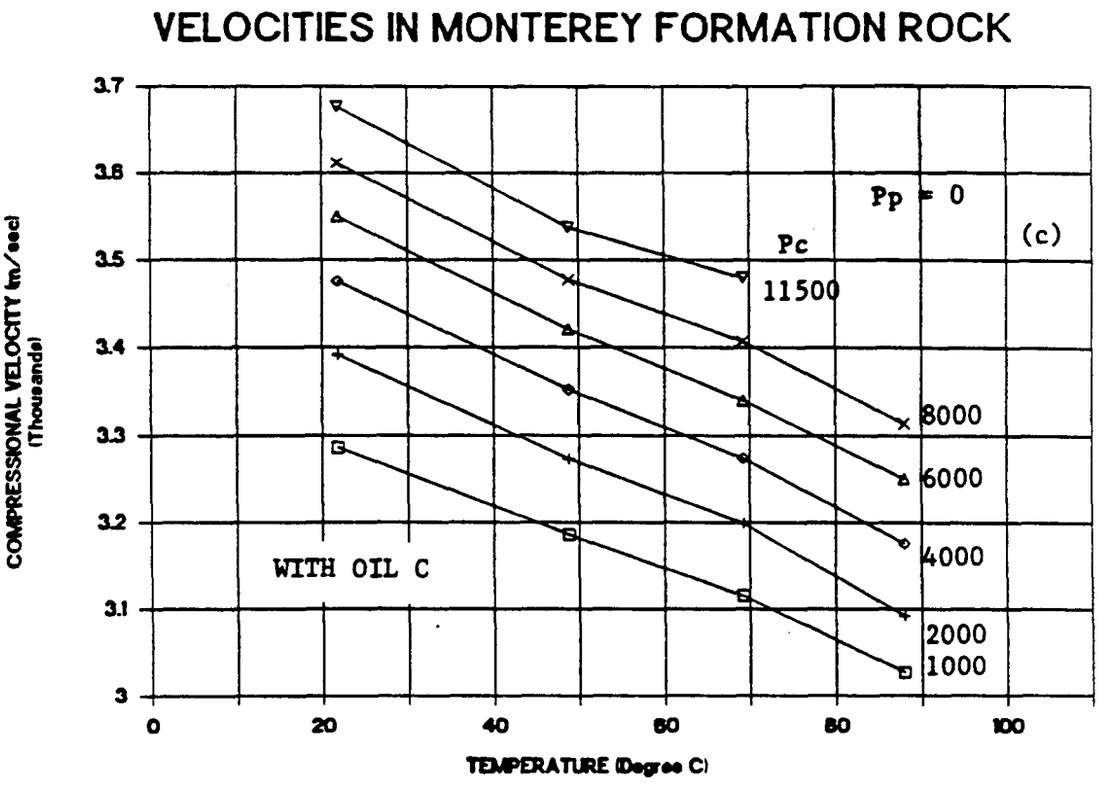
VELOCITIES IN MONTEREY FORMATION ROCK
COMPRESSIONAL VELOCITY (m/sec) (Thousands)
3.7
3.6
3.5
3.4
3.3
3.2
3.1
3
Pp = 0
(c)
Pc
11500
8000
6000
4000
2000
1000
WITH OIL C
0
20
40
60
80
100
TEMPERATURE (Degree C)

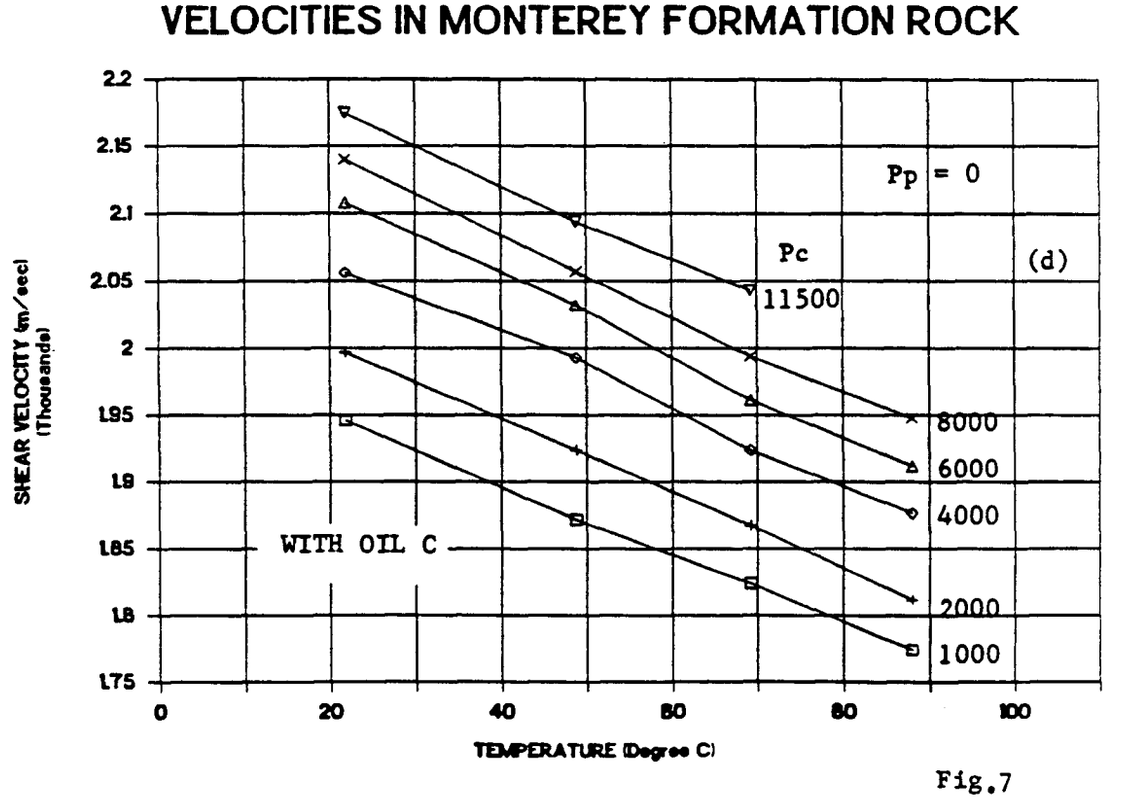
VELOCITIES IN MONTEREY FORMATION ROCK
SHEAR VELOCITY (m/sec) (Thousands)
2.2
2.15
2.1
2.05
2
1.95
1.9
1.85
1.8
1.75
Pp = 0
(d)
Pc
11500
8000
6000
4000
2000
1000
WITH OIL C
0
20
40
60
80
100
TEMPERATURE (Degree C)

Fig.7

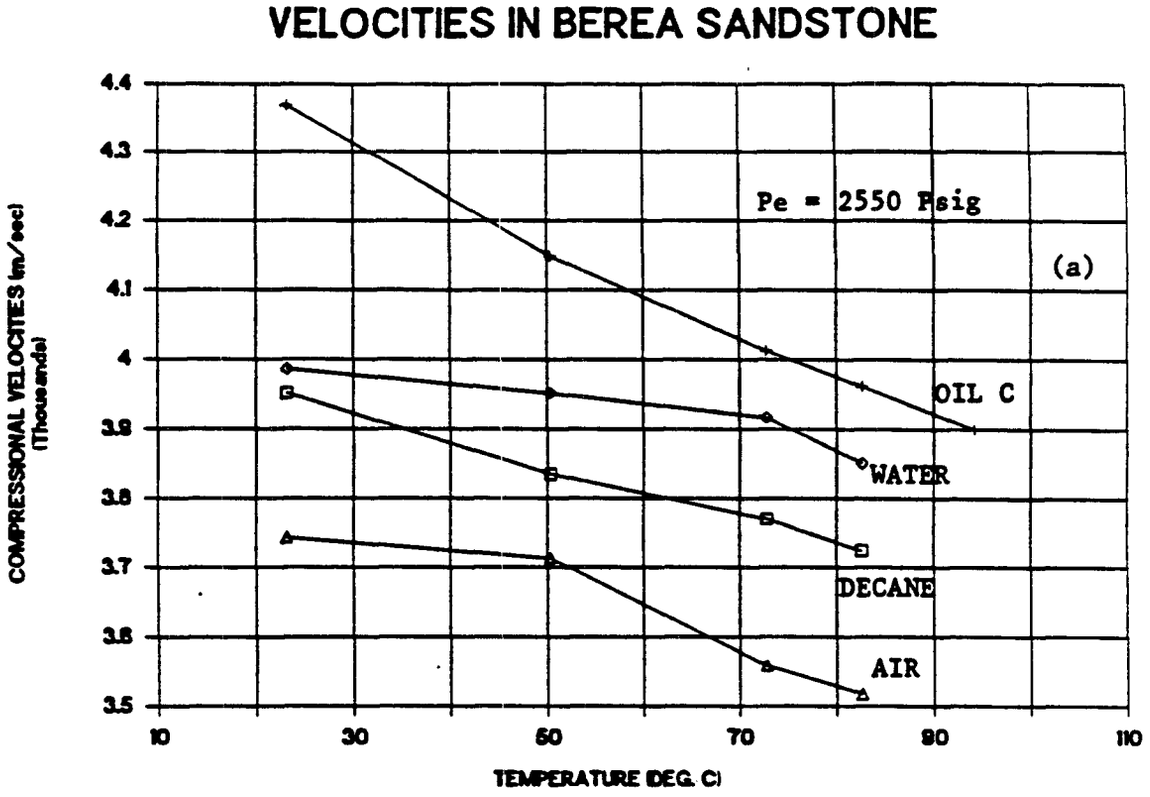
VELOCITIES IN BEREA SANDSTONE
COMPRESSIONAL VELOCITIES (m/sec) (Thousands)
4.4
4.3
4.2
4.1
4
3.9
3.8
3.7
3.6
3.5
10
30
50
70
90
110
TEMPERATURE (DEG. C)
Pe = 2550 Psig
(a)
OIL C
WATER
DECANE
AIR

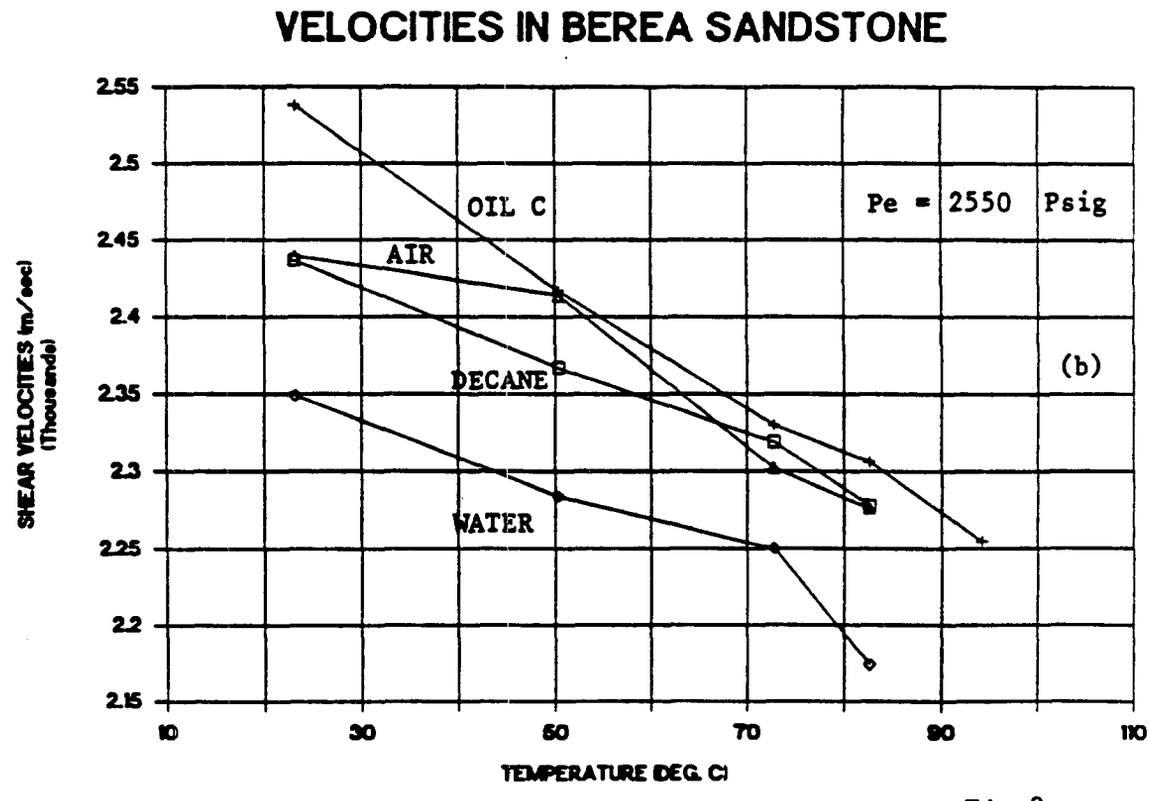
VELOCITIES IN BEREA SANDSTONE
SHEAR VELOCITIES (m/sec) (Thousands)
2.55
2.5
2.45
2.4
2.35
2.3
2.25
2.2
2.15
10
30
50
70
90
110
TEMPERATURE (DEG. C)
OIL C
Pe = 2550 Psig
AIR
DECANE
(b)
WATER

Fig.8

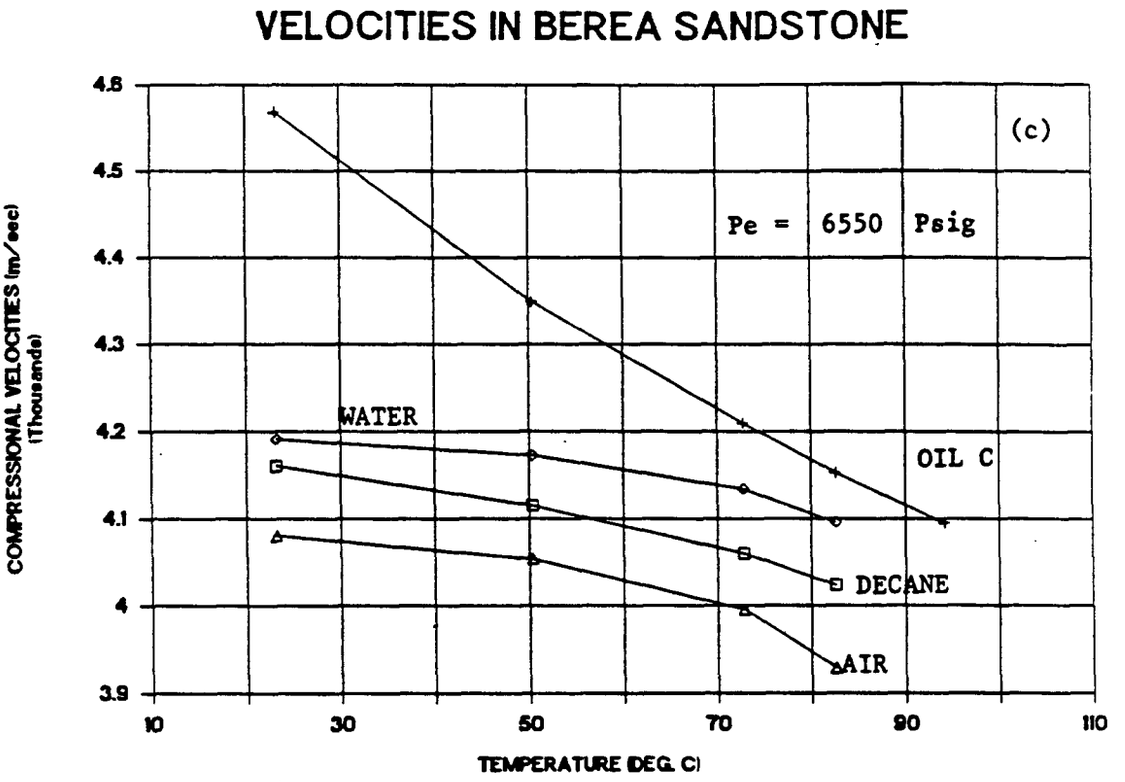
VELOCITIES IN BEREA SANDSTONE
COMPRESSIONAL VELOCITIES (m/sec)
(Thousands)
4.6
4.5
4.4
4.3
4.2
4.1
4
3.9
10
30
50
70
90
110
TEMPERATURE (DEG. C)
(c)
Pe = 6550 Psig
WATER
OIL C
DECANE
AIR

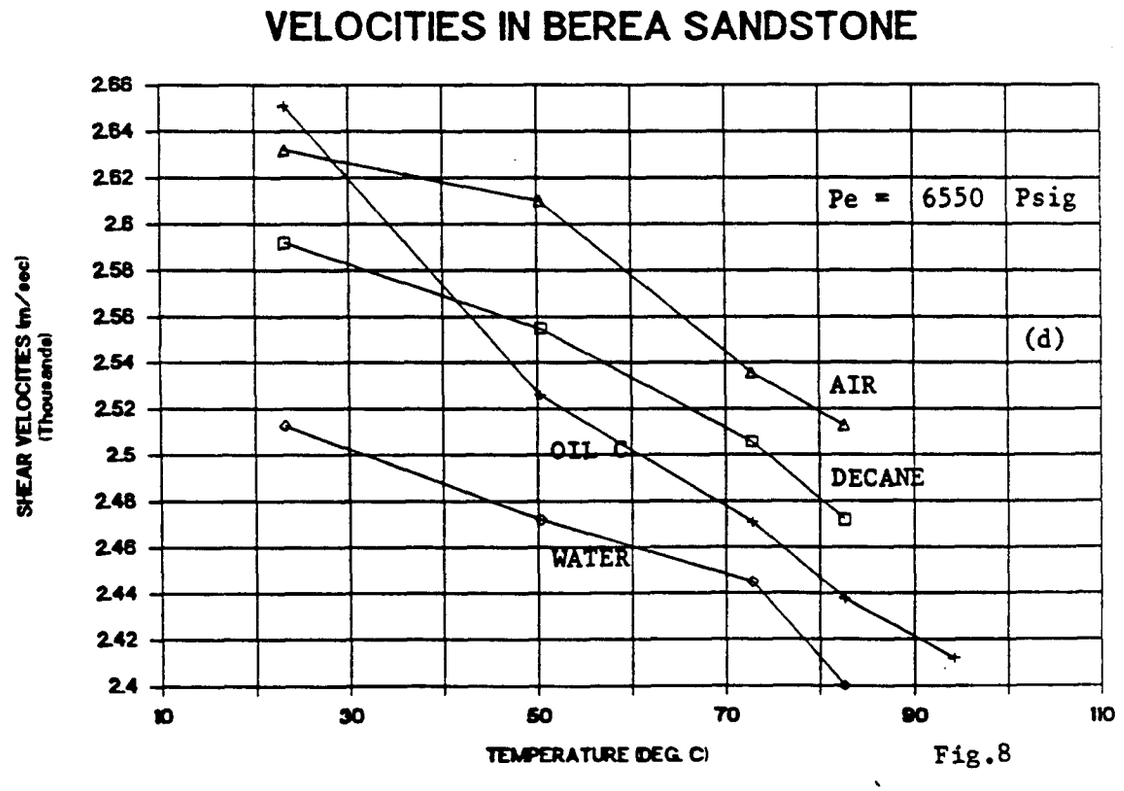
VELOCITIES IN BEREA SANDSTONE
SHEAR VELOCITIES (m/sec)
(Thousands)
2.66
2.64
2.62
2.6
2.58
2.56
2.54
2.52
2.5
2.48
2.46
2.44
2.42
2.4
10
30
50
70
90
110
TEMPERATURE (DEG. C)
Pe = 6550 Psig
(d)
AIR
OIL C
DECANE
WATER

Fig.8

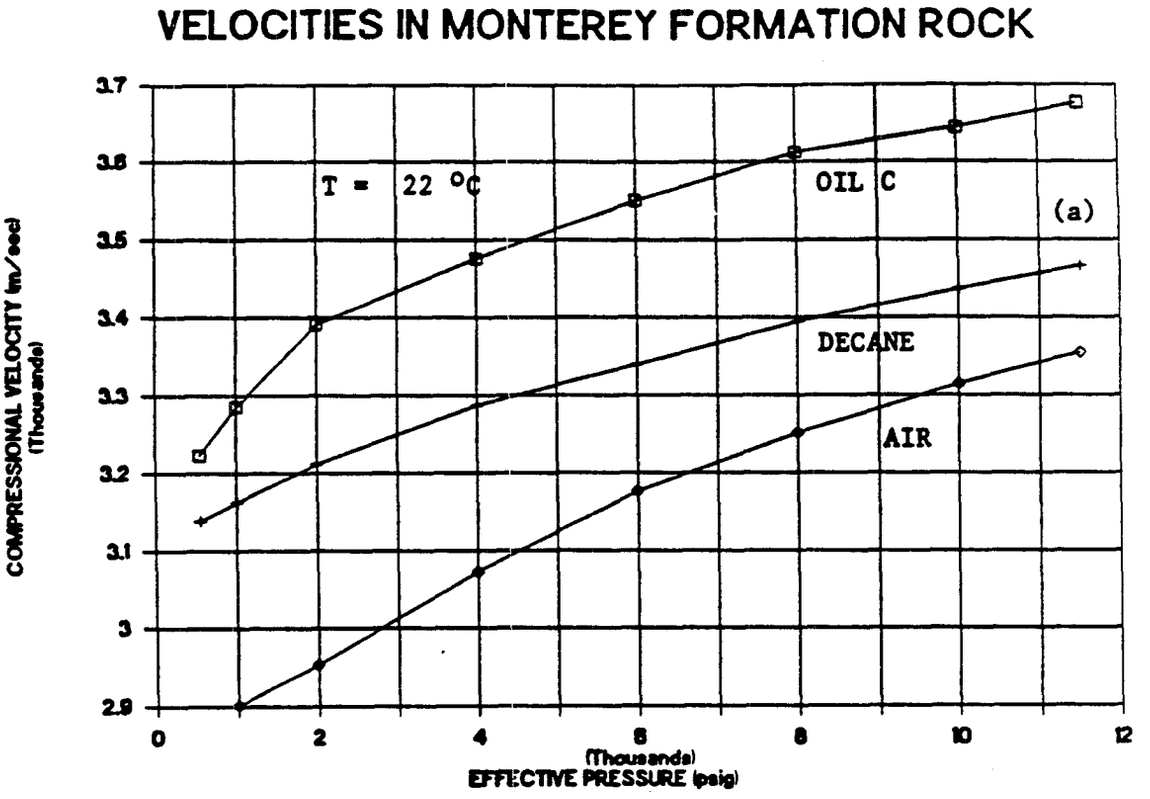
VELOCITIES IN MONTEREY FORMATION ROCK
COMPRESSIONAL VELOCITY (m/sec)
(Thousands)
3.7
3.6
3.5
3.4
3.3
3.2
3.1
3
2.9
T = 22 °C
OIL C
(a)
DECANE
AIR
0
2
4
6
8
10
12
(Thousands)
EFFECTIVE PRESSURE (psig)

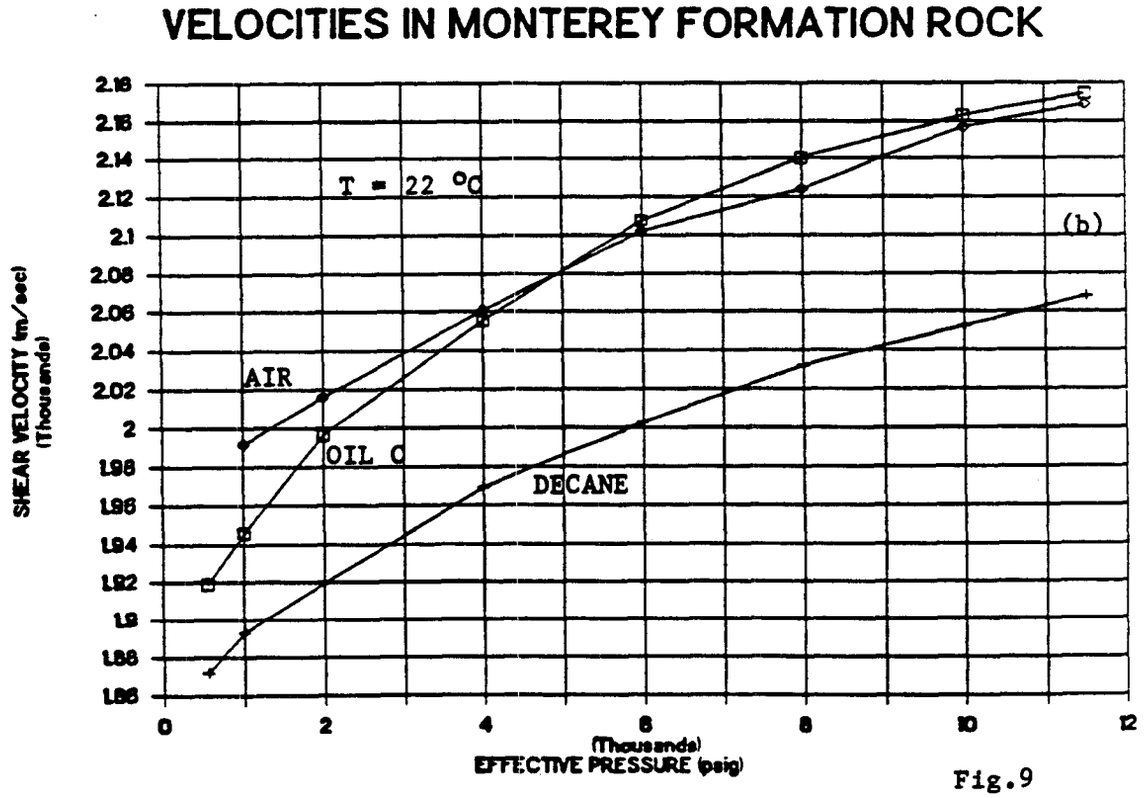
VELOCITIES IN MONTEREY FORMATION ROCK
SHEAR VELOCITY (m/sec)
(Thousands)
2.18
2.16
2.14
2.12
2.1
2.08
2.06
2.04
2.02
2
1.98
1.96
1.94
1.92
1.9
1.88
1.86
T = 22 °C
(b)
AIR
OIL C
DECANE
0
2
4
6
8
10
12
(Thousands)
EFFECTIVE PRESSURE (psig)

Fig.9

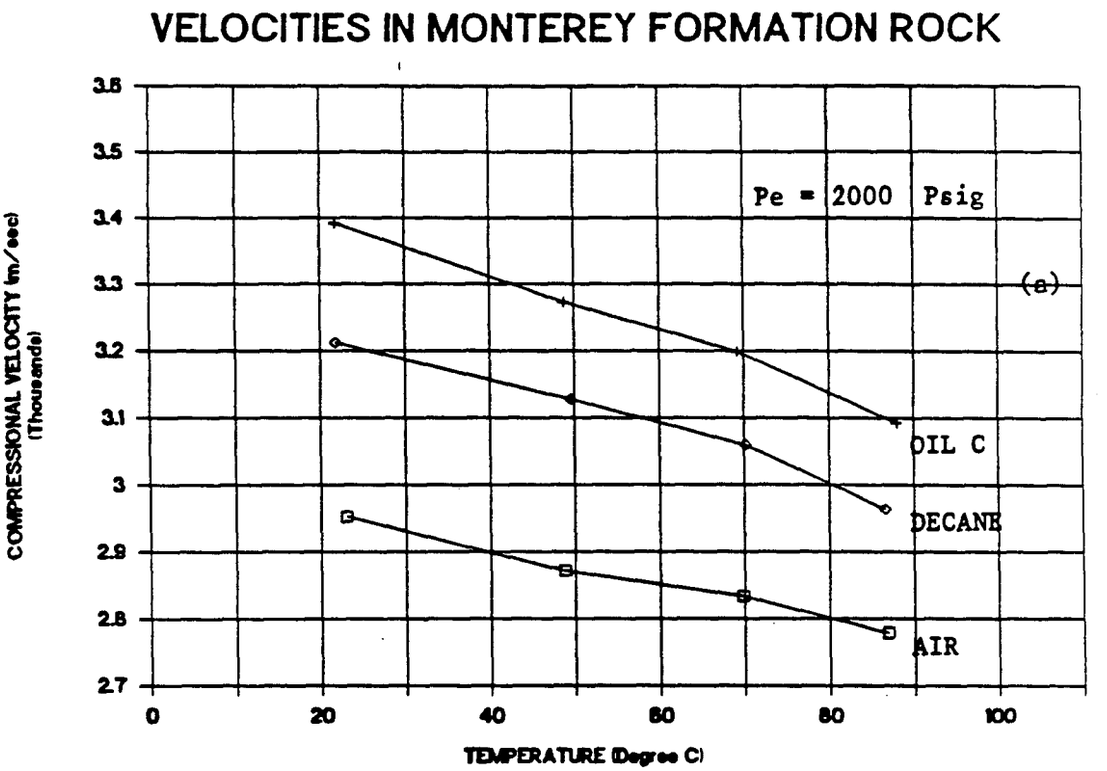
VELOCITIES IN MONTEREY FORMATION ROCK
COMPRESSIONAL VELOCITY (m/sec) (Thousands)
3.6
3.5
3.4
3.3
3.2
3.1
3
2.9
2.8
2.7
Pe = 2000 Psig
(a)
OIL C
DECANE
AIR
0
20
40
60
80
100
TEMPERATURE (Degree C)

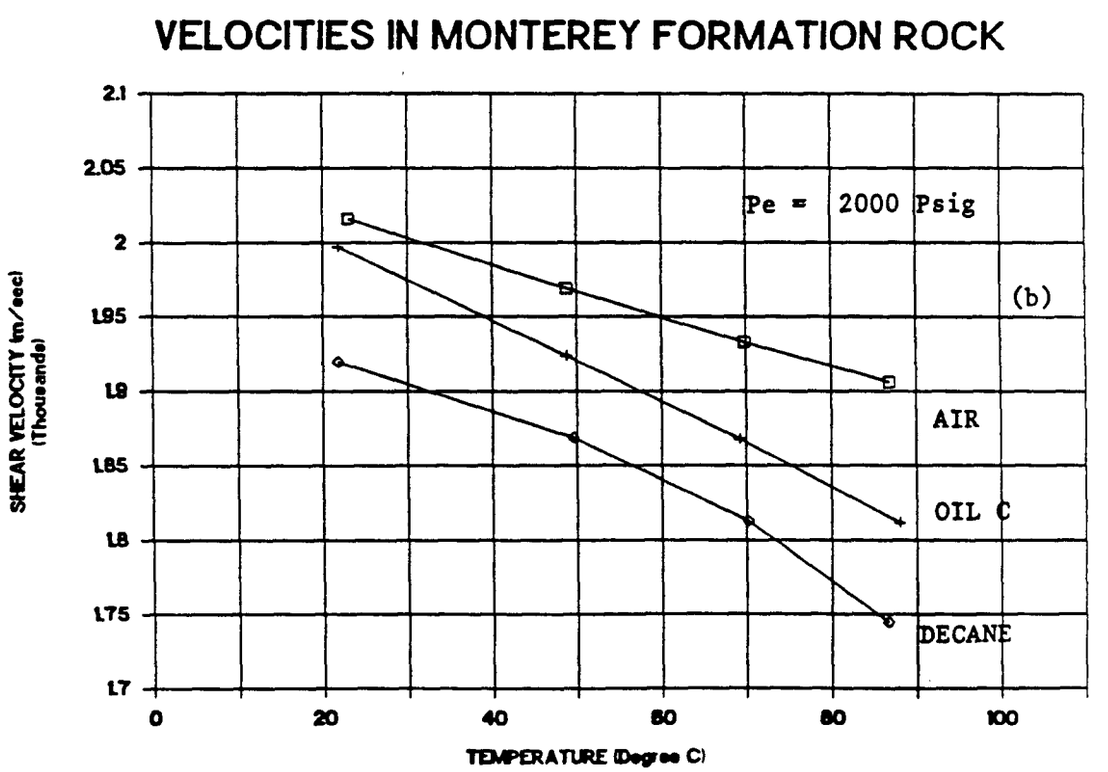
VELOCITIES IN MONTEREY FORMATION ROCK
SHEAR VELOCITY (m/sec) (Thousands)
2.1
2.05
2
1.95
1.9
1.85
1.8
1.75
1.7
Pe = 2000 Psig
(b)
AIR
OIL C
DECANE
0
20
40
60
80
100
TEMPERATURE (Degree C)

Fig.10

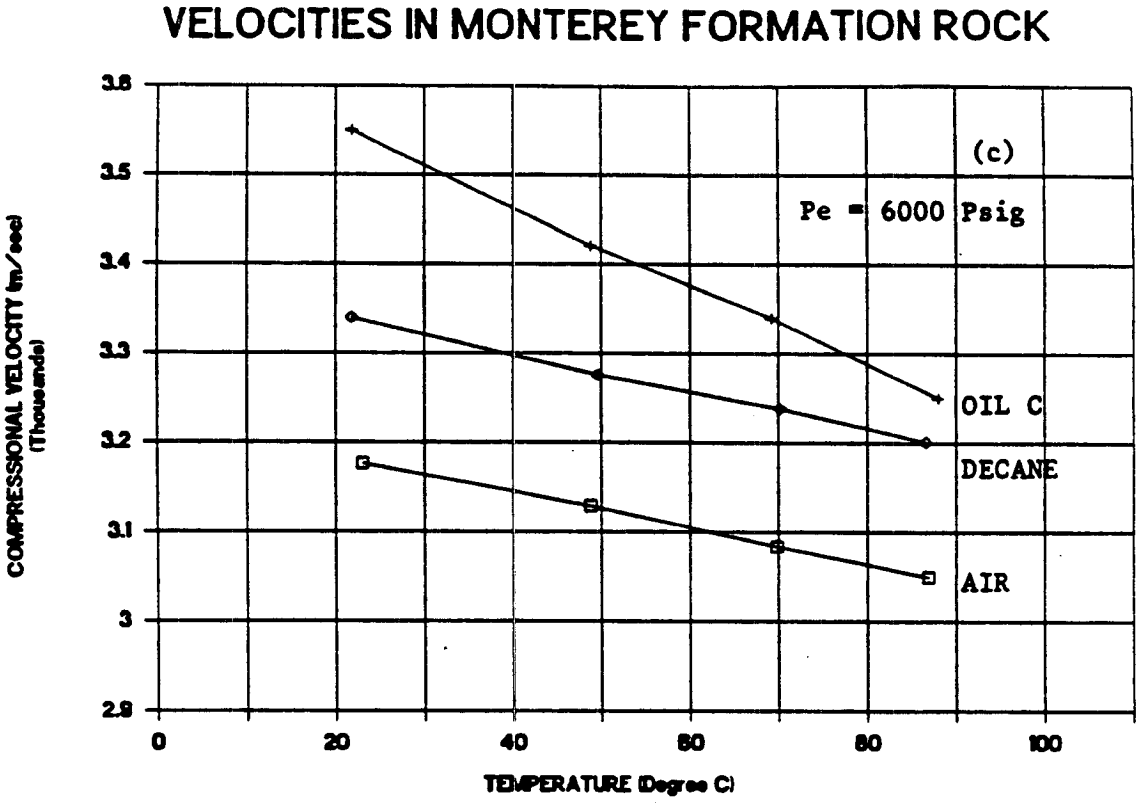
VELOCITIES IN MONTEREY FORMATION ROCK
COMPRESSIONAL VELOCITY (m/sec) (Thousands)
3.6
3.5
3.4
3.3
3.2
3.1
3
2.9
0
20
40
60
80
100
TEMPERATURE (Degree C)
(c)
Pe = 6000 Psig
OIL C
DECANE
AIR

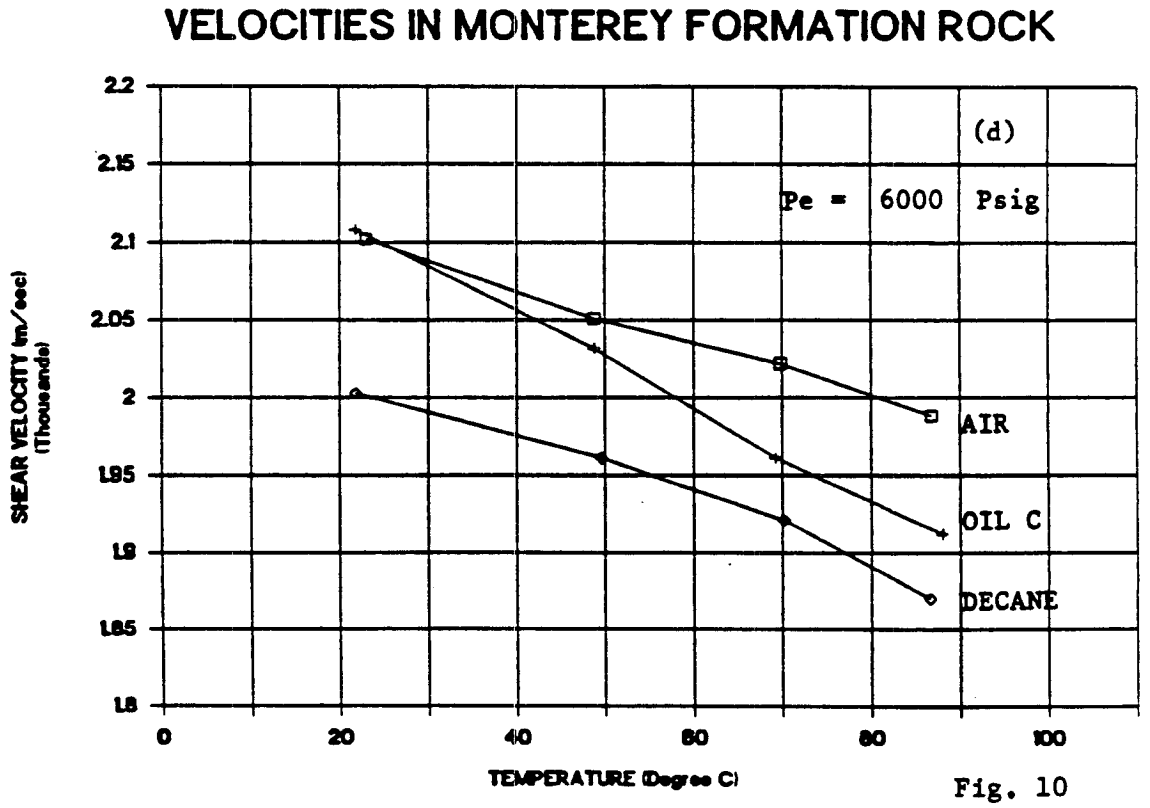
VELOCITIES IN MONTEREY FORMATION ROCK
SHEAR VELOCITY (m/sec) (Thousands)
2.2
2.15
2.1
2.05
2
1.95
1.9
1.85
1.8
0
20
40
60
80
100
TEMPERATURE (Degree C)
(d)
Pe = 6000 Psig
AIR
OIL C
DECANE

Fig. 10

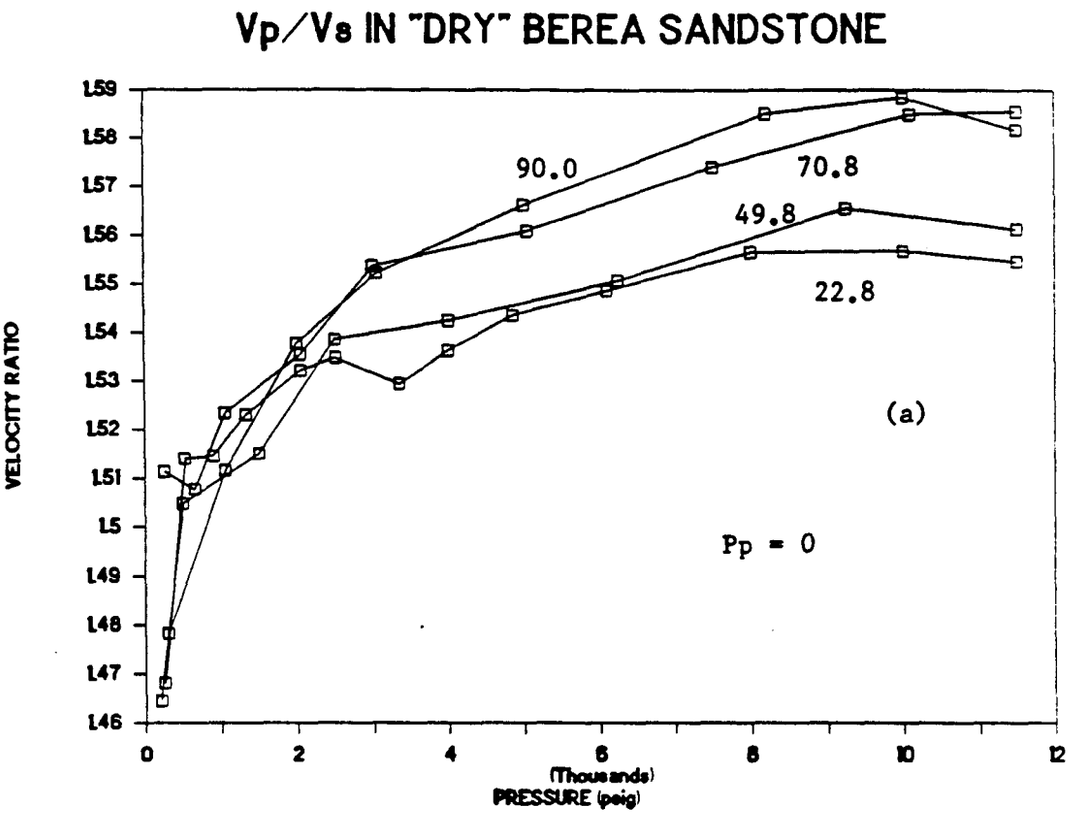
Vp/Vs IN "DRY" BEREA SANDSTONE
VELOCITY RATIO
1.59
1.58
1.57
1.56
1.55
1.54
1.53
1.52
1.51
1.5
1.49
1.48
1.47
1.46
90.0
70.8
49.8
22.8
(a)
Pp = 0
0
2
4
6
8
10
12
(Thousands)
PRESSURE (psig)

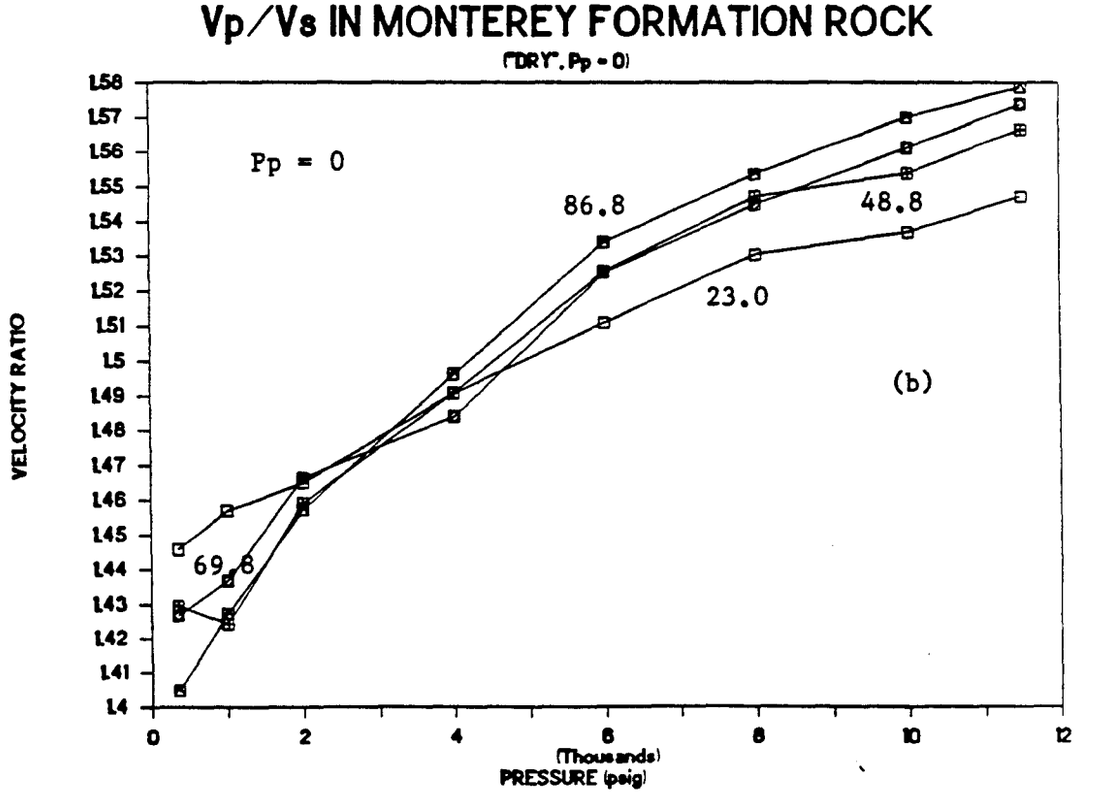
Vp/Vs IN MONTEREY FORMATION ROCK
("DRY", Pp = 0)
VELOCITY RATIO
1.58
1.57
1.56
1.55
1.54
1.53
1.52
1.51
1.5
1.49
1.48
1.47
1.46
1.45
1.44
1.43
1.42
1.41
1.4
Pp = 0
86.8
48.8
23.0
69.8
(b)
0
2
4
6
8
10
12
(Thousands)
PRESSURE (psig)

Fig. 11

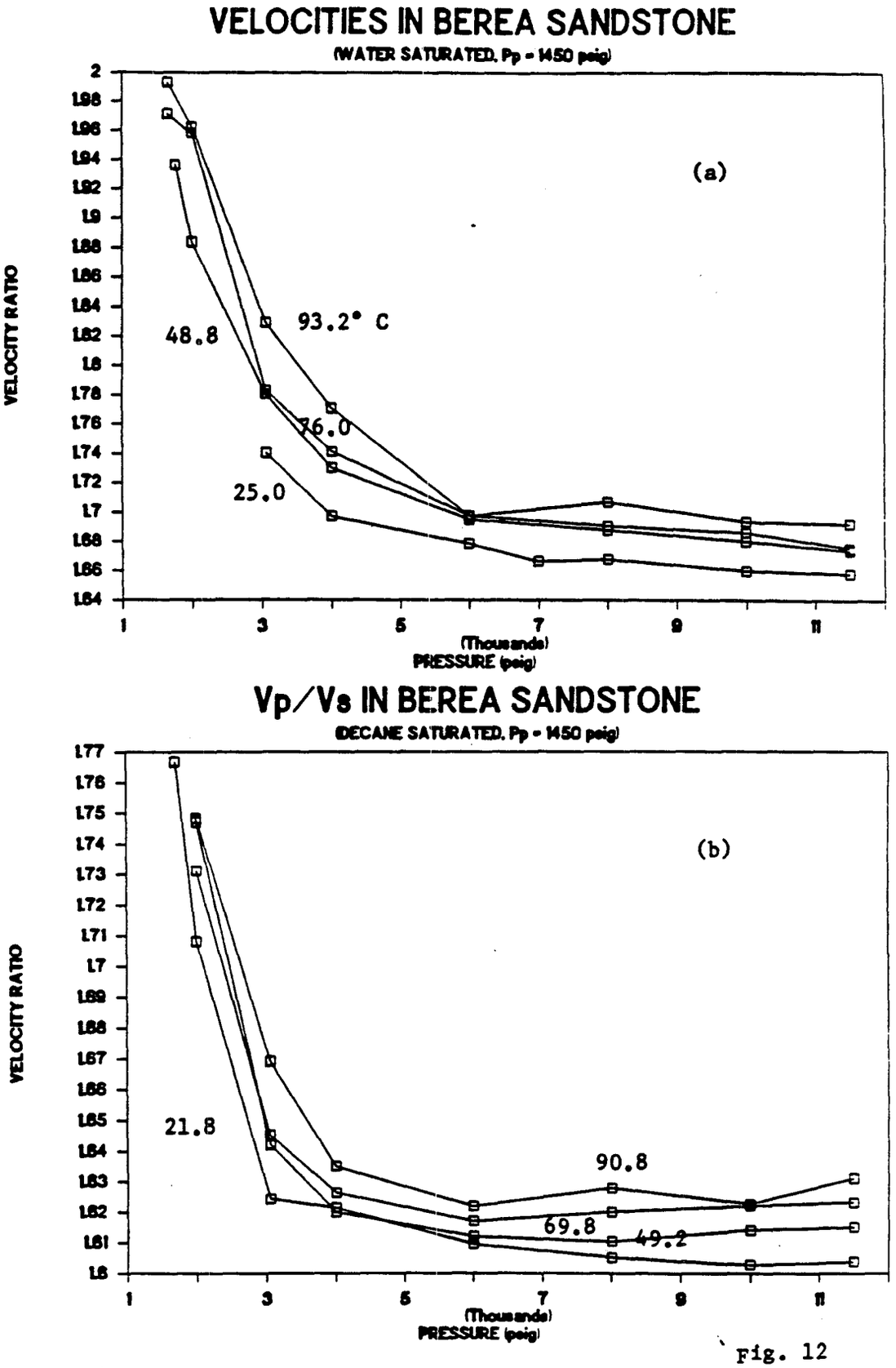
VELOCITIES IN BEREA SANDSTONE
(WATER SATURATED, Pp = 1450 psig)
VELOCITY RATIO
2
1.98
1.96
1.94
1.92
1.9
1.88
1.86
1.84
1.82
1.8
1.78
1.76
1.74
1.72
1.7
1.68
1.66
1.64
(a)
93.2° C
48.8
76.0
25.0
1
3
5
7
9
11
(Thousands)
PRESSURE (psig)
Vp/Vs IN BEREA SANDSTONE
(DECANE SATURATED, Pp = 1450 psig)
VELOCITY RATIO
1.77
1.76
1.75
1.74
1.73
1.72
1.71
1.7
1.69
1.68
1.67
1.66
1.65
1.64
1.63
1.62
1.61
1.6
(b)
21.8
90.8
69.8
49.2
1
3
5
7
9
11
(Thousands)
PRESSURE (psig)

Fig. 12

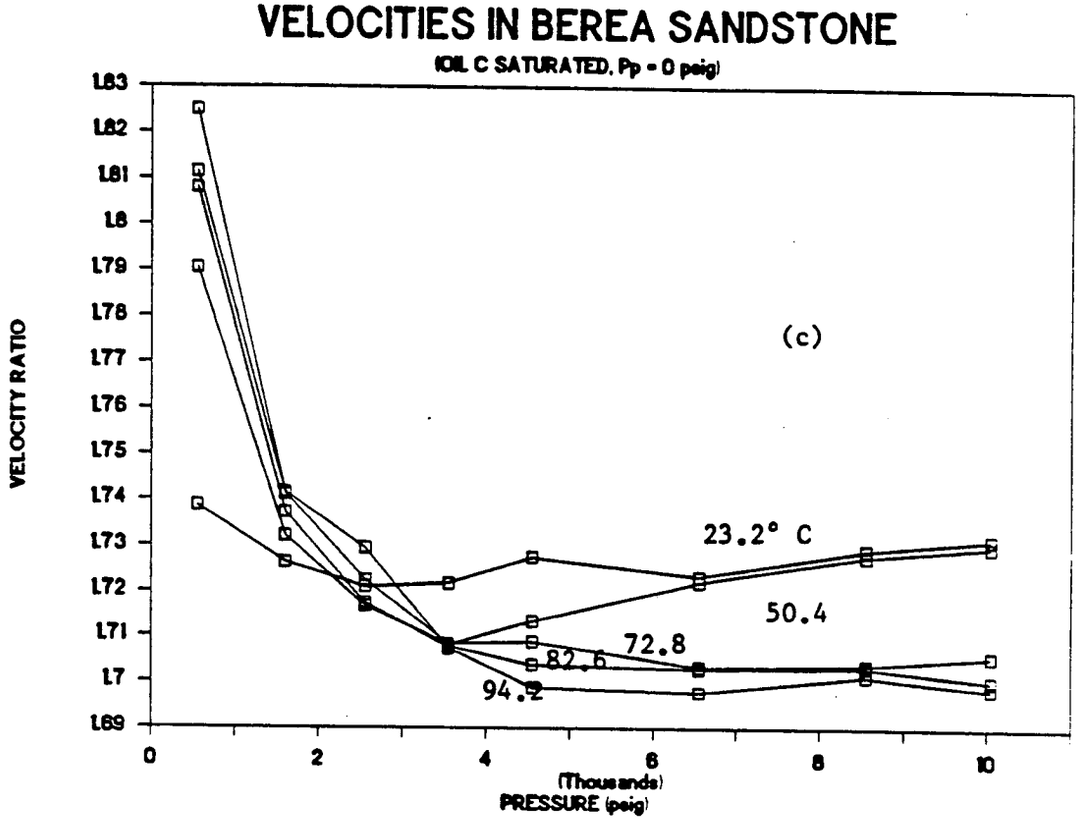
VELOCITIES IN BEREA SANDSTONE
(OIL C SATURATED, Pp = 0 psig)
VELOCITY RATIO
1.83
1.82
1.81
1.8
1.79
1.78
1.77
1.76
1.75
1.74
1.73
1.72
1.71
1.7
1.69
(c)
23.2° C
50.4
72.8
82.6
94.2
0
2
4
6
8
10
(Thousands)
PRESSURE (psig)

Fig.12

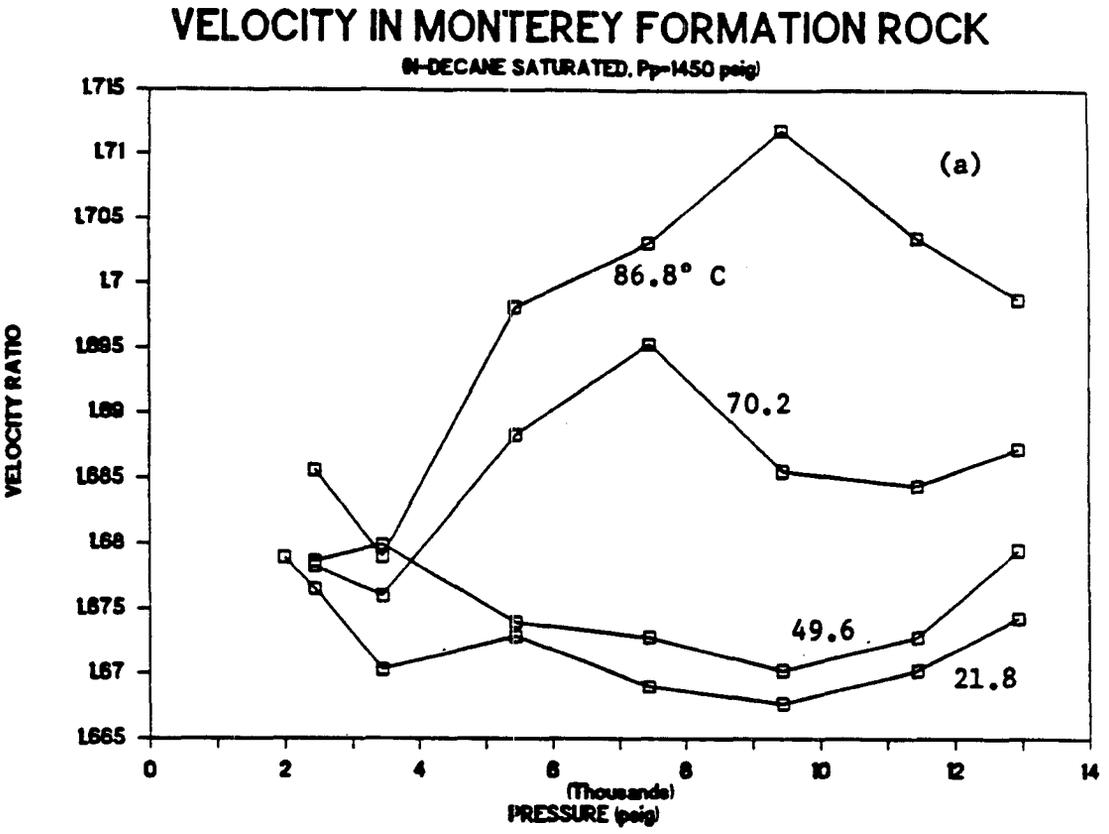
VELOCITY IN MONTEREY FORMATION ROCK
(N-DECANE SATURATED, Pp=1450 psig)
VELOCITY RATIO
1.715
1.71
1.705
1.7
1.695
1.69
1.685
1.68
1.675
1.67
1.665
(a)
86.8° C
70.2
49.6
21.8
0
2
4
6
8
10
12
14
(Thousands)
PRESSURE (psig)

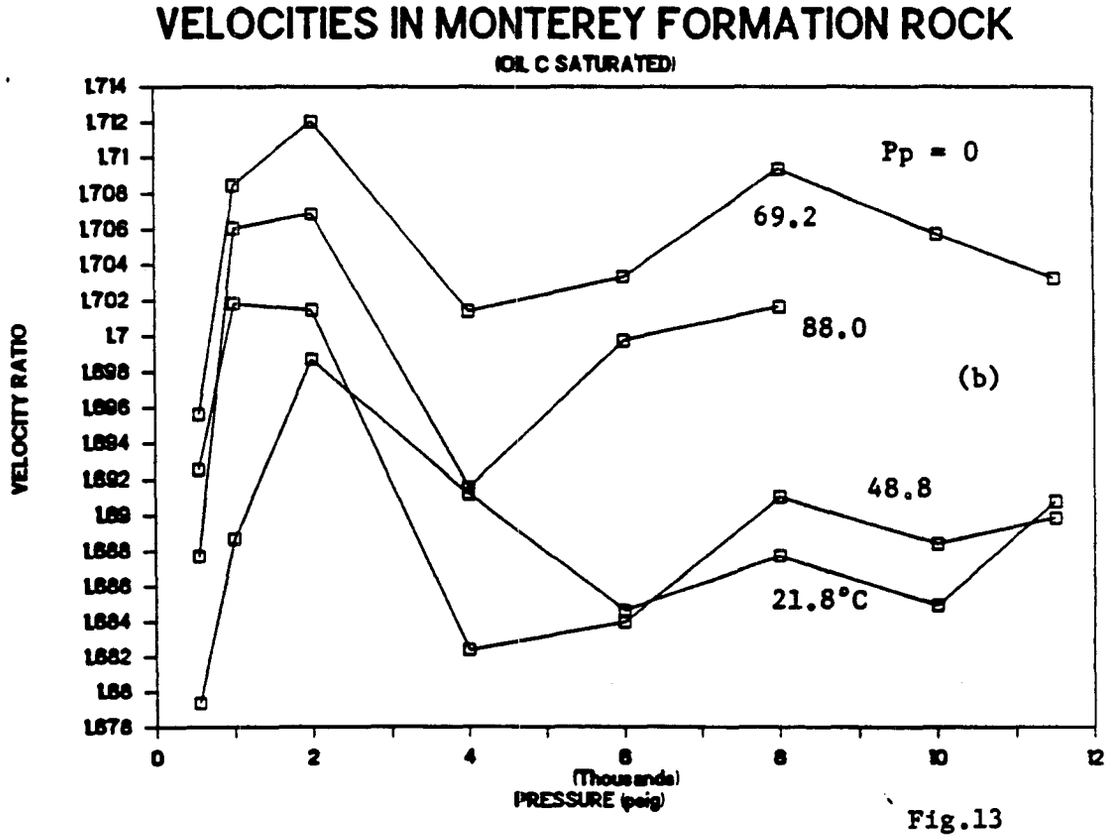
VELOCITIES IN MONTEREY FORMATION ROCK
(OIL C SATURATED)
VELOCITY RATIO
1.714
1.712
1.71
1.708
1.706
1.704
1.702
1.7
1.698
1.696
1.694
1.692
1.69
1.688
1.686
1.684
1.682
1.68
1.678
Pp = 0
69.2
88.0
(b)
48.8
21.8°C
0
2
4
6
8
10
12
(Thousands)
PRESSURE (psig)

Fig.13

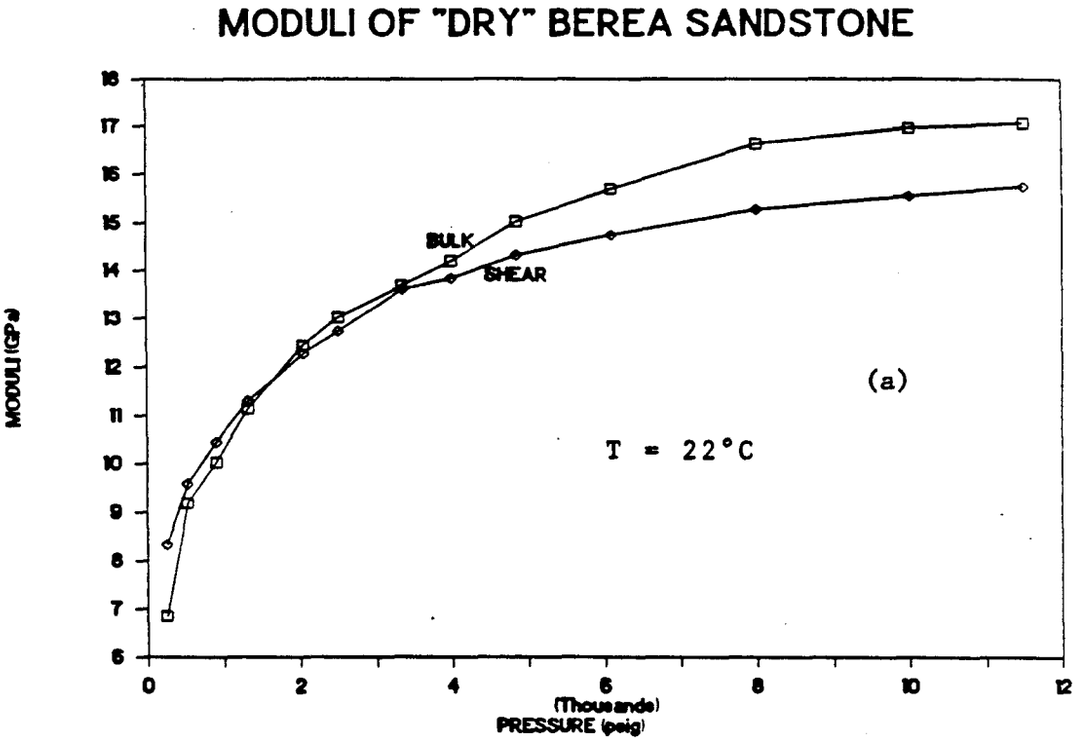
MODULI OF "DRY" BEREA SANDSTONE
MODULI (GPa)
BULK
SHEAR
(a)
T = 22°C
PRESSURE (psig)
(Thousands)

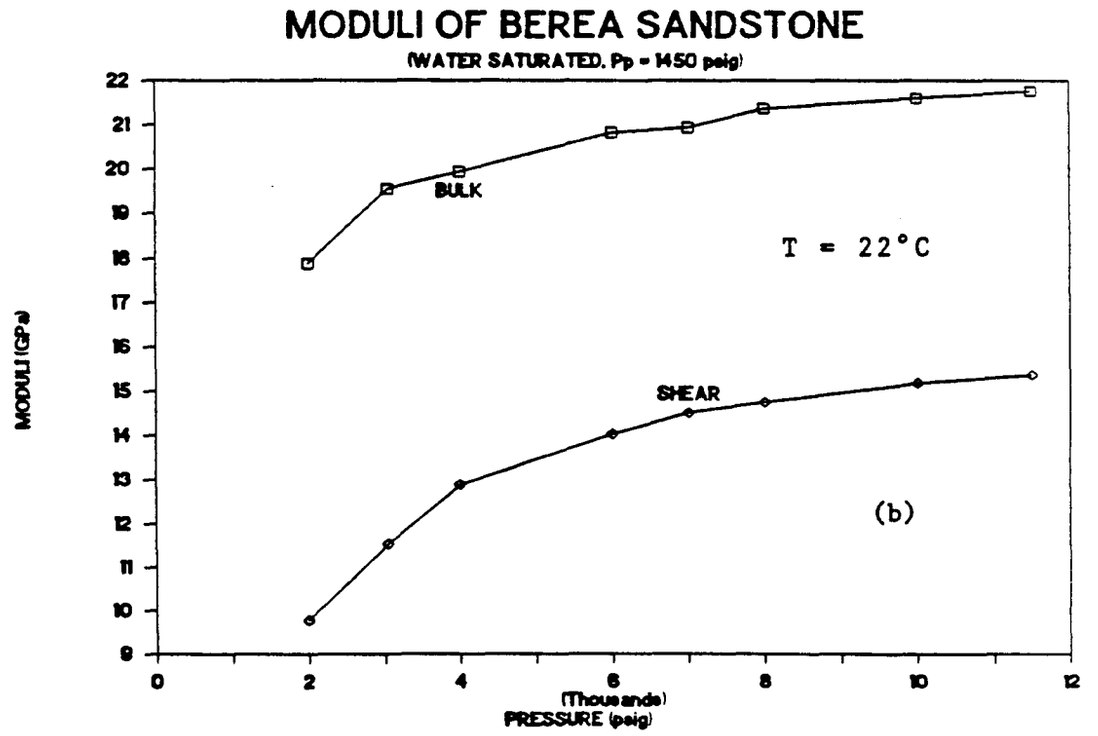
MODULI OF BEREA SANDSTONE
(WATER SATURATED, Pp = 1450 psig)
MODULI (GPa)
BULK
SHEAR
T = 22°C
(b)
PRESSURE (psig)
(Thousands)

Fig.14

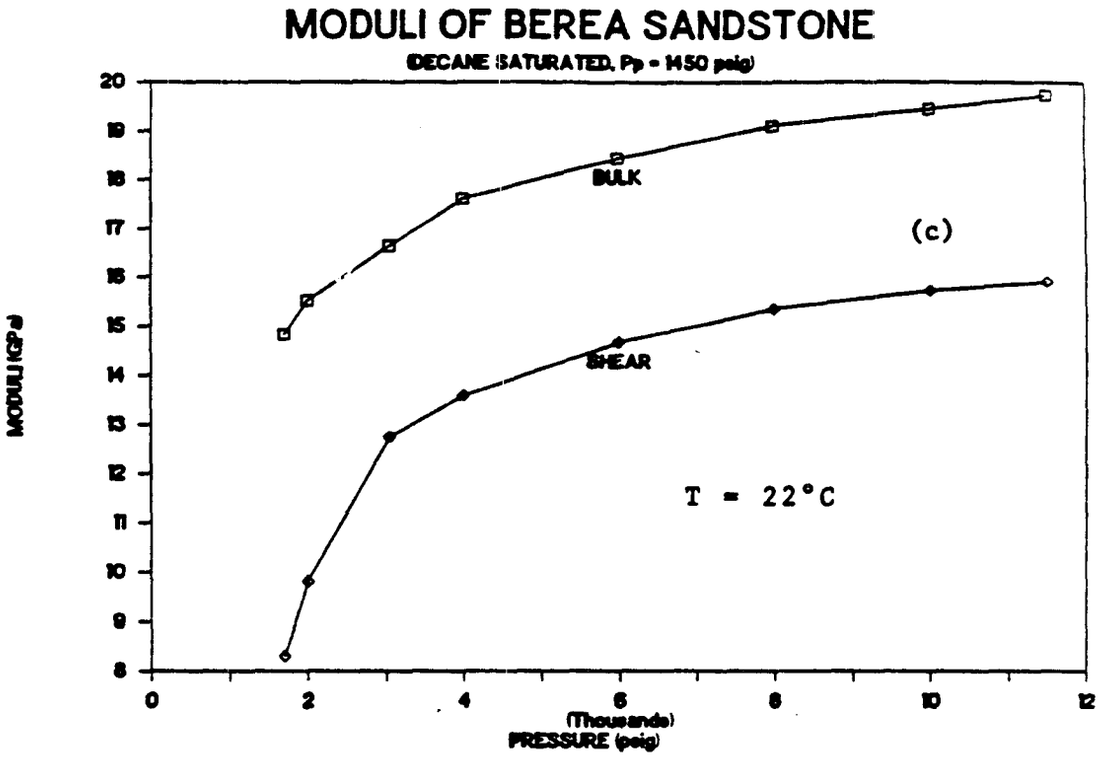
MODULI OF BEREA SANDSTONE
(DECANE SATURATED, Pp = 1450 psig)
BULK
SHEAR
(c)
T = 22°C
MODULI (GPa)
PRESSURE (psig)
(Thousands)

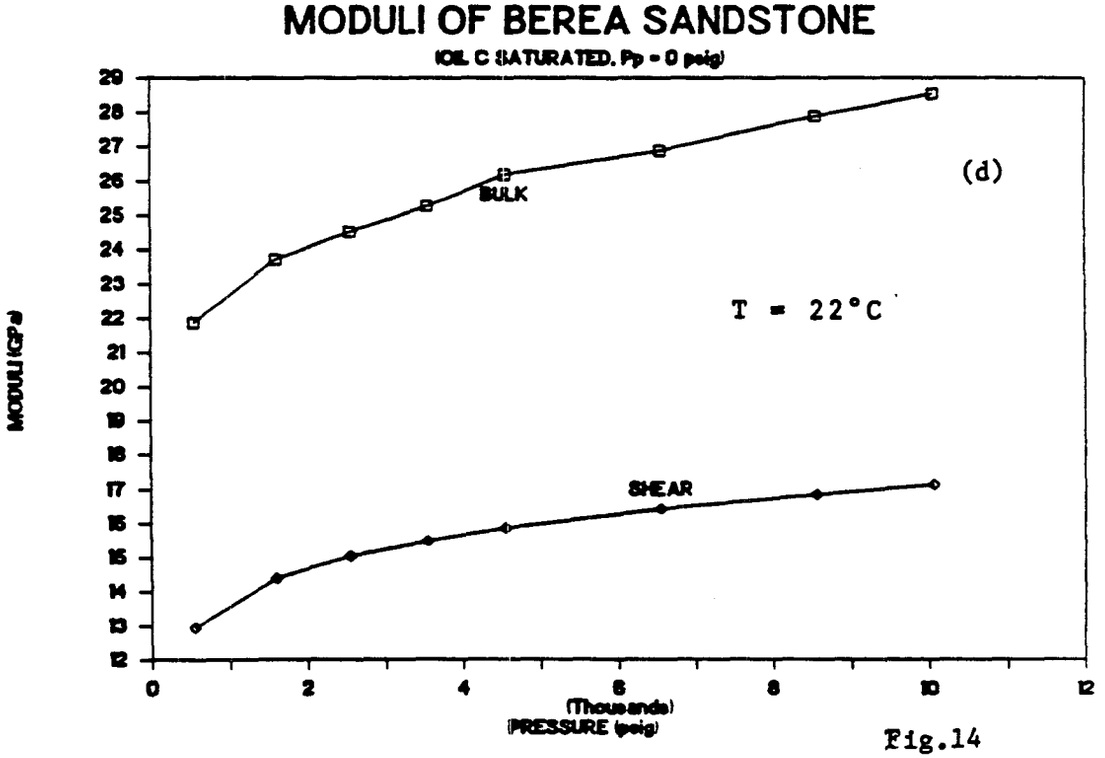
MODULI OF BEREA SANDSTONE
(OIL C SATURATED, Pp = 0 psig)
BULK
SHEAR
(d)
T = 22°C
MODULI (GPa)
PRESSURE (psig)
(Thousands)

Fig.14

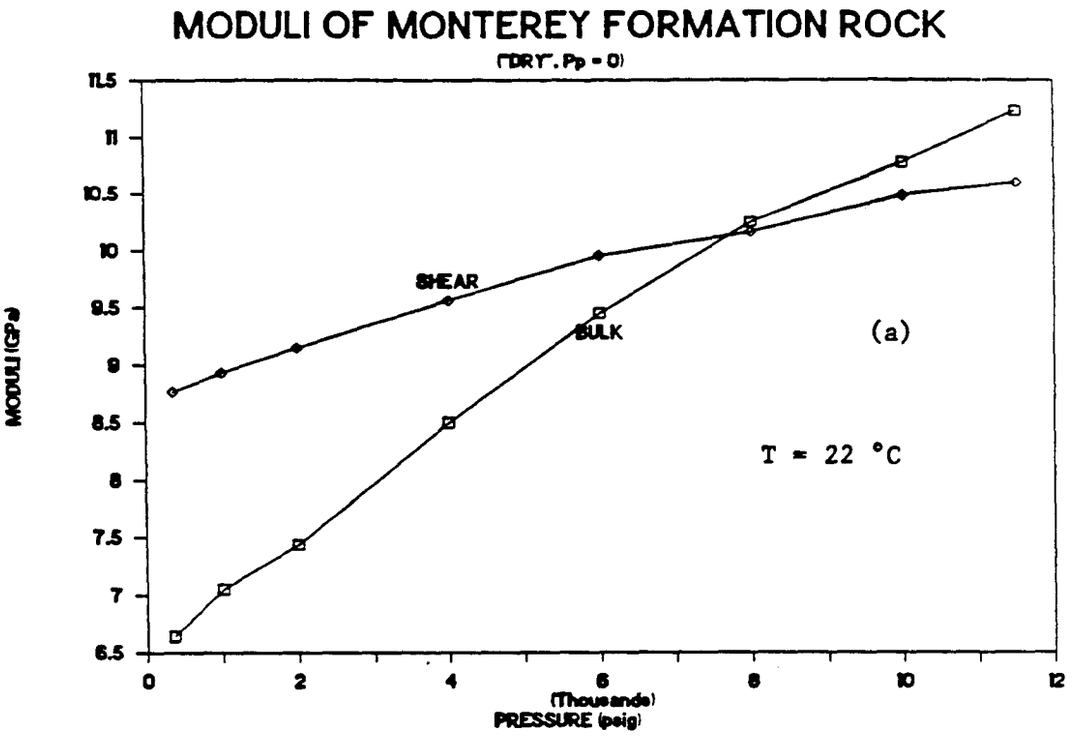
MODULI OF MONTEREY FORMATION ROCK
("DRY", Pp = 0)
MODULI (GPa)
11.5
11
10.5
10
9.5
9
8.5
8
7.5
7
6.5
SHEAR
BULK
(a)
T = 22 °C
0
2
4
6
8
10
12
(Thousands)
PRESSURE (psig)

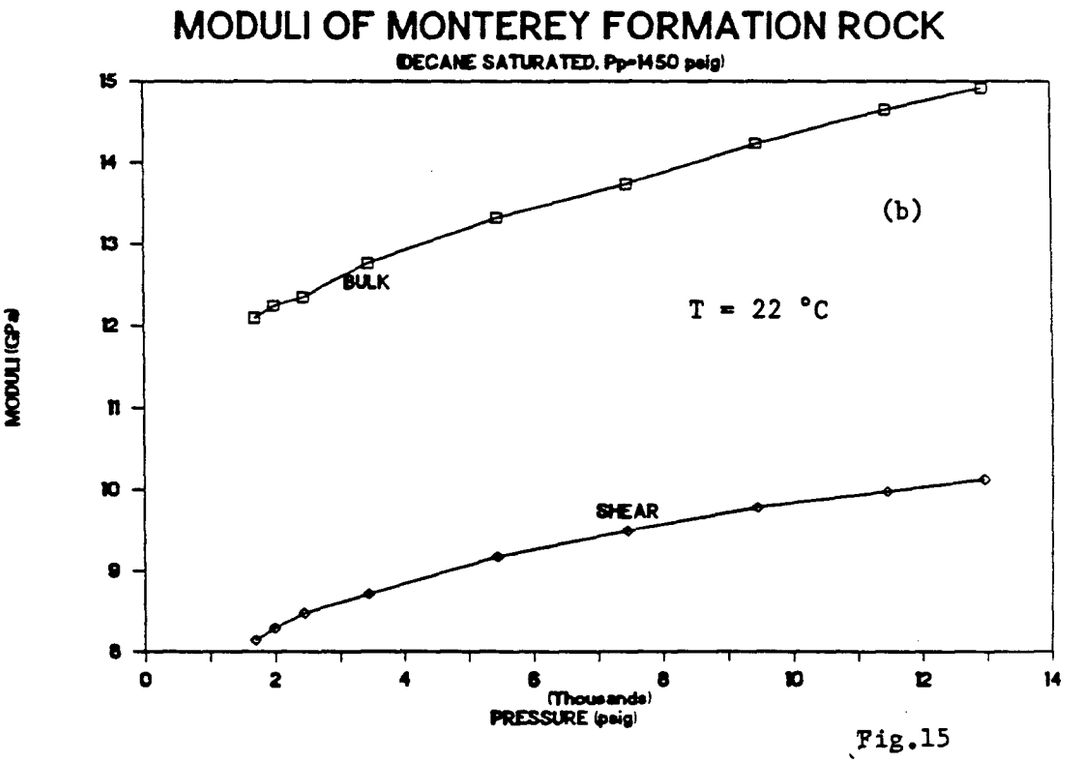
MODULI OF MONTEREY FORMATION ROCK
(DECANE SATURATED, Pp=1450 psig)
MODULI (GPa)
15
14
13
12
11
10
9
8
BULK
(b)
T = 22 °C
SHEAR
0
2
4
6
8
10
12
14
(Thousands)
PRESSURE (psig)

Fig.15

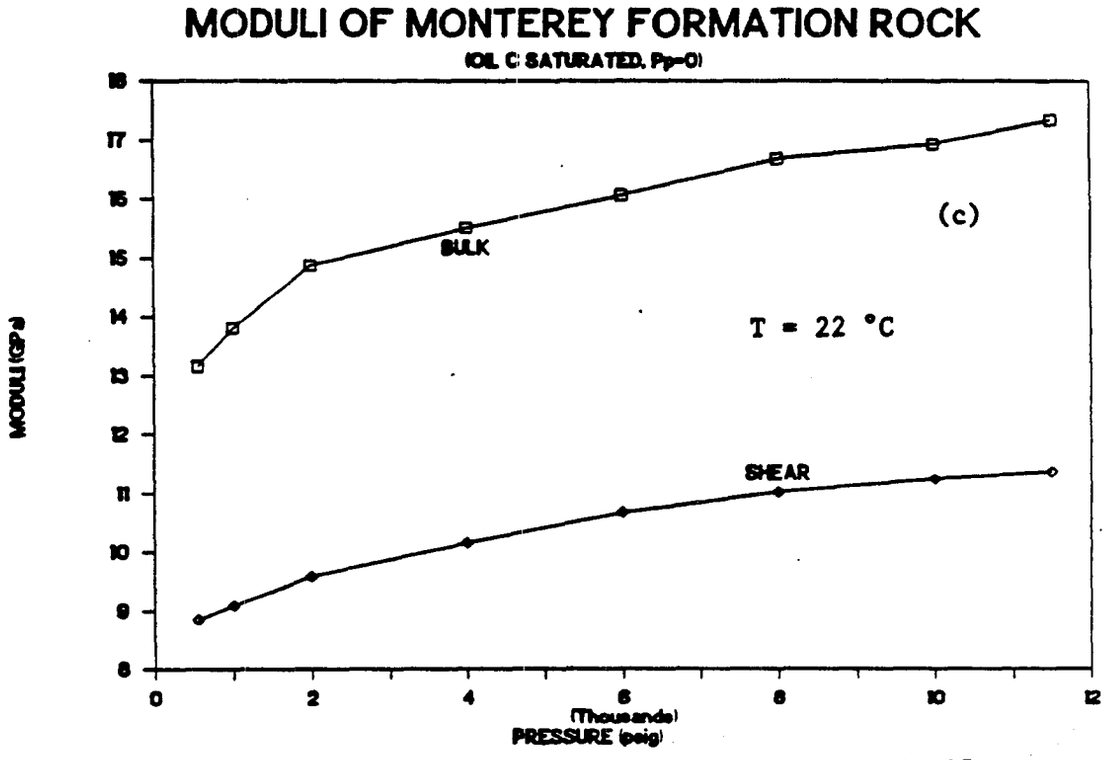
MODULI OF MONTEREY FORMATION ROCK
(OIL C: SATURATED, Pp=0)
(c)
BULK
T = 22 °C
SHEAR
MODULI (GPa)
PRESSURE (psig)
(Thousands)
0
2
4
6
8
10
12

Fig.15

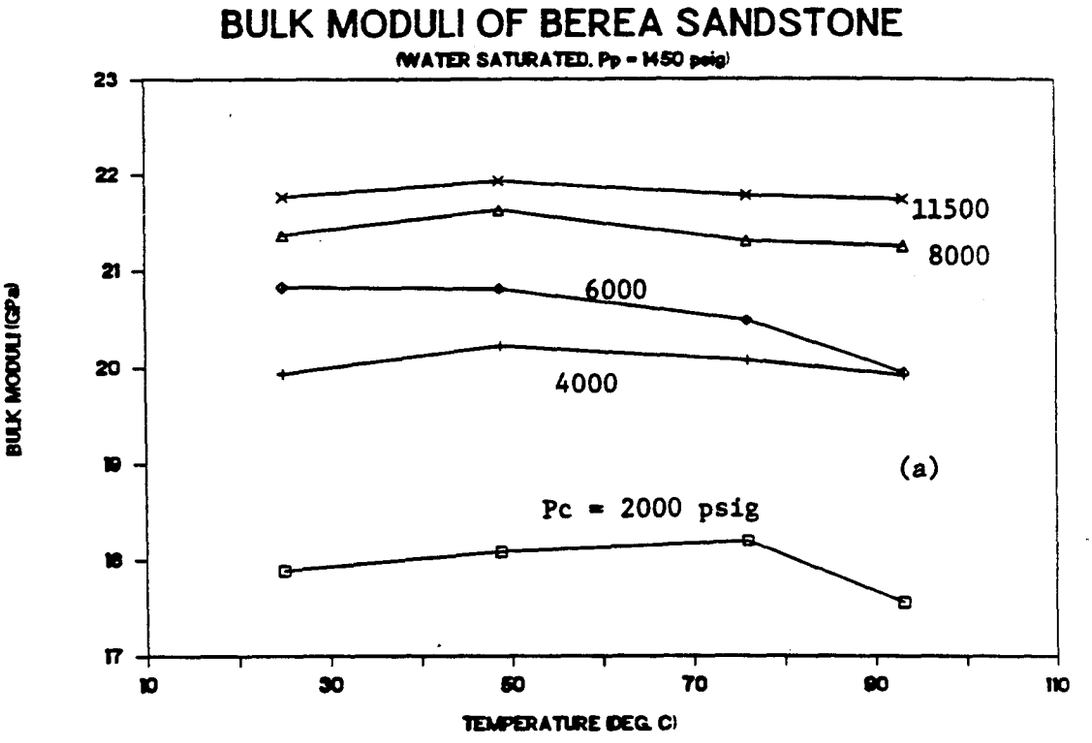
BULK MODULI OF BEREA SANDSTONE
(WATER SATURATED. Pp = 1450 psig)
BULK MODULI (GPa)
23
22
21
20
19
18
17
10
30
50
70
90
110
TEMPERATURE (DEG. C)
11500
8000
6000
4000
(a)
Pc = 2000 psig

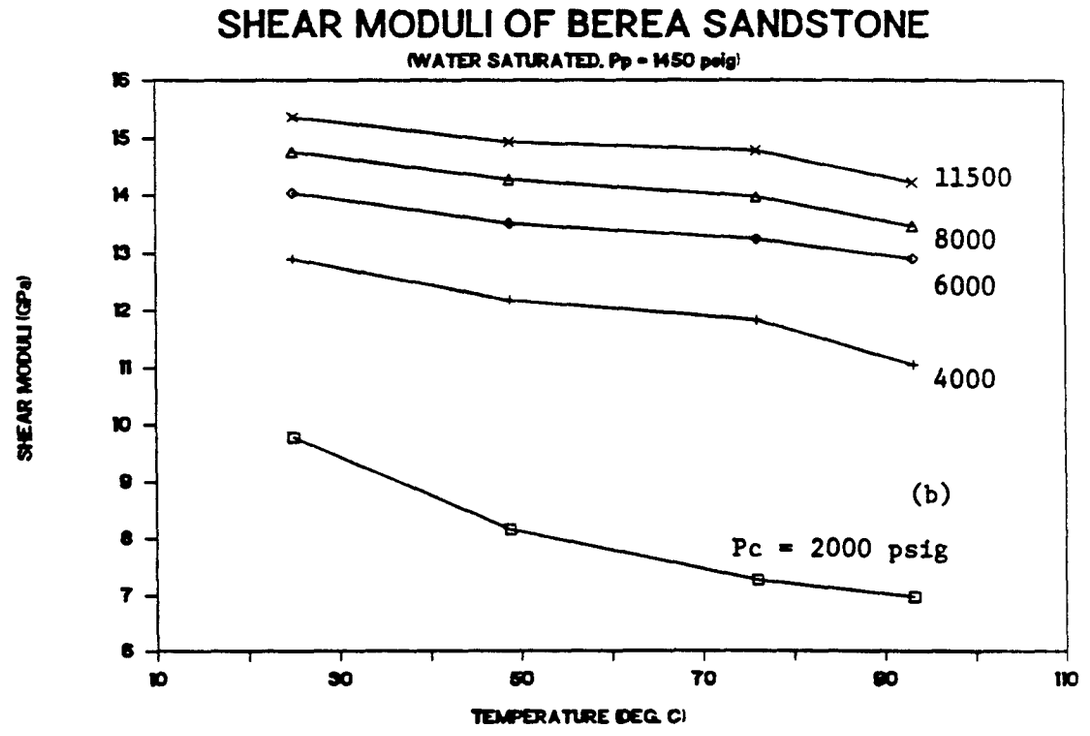
SHEAR MODULI OF BEREA SANDSTONE
(WATER SATURATED. Pp = 1450 psig)
SHEAR MODULI (GPa)
16
15
14
13
12
11
10
9
8
7
6
10
30
50
70
90
110
TEMPERATURE (DEG. C)
11500
8000
6000
4000
(b)
Pc = 2000 psig

Fig.16

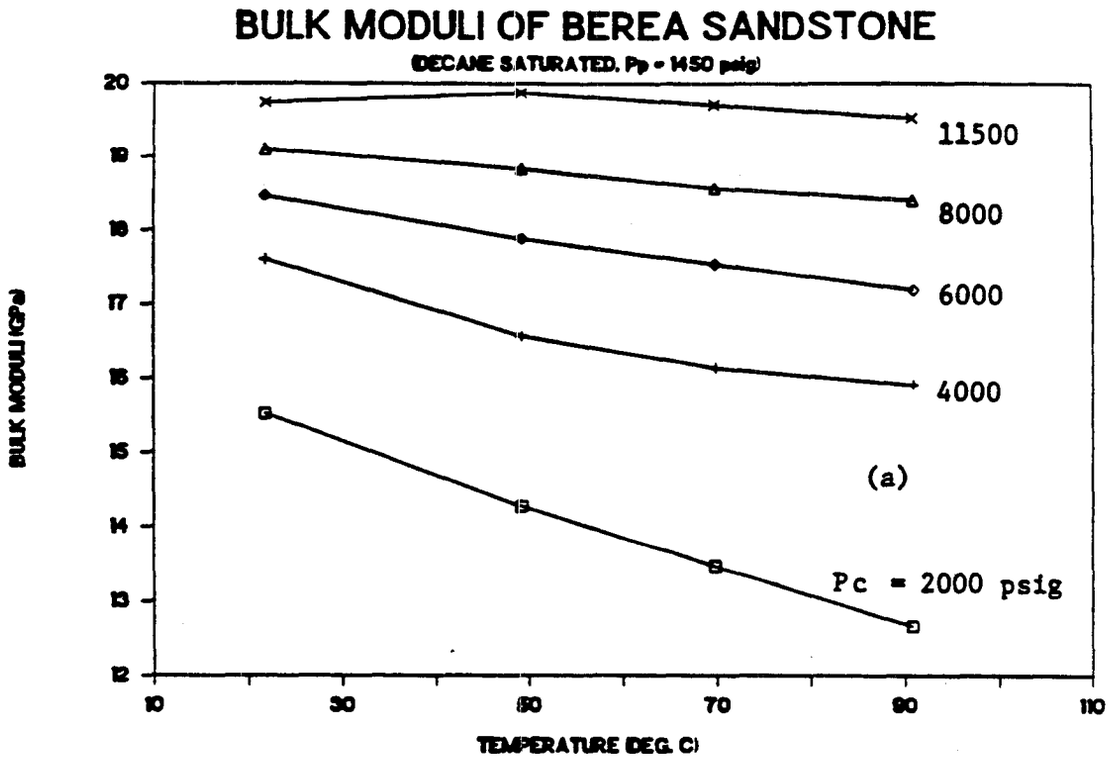
BULK MODULI OF BEREA SANDSTONE
(DECANE SATURATED, Pp = 1450 psig)
BULK MODULI (GPa)
TEMPERATURE (DEG. C)
11500
8000
6000
4000
(a)
Pc = 2000 psig

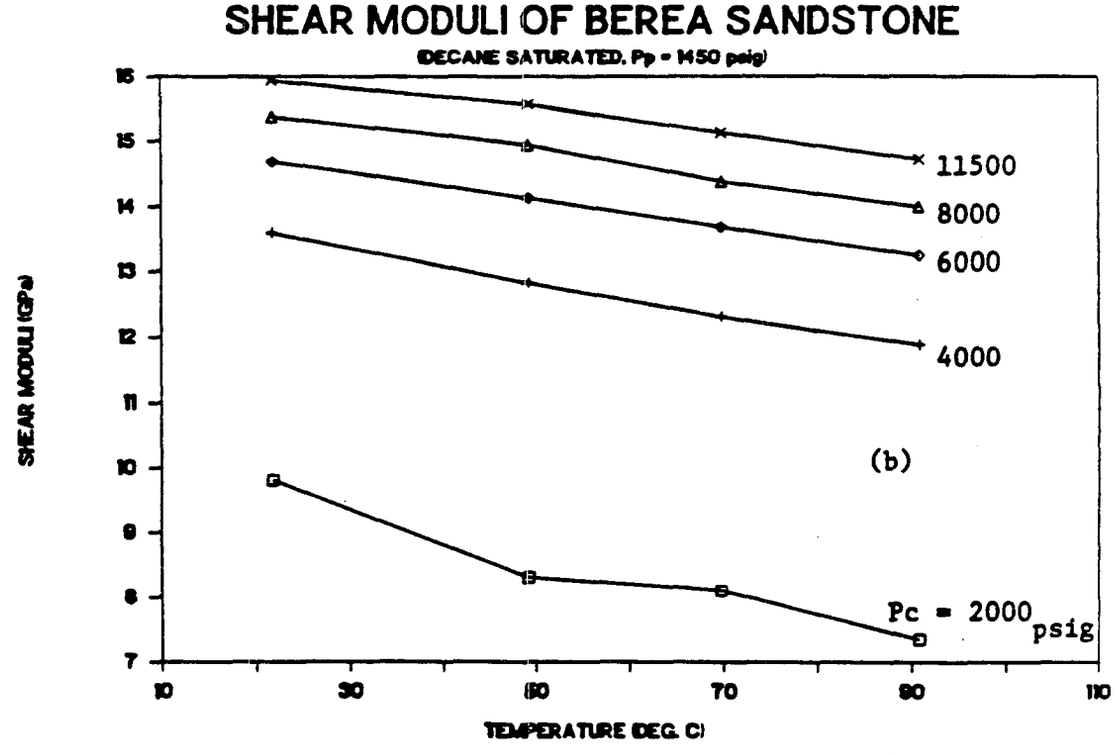
SHEAR MODULI OF BEREA SANDSTONE
(DECANE SATURATED, Pp = 1450 psig)
SHEAR MODULI (GPa)
TEMPERATURE (DEG. C)
11500
8000
6000
4000
(b)
Pc = 2000 psig

Fig.17

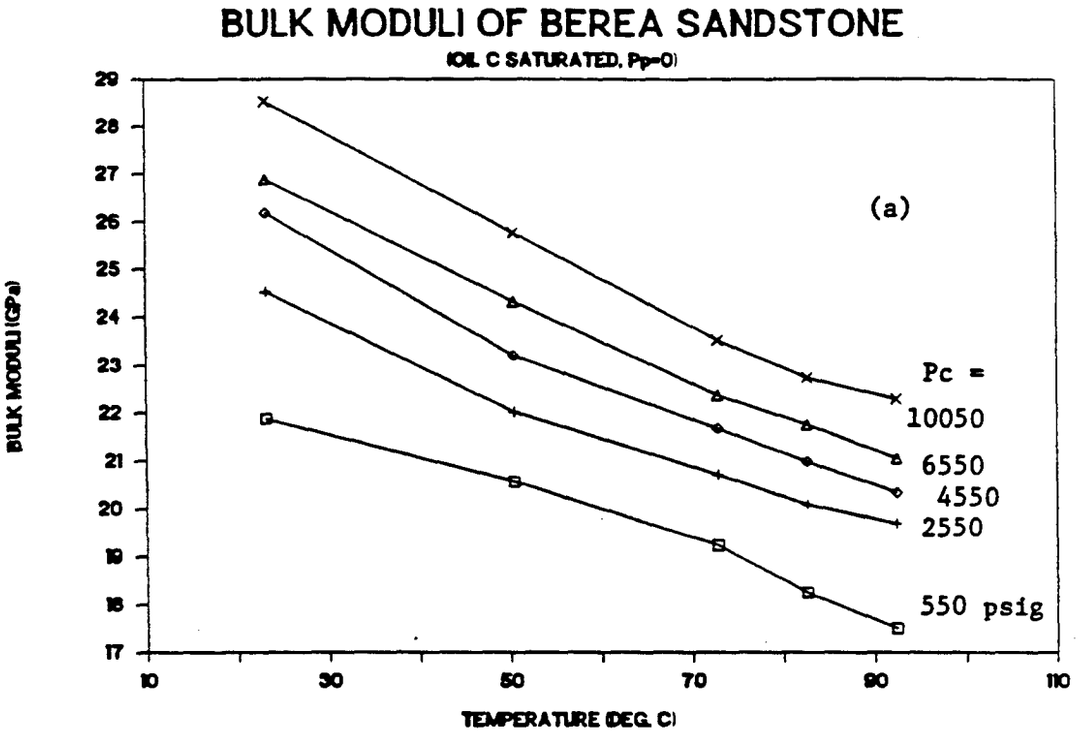
BULK MODULI OF BEREA SANDSTONE
(OIL C SATURATED, Pp=0)
BULK MODULI (GPa)
TEMPERATURE (DEG. C)
(a)
Pc =
10050
6550
4550
2550
550 psig

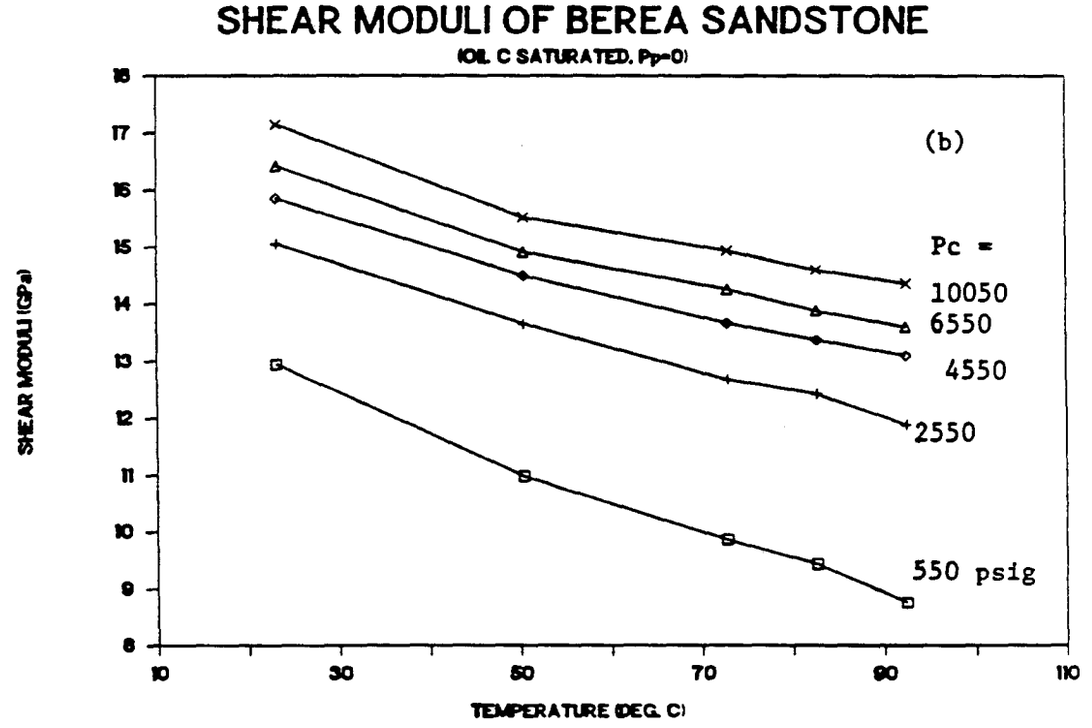
SHEAR MODULI OF BEREA SANDSTONE
(OIL C SATURATED, Pp=0)
SHEAR MODULI (GPa)
TEMPERATURE (DEG. C)
(b)
Pc =
10050
6550
4550
2550
550 psig

Fig.18

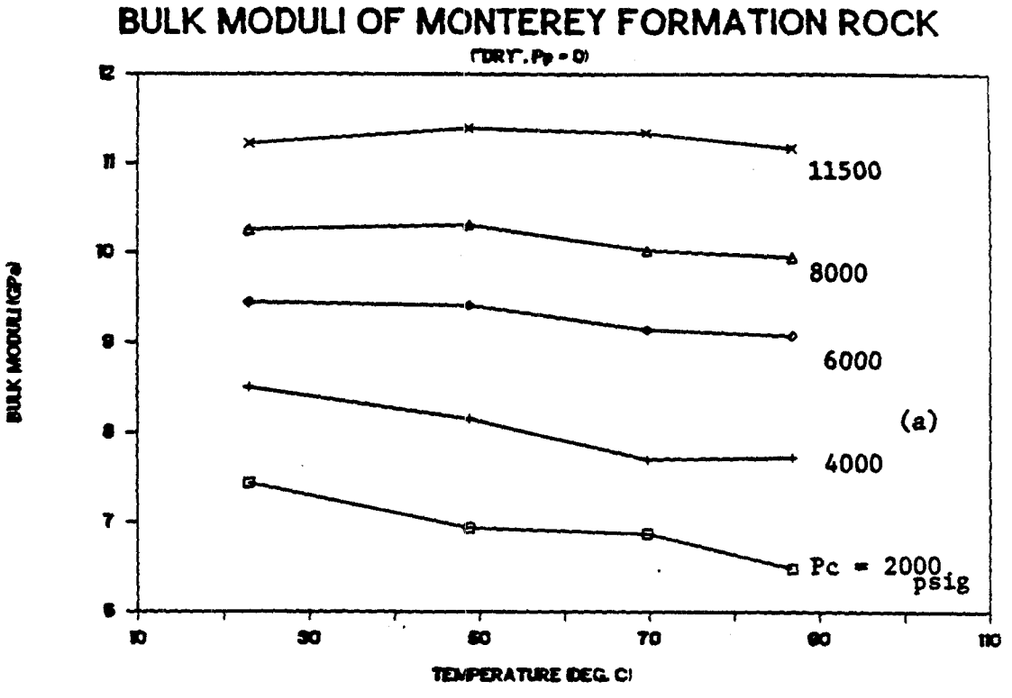
BULK MODULI OF MONTEREY FORMATION ROCK
("DRY", Pp = 0)
BULK MODULI (GPa)
TEMPERATURE (DEG. C)
11500
8000
6000
4000
Pc = 2000 psig
(a)

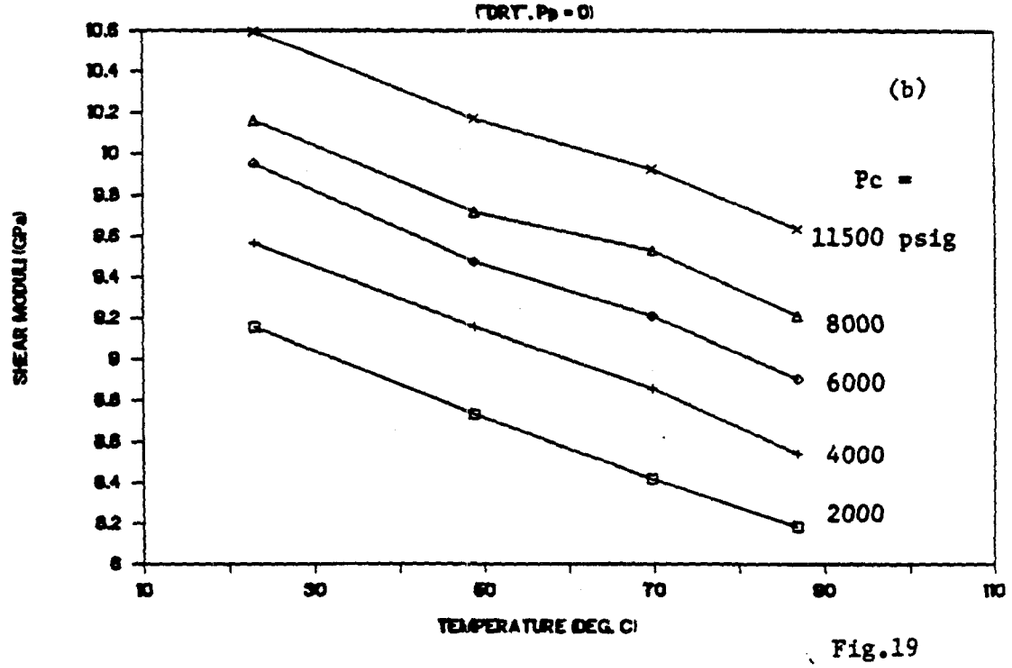
SHEAR MODULI OF MONTEREY FORMATION ROCK
("DRY", Pp = 0)
SHEAR MODULI (GPa)
TEMPERATURE (DEG. C)
(b)
Pc =
11500 psig
8000
6000
4000
2000

Fig.19

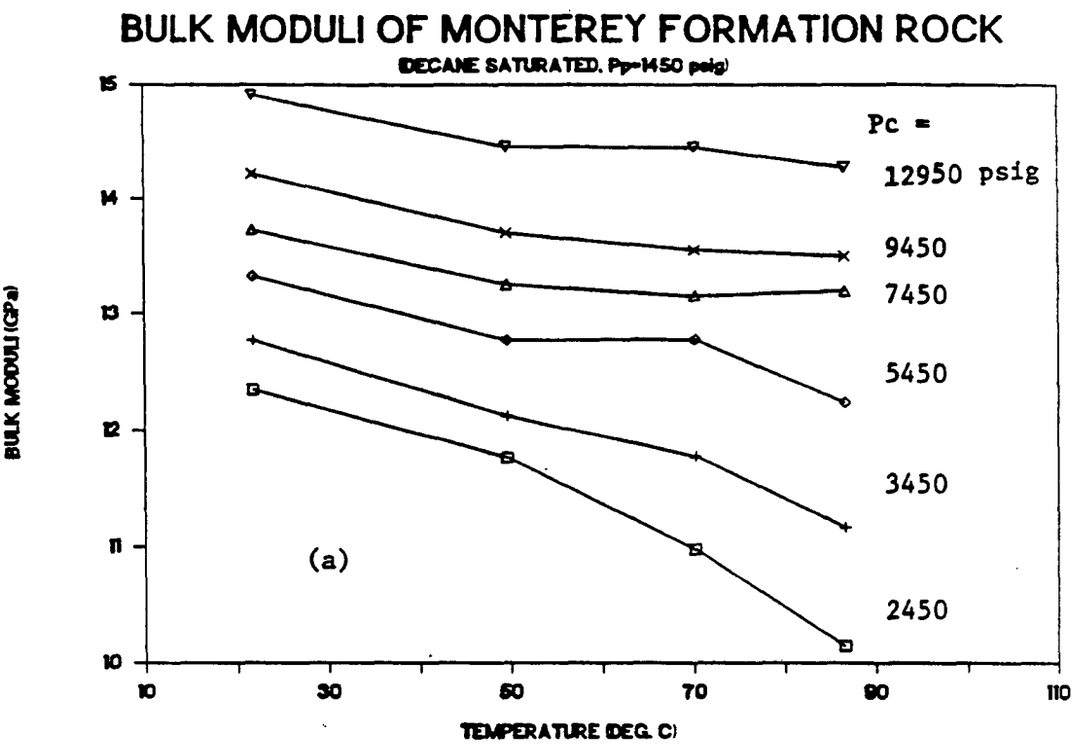
BULK MODULI OF MONTEREY FORMATION ROCK
(DECANE SATURATED, Pp=1450 psig)
BULK MODULI (GPa)
TEMPERATURE (DEG. C)
Pc =
12950 psig
9450
7450
5450
3450
2450
(a)
15
14
13
12
11
10
10
30
50
70
90
110

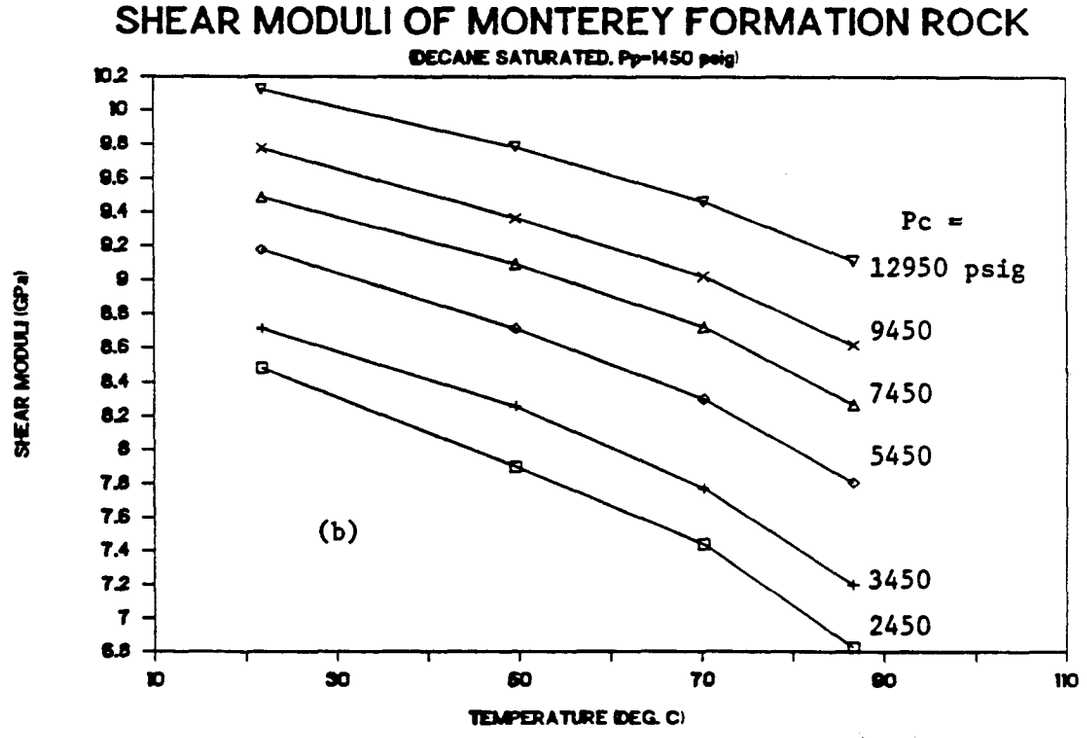
SHEAR MODULI OF MONTEREY FORMATION ROCK
(DECANE SATURATED, Pp=1450 psig)
SHEAR MODULI (GPa)
TEMPERATURE (DEG. C)
Pc =
12950 psig
9450
7450
5450
3450
2450
(b)
10.2
10
9.8
9.6
9.4
9.2
9
8.8
8.6
8.4
8.2
8
7.8
7.6
7.4
7.2
7
6.8
10
30
50
70
90
110

Fig.20

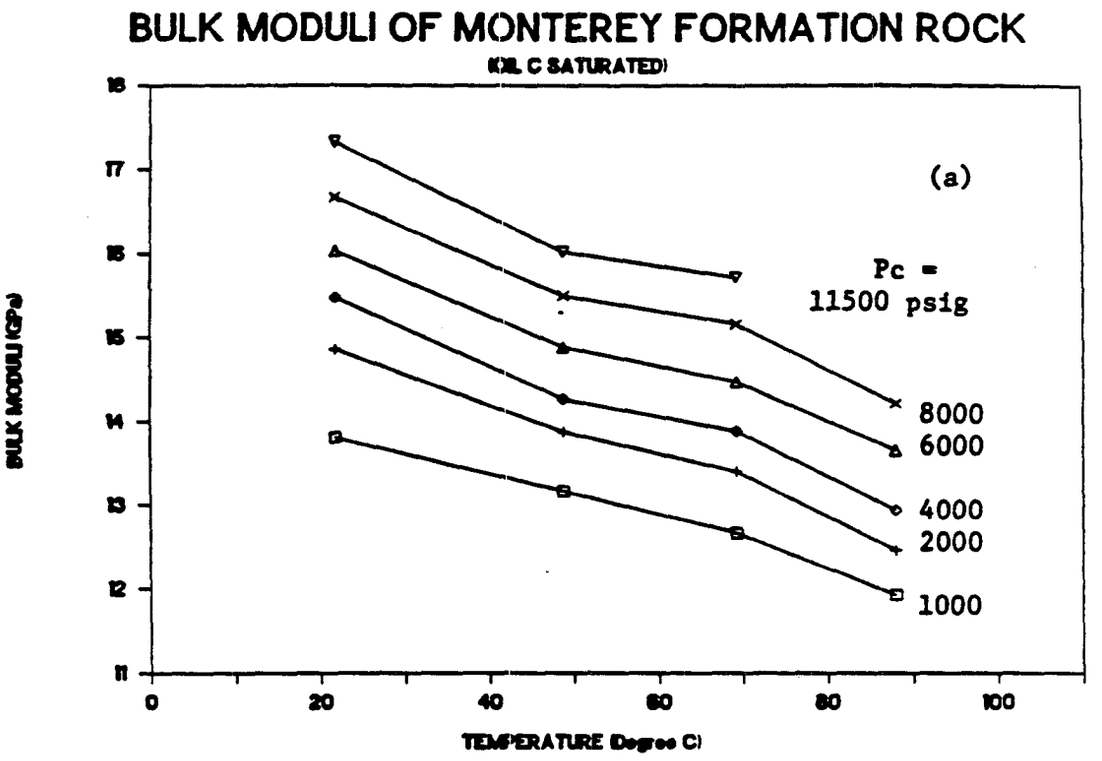
BULK MODULI OF MONTEREY FORMATION ROCK
(OIL C SATURATED)
BULK MODULI (GPa)
TEMPERATURE Degree C)
(a)
Pc =
11500 psig
8000
6000
4000
2000
1000

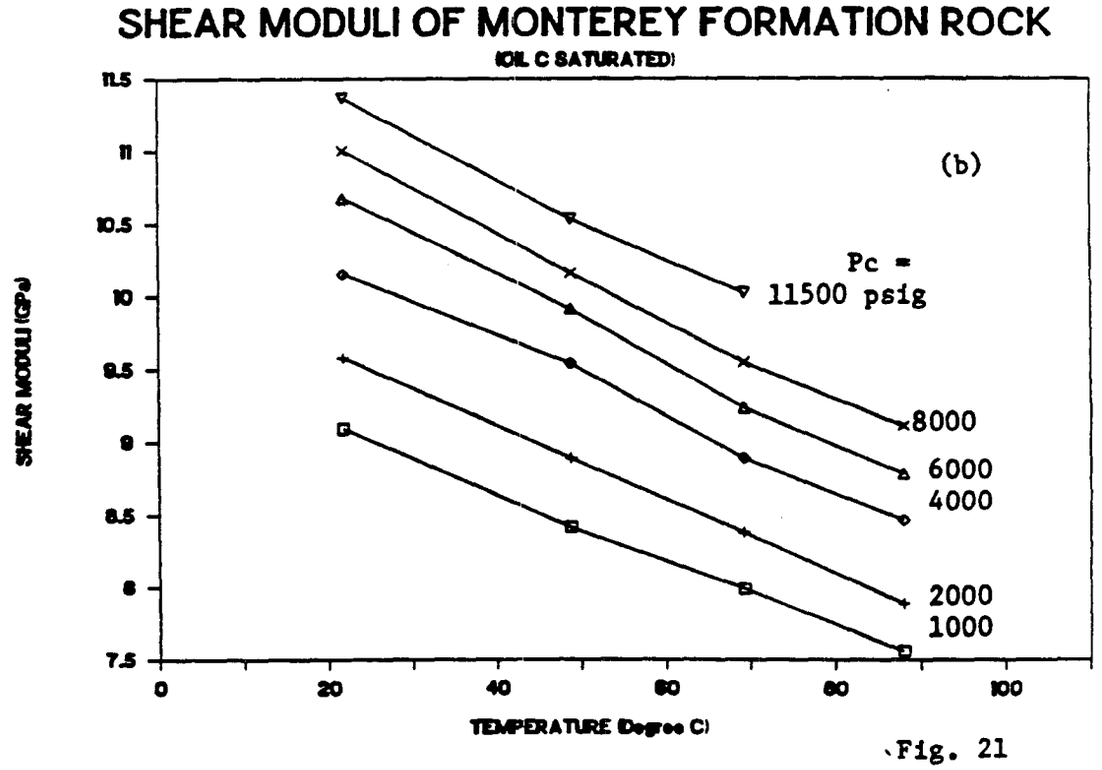
SHEAR MODULI OF MONTEREY FORMATION ROCK
(OIL C SATURATED)
SHEAR MODULI (GPa)
TEMPERATURE Degree C)
(b)
Pc =
11500 psig
8000
6000
4000
2000
1000

Fig. 21

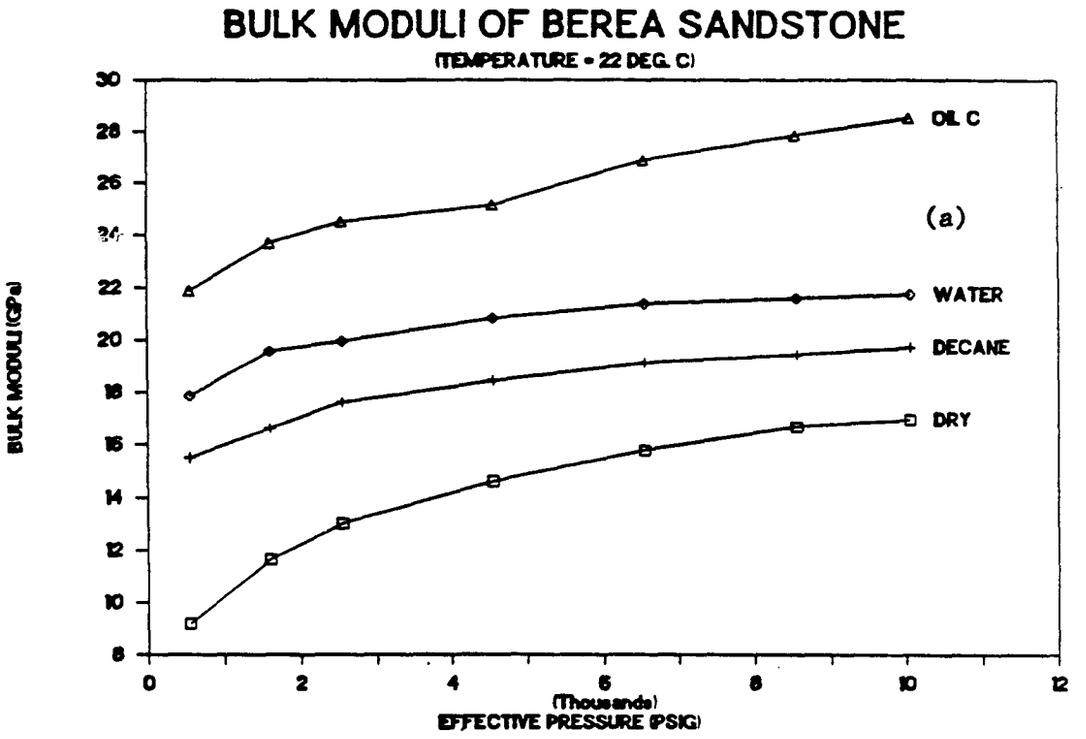
BULK MODULI OF BEREA SANDSTONE
(TEMPERATURE = 22 DEG. C)
BULK MODULI (GPa)
30
28
26
24
22
20
18
16
14
12
10
8
0
2
4
6
8
10
12
(Thousands)
EFFECTIVE PRESSURE (PSIG)
OIL C
(a)
WATER
DECANE
DRY

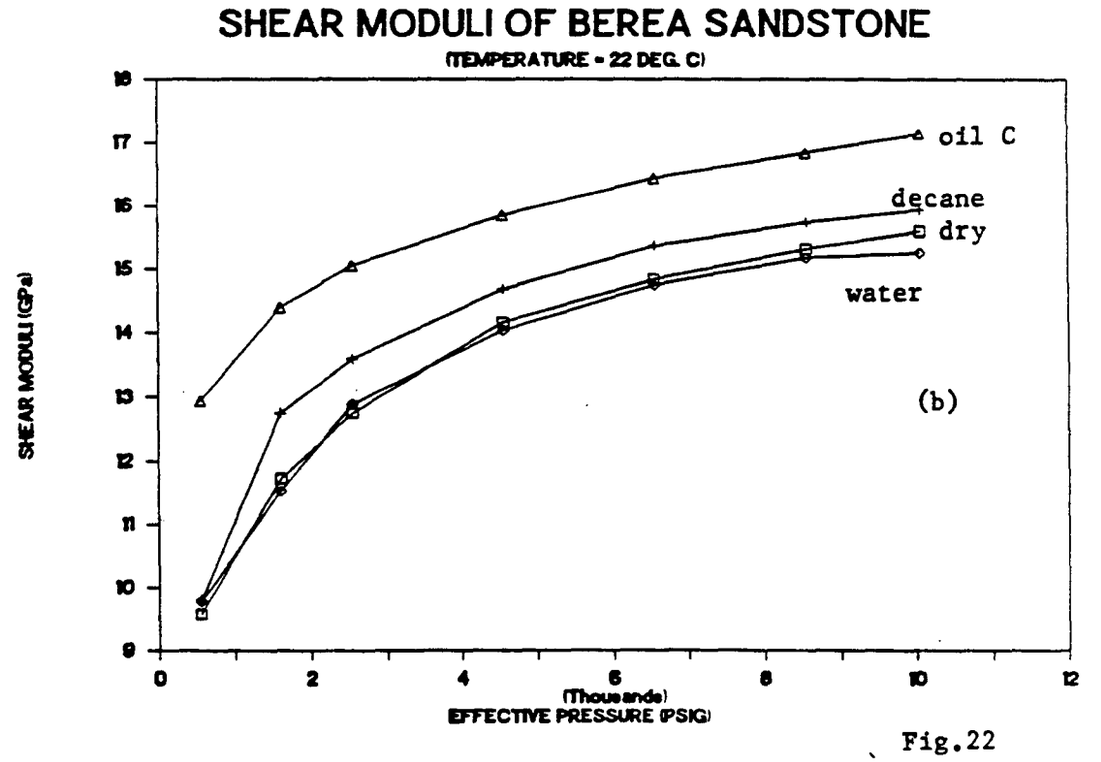
SHEAR MODULI OF BEREA SANDSTONE
(TEMPERATURE = 22 DEG. C)
SHEAR MODULI (GPa)
18
17
16
15
14
13
12
11
10
9
0
2
4
6
8
10
12
(Thousands)
EFFECTIVE PRESSURE (PSIG)
oil C
decane
dry
water
(b)

Fig.22

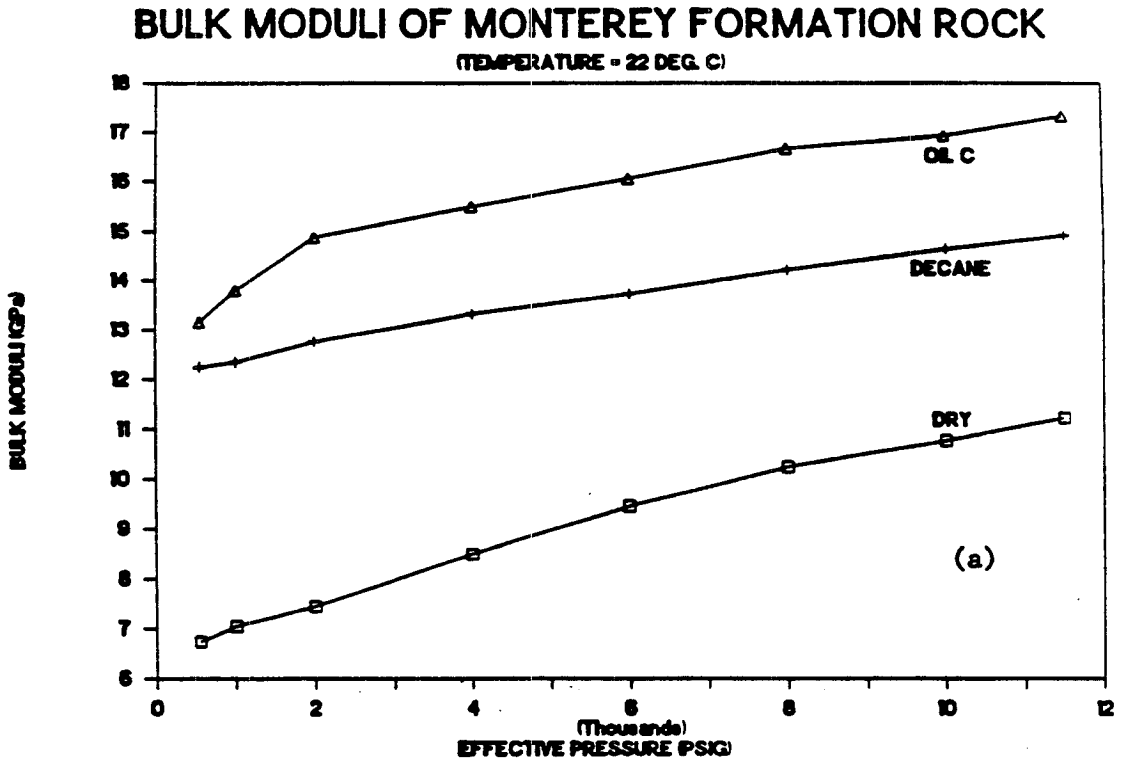
BULK MODULI OF MONTEREY FORMATION ROCK
(TEMPERATURE = 22 DEG. C)
BULK MODULI (GPa)
OIL C
DECANE
DRY
(a)
(Thousands)
EFFECTIVE PRESSURE (PSIG)

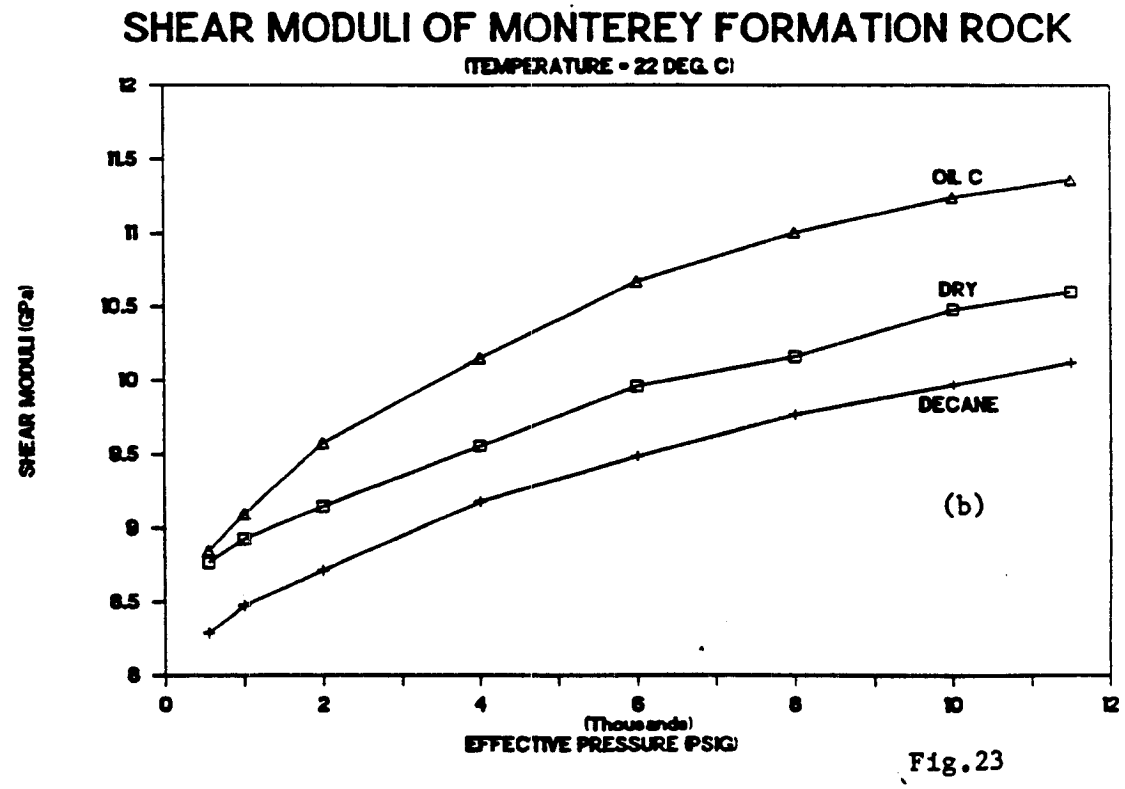
SHEAR MODULI OF MONTEREY FORMATION ROCK
(TEMPERATURE = 22 DEG. C)
SHEAR MODULI (GPa)
OIL C
DRY
DECANE
(b)
(Thousands)
EFFECTIVE PRESSURE (PSIG)

Fig.23

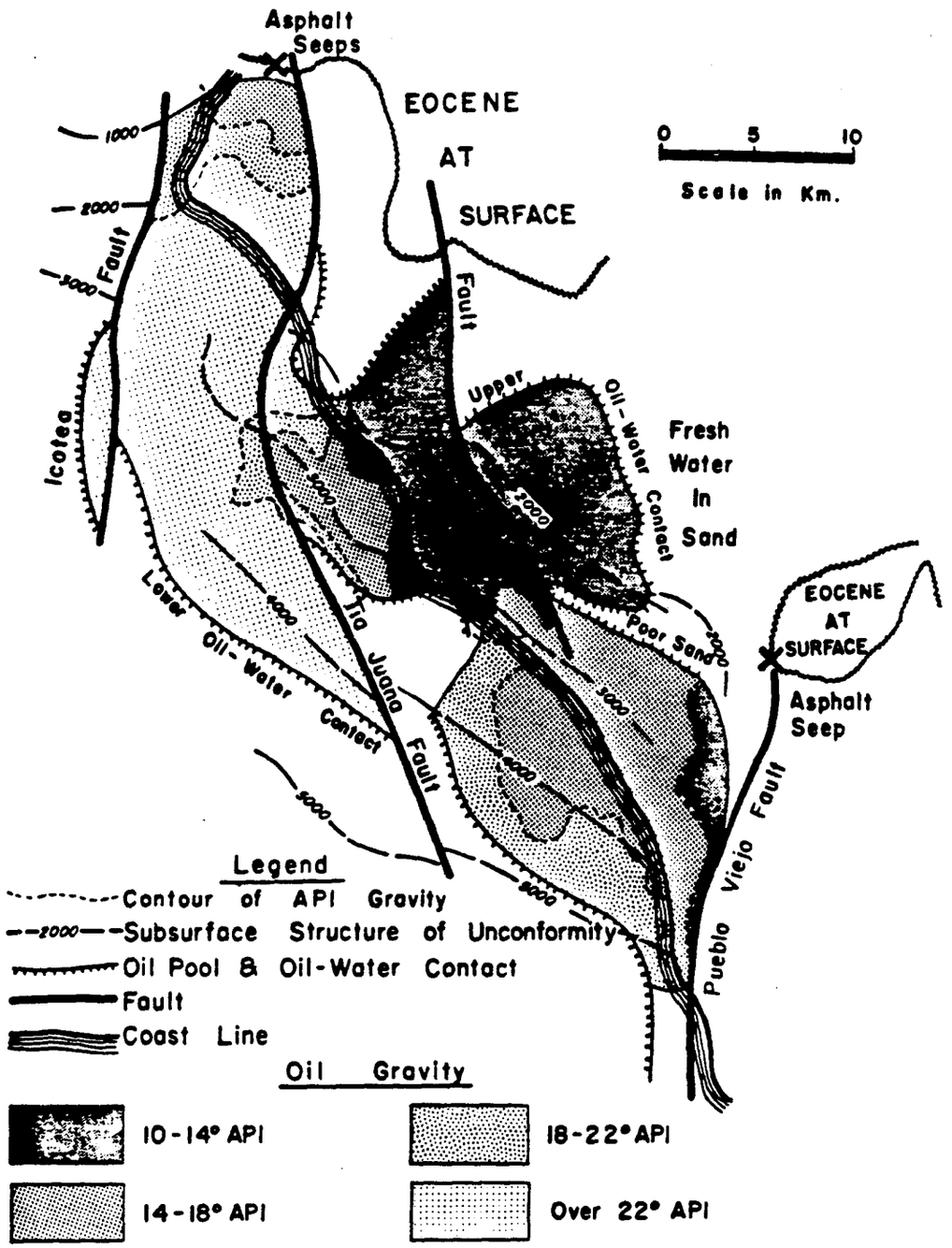
Asphalt Seeps
EOCENE AT SURFACE
0 5 10
Scale in Km.
1000
2000
3000
Fault
Icotea
Fault
Upper
Oil-Water Contact
Fresh Water In Sand
2000
3000
4000
Lower Oil-Water Contact
Tia Juana Fault
Poor Sand
3000
4000
5000
EOCENE AT SURFACE
Asphalt Seep
Pueblo Viejo Fault
Legend
Contour of API Gravity
2000 Subsurface Structure of Unconformity
Oil Pool & Oil-Water Contact
Fault
Coast Line
Oil Gravity
10-14° API
14-18° API
18-22° API
Over 22° API

Fig.24

CHAPTER 8

DISPERSION ANALYSIS OF VELOCITIES IN ROCKS

ABSTRACT

Velocity dispersions in three rocks saturated with water, normal decane, and two heavy oils, respectively, are calculated in this chapter, using Winkler's method. The results show that the apparent velocity dispersions in light fluids (water and normal decane) saturated rocks are relatively small, usually less than 3 to 5 percent, while those in the same rocks saturated with heavy oils are much larger. Such apparent velocity dispersions are well explained by the "local flow" mechanism which relates the dispersions to the viscosity of the pore fluid, the pore geometry and permeability of the rock, and the effective pressure and temperature.

The Biot velocity dispersions calculated using the Biot low and high frequency limits of the velocities in the rocks are very small, typically less than 2 percent. Such Biot velocity dispersions are explained in terms of the Biot theory which relates the Biot dispersion to the viscosity of the pore fluid and the permeability of the rock in a way which is just opposite to the "local flow" mechanism.

According to either the "local flow" mechanism or the Biot theory, the temperature dependence of the compressional wave velocities in heavy oil saturated rocks in the seismic frequency band should be about the same as that observed in the laboratory at 1 MHz frequency, which means that the laboratory results can be directly applied in the field. Therefore, in-situ seismic monitoring thermal EOR processes and tracking the thermal fronts in such processes are possible.

INTRODUCTION

It has been known that acoustic wave velocities in fluid saturated rocks are dispersive (i.e., they are function of frequency). Unfortunately, very few quantitative measurements or estimation of such velocity dispersions exist in the literature. Even up to now, we still do not know exactly how much velocity dispersion occurs in fluid saturated rocks from seismic to laboratory ultrasonic frequencies, which is mainly due to the fact that it is very difficult to measure such dispersions quantitatively both in the field and in the laboratory.

The study of velocity dispersions in rocks is very important and yet poorly understood. Basically, in seismic explorations the wave frequencies are in the band of 10 to 200 Hz, and in acoustic well logging, the frequencies of the acoustic waves cover a range of several hundred Hertz to about 100 KHz, while in the laboratory, waves of ultrasonic frequencies (500 KHz to several MHz) are usually employed. Therefore, in order to apply the laboratory velocity data in seismic and log interpretations, it is apparently necessary to know quantitatively the dispersion values of the velocities. However, such quantitative knowledge about velocity dispersions is usually difficult to obtain, since up to now there is no reliable method which can measure the velocities as a continuous function of frequency over a broad band either in the field or in the laboratory.

On one hand, in the field it is very difficult to use high frequency waves in relatively large scale explorations due to their fast attenuations. On the other hand, in the laboratory one can not arbitrarily lower the wave frequency since the measurements are usually affected by the scaling or boundary conditions when the rock sample is shorter than a half wavelength. Knowing these difficulties, Winkler (1983, 1985, 1986) developed a method which can estimate the velocity dispersions in fluid saturated rocks. This method is simple and straightforward and gives relatively accurate dispersion estimations.

In this chapter, we follow Winkler's method and calculate the velocity dispersions in three rocks saturated with various pore fluids. The calculated results are interpreted in terms of the "local flow" mechanism and other factors which may affect the calculations.

METHOD AND CALCULATIONS

As has been known, the Gassmann equation (Gassmann, 1951) is regarded as the low frequency approach of wave propagations in porous media. It relates the moduli of the fluid saturated porous medium to those of the frame and grains of the porous material and of the pore fluid. In our treatment, we refer the difference between the measured velocities and those calculated using the Gassmann equation as the absolute apparent dispersion. Therefore, the apparent dispersion is defined as

$$Apparent\ \ Dispersion = \frac{V_{Measured} - V_{Gassmann}}{V_{Measured}}.$$

In the Biot theory, Biot (1956) gave two frequency limits of the acoustic velocities in porous media. The low frequency limit is actually the Gassmann equation, and the expression of the velocity at the high frequency limit will be given later. We refer the absolute Biot dispersion as the difference between the calculated velocities by using the Biot high frequency limit and the Gassmann equation. Therefore, the Biot dispersion is defined as

$$Biot\ \ Dispersion = \frac{V_{Biot} - V_{Gassmann}}{V_{Biot}}.$$

In the calculation, the only major assumption needed is that there is no velocity dispersion in dry rocks, which is supported by experiments (Peselnick and Outerbridge, 1961; Spencer, 1981). The Gassmann equation, which is also the low frequency limit of the Biot theory, is used to calculate the velocities in fluid saturated rocks at essentially zero frequency. The equations used in such calculations are as following:

$$V_{pl}^{\,2} = \frac{1}{\rho_c}\left[\frac{(K_s - K_d)^2}{K_s[1 - \phi - (K_d/K_s) + \phi(K_s/K_f)]} + K_d + \frac{4}{3}N\right],$$

and

$$V_{sl}^{\,2} = N/\rho_c,$$

where

$$K_d = \rho_d\left(V_{Pd}^{\,2} - \frac{4}{3}V_{Sd}^{\,2}\right)$$

and

$$N = \rho_d V_{sd}^{\,2}$$

are the bulk and shear moduli of, $\rho_d = (1 - \phi)\rho_s$ is the density of, and V_{Pd} and V_{sd} are the compressional and shear wave velocities in, the dry rock, respectively. The other notations are:

ϕ porosity;

ρ_s density of the solid grains of the rock;

K_f bulk modulus of the pore fluid;

K_s bulk modulus of the solid grains;

ρ_f density of the pore fluid;

$\rho_c = (1 - \phi)\rho_s + \phi\rho_f$ density of the saturated rock;

V_{Pl} low frequency limit compressional velocities in the saturated rock;

V_{Sl} low frequency limit shear velocities in the saturated rock;

V_{Ph} high frequency limit compressional velocities in the saturated rock;

V_{Sh} high frequency limit shear velocities in the saturated rock.

The high frequency limit of the velocities in the Biot theory is used to calculate the high frequency limit velocities in fluid saturated rocks. The formulations are shown in the following.

Shear wave velocity

$$V_{Sh}{}^2 = \frac{N}{\rho_d + [1 - (1/\alpha)]\phi\rho_f}.$$

Compressional wave velocity

$$V_{Ph}{}^2 = \frac{A + [A^2 - 4B(PR - Q^2)]^{1/2}}{2B},$$

where

$$A = P\rho_{22} + R\rho_{11} - 2Q\rho_{12},$$

$$B = \rho_{11}\rho_{22} - \rho_{12}{}^2,$$

$$P = \frac{(1-\phi)[1 - \phi - (K_d/K_s)]K_s + \phi(K_s/K_f)K_d}{D} + \frac{4}{3}N,$$

$$R = \phi^2 K_s/D,$$

$$Q = \frac{[1 - \phi - (K_d/K_s)]\phi K_s}{D},$$

$$D = 1 - \phi - \frac{K_d}{K_s} + \phi\frac{K_s}{K_f},$$

$$\rho_{11} + \rho_{12} = \rho_d,$$

$$\rho_{22} + \rho_{12} = \phi\rho_f,$$

$$\rho_{12} = (1-\alpha)\phi\rho_f,$$

and α is called the tortuosity parameter which is defined in the Biot theory as a non-dimensional parameter that is dependent on the pore geometry of the porous medium. For pores of parallel tubes, $\alpha = 1$. For typical sandstones, a value of $\alpha = 2$ seems to be reasonable (Winkler, 1986; Johnson, 1982). In fact, the value of α only affects the Biot dispersion calculations as seen in the above equations.

Calculations using the Gassmann equation and the Biot high frequency limit are made for three rocks, namely, Berea sandstone, the Monterey dolomitic chert, and Massillon sandstone. The pore fluids are distilled water, normal decane, the heavy oil C, and the heavy oil 2, respectively. The compressional wave velocities and densities (and hence the bulk moduli) of the distilled water as a function of temperature and pressure can be found in the CRC Handbook of Chemistry and Physics and Wilson (1959). Those of the heavy oils C and 2 can be found in chapter 3 and chapter 5, respectively. The properties of the normal decane can be found in chapters 3 and 4.

The input parameters of ρ_s, α, K_s, and the temperature and pressure dependences of the densities of the dry rocks (ρ_d) are listed in the following table.

Parameter	Berea	Monterey	Massillon
Porosity at 2000 psig	0.18	0.15	0.22
Porosity at 6000 psig	0.17	0.15	0.21
Grain Density ρ_s, kg/m^3	2650	2670	2650
Grain Bulk Modulus K_s, GPa	44	38	40
Tortuosity α	2	3	2
T Dependence of ρ_d, $(g/cm^3)/^\circ C$	-5×10^{-4}	-5×10^{-4}	-5×10^{-4}
P Dependence of ρ_d, $(g/cm^3)/psi$	10^{-5}	10^{-5}	10^{-5}

In the above table, K_s is calculated from the compressional and shear wave velocities in the rock grains. For the Berea sandstone, we used Vp = 6000 m/sec and Vs = 3800 m/sec; for the Massillon sandstone K_s is chosen according to Han (1987); and for the Monterey dolomitic chert, the Vp and Vs of the rock grains are calculated through the empirical equation given by Han (1987):

$$Vp = 5590 - 2190C \qquad (m/sec),$$

$$Vs = 3520 - 1890C \qquad (m/sec),$$

where C is the clay content (by volume in percentage) of the rock. Since the dolomitic chert contains about 8% (by volume) clay, we have the Vp = 5415 m/sec and Vs = 3369 m/sec for the rock grains, which yields K_s = 38 GPa.

The porosity of the rock is assumed to be not affected by temperature changes, but varies a little as pressure changes as shown in the above table.

The uncertainty in choosing K_s for the rocks may yield errors in the compressional wave velocity calculations. However, as one can see from the Gassmann equation and the Biot high frequency limit, the compressional wave velocities to be calculated are not very sensitive to the values of K_s. We checked the sensitivity of the compressional wave velocities to K_s by changing K_s of the Monterey dolomitic chert from 38 GPa to 48 GPa, the calculated compressional wave velocities only resulted about 1.5% increase. Therefore the uncertainty in choosing the values of K_s does not contribute much to the uncertainty in the calculated Vp, as long as such choosing is reasonable.

The pressure and temperature dependences of the dry rock densities assumed in the above table are believed reasonable within an order of magnitude in the measurement ranges of the pressure (2000 to 6550 psig, or 13.8 to 45.2 MPa) and temperature (21 to 120° C). Such assumptions are based on the observations on other materials (e.g., for Aluminum, the thermal expansivity is 2.4×10^{-5} /° C, CRC Handbook of Chemistry and Physics).

It should also be pointed out that all the moduli in the Gassmann equation and the Biot high frequency limit are dynamic. Especially in the Gassmann equation, the calculated velocities are essentially of "zero" frequency, but they are different from those velocities derived from "static" measurements, since the "static" moduli are usually measured at much higher strain amplitudes (usually higher than 10^{-5}), while the

moduli in the Gassmann equation and Biot theory are dominated by the wave phenomenon with strain amplitude of less than 10^{-6} — 10^{-7}.

RESULTS AND INTERPRETATIONS

Velocity Dispersion in Water-saturated Rocks

Shown in figures 1a to 1d are the calculated compressional and shear wave velocities, along with those measured, in the water saturated Berea sandstone using the Gassmann equation and the high frequency limit of the Biot theory. At lower effective pressure of 2550 psig (176 bars or 17.6 MPa), the calculated compressional wave velocity dispersion is less than 3.5% (figure 1a), while at higher effective pressure of 6550 psig (452 bars or 45.2 MPa), the compressional wave velocity has virtually no dispersion (figure 1b). i.e., for the water saturated Berea sandstone, the Gassmann equation can predict fairly accurate compressional wave velocities at higher pressures.

The shear wave velocities in the water saturated Berea sandstone have approximately negative dispersions, especially at the higher pressure (figures 1c and 1d). This phenomenon may be caused by the chemical interactions between the rock frame and the pore water since in both the Gassmann equation and the Biot theory, the chemical weakening effect of the pore fluid on the rock frame is not included. On the other hand, it may also be caused by the fact that the input K_d and N values in the calculation are those of the dry rock (the Berea sandstone was dried in a vacuum oven under modest temperature for several days before measurement) instead of those of the drained rock (a few percent moisture saturation) as required by the Biot theory (Biot, 1956). And hence the calculated velocities might be a little overestimated. Nevertheless, one can see that the Gassmann equation and the Biot theory can predict fairly accurate velocities for the water saturated Berea sandstone.

Unlike the Berea sandstone, the Massillon sandstone was room dried. Hence in the calculation, the input values of K_d and N are those of the drained rock (about 3%

water saturation). Figures 2a and 2b show the calculated compressional and shear wave velocities, respectively, using the Gassmann equation and the Biot high frequency limit, along with the measured velocities. The calculated apparent dispersion for the compressional wave velocity is around 2%, while that for the shear wave velocity is around 5%. The amount of dispersions is reasonable for both Vp and Vs, comparing to the calculated results by others (Winkler, 1986; Han, 1987).

Comparing the calculations for the Berea sandstone and the Massillon sandstone, one can see that it is the moduli of the drained rock, not the dry rock, that should be used in the velocity calculations. The physical aspect behind this statement is that one simply eliminates the effects of chemical weakening and probably wetting of the pore fluids on the calculated velocities if the moduli of the drained rock are used. In practice, the drained rock can well be referred as the room-dried rock.

Velocity Dispersion in N-decane-saturated Rocks

For the normal decane saturated Berea sandstone, the calculated, along with those measured, compressional and shear wave velocities are shown as a function of temperature at two effective pressures in figures 3a through 3d. The apparent dispersions of the compressional wave velocities are around 3.0 to 4.5% at effective pressure of 2550 psig (176 bars, or 17.6 MPa), and decrease to about 1.0 to 2.5% at effective pressure of 6550 psig (452 bars or 45.2 MPa) (the pressure dependence of velocity dispersion will be discussed later). The apparent dispersions for the shear wave velocities are about 3% at 2550 psig and decrease to about 1% at 6550 psig.

Comparing the calculated velocity results in the water saturated and normal decane saturated Berea sandstone, one can see the wetting or chemical weakening effect of the pore fluids on the velocities. The input rock parameters for these two calculations are exactly the same, but the calculated apparent dispersions for the normal decane saturated rock (the same rock sample was also used for water saturation) are obviously higher than those in the water saturated rock. Since the rock sample was dry

before saturation, saturation of the rock with water apparently weakened the rock frame, and which in turn lowered the measured velocities (both Vp and Vs). However, the normal decane saturated to the rock did not weaken the rock frame much since the Berea sandstone is essentially water (not oil) wet and also the normal decane is less chemically reactive than water.

From the above discussion, one can see that the effects of wetting and chemical weakening of the pore fluids on the velocities should be counted in calculating the apparent dispersions of the velocities. Therefore, we suggest that for velocity and apparent velocity dispersion calculations in water saturated rocks using the Gassmann equation or the Biot theory, the input K_d and N should be those of the drained or room dried rock; while for the calculations in oil or other non-wetting fluid saturated rocks, the input K_d and N should be those of the dry rock. Otherwise, one would either underestimate (if using the moduli of the dry rock in the case of the water saturated rock) or overestimate (if using the moduli of the drained rock in the case of oil or non-wetting fluid saturated rock) the apparent velocity dispersions.

Shown in figures 4a and 4b are the calculated and measured compressional wave velocities in the Monterey dolomitic chert saturated with normal decane. Basically, the compressional wave velocities do not have dispersions in this rock (less than 1%). However, the shear wave velocities all have negative dispersions (figures 4c and 4d), which may be caused by the clays in the rock. As mentioned earlier, liquid in the rock pores "lubricates" the rock grains. When the rock contains clays, the surface area of the grains increases (clays are usually very fine-grained and have very high surface to volume ratio), which enhances the lubrication effect. Such lubrication effect decreases the rigidity (shear modulus) of the rock, so that the measured shear wave velocities are usually lower than those predicted by either the Gassmann equation or the Biot theory, as shown in figures 4c and 4d.

Velocity Dispersion in Heavy Oil-saturated Rocks

As have been seen, the compressional wave velocities in the water and normal decane saturated rocks are not much dispersive. But for heavy oil saturated rocks, the compressional wave velocities can have dispersions as large as of 10% (at Pe = 2550 psig or 17.6 MPa). Figures 5a and 5b show such dispersions and the measured and calculated compressional wave velocities in the Berea sandstone saturated with the heavy oil C. The compressional wave velocity dispersions decrease as either temperature or pressure increases. i.e., at both high pressure and high temperature, the dispersion becomes small (figure 5b).

Not only the compressional wave velocities are very much dispersive, but also are the shear wave velocities in the heavy oil C saturated Berea sandstone (figures 5c and 5d). However, such shear wave velocity dispersions are only significant at lower temperatures and pressures. i.e., they decrease as temperature or pressure increases. For instance, at 22^{o} C and 2550 psig effective pressure, the measured shear wave velocity is about 8% higher than that calculated by the Gassmann equation, while at 94^{o} C and 6550 psig effective pressure, the measured shear wave velocity is approximately equal to that calculated by the Gassmann equation.

One may have noticed that the apparent dispersions of the compressional wave velocities are also contributed by those of the the shear wave velocities. Usually, such contribution is relatively small. For example, 7% shear wave velocity dispersion only causes about 2 to 3% dispersion in the compressional wave velocity. Therefore, apparent dispersions of the compressional wave velocities are not only caused by the shear, but also the bulk, modulus dispersions.

Even though relatively large apparent dispersions are found in both compressional and shear wave velocities in the heavy oil C saturated Berea sandstone, such dispersions are very small in the Monterey dolomitic chert saturated with the same heavy oil (figures 6a to 6d). The apparent dispersions of the compressional wave velocities are

essentially negative, which means that either the rock sample was too dry in the velocity measurements of the dry sample or the chert sample contains only round pores (the pores do not have compliance heterogeneity), or both. According to the "local flow" mechanism, the velocity dispersions in rocks are caused by the compliance heterogeneity of the pores. If a rock contains only round pores, the compliance of the pores is the same, so that there is no wave-induced pore fluid flow when the rock is fully saturated, and thus there is no velocity dispersion (We will discuss this later). Nevertheless, the compressional wave velocities calculated by the Gassmann equation and the Biot high frequency limit fit the measured values satisfactorily in the heavy oil C saturated chert.

The apparent dispersions of the shear wave velocities in the heavy oil C saturated chert are around 2 to 3%. The higher dispersions at lower temperatures are caused by the viscous skinning effect on the measured values of the shear wave velocity, as discussed in the previous chapter. The negative dispersions may also be caused by the lubrication effect of the pore fluid on the shear modulus.

The calculated and measured velocities, along with their apparent dispersions, in the Massillon sandstone saturated with oil 2 are shown in figures 7a and 7b, respectively. The calculated compressional wave velocities fit the measured values fairly well, while the shear wave velocities have about 5 to 7% dispersions.

DISCUSSIONS

Our calculation results show that the Biot dispersions of both Vp and Vs are relatively small (usually less than 2%). The mechanism is explained in the Biot theory that the velocity dispersions are caused by the inertial drag of the pore fluid: i.e., when an acoustic wave passes through a fluid saturated porous medium, the pore fluid moves under the differential pressure generated by the passing wave behind the solid frame due to the density difference between the rock frame and the pore fluid. At low

frequencies, the pore fluid is "locked" on the frame so there is no relative motion between the pore fluid and the solid frame. Hence there is no velocity dispersion at low frequencies. At high frequencies, the effect of inertia caused by the density difference causes the motion of the pore fluid to lag behind the that of the solid frame, which in turn leads to higher velocities.

Since the Biot low and high frequency limits were used in the velocity calculations, the calculated Biot dispersions are the maximum dispersion values that the Biot theory can predict. Obviously, the calculated apparent dispersion (absolute values) is always higher than the Biot dispersion, which means that besides the Biot mechanism, there must exist some other non-Biot mechanism(s) which is responsible for the additional dispersion.

A possible mechanism which can explain the velocity dispersions is the "local flow" model. "Local flow" means the flow is controlled by the "local" fluctuations of the compressibility of the pore spaces. And "local" means that the compressibility fluctuations are on the scale of pore size.

The "local flow" mechanism has been discussed by various investigators (e.g., O'Connell and Budiansky, 1977; Mavko and Nur, 1979; Murphy et al., 1984). The essential assumption in this mechanism is that some parts of the pore space are more compliant than other parts. A passing acoustic wave deforms the pore space and hence causes the pore fluid in the more compliant parts to tend to flow to the less compliant parts. For example, the pore fluid in a crack oriented with the long axis perpendicular to the wave direction tends to flow to the crack with long axis parallel to the wave direction, or to the high aspect ratio or round pores connected to the crack (figure 8). In a partially saturated rock, pore fluid tends to flow to the empty regions of the pore space.

The "local flow" mechanism is apparently related to the viscosity of the pore fluid, the permeability of the rock, the appearance of thin cracks and their aspect

ratios, and the connectivity of the thin cracks to the round pores.

If the "local flow" mechanism is the right model in interpreting the velocity dispersions, the magnitude of the velocity dispersions should be partly controlled by the viscosity of the pore fluid. The results shown in this chapter clearly indicate that such argument is true. The apparent Vp dispersions in light fluids (water and normal decane) saturated rocks are very small (usually less than 3%), while in the heavy oil (oil C) saturated Berea sandstone, such velocity dispersions can be as large as 10% (figures 5a to 5d) at effective pressure of 2550 psig. In terms of the "local flow" mechanism, such phenomenon can be explained that for low viscosity fluid saturated rocks, the pore pressure usually has enough time to get to equilibrium in the time interval of a half period of the acoustic wave passing through, so the rock-fluid aggregate is at the "relaxed" state or almost "relaxed" state. Therefore, the apparent dispersion of the velocity is zero or very small. When the rock is saturated with a fluid of high viscosity, the time for the "local flow" to stop (or the pore pressure to equilibrate) is much longer due to the low mobility of the pore fluid. Such time is usually longer than a half period of the acoustic wave, so the saturated rock sample is at the "unrelaxed" state. As a result, the apparent dispersion of the velocity is larger since the measured velocity is higher.

The effect of pore fluid viscosity on the apparent velocity dispersions in Berea sandstone was also found by Winkler (1985). Figure 9 from Winkler depicts that for water saturated Berea sandstone the apparent dispersion of the compressional wave velocity is relatively small (less than 4%), while such dispersion can be as high as 17% in the same sandstone saturated with an oil with viscosity of 300 cp (0.3 Pa.s). Again, the "local flow" mechanism can well be applied in the interpretation of such a phenomenon.

In the aspect of acoustic wave propagations in porous rocks, the "local flow" mechanism predicts that both attenuation and velocity of the wave depend on the

product of wave frequency and the pore fluid viscosity (O'Connell and Budiansky, 1977; Jones, 1986). Laboratory results have shown that there appears an attenuation peak of the acoustic waves traveling in a fluid saturated porous medium. Such peak usually sits in the interval where the product of the wave frequency (f) and the pore fluid viscosity (η) equals to 1 to 10 Hz.Pa.s (see Jones, 1986). Since attenuation and velocity dispersion are closely related (Kjartansson, 1980; Nur, 1982), the point on the $f\ \eta$ axis at which the attenuation peak appears is usually also the inflection point of the velocity curve (see Jones, 1986).

Therefore, if we take $f\ \eta = 1\ Hz.Pa.s$, for a water ($\eta = 0.001\ Pa.s$) saturated rock, the attenuation peak of the acoustic wave will appear at the frequency of 1000 Hz, which means even at sonic logging frequencies, the wave velocities are dispersive. In other words, the acoustic velocities extracted from sonic well logging results can not represent those at seismic frequencies. On the other hand, for a heavy oil (say $\eta = 1\ Pa.s$, or 1000 cp) saturated rock, the attenuation peak will appear at the frequency of 1 Hz, which means that even at seismic frequency, the acoustic velocities are dispersive. In other words, for heavy oil saturated rocks, laboratory results of velocities measured at ultrasonic frequencies (0.5 to 1 MHz) may well represent those at seismic frequencies, since the velocities at both seismic and ultrasonic frequencies are all dispersive. Therefore laboratory results can be directly used in the field. We will discuss some applications of this discovery in the next section.

The "local flow" mechanism predicts an attenuation peak of the velocities in water or light (low viscosity) fluids saturated rocks in the frequency range of 1 to 10 KHz, while the Biot theory predicts an attenuation peak in about the same frequency range, usually at about 1 KHz. In the Biot theory, the attenuation peak occurs when the viscous skin depth of the wave is approximately equal to the pore size of the rock. The frequency at which the peak occurs is given by

$$f_c = \frac{\eta}{\pi \rho_f r^2},$$

where η and ρ_f are the viscosity and density of the pore fluid, respectively, and r is the pore radius. For a water saturated rock of pore diameter of 40 μm, $f_c \approx 800\ Hz$. However, for a heavy oil (say $\eta = 2000\ cp$) saturated rock, the attenuation peak is shifted to a much higher frequency ($f_c \approx 1.6\ MHz$). Therefore, according to the Biot theory, for heavy oil saturated rocks, we are still measuring the acoustic velocities in the low frequency range at 1 MHz, which means that the wave propagation characteristics at about 1 MHz frequency in heavy oil saturated rocks are the same as those at seismic frequencies. Hence the laboratory results can be directly applied in the field survey of seismic or acoustic logging frequency.

The apparent dispersions of velocities explained in terms of the "local flow" mechanism depend not only on the viscosity of the pore fluid, but also on the thin crack appearance and the aspect ratios of the thin cracks. If the pore space of a rock is only composed of round pores or channels with round cross section, the velocity will basically have no dispersion since in this case all the parts of the pore space have the same compliance and hence there is no local flow to occur. This may well be the case for the Monterey dolomitic chert, since the pore space of this chert mainly consists of round pores. Therefore, the dispersion of the velocities in this rock is small (figures 4a to 4d and 6a to 6d), even for the heavy oil saturated rock.

The "local flow" mechanism also requires crack-crack and crack-pore connections in order to explain the dispersion results. That is to say, in order for the "local flow" to occur, the cracks and cracks and pores should be connected as shown in figure 8. As the effective pressure increases, the crack tips (or even the whole cracks) connecting to the pores or other cracks are closed, and hence the "local flow" activity of the pore fluid is limited and greatly decreased, which results less apparent dispersions of the acoustic velocities. Such arguments are strongly supported by the experimental and calculation results shown in figures 1a through 6d and figure 9. In the results, the apparent dispersions of all the velocities in all the rocks decrease with increasing

effective pressure. Such decreases are obviously caused by the decreased connectivity of cracks and cracks and pores as explained above.

The "local flow" mechanism is also related to the permeability of the rock. Low permeability rocks usually contain cracks of small aspect ratios (e.g., some granites and sandstones). For low permeability rocks in which the cracks are still connected, the apparent dispersion of the acoustic velocities should be higher than that for high permeability rocks, since the "local flow" takes longer time to get to equilibrium in low permeability rocks. Figure 10 shows the apparent dispersions of the compressional wave velocities in 33 sandstones saturated with water versus the logarithmic permeabilities of the rocks (dispersion data are taken from Han, 1987). At effective pressure of 100 bars (1450 psig, or 10 MPa), the velocity dispersion is systematically related to the logarithmic permeability of the sandstones, although the data are very scattered. At effective pressure of 400 bars (5800 psig, or 40 MPa), such a relationship still exists.

In low permeability rocks at higher effective pressures, those very small aspect ratio cracks are closed, but the high pressure also creates some cracks from those not ready to be closed larger aspect ratio cracks. Hence there still exist some interconnected cracks, and as a result, the dispersion still depends on the permeability. In high permeability rocks, the thin crack content is usually small, so at high effective pressures, the thin cracks are completely closed and what left open are those high aspect ratio or round pores. At this stage, the "local flow" activity of the pore fluid is both limited and easy to get to equilibrium, so that the dispersion becomes more or less independent of the permeability of the rock.

Note that the magnitude of the apparent dispersions of the compressional wave velocities in all the 33 sandstones decreases with increasing effective pressure (figure 10), which is expected from the arguments made above.

The plotted data in figure 10 are only from the water saturated sandstones. We do not have the dispersion data for these sandstones saturated with high viscosity oils.

However, we expect that the apparent velocity dispersions would be higher and more dependent on the permeabilities of such oil saturated rocks, since the "local flow" of the pore fluid would take more time to get to equilibrium due the high viscosities of oils.

The Biot dispersions of the compressional wave velocities in the 33 sandstones are shown in figure 11 versus the logarithmic permeabilities of the rocks. The Biot dispersions of the compressional wave velocities at both 100 and 400 bars of effective pressures increase systematically with increasing permeability, which is just the opposite to the permeability behavior of the apparent velocity dispersions. This is not surprising since the "local flow" and the Biot mechanisms are different. As stated earlier, the Biot dispersion is caused by that the motion of the pore fluid lags behind that of the solid frame in response to the passing acoustic wave due to the density difference. In low permeability rocks, the pore fluid is effectively "locked" on the solid frame so that it moves with the frame, which is resemble to the situation of low frequencies. Therefore for low permeability rocks, the Biot dispersion of the compressional wave velocities is small or effectively vanishes for rocks with isolated pores (zero permeability).

As the permeability of the rock increases, the relative motion between the pore fluid and the solid frame is enhanced due to the increased mobility of the pore fluid. Hence the Biot dispersion increases (figure 11).

One also notices that the Biot dispersion of the compressional wave velocities increases with increasing effective pressure (figure 11). Furthermore, Winkler (1985) also showed such a relation between the Biot dispersion of the compressional wave velocity and the effective pressure without giving explanations. This phenomenon is contradictory to the above explanations since the permeability of a rock decreases as the effective pressure increases. However, such contradiction is caused by both the calculation artifacts and the modulus increases of the dry rocks as the effective pressure increases. In the velocity calculations using the Biot high frequency limit, the tortuosity

parameter α was assumed to be a constant of 2 (see Han, 1987). However, α increases with increasing effective pressure, since at higher effective pressure, some pore or crack throats are closed so that the pore spaces are more tortuous. The Biot velocity dispersion decreases as α increases. Therefore, the Biot dispersion at higher effective pressures is overestimated in the calculations due to the assumption that α is a constant.

In the Biot theory, the Biot velocity dispersions are also related to the bulk modulus of the dry rock: i.e., the higher the bulk modulus of the dry rock, the lager the Biot dispersion will be, although such modulus effect is relatively small. For poorly-consolidated rocks or rocks at low effective pressures, there may exist relative slidings or motions among the rock grains as the acoustic wave passes through. Such slidings or relative motions among the rock grains cancel partly the relative motion between the pore fluid and the rock grains, which in turn decreases the Biot dispersion. For rocks with high bulk moduli or rocks at high effective pressures, the rock grains are confined together tightly, so that the slidings or relative motions among the rock grains are highly restricted, and as a result, the Biot dispersion is larger.

In Winkler's (1985) calculations, the density of the dry rock and the porosity were assumed to be constant as the effective pressure increases. Such assumptions apparently underestimate the calculated velocities and in turn overestimate the apparent dispersions at higher effective pressures. The Biot dispersions are less affected since they are inferred from the velocities calculated by the Gassmann equation and the Biot high frequency limit.

In the velocity calculations using the Gassmann equation and the Biot high frequency limit, errors might come from the uncertainties in measuring the velocities in the dry rock, the density and porosity measurements and their dependences on temperature and pressure, the estimation of the grain density and bulk modulus of the rock, and the tortuosity factor α. However, α only appears in the Biot high frequency limit so that it does not affect the apparent dispersions of the velocities. The

uncertainties in measuring the velocities in both the dry and the saturated rocks are around 2%. Such uncertainties do not contribute much error to the calculated dispersions since they exist in both the calculated and the measured velocities in the saturated rock and since the calculated velocity dispersions are relative values. Therefore, the major error in the calculated velocity dispersions may mainly contributed by the uncertainties in measuring or estimating the density and the porosity of the rock and their temperature and pressure dependences, and in estimating the density and the bulk modulus of the rock grains. Such errors are estimated at about ± 1.0 to 1.5%.

APPLICATION:

Applicability of Seismic Monitoring Thermal EOR Processes

Both our previous (Wang and Nur, 1986; Nur and Wang, 1987; Wang and Nur, 1987) and present experimental results show that the compressional wave velocities in heavy oil saturated rocks decrease very fast as temperature increases. Such decreases usually range 10 to 15% in well-consolidated rocks as temperature increases by 100^{o} C. Therefore, we proposed that seismic, especially high frequency high resolution seismic, methods could be used to monitor thermal enhanced oil recovery (EOR) processes such as steam floodings and in-situ combustions.

However, the experimental results were gathered in the laboratory at about 1 MHz frequency. It has been doubted that the acoustic properties of rocks measured at high frequencies may not represent the same properties at low frequencies, and vice versa. Therefore, it is the main task of this section to confirm the applicability of seismic monitoring thermal EOR processes.

As analyzed in the previous section, if the Biot mechanism is dominant, the measured acoustic velocities in heavy oil saturated rocks at about 1 MHz frequency are still in the low frequency range. This means that at lower temperatures, the compressional wave velocities at seismic and 1 MHz frequencies are essentially the same for heavy oil

saturated rocks. As temperature increases, the viscosity of the heavy oil decreases very fast, so that the characteristic frequency defined in the Biot theory (Biot, 1956) decreases rapidly from the megahertz to kilohertz ranges. Therefore at higher temperatures, the measured velocities at 1 MHz frequency are in the Biot high frequency range, which means that at seismic frequencies the velocities are lower than those measured in the laboratory. Therefore, the temperature effect on the compressional wave velocities in heavy oil reservoirs is larger at seismic frequencies than at 1 MHz (figure 12). That is, the compressional wave velocities would decrease faster at seismic frequencies as temperature increases, according to the Biot theory.

In terms of the "local flow" mechanism, our analysis shows that the acoustic velocities in heavy oil saturated rocks are dispersive even at very low frequencies. For example, for a sandstone saturated with a heavy oil of 1000 cp (1 Pa.s) viscosity, the attenuation peak would appear at the frequency of 1 Hertz. Furthermore, viscosities of heavy oils can well exceed 1000 cp at in-situ conditions in many heavy oil or tar sand reservoirs. This suggests that the acoustic velocity behaviors in the field at seismic and logging frequencies may well resemble those measured in the laboratory at 1 MHz frequency. Therefore, if the "local flow" mechanism is dominant, the measured behaviors of the velocities in the laboratory can be directly applied in the field at seismic or logging frequencies.

Besides the above analyses, steam flooding and especially in-situ combustion processes cause the temperature of the flooded zones to increase usually more than 100^{o} C (could be several hundred degree Celcius in in-situ combustion processes). Furthermore, the thermal cracking of rocks in the flooded zones and higher pore pressures at the steam or fire front all cause more decreases of the acoustic velocities.

Therefore, the temperature effects on the acoustic wave velocities measured in the laboratory at 1 MHz frequency should be about the same as on those at seismic frequencies. Therefore, seismic monitoring thermal EOR processes and tracking the

thermal fronts in such processes are highly possible in the field.

SUMMARY AND CONCLUSION

Using the Gassmann equation and the Biot theory to calculate or estimate the velocity dispersions in fluid saturated rocks gives us an insight in understanding the dispersion problems of acoustic velocities. It also leads us to a way to better apply the velocity data gathered in the laboratory or from acoustic well logging data to seismic explorations and monitorings. Such calculations usually can be fairly accurate if the input parameters to the Gassmann equation and the Biot theory are accurate.

In the calculations, for water saturated rocks the input moduli of the dry rock should be those of the drained rock (with about 3 to 5% moisture saturation), while for oil saturated rocks, the input moduli should be those of the completely dried rock (with no moisture content).

Our results show that the apparent dispersions of the velocities in light fluid saturated rocks are relatively small (usually less than 3 to 5%), while those in heavy oil saturated rocks are much larger. This phenomenon can be well explained by the "local flow" mechanism which is related to the pore fluid viscosity, the pore geometry and permeability of the rock, and the effective pressure and temperature.

The Biot mechanism is different from the "local flow" mechanism, so that it predicts different values and different dependences of the velocity dispersions on the pore fluid viscosity, the pore geometry and permeability of the rock, and the effective pressure and temperature.

The Biot mechanism is also different from the "local flow" mechanism in predicting the position of the attenuation peak and its direction of movement as the viscosity of the pore fluid changes. As the viscosity increases, the "local flow" mechanism predicts that the attenuation peak moves to the lower frequency direction, while the Biot theory predicts that the peak moves to the higher frequency direction. Therefore.

they give different frequency intervals in which the velocities are dispersive.

The "local flow" mechanism predicts that velocity dispersions can occur at very low frequencies, even much lower than the seismic frequencies, which suggests that the acoustic velocity behaviors in the field at seismic and logging frequencies may well resemble those measured in the laboratory at 1 MHz frequency.

According to the Biot theory, our measured velocities in heavy oil saturated rocks at 1 MHz are still in the low Biot frequency range, due to the high viscosity of the pore fluid. Therefore, in the seismic frequency band, the velocities and their behaviors should be approximately the same as those measured in the laboratory.

According to either the "local flow" mechanism or the Biot theory, the temperature dependence of the compressional wave velocities in heavy oil saturated rocks in the seismic frequency band should be about the same as that observed in the laboratory at 1 MHz frequency, which means that the laboratory results can be directly applied in the field. Therefore, in-situ seismic monitoring thermal EOR processes and tracking the thermal fronts in such processes are possible.

REFERENCES

Biot, M. A., 1956. Theory of propagation of elastic waves in a fluid saturated porous solid, I, Low frequency range. J. Acoust. Soc. Am., vol. 28, 168-178. II, high frequency range. J. Acoust. Soc. Am., vol. 28, 179-191.

Gassmann, F., 1951. Uber die elastizitat poroser medien, Vierteljahrsschr. Naturforsh. Ges. Zuerich, vol. 96, 1-23.

Han, D., 1987. Effects of porosity and clay content on acoustic properties of sandstones and unconsolidated sediments. Ph.D. thesis, Stanford University.

Johnson, D. L., 1982. Acoustic propagation in porous media. In: excitations in disordered media, edited by M. F. Thorpe. Plenum, New York.

Jones, T. D., 1986. Pore fluids and frequency-dependent wave propagation. Geophysics, vol. 51, 1939-1953.

Kjartansson, E., 1980. Attenuation of seismic waves in rocks and applications in energy

exploration. Ph.D. thesis, Stanford University.

Mavko, G. and Nur, A. M., 1979. Wave attenuation in partially saturated rocks. Geophysics, vol. 44, 161-178.

Murphy, W. F., K. W. Winkler and R. L. Kleinberg, 1984. Contact microphysics and viscous relaxation in sandstones. In: Physics and chemistry of porous media. edited by D. L. Johnson and P. N. Sen. Am. Inst. Phys., New York, 176-190.

Nur, A. M. and Wang, Z., 1987. In-situ seismic monitoring EOR: The petrophysical basis. SPE paper 16865.

Nur, A. M., 1982. Wave propagation in porous media. Stanford Rock Physics Project, vol. 13. 121pp.

O'Connell, R. J. and Budiansky, B., 1977. Viscoelastic properties of fluid-saturated cracked solids. J. Geophys. Res., vol. 82, 5719-5736.

Peselnick, L. and Outerbridge, W. F., 1961. Internal friction in shear and shear modulus of Solenhofen limestone over a frequency range of 10^7 cycles per second. J. Geophys. Res., vol. 66, 581-588.

Spencer, J. W., 1981. Stress relaxations at low frequencies in fluid saturated rocks: Attenuation and modulus dispersion. J. Geophys. Res., vol. 86, 1803-1812.

Wang, Z., 1987. Acoustic velocities in oils and the effects on velocities in rocks, Part II: The effects on velocities in rocks. Internal Repor: ARCO Oil and Gas Co., 119pp.

Wang, Z. and A. M. Nur, 1986. Effect of temperature on wave velocities in sands and sandstones with heavy hydrocarbons. SEG Expanded Abs., 3-5.

Wang, Z. and Nur, A. M., 1987. Velocities in hydrocarbons and hydrocarbon-saturated rocks and sands. SEG Expanded Abs., 1-4.

Wilson, W. D., 1959. Speed of sound in distilled water as a function of temperature and pressure. J. Acoust. Soc. Am., vol. 31, 1067-1072.

Winkler, K. W., 1983. Frequency dependent ultrasonic properties of high-porosity sandstones. J. Geophys. Res., vol. 88, 9493-9499.

Winkler, K. W.,1985. Dispersion analysis of velocity and attenuation in Berea sandstone. J. Geophys. Res., vol. 90, 6793-6800.

Winkler, K. W., 1986. Estimates of velocity dispersion between seismic and ultrasonic frequencies. Geophysics, vol. 51, 183-189.

FIGURE CAPTIONS

Figure 1. Measured and calculated compressional (a, b) and shear (c, d) wave velocities and apparent dispersions in Berea sandstone saturated with water at effective

pressures of 2550 and 6550 psig, respectively.

Figure 2. Measured and calculated compressional (a) and shear (b) wave velocities and apparent dispersions in Massillon sandstone saturated with water at effective pressure of 2750.

Figure 3. Measured and calculated compressional (a, b) and shear (c, d) wave velocities and apparent dispersions in Berea sandstone saturated with normal decane at effective pressures of 2550 and 6550 psig, respectively.

Figure 4. Measured and calculated compressional (a, b) and shear (c, d) wave velocities and apparent dispersions in Monterey dolomitic chert saturated with normal decane at effective pressures of 2000 and 6000 psig, respectively.

Figure 5. Measured and calculated compressional (a, b) and shear (c, d) wave velocities and apparent dispersions in Berea sandstone saturated with oil C at effective pressures of 2550 and 6550 psig, respectively.

Figure 6. Measured and calculated compressional (a, b) and shear (c, d) wave velocities and apparent dispersions in Monterey dolomitic chert saturated with oil C at effective pressures of 2000 and 6000 psig, respectively.

Figure 7. Measured and calculated compressional (a) and shear (b) wave velocities and apparent dispersions in Massillon sandstone saturated with oil 2 at effective pressure of 2750 psig.

Figure 8. Sketch of the "local flow" mechanism.

Figure 9. Compressional wave velocities in Berea sandstone saturated with water and a 300 cp viscosity oil and their dispersions (From Winkler, 1985).

Figure 10. Apparent dispersions of the compressional wave velocities in 33 sandstones saturated with water versus the logarithmic permeabilities of the rocks (dispersion data taken from Han, 1987) at two effective pressures.

Figure 11. Biot dispersions of the compressional wave velocities in 33 sandstones saturated with water versus the logarithmic permeabilities of the rocks (dispersion data taken from Han, 1987) at two effective pressures.

Figure 12. Sketch of the temperature dependence of compressional wave velocities in heavy oil-saturated rocks, according to the Biot theory.

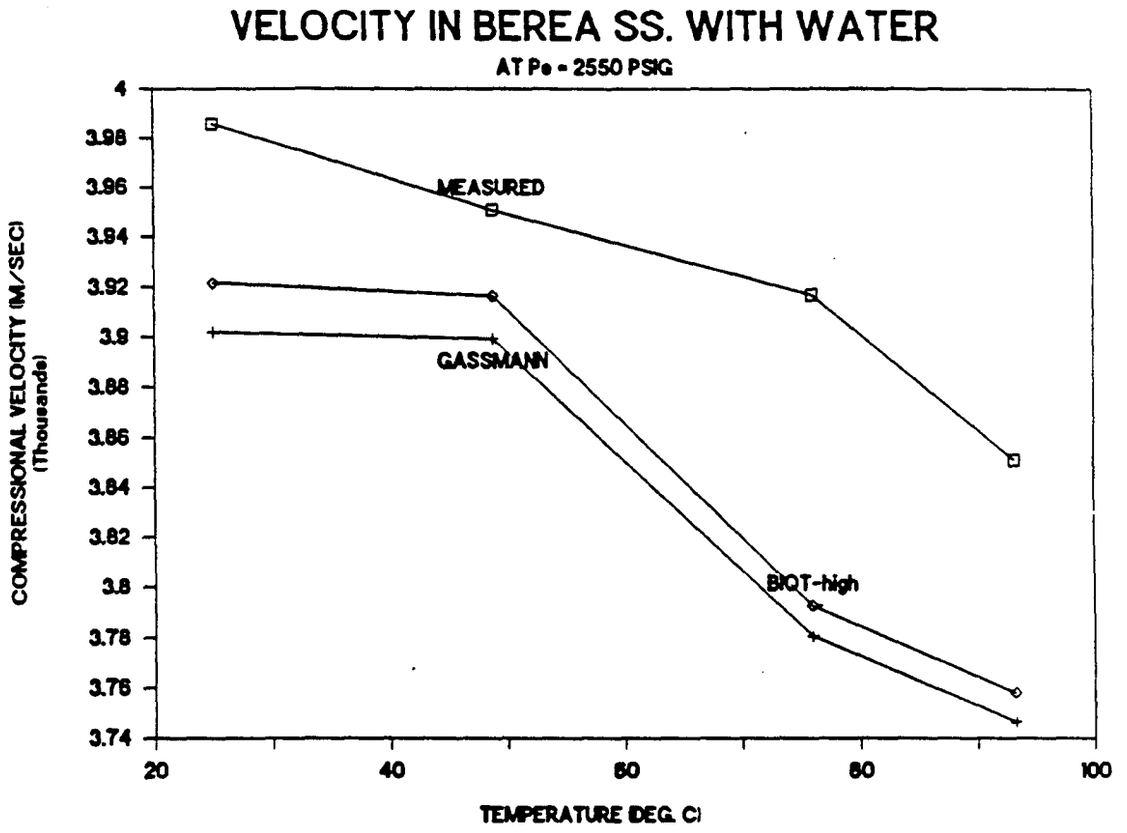
VELOCITY IN BEREA SS. WITH WATER
AT Pe = 2550 PSIG
COMPRESSIONAL VELOCITY (M/SEC)
(Thousands)
4
3.98
3.96
3.94
3.92
3.9
3.88
3.86
3.84
3.82
3.8
3.78
3.76
3.74
MEASURED
GASSMANN
BIOT-high
20
40
60
80
100
TEMPERATURE (DEG. C)

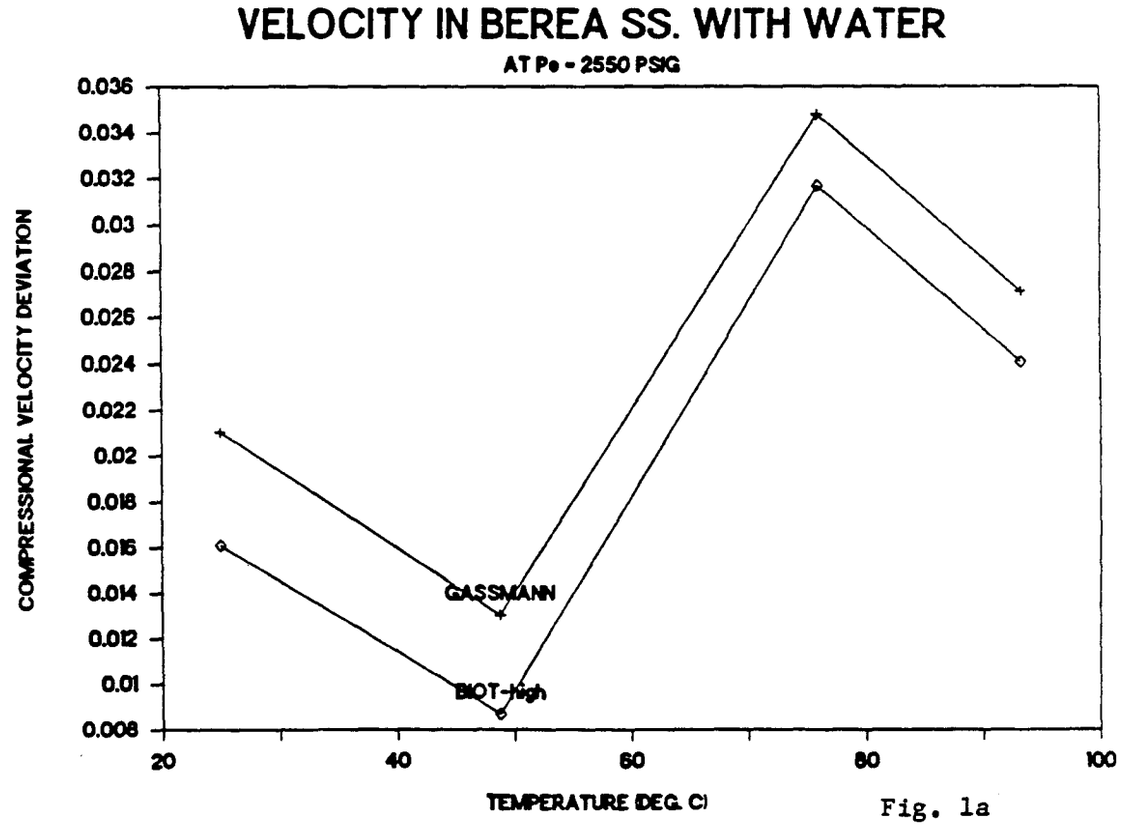
VELOCITY IN BEREA SS. WITH WATER
AT Pe = 2550 PSIG
COMPRESSIONAL VELOCITY DEVIATION
0.036
0.034
0.032
0.03
0.028
0.026
0.024
0.022
0.02
0.018
0.016
0.014
0.012
0.01
0.008
GASSMANN
BIOT-high
20
40
60
80
100
TEMPERATURE (DEG. C)

Fig. 1a

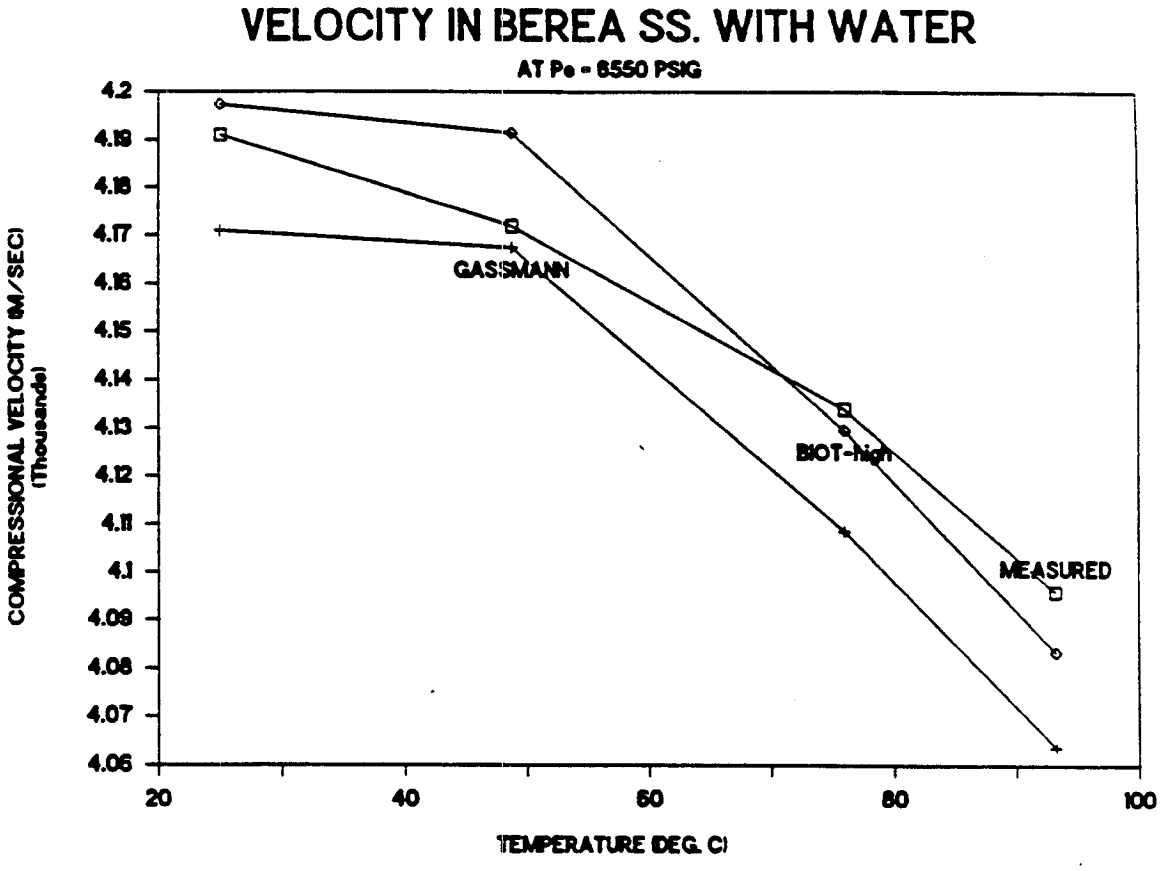
VELOCITY IN BEREA SS. WITH WATER
AT Pe = 6550 PSIG
COMPRESSIONAL VELOCITY (M/SEC) (Thousands)
4.2
4.19
4.18
4.17
4.16
4.15
4.14
4.13
4.12
4.11
4.1
4.09
4.08
4.07
4.06
GASSMANN
BIOT-high
MEASURED
20
40
60
80
100
TEMPERATURE DEG. C)

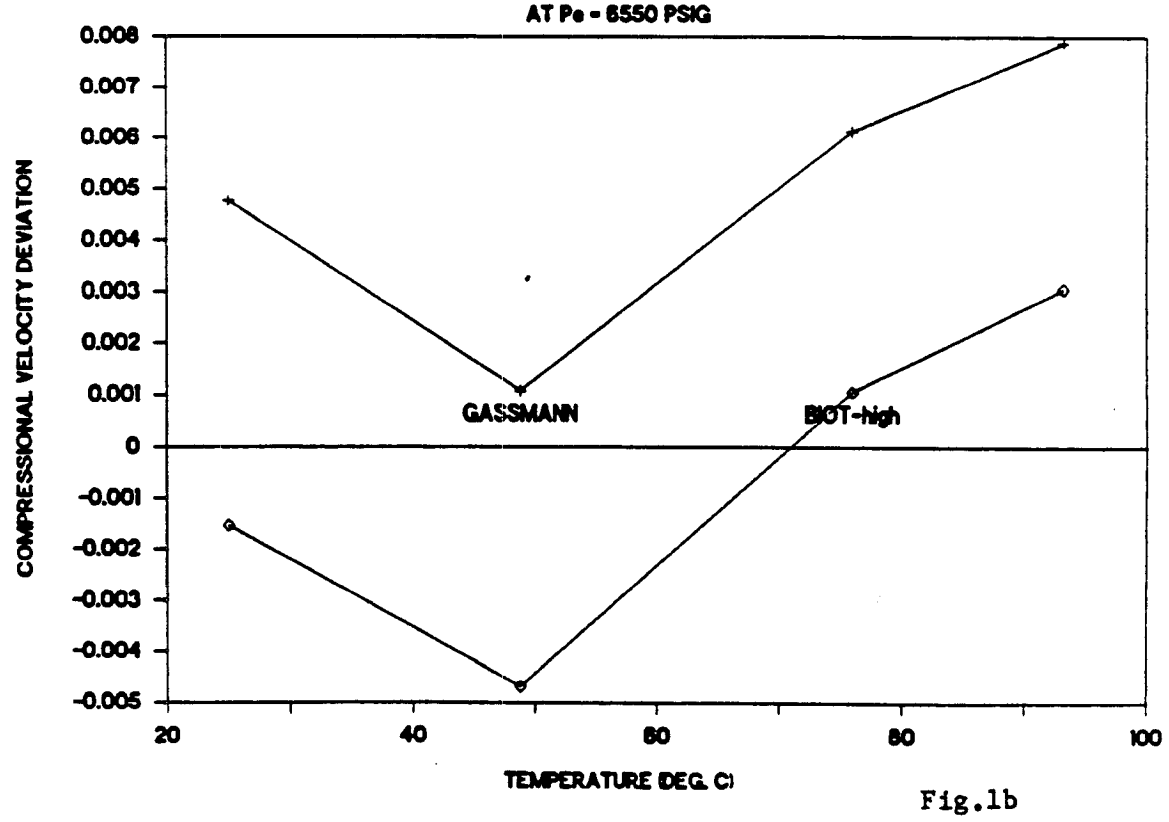
VELOCITY IN BEREA SS. WITH WATER
AT Pe = 6550 PSIG
COMPRESSIONAL VELOCITY DEVIATION
0.008
0.007
0.006
0.005
0.004
0.003
0.002
0.001
0
-0.001
-0.002
-0.003
-0.004
-0.005
GASSMANN
BIOT-high
20
40
60
80
100
TEMPERATURE DEG. C)

Fig.1b

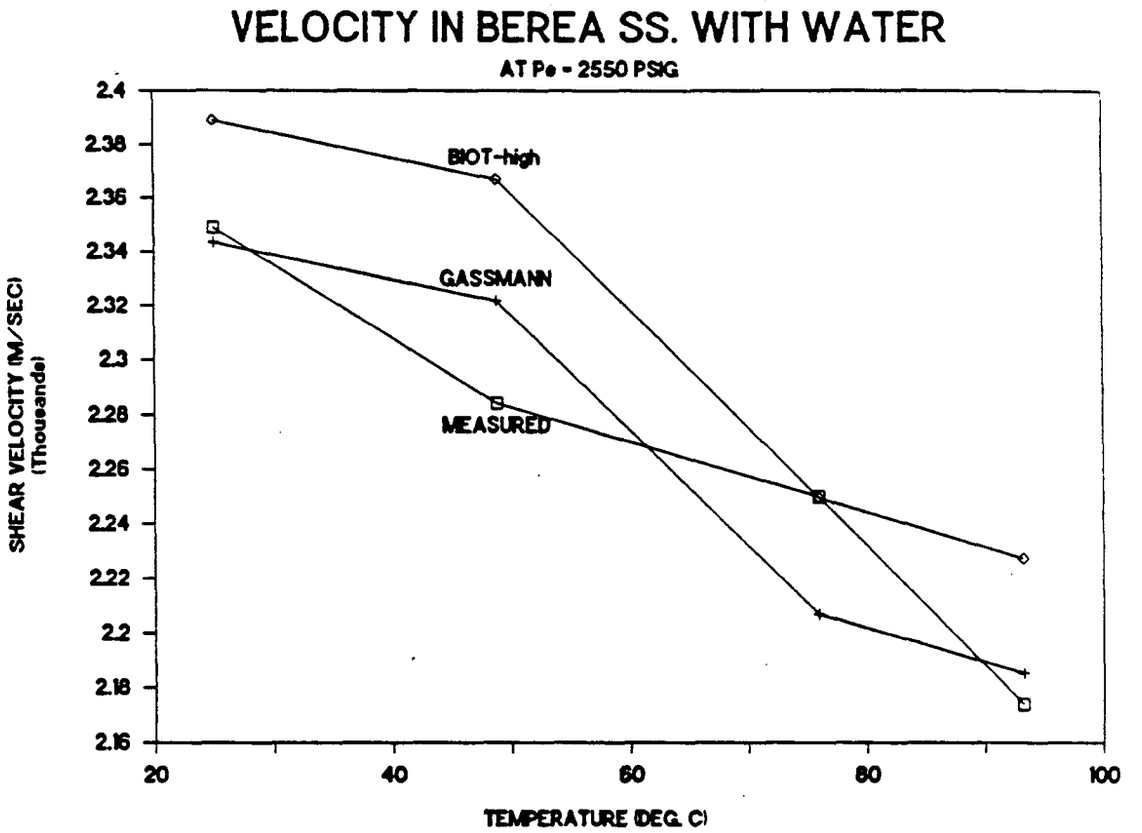
VELOCITY IN BEREA SS. WITH WATER
AT Pe = 2550 PSIG
SHEAR VELOCITY (M/SEC)
(Thousands)
2.4
2.38
2.36
2.34
2.32
2.3
2.28
2.26
2.24
2.22
2.2
2.18
2.16
BIOT-high
GASSMANN
MEASURED
20
40
60
80
100
TEMPERATURE (DEG. C)

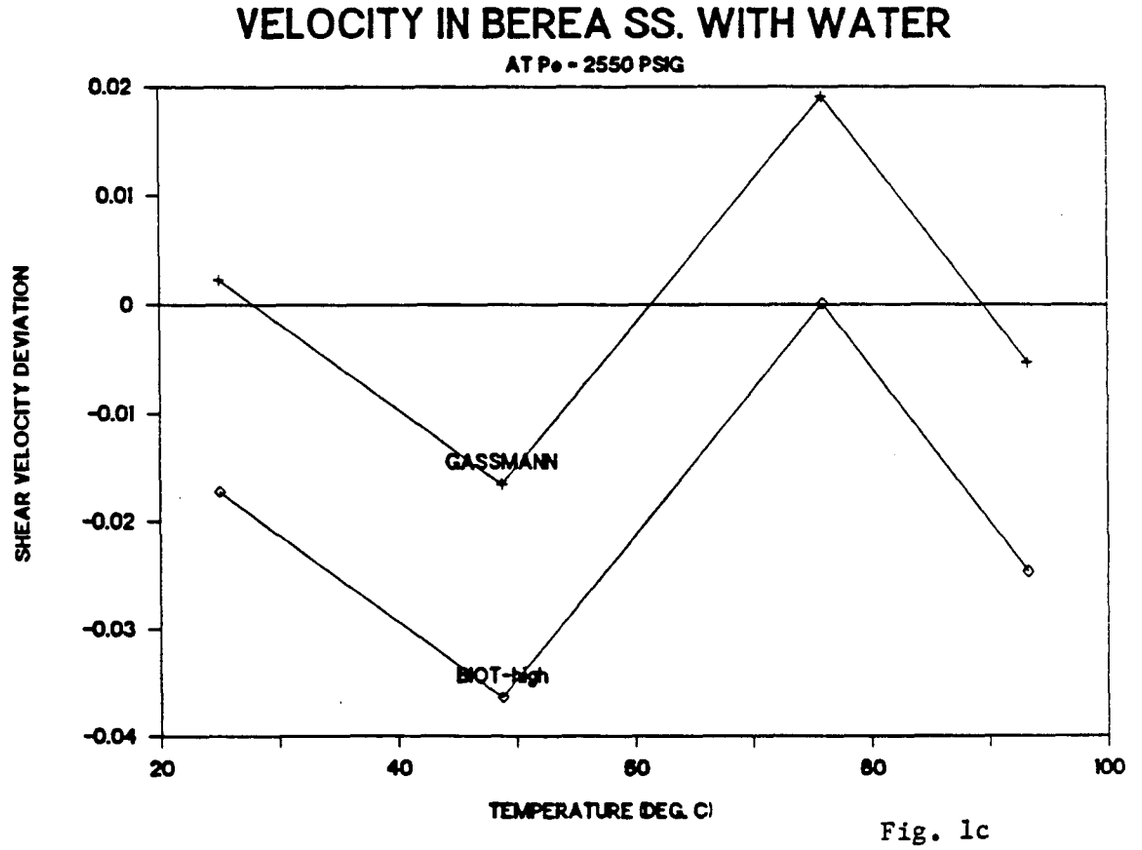
VELOCITY IN BEREA SS. WITH WATER
AT Pe = 2550 PSIG
SHEAR VELOCITY DEVIATION
0.02
0.01
0
-0.01
-0.02
-0.03
-0.04
GASSMANN
BIOT-high
20
40
60
80
100
TEMPERATURE (DEG. C)

Fig. 1c

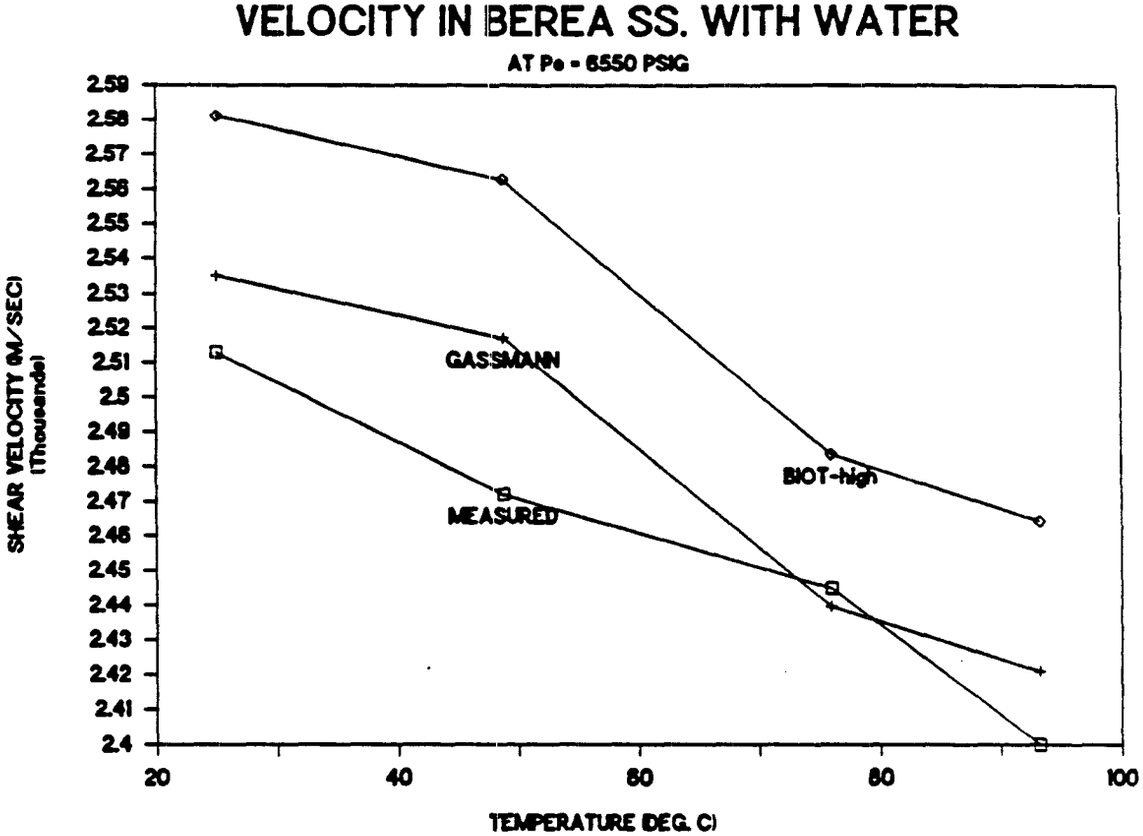
VELOCITY IN BEREA SS. WITH WATER
AT Pe = 6550 PSIG
SHEAR VELOCITY (M/SEC)
(Thousands)
2.59
2.58
2.57
2.56
2.55
2.54
2.53
2.52
2.51
2.5
2.49
2.48
2.47
2.46
2.45
2.44
2.43
2.42
2.41
2.4
GASSMANN
BIOT-high
MEASURED
20
40
60
80
100
TEMPERATURE (DEG. C)

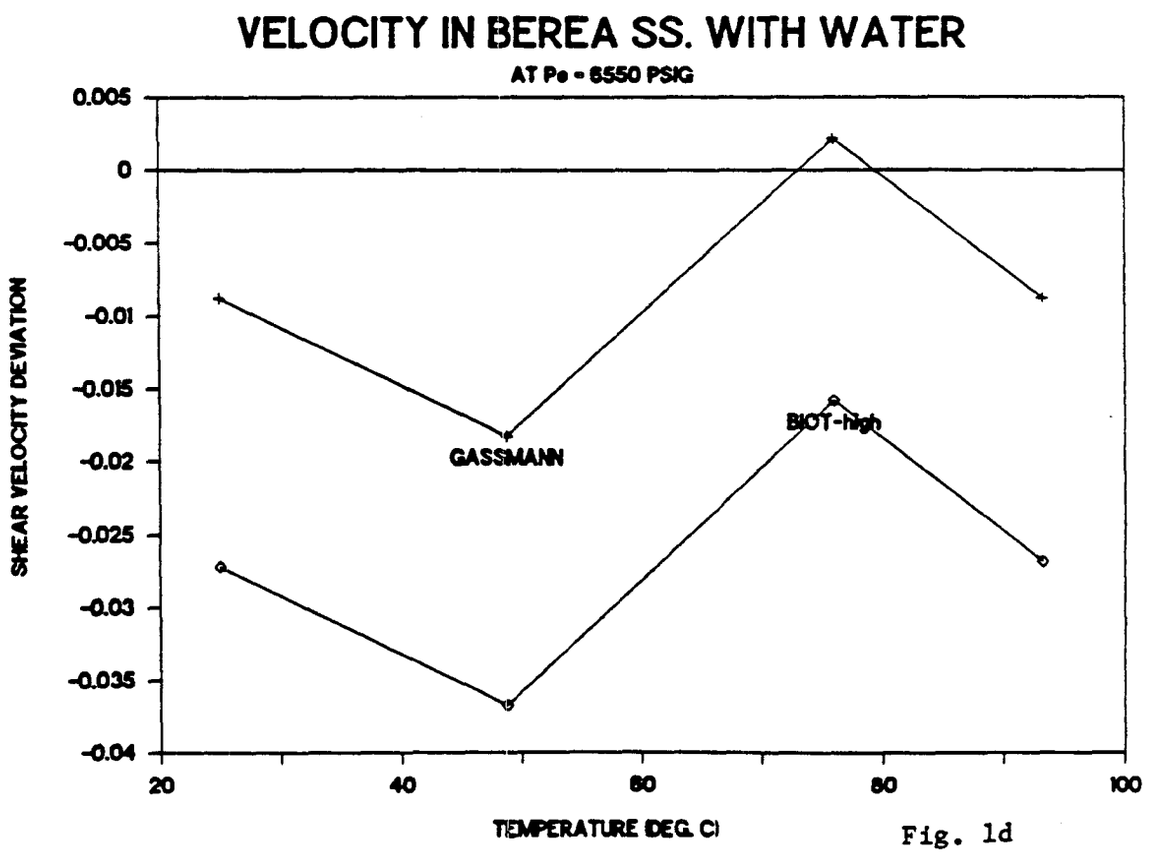
VELOCITY IN BEREA SS. WITH WATER
AT Pe = 6550 PSIG
SHEAR VELOCITY DEVIATION
0.005
0
-0.005
-0.01
-0.015
-0.02
-0.025
-0.03
-0.035
-0.04
GASSMANN
BIOT-high
20
40
60
80
100
TEMPERATURE (DEG. C)

Fig. 1d

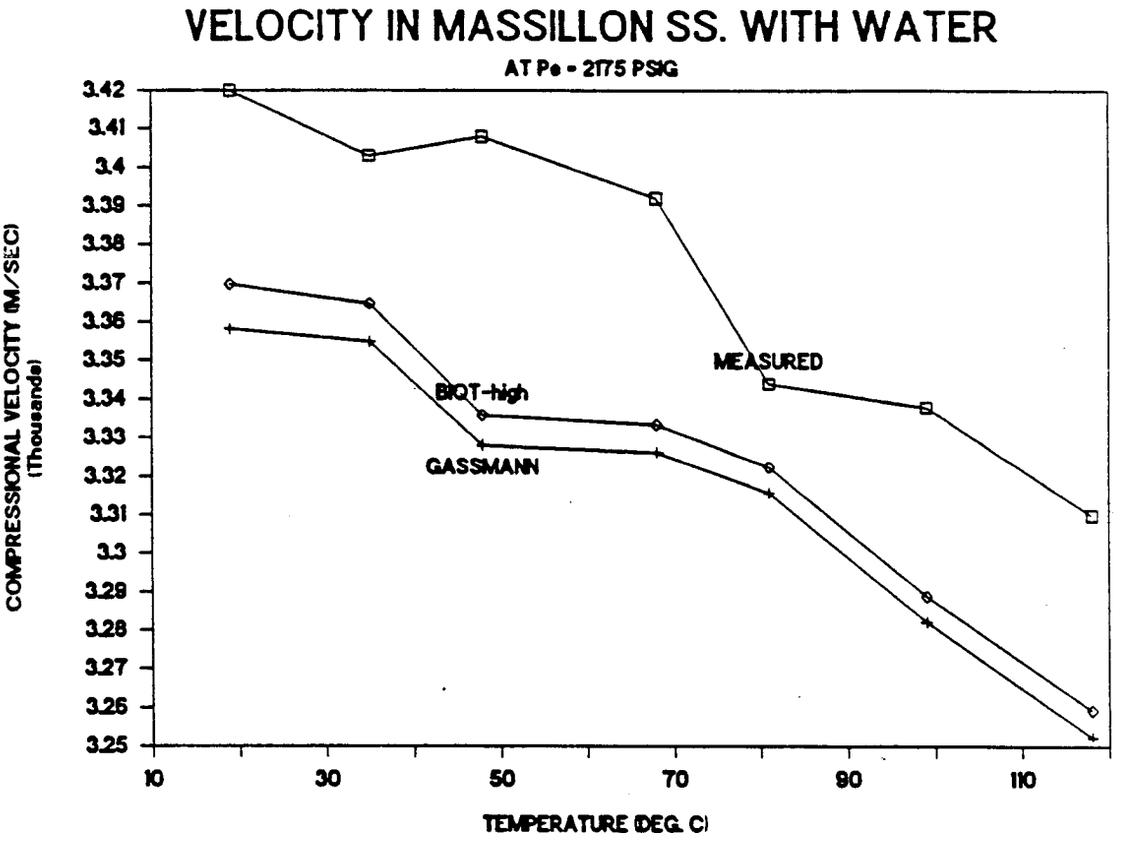
VELOCITY IN MASSILLON SS. WITH WATER
AT Pe = 2175 PSIG
COMPRESSIONAL VELOCITY (M/SEC) (Thousands)
3.42
3.41
3.4
3.39
3.38
3.37
3.36
3.35
3.34
3.33
3.32
3.31
3.3
3.29
3.28
3.27
3.26
3.25
MEASURED
BIOT-high
GASSMANN
10
30
50
70
90
110
TEMPERATURE (DEG. C)

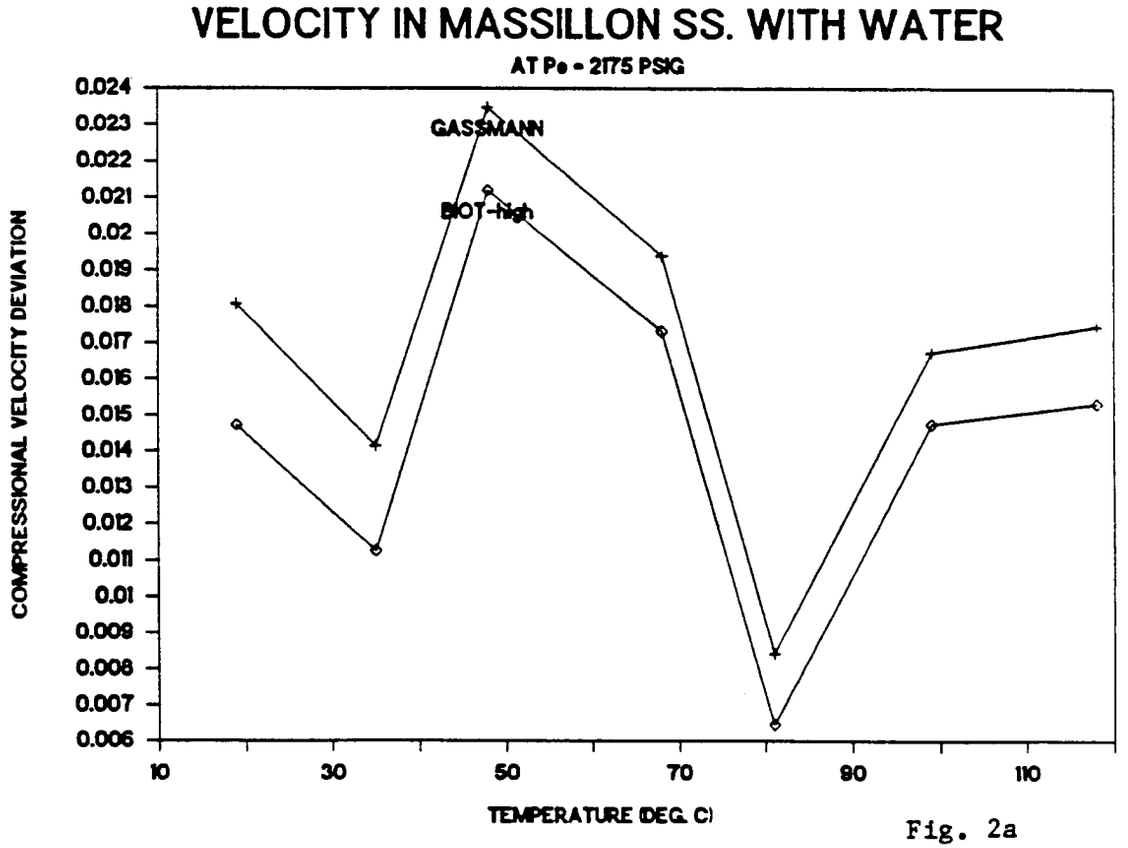
VELOCITY IN MASSILLON SS. WITH WATER
AT Pe = 2175 PSIG
COMPRESSIONAL VELOCITY DEVIATION
0.024
0.023
0.022
0.021
0.02
0.019
0.018
0.017
0.016
0.015
0.014
0.013
0.012
0.011
0.01
0.009
0.008
0.007
0.006
GASSMANN
BIOT-high
10
30
50
70
90
110
TEMPERATURE (DEG. C)

Fig. 2a

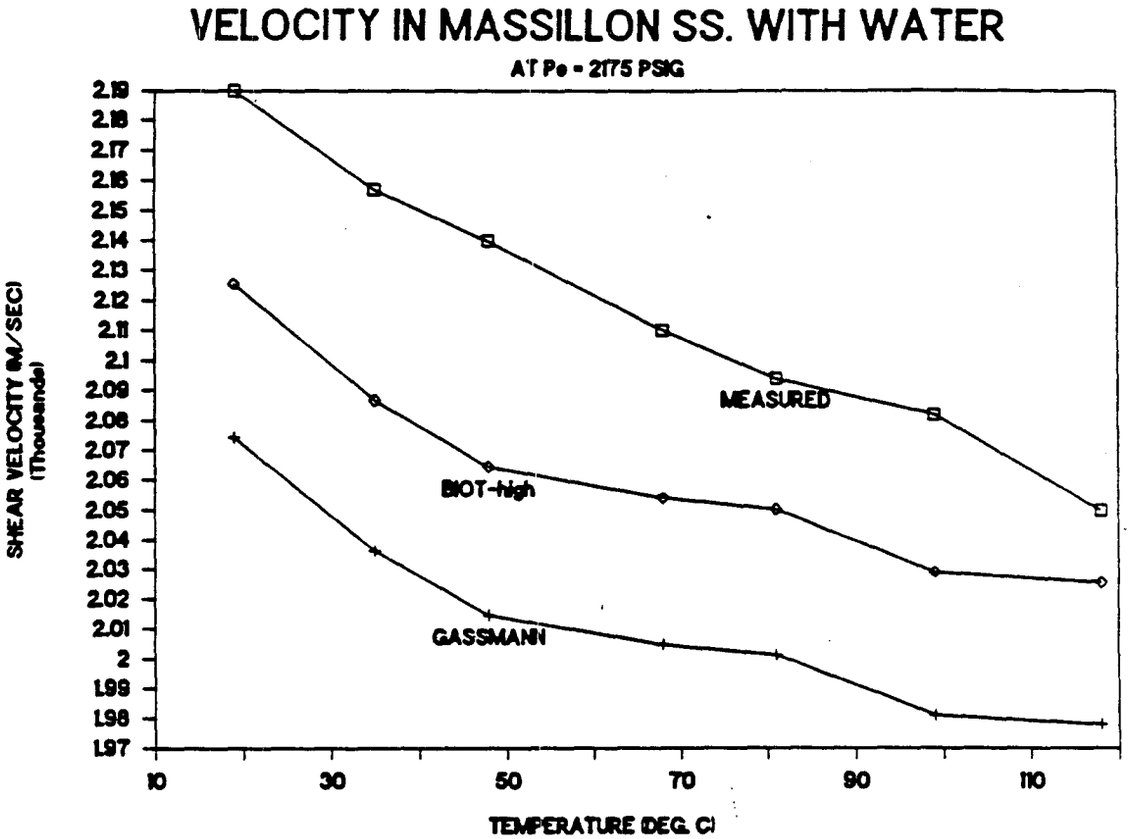
VELOCITY IN MASSILLON SS. WITH WATER
AT Pe = 2175 PSIG
SHEAR VELOCITY (M/SEC) (Thousands)
2.19
2.18
2.17
2.16
2.15
2.14
2.13
2.12
2.11
2.1
2.09
2.08
2.07
2.06
2.05
2.04
2.03
2.02
2.01
2
1.99
1.98
1.97
MEASURED
BIOT-high
GASSMANN
10
30
50
70
90
110
TEMPERATURE DEG. C

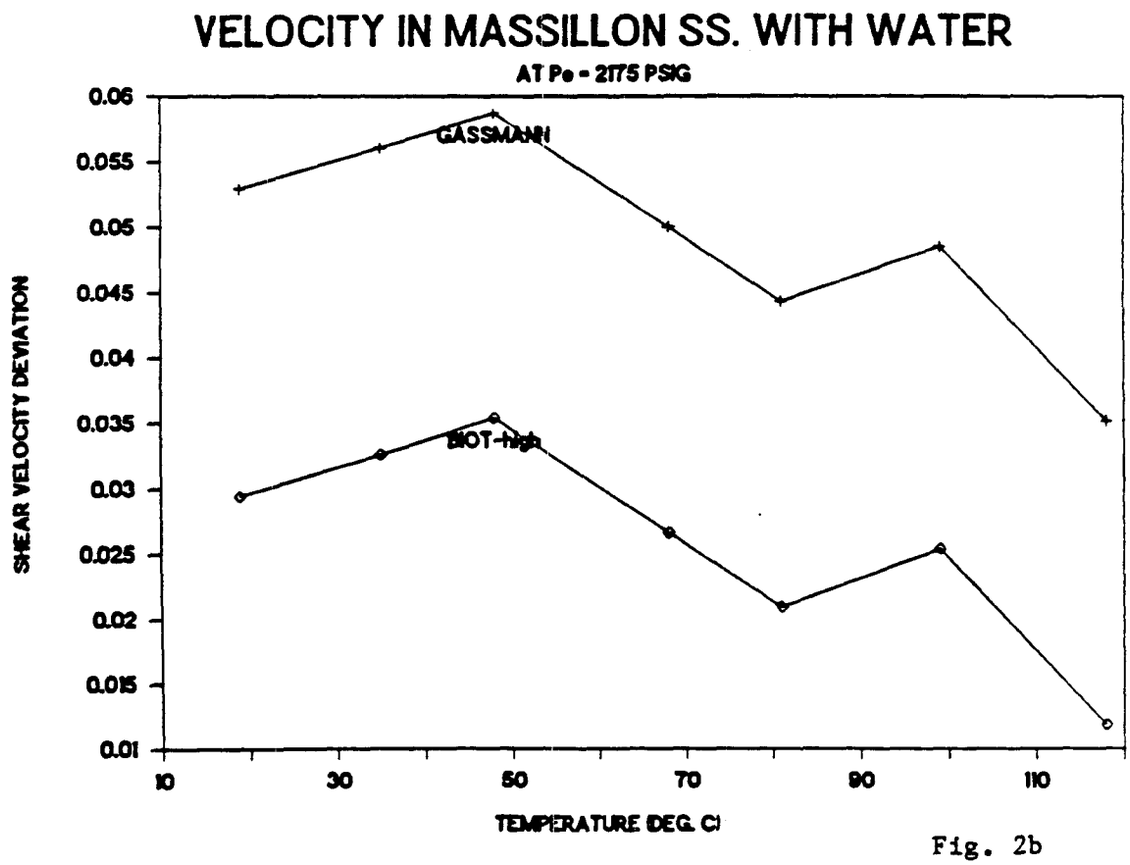
VELOCITY IN MASSILLON SS. WITH WATER
AT Pe = 2175 PSIG
SHEAR VELOCITY DEVIATION
0.06
0.055
0.05
0.045
0.04
0.035
0.03
0.025
0.02
0.015
0.01
GASSMANN
BIOT-high
10
30
50
70
90
110
TEMPERATURE DEG. C

Fig. 2b

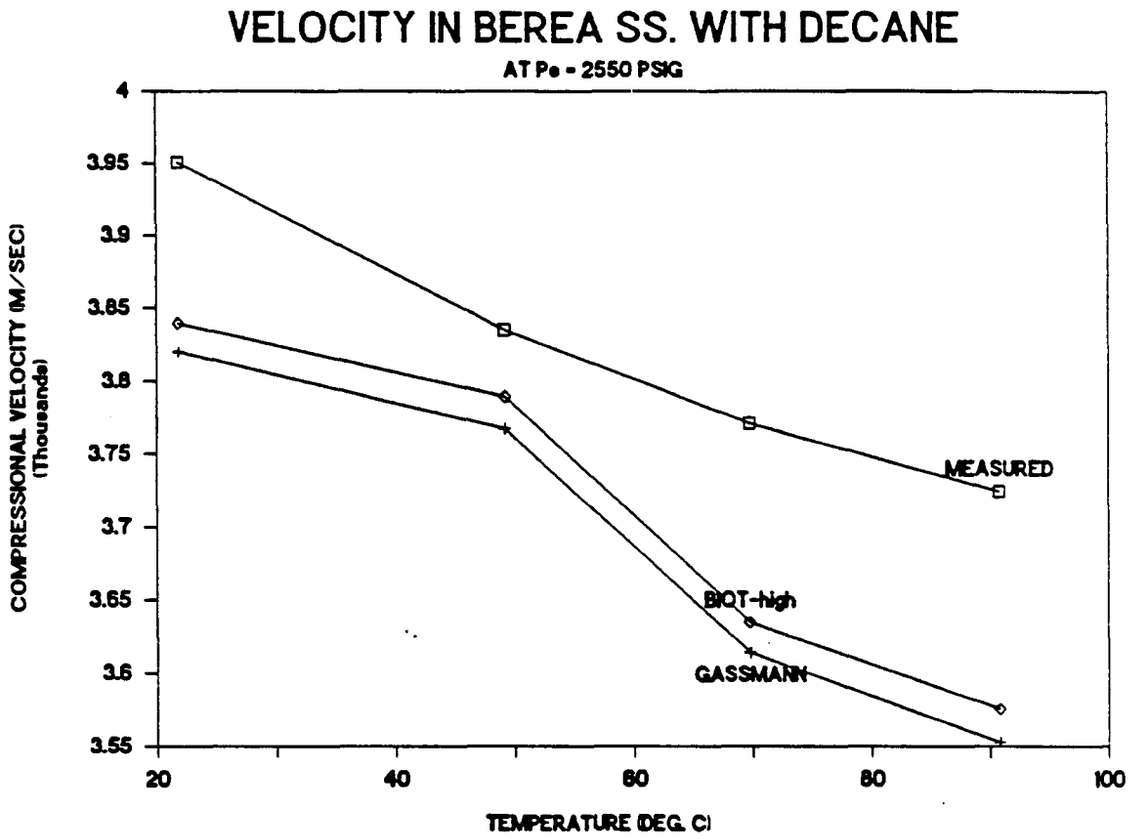
VELOCITY IN BEREA SS. WITH DECANE
AT Pe = 2550 PSIG
COMPRESSIONAL VELOCITY (M/SEC)
(Thousands)
4
3.95
3.9
3.85
3.8
3.75
3.7
3.65
3.6
3.55
MEASURED
BIOT-high
GASSMANN
20
40
60
80
100
TEMPERATURE (DEG. C)

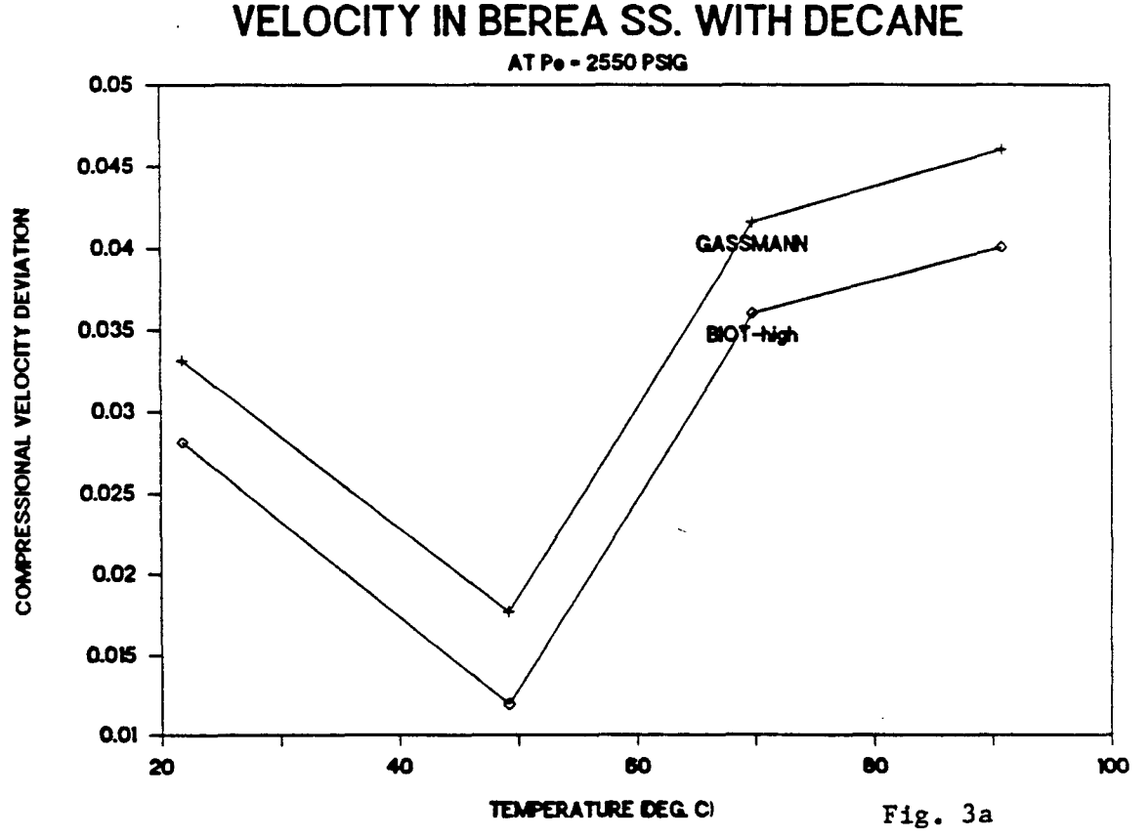
VELOCITY IN BEREA SS. WITH DECANE
AT Pe = 2550 PSIG
COMPRESSIONAL VELOCITY DEVIATION
0.05
0.045
0.04
0.035
0.03
0.025
0.02
0.015
0.01
GASSMANN
BIOT-high
20
40
60
80
100
TEMPERATURE (DEG. C)

Fig. 3a

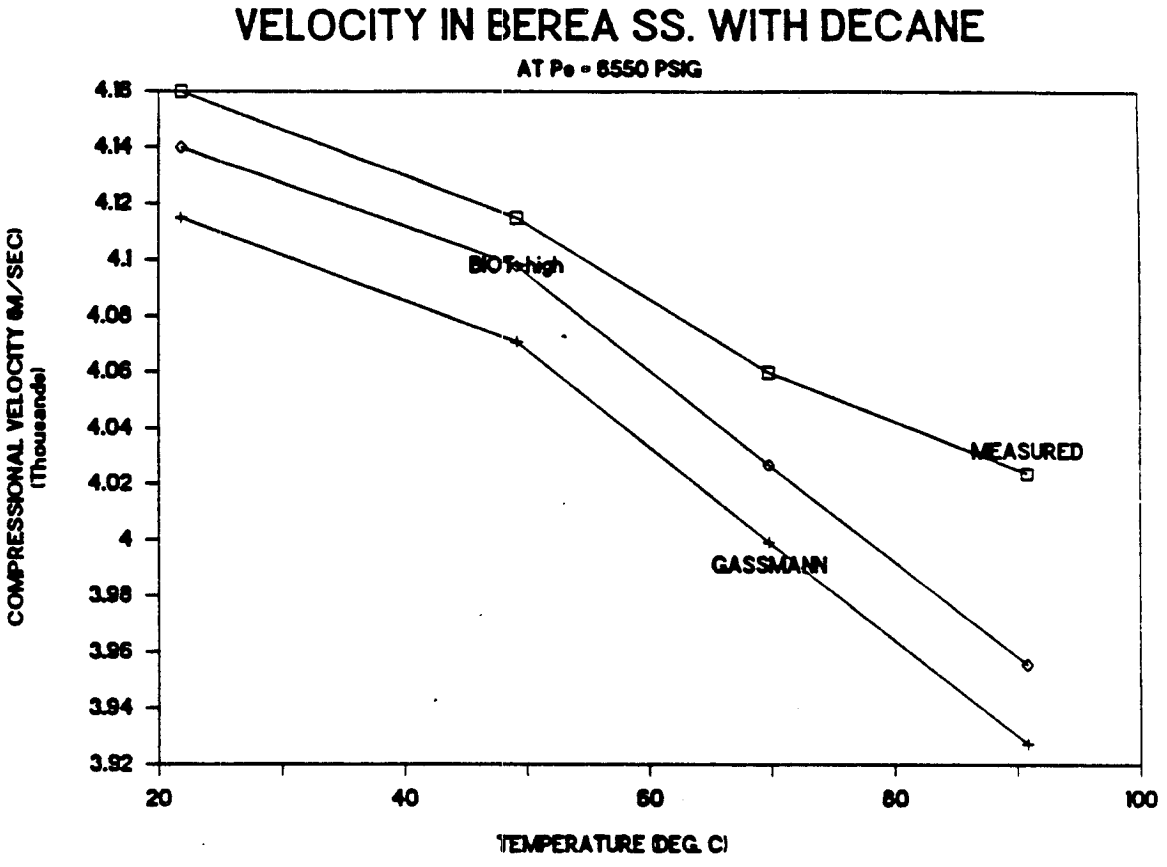
VELOCITY IN BEREA SS. WITH DECANE
AT Pe = 6550 PSIG
COMPRESSIONAL VELOCITY (M/SEC)
(Thousands)
4.16
4.14
4.12
4.1
4.08
4.06
4.04
4.02
4
3.98
3.96
3.94
3.92
BIOT-high
MEASURED
GASSMANN
20
40
60
80
100
TEMPERATURE (DEG. C)

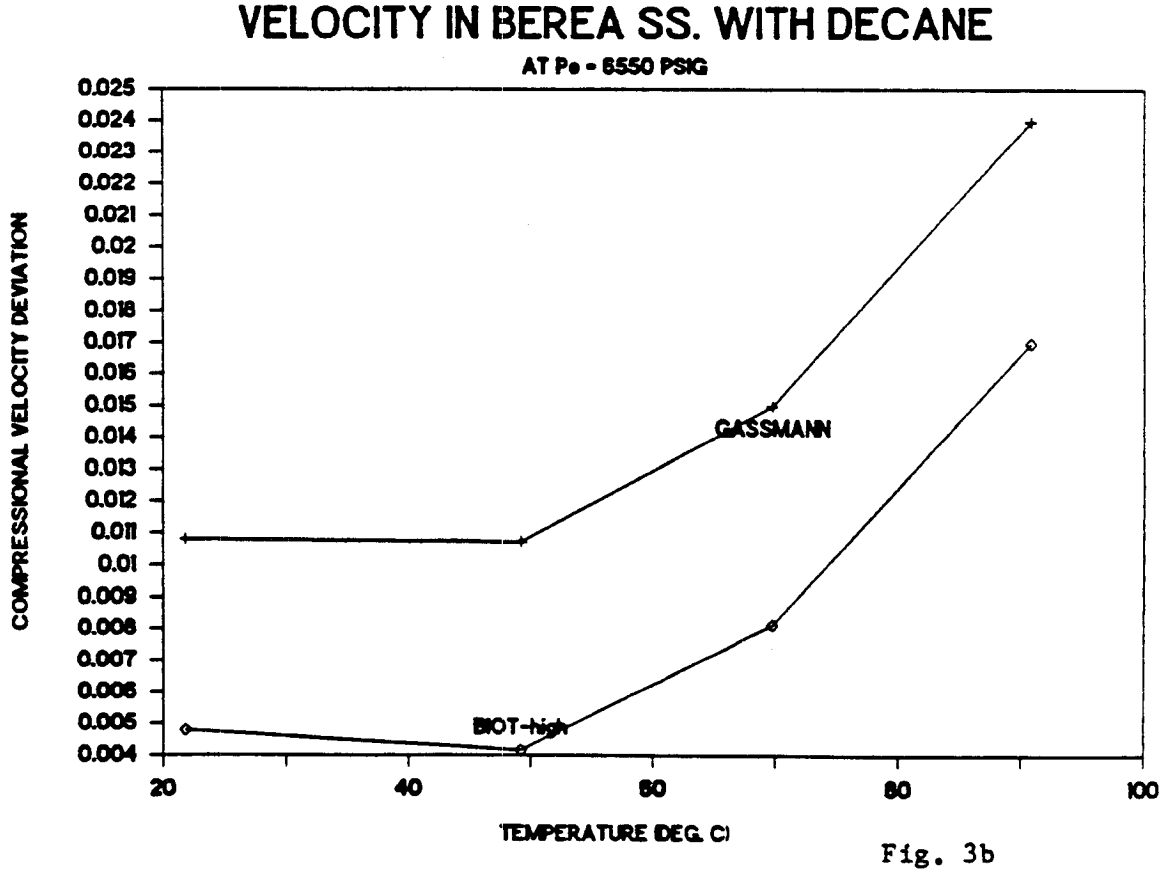
VELOCITY IN BEREA SS. WITH DECANE
AT Pe = 6550 PSIG
COMPRESSIONAL VELOCITY DEVIATION
0.025
0.024
0.023
0.022
0.021
0.02
0.019
0.018
0.017
0.016
0.015
0.014
0.013
0.012
0.011
0.01
0.009
0.008
0.007
0.006
0.005
0.004
GASSMANN
BIOT-high
20
40
60
80
100
TEMPERATURE (DEG. C)

Fig. 3b

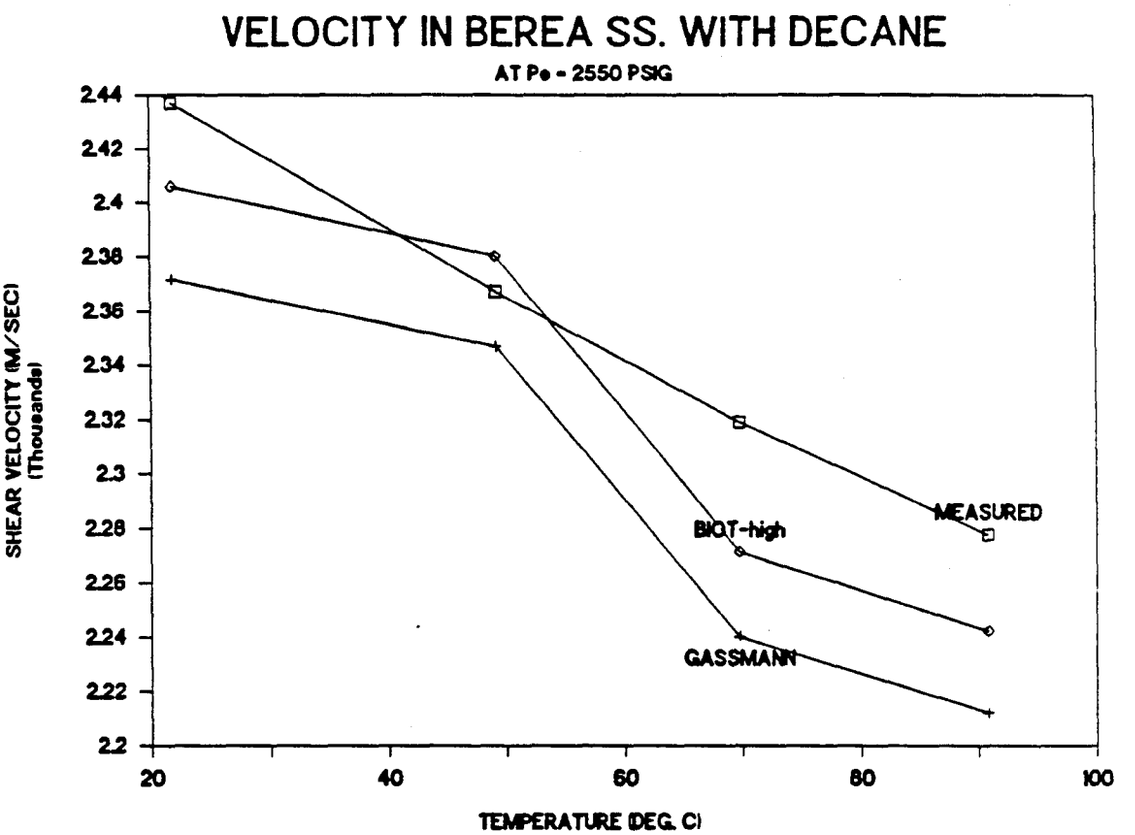
VELOCITY IN BEREA SS. WITH DECANE
AT Pe = 2550 PSIG
SHEAR VELOCITY (M/SEC) (Thousands)
2.44
2.42
2.4
2.38
2.36
2.34
2.32
2.3
2.28
2.26
2.24
2.22
2.2
20
40
60
80
100
TEMPERATURE (DEG. C)
MEASURED
BIOT-high
GASSMANN

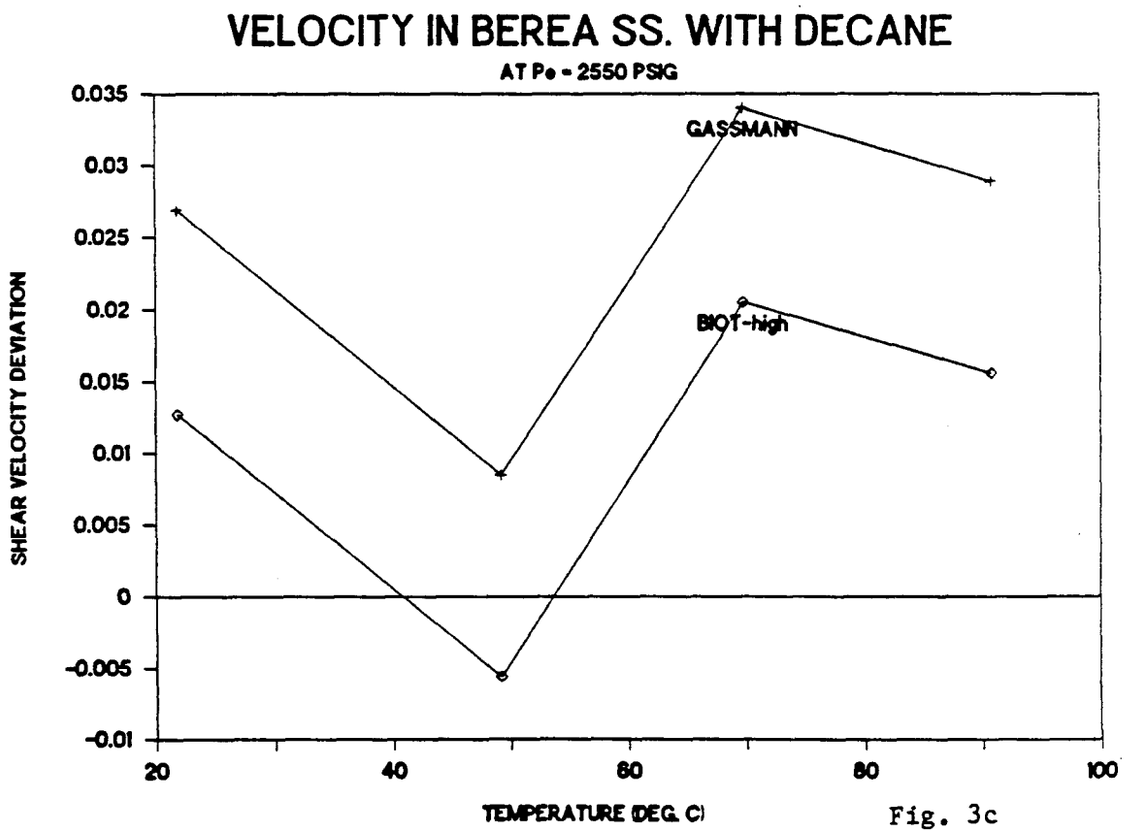
VELOCITY IN BEREA SS. WITH DECANE
AT Pe = 2550 PSIG
SHEAR VELOCITY DEVIATION
0.035
0.03
0.025
0.02
0.015
0.01
0.005
0
-0.005
-0.01
20
40
60
80
100
TEMPERATURE (DEG. C)
GASSMANN
BIOT-high

Fig. 3c

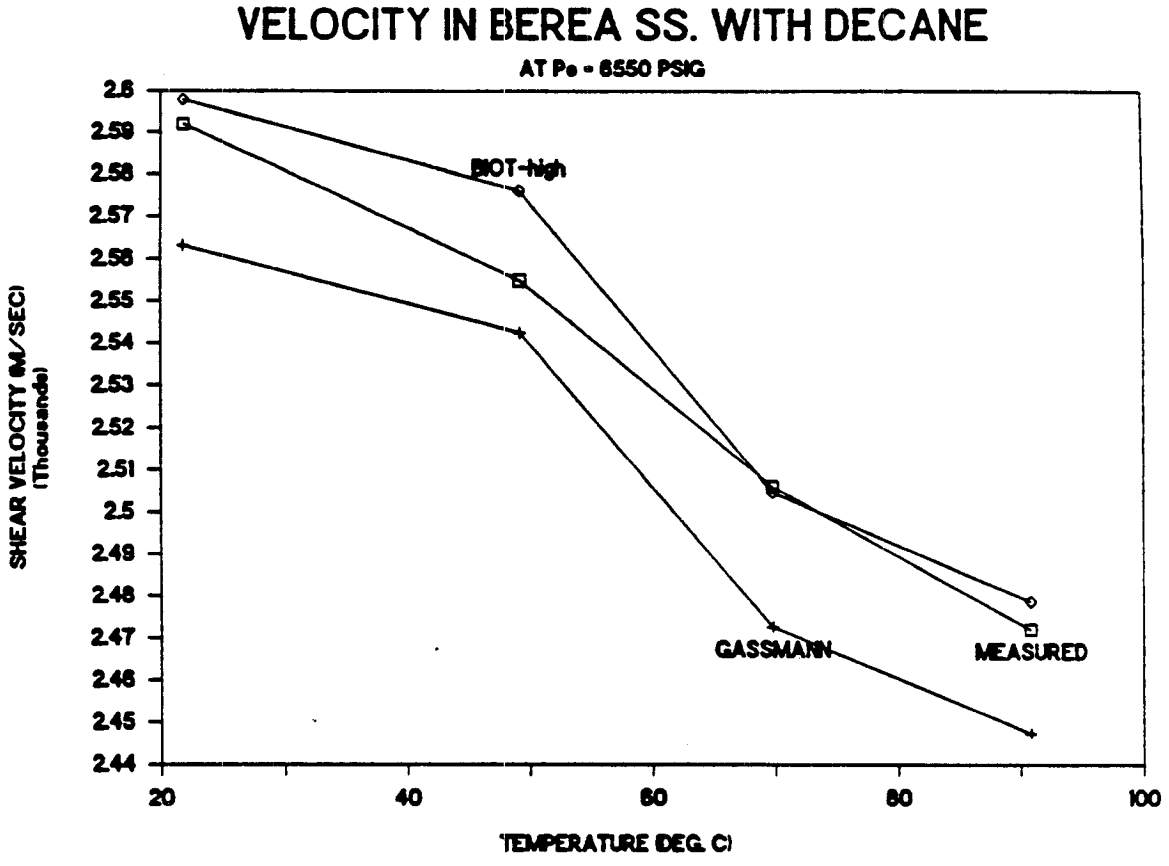
VELOCITY IN BEREA SS. WITH DECANE
AT Pe = 6550 PSIG
SHEAR VELOCITY (M/SEC) (Thousands)
2.6
2.59
2.58
2.57
2.56
2.55
2.54
2.53
2.52
2.51
2.5
2.49
2.48
2.47
2.46
2.45
2.44
BIOT-high
GASSMANN
MEASURED
20
40
60
80
100
TEMPERATURE (DEG. C)

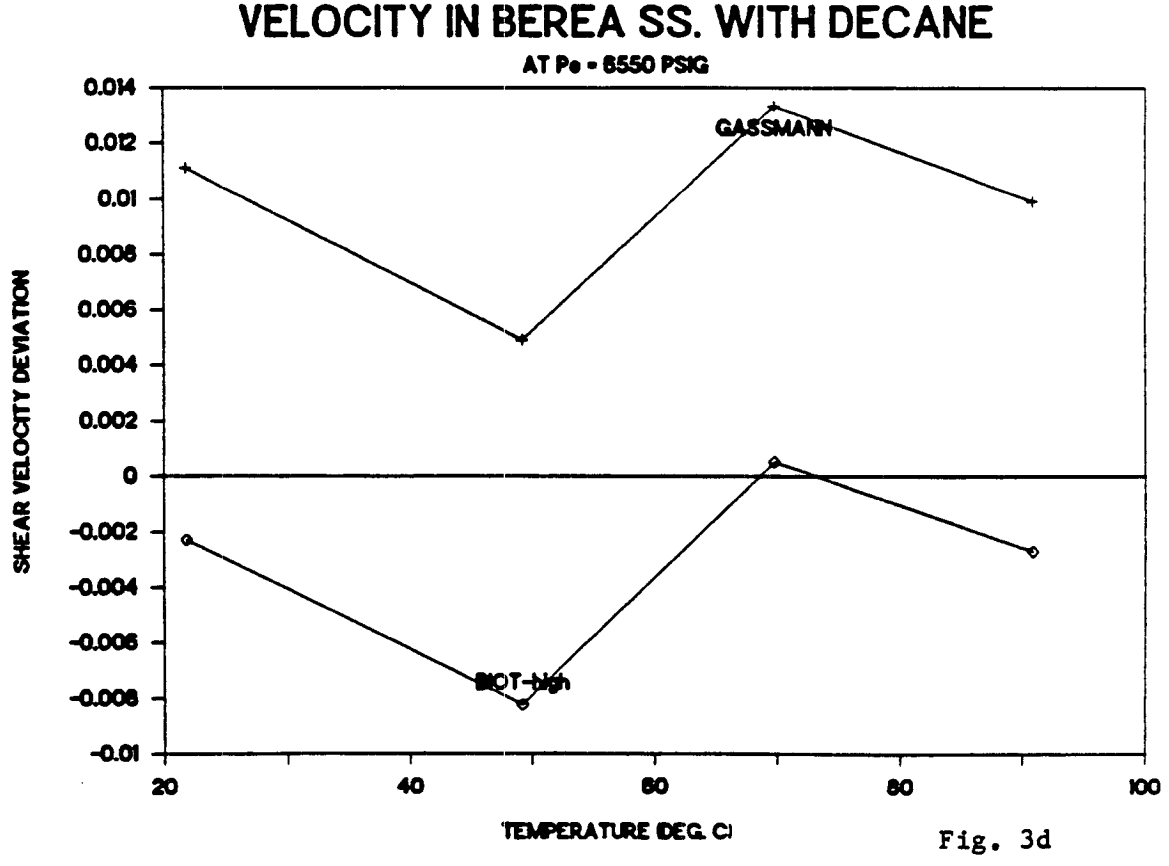
VELOCITY IN BEREA SS. WITH DECANE
AT Pe = 6550 PSIG
SHEAR VELOCITY DEVIATION
0.014
0.012
0.01
0.008
0.006
0.004
0.002
0
-0.002
-0.004
-0.006
-0.008
-0.01
GASSMANN
BIOT-high
20
40
60
80
100
TEMPERATURE (DEG. C)

Fig. 3d

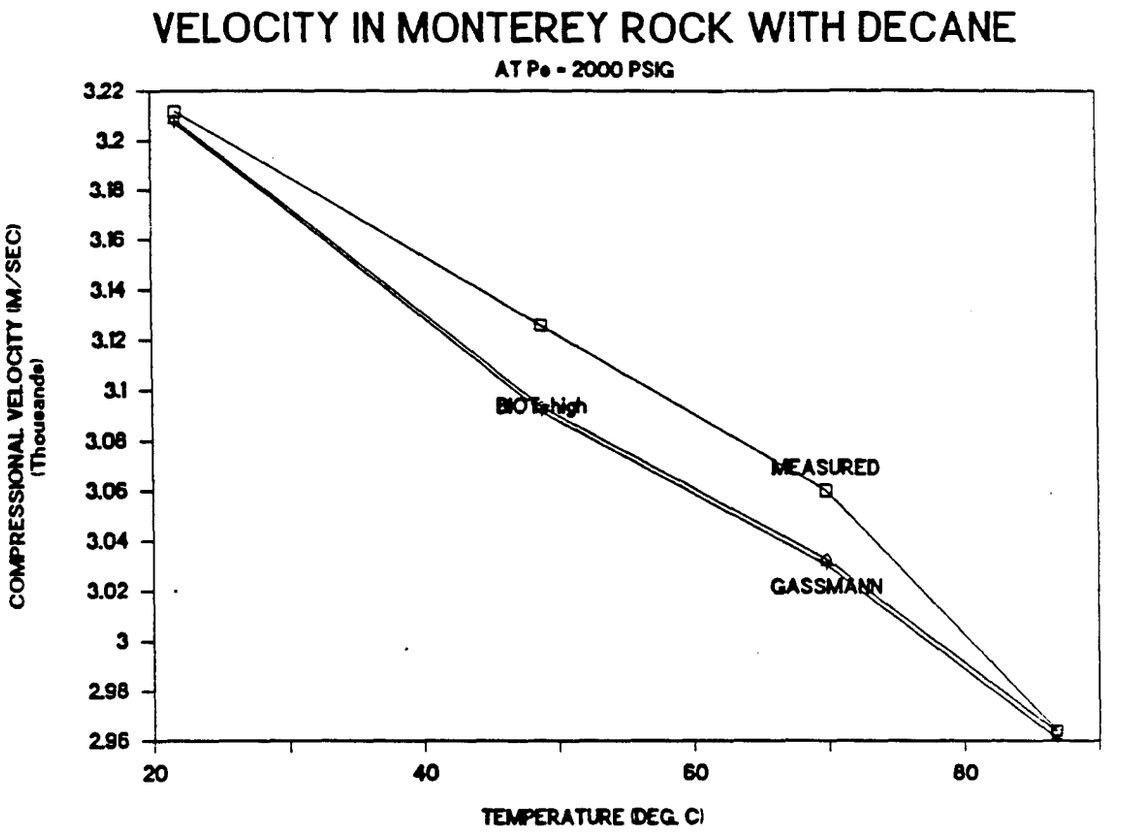
VELOCITY IN MONTEREY ROCK WITH DECANE
AT Pe = 2000 PSIG
COMPRESSIONAL VELOCITY (M/SEC)
(Thousands)
3.22
3.2
3.18
3.16
3.14
3.12
3.1
3.08
3.06
3.04
3.02
3
2.98
2.96
20
40
60
80
TEMPERATURE (DEG. C)
BIOT-high
MEASURED
GASSMANN

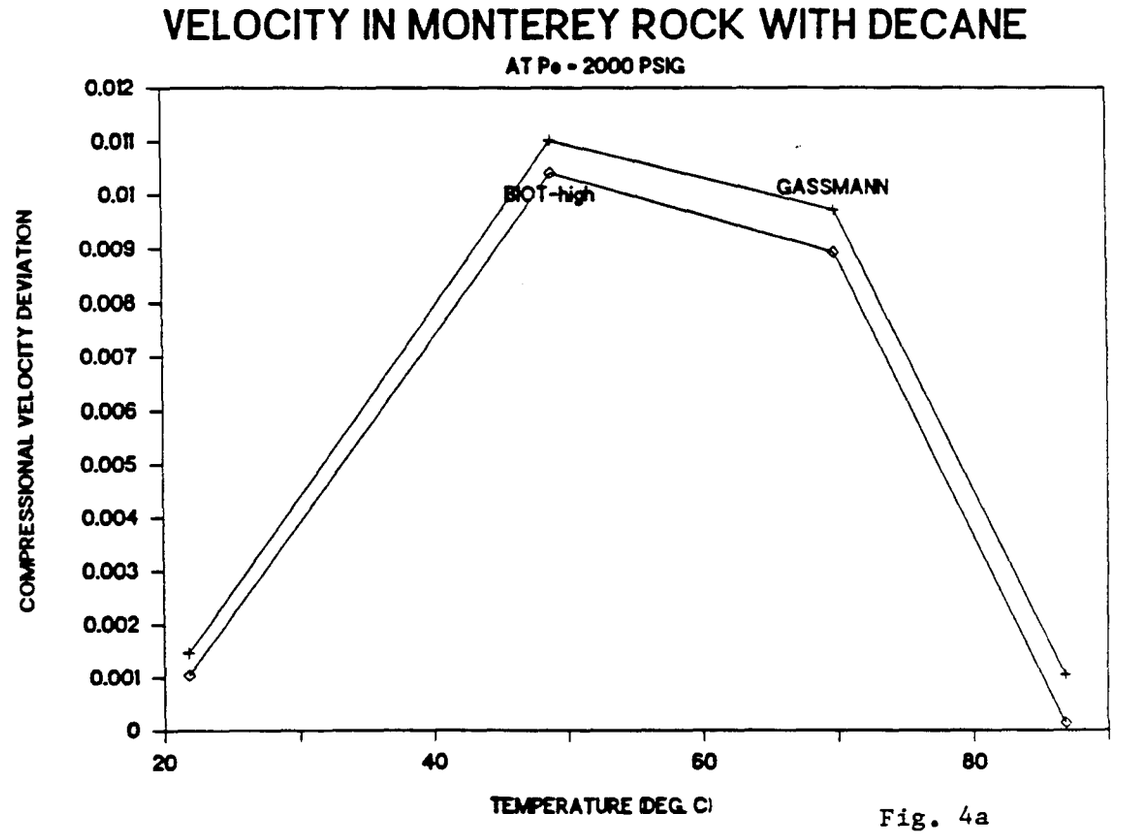
VELOCITY IN MONTEREY ROCK WITH DECANE
AT Pe = 2000 PSIG
COMPRESSIONAL VELOCITY DEVIATION
0.012
0.011
0.01
0.009
0.008
0.007
0.006
0.005
0.004
0.003
0.002
0.001
0
20
40
60
80
TEMPERATURE (DEG. C)
BIOT-high
GASSMANN

Fig. 4a

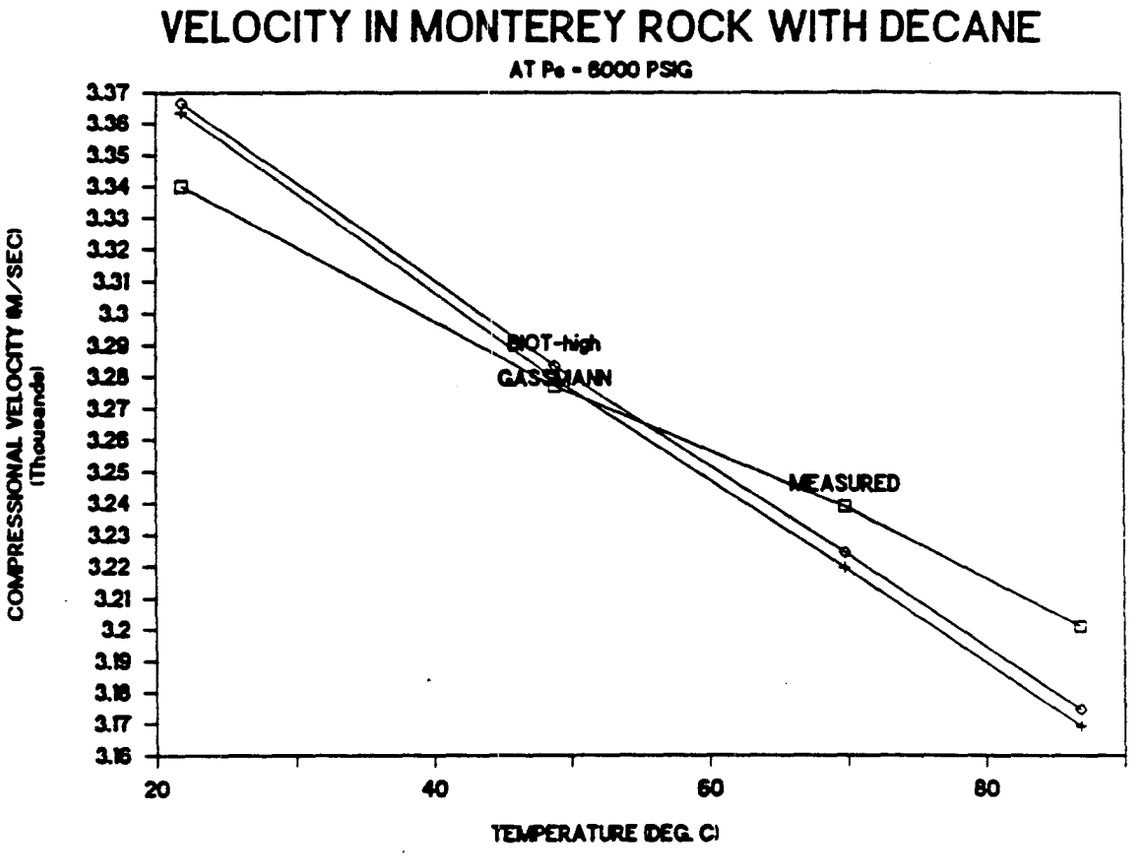
VELOCITY IN MONTEREY ROCK WITH DECANE
AT Pe = 6000 PSIG
COMPRESSIONAL VELOCITY (M/SEC)
(Thousands)
3.37
3.36
3.35
3.34
3.33
3.32
3.31
3.3
3.29
3.28
3.27
3.26
3.25
3.24
3.23
3.22
3.21
3.2
3.19
3.18
3.17
3.16
BIOT-high
GASSMANN
MEASURED
20
40
60
80
TEMPERATURE (DEG. C)

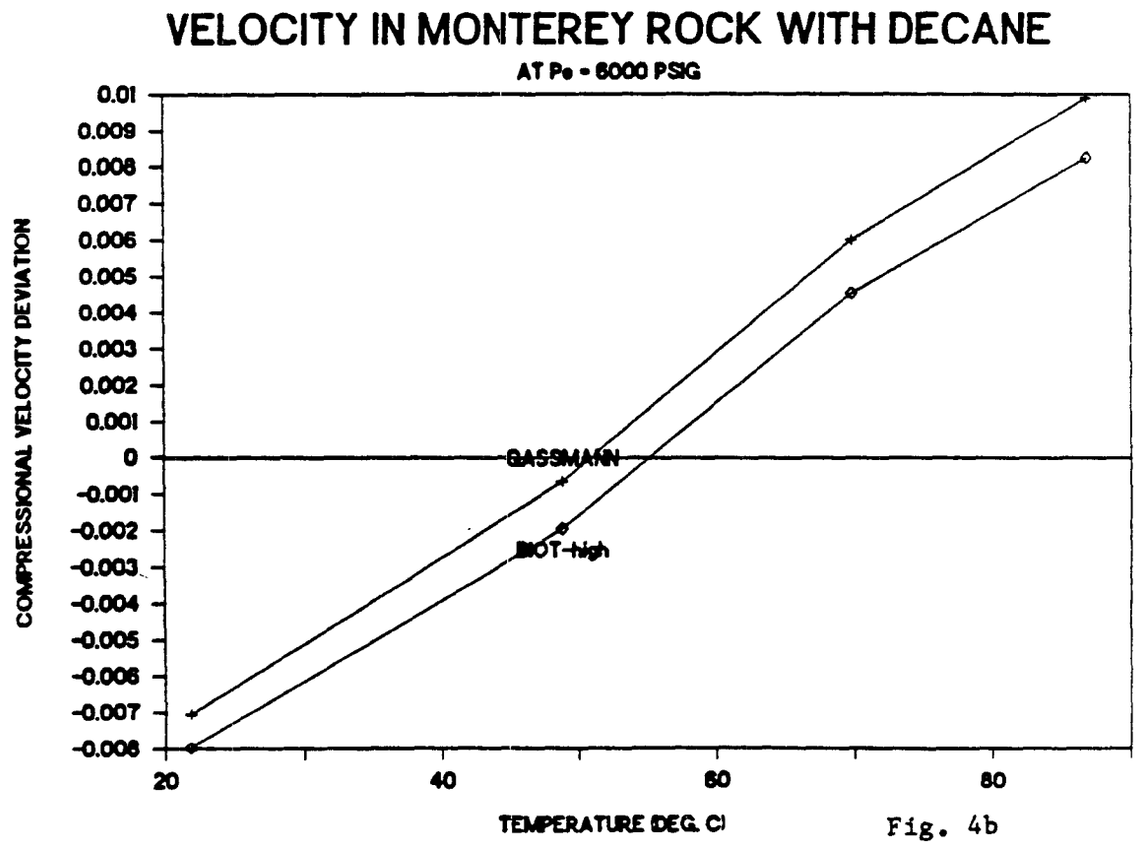
VELOCITY IN MONTEREY ROCK WITH DECANE
AT Pe = 6000 PSIG
COMPRESSIONAL VELOCITY DEVIATION
0.01
0.009
0.008
0.007
0.006
0.005
0.004
0.003
0.002
0.001
0
-0.001
-0.002
-0.003
-0.004
-0.005
-0.006
-0.007
-0.008
GASSMANN
BIOT-high
20
40
60
80
TEMPERATURE (DEG. C)

Fig. 4b

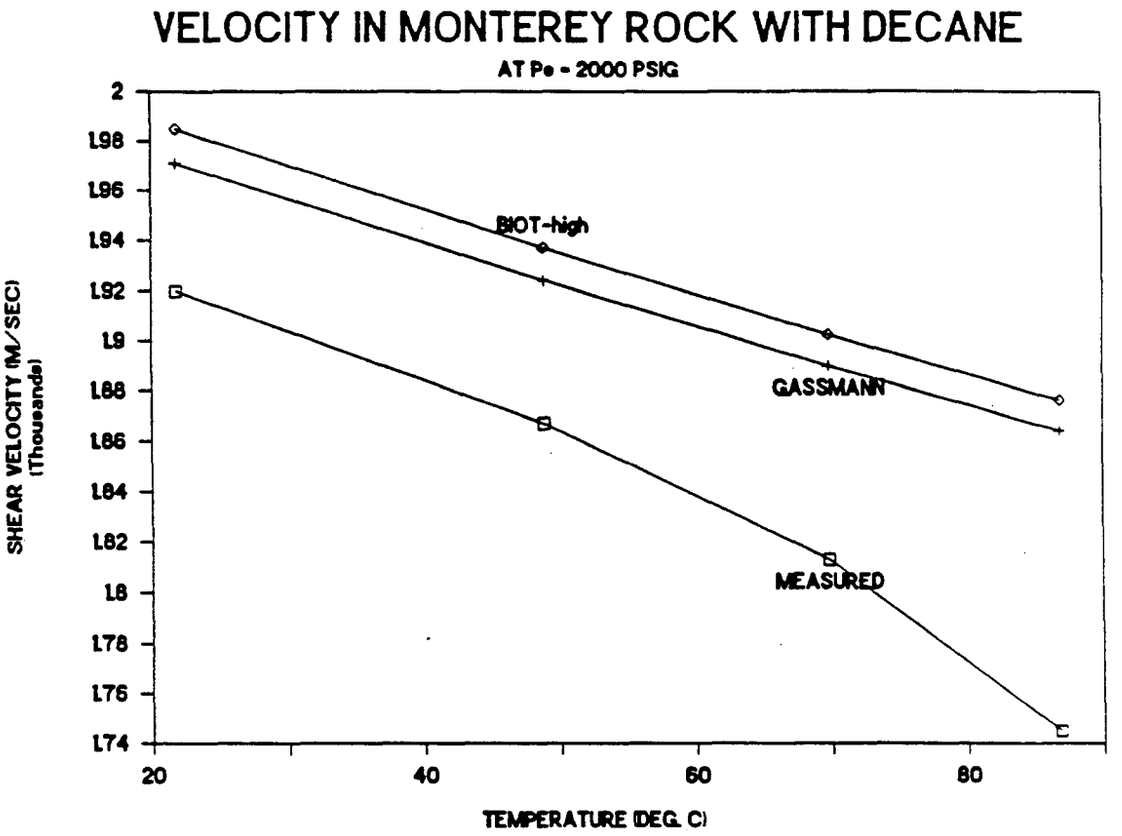
VELOCITY IN MONTEREY ROCK WITH DECANE
AT Pe = 2000 PSIG
SHEAR VELOCITY (M/SEC)
(Thousands)
2
1.98
1.96
1.94
1.92
1.9
1.88
1.86
1.84
1.82
1.8
1.78
1.76
1.74
BIOT-high
GASSMANN
MEASURED
20
40
60
80
TEMPERATURE (DEG. C)

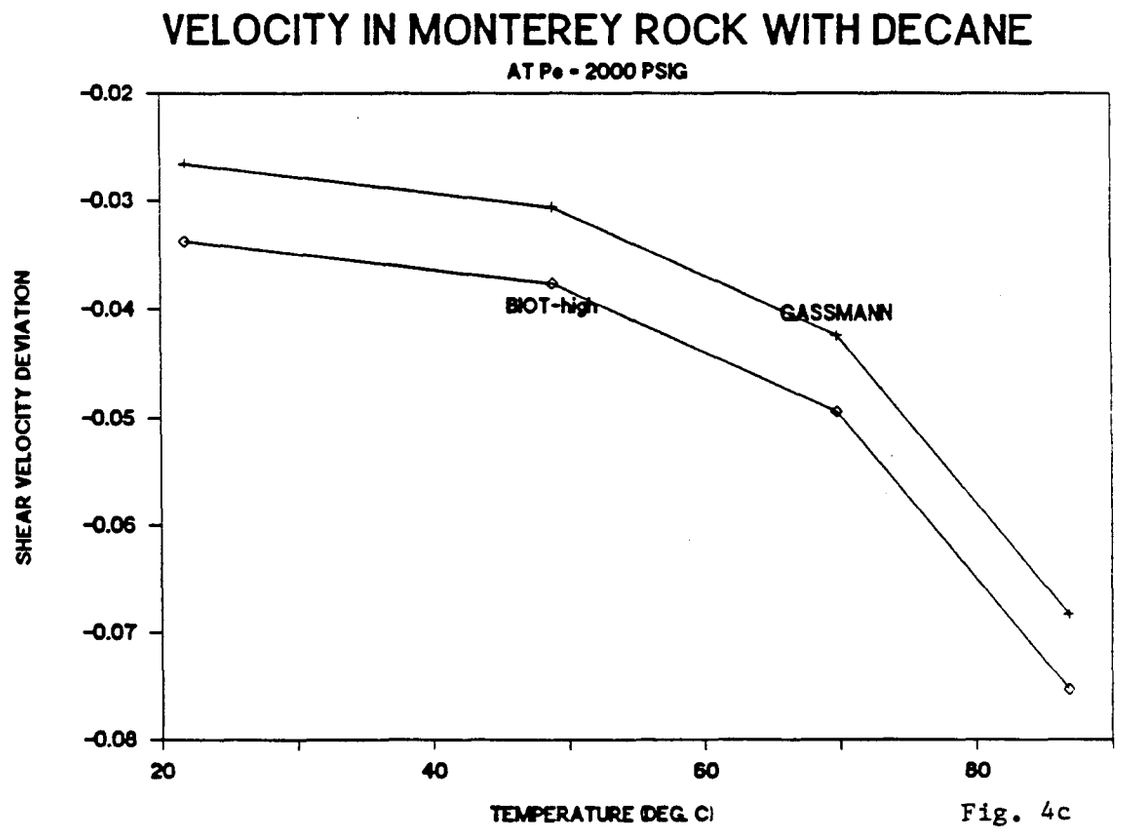
VELOCITY IN MONTEREY ROCK WITH DECANE
AT Pe = 2000 PSIG
SHEAR VELOCITY DEVIATION
-0.02
-0.03
-0.04
-0.05
-0.06
-0.07
-0.08
BIOT-high
GASSMANN
20
40
60
80
TEMPERATURE (DEG. C)

Fig. 4c

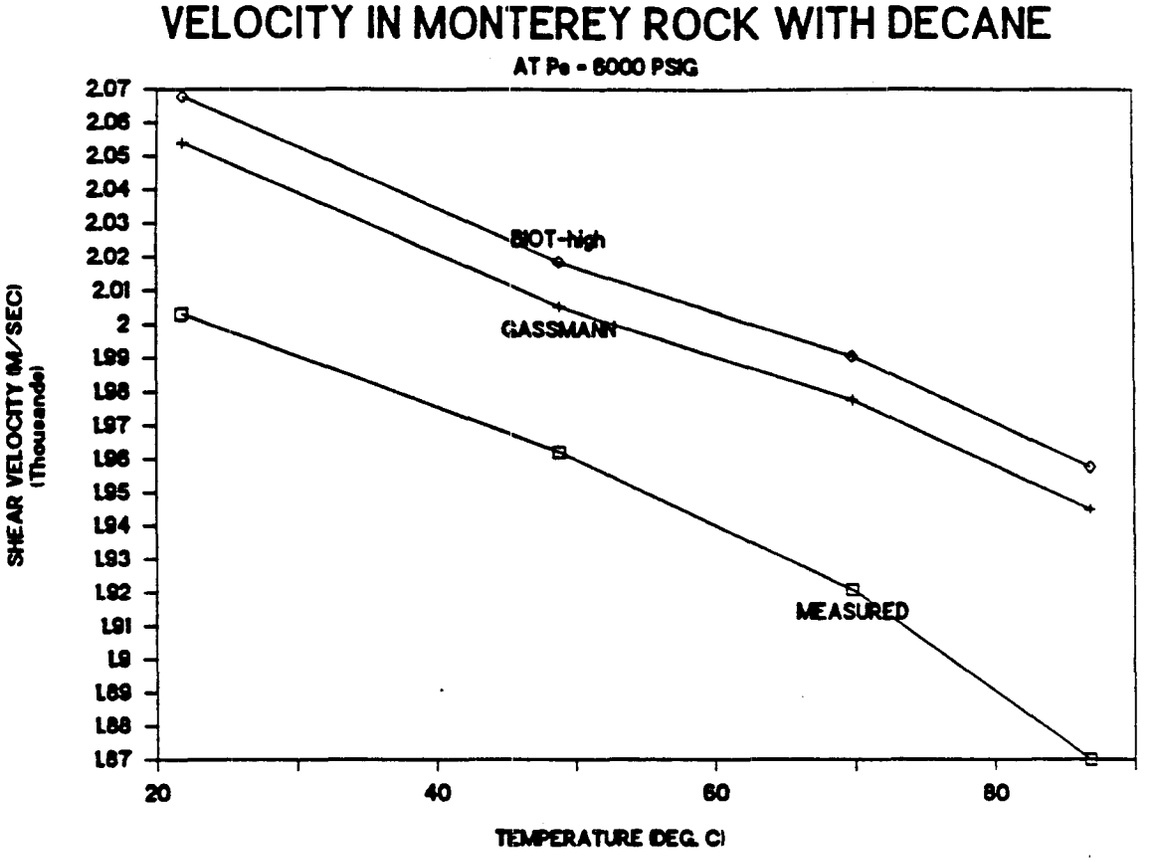
VELOCITY IN MONTEREY ROCK WITH DECANE
AT Pe = 6000 PSIG
SHEAR VELOCITY (M/SEC)
(Thousands)
2.07
2.06
2.05
2.04
2.03
2.02
2.01
2
1.99
1.98
1.97
1.96
1.95
1.94
1.93
1.92
1.91
1.9
1.89
1.88
1.87
BIOT-high
GASSMANN
MEASURED
20
40
60
80
TEMPERATURE DEG. C)

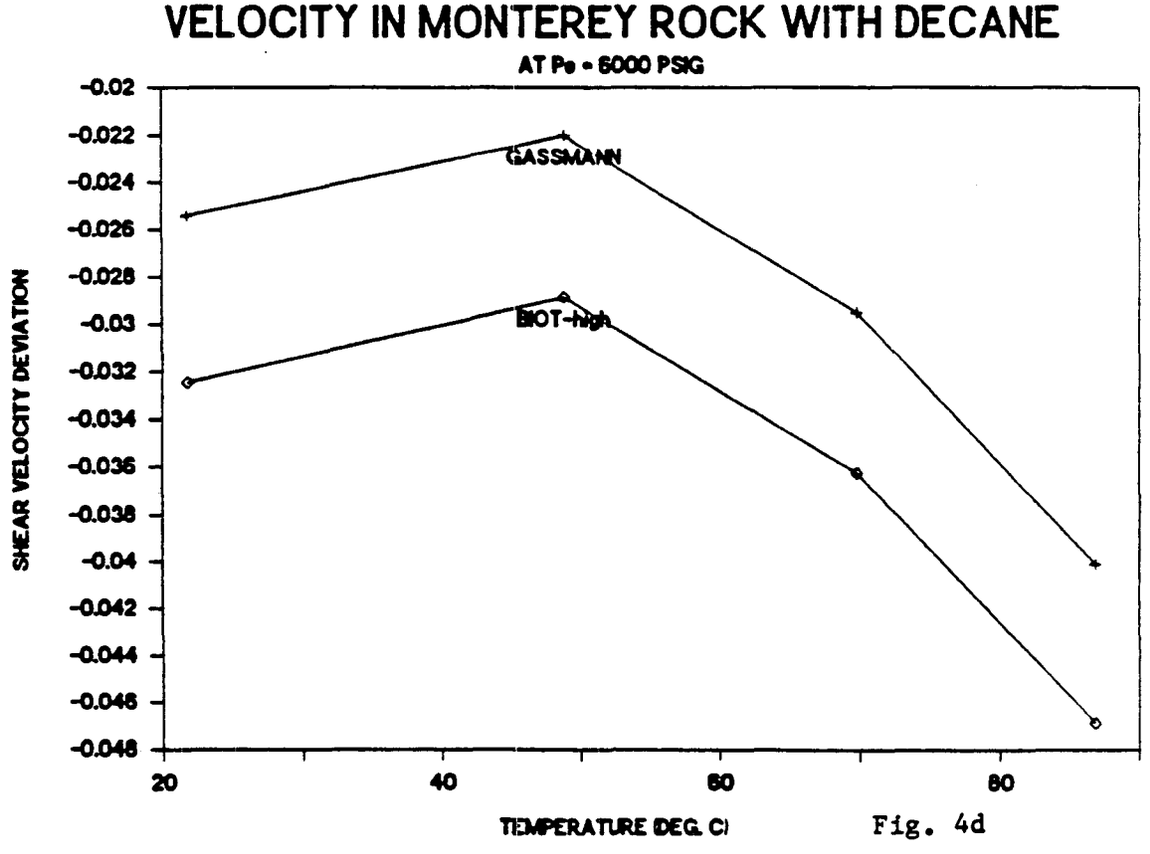
VELOCITY IN MONTEREY ROCK WITH DECANE
AT Pe = 6000 PSIG
SHEAR VELOCITY DEVIATION
-0.02
-0.022
-0.024
-0.026
-0.028
-0.03
-0.032
-0.034
-0.036
-0.038
-0.04
-0.042
-0.044
-0.046
-0.048
GASSMANN
BIOT-high
20
40
60
80
TEMPERATURE DEG. C)

Fig. 4d

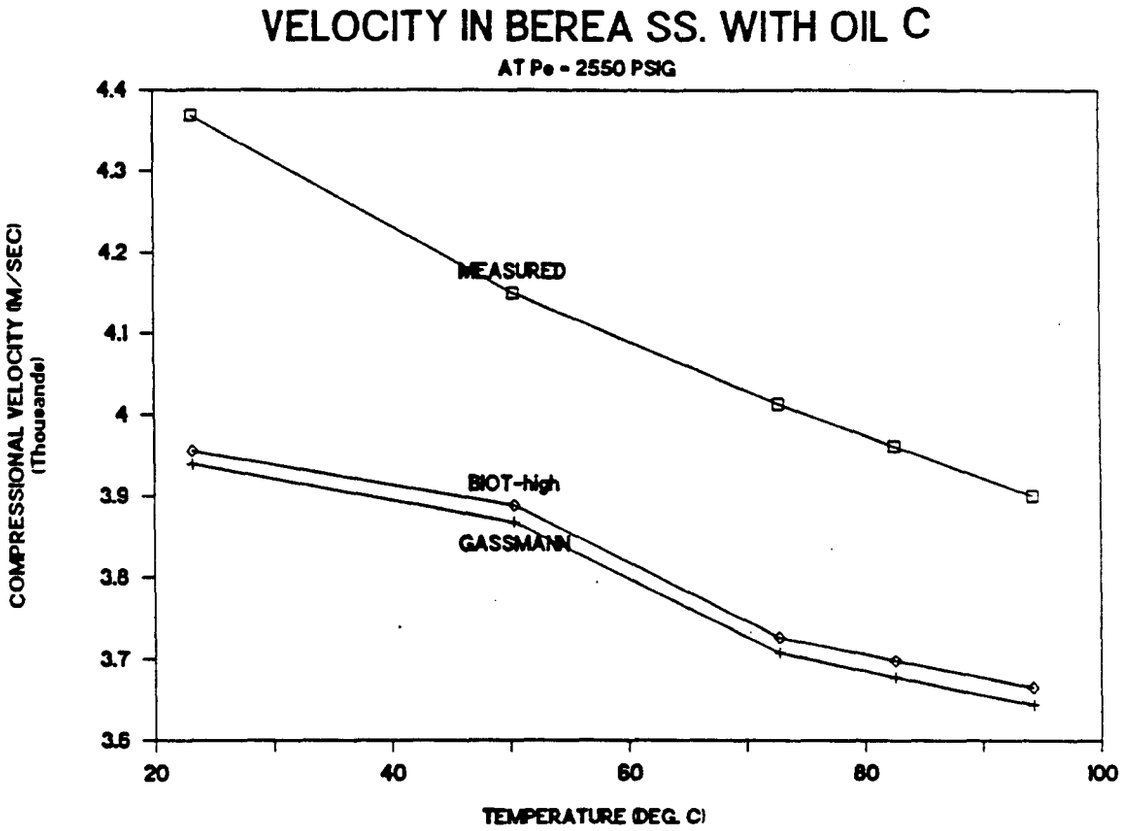
VELOCITY IN BEREA SS. WITH OIL C
AT Pe = 2550 PSIG
COMPRESSIONAL VELOCITY (M/SEC) (Thousands)
4.4
4.3
4.2
4.1
4
3.9
3.8
3.7
3.6
MEASURED
BIOT-high
GASSMANN
20
40
60
80
100
TEMPERATURE (DEG. C)

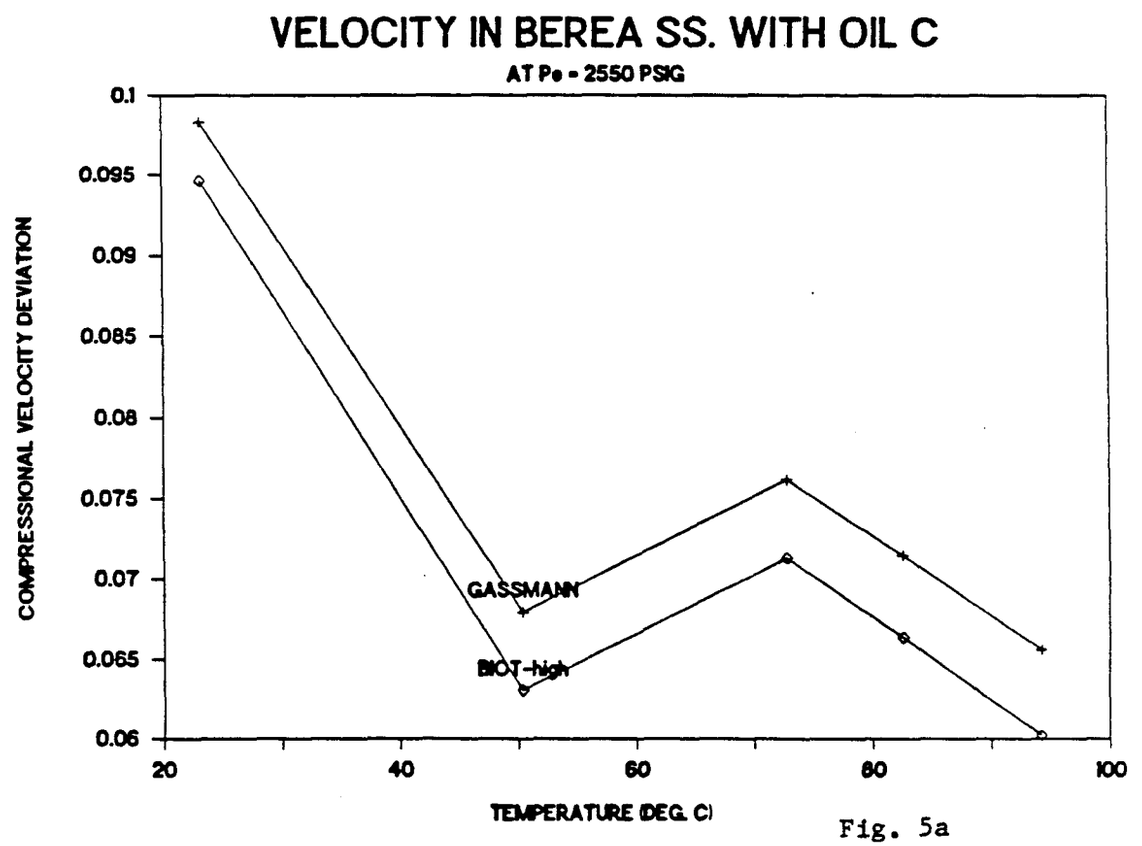
VELOCITY IN BEREA SS. WITH OIL C
AT Pe = 2550 PSIG
COMPRESSIONAL VELOCITY DEVIATION
0.1
0.095
0.09
0.085
0.08
0.075
0.07
0.065
0.06
GASSMANN
BIOT-high
20
40
60
80
100
TEMPERATURE (DEG. C)

Fig. 5a

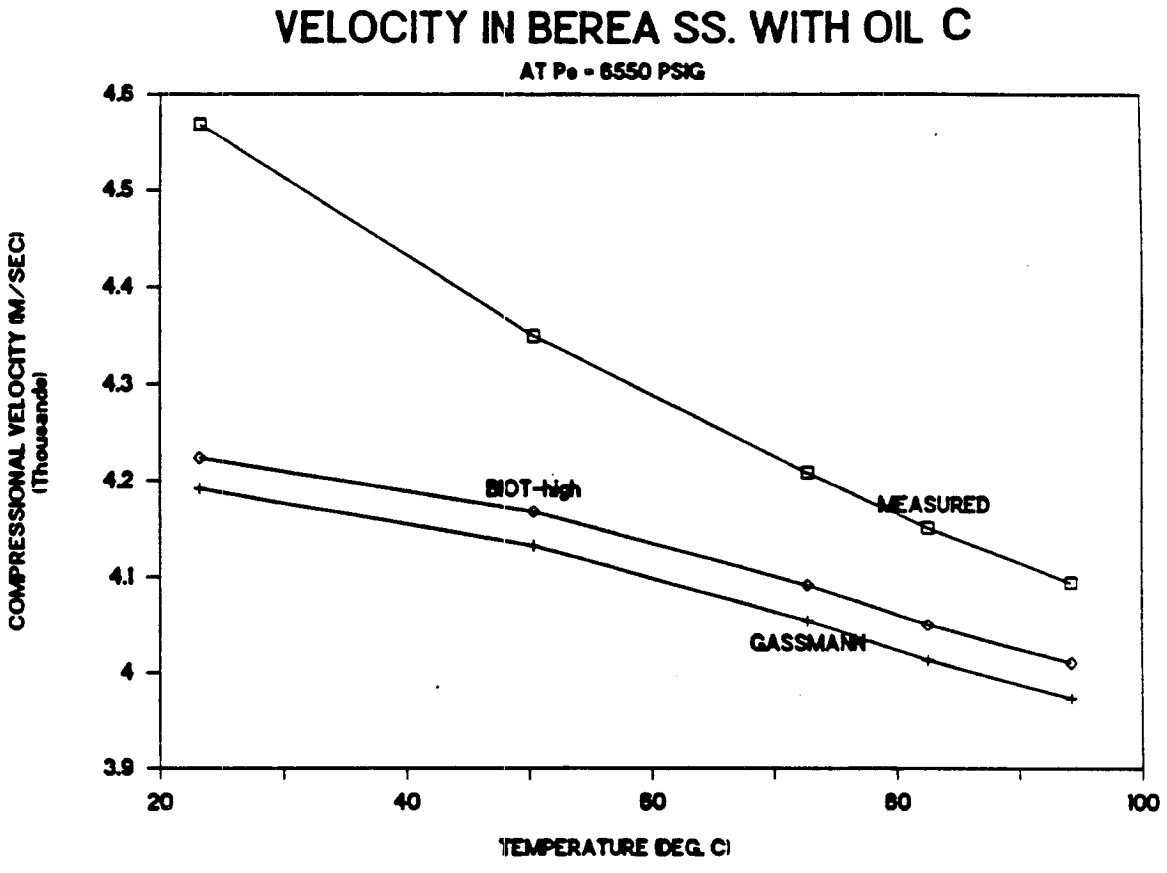
VELOCITY IN BEREA SS. WITH OIL C
AT Pe = 6550 PSIG
COMPRESSIONAL VELOCITY (M/SEC) (Thousands)
4.6
4.5
4.4
4.3
4.2
4.1
4
3.9
BIOT-high
MEASURED
GASSMANN
20
40
60
80
100
TEMPERATURE (DEG. C)

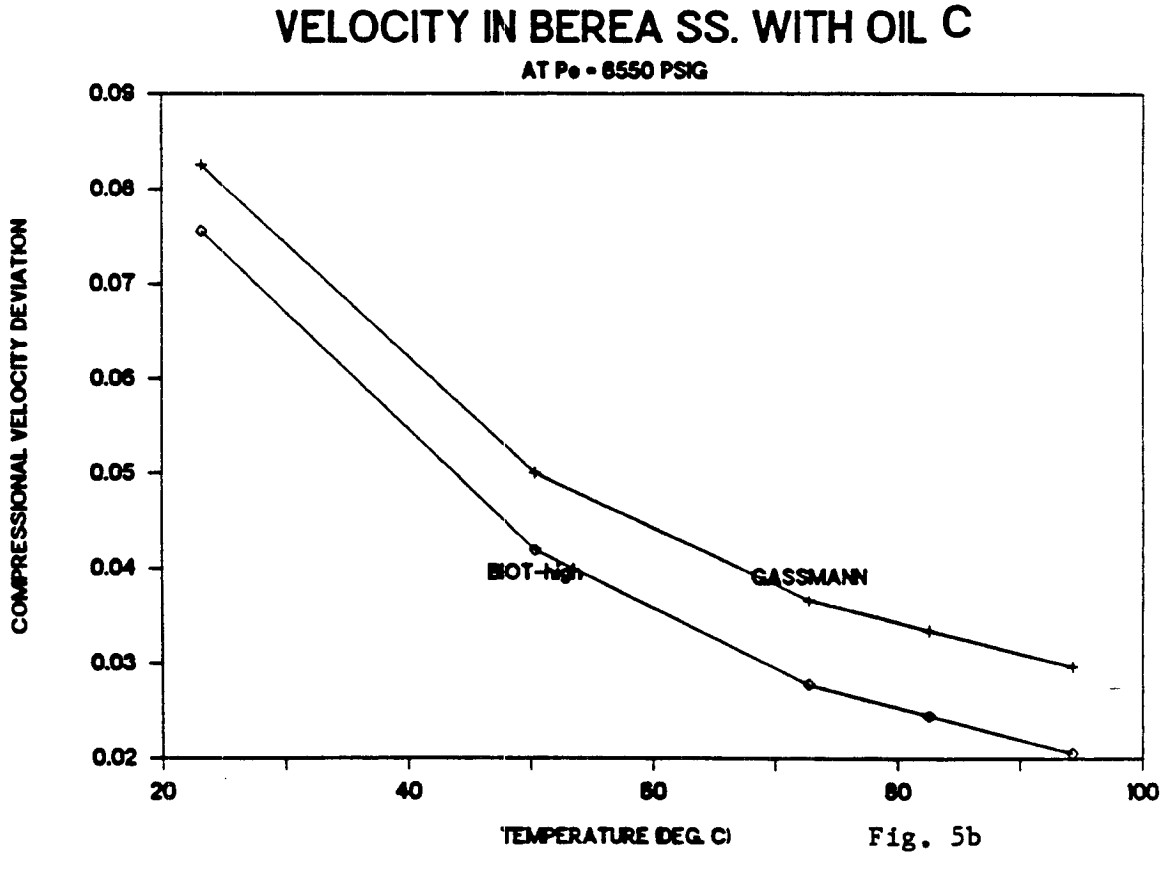
VELOCITY IN BEREA SS. WITH OIL C
AT Pe = 6550 PSIG
COMPRESSIONAL VELOCITY DEVIATION
0.09
0.08
0.07
0.06
0.05
0.04
0.03
0.02
BIOT-high
GASSMANN
20
40
60
80
100
TEMPERATURE (DEG. C)

Fig. 5b

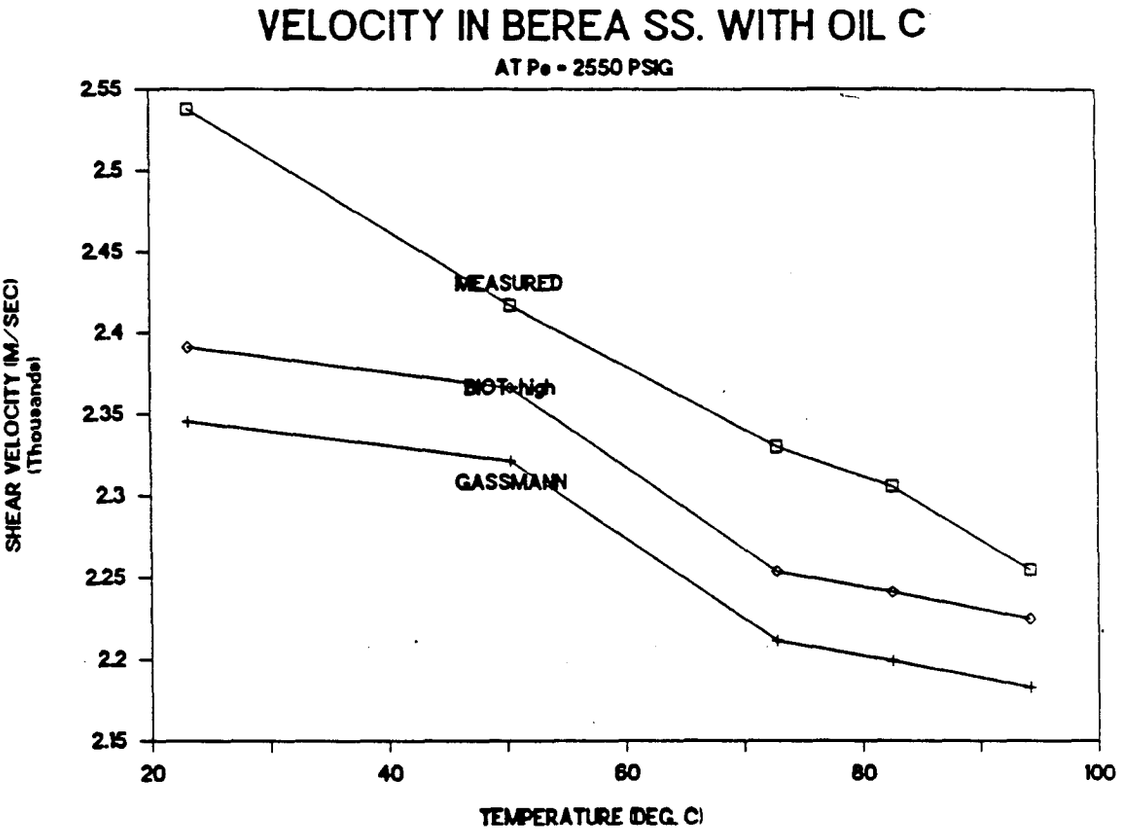
VELOCITY IN BEREA SS. WITH OIL C
AT Pe = 2550 PSIG
SHEAR VELOCITY (M/SEC)
(Thousands)
2.55
2.5
2.45
2.4
2.35
2.3
2.25
2.2
2.15
MEASURED
BIOT-high
GASSMANN
20
40
60
80
100
TEMPERATURE (DEG. C)

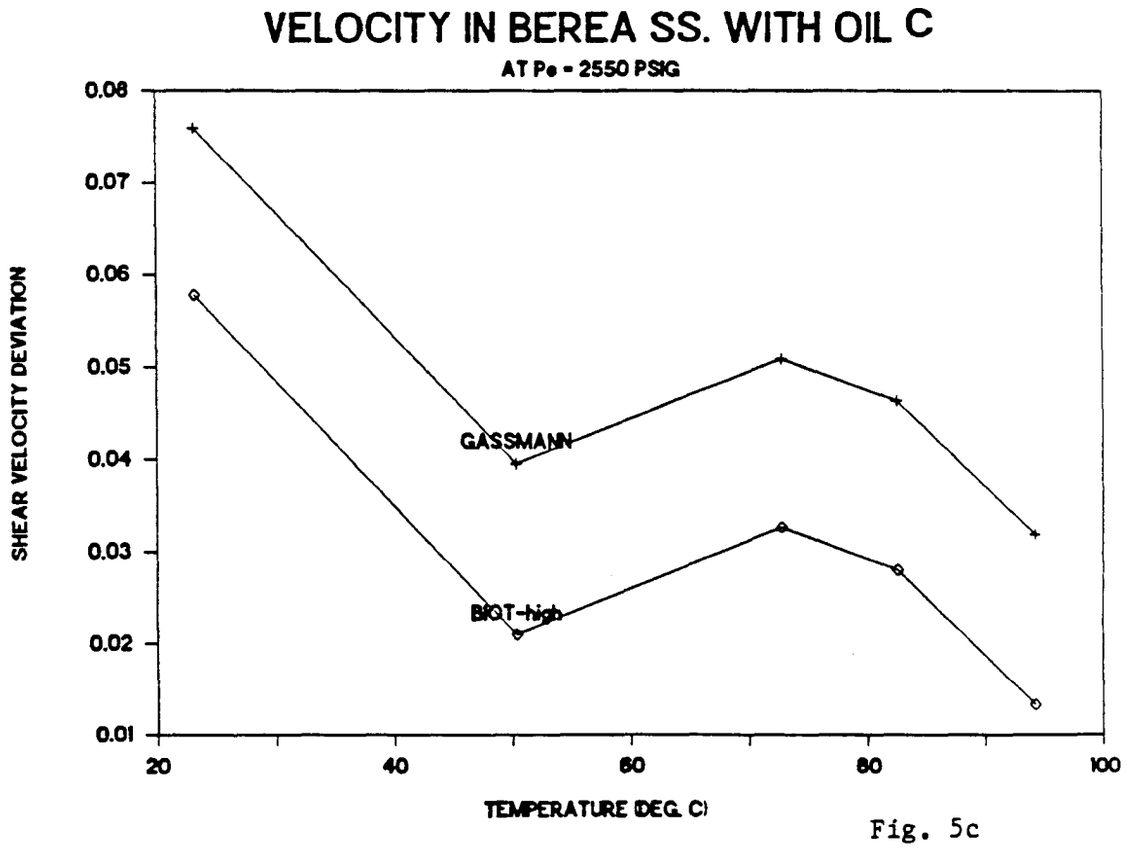
VELOCITY IN BEREA SS. WITH OIL C
AT Pe = 2550 PSIG
SHEAR VELOCITY DEVIATION
0.08
0.07
0.06
0.05
0.04
0.03
0.02
0.01
GASSMANN
BIOT-high
20
40
60
80
100
TEMPERATURE (DEG. C)

Fig. 5c

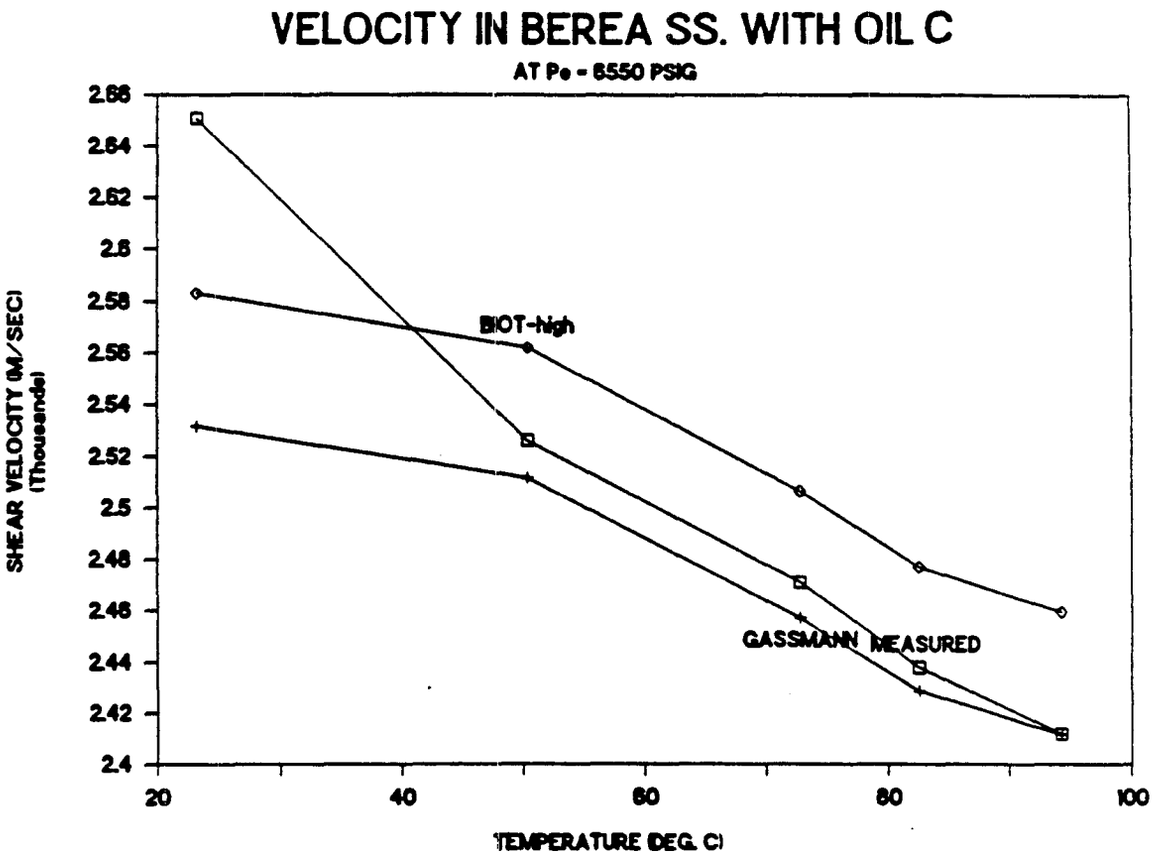
VELOCITY IN BEREA SS. WITH OIL C
AT Pe = 6550 PSIG
SHEAR VELOCITY (M/SEC)
(Thousands)
2.66
2.64
2.62
2.6
2.58
2.56
2.54
2.52
2.5
2.48
2.46
2.44
2.42
2.4
BIOT-high
GASSMANN
MEASURED
20
40
60
80
100
TEMPERATURE DEG. C)

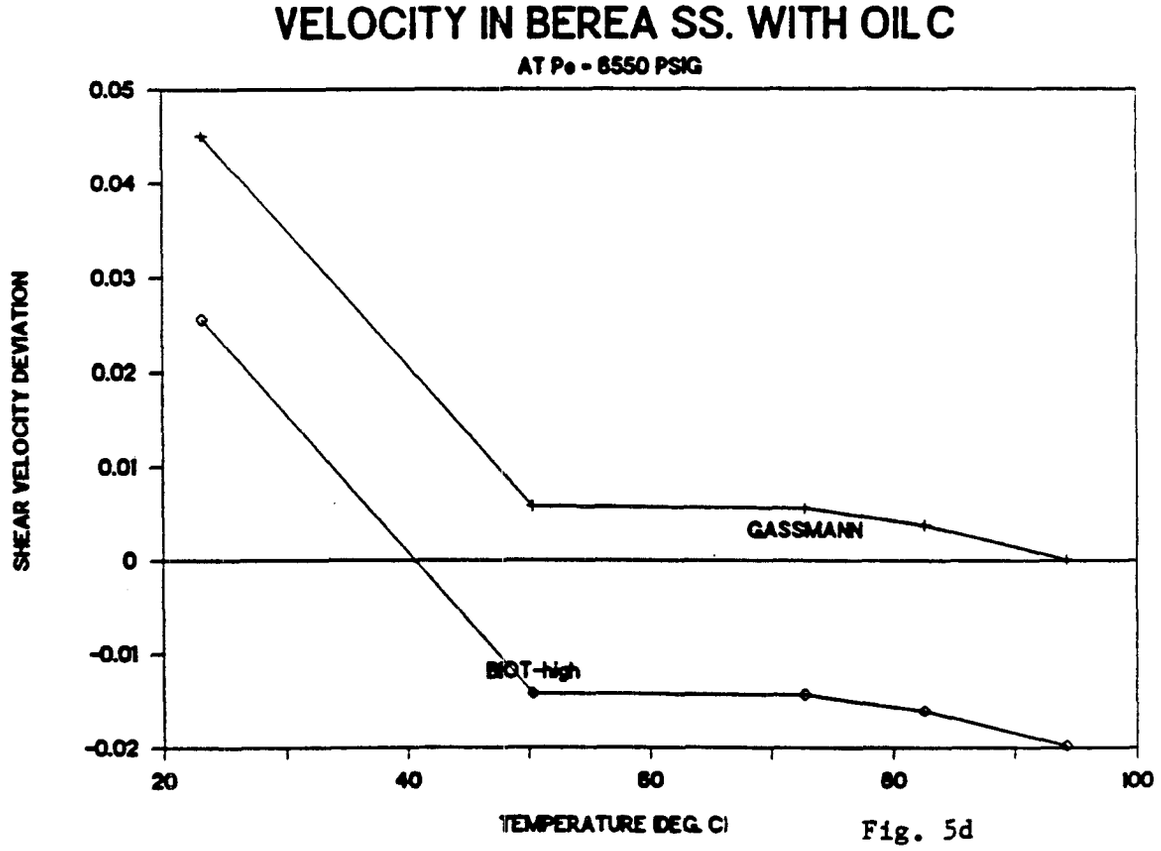
VELOCITY IN BEREA SS. WITH OIL C
AT Pe = 6550 PSIG
SHEAR VELOCITY DEVIATION
0.05
0.04
0.03
0.02
0.01
0
-0.01
-0.02
GASSMANN
BIOT-high
20
40
60
80
100
TEMPERATURE DEG. C)

Fig. 5d

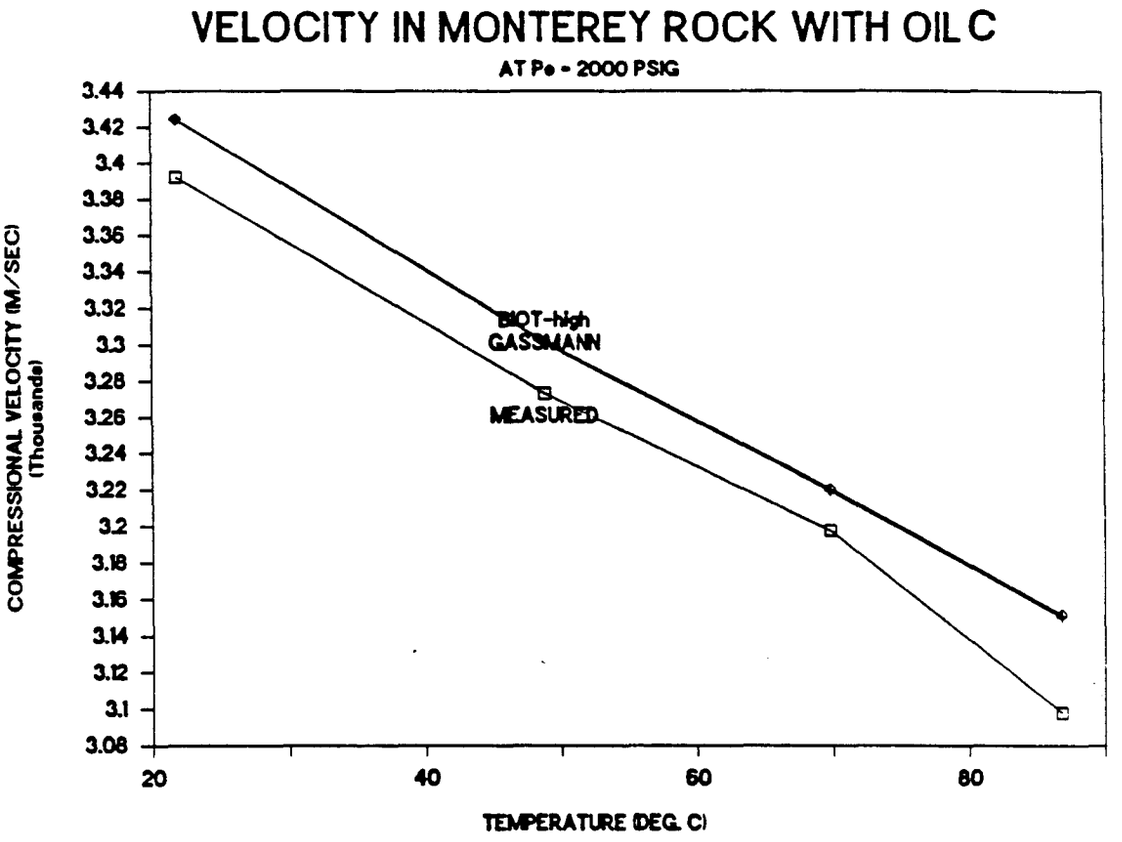
VELOCITY IN MONTEREY ROCK WITH OIL C
AT Pe = 2000 PSIG
COMPRESSIONAL VELOCITY (M/SEC)
(Thousands)
3.44
3.42
3.4
3.38
3.36
3.34
3.32
3.3
3.28
3.26
3.24
3.22
3.2
3.18
3.16
3.14
3.12
3.1
3.08
BIOT-high
GASSMANN
MEASURED
20
40
60
80
TEMPERATURE (DEG. C)

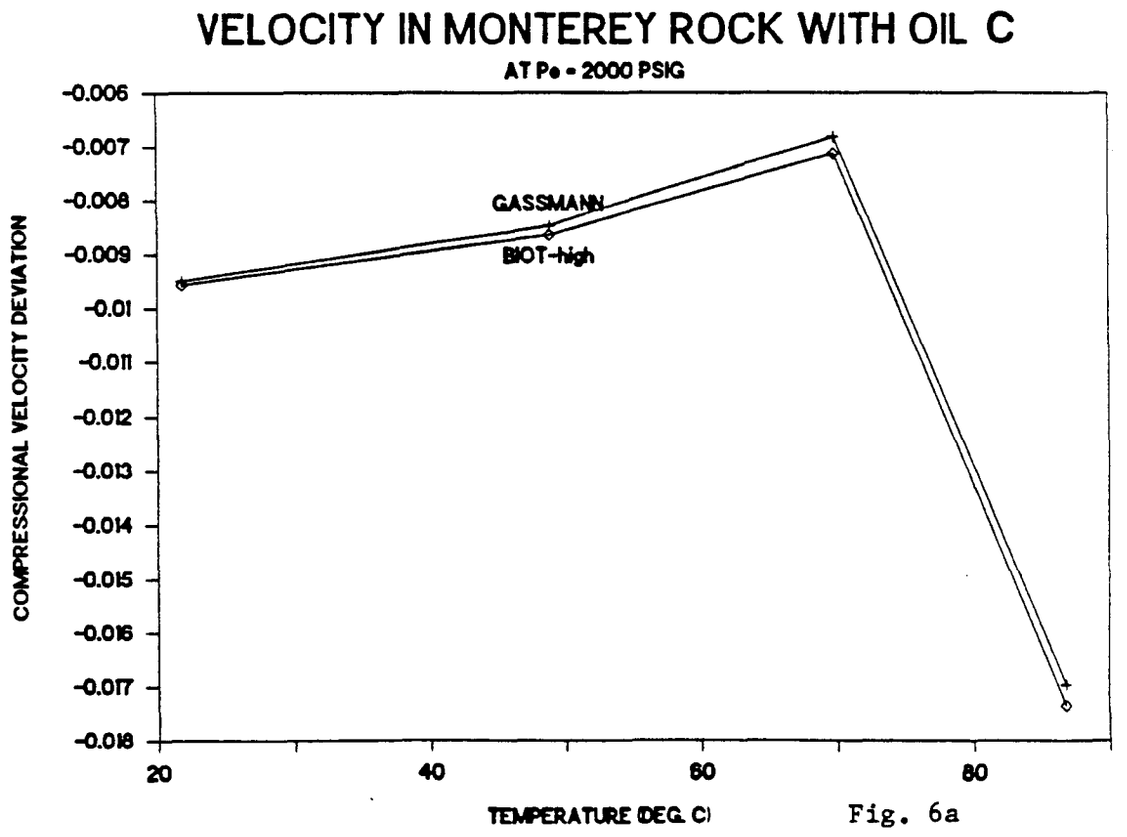
VELOCITY IN MONTEREY ROCK WITH OIL C
AT Pe = 2000 PSIG
COMPRESSIONAL VELOCITY DEVIATION
-0.006
-0.007
-0.008
-0.009
-0.01
-0.011
-0.012
-0.013
-0.014
-0.015
-0.016
-0.017
-0.018
GASSMANN
BIOT-high
20
40
60
80
TEMPERATURE (DEG. C)

Fig. 6a

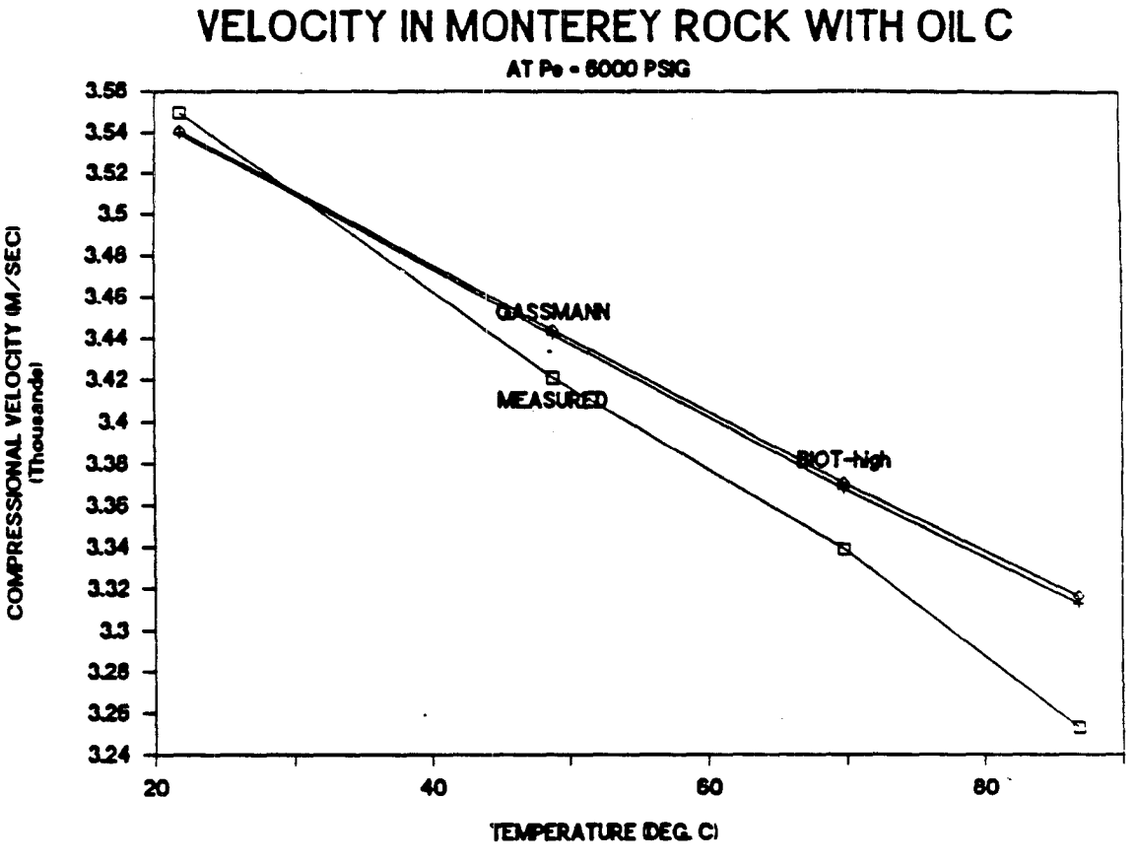
VELOCITY IN MONTEREY ROCK WITH OIL C
AT Pe = 6000 PSIG
COMPRESSIONAL VELOCITY (M/SEC)
(Thousands)
3.56
3.54
3.52
3.5
3.48
3.46
3.44
3.42
3.4
3.38
3.36
3.34
3.32
3.3
3.28
3.26
3.24
GASSMANN
MEASURED
BIOT-high
20
40
60
80
TEMPERATURE (DEG. C)

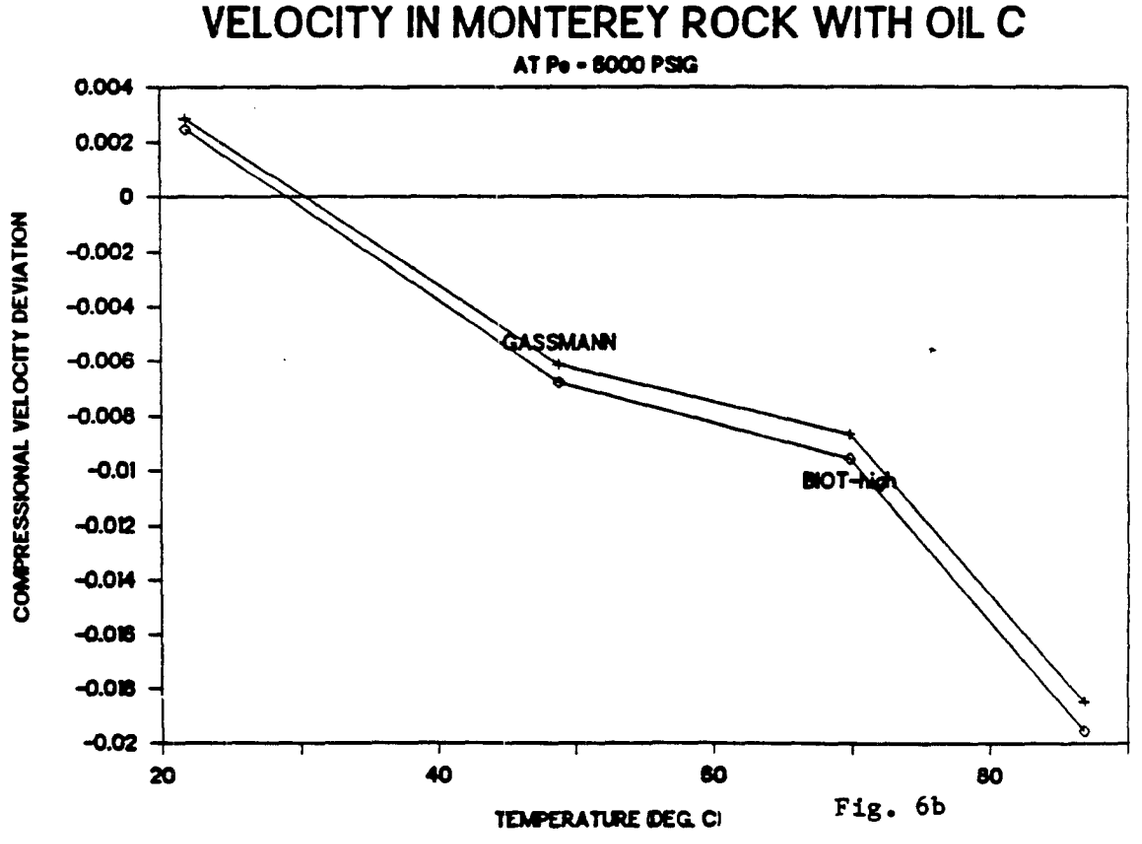
VELOCITY IN MONTEREY ROCK WITH OIL C
AT Pe = 6000 PSIG
COMPRESSIONAL VELOCITY DEVIATION
0.004
0.002
0
-0.002
-0.004
-0.006
-0.008
-0.01
-0.012
-0.014
-0.016
-0.018
-0.02
GASSMANN
BIOT-high
20
40
60
80
TEMPERATURE (DEG. C)

Fig. 6b

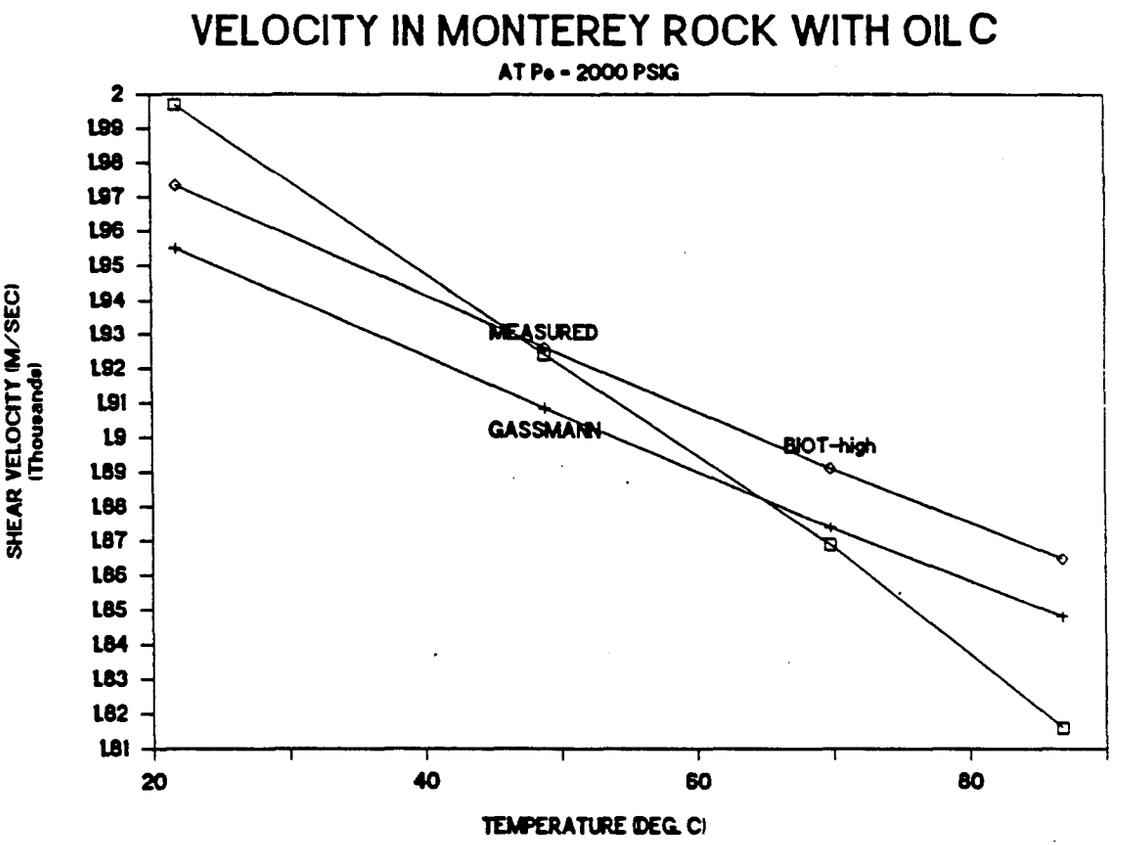
VELOCITY IN MONTEREY ROCK WITH OIL C
AT Pe = 2000 PSIG
SHEAR VELOCITY (M/SEC)
(Thousands)
2
1.99
1.98
1.97
1.96
1.95
1.94
1.93
1.92
1.91
1.9
1.89
1.88
1.87
1.86
1.85
1.84
1.83
1.82
1.81
MEASURED
GASSMANN
BIOT-high
20
40
60
80
TEMPERATURE (DEG. C)

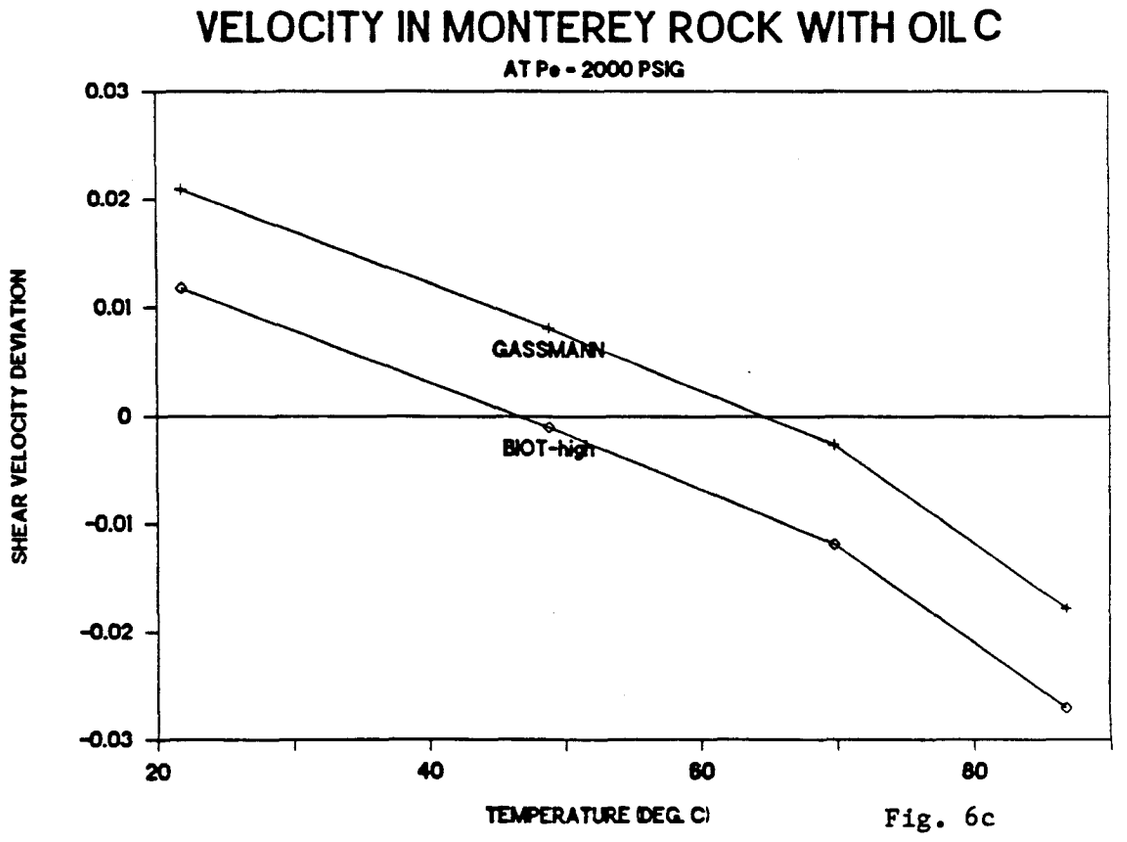
VELOCITY IN MONTEREY ROCK WITH OIL C
AT Pe = 2000 PSIG
SHEAR VELOCITY DEVIATION
0.03
0.02
0.01
0
-0.01
-0.02
-0.03
GASSMANN
BIOT-high
20
40
60
80
TEMPERATURE (DEG. C)

Fig. 6c

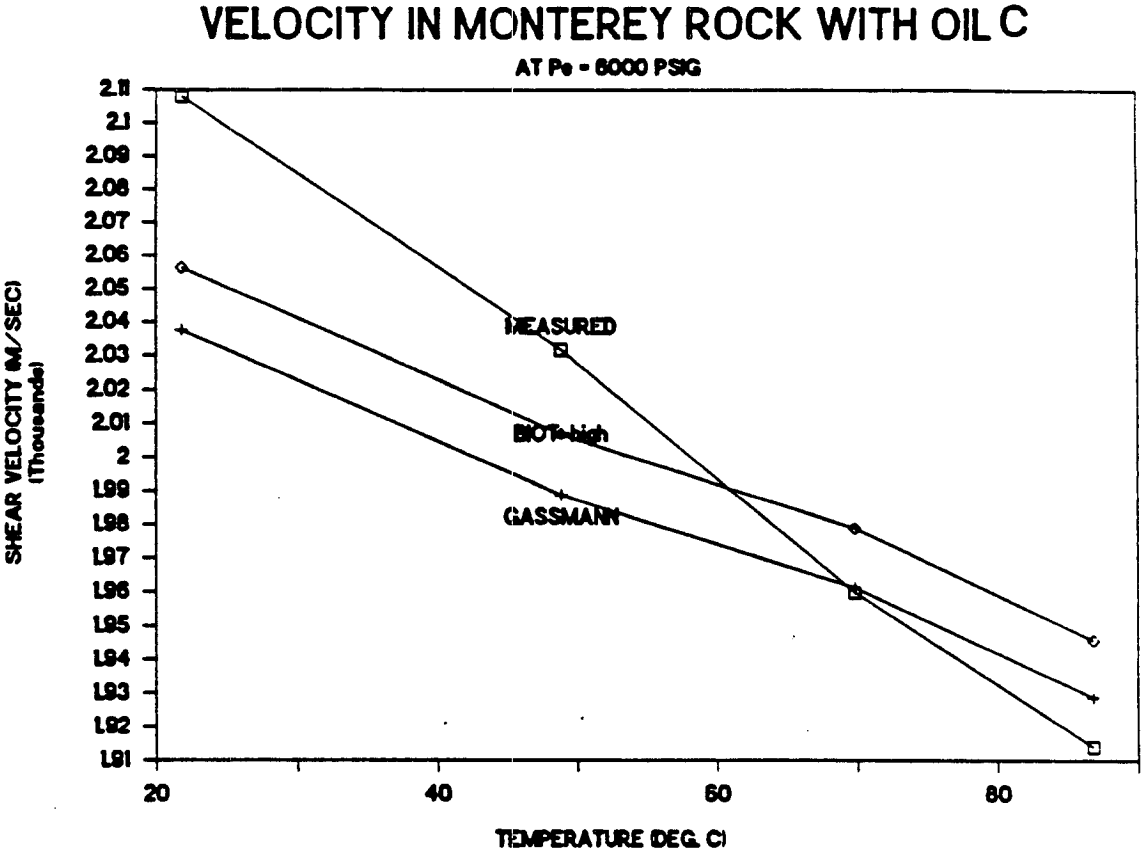
VELOCITY IN MONTEREY ROCK WITH OIL C
AT Pe = 6000 PSIG
SHEAR VELOCITY (M/SEC)
(Thousands)
2.11
2.1
2.09
2.08
2.07
2.06
2.05
2.04
2.03
2.02
2.01
2
1.99
1.98
1.97
1.96
1.95
1.94
1.93
1.92
1.91
MEASURED
BIOT-high
GASSMANN
20
40
60
80
TEMPERATURE (DEG. C)

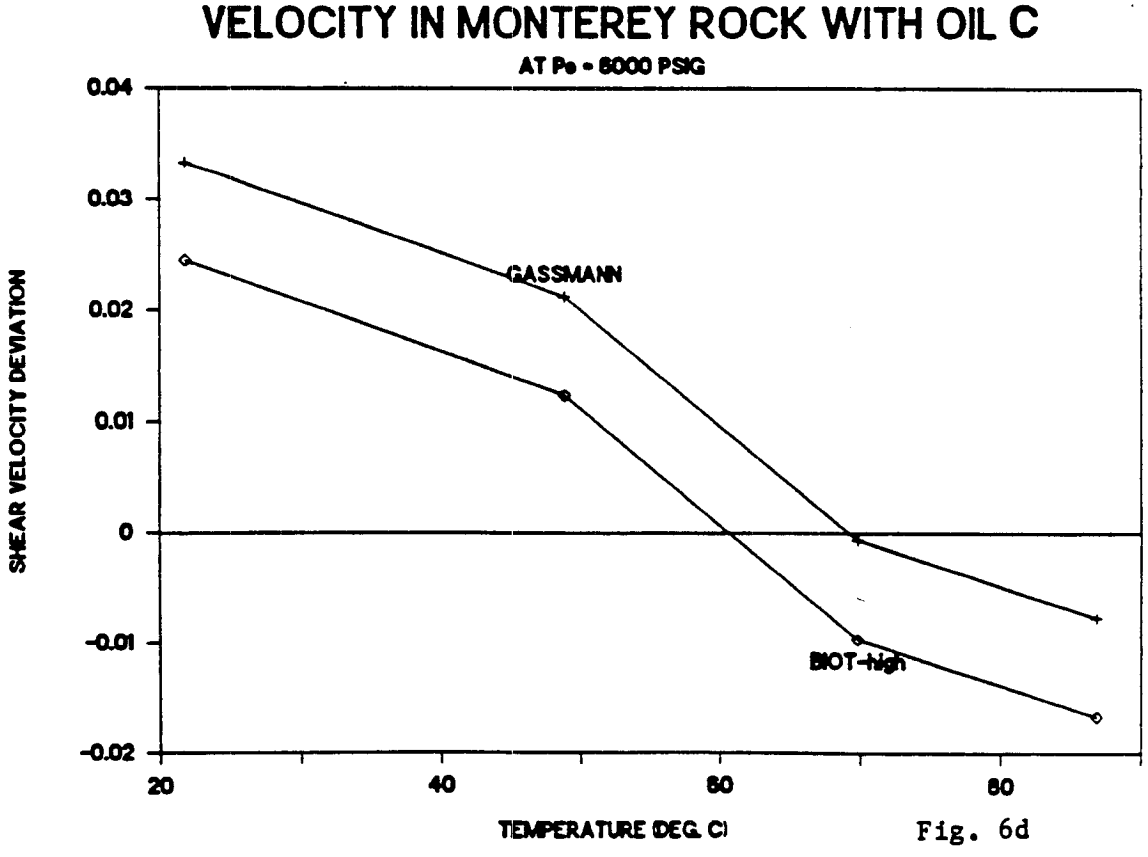
VELOCITY IN MONTEREY ROCK WITH OIL C
AT Pe = 6000 PSIG
SHEAR VELOCITY DEVIATION
0.04
0.03
0.02
0.01
0
-0.01
-0.02
GASSMANN
BIOT-high
20
40
60
80
TEMPERATURE (DEG. C)

Fig. 6d

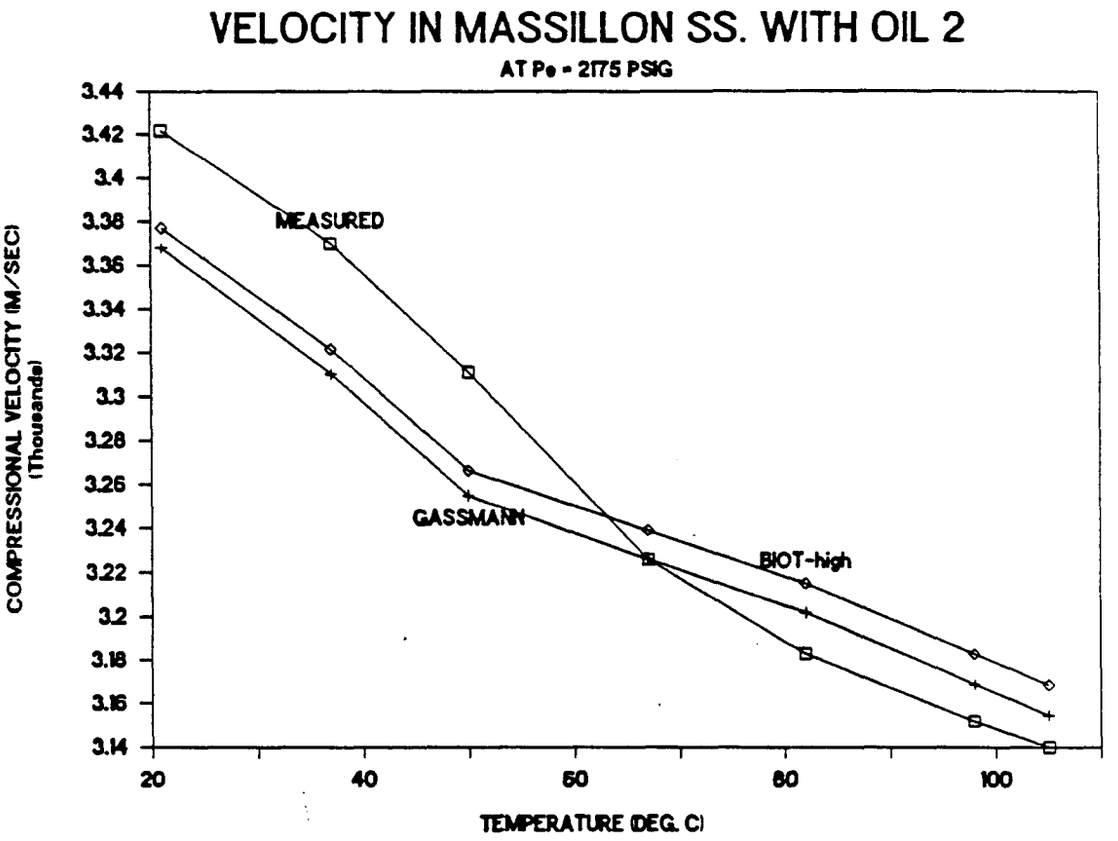
VELOCITY IN MASSILLON SS. WITH OIL 2
AT Pe = 2175 PSIG
COMPRESSIONAL VELOCITY (M/SEC)
(Thousands)
3.44
3.42
3.4
3.38
3.36
3.34
3.32
3.3
3.28
3.26
3.24
3.22
3.2
3.18
3.16
3.14
MEASURED
GASSMANN
BIOT-high
20
40
60
80
100
TEMPERATURE (DEG. C)

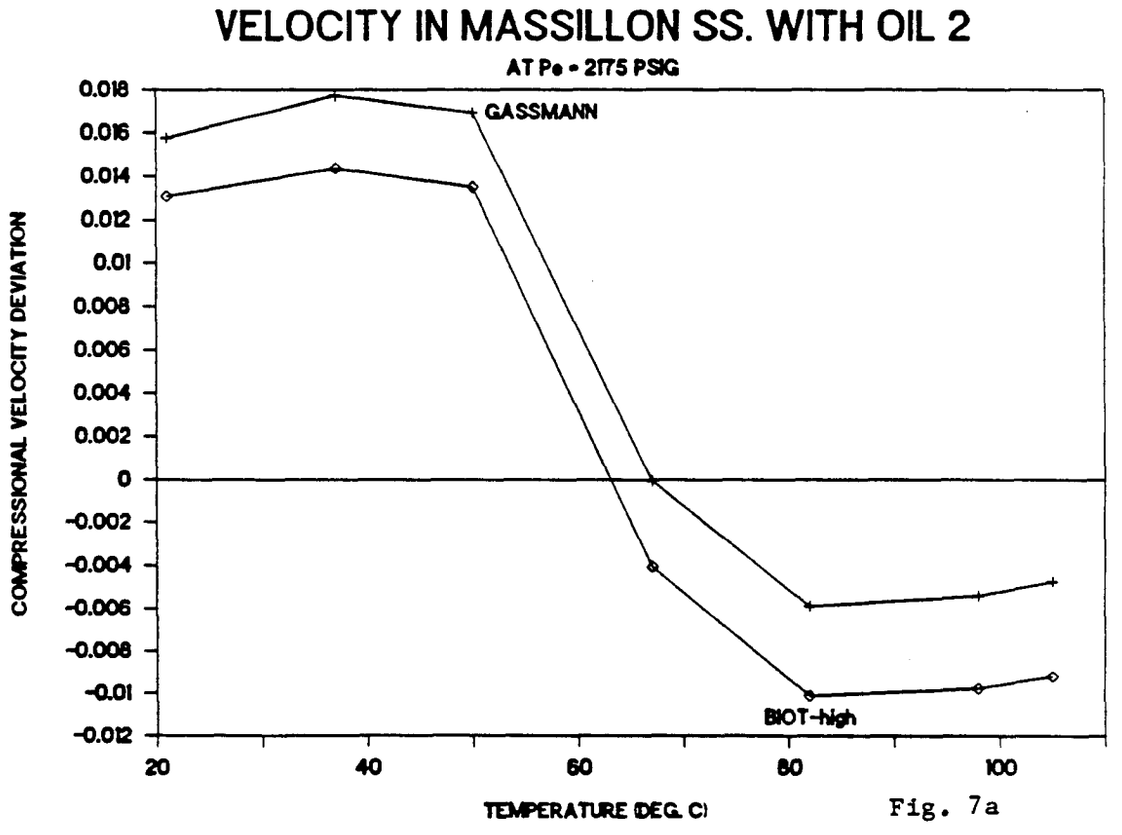
VELOCITY IN MASSILLON SS. WITH OIL 2
AT Pe = 2175 PSIG
COMPRESSIONAL VELOCITY DEVIATION
0.018
0.016
0.014
0.012
0.01
0.008
0.006
0.004
0.002
0
-0.002
-0.004
-0.006
-0.008
-0.01
-0.012
GASSMANN
BIOT-high
20
40
60
80
100
TEMPERATURE (DEG. C)

Fig. 7a

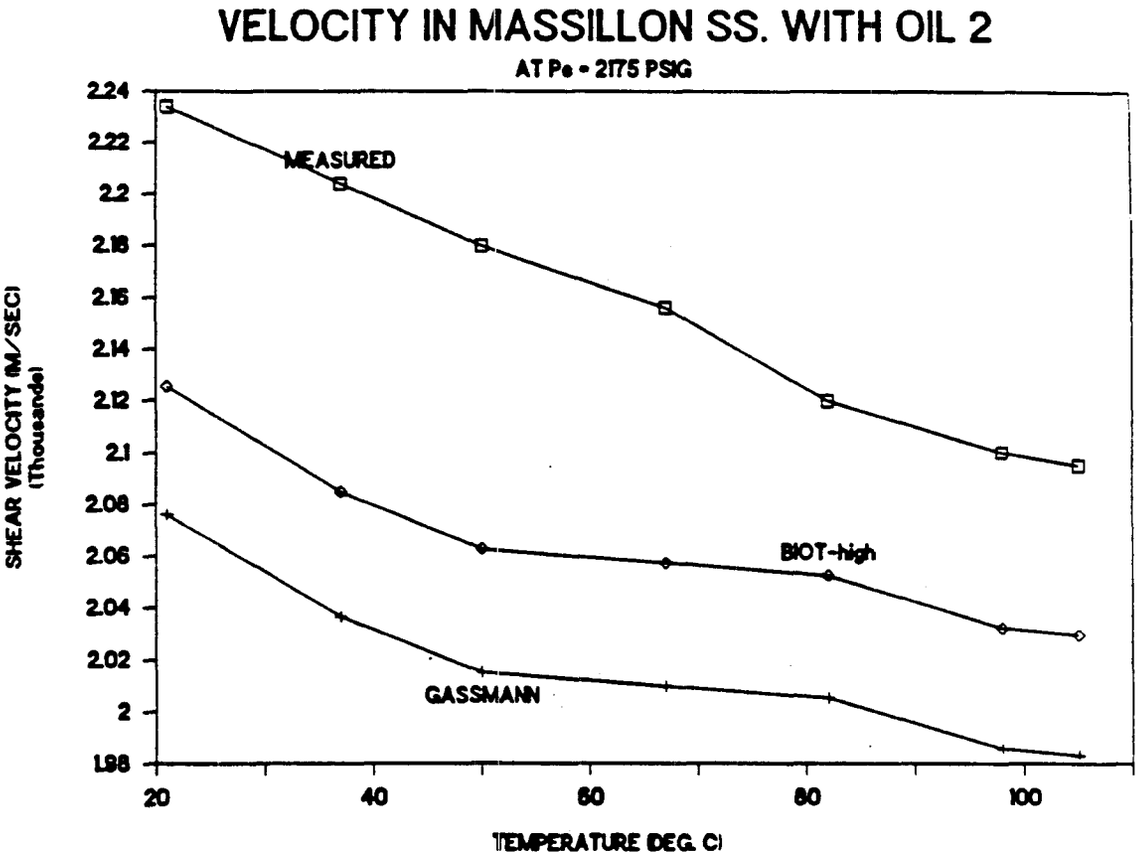
VELOCITY IN MASSILLON SS. WITH OIL 2
AT Pe = 2175 PSIG
SHEAR VELOCITY (M/SEC)
(Thousands)
2.24
2.22
2.2
2.18
2.16
2.14
2.12
2.1
2.08
2.06
2.04
2.02
2
1.98
MEASURED
BIOT-high
GASSMANN
20
40
60
80
100
TEMPERATURE DEG. C)

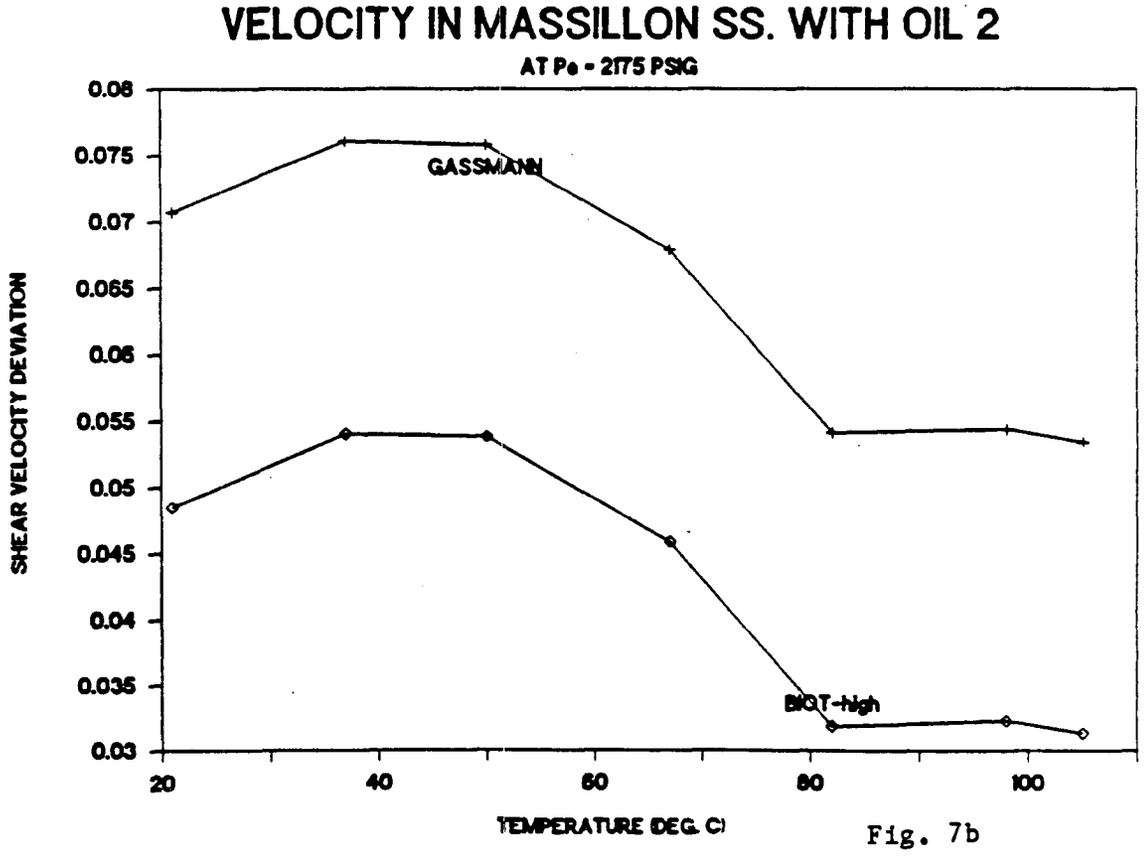
VELOCITY IN MASSILLON SS. WITH OIL 2
AT Pe = 2175 PSIG
SHEAR VELOCITY DEVIATION
0.08
0.075
0.07
0.065
0.06
0.055
0.05
0.045
0.04
0.035
0.03
GASSMANN
BIOT-high
20
40
60
80
100
TEMPERATURE DEG. C)

Fig. 7b

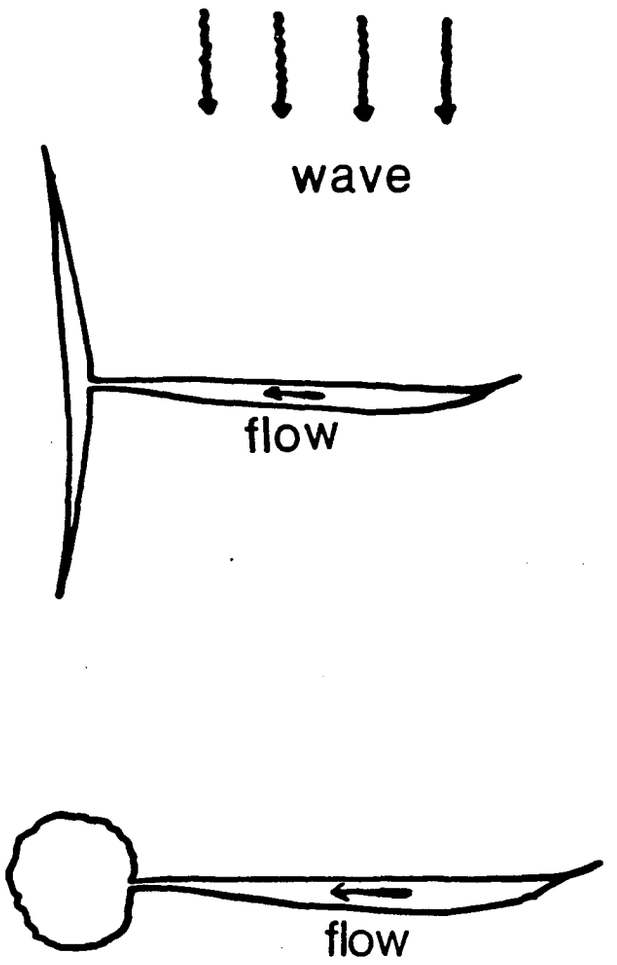

Fig. 8

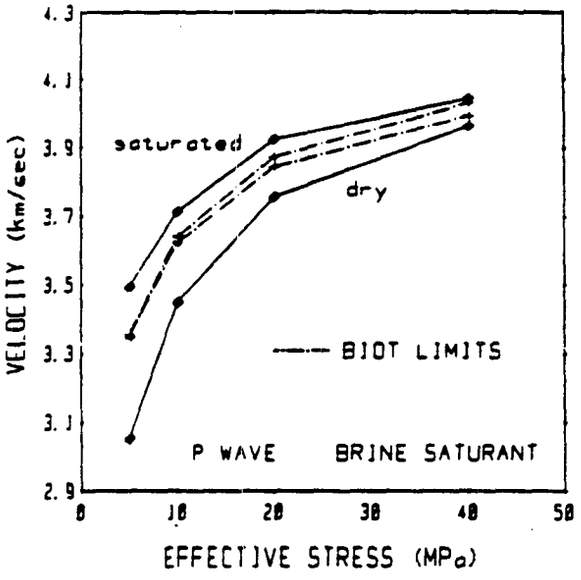

Compressional phase velocity as function of effective stress in Berea sandstone. Data are shown for dry and brine-saturated samples at 400 kHz. Biot low- and high-frequency limits are shown on dashed lines.

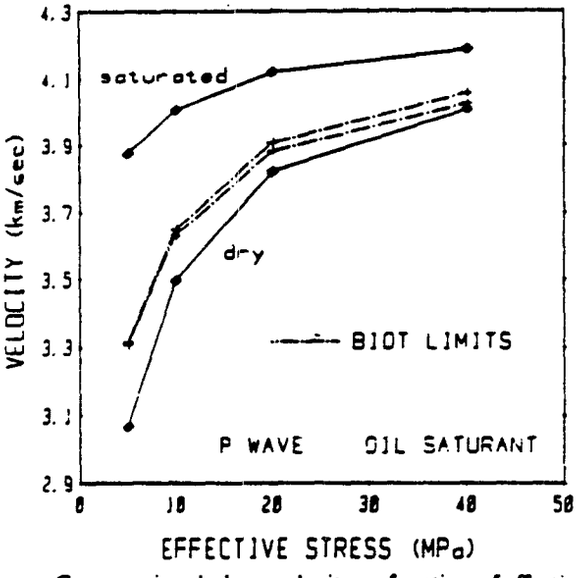

Compressional phase velocity as function of effective stress in Berea sandstone. Data are shown for dry and oil-saturated samples at 400 kHz. Biot low- and high-frequency limits are shown on dashed lines.

Fig. 9

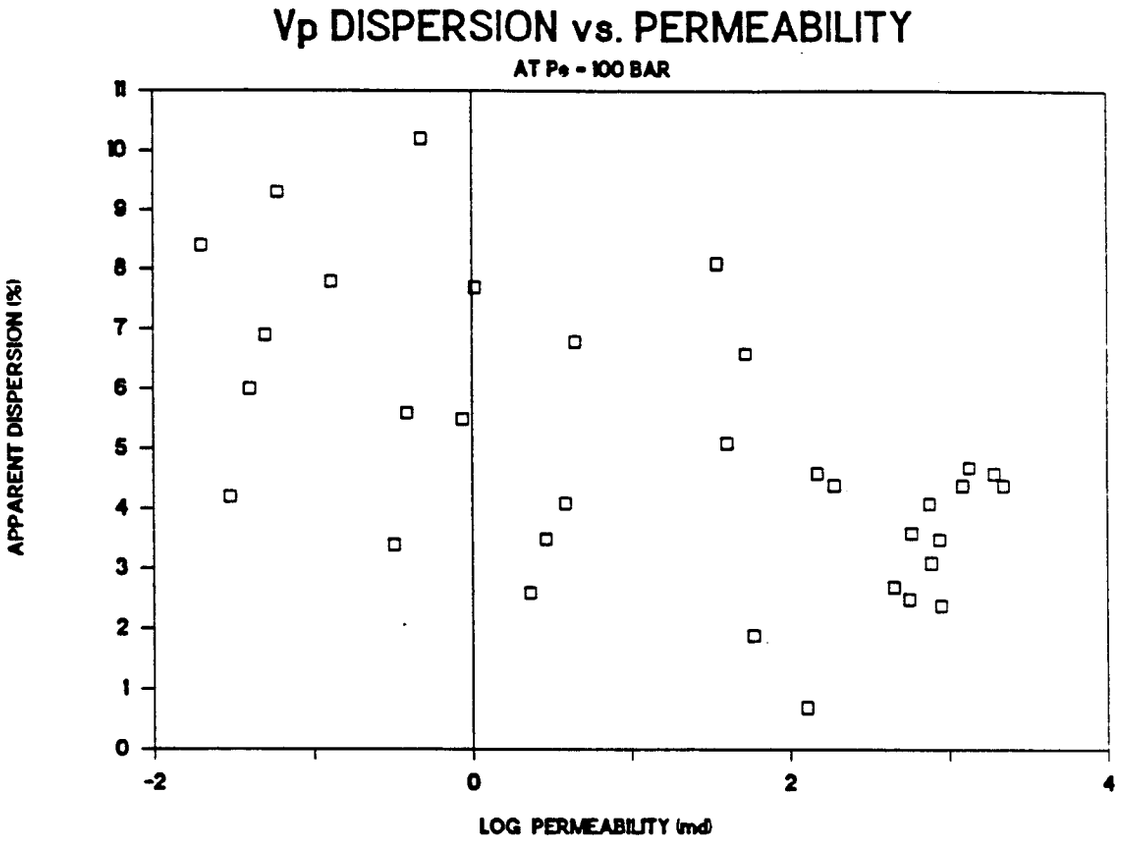
Vp DISPERSION vs. PERMEABILITY
AT Pe = 100 BAR
APPARENT DISPERSION (%)
LOG PERMEABILITY (md)
0
1
2
3
4
5
6
7
8
9
10
11
-2
0
2
4

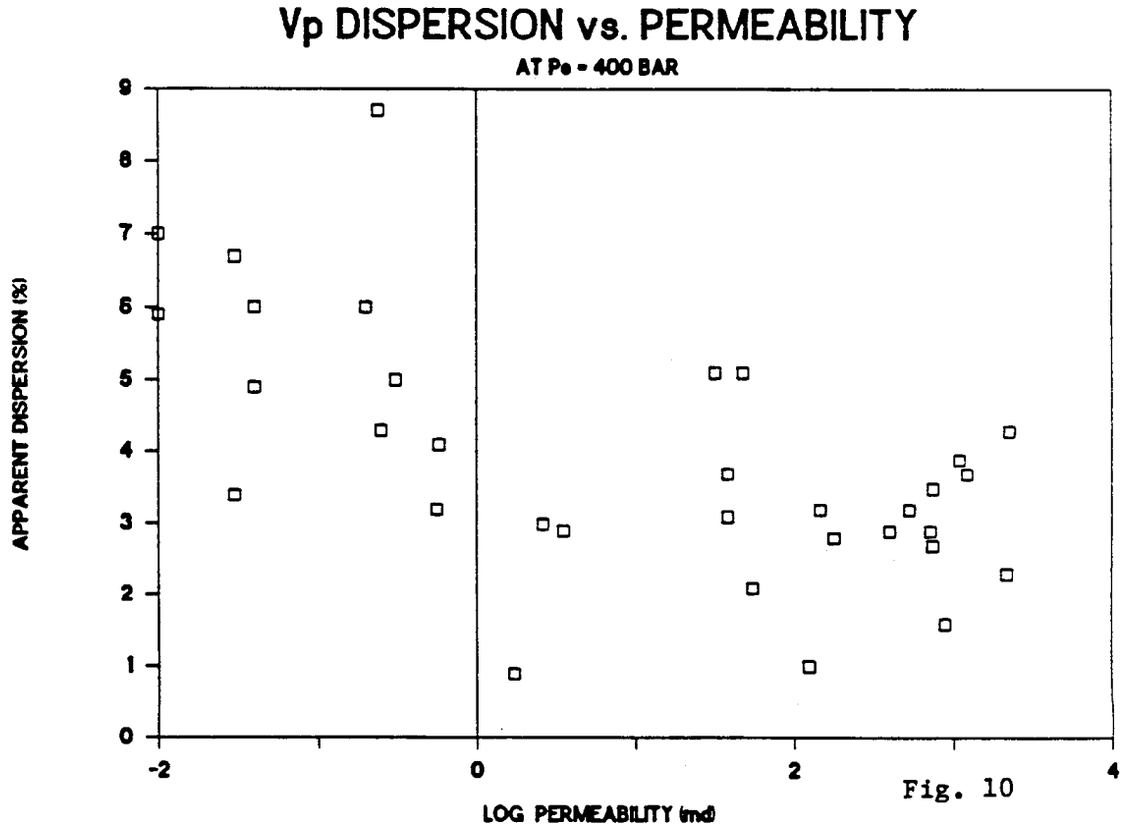
Vp DISPERSION vs. PERMEABILITY
AT Pe = 400 BAR
APPARENT DISPERSION (%)
LOG PERMEABILITY (md)
0
1
2
3
4
5
6
7
8
9
-2
0
2
4

Fig. 10

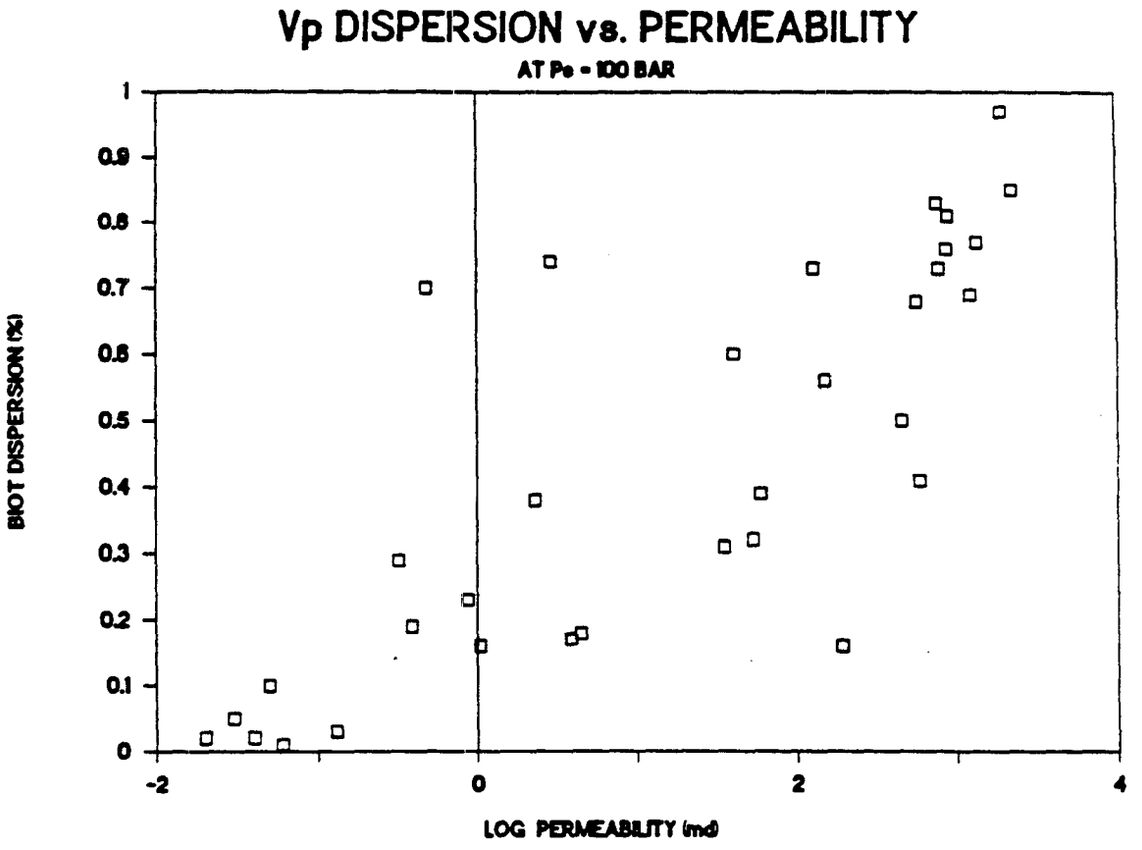
Vp DISPERSION vs. PERMEABILITY
AT Pe = 100 BAR
BIOT DISPERSION (%)
1
0.9
0.8
0.7
0.6
0.5
0.4
0.3
0.2
0.1
0
-2
0
2
4
LOG PERMEABILITY (md)

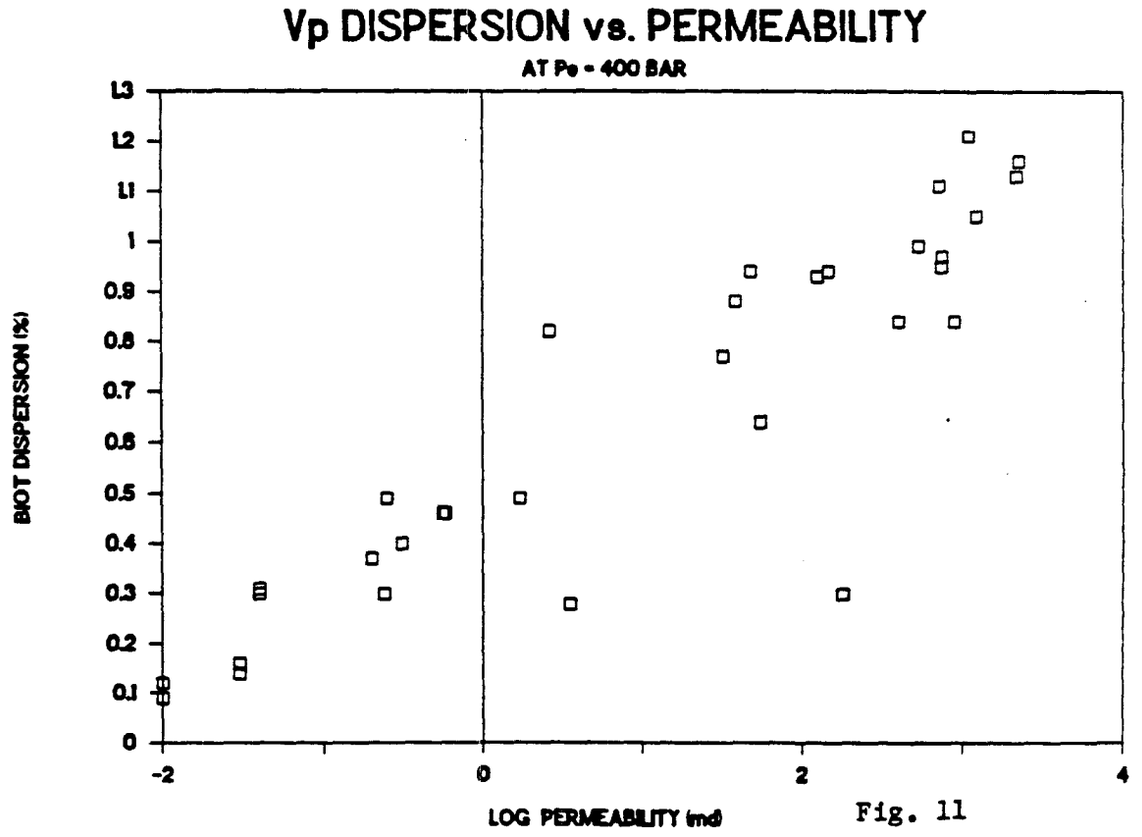
Vp DISPERSION vs. PERMEABILITY
AT Pe = 400 BAR
BIOT DISPERSION (%)
1.3
1.2
1.1
1
0.9
0.8
0.7
0.6
0.5
0.4
0.3
0.2
0.1
0
-2
0
2
4
LOG PERMEABILITY (md)

Fig. 11

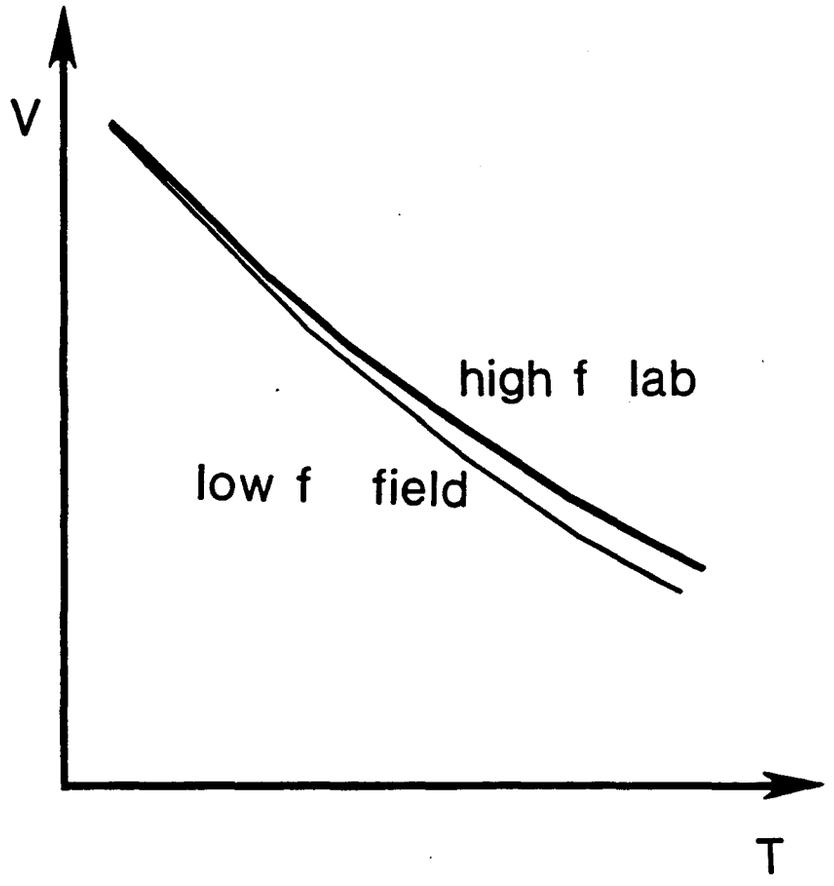

Fig. 12

CHAPTER 9

DISCUSSIONS ON SEISMIC MONITORING EOR AND PRODUCTION PROCESSES

ABSTRACT

This chapter serves as a summary on seismic monitoring various enhanced oil recovery (EOR) and production processes. It discusses factors effecting seismic wave velocities in hydrocarbon reservoirs and the possibilities and petrophysical bases of using seismic methods to monitor various EOR and production processes.

INTRODUCTION

As nearly two-thirds of the original oil in place can not be recovered by conventional recovery methods in most oil reservoirs, methods of enhanced oil recoveries become more and more important. However, success of an EOR process is often dependent on whether it is effectively controlled. For example, during an EOR process, field engineers often need to modify the EOR process, to adjust the rate and pressure of the injection, to change the viscosity of the fluids to be injected, and/or even to shut in some injection well(s) in order to get better oil sweep efficiency and to prevent early break-through of the injected fluids. That is to say, effective methods for monitoring EOR processes are apparently needed.

Chemical tracers have been widely used in monitoring fluid break-throughs in EOR processes, but, as mentioned earlier in chapter 6, they may cause polymerization of reservoir fluids and thus chemical precipitations. Such chemical precipitations in turn may reduce the effective permeability of the reservoir rocks. Moreover, chemical

tracers can not provide information regarding the degree of oil saturation of reservoir rocks and the position of the front of the injected fluids before they reach the monitor well(s).

In contrast to the method of chemical tracers, seismic methods are very promising in monitoring various EOR processes. And the advantages of such methods are obvious: (1) They do not cause precipitations of reservoir fluids; (2) They are economical since seismic data acquisition and processing are both routine; (3) They do not require shut-in wells (except borehole seismic methods) and cause damage to wells and formations.

Whether seismic methods can be used to monitor an EOR process mainly depends on that if the seismic wave velocities and/or amplitudes are affected by such process, besides the resolution of the seismic methods. Amplitude changes of seismic waves are more difficult to measure accurately both in the laboratory and in the field. But in the future, with the rapid development of geophysical technologies, both amplitude and velocity changes will certainly be measured with great accuracy in seismic surveys. Nevertheless, our discussions in this chapter are mainly based on the velocity changes caused by EOR processes.

Velocity changes of seismic waves in hydrocarbon reservoirs may be caused by:

(1). Temperature changes and vapor appearance in thermal EOR processes such as steam flooding, in-situ combustion, and hot water injection. Both increase in reservoir temperature and vapor appearance decrease the velocities.

(2). Compressibility changes of the pore fluid in the processes of CO_2 flooding and gas drive. In such processes, CO_2, Nitrogen gas, or light hydrocarbon gas displace liquid hydrocarbons in the pore space, which causes the compressibility of the reservoir rock to increase and thus the seismic wave velocity to decrease.

(3). Pore pressure changes which occur in all the EOR processes involving fluid injections. The injected fluids usually cause high pore pressure zones in which

seismic waves travels with lower velocities.

(4). Production processes such as water intrusion and gas-cap appearance or disappearance.

In this chapter, we discuss how the above factors affect seismic wave velocities in hydrocarbon reservoirs, and the possibilities and petrophysical bases of using seismic methods to monitor various EOR processes.

EOR RELATED TO TEMPERATURE CHANGES

One of the problems faced by a variety of EOR schemes is the need to determine, with accuracy yet not possible, the spatial distribution of reservoir properties and their changes with time. In thermal EOR, it is especially important to try to determine the direction of propagation and details of the shape, rate of movement and spatial heterogeneity of the fire or steam fronts. To accomplish such determinations we ideally would like to continuously monitor reservoirs throughout their volume, using remote seismic methods.

Increased temperature by thermal EOR such as steam flooding and in-situ combustion decreases seismic wave velocities in reservoir rocks, as shown in the previous chapters. Fast temperature increase of the reservoir subjecting in-situ combustion also causes partial gas saturation and thermal cracking of the reservoir rocks, which further decreases seismic wave velocities.

The velocity decreases in turn will cause travel time delay of the seismic waves. Figure 1, taken from Britton et al (1983), shows the effect of such velocity decreases in the heated zone around the injection well of steam. A conventional seismic survey was done to map the steam-flooded zones at the Street Ranch pilot, Texas. The seismic section clearly shows travel time delay and changes in wavelet shape around the injection well. As the distance increases from the injection well, such anomalies decrease as a result of decrease in temperature. The seismic section also shows that the injected

steam flows with different speed in different directions, which suggests permeability heterogeneities of the reservoir rocks.

Greaves and Fulp (1987) reported that a 3-D seismic reflection method was used to monitor the progress of an in-situ combustion EOR process. The resulting "different volume" of 3-D seismic data showed anomalies in association with the development of "bright spot" and "dim spot". Such anomalies are apparently caused by the temperature increases and thus velocity decreases in the reservoir rocks; the increased gas saturation along the top of the reservoir boundary which decreases both the compressional wave velocity and the density, and hence the impedance; and attenuation increases in association with the high temperature alterations of the reservoir rocks.

In both seismic surveys mentioned above, the shape, orientation, and volume of the heated zones interpreted from the seismic data were confirmed by temperature monitor wells and post-burn coring.

Recent seismic measurements before and after steam injection were obtained by Macrides et al (1988) for the purpose of delineating the fluid-invaded zone. The experiment, despite its limited temporal and spatial sampling, showed significant changes in seismic signiture after steam injection. The received seismic wave signals traveled through the steam-invaded zone are clearly delayed duo to the lowered velocities.

All in all, both our laboratory results and field experiments of others have proven that seismic methods can be used in monitoring thermal EOR processes. Field activities in such exercises are fast increasing. For instance, Pullin et al (1987) recently reported some techniques applied to obtain very high resolution 3-D seismic imaging at an Athabasca tar sands thermal pilot. The primary purpose of their survey is to use the high resolution 3-D seismic results as a basis of comparison with future surveys of a similar type in order to locate and monitor the progress of in-situ heat movement. There is little doubt that such seismic surveys will become routine in the very near future to probe and track reservoir production and EOR processes of complex oil fields.

EOR RELATED TO PORE FLUID COMPRESSIBILITY CHANGES

CO_2 Flooding. In CO_2 flooding, the injected CO_2 displaces hydrocarbons in reservoir rocks. Since CO_2 has very high compressibility even at high pressures and furthermore very high density (see Chapter 6), substitution of CO_2 for the liquid hydrocarbons in the pore space of reservoir rocks increases the compressibility and hence decreases the compressional wave velocity of the rocks. Our laboratory experimental results shown in Chapter 6 revealed that compressional wave velocities in hydrocarbon saturated rocks decreased significantly as the rocks were flooded by CO_2. Such decreases should also take place in-situ upon CO_2 flooding of hydrocarbon reservoirs. Therefore, it was concluded that seismic methods should be very useful for monitoring CO_2 flooding processes in-situ.

Gas Drive. Current technologies of gas drive include using enriched hydrocarbon gas, high pressure hydrocarbon gas, and nitrogen gas to displace oil in reservoir rocks. Since all of these gases are highly compressible, the compressibility of the pore fluid and hence that of the whole rock-fluid aggregate increase significantly after the oils in the rock pores are displaced or partially displaced. As a consequence, the compressional wave velocities in the rock are decreased.

Beside the compressibility increases of the pore fluids caused by the gas drive, high pore pressures generated by the high pressure hydrocarbon gas and nitrogen gas drives also decrease the wave velocities in rocks. These combined effect of gas saturation and high pore pressure certainly gives us possibilities to use seismic methods to monitor EOR processes of gas drives.

Foam Injection. Foams are accumulations of gas bubbles, separated from each other by thin films of liquid. The injection of foam into reservoir rocks saturated with oil creates a large number of resilient interfaces, which exert a piston-like force on the oil. The process is highly efficient since the foam first finds its way into the largest pores. The smaller pores are next invaded, and so on until the entire permeable section

has accepted the foam (Latil, 1980).

The "quality" of the foam is defined as the ratio of the contained gas volume to the total foam volume. Such "quality" in reality can achieve to 0.96, which means that the foam contains large amount of gas. When the reservoir rocks saturated with oil are invaded by the foam, they become partially saturated since some of the oil is displaced, and the compressibility of the rock-fluid aggregate is increased. Hence in seismic survey, the compressional wave velocity is decreased. Therefore it is also possible to use seismic methods to monitor the foam injection process in-situ.

EOR RELATED TO PORE PRESSURE CHANGE

In all EOR processes involving injection, the injected fluids usually generate high pore pressure zones. Laboratory experimental results have proven that high pore pressures decrease both compressional and shear wave velocities in reservoir rocks. Figure 2 taken from Nur and Wang (1987) schematically shows the effect of high pore pressure on wave velocities. Therefore, seismic methods may be also used to detect the high pore pressure bank and track its propagations.

PRODUCTION PROCESS AND WATER FLOODING

Production Process. In hydrocarbon reservoirs which contain saturated gases, after a period of production, gas-caps may form at the top of the reservoirs. In such gas-caps, both seismic wave velocity in and the density of the reservoir rocks are decreased, so that "bright spot" may appear at the interface of the gas-cap and the lower part of the reservoir. Seismic methods can be used to track the movement of the "bright-spot" and as a consequence to monitor production processes.

Water Injection. In hydrocarbon reservoirs with gas-caps, "bright spot" usually appear at the saturation interface of gas and liquid (either oil or water). As the activity of water injection goes on, the injected water lifts and pushes the oil bank toward the

direction of production wells (figure 3). The gas-cap gradually moves also toward the direction of production wells and disappears as more water is injected. In seismic profiles, we would see that the "bright spot" vanishes from the injection well gradually toward the direction of production wells. As more and more water is injected, the "bright spot" would vanish completely. Therefore, seismic methods can be used to monitor water injection processes in-situ as well.

EOR RELATED TO ATTENUATION CHANGES

Although no experimental results have been reported on the effects of various EOR processes on attenuations of seismic waves, it is well doubted that most EOR processes, such as thermal EOR (in-situ combustion, steam flooding), miscible floodings, and immiscible floodings, would have such effects which are measurable in-situ. For example, polymer and surfactant floodings may not have dramatic effects on seismic wave velocities, but they may affect seismic wave attenuations since both polymers and surfactants are usually highly attenuative for seismic waves. Therefore, much work is needed in this aspect.

CONCLUSIONS

The richness of the seismic effects discussed above, and the sensitivity of velocity to reservoir parameters clearly indicate the future direction of reservoir seismology: growing efforts to describe reservoirs in more detail, and monitoring their recovery processes, using high resolution seismic methods. Much of the methodology required remains to be developed. Although 3-D and VSP surveys already contribute significantly to reservoir description, cross-hole tomography and inverted vertical seismic profiles (VSP), using downhole sources and a very large number of surface receives, are just beginning to emerge. With data densities which are much greater than those needed for exploration through rock volumes (reservoirs, production zones.

etc.) which are quite small, it should thus become very practical to use seismic probing routinely in development and production. The velocities and amplitude data obtained can then be converted to desired reservoir parameters, using the effects described in this chapter.

REFERENCES

Britton, M. W., W. L. Martin, R. J. Leibrecht, and R. A. Harmon, 1983. Street Ranch pilot test of fracture-assisted steamflood technology. J. Petro. Tech., vol. 35, 511-522.

Greaves, R. J. and T. J. Fulp, 1987. Three-dimensional seismic monitoring of an enhanced oil recovery process. Geophys., vol. 52, 1175-1187.

Latil, M., 1980. Enhanced oil recovery. Gulf Pub. Co.: Houston.

Macrides, C. G., E. R. Kanasewich, and S. Bharatha, 1988. Multiborehole seismic imaging in steam injection heavy oil recovery projects. Geophys., vol. 53, 65-75.

Nur, A. M. and Z. Wang, 1987. In-situ seismic monitoring EOR: The petrophysical basis. Proc. of the 62nd Annual Tech. Conf. and Exhib., vol. Φ, 307-314.

Pullin, N., L. Matthews, and K. Hirche, 1987. Techniques applied to obtain very high resolution 3-D seismic imaging at an Athabasca tar sands thermal pilot. Geophys.: The Leading Edge. vol. 6, 10-15.

FIGURE CAPTIONS

Figure 1. Conventional seismic survey in a Street Ranch Steamflood pilot. (a). Seismic line and well configurations; (b). Resulting seismic profile; (c). Seismic Anomalies caused by steam flooding (after Britton et al, 1983).

Figure 2. Schematic velocity profiles showing the effect of high pore pressures (after Nur and Wang, 1987).

Figure 3. Sketch of effect of water flooding process on gas-cap movement (after Latil, 1980).

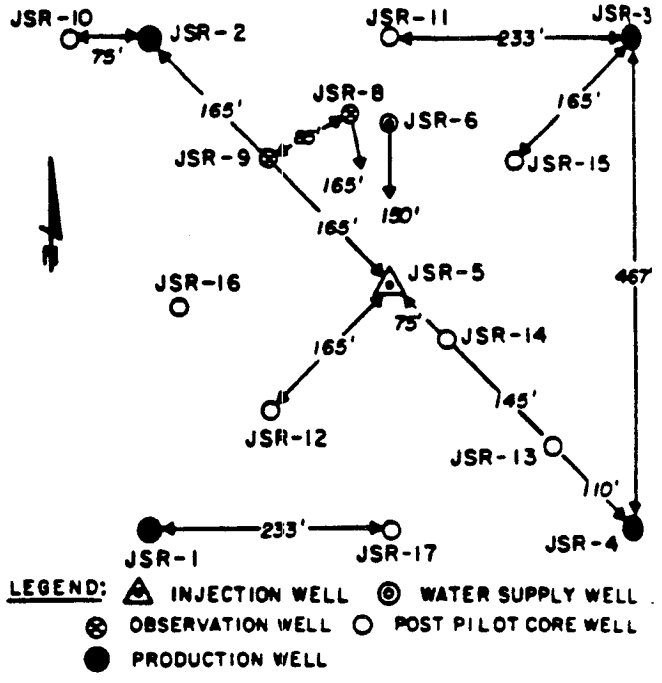
JSR-10
JSR-2
75'
JSR-11
233'
JSR-3
165'
JSR-8
JSR-6
JSR-9
165'
165'
JSR-15
165'
150'
JSR-16
JSR-5
467'
75'
JSR-14
165'
145'
JSR-12
JSR-13
10'
233'
JSR-1
JSR-17
JSR-4
LEGEND: INJECTION WELL WATER SUPPLY WELL
OBSERVATION WELL POST PILOT CORE WELL
PRODUCTION WELL

(a)

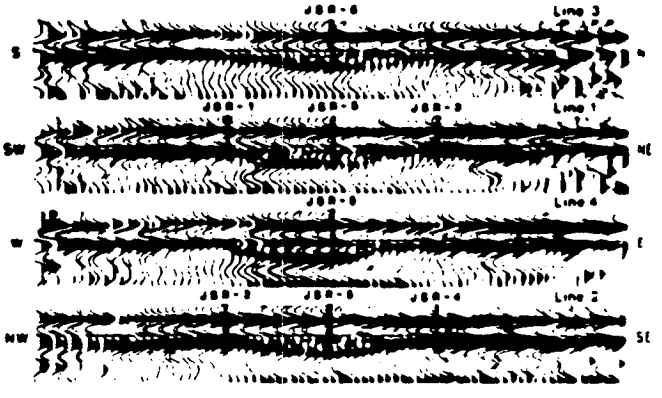

(b)

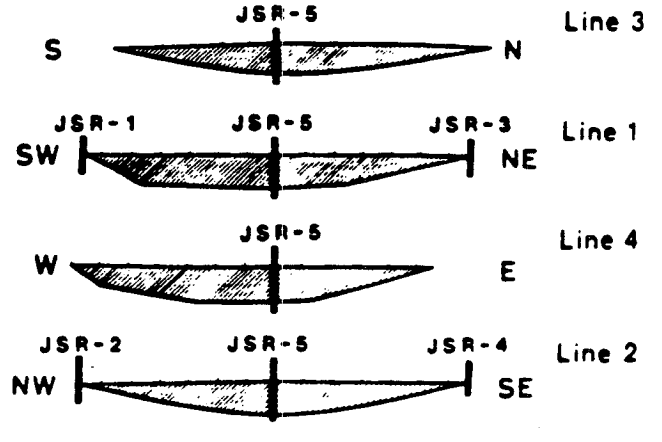
JSR-5
S
N
Line 3
JSR-1
JSR-5
JSR-3
SW
NE
Line 1
JSR-5
W
E
Line 4
JSR-2
JSR-5
JSR-4
NW
SE
Line 2

(c)

Fig. 1

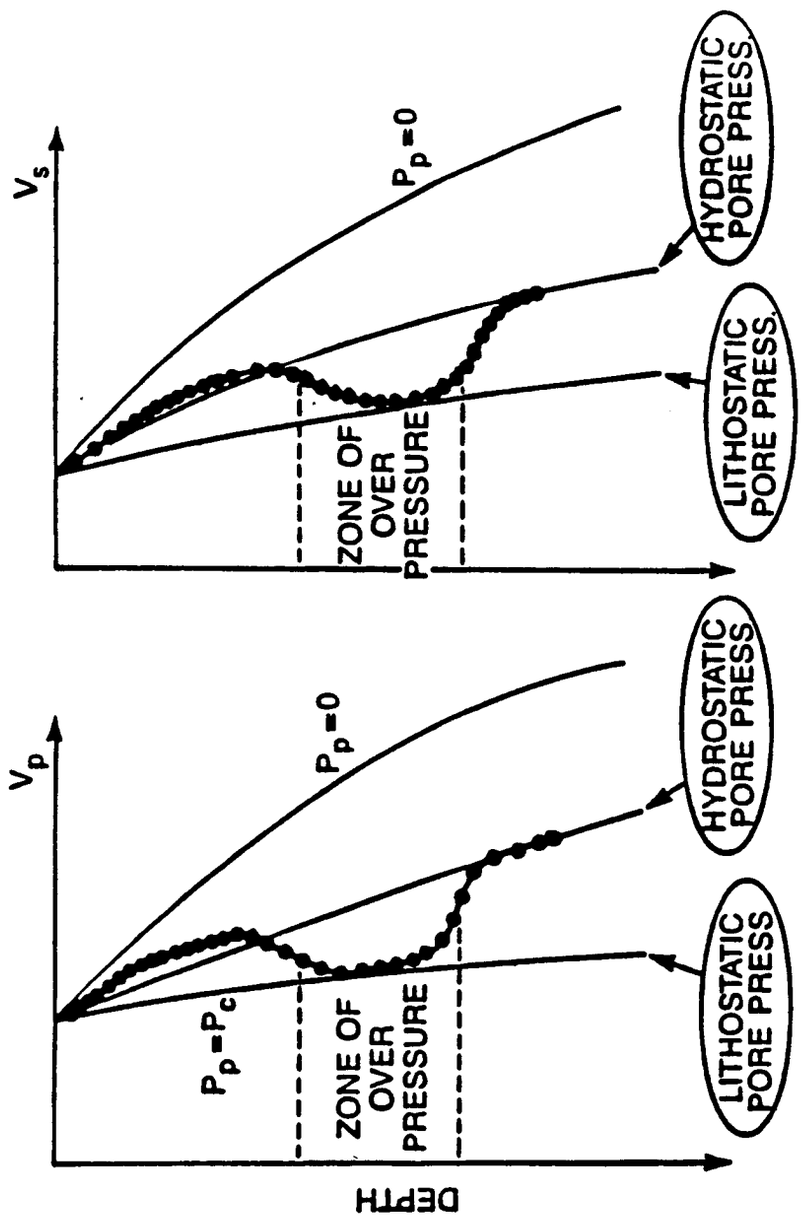
V_s
$P_p=0$
HYDROSTATIC PORE PRESS.
LITHOSTATIC PORE PRESS.
ZONE OF OVER PRESSURE
V_p
$P_p=0$
HYDROSTATIC PORE PRESS
LITHOSTATIC PORE PRESS
$P_p=P_c$
ZONE OF OVER PRESSURE
DEPTH

Fig. 2

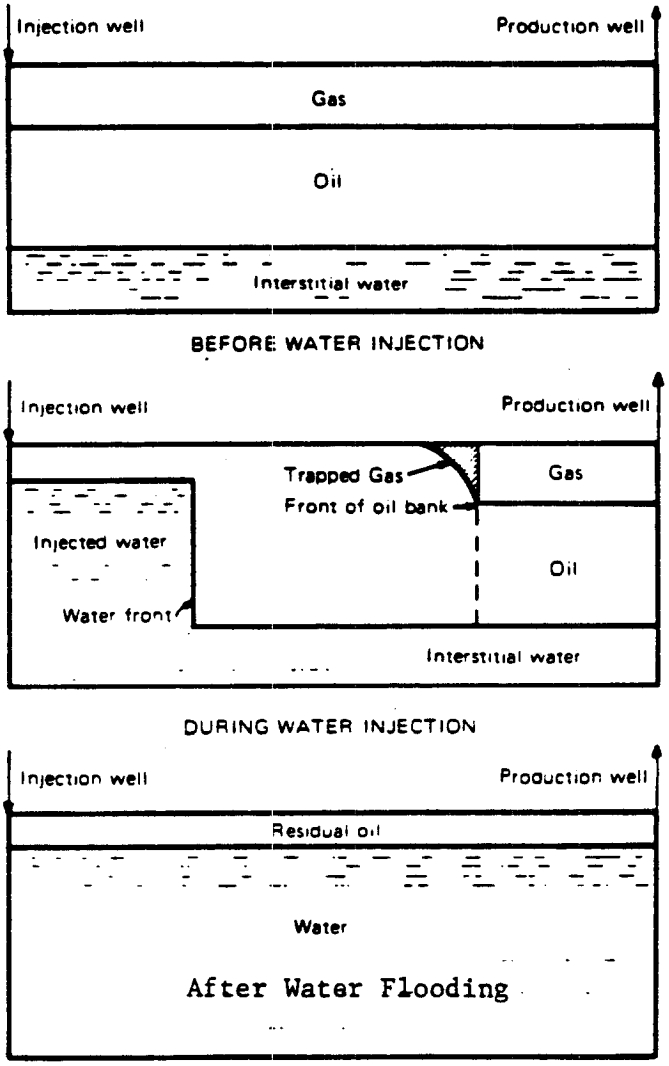
Injection well
Production well
Gas
Oil
Interstitial water
BEFORE WATER INJECTION
Injection well
Production well
Trapped Gas
Front of oil bank
Gas
Injected water
Oil
Water front
Interstitial water
DURING WATER INJECTION
Injection well
Production well
Residual oil
Water
After Water Flooding

Fig. 3

CHAPTER 10

OTHER RELATED PUBLICATIONS AND REPORTS BY THE AUTHOR

The Effects of Sample Sizes on Wave Attenuations and Velocities in the Resonant-Bar Technique

Zhijing Wang and Amos Nur, 1985. Stanford Rock Physics Project, 25, 331-367.

The resonant bar technique has been used for more than half a century in measurements of wave attenuations and velocities of different materials. However, the effect of sample size on the measured attenuations and velocities has not been carefully studied. In our experiments, four bar-shaped Massillon light sandstone samples and seven Lucite samples of different diameters but the same length have been tested. Attenuations and velocities of Massillon light sandstone measured by this technique are plotted as functions of water saturation at different diameters, and those of Lucite are plotted as functions of sample diameters.

Several summaries were made from our experimental results and analyses.

(1) Change in sample diameters of porous rocks does not affect the attenuation factors in dry materials of sample diameters between 0.75 in. and 1.25 in. in the resonant bar technique.

(2) Change in sample diameter does not change the shear attenuation factor of both dry and water-saturated porous rocks, which is also true for Lucite. Therefore, shear attenuation measured by the resonant bar technique is independent of sample diameter.

(3) Sample size affects the measured attenuations when the rock samples are water-saturated. Such effect may be caused by either fluid flow in the samples or their drying processes, or both.

(4) Extensional wave velocities change systematically with change of sample size, which suggests velocity transitions from extensional to compressional as the sample size increases.

(5) All in all, the resonant bar technique is good for measuring shear attenuation and velocities. For extensional (or longitudinal) waves, corrections of sample size effect must be made on the measured velocities and attenuations.

Effects of Pore Fluid Viscosity on Acoustic Wave Velocities in Porous Rocks.

Zhijing Wang and Amos Nur, 1985. J. Acoust. Soc. Am., 78(s1), p32-33. Also: Stanford Rock Physics Project, 26, 131-166.

A series of laboratory experiments on acoustic wave propagation in porous rocks saturated with fluids of a wide range of viscosity were achieved both in *KHz* and *MHz* frequency ranges. The experimental results of the wave velocities were plotted as a function of pore fluid viscosities. It was shown that the measured wave velocities increased with increasing pore fluid viscosity in *KHz* frequency range, while in *MHz* frequency range, the pore fluid viscosity had very little effect on the velocities.

The experimental results were discussed in terms of theories of acoustic wave propagation in both viscous fluids and in the saturated porous rocks.

In the light of the classical theory of wave propagation in viscous fluids, shear wave velocities are dependent on the viscosities of the fluids. And in turn, they should also depend on the pore fluid viscosities of the porous rocks saturated with viscous fluids. However, this dependence is also controlled by the skin depths of the shear waves. When the skin depth is greater than the pore diameters, the shear waves can travel through the pore fluids with velocities proportional to the square root of the

product of the viscosity and the wave frequency. When it is less than the pore diameters, shear waves can not propagate through the pore fluids, and therefore saturation of the viscous fluid to the porous rocks does not affect the shear wave velocities in the rock-fluid aggregate. The skin depth is inversely proportional to the square root of the wave frequency. Hence the pore fluid viscosity has more effect on the shear wave velocities in the rock-fluid aggregate at low frequencies than it has at high frequencies.

The relaxational theory of wave propagation in viscous fluids theory assumes that the viscosity of the fluid is dependent on the wave frequency. The fluid behaves less viscous at high frequencies than at low frequencies. At very low frequencies, the compressional wave velocity becomes independent of the viscosity of the fluid. We could unfortunately not be able to prove this since the wave frequencies could not be lowered very far in our experiments. According to this theory, pore fluid viscosity should have more effect on the wave velocities measured at *KHz* frequencies than on those measured at *MHz* frequencies, which is accordant with our experimental results.

In the Biot theory of wave propagation in porous solids saturated with viscous fluids, the shear wave velocities are proportional to the pore fluid viscosity in a manner of a second order at low frequencies. In terms of a reference frequency defined in the Biot theory, our *KHz* frequency measurements were treated to be in low frequency range, and those at *MHz* in high frequency range in which the wave velocities are independent of the pore fluid viscosity. However, our experimental results contradict with the Biot theory since the Biot theory predicts that the shear wave velocity in the porous rocks saturated with viscous fluids decreases as the pore fluid viscosity increases. The contradiction may arise from the assumption of the frequency independence of the pore fluid viscosity in the Biot theory.

From the experimental results and discussions shown in the paper, one can see that the pore fluid viscosity of the porous rocks does affect the shear wave velocities in *KHz* frequency range, while in *MHz* frequency range, this effect is very small. And its

effect on compressional wave velocities is always very small.

In-Situ Seismic Monitoring EOR: The Petrophysical Basis.

Amos Nur and Zhijing Wang, 1987. Proc. 62nd Ann. Tech. Conf. Exhib, vol. Φ. 307-314.

This paper presents laboratory experimental results on wave velocities in hydrocarbons, rocks and sands versus saturation, pore and confining pressures, temperature, and CO_2 content. The results suggest that seismic, especially high resolution seismic, methods can be used in detecting anomalous pore pressures, tracking thermal fronts and mapping high temperature regions in thermal enhanced oil recovery processes, and monitoring CO_2 flooding and water flooding processes in reservoirs in-situ. However, much of the methodology and technology required still remains to be developed before routine field applications can be made.

In this paper, various applications of the laboratory velocity results are discuused.

Recent Advances and Developments in Rock Physics, Part I, Elastic Wave Propagation in Rocks.

Zhijing Wang, De-hua Han, and Amos Nur, 1987. Collections of Geophysical Technology (in Chinese), edited by the Editorial Board of "Oil Geophysical Prospecting", 7, 1-17.

This paper reviews recent advances and developments in rock physics researches. It includes review on Biot theory, wave velocities in rocks and their relations with various parameters such as temperature, confining and pore pressures, pore fluid saturation, frequency, clay content, density, rock age, lithology, porosity, permeability, fluid flow, etc., and wave attenuations in rocks and various attenuation mechanisms. It serves as summaries of recent research results in the aspect of elastic wave

propagations in porous rocks.

Recent Advances and Developments in Rock Physics, Part II, Electrical Properties and Modeling of Rocks.

Zhijing Wang and Amos Nur, 1988. Collections of Geophysical Technology (in Chinese), edited by the Editorial Board of "Oil Geophysical Prospecting", 8, 1-34.

This paper surveys recent research results in the aspects of electrical properties and different models of porous rocks. The first part of this paper summarizes the nature of electrical resistivity of rocks and the effects of various parameters including confining and pore pressures, temperature, saturation, pore fluid type, porosity, permeability, clay content, wettability, and others. Some results in dielectric properties of rocks are also discussed. The second part summarizes different models of porous rocks, including elastic models such as Gassmann equation, Biot-Geertsma equation, static and dynamic moduli, bound models and theories, models related to pore geometries, and their applications. Others such as electrical and fluid flow models are also discussed. The final part discusses the present, future, importance, applications, and problems in the field of rock physics research.

BIBLIOGRAPHY

Anderson, A. L. and L. D. Hampton, 1980. Acoustics of gas bearing sediments I. Background. J. Acoust. Soc. Am., 67, 1865-1889.

Anderson, A. L. and L. D. Hampton, 1980. Acoustics of gas bearing sediments II. Measurements and models. J. Acoust. Soc. Am., 67, 1890-1903.

Bacri, J. and D. Salin, 1986. Sound velocity of a sandstone saturated with oil and brine at different concentrations. Geophys. Res. Let., 13, 326-328.

Birch, F. and B. Dow, 1936. Compressibility of rocks and glasses at high temperatures and pressures: seismological application. Bull. Geol. Soc. Am., 31, 1235-1255.

Birch, F., 1961. The velocity of compressional waves in rocks to 10 Kilobars, Part 2. J. Geophys. Res., 66, 2199-2223.

Brennan, B. J. and D. E. Smylie, 1981. Linear viscoelasticity and dispersion in seismic wave propagation. Rev. Geophys. Space Phys., 19, 233-246.

Budiansky, B. and R. J. O'Connell, 1976. Elastic moduli of a cracked solid. Int. J. Solids Struct. 12, 81-97.

Carlson, R. L. and A. F. Gangi, 1985. Effect of cracks on the pressure dependence of P wave velocities in crystalline rocks. J. Geophys. Res., 90, 8675-8684.

Castagna, J. P., M. L. Batzle, and R. L. Eastwood, 1985. Relationships between compressional-wave and shear-wave velocities in clastic silicate rocks. Geophys., 50, 571-581.

Cheng, C. H. and M. N. Toksoz, 1979. Inversion of seismic velocities for the pore aspect ratio spectrum of a rock. J. Geophys. Res., 84, 7533-7543.

Christensen, N. I. and H. F. Wang, 1985. The influence of pore pressure and confining pressure on dynamic elastic properties of Berea sandstone. Geophys., 50, 207-213.

Clark, V. A., B. R. Tittmann, and T. W. Spencer, 1980. Effect of volatiles on attenuation and velocity in sedimentary rocks. J. Geophys. Res., 85, 5190-5198.

Cleary, M. P., 1978. Elastic and dynamic response regimes of fluid-impregnated solids with diverse microstructures. Int. J. Solids Struct., 14, 795-819.

Crampin, S., 1984. Effective anisotropic elastic constants for wave propagation through cracked solids. Geophys. J. R. Astr. Soc., 76, 133-145.

Domenico, S. N., 1976. Effect of brine-gas mixture on velocity in an unconsolidated sand reservoir. Geophys., 41, 882-894.

Domenico, S. N., 1977. Elastic properties of unconsolidated porous sand reservoirs. Geophys., 42, 1339-1368.

Domenico, S. N., 1984. Rock lithology and porosity determination from shear and compressional wave velocities. Geophys., 49, 1188-1195.

Dutta, N. C. and H. Ode, 1979. Attenuation and dispersion of compressional waves in fluid-filled porous rocks with partial gas saturation (White model) -- Part I: Biot theory. Geophys., 44, 1777-1788.

Dutta, N. C. and H. Ode, 1979. Attenuation and dispersion of compressional waves in fluid-filled porous rocks with partial gas saturation (White model) -- Part II: Results. Geophys., 44, 1789-1805.

Elliot, S. E. and B. F. Wiley, 1975. Compressional velocities of partially saturated, unconsolidated sands. Geophys., 40, 949-954.

Faust, L. Y., 1951. Seismic velocity as a function of depth and geologic time. Geophys., 16, 192-206.

Geertsma, J. and D. C. Smit, 1961. Some aspects of elastic wave propagation in fluid-saturated porous solids. Geophys., 26, 169-181.

Gordon, R. B. and L. A. Davis, 1968. Velocity and attenuation of seismic waves in imperfectly elastic rock. J. Geophys. Res., 73, 3917-3935.

Gregory, A. R., 1976. Fluid saturation effects on dynamic elastic properties of sedimentary rocks. Geophys., 41, 895-921.

Hamdi, F. and D. T. Smith, 1982. The influence of permeability on compressional wave velocity in marine sediments. Geophys. Prosp., 30, 622-640.

Hamilton, E. L., 1971. Elastic properties of marine sediments. J. Geophys. Res., 76, 579-604.

Han, D., A. Nur and D. Morgan, 1986. Effects of porosity and clay content on wave velocities in sandstones. Geophys., 51, 2093-2107.

Hartley, K. B., 1981. Factors affecting sandstone acoustic compressional velocities and an examination of empirical correlations between velocities and porosities. SPWLA 22nd Annual Log. Symp., paper PP.

Hartley, K. B., 1981. Factors affecting sandstone acoustic compressional velocities and an examination of empirical correlations between velocities and porosities. SPWLA 22nd Annual Log. Symp., paper PP. (20pp.)

Hashin, Z. and S. Shtrikman, 1963. A variational approach to the theory of the elastic behavior of multiphase materials. J. Mech. Phys. Solids, 11, 127-140.

Helbig, K., 1983. Elliptical anisotropy -- its significance and meaning. Geophys., 48, 825-832.

Hudson, J. A., 1981. Wave speeds and attenuation of elastic waves in materials containing cracks. Geophys. J. R. Astr. Soc., 64, 133-150.

Hughes, D. S. and J. H. Cross, 1951. Elastic wave velocities in rocks at high pressures and temperatures. Geophys., 16, 577-593.

Hughes, D. S. and J. L. Kelly, 1952. Variation of elastic wave velocity with saturation in sandstone. Geophys., 17, 739-952.

Ide, J. M., 1937. The velocity of sound in rocks and glasses as a function of temperature. J. Geol., 45, 689-716.

Ito, H., J. DeVilbiss and A. Nur, 1979. Compressional and shear waves in saturated rock during water-steam transition. J. Geophys. Res., 84, 4731-4735.

Jankowsky, W., 1970. Empirical investigation of some factors affecting elastic wave velocities in carbonate rocks. Geophysical Prospecting, 18, 103-118.

Jones, L. A. and H. F. Wang, 1981. Ultrasonic velocities in Cretaceous shales from the Williston basin. Geophys., 46, 288-297.

Jones, T. D., 1986. Pore fluid and frequency-dependent wave propagation in rocks. Geophys., 51, 1939-1953.

Jones, T. and A. Nur, 1983. Velocity and attenuation in sandstone at elevated temperatures and pressures. Geophys. Res. Let., 10, 140-143.

King, M. S., 1966. Wave velocities in rocks as a function of changes in overburden pressure and pore fluid saturation. Geophys., 31, 50-73.

Kowallis, B. J., L. E. A. Jones, and H. F. Wang, 1984. Velocity-porosity-clay content systematics of poorly consolidated sandstones. J. Geophys. Res., 89, 10355-10364.

Kuster, G. T. and M. N. Toksoz, 1974. Velocity and attenuation of seismic waves in two-phase media: Part I: theoretical formulations, Part II: experimental results. Geophys. 39, 587-618.

Levin, F. K., 1979. Seismic velocities in transversely isotropic media, Geophys., 44, 918-936.

Liu, H. P., D. L. Anderson and H. Kanamori, 1976. Velocity dispersion due to anelasticity; implications for seismology and mantle composition. Geophys. J. R. Astr. Soc. 47, 41-58.

Lockner, D. A., J. B. Walsh, and J. D. Byerlee, 1977. Changes in seismic velocity and

attenuation during deformation of granite. J. Geophys. Res., 82, 5374-5378.

Lynn, W. S. and J. Claerbout, 1982. Velocity estimation in laterally varying media. Geophys., 47, 884-897.

Mavko, G. M. and A. Nur, 1978. The effect of nonelliptical cracks on the compressibility of rocks. J. Geophys. Res., 83, 4459-4468.

Mavko, G. M., 1980. Velocity and attenuation in partially molten rocks. J. Geophys. Res., 85, 5173-5189.

Murphy, W. F., III, 1984. Acoustic measures of partial gas saturation in tight sandstones. J. Geophys. Res., 89, 11549-11559.

Murphy, W. F., III, 1984. Seismic to ultrasonic velocity drift: intrinsic absorption and dispersion in crystalline rock. Geophys. Res. Let., 11, 1239-1242.

Murphy, W. F., III, 1985. Sonic and ultrasonic velocities: theory versus experiment. Geophys. Res. Let., 12, 85-88.

Murphy, W. F., III, K. W. Winkler, and R. L. Kleinberg, 1984. Frame modulus reduction in sedimentary rocks: The effect of adsorption on grain contacts. Geophys. Res. Let., 1, 805-808.

Nur, A. and G. Simmons, 1969. Strees-induced velocity anisotropy in rock: an experimental study. J. Geophys. Res., 74, 6667-6674.

Nur, A. and G. Simmons, 1969. The effect of saturation on velocity in low porosity rocks. Earth Planet. Sci. Let., 7, 183-193.

Nur, A. and G. Simmons, 1969. The effect of viscosity of a fluid phase on velocity in low porosity rocks. Earth Planet. Sci. Let., 7, 99-108.

Nur, A. and Z. Wang, 1987. In-situ seismic monitoring EOR: The petrophysical basis. Proc. 62nd Annual Tech Conf. Exhib. SPE, vol. Φ, 307-314.

Nur, A., 1971. Effect of stress on velocity anisotropy in rocks with cracks. J. Geophys. Res., 76, 2022-2034.

O'Connell, R. J. and B. Budiansky, 1974. Seismic velocities in dry and saturated cracked solids. J. Geophys. Res., 35, 5412-5426.

Ogushwitz, P. R., 1984. Applicability of the Biot Theory. I. Low-porosity materials. J. Acoust. Soc. Am., 77, 429-440.

Ogushwitz, P. R., 1984. Applicability of the Biot Theory. II. Suspensions. J. Acoust. Soc. Am., 77, 441-451.

Ogushwitz, P. R., 1984. Applicability of the Biot Theory. III. . Jve speeds versus depth in marine sediments. Acoust. Soc. Am., 77, 452-463.

Pennebaker, E. S., Jr, 1968. Seismic data indicate depth, magnitude of abnormal pressures. World Oil, June, 1968, 73-77.

Rafavich, F., C. H. St. C. Kendall, and T. P. Todd, 1984. The relationship between acoustic properties and the petrographic character of carbonate rocks. Geophys., 49, 1622-1636.

Raymer, L. L., E. R. Hunt, and J. S. Gardner, 1980. An improved sonic transit time-to-porosity transform. SPWLA 21st Annual Log. Symp., paper P.

Rybach, L. and G. Buntebarth, 1982. Relationships between the petrophysical properties density, seismic velocity, heat generation, and mineral constitution. Earth Planet. Sci. Let., 57, 367-376.

Sarmiento, R., 1961. Geological factors influencing porosity estimates from velocity logs. Bull. Am. Ass. Petro. Geol., 45, 633-644.

Sayers, C. M., 1980. Ultrasonic velocity dispersion in porous materials. J. Phys., 14, 413-420.

Seeburger, D. A. and A. Nur, 1984. A pore space model for rock permeability and bulk modulus. J. Geophys. Res., 89, 527-536.

Shumway, G., 1958. Sound velocity ve. temperature in water-saturated sediments. Geophys., 23, 494-505.

Simmons, G. and W. F. Brace, 1965. Comparison of static and dynamic measurements of compressibility of rocks. J. Geophys. Res., 70, 5649-5656.

Spencer, J. W., Jr, 1981. Stress relaxations at low frequencies in fluid-saturated rocks: attenuation and modulus dispersion. J. Geophys. Res., 86, 1803-1812.

Spencer, J. W., Jr. and A. Nur, 1976. The effect of pressure, temperature, and pore water on velocities in Westerly granite. J. Geophys. Res., 81, 899-904.

Thomsen, L., 1986. Weak elastic anisotropy. Geophys., 51, 1954-1966.

Timur, A., 1968. Velocity of compressional waves in porous media at permafrost temperatures. Geophys., 33, 584-595.

Timur, A., 1977. Temperature dependence of compressional and shear wave velocities in rocks. Geophys., 42, 950-956.

Toksoz, M. N., C. H. Cheng, and A. Timur, 1976. Velocities of seismic waves in porous rocks. Geophys., 41, 621-645.

Tosaya, C. and A. Nur, 1982. Effects of diagenesis and clays on compressional velocities in rocks. Geophys. Res. Let., 9, 5-8.

Tosaya, C., A. Nur, D. Vo-Thanh, and G. Da Prat, 1987. Laboratory seismic methods for remote monitoring of thermal EOR. SPE Res. Eng., May, 1987, 235-242.

Uhrig, L. F. and F. A. Van Melle, 1955. Velocity anisotropy in stratified media. Geophys., 20, 774-779.

Walsh, J. B., 1965. The effect of cracks on the compressibility of rock. J. Geophys. Res., 70, 381-389.

Wang, Z. and A. Nur, 1985. The Effect of Sample Size on Wave Attenuations and Velocities in the Resonant Bar Technique. Stanford Rock Physics Project, vol. 25, 331-367.

Wang, Z. and A. Nur, 1985. Effects of Pore Fluid Viscosity on the Acoustical Velocities in Porous Rocks, Journal of Acoustical Society of America, vol. 78(s1), p32-33. Also in "Stanford Rock Physics Proj., vol. 26, 131-166.

Wang, Z. and A. Nur, 1986. Effect of Temperature on the Seismic Wave Velocities in Sandstones and Sand with Heavy Hydrocarbons, SEG Extended Abstract, Presented at the Annual International Meeting of Society of Exploration Geophysicists, Houston, 1986. Also in "Stanford Rock Phys. Proj., vol. 26, 167-216.

Wang, Z. and A. Nur, 1986. The Effect of Temperature on the Seismic Wave Velocities in Rocks Saturated with Hydrocarbons, SPE paper 15646, Presented at the 61st Annual International Meeting of Society of Petroleum Engineers, New Orleans, 1986. Also in "SPEJ: Reservoir Engineering", Feb., 1988, 158-164.

Wang, Z. and A. Nur, 1987. Ultrasonic Wave Velocities in Hydrocarbons, Stanford Rock and Borehole Geophysics Project, vol. 31, 59-118.

Wang, Z., D. Han, and A. Nur, 1987. Recent Advances and Developments in Rock Physics, Part I, Seismic wave Velocities and Attenuations, in: "Collections of Geophysical Technology", vol. 7 (in Chinese) 1-17.

Wang, Z. and A. Nur, 1988. Recent Advances and Developments in Rock Physics, Part II, Electrical Properties and Modeling of Rocks, in: "Collections of Geophysical Technology", vol. 8 (in Chinese), 1-34.

Wang, Z. and A. Nur, 1987. Wave Velocities in Pure Hydrocarbon Saturated Sandstones and Sand. "Stanford Rock and Borehole Geophysics Project", vol. 31, 119-158.

Wang, Z. and A. Nur, 1987. Wave Velocities in Hydrocarbons and Hydrocarbon Saturated Rocks, Presented at the 1987 SEG Meeting, New Orleans.

Wang, Z. and A. Nur, 1988. Wave Velocities in Hydrocarbons and Hydrocarbon Saturated Rocks and Sands. to be submitted to "Geophysics".

Wang, Z., 1987. Acoustic velocities in oils and the effect on velocities in the saturated rocks, Part I: Acoustic velocities in oils. Internal Report, ARCO Oil and Gas Co., 120pp. Also to be submitted.

Wang, Z., 1987. Acoustic velocities in oils and the effect on velocities in the saturated rocks, Part II: The effects on rocks. Internal Report, ARCO Oil and Gas Co., 119pp. Also to be submitted.

Wang, Z. and A. Nur, 1988. Effect of CO2 flooding on wave velocities in sandstones and sand with hydrocarbons. SPE/DOE 4th EOR Symp..

White, J. E., 1975. Computed seismic speeds and attenuation in rocks with partial gas saturation. Geophys., 40, 224-232.

White, J. E., L. Martineau-Nicoletis, and C. Monash, 1983. Measured anisotropy in Pierre shale. Geophys. Prosp. 31, 709-725.

Wilkens, R., G. Simmons, and L. Caruso, 1984. The ratio of Vp/Vs as a discriminant of composition for siliceous limestones. Geophys., 49, 1850-1860.

Winkler, K. W., 1983. Frequency dependent ultrasonic properties of high-porosity sandstones. J. Geophys. Res., 88, 9493-9499.

Winkler, K. W., 1985. Dispersion analysis of velocity and attenuation in Berea sandstone. J. Geophys. Res., 90, 6793-6800.

Winkler, K. W., 1986. Estimates of velocity dispersion between seismic and ultrasonic frequencies. Geophys., 51, 183-189.

Wuenschel, P. C., 1965. Dispersive body waves -- an experimental study. Geophys., 30, 539-551.

Wyllie, M. R. J., A. R. Gregory, and L. W. Gardner, 1956. Elastic wave velocities in heterogeneous and porous media. Geophys., 21, 41-70.

Wyllie, M. R., A. R. Gregory, and G. H. F. Gardner, 1958. An experimental investigation of factors affecting elastic wave velocities in porous media. Geophys., 23, 459-493.

Zimmerman, R. W. and M. S. King, 1986. The effect of the extent of freezing on seismic velocities in unconsolidated permafrost. Geophys., 51, 1285-1290.